

Universidade do Minho
Escola de Engenharia

Monica Patricia Santamaria Ariza

Risk-informed Decision Making for Resilient Transport Infrastructure Systems

April 2024

Risk-informed Decision Making for Resilient Transport Infrastructure Systems
Monica Patricia Santamaria Ariza
UMinho | 2024



Universidade do Minho
Escola de Engenharia

Monica Patricia Santamaria Ariza

Risk-informed Decision Making for Resilient Transport Infrastructure Systems

Doctoral Thesis
Doctoral Program in Civil Engineering

Work developed under the supervision of
Professor José Campos e Matos
Professor Hélder Sousa
Professor Michael Faber

April 2024

DIREITOS DE AUTOR E CONDIÇÕES DE UTILIZAÇÃO DO TRABALHO POR TERCEIROS

Este é um trabalho académico que pode ser utilizado por terceiros desde que respeitadas as regras e boas práticas internacionalmente aceites, no que concerne aos direitos de autor e direitos conexos. Assim, o presente trabalho pode ser utilizado nos termos previstos na licença abaixo indicada. Caso o utilizador necessite de permissão para poder fazer um uso do trabalho em condições não previstas no licenciamento indicado, deverá contactar o autor, através do RepositóriUM da Universidade do Minho.

Licença concedida aos utilizadores deste trabalho



Atribuição CC BY

https://creativecommons.org/licenses/by/4.0/

Acknowledgements

The completion of this doctoral degree signifies the fulfillment of a goal that began five years ago. This journey, marked by a spectrum of emotions ranging from excitement to frustration, has been an arduous yet rewarding path. It is with deep appreciation that I acknowledge the invaluable support and guidance provided by many people throughout this endeavor.

First and foremost, I would like to express my gratitude to my supervisors at the University of Minho, José Matos and Hélder Sousa. Your trust and mentorship gave me a valuable opportunity to be part of a stimulating research environment. I am also deeply thankful to my supervisor Michael Faber from Aalborg University, for his encouragement and generous support throughout my academic journey. I extend my sincere thanks to Min Liu for her invaluable guidance and readiness to collaborate. Lastly, my gratitude goes to Prof. Juliana Mendes from the University of Porto, whose generous contribution in clarifying hydrological modeling concepts and software was immensely helpful.

I should also acknowledge the financial support provided by national funds through the Portuguese Foundation for Science and Technology (FCT), via the Ph.D. grant SFRH/BD/144749/2019, and the financial support through the SAFEWAY project, within the framework of the European Union's Horizon 2020 research and innovation programme, under Grant Agreement No. 769255. Additionally, I acknowledge the support from Infraestruturas de Portugal for sharing essential data for the case studies, which were fundamental in developing this thesis.

I also wish to express my heartfelt thanks to my research group colleagues, with whom I not only collaborated but also became friends: João, Neryvaldo, Edward, Erica, Fereshteh, Carlos, and all those I have met over these years who have offered me unconditional support and close friendship: Yina, Andrea, Norma, Leidy, Sinem, Harley, Luis, Oscar, Jairo, and Diddyer.

My eternal gratitude is extended to my parents, my sister, and her family - with special mention to those little ones, Isa and Sebas, who have continually buoyed me with their emotional support and encouragement, even from afar. Your unwavering faith has been my pillar of strength. I also dedicate this to my grandmother, who passed away during the completion of this work but whose prayers and concerns for me always remained.

Finally, I wish to convey my profound thanks to my partner in life, Carlos, and his family, for embracing me as their own. Embarking on this Ph.D. journey brought me the fortune of meeting you. Walking this path alongside you has been an adventure, replete with challenges yet filled with joy and love. This accomplishment is wholeheartedly dedicated to my entire family.

STATEMENT OF INTEGRITY

I hereby declare having conducted this academic work with integrity. I confirm that I have not used plagiarism or any form of undue use of information or falsification of results along the process leading to its elaboration. I further declare that I have fully acknowledged the Code of Ethical Conduct of the University of Minho.

Resumo

Os sistemas de infraestruturas de transporte são suscetíveis ao envelhecimento e a perigos naturais e antrópicos, que afetam a sua capacidade de serviço e levam a consequências para a sociedade. Dado que os recursos disponíveis são limitados, as decisões sobre a manutenção e melhoria das infraestruturas de transporte devem ser abordadas através de uma perspetiva informada pelo risco. A quantificação dos riscos nestes sistemas requer a modelação espacial do evento extremo, a caracterização do desempenho das numerosas infraestruturas interligadas, e a estimativa das consequências diretas e indiretas de falhas, incluindo impactos monetários, ambientais e sociais. A integração destes modelos, ao nível da rede e com uma perspetiva de ciclo de vida, requer consistência no tratamento de incertezas, que envolve complexidade no processo de modelação e custos computacionais substanciais.

Este trabalho introduz avanços recentes em modelação e análise de sistemas complexos de modo a quantificar os riscos dos sistemas de infraestruturas de transporte ao longo do ciclo de vida. Assim, esta quantificação apoia o processo de tomada de decisão e aumenta a sua resiliência contra perigos naturais, particularmente aqueles associados a efeitos de mudanças climáticas, como inundações. Inicialmente, técnicas probabilísticas Bayesianas são introduzidas para modelar eventos de inundação, capturando incertezas e fornecendo uma representação espácio-temporal dos impactos das inundações nas infraestruturas de transporte. Posteriormente, apresenta metodologias para avaliar as vulnerabilidades das infraestruturas, incluindo técnicas de aprendizagem automática para prever a deterioração ao longo do seu ciclo de vida. As metodologias são enquadradas no âmbito da avaliação de risco de ciclo de vida, utilizando uma abordagem de modelação de sistemas baseada em cenários, e técnicas de aprendizagem automática são ainda introduzidas para melhorar a eficiência computacional na quantificação das consequências económicas, humanas e ambientais resultantes da disrupção da funcionalidade do transporte. Este enquadramento integrado facilita a identificação de infraestruturas críticas cuja potencial falha afeta significativamente os riscos e define uma priorização de estratégias de mitigação. Além disso, as decisões sobre a priorização da recuperação também são auxiliadas, visando reduzir as consequências indiretas e, assim, aumentar a resiliência dos transportes, restabelecendo eficientemente a funcionalidade após disrupções. Por último, o conceito de probabilidade de falha de resiliência, definida como o esgotamento da capacidade do sistema de transporte para restaurar a funcionalidade sem apoio externo, é introduzido para ter em conta as decisões sobre a preparação da sociedade para lidar com eventos disruptivos.

Palavras chave: Avaliação dos riscos de inundações; Deterioração de infraestruturas; Redes Bayesianas; Resiliência de redes de transporte; Técnicas de aprendizagem automática.

Abstract

Transport infrastructure systems are susceptible to aging and natural and anthropogenic hazards, affecting their serviceability and leading to societal consequences. As available resources are limited, decisions about maintaining and developing transport infrastructures must be addressed from a risk-informed perspective. Quantifying risk in these systems requires the spatial modeling of hazardous events, characterizing the joint performance of numerous interconnected infrastructures, and estimating direct and indirect consequences of failures, including monetary, environmental, and social impacts. Integrating these probabilistic models at the network level within a life cycle perspective while ensuring consistency in uncertainty treatment involves modeling complexity and substantial computational costs.

This thesis introduces recent advances in systems modeling and analysis to quantify transport infrastructure risks throughout their life cycle, thereby aiding the decision-making process to enhance their resilience against natural hazards, particularly those associated with climate change effects like flooding. It first introduces Bayesian probabilistic techniques for modeling flood events, capturing uncertainties, and providing a spatiotemporal representation of flood impacts on transport infrastructures. Subsequently, it outlines methodologies for assessing infrastructure vulnerabilities, including machine learning techniques for predicting deterioration over their life cycle. The methodologies are integrated into a life cycle risk assessment framework utilizing a scenario-based system modeling approach, and machine learning techniques are further introduced to improve computational efficiency in quantifying economic, health, and environmental consequences resulting from disturbances in transportation functionality. The integrated framework facilitates the identification of critical infrastructures significantly contributing to risks and informs the prioritization of mitigation strategies. Furthermore, decisions about recovery prioritization are also aided, aiming at reducing the indirect consequences and thereby enhancing transportation resilience by efficiently restoring functionality after disturbances. Lastly, decisions on the societal preparedness to cope with disturbance events were enabled by establishing a probability of resilience failure, defined as the exhaustion of the capacity of the transportation system to restore functionality without external support.

Keywords: Bayesian networks; Flood risk assessment; Infrastructure deterioration; Machine learning techniques; Resilience of transportation systems.

Contents

Resumo v

Abstract vi

List of Figures xii

List of Tables xviii

Abbreviations xx

Symbols xxii

1 Introduction 1
- 1.1 Background and motivation . . . 1
- 1.2 Aim and objectives . . . 5
- 1.3 Thesis outline and overview . . . 6
  - 1.3.1 Case study: Santarém, Portugal . . . 10
- 1.4 Supplementary scientific contributions . . . 10
  - 1.4.1 Journal Publications . . . 12
  - 1.4.2 Conference Publications . . . 12
  - 1.4.3 Technical reports . . . 14

2 An exploratory bibliometric analysis of risk, resilience, and sustainability management of transport infrastructure systems 15
- 2.1 Introduction . . . 16
- 2.2 Methodology for the bibliometric analysis . . . 21
  - 2.2.1 Step I: Research design . . . 21
    - 2.2.1.1 Aim of the bibliometric study . . . 22
    - 2.2.1.2 Scope of the study: System identification . . . 23
  - 2.2.2 Step II: Data compilation . . . 29
    - 2.2.2.1 Search query . . . 29
    - 2.2.2.2 Data collection and cleaning . . . 30
  - 2.2.3 Step III: Bibliometric networks construction . . . 32

2.2.3.1 Term co-occurrence network visualizations . . . 32
2.2.3.2 Bibliographic coupling network visualizations . . . 33
2.2.4 Step IV: Analysis of results . . . 34
2.3 Results . . . 35
2.3.1 Historical evolution and growth of research in system characteristics of TIS . 35
2.3.2 Multi-disciplinary composition of research in system characteristics of TIS . . 35
2.3.3 Term co-occurrence analysis results . . . 38
2.3.4 Bibliographic coupling analysis results . . . 46
2.4 Discussion . . . 58
2.5 Conclusions . . . 61

3 Bayesian probabilistic representation of flood events on Transport Infrastructure Systems 64
3.1 Introduction . . . 65
3.2 Methodology for probabilistic flood representation using Bayesian networks (BN) . . . 68
3.2.1 Extreme Value Analysis: Peak-over-thresholds . . . 70
3.2.2 Hydrologic and Hydraulic modeling . . . 70
3.2.3 Bayesian networks (BNs) . . . 71
3.2.4 Learning Bayesian networks . . . 73
3.2.4.1 Parameter Learning . . . 74
3.2.4.2 Structure Learning . . . 74
3.2.5 Bayesian Inference . . . 75
3.3 Case Study Application . . . 76
3.3.1 Study Area . . . 76
3.3.2 Data and Methods . . . 77
3.3.2.1 Extreme Value Analysis: POT . . . 78
3.3.2.2 Hydrologic Model . . . 81
3.3.2.3 BN representation . . . 83
3.4 Results and discussion . . . 85
3.5 Conclusions . . . 88

4 Comparison of deterioration models for transport infrastructures 92
4.1 Introduction . . . 93
4.2 Database Pre-processing . . . 95
4.3 Discrete Markov Models . . . 98
4.4 Semi Markov models . . . 100
4.5 Hidden Markov models . . . 102
4.6 Neural Networks . . . 105
4.7 Results . . . 107
4.8 Discussion . . . 109
4.9 Conclusions and future directions . . . 111

5 Fragility assessment of transport infrastructures subjected to flood events 113
5.1 Introduction . . . 114
5.2 Methodology for portfolio-level flood fragility functions . . . 117
5.2.1 Bridge component failure modes . . . 119
5.2.2 Component Limit State Functions . . . 125
5.2.3 Bridge System Fragility . . . 126
5.2.4 Time-dependent Fragility . . . 127
5.3 Flood actions on bridges . . . 129
5.3.1 Hydrodynamic forces on bridge decks . . . 129
5.3.2 Hydrodynamic forces on bridge piers . . . 131
5.3.3 Scour at substructures . . . 132
5.4 Case study of Santarém area bridges . . . 138
5.4.1 Single span RC bridge . . . 141
5.4.2 Multiple-span RC bridge (continuous) with shallow foundation . . . 148
5.4.3 Multiple-span RC bridge (simply supported) with shallow foundation . . . 154
5.4.4 Multiple-span RC bridge with deep foundation . . . 156
5.4.5 Masonry arch bridges with shallow foundation . . . 162
5.4.6 Multiple-span steel truss bridges on masonry piers . . . 171
5.5 Conclusions . . . 179

6 Long-term flood risk and recovery prioritization for Resilient Transport Infrastructure Systems 182
6.1 Introduction . . . 183
6.2 Risk modeling framework for decision-analysis of Transport Infrastructure Systems . . . 185
6.2.1 Exposure modeling . . . 187
6.2.2 Modeling of direct consequences: Vulnerability . . . 187
6.2.3 Modeling of indirect consequences: Robustness . . . 190
6.2.3.1 Economic consequences to users . . . 191
6.2.3.2 Environmental consequences . . . 192
6.2.3.3 Consequences to health . . . 193
6.3 Risk-informed Methodology for Resilient Transportation recovery . . . 195
6.3.1 NN model for Traffic Modeling . . . 195
6.3.2 Recovery Modeling . . . 198
6.4 Case study: Santarém transportation network . . . 204
6.4.1 Vulnerability modeling . . . 204
6.4.2 NN model for Static Traffic Assignment . . . 208
6.4.3 Indirect costs of failures . . . 214
6.4.4 Recovery model . . . 218
6.5 Results and discussion . . . 219
6.6 Conclusions . . . 231

7 Risk- and Resilience-informed decision making for Transport Infrastructure Systems 233

7.1 Introduction . . . 234
7.2 System representation of TIS for assessing resilience . . . 236
7.2.1 Resilience modeling and quantification . . . 238
7.3 Decision support framework for interlinked TIS . . . 241
7.4 Santarém Case Study . . . 242
7.4.1 System representation of roadway networks for decision support . . . 242
7.4.1.1 Management system . . . 242
7.4.1.2 Infrastructure system . . . 245
7.4.1.3 Geo-hazard system . . . 247
7.4.1.4 Social system . . . 247
7.4.2 Economic Model . . . 248
7.4.3 System failure consequences . . . 252
7.5 Results and discussion . . . 254
7.6 Conclusions . . . 259

8 Conclusions and future developments 261
8.1 Contributions to research domain . . . 261
8.2 Conclusions . . . 263
8.3 Limitations and recommendations for future research . . . 266

A Bibliometric networks construction 270

B Supplementary information for the flood hazard modeling 274
B.1 Study Area . . . 274
B.2 Input Data Treatment . . . 275
B.2.1 Rainfall data . . . 275
B.3 Extreme Value Analysis - Peak Over Threshold . . . 277
B.3.1 Mean Residual Life . . . 277
B.3.2 Parameter Stability . . . 278
B.3.3 Return Value Stability . . . 278
B.4 Hydrological Model in HEC-HMS . . . 280
B.4.1 Basin Model . . . 280
B.4.2 Loss method . . . 282
B.4.3 Transform method . . . 287
B.4.4 Baseflow method . . . 287
B.4.5 Routing method . . . 288
B.4.6 Model Calibration and Evaluation . . . 289

C Dataset of Roadway bridges 293
C.1 Hydrodynamic forces on decks . . . 293

D Traffic Model **300**
D.1 Traffic Model: Infraestruturas de Portugal 300
D.2 Santarém Roadway Network 304
D.3 AequilibraE Traffic Model 304

Bibliography **308**

List of Figures

1.1 Illustration of modeling framework in the context of Management of Transport Infrastructure Systems. Adapted from [1] . . . 5
1.2 Thesis outline . . . 9
1.3 a) Location of the Santarém district, Portugal; b) Flood events along Tagus River with c) Isolation of Reguengo de Alviela village. Pictures source: [2] . . . 11

2.1 Connections between risk, resilience, and sustainability with assessment metrics and techniques. Adapted from Faber [3]. . . . 20
2.2 Workflow of the methodology for conducting the bibliometric analysis . . . 22
2.3 System representation of TIS at different spatial scales . . . 27
2.4 Workflow of search queries for the bibliometric analysis . . . 31
2.5 Evolution of research in (a) system characteristics of TIS (n_1 - n_4) (b) under flood exposure (n_5 - n_8) . . . 36
2.6 Main subject areas in TIS research on (a) risk and vulnerability (b) robustness (c) resilience (d) sustainability. . . . 37
2.7 (a) Network map of research in the domain of risk and vulnerability of TIS (n_1) (b) under flood events (n_5) . . . 40
2.8 Network map of research in the domain of robustness of TIS (n_2) . . . 41
2.9 (a) Network map of research in the domain of resilience of TIS (n_3) (b) under flood events (n_7) . . . 43
2.10 (a) Network map of research in the domain of sustainability of TIS (n_4) (b) under flood events (n_8) . . . 45
2.11 Network map of research in the domain of (a) uncertainties in the system characteristics of TIS (n_9) and (b) dependencies (n_{10}) . . . 47
2.12 Network map of research in the domain of decision-making preferences for TIS management (n_{11}) . . . 48
2.13 Bibliographic coupling of vulnerability and risk of TIS . . . 50
2.14 Bibliographic coupling of vulnerability and risk of TIS under flood events . . . 51
2.15 Bibliographic coupling of robustness of TIS . . . 52
2.16 Bibliographic coupling of resilience of TIS . . . 54
2.17 Bibliographic coupling of resilience of TIS under flood events . . . 55
2.18 Bibliographic coupling of sustainability of TIS . . . 56
2.19 Bibliographic coupling of sustainability of TIS under flood events . . . 57

3.1 Proposed methodology for probabilistic representation of flood events 69
3.2 Illustration of a parent set $X_{Pa(i)}$ of a child node X_i in a BN (adapted from [4]) . . . 72
3.3 Location of the Central Tagus River basin and data observation locations (hydrometric stations). Source data: [5–7] 77
3.4 Daily rainfall at Chouto weather station exceeding a threshold of 25mm (generated with [8]) 79
3.5 Diagnostic plot of the GP distribution fitting to observed extreme values (black dots), including return values, PDF, Q-Q, and P-P plots (generated with [8]) 80
3.6 Discretization of variables a) Q_P at "Almon-1" hydrologic element, and b) Q_P at "Alvie-1" hydrologic element 86
3.7 Illustration of the BN model structure learned 87
3.8 Joint distribution of Q_P and H at "Almon-1" hydrologic element 89
3.9 Samples from the joint distribution of the BN model given historical (blue) and climate-adjusted (orange) GP distributions 90

4.1 Distribution of bridges by year of construction and deck structure type 97
4.2 Normalized importance of the independent variables 106
4.3 Deterioration curves for bridge decks 108

5.1 Schematic illustration of a) damage function model; b) fragility model 115
5.2 Methodology for time-dependent flood fragility functions for bridge portfolio 120
5.3 Illustration of the two-phase scenario-based failure propagation model. Source: [9] . . 121
5.4 Schematic illustration of a) Bridge system fragility with upper and lower bounds; b) Bridge system fragility at different time periods 127
5.5 Modeling of corrosion effects on bridge components (a) Area reduction of the column reinforcement (b) Shear strength deterioration of anchor bolts. Source: [10] 128
5.6 Hydrodynamic forces on inundated bridge decks (adapted from [11]) 130
5.7 Hydrodynamic forces on submerged bridge piers 132
5.8 a) Total scour and scour components (source: [12]) ; b) Local scour processes at a cylindrical pier (source: [13]) 134
5.9 Example of predicted local scour depths for different flood durations 137
5.10 Location of transportation assets from the Santarém study area (source of data: Infraestruturas de Portugal) 140
5.11 Distribution of a) transport infrastructure types; b) river-crossing bridge structural types, in the Santarém case study (source of data: Infraestruturas de Portugal) 142
5.12 Illustration of bridges belonging to class 1: Single span RC bridges 143
5.13 Slope stability failure of the abutment embankment. Source: [14] 147
5.14 Time-dependent system fragility function for a single-span RC bridge (class 1) 148
5.15 Illustration of bridges belonging to class 2: Multiple continuous-span RC bridges with shallow foundations 149
5.16 a) Combined bridge failure mode in the longitudinal direction; (b) local scour cavity at the affected pier foundation; (c) triangular scour cavity approximation. Source: [15] . . 150

5.17 a) Decrease in limit load as a function of the horizontal scour extent; (b) Bridge types (BT) depending on adjacent deck support conditions and deck-pier connection. Source: [16] . . . 152
5.18 Time-dependent system fragility function for multiple continuous-span RC bridges with shallow foundations (class 2) . . . 154
5.19 Illustration of bridges belonging to class 3: Multiple-span simply supported RC bridges with shallow foundations . . . 155
5.20 Time-dependent system fragility function for multiple-span simply supported RC bridges with shallow foundations (class 3) . . . 156
5.21 Illustration of bridges belonging to class 4: Multiple-span RC bridges with deep foundation; a) longitudinal view; b) cross-section of the pier-foundation system . . . 158
5.22 Time-dependent system fragility function for multiple-span simply supported RC bridges with deep foundations (class 4) . . . 163
5.23 a) Illustration of bridges belonging to class 5: Masonry arch bridges (MAB) with shallow foundation; b) MAB example in the study area (source: Infraestruturas de Portugal) . . . 164
5.24 DLO model for the multiple span masonry arch bridge in LimitState:GEO [17] . . . 165
5.25 Symmetric scour configurations a) 1m scour depth cavity and its b) failure mechanism; c) 2m scour depth cavity and its d) failure mechanism, obtained through DLO in LimitState:GEO [17] . . . 166
5.26 Asymmetric scour configurations a) 1m scour depth cavity and its b) failure mechanism; c) 2m scour depth cavity and its d) failure mechanism, obtained through DLO in LimitState:GEO [17] . . . 167
5.27 Mean Adequacy Factor (AF) variation at increasing dimensionless scour depths for both symmetric ($AF_{s,sym}$) and asymmetric configurations ($AF_{s,asym}$) . . . 168
5.28 Time-dependent system fragility functions for masonry arch bridges with shallow foundations (class 5) for different flow angles: a) $0°$; b) $15°$; c) $30°$ . . . 172
5.29 General layout of bridges belonging to class 6: Multiple-span steel truss bridges on masonry piers . . . 173
5.30 Presence of local scour in Dom Luís bridge (a) sub-aquatic inspection (b) “washed away” of protective fills. Source: Infraestruturas de Portugal . . . 173
5.31 a) Example of a typical masonry pier of class 6 bridges and supporting soil modeled in LimitState:GEO, and its b) failure mechanism obtained through DLO [17] . . . 174
5.32 a) Modeling of scour cavity around the masonry pier for 8m of scour depth, and its b) failure mechanism obtained through DLO [17] . . . 175
5.33 a) Extreme scour conditions undermining the pier foundation base and its b) failure mechanism obtained through DLO [17] . . . 176
5.34 Mean Adequacy Factor (AF) variation at increasing scour depths around the masonry pier . . . 177
5.35 Time-dependent system fragility function for multiple-span steel truss bridges on masonry piers (class 6) . . . 179

6.1 Illustration of systems modeling framework for decision analysis. Source: [18] . . . 186
6.2 Relationship between traffic congestion and deaths due to road accidents. Source: [19] 194

6.3 Methodology for risk-informed recovery of transportation networks after bridge failures 196
6.4 Schematic structure of the Neural Network (NN) model for traffic-related metrics . . . 198
6.5 Functionality recovery curves for a transportation system 199
6.6 Bridge recovery patterns associated with different types of damage. Source: adapted from [20] 200
6.7 Illustrative traffic-related user costs during recovery period 203
6.8 Bridge network in Santarém, Portugal 205
6.9 Annual failure probability of bridges over time 206
6.10 Traffic network of Santarém district, Portugal. Source of data: Infraestruturas de Portugal 209
6.11 Comparison of training and validation losses of a NN model with various hidden layer sizes and 30 neurons 212
6.12 Comparison of training and validation losses of a NN model with various numbers of neurons and one hidden layer 213
6.13 Training and validation loss curves of the NN model for each dataset 215
6.14 Observed versus predicted traffic-related metrics with the NN model 216
6.15 Annual Exceedance Probability curves of a) direct economic losses and b) direct environmental losses 220
6.16 Time-variant expected value of a) direct economic losses and b) direct environmental losses 221
6.17 Accumulated indirect costs to users during transportation network recovery for different preparedness levels 222
6.18 Accumulated indirect environmental consequences during transportation network recovery for different preparedness levels 223
6.19 Annual Exceedance Probability curves of indirect economic losses at a) current year and b) projected for 75 years 224
6.20 Annual Exceedance Probability curves of indirect environmental losses at a) current year and b) projected for 75 years 225
6.21 Time-variant expected value of indirect a) economic losses; b) environmental losses; and c) fatality losses 227
6.22 Cumulative distribution function (CDF) of the robustness index for the three preparedness levels a) economic losses and b) environmental losses. 228
6.23 Bridge criticality in the roadway network based on the robustness index conditional on economic losses 229
6.24 Critical damage failure scenarios exceeding the 99^{th} percentile of expected a) economic losses and b) environmental losses, computed at the time of 75 years. 229
6.25 Predominant failure modes for critical failure scenarios computed at a) current year; and b) at the end of 75 years. 230

7.1 Illustration of principal model for resilience assessment 235
7.2 Illustration of interlinked systems for assessing resilience. Adapted from [9] 237
7.3 Resilience model in terms of benefit generation and economic capacity (a) Scenario with no resilience failure (b) Scenario with resilience failure 240

7.4 Decision support framework for interlinked Transport Infrastructure Systems 243
7.5 Flood load intensity S_i at the first six bridges 248
7.6 Expected net economic output (benefit) over the life cycle for the different decision alternatives 254
7.7 Expected embodied emissions over the life cycle for the different decision alternatives due to a) maintenance and b) reconstruction 255
7.8 Expected emissions from rerouting over the life cycle for the different decision alternatives 256
7.9 Expected fatalities over the life cycle for the different decision alternatives 256
7.10 Annual Probability of Resilience Failure: Low-reliability decision alternatives 257
7.11 Annual Probability of Resilience Failure: Medium-reliability decision alternatives 258
7.12 Annual Probability of Resilience Failure: High-reliability decision alternatives 258

8.1 Global surface temperature change relative to 1850–1900. Source: [21] 267

B.1 Location of Tagus River basin and reservoirs. Source: [22] 275
B.2 Annual and Monthly Average Precipitation in the Tagus River Basin. Source: [23] . . . 276
B.3 Hourly precipitation recorded at Chouto station and monthly seasonality 276
B.4 Exceedance probability of observed (black dots) and simulated (red line) hourly rainfall values (generated with NEOPRENE [24]) 276
B.5 Rainfall disaggregation plot. Blue (observation) and red (simulated) lines correspond to observed and simulated series at a daily scale, respectively. Back lines indicate the hourly disaggretation simulated with the model (generated with NEOPRENE [24]) . . . 277
B.6 Mean residual plot (generated with [8]) 278
B.7 Parameter stability plot (generated with [8]) 279
B.8 Return value stability plot (generated with [8]) 279
B.9 Flowchart for the development of HEC-HMS model 281
B.10 Sub-basins of the Tagus River basin. Source: [25] 282
B.11 HEC-HMS model of Central Tagus River Basin 283
B.12 Comparison of the observed flow with simulation outputs performed with the calibrated CN values for AMC I 291
B.13 Comparison of the observed flow with simulation outputs performed with the calibrated CN values for AMC II 291
B.14 Comparison of the observed flow with simulation outputs performed with the calibrated CN values for AMC III 292

C.1 Bridge network in Santarém, Portugal (reproduced from Chapter 6) 294
C.2 River channel approximation as a) Trapezoidal channel; b) Compound channel 294
C.3 Geotechnical profile at Pier 5 - Dom Luís bridge 296
C.4 Hydrodynamic forces on decks: Drag force (F_{drag}), Lift force (F_{lift} and Overturning moment (M_{cg}) 296

D.1 Traffic Model Infraestruturas de Portugal (IP). Source: [26] 301
D.2 Volume-delay functions for each link type in IP's traffic model. Source: [26] 303

D.3 Accurracy of IP's Traffic Model. Source: [26] 303
D.4 Roadway network of Santarém district, Portugal. Source of data: Infraestruturas de Portugal 305
D.5 Traffic flows (heavy vehicles) in Santarém roadway network. Source of data: Infraestruturas de Portugal 306
D.6 Link capacity of Santarém roadway network. Source of data: Infraestruturas de Portugal 307

List of Tables

3.1 HEC-HMS components, methods and parameters . . . 82
3.2 Variables in the flood hazard database . . . 83

4.1 Condition rating system for decks used in the National Bridge Inventory (NBI) [27] . . . 96
4.2 Distribution of bridges according to selected parameters for each dataset . . . 98
4.3 Input parameters for the Semi Markov process . . . 102
4.4 MSE and MAE accuracy measures . . . 108

5.1 Common failure modes per bridge component type . . . 123
5.2 Distribution parameters for random variables to evaluate $G^{d,t}$, $G^{d,o}$, $G^{d,u}$, and $G^{a,s}$ . . . 147
5.3 Distribution parameters for random variables to evaluate $G^{p,u}$ and $G^{a,u}$ . . . 153
5.4 Distribution parameters for random variables to evaluate $G^{f,q}$ and $G^{f,b}$ . . . 162
5.5 Distribution parameters for random variables to evaluate $G^{ma,u}$ . . . 170
5.6 Distribution parameters for random variables to evaluate $G^{mp,u}$ . . . 178

6.1 Restoration tasks and duration per bridge failure mode for a reference 3-span pre-stressed concrete bridge . . . 207
6.2 Parameters of random variables associated with direct consequences evaluation . . . 208
6.3 Parameters of random variables associated with indirect consequences evaluation . . . 217
6.4 Recovery factors and parameters for different preparedness levels . . . 218

7.1 Decision scenarios with predefined levels (low (l), medium (m), and high (h)) . . . 245
7.2 Distribution parameters for the Limit State Function . . . 247

8.1 Research gaps from bibliometric analysis . . . 261

A.2 Search query combinations . . . 271
A.3 Scopus subject areas excluded from the search . . . 271
A.4 Context areas excluded from the search . . . 272
A.5 Non-context-specific terms excluded from visualizations . . . 272
A.6 VOSviewer specifications for term co-occurrence analysis networks . . . 273
A.7 VOSviewer specifications for bibliographic coupling analysis networks . . . 273

B.1 Sub-basins characteristics . . . 284
B.2 Characteristics of reach elements . . . 285

B.3 Estimated CN values per sub-basin for each AMC level 286
B.4 Antecedent moisture conditions relative to the total precipitation in the five days prior [28] 286
B.5 Estimated response time and concentration time for each sub-basin 288

C.1 Applicable limit state functions (LSF) per bridge (1= Apply; 0=Not Apply) 295
C.2 Characteristics of the river channel at the asset location 297
C.3 Bridge dimensions and rebuilding costs 298
C.4 Mean values of soil-related parameters per bridge 299
C.5 Pier-foundation dimensions and characteristics (Shape: 0= Circular; 1=Rectangular) . 299
C.6 Pile-supported foundation dimensions and characteristics (Shape: 0= Circular; 1=Rectangular) 299

D.1 Characteristics of links and VDF functions. Source: Infraestruturas de Portugal 302

Abbreviations

ADT	Average Daily Traffic
ADTT	Average Daily Truck Traffic
AF	Adequacy Factor
AMC	Antecedent Moisture Condition
AMS	Annual Maximum Series
APA	Portuguese Environment Agency
BMS	Bridge Management Systems
BPN	Bayesian Probabilistic Network
CFD	Computational Fluid Dynamics
CI	Congestion Index
CN	Curve Number
DAG	Directed Acyclic Graph
DEM	Digital Elevation Model
DS	Damage State
ELSS	Earth Life Support System
FFA	Flood Frequency Analysis
GIS	Geographic Information System
GDP	Gross Domestic Product
GHG	Greenhouse Gases
GP	Generalized Pareto
JCSS	Joint Committee on Structural Safety

LQI	Life Quality Index
LSF	Limit State Function
LT	Lost Trips
MLE	Maximum likelihood estimation
MLP	Multilayer Perceptron Network
NBI	National Bridge Inventory
NN	Neural Networks
PCU	Passenger Car Unit
PDS	Partial Duration Series
POT	Peaks Over Threshold
SCS	Soil Conservation Service
SHM	Structural Health Monitoring
SVSL	Societal Value of a Statistical Life
TIS	Transport Infrastructure Systems
TPM	Transition Probability Matrix
UE	User Equilibrium
VDF	Volume-delay function
VHT	Vehicle Hours Traveled
VKT	Vehicle Kilometers Traveled
VoI	Value of Information

Symbols

A	Factor in production function
a or $\boldsymbol{a}$	Decision alternatives
b_{d}	Deck width
b_{f}	Foundation width
b_{p}	Pier width
BF_{L}	Buoyancy force
C_{D}	Direct consequences
$C_{\mathrm{D,d}}$	Drag coefficient on deck
$C_{\mathrm{D,env}}$	Direct environmental consequences
$C_{\mathrm{D,fa}}$	Direct consequences due to fatalities given bridge damage
$C_{\mathrm{D,p}}$	Drag coefficient on pier
$C_{\mathrm{D,reb}}$	Direct consequences due to rebuilding
$C_{\mathrm{ID,env}}$	Indirect consequences due to environmental emissions
$C_{\mathrm{ID,fa}}$	Indirect consequences due to road accident fatalities
$C_{\mathrm{ID,lc}}$	Indirect consequences due to connectivity loss
$C_{\mathrm{ID,pt}}$	Indirect consequences due to prolongation of travel costs
$C_{\mathrm{L,d}}$	Lift coefficient on deck
$C_{\mathrm{L,p}}$	Lift coefficient on pier
$C_{\mathrm{M,d}}$	Moment coefficient on deck
D_{50}	Soil median size diameter

D_{eff}	Effective pier diameter
F_{D}	Hydrodynamic drag force
H	Water depth
h_{d}	Deck height
h_{f}	Foundation height
h_{p}	Pier height
HF_{L}	Hydrodynamic lift force
I	Savings into reconstruction
I_R	Robustness Index
K	Amount of infrastructure capital
l_{f}	Foundation length
l_{p}	Pier length
l_{s}	Span length
M	Investment into maintenance
M_{CG}	Hydrodynamic overturning moment
n_{m}	Manning coefficient
P_{RF}	Probability of resilience failure
P_{F}	Probability of failure
Q_P	Peak flow discharge
Q_W	Hydrograph duration
R_{D}	Risk due to direct consequences
R_D	Rainfall depth
R_{ID}	Risk due to indirect consequences
R_{r}	Economic capacity with respect to resilience
R_W	Rainfall duration
r_γ	Discount rate
S_{r}	Economic demand due to reconstruction
t_{eq}	Time to reach equilibrium scour depth
t_{hyd}	Flood duration

U_{ov}	Value of vehicle operating costs
U_{tt}	Value of user travel time
V	Flow velocity
Y	Economic output
y_{s}	Scour depth
z	Safety design parameter
$\boldsymbol{E}$	A set of directed edges (or connections) between variables in a BN
$\boldsymbol{X}$	A set of random variables
$\boldsymbol{\Theta}_{\mathcal{G}}$	Set of model parameters that define the conditional distributions
θ_{f}	Flow skew angle
θ_{s}	Internal soil friction angle
ρ_{w}	Density of water
β	Reliability index
χ	Percentage of benefit savings
γ_{E}	Embodied CO_2 per unit of the considered material
α_c	Marginal increase in economic output relative to infrastructure capital
λ_M	Maintenance investment ratio

Chapter 1

Introduction

1.1 Background and motivation

Modern societies rely heavily on critical infrastructures, including water supply and sanitation, power, telecommunications, transportation, and emergency services. Among these, transport infrastructure systems (TIS) are particularly relevant as any reduction in their functionality directly impacts the performance of various interdependent socio-technical systems [29]. However, concern about the safety of these systems is growing, primarily due to the degradation of infrastructures, coupled with exposure to various natural and anthropogenic hazards. In addition, most of Europe's bridge stock was constructed several decades ago and designed for a service life of 50 to 100 years. Still, many of these bridges remain operational beyond their intended service lives and carry traffic loads that exceed their original design specifications [30]. Therefore, there is an urgent need for efficient infrastructure management by means of inspection and monitoring, maintenance, and possibly rehabilitation or rebuilding to guarantee the safety of existing infrastructures and to promote the optimized design of new ones. This is crucial to prevent infrastructure failures, which can lead to casualties and significant economic losses and cause extensive disruptions in transportation systems, as exemplified by the recent Morandi's Polcevera bridge collapse in Genoa, Italy [31]. On the other hand, transport infrastructure managers are facing additional challenges in maintaining the operational state of their networks due to the changing climate. Essentially,

the warming of the climate system due to anthropogenic emissions of greenhouse gases (GHG) has led to an increased frequency of more intense and more widespread severe weather events [21]. For instance, in mid-July 2021, extreme precipitation affected parts of Belgium, Germany, and the Netherlands, leading to unprecedented flooding that severely impacted transport infrastructure [32, 33]. Germany experienced the most significant damage, with cost estimates for repairing road and railway infrastructure reaching approximately €2 billion. The flooding resulted in the destruction of 62 bridges and severe damage to 13 others in the Ahr valley, leading to critical damage over more than 74 km of roads, paths, and bridges. In Belgium, the railway infrastructure suffered considerable damage, with repair costs estimated to be between €30 and €50 million. Although the Netherlands was less severely affected, it still experienced some flooding-related disruptions. Events like these have exposed the vulnerability of transport infrastructures to natural hazards and underscored the escalating risks in the context of climate change. Therefore, in addition to the need for enhanced risk assessment to inform decisions on loss reduction, the concept of resilience has emerged as a key objective in the management of transport infrastructure systems. Essentially, resilience is a more holistic system-level concept, which can be understood as the ability of interlinked socio-technical systems to sustain and recover from disturbances over time without support from the exterior [18]. In this sense, risk-informed decision support can be enhanced by the concept of systems resilience to identify decision alternatives that increase the system capacity, which is critical for successful and rapid reorganization, adaptation, and restoration of service after disturbance events.

Although the concept of risk has long been utilized for decision support for engineered systems as a measure for handling and communicating the uncertainties [34, 35], understanding the risks inherent to transport infrastructure systems is a challenging task. This is largely due to the complexity of modeling the performance of TIS, which is characterized by the joint performance of numerous interconnected physical assets. In the case of an extreme natural event, physical damage to one or several assets may occur, leading to varying direct and indirect impacts. Considering the extent of the transportation system and budget limitations, it is evident that strengthening all transport infrastructure assets to a very high safety level is neither cost-effective [36] nor sustainable [3]. Hence, the system modeling should facilitate the identification of relevant scenarios that significantly contribute to risks. An illustration of a modeling framework in the context of the management of transport infrastructure systems is depicted in Figure 1.1. The general

idea is that decisions for managing TIS are fundamentally reliant on models, which serve as representations of the real world. The formulation of these models is facilitated by the use of indicators, which enable including observations into the systems modeling, which are related to the system performance [37]. In this modeling framework, applied throughout this thesis, the system representation for risk assessment includes the modeling of the exposure or hazards, the modeling of direct consequences, which comprise any loss associated with the failure of individual infrastructure components, and the modeling of indirect consequences, which are wider and include monetary, environmental, and societal consequences due to loss of network connectivity, loss of functionality and business interruption. The distinction between direct and indirect consequences facilitates the modeling of two system characteristics, namely vulnerability and robustness. The relation between exposure or hazards and the direct consequences is termed vulnerability, and the link between the direct consequences and the indirect consequences is related to the concept of robustness [38]. Essentially, the vulnerability of a system indicates the degree to which exposures generate direct consequences, while robustness characterizes the degree to which a system is able to contain or limit indirect consequences associated with a hazard event [39].

Subsequently, these models are used for the identification of effective and potentially optimal decision-making alternatives. The plausible decision alternatives for managing TIS may vary over the time horizon, i.e., in the situations before, during, and after the occurrence of a hazard event. Before a hazard occurs, the focus is to optimize available resources for designing and strengthening infrastructures and developing preparedness and emergency plans. During the event, the main concern is to limit the consequences by containing damages and by means of evacuation and rescue actions. After the event, the challenge is to assess the damages and rehabilitate/rebuild the affected constituents to re-establish the system's functionality [40]. In addition, decision alternatives can be differentiated according to the type of measures they refer to, namely physical, organizational, and collection of information. Physical measures refer to repairs, strengthening, and renewals of existing infrastructure or the building of new infrastructure. These types of measures are focused on reducing vulnerability and increasing the robustness and redundancy of the transportation system. Organizational measures refer to decisions on governance, such as policies over the safety level of constituents, the value of savings from the benefits, the development of emergency and evacuation plans, and functionality recovery plans, among others. The emphasis of these measures

is to increase the preparedness, rapidity of recovery, and resourcefulness of the system. Finally, collection of information as a type of measure refers to gathering additional information about the system to improve the knowledge about the system and, thereby, our models. This particular aspect relates to the value of information analysis (VoI), which is closely linked to pre-posterior Bayesian decision analysis [41]. Fundamentally, this approach evaluates the value of gathering new information about various performance characteristics before actually collecting it [1, 42]. The application of the VoI concept in the field of risk-based inspection (RBI), represents a strong means to optimize decisions regarding inspection locations and methods, as well as timing and approaches for repairs. Additionally, VoI analysis has raised significant research interest for decision making related to the arrangement and operation of Structural Health Monitoring (SHM) systems (see [43] for a review).

The plausible decision alternatives evaluated in this thesis for managing the transportation system include both physical and organizational measures. Decisions regarding collecting information are not covered in this thesis, as applying the VoI concept would necessitate robust prior models that ensure consistent treatment of available knowledge. Although there have been significant research contributions in assessing risks in transport infrastructure systems (e.g., [44–47]), the development of prior models to the extent necessary for VoI analysis is not readily available. Consequently, VoI is planned for future research as a means to improve the knowledge basis. Additionally, this thesis considers decision alternatives for situations before and after a hazardous event. While decision making during hazardous events is recognized as crucial due to the role of transportation systems in evacuation and emergency response, this aspect falls outside the scope of this thesis.

Some of the challenges in building the prior models include the extensive data required for developing each model, the computational demands of the models (especially structural finite element models and traffic assignment models), and the substantial uncertainties in the predicted system performance. Consequently, this thesis focuses on implementing probabilistic modeling of systems and machine learning techniques to enhance risk modeling. The proposed approaches ensure consistency in the treatment of available knowledge and contribute to understanding the performance of transport infrastructure systems.

This thesis addresses risks associated with infrastructure deterioration and flooding hazards. This focus is chosen due to two factors: firstly, floods cause the most significant economic damage to the transport

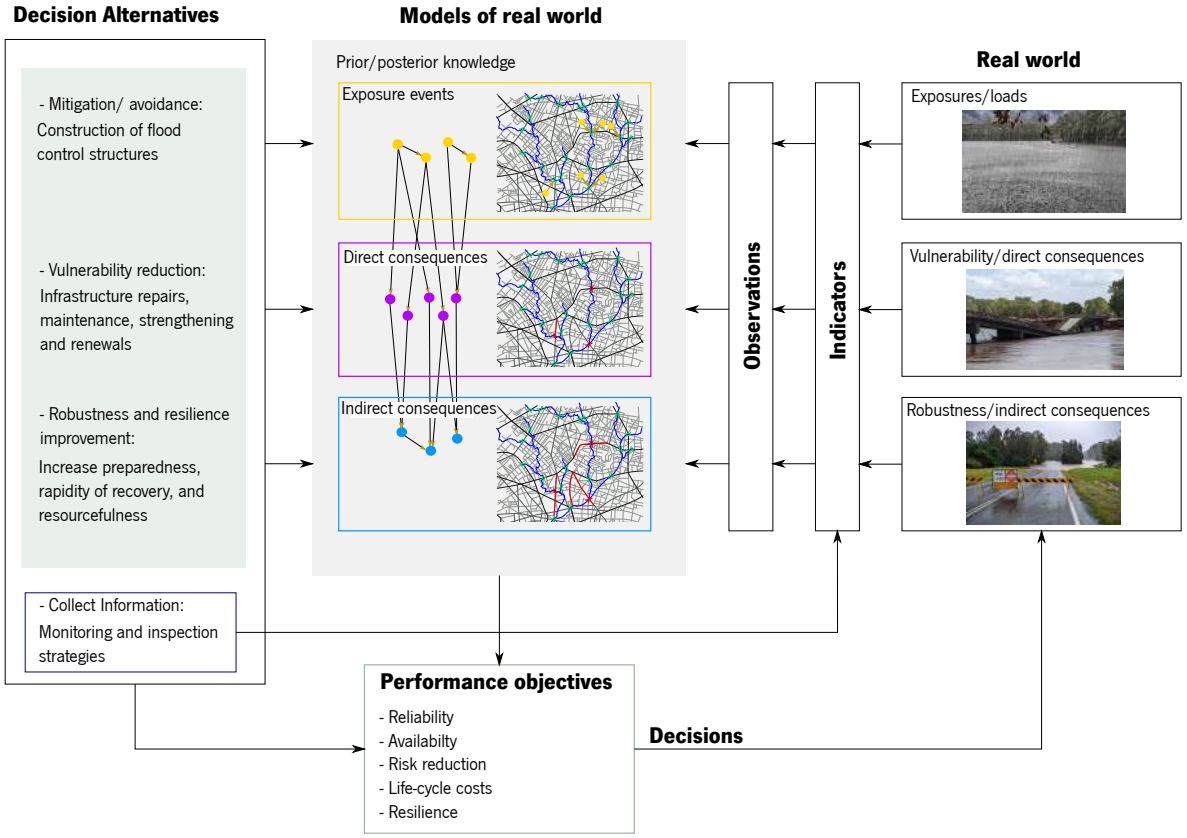


Figure 1.1: Illustration of modeling framework in the context of Management of Transport Infrastructure Systems. Adapted from [1]

sector among weather-related disasters [36], and secondly, the flooding exposure in the case study used for this thesis, as detailed in Section 1.3.1. This case study was selected based on data availability from the SAFEWAY project [48], an H2020 European research initiative in which the author participated.

1.2 Aim and objectives

This thesis aims to enhance risk-informed decision making for resilient transportation systems, particularly for infrastructure deterioration and flooding hazards, by introducing recent advances in the probabilistic modeling of systems and machine learning techniques. These advances facilitate a comprehensive representation of the transportation system performance, including exposure modeling, structural response of

transport infrastructures, and the modeling of consequences at the system level. The models established through this approach offer a robust framework, enabling an improved understanding of the relevant transportation network characteristics that influence the risks. The accomplishment of this overall aim is achieved through the fulfillment of the following specific objectives:

1. Implementation of Bayesian probabilistic modeling techniques to establish the representation of flood events impacting transport infrastructure systems, consistently integrating available and potential future knowledge and information while systematically addressing uncertainties inherent in exposure modeling.

2. Application of machine learning techniques for improving the understanding of transport infrastructure systems performance and reducing the computational cost associated with complex consequence modeling tasks while maintaining a high level of model accuracy.

3. Quantification of life cycle risks at the network level scale, accounting for individual infrastructure's response to the common hazard event throughout their service life, with consistent treatment of uncertainties and dependencies and aggregating consequences at the transportation network level.

4. Establishment of a decision-making methodology integrating resilience concepts to facilitate the identification of decision alternatives that reduce the risks, improve the resilience of the transport infrastructure system, and examine the impacts of these decisions on sustainability.

1.3 Thesis outline and overview

This thesis is structured into eight chapters, with the organization and interaction among them depicted in Figure 1.2. The color coding in this figure corresponds to that used in the illustration of the modeling framework from Figure 1.1. This correspondence is intended to demonstrate how each chapter contributes to the overall modeling framework and to identify areas designated for future research. It is noted that some of the chapters have been published in Journal and Conference papers, as indicated at the beginning of each chapter.

Chapter 1 is the introductory chapter and presents the background, motivation, and the aim and objectives of the thesis. Additionally, it provides an overview of the thesis structure and supplementary scientific contributions.

Chapter 2 presents an exploratory bibliometric analysis to map the current knowledge in risk, resilience, and sustainability management of TIS. This chapter highlights the interdisciplinary contributions, research trends, gaps, relevant authors, and geographical distribution of research. The research conducted in this thesis aims to address several of these identified gaps, as detailed in subsequent chapters. A summary of the contributions made in relation to these research gaps is provided in the concluding chapter of the thesis (Chapter 8). It is important to note that this thesis predominantly uses "Transport Infrastructure Systems", or its acronym TIS, to denote a socio-technical system comprising all infrastructures that enable terrestrial travel of people and goods. As elaborated in Chapter 2, the literature employs a variety of terms to describe these systems, including "transportation networks", "roadway networks", "highway networks", and even more specific terms like "bridge networks" when focusing on bridges as key vulnerable assets. Despite these varied terminologies, they all fundamentally refer to the same technical system. While the applications presented in this thesis are particularly oriented toward bridges in a roadway network, the chosen terminology is intended to reflect the broad nature of the studied system. (https://doi.org/10.1016/j.ijdrr.2023.104063).

In Chapter 3, the implementation of Bayesian probabilistic modeling techniques is proposed to create probabilistic models for flood events affecting transportation infrastructure systems. The approach leverages Bayesian networks to incorporate expert knowledge, observational data, and simulation outputs. A case study from the Tagus River basin in central Portugal demonstrates the development and application of this model, particularly for simulating extreme events impacting transport infrastructure over time, capturing the uncertainties inherent in flood hazard modeling, and providing a spatio-temporal view of flood impacts, which is crucial for risk assessment.

Chapter 4 evaluates the accuracy of various forecasting models for predicting deterioration over the infrastructure service life. This chapter compares the performance of stochastic Markov, Semi-Markov, Hidden Markov models, and Neural Networks (NN). It evaluates how well the models fit the observed data and highlights the superior accuracy of the NN model. Furthermore, it examines the limitations of current

condition assessment practices, including the subjectivity of visual inspections, and advocates for more advanced and objective approaches for managing transport infrastructures. (https://doi.org/10.1002/suco.201900434).

Chapter 5 introduces a generic methodology for developing flood fragility functions for transport infrastructures, particularly bridges, suitable for application at the infrastructure network scale. This chapter first reviews current fragility functions for flood-exposed bridges. Based on the gaps identified, a comprehensive methodology is then proposed. This includes identifying the bridge failure modes, formulating limit state functions, defining bridge classes, evaluating the system fragility, and incorporating time-dependent considerations. The methodology is applied to a bridge portfolio of a Portuguese case study, where the use of simplified yet sufficiently accurate models is advocated, striking a balance with the required level of detail for assessing network-level risks.

Chapter 6 tackles the challenge of prioritizing risk mitigation strategies for transportation systems, considering the spatial flooding characterization, asset fragility and correlations, aleatory and epistemic uncertainties, and direct and indirect consequences of infrastructure failures. This chapter uses a scenario-based modeling approach to comprehensively understand which infrastructure failures contribute the most to the expected total losses. Additionally, various decision-making options concerning preparedness levels for recovery are evaluated to understand their effect on the network's resilience.

Chapter 7 presents a decision analysis framework where transport infrastructure networks are modeled as interconnected systems involving social, infrastructure, and geo-hazard systems, all managed by governance and regulatory systems. This chapter extends the scenario-based modeling approach from the previous chapter to include the economic benefits of these interlinked systems. It also introduces the concept of the probability of resilience failure, defined as the inability of the system to restore transportation network functionality. The proposed methodology facilitates the comparison of decision alternatives that balance economic, social, and environmental outcomes.

Finally, Chapter 8 summarizes this thesis' contributions to the research domain and concluding remarks. It also discusses the identified limitations and potential for future research directions.

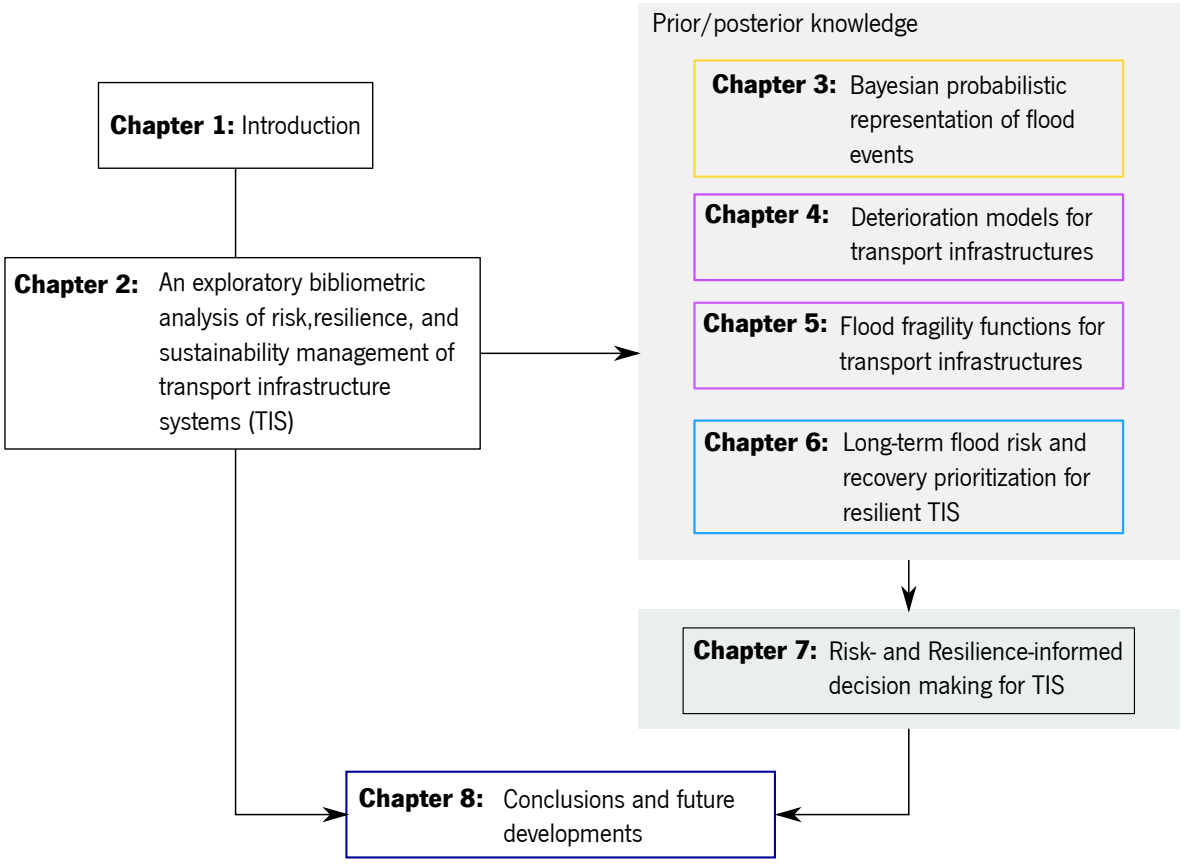


Figure 1.2: Thesis outline

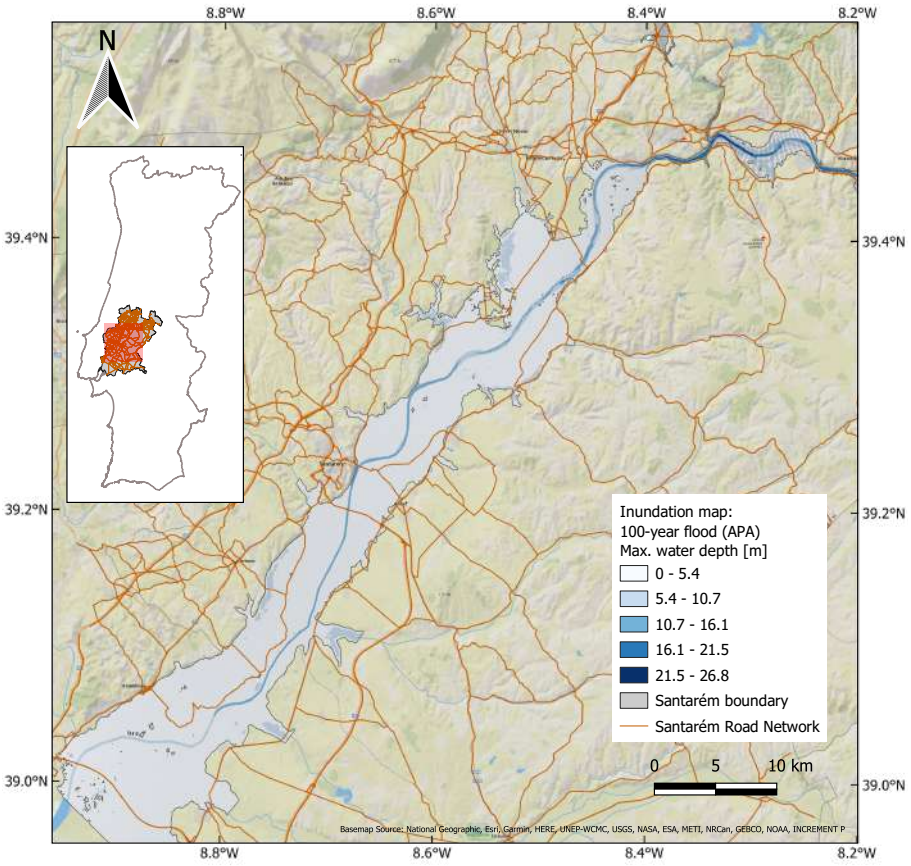
Four appendices supplement the main chapters. Appendix A contains the supporting information for the bibliometric analysis conducted in Chapter 2. Appendix B provides further details regarding methods and data treatment for the flood hazard modeling from Chapter 3. Appendix C contains the inventory data required in Chapter 5 to assess the performance of bridges under flooding events. Lastly, Appendix D outlines the details regarding the development and modeling considerations pertinent to the traffic model, which is necessary for computing the indirect consequences of infrastructure failures in Chapter 6 and Chapter 7.

1.3.1 Case study: Santarém, Portugal

Throughout this thesis, a case study from the Santarém district area in Portugal (Figure 1.3a) is primarily employed to demonstrate the application of the proposed modeling approaches, methodologies, and decision-making framework within a real-world context. The Santarém region, located alongside the Tagus River, has been recurrently affected by severe flood events. Figure 1.3b depicts the increased water levels in the Tagus River, leading to the inundation of surrounding floodplains, as exhibited during the April 2013 floods. This particular event led to the isolation of a small village, as shown in Figure 1.3c. Such isolation is common during extreme floods in this region, along with road closures that can extend for one or more weeks. Another recent example is the floods in December 2019, which resulted from two powerful storms that struck the Iberian Peninsula. These storms caused extensive damage to the area, disrupting train services by inundating rail tracks, downing power lines, which left thousands of inhabitants without electricity, and damaging the road infrastructure, including embankments, slopes, and culverts. The Médio Tejo Intermunicipal Community (CIMT) estimated the impacts of these events at €7.7 million [49]. Due to these frequent events, the Portuguese Environment Agency (APA) has identified this region as the river basin district most affected by floods in terms of the population impacted. It is also recognized as the area where critical investments are most urgently needed to mitigate catastrophic impacts. The APA's plan for 2016-2021 outlined 81 measures, estimated to cost €70 million, aimed at reducing flood risks [50]. These proposed measures encompass a variety of strategies, including structural and green measures for reducing exposure and vulnerability and initiatives for enhancing learning and recovery capabilities.

1.4 Supplementary scientific contributions

In addition to the research contributions presented within the main chapters of this thesis, research work has emerged from collaborative efforts with peers. These collaborations have not only extended the scope of the original research topic but have also led to the exploration and discovery of new, related subjects. These endeavors have been documented in the publications listed below, which provide further insights and extend the discourse beyond the scope of this thesis.



(a)



(b) (c)

Figure 1.3: a) Location of the Santarém district, Portugal; b) Flood events along Tagus River with c) Isolation of Reguengo de Alviela village. Pictures source: [2]

1.4.1 Journal Publications

(i) Shahdani, F.J.; **Santamaria-Ariza, M.**; Sousa, H.S.; Coelho, M.; Matos, J.C. Assessing flood indirect impacts on road transport networks applying mesoscopic traffic modelling: The case study of Santarém, Portugal. Appl. Sci. 2022, 12, 3076. https://doi.org/10.3390/app12063076.

(ii) Mendoza Cabanzo, C.; **Santamaria-Ariza, M.**; Sousa, H.S.; Matos, J.C. In-Plane Fragility and Parametric Analyses of Masonry Arch Bridges Exposed to Flood Hazard Using Surrogate Modeling Techniques. Appl. Sci. 2022, 12, 1886. https://doi.org/10.3390/app12041886.

(iii) Eidsvig, U.; **Santamaria-Ariza, M.**; Galvão, N.; Tanasic, N.; Piciullo, L.; Hajdin, R.; Nadim, F.; Sousa, H.S.; Matos, J. Risk Assessment of Terrestrial Transportation Infrastructures Exposed to Extreme Events. Infrastructures 2021, 6, 163. https://doi.org/10.3390/infrastructures6110163.

(iv) Zambon I., **Santamaria-Ariza, M.**, Matos J.C., Strauss A.. (2020). Value of Information (VoI) for the Chloride Content in Reinforced Concrete Bridges. Applied Sciences. 10(2), 567. doi.org/10.3390/app10020567.

1.4.2 Conference Publications

(i) **Santamaria-Ariza, M.**; Liu M., Sousa H.S., Matos J.C., Faber M.H.. (2023). Probabilistic resilience model for management of road infrastructure systems subject to flood events. In: International Conference on Applications of Statistics and Probability in Civil Engineering, ICASP 14. Dublin, Ireland. 09-13 July 2023. http://hdl.handle.net/2262/103586.

(ii) Arango E., **Santamaria-Ariza, M.**, Nogal M., Sousa H.S., Matos J.C.. (2022). Flood risk assessment for road infrastructures using Bayesian networks: case study of Santarem - Portugal. In: International Probabilistic Workshop – IPW2022. Stellenbosch, South Africa. 08-09 September 2022. pp. 33-46. https://doi.org/10.14311/app.2022.36.0033.

(iii) Arango E., **Santamaria-Ariza, M.**, Sousa H.S., Matos J.C. (2022) Reliability-Based Bayesian Updating Using Visual Inspections of Existing Bridges. In: Pellegrino C., Faleschini F., Zanini M.A., Matos J.C., Casas J.R., Strauss A. (eds) Proceedings of the 1st Conference of the European

Association on Quality Control of Bridges and Structures. EUROSTRUCT 2021. Lecture Notes in Civil Engineering, vol 200. Springer, Cham. https://doi.org/10.1007/978-3-030-91877-4_19.

(iv) Shahdani F.J., **Santamaria-Ariza, M.**, Coelho M., Sousa H.S., Matos J.C.. (2021). The indirect impact of flooding on the road transport network: A case study of Santarém region in Portugal. In: 30th European Safety and Reliability Conference (ESREL). Angers, France. 19-23 September 2021. pp. -. ISBN: 978-981-18-2016-8. https://doi.org/10.3850/978-981-18-2016-8_591-cd.

(v) Santos C., **Santamaria-Ariza, M.**, Coelho M., Sousa H.S., Matos J.C.. (2021). Stochastic methodology to forecast concrete deterioration based on corrosion mechanisms. In: fib Symposium 2021, Concrete Structures: New trends for eco-efficiency and performance. Lisbon, Portugal. 14-16 June 2021. pp. 1519-1528. ISBN: 978-2-940643-08-0.

(vi) Mendoza-Cabanzo, C., **Santamaria-Ariza, M.**, Sousa H.S., Matos J.C.. (2021). Reliability-based assessment of a masonry arch bridge under flood events. In: 8th International Conference on Computational Methods in Structural Dynamics and Earthquake Engineering (COMPDYN). Athens, Greece. 28-30 June 2021. pp. 3377-3388. ISBN: 978-618-85072-4-1.

(vii) **Santamaria-Ariza, M.**, Sousa H.S., Fernandes J., Matos J.C.. (2019). Reliability analysis of a post-tensioned railway bridge exposed to corrosion effects. In: IPW2019 – 17th International Probabilistic Workshop. Edinburgh, United Kingdom. 11-13 September 2019. pp. 81-86.

(viii) Moscoso Y.F.M., **Santamaria-Ariza, M.**, Sousa H.S., Matos J.C.. (2021). Stochastic degradation model of concrete bridges using Data Mining tools. In: 18th International Probabilistic Workshop. IPW 2021. pp. 767-777. https://doi.org/10.1007/978-3-030-73616-3_59.

(ix) Fernandes J., **Santamaria-Ariza, M.**, Matos J.C., Oliveira D.V., Henriques A.A. (2021). Risk Assessment of a Railway Bridge Subjected to a Multi-hazard Scenario. In: 18th International Probabilistic Workshop. IPW 2021. pp. 661-672. https://doi.org/10.1007/978-3-030-73616-3_51.

(x) Santos C., Coelho M., **Santamaria-Ariza, M.**, Matos J.C., Sanchéz-Silva M. . (2021). Life-Cycle Cost Analysis of a Viaduct Considering Uncertainties on the Interventions Plan. In: 18th International Probabilistic Workshop. IPW 2021. pp. 481-493. https://doi.org/10.1007/978-3-030-73616-3_36.

(xi) **Santamaria-Ariza, M.**, Fernandes J., e Matos, J. .(2019). Overview on performance predictive models: Application to Bridge Management Systems. In: IABSE Symposium 2019 Guimarães. Towards a Resilient Built Environment - Risk and Asset Management. Guimarães, Portugal. 27-29 March 2019. pp. 1222-1229. ISBN: 978-3-85748-163-5.

(xii) Fernandes J., **Santamaria-Ariza, M.**, e Matos, J., Oliveira D., Costa L., Henriques A. . (2019). Overview of the infrastructure management system process with an application to a case study. In: IABSE Symposium 2019 Guimarães. Towards a Resilient Built Environment - Risk and Asset Management. Guimarães, Portugal. 27-29 March 2019. pp. 168-175. ISBN: 978-3-85748-163-5.

1.4.3 Technical reports

(i) **Santamaria-Ariza, M.**, Arango E., Jafari F., Sousa H.S., Eidsvig U., Nadim F., Piciullo L., Steinholt I.H., Klaeboe R., Ludvigsen J., Hadjidemetriou G., Matos, J.C., Morais M.. (2021). Dynamic Risk-based Predictive Models, SAFEWAY Deliverable 5.1. Grant Agreement No. 769255.

Chapter 2

An exploratory bibliometric analysis of risk, resilience, and sustainability management of transport infrastructure systems

Monica Santamaria-Ariza, Hélder S. Sousa, José C. Matos, Michael H. Faber

International Journal of Disaster Risk Reduction

Volume 97, 15 October 2023, 104063

https://doi.org/10.1016/j.ijdrr.2023.104063

Abstract: Transport infrastructure systems (TIS) are key enablers of economic development and welfare. However, such infrastructures are exposed to natural and anthropogenic hazards that have caused structural failures, traffic disruptions, injuries and fatalities, and damages to the environment. These past events have underscored the need for more resilient transportation systems. However, reducing risks and achieving more resilient infrastructure systems may result in greater resource consumption and environmental impacts, demanding the consideration of sustainability requirements in the management of TIS. Therefore, this chapter conducts an exploratory study to map the current knowledge in the domain of risk, resilience, and sustainability management of TIS. As a first step, the system identification of TIS in the context of their management is conducted for the purpose of providing the basis for searching for relevant

information. This step sets the baseline for conducting a bibliometric analysis of 16,395 scientific works extracted from the Scopus database between 1990 and 2022. Two quantitative bibliometric techniques are used, namely term co-occurrence and bibliographic coupling. The former technique allows to distinguish the different disciplinary contributions and to identify research gaps. The latter technique facilitates the identification of the main contributors (authors and countries) and the relatedness of research communities. The bibliometric analysis performed provides the basis for future research and development to improve the management of TIS and highlights the potential for transferring knowledge from other research domains.

2.1 Introduction

Transport infrastructures have a wide range of beneficial impacts on economic welfare and equity, as well as on reducing prices and boosting levels of investment, trade, and productivity [51]. It is estimated that low and middle-income countries will need to invest in new transport infrastructure between 0.5% and 3.3% of their gross domestic product (GDP) annually (US$157 billion to US$1 trillion) by 2030, plus an additional 1.1% to 2.1% of GDP annually for maintenance of existing and new transport infrastructure [52]. Maintenance costs are even more relevant than new investment costs for countries with large transportation networks, such as European countries, with the aggravating fact that failing to perform routine maintenance will result in poor service and will cost 50% more overall because of additional rehabilitation needs [52].

Transportation networks have a wide geographical extension, exposing each infrastructure asset to stressors such as floods, earthquakes, tsunamis, landslides, hurricanes, wildfires, or extreme temperatures. This exposure, in combination with the inherent vulnerability of transportation assets, have led in the past to huge economic losses. According to Koks et al. [36], Global Expected Annual Damages (EAD) due to direct damage from natural hazards to road and railway assets range from US$3.1 to US$22 billion, of which approximately 73% is caused by surface and river flooding. The estimated EAD can reach 0.5% to 1% of GDP annually in some countries, which corresponds almost to their national transport infrastructure budget. Natural hazards not only damage physical assets but also disrupt infrastructure services,

with significant impacts on businesses and people. The World Bank estimated in $107 billion a year the impacts of transport infrastructure disruption on the capacity utilization rates of businesses from low- and middle-income countries [53]. The impacts included business losses and delayed supplies and deliveries. Other indirect impacts in the long-term were not covered, such as loss of international competitiveness, which highlights the substantial cost of unreliable infrastructure networks.

Challenges in the management of transport infrastructure systems are likely to be exacerbated due to the increase in frequency and magnitude of extreme weather events attributed to the warming of the climate system due to anthropogenic emissions of greenhouse gases [21]. In fact, the World Meteorological Organization (WMO) has shed light on the escalating impact of weather-related disasters over the past five decades (1970-2019). Drawing from EM-DAT records, the report highlights an increase of seven times in economic losses from the 1970s to the 2010s. Specifically, the losses documented during 2010–2019 averaged at US$ 383 million per day over the decade, a sevenfold increase compared to the amount reported from 1970–1979 (US$ 49 million) [54]. The large evidence of direct and indirect impacts that transport infrastructure networks face due to natural hazards at the global level has attracted the attention of the research community and the public authorities at local and global scales to allocate resources in terms of knowledge, time, and money, for improved risk and resilience management of existing and new transport infrastructure systems. The concept of risk as a measure to deal with and communicate the uncertainties associated with the outcomes of decisions has been used for decision support in engineered systems over many years ([34, 35]), and has been incorporated into standards and regulations (e.g., [55, 56]). However, conducting a risk assessment for transportation networks can be particularly challenging. Transport infrastructure systems have become increasingly complex due to the large number of interconnected physical assets and the different services that the system provides. In the case of an extreme natural event, physical damage may occur to one asset or to several assets simultaneously, in which each particular case would induce different direct and indirect impacts. Moreover, they are interconnected with other complex systems such as communication, power, and building infrastructure systems. Given the extent of the system and budget constraints, it is evident that strengthening all transport infrastructure assets to a very high safety level is not a cost-effective measure [36]. Thus, the system modeling should enable the identification of the more relevant scenarios contributing the most to the risks to prioritize the mitigation measures for the more critical assets, which

could guarantee a minimum transportation functionality despite disrupted parts of the network. Several approaches have been developed to assess risks for transport infrastructure networks (e.g., [44, 45, 47]). Nevertheless, there is usually a lack of completeness in integrating all modeling aspects consistently across spatial and temporal scales, i.e., hazard modeling, fragility assessment of system constituents, transportation network analysis, assessment of consequences to health, environment, and economy, and particularly in integrating the quantitative risk modeling results into decision-making processes for the definition of mitigation measures. Significant challenges for implementing these modeling frameworks arise from gathering all relevant data, computational costs associated with complex models (e.g., finite element structural models, agent-based traffic models), and major uncertainties involved in modeling and predicting the performance of TIS. In addition, consequences typically considered are too narrowly defined to the transportation sector and do not consider inequality of impacts across the population [57].

On the other hand, compared to risk assessment, resilience management of engineered systems is a more recent research field despite the concept being introduced some decades ago in the field of ecology [58]. Resilience is a more holistic system-level approach and can be understood as the ability of interlinked socio-technical systems to sustain and recover from disturbances over time without support from the exterior [18]. Several methodologies for resilience assessment of TIS have been proposed in literature, ranging from qualitative and semi-qualitative to fully quantitative methods, using a wide variety of resilience indicators and metrics which are typically selected depending on the perspective, objective and scale of the analysis (see, e.g., [59–63] for an overview). Generally, the resilience of TIS has been quantified using the system recovery curve, also known as the resilience curve, through different mathematical formulations. The first and most influential formulation introduced by Bruneau et al. [64] for seismic resilience of communities has been broadly used and adapted for resilience analysis of TIS. Following this approach, resilience is quantified as the integral over time of the system recovery curve after a disturbance event. Therefore, resilience is characterized by the drop in the service provision after a disturbance event which relates to the robustness of the system, and the particular shape of the recovery curve is related to systems characteristics such as preparedness and adaptive capacity, which determine the time to fully recover the service and the rapidity of recovery. Resilience loss is then assessed by the difference between the service provided if no disturbance event occurs and the service provided if a disturbance event occurs, often referred to as the resilience triangle. More recent approaches have proposed

extensions to this formulation, e.g., systems recovering to higher/lower service provision than before the disturbance event (e.g., [65], as well as more advanced mathematical formulations for resilience analysis and metrics (e.g., [66]). In addition, great attention has been given to the representation of the impacts of disturbance events on the service provision (e.g., [67, 68]), and the characteristics of the recovery phase to define optimal strategies in terms of resource coordination and sequence of repairs following the event (e.g.[20, 69, 70]). However, as highlighted in [9, 18], systems resilience models and assessments should also explicitly address the generation of system capacity, which is critical for successful and rapid reorganization, adaptation and restoration of service after disturbance events. This capacity develops over time through the service provided by the system. When a disturbance event occurs, some of this capacity is lost as it is needed to restore system functionality. At any given time, if any of the available system capacities, economic, social, and/or environmental, are no longer sufficient to restore system functionality, this can be defined as a resilience failure event. Therefore, systems resilience should be approached probabilistically and within a life cycle framework as the one proposed by Faber et al. [18], in which scenarios of benefit generation and losses are modeled and analyzed. In addition, the resilience of infrastructure systems is generally addressed at a small geographic scale, i.e., at the community or regional level, and at a short-term time scale. However, when the boundaries of resilience assessment are extended to the global scale and the long-term time scale, the capacities considered in the modeling of resilience failure must include the Earth system capacities, implying an evident coupling with sustainability. Therefore, by analogy with resilience failure, sustainability failure can be introduced as the event in which one or more of the Earth system's capacities to sustain human activities is exceeded. These formulations imply that sustainability and resilience failures are equivalent at the global Earth scale, and at the local level, resilience is conditional on sustainability [18]. Figure 2.1 illustrates these interrelations between risk, resilience, and sustainability in the context of decision support for resilient and sustainable societal developments [3]. It can be observed that a resilient infrastructure system provides benefits to society in terms of economy, livelihoods, safety, and health, but, at the same time, imposes resource consumption and emissions to the environment. Thus, these trade-offs must be well understood when deciding how to optimize the resilience of infrastructure systems while guaranteeing long-term sustainability. These interrelations and conflicts between resilient and sustainable infrastructure systems have been recognized over the past years and have received increased attention (see e.g. Gardoni and Murphy

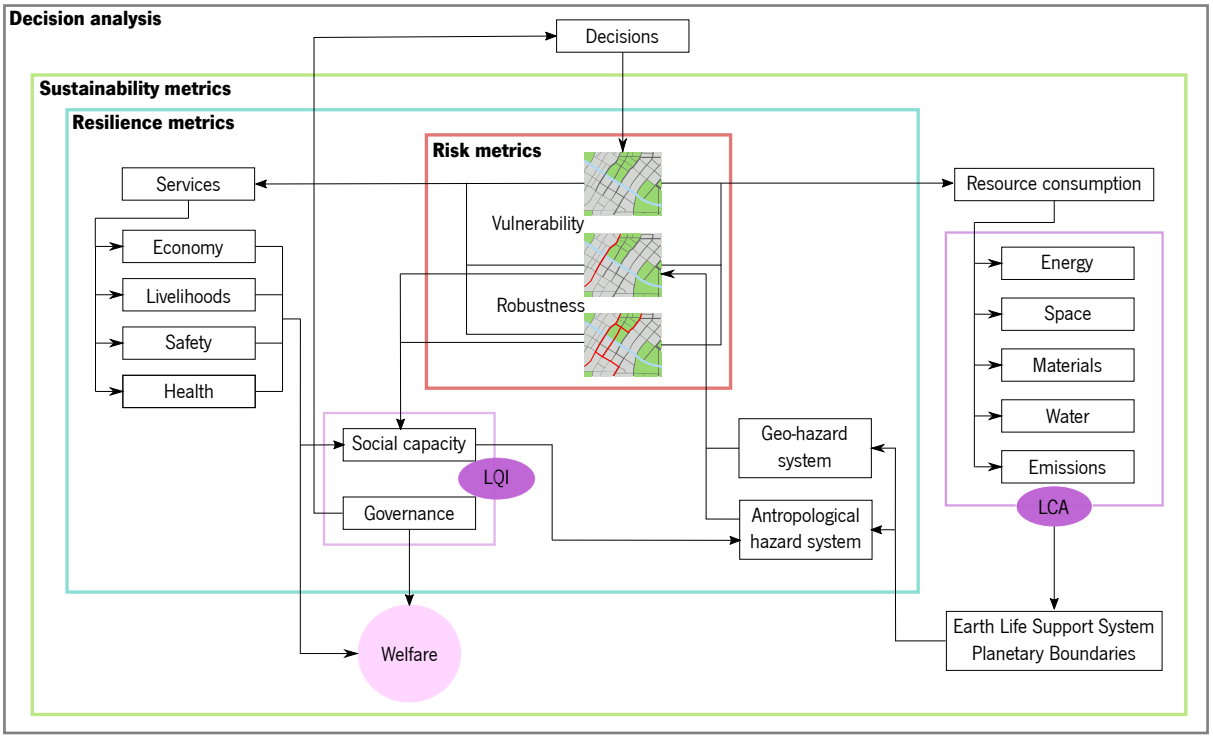


Figure 2.1: Connections between risk, resilience, and sustainability with assessment metrics and techniques. Adapted from Faber [3].

[57], Saunders and Becker [71], Lounis and McAllister [72], Gardoni [73]).

Based on the foregoing outlined challenges, the study presented in this chapter aims to establish a better understanding of the current state-of-the-art in the domain of risk, resilience, and sustainability management of TIS, with a focus on flood hazards. This focus is chosen given the challenges posed by climate change effects and the fact that floods generate the largest amount of economic damage for the transport sector among weather-related disasters. Previous state-of-the-art reviews do not concurrently address the concepts of risk, resilience, and sustainability, and do not analyze the context of the TIS in terms of decision makers, stakeholders and their preferences, decision alternatives, and state of knowledge for managing the system. To that aim, this chapter outlines a generic and comprehensive system identification of TIS following the systems modeling framework of the JCSS [40]. This step sets the baseline for conducting a bibliometric analysis, which is a quantitative method for exploring and analyzing large volumes of scientific data, along with science mapping, that can facilitate deciphering and mapping a particular knowledge domain [74, 75]. Two quantitative bibliometric techniques, namely term co-occurrence and bibliographic coupling networks, were employed to analyze the scientific literature from the emergence of the field in

1990 until 2022. The Scopus database was selected due to its extensive publication coverage within the research domain under study. The term co-occurrence technique is useful for identifying patterns and trends in the research field, studying how different sub-fields are interconnected, finding potential opportunities for bridging the gaps between sub-fields, and searching for approaches in other research domains which could be imported. The bibliographic coupling technique identifies the main contributors to the research domain (authors) and their geographic distribution (countries).

Section 2.2 describes the methodology proposed for performing the bibliometric analysis. Section 2.3 presents the results and interpretation of the bibliometric analysis. Section 2.4 discusses the main research findings and the potential for filling out the identified gaps, which provide the basis for future developments. Finally, Section 2.5 provides conclusions and an outlook for future research to improve the risk, resilience, and sustainability management of TIS.

2.2 Methodology for the bibliometric analysis

The methodology followed for conducting the bibliometric analysis consisted of four main steps, as depicted in Figure 2.2. The first step is termed the research design and comprises the definition of the aim of the analysis and the system identification for the purpose of setting the scope of the analysis. The second step involves the definition of the search queries based on the research design and the data collection and cleaning. In the third step, the techniques for the bibliometric analysis are selected, and the networks to visualize the results are constructed. Finally, the fourth step consists of data interpretation and analysis. Further details concerning each of the steps are given in the following.

2.2.1 Step I: Research design

The first step in any bibliometric analysis is planning the research. This includes determining the main objective of the study and defining the research questions. In addition, the scope of the study should be defined, which requires an understanding of the system under study. Usually, the scope of a bibliometric study is defined by search terms selected by experts. In this work, the system identification is proposed

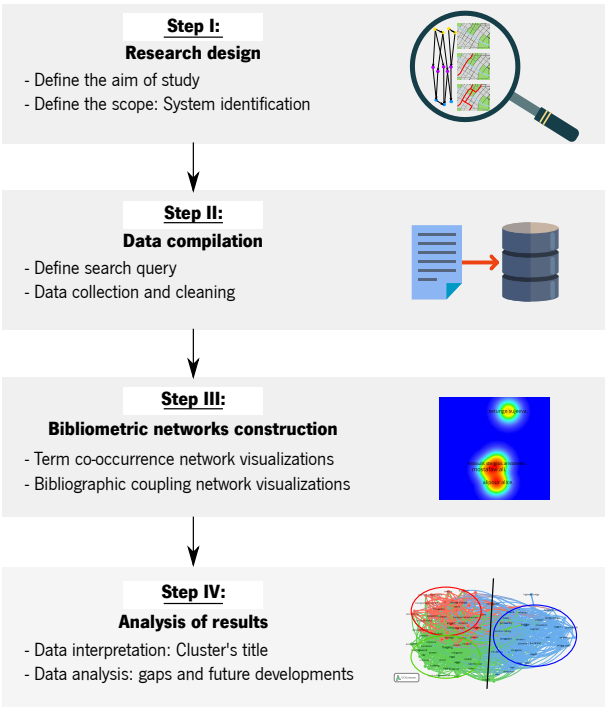


Figure 2.2: Workflow of the methodology for conducting the bibliometric analysis

as the basis for defining the scope of the bibliometric study. This approach allows for a thorough understanding of the system under study, i.e., transport infrastructure systems, and provides the logic for searching the relevant information in the context of their management.

2.2.1.1 Aim of the bibliometric study

The main goal of the bibliometric analysis in this study is to understand the current state of the art in the domain of risk, resilience, and sustainability of TIS affected by flood events in the context of managing and governing the system. To gain this understanding, the following research questions are formulated: *i)* How has the research domain grown over the past few decades? *ii)* What are the main disciplines contributing to this research area? *iii)* Are there potential gaps (research needs) in the existing knowledge? *iv)* Are there approaches in other research areas outside the specific context of floods that could be imported (knowledge transfer)? *v)* How is the distribution of the research among expert communities and countries? It should be noted that bibliometric studies allow us to identify where the major research streams have

been concentrated, and the observations that can be derived are consistent with this big picture, where outliers are not the focus.

2.2.1.2 Scope of the study: System identification

The system identification comprises a description of the system's physical characteristics, temporal and spatial boundaries, main functionalities, exposure events and potential associated consequences, decision makers, stakeholders and their preferences, and plausible decision alternatives for managing the system and their effects on system performance [40, 76]. When analyzing TIS, there may be different choices of scale to represent the system. For instance, Figure 2.3 depicts an illustration of different choices of the spatial scale for the system representation. At the first scale (Level 1), the system can be a roadway network, and the constituents are different infrastructure assets, namely bridges, embankments, tunnels, retaining walls, and pavements, among others, which interact with each other to provide their intended service, i.e., transportation for people and goods. At the second scale (Level 2), each infrastructure asset is a system that provides connectivity at one specific location in the network. The asset system is comprised of several interacting constituents, namely structural components (e.g., bridge components might be deck, piers, abutments, foundation, bearing devices), non-structural components (e.g., pavements, guardrails), as well as monitoring and control systems installed at the assets (e.g., structural health monitoring devices). Each component can be considered a subsystem, constituting the third scale (Level 3). Each subsystem consists of interacting constituents, e.g., the foundation subsystem can comprise individual piles and a pile cap. Therefore, the system representation for decision analysis must be chosen in a way that facilitates the quantification of the expected values of benefits corresponding to the decision alternatives under consideration. The decision alternatives can thus be considered as the drivers for identifying the appropriate scale for the system model [1]. Figure 2.3 presents some examples of relevant decision alternatives depending on the spatial scale of the system. At Level 1, decisions may relate to, e.g., the minimum safety level required for individual bridges, guaranteeing certain network functionality and connectivity for evacuation routes, among others. At level 2, decisions may pertain to strengthening bridge components to achieve safety, defining the optimal frequency of inspection and maintenance, installing sensors to monitor the condition of components, and others. Finally, at Level 3, decisions are

more specific to the component under study, e.g., for a pier foundation subjected to scour, plausible alternatives may be to protect the foundation using riprap, installing sensors for monitoring the scour depth, among others. Moreover, the temporal scale of the system representation should also be consistent with the planning horizon of the decision problem. For instance, decisions made at the strategic level typically have a long-term perspective, which requires modeling the system in the long run. Conversely, at the operational level, decisions generally concern the management of the system from a more short-term perspective, focusing on day-to-day inspection, monitoring, maintenance, and repair activities. Lastly, at the tactical management level, which generally concerns loss reduction, it would be relevant to have a temporal system representation that supports decisions to react during the hazard event, e.g., evacuation and emergency response plans.

Depending on the spatial and temporal scale of the system representation, the definition of the exposure of the system and the consequences would also vary. In general, TIS exposure may comprise any threat that potentially results in the failure of physical infrastructure or disruptions to their functionality. Characterizing these exposures requires a joint probabilistic model considering all relevant impacts relative to time and space. Since the emphasis of the present study is given to flood hazards, the system representation of Figure 2.3 provides examples of exposure events related to traffic overloading, floods, and degradation, at each spatial scale of the system. At Level 1, the exposure characterization requires consideration of the spatial correlation between hazard intensities at each asset location in the network. In addition, individual assets may be threatened by different degradation processes that should be characterized, such as corrosion, fatigue, erosion, among others. At Level 2, the characterization of exposure is asset specific and should take into account the correlation of hazard intensities acting on each component and the degradation processes applicable to each bridge component. Similarly, the Level 3 exposure characterization is component-specific and may address in more detail the modeling of each phenomenon, e.g., using a computational fluid dynamics model to determine the hydrodynamic forces acting on each pile of a pier foundation to derive the local scour depth. Given the exposure events defined, the systems modeling approach recommended by the Joint Committee for Structural Safety [40] can be utilized to divide the scenarios of events leading to consequences into direct and indirect consequences to health, environment, and economy. Direct consequences consist of all losses caused directly by the hazard event and/or caused by the failure (or damage) of the constituents of the system. Indirect consequences

comprise all losses caused in the process of internal redistribution after the hazard event or any consequence associated with the loss of the system's functionalities. When the system under analysis is the pier foundation from Figure 2.3 (Level 3), a direct consequence of local scour would be pile failure due to the loss of lateral support, which could trigger loss of lives and injuries, and damage to the environment, e.g., pollution due to collapsed pile debris, while indirect consequences would be foundation failure due to lack of robustness and redundancy in the pile group capacity, together with additional losses imposed to health and environment. On the other hand, if the bridge is the system under analysis (Level 2), a direct consequence of an extreme flow discharge acting on the structure would be physical damage to any of the elements, loss of lives and injuries, and damage to the environment caused by the failure of any bridge component (e.g., foundation failure), while indirect consequences would be additional losses due to complete bridge failure. Finally, when the roadway network is the system under analysis (Level 1), the direct consequences of a flooding event would be any loss associated with the failure of individual bridges, while the indirect consequences would be wider and include monetary, environmental, and social consequences due to loss of network connectivity, loss of functionality and business interruption. The distinction between direct and indirect consequences facilitates the modeling of two system characteristics, namely vulnerability and robustness. As depicted in Figure 2.3, the relation between exposure or hazards and the direct consequences is termed vulnerability, and the link between the direct consequences and the indirect consequences is related to the concept of robustness. Essentially, the vulnerability of a system indicates the degree to which exposures generate direct consequences, while robustness characterizes the degree to which a system is able to contain or limit indirect consequences associated with a hazard event [39]. If the indirect consequences of a scenario outweigh the direct consequences, then the system lacks robustness with respect to this scenario. The other two system characteristics which are crucial for the management of TIS are resilience and sustainability. When modeling these system characteristics, not only the losses but the capacity of the system (economic, social, and/or environmental) to sustain, adapt, and recover from adverse effects should be considered. The economic capacity is based on the benefits that TIS generates through the provision of services, i.e., mobility for people and goods through taxes or toll roads. In some cases, infrastructure assets such as bridges or viaducts may also provide a cultural and historical value that is transformed into an economical service related to tourism (refer to

Turksezer et al. [77]). Moreover, transport infrastructure assets can assume other types of functionalities for economic benefits, such as carrying power and telecommunication lines, oil and gas pipelines, or water pipelines. The social capacity in the context of TIS encompasses the ability of the governance system (comprised of infrastructure owners/operators, local and national public authorities) to deal with hazardous events in terms of reorganization, restructuring, and adaptive learning in and after an event [18]. Lastly, the environmental capacity may relate to, e.g., emissions of CO_2 or the availability of natural resources for the development and maintenance of TIS, such as raw materials, space, and water.

Another relevant issue when defining the appropriate system representation is that it should be consistent with available knowledge about the system, and it should facilitate that risks may be updated according to knowledge that may be available in the future. The knowledge about the system to be managed is a crucial factor for optimal decision making. Basically, the "best" of our knowledge is used to formulate models of the real world, and these models are the basis for our decision making. Generally, the best available knowledge about a system comprises phenomenological physical understanding and experience paired with information (commonly referred to as evidence) that has been gathered and processed over time [37]. Lack of knowledge or uncertainty, describes the typical condition in real-world decision making. In the context of the management of TIS, there are large uncertainties involved since transport infrastructures such as bridges are designed for a long service life of 50 to 75 years, which sometimes is even extended beyond this period. Then, our knowledge about the future state of the system is incomplete in regard to, e.g., the structural condition, changing climate, socioeconomic developments, among others. Thus, it is crucial to appropriately represent and treat uncertainties consistently to allow for more rational decision making. In addition, when modeling complex systems such as TIS, possible dependencies exist among random input variables and random events, which need to be properly accounted for when assessing risks. There are different types of dependencies that can be grouped into statistical dependence and functional dependence [40]. Statistical dependence exists when events or variables exhibit some correlation, e.g., spatial correlation or correlated information sources. For instance, if near bridges in a road network have been constructed around the same time, using concrete produced from a small concrete production plant near the construction site, as well as employing the same design standards, their structural capacity will have a statistical dependence which may be appropriately represented through correlation of the random variables used to model the capacities in the probabilistic modeling [40]. On the other hand, functional

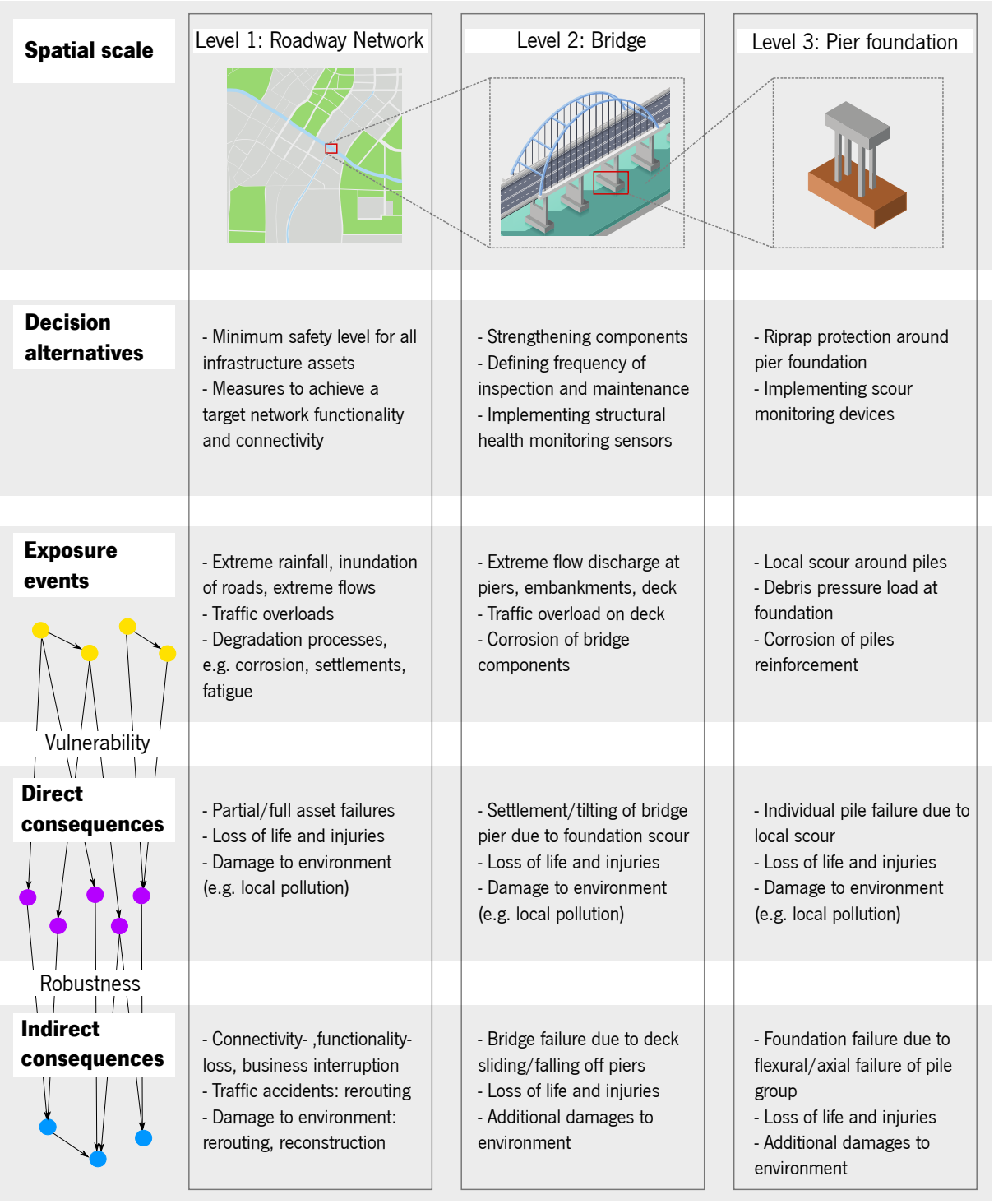


Figure 2.3: System representation of TIS at different spatial scales

dependence exists when various constituent failures are dependent. This type of dependence may have different representations, such as common cause failures (CCF), cascading failures, or relief [78]. It is widely acknowledged that neglecting dependencies can lead to underestimating the risk associated with the functioning of complex infrastructure systems (see e.g. Bayraktarli and Faber [79]). Therefore, to aggregate the risks for a portfolio of infrastructure systems correctly, it is necessary to account for all prevailing dependencies.

Lastly, the system identification should include the recognition of decision makers and stakeholders involved, along with understanding their organizational structure. Typically, decision makers and stakeholders of TIS are organized hierarchically at local, national, and global levels, and are connected by governance structures. At the local level (municipality or community level), decision makers are private or public asset infrastructure owners, managers, or operators in charge of operational decisions of maintenance and repair activities at the asset level in the short- to mid-term, as well as strategical decisions for the management of individual local projects at long-term. At the regional/state level, network managers are in charge of the entire transportation network or all infrastructure assets in a large geographical area. At the national to the global level, the governance system manages all previous levels based on its objectives, which include but are not limited to maximizing benefits, minimizing economic losses, satisfying population demands, maximizing the welfare of people, and minimizing environmental damage at local and global levels. The extent by which an objective is accomplished can be measured by attributes or criteria, e.g., safety, monetary cost, minimum level of service, life quality, emissions to the environment, among others. Through the use of utility theory, several attributes can be transformed (weighted) into a single metric - utility, which consistently reflects the preferences of decision makers and allows assessing the optimality of different decision alternatives [41, 80]. Finally, the governance system ensures the achievement of its objectives by means of regulations. In other words, decision alternatives considered for the purpose of managing the system must comply with the boundary conditions and/or constraints imposed through codes, standards, and trans/national or global scale regulations. For instance, in the National Annexes of the European civil engineering technical standards (Eurocodes), individual nations specify their National Determined Parameters (NDPs) and decide on the level of safety for the design of new structures and assessment of existing ones.

2.2.2 Step II: Data compilation

2.2.2.1 Search query

The identification of search terms is one of the most critical steps in bibliometric analysis since it significantly influences the outcomes of the study. The system identification from Section 2.2.1.2 is used as a basis to formulate the different search queries. Five groups of search terms were first established and were organized into eleven search queries as illustrated in the workflow given in Figure 2.4.

The first group provides the context to the technical system under study: Transport infrastructure systems. As described in Section 2.2.1.2, TIS can be modeled at different scales, i.e., from the component level to the asset level to the network level. Then, in an effort to reach research at any spatial scale and understand possible effects of the considered scale of the system, search terms in this group include component-level terms (e.g., bridge pier, bridge pile), asset-level terms (e.g., highway bridge, transportation asset), as well as network-level terms (e.g., road network, bridge network). It should be noted that terms used to refer to Transport Infrastructure Systems (as referred to in this study) are semantically different across many articles. For instance, some authors refer to them as highway networks (e.g., [81]), transportation networks (e.g., [82]), road networks (e.g., [44, 83, 84]), bridge networks - when the focus is given to bridges as the most vulnerable asset in the network (e.g.[20, 85]), traffic networks (e.g., [86]), and so on. However, they refer to the same technical system under study, i.e., a system comprised of all infrastructures enabling terrestrial traveling of people and goods. Thus, an extensive literature screening was conducted to find semantically-related terms and complete the collection of keywords to refer to the same technical system (the complete list of terms belonging to each group is provided in Appendix A). Moreover, wildcards are used to represent different combinations of characters in the construction of a query (e.g., "road* *structure" to represent road structure, roadway infrastructure). Lastly, the Boolean operator "OR" was employed to retrieve records containing any of the terms from Group 1 (n_0).

The second group corresponds to the system characteristics explained in section 2.2.1.2: vulnerability, robustness, resilience, and sustainability. Risk is included in the search query together with vulnerability since the structural engineering community tends to employ the term risk more than vulnerability. Separate searches (n_1 – n_4) are conducted to identify methods and indicators/metrics to characterize the

different system characteristics. A combined search of all system characteristics with the "OR" operator (n_{OR}) was also performed for a subsequent search query combination with Group 4 and Group 5 terms (see Figure 2.4).

The third group corresponds to the flood hazard to give the emphasis of the present study to understand particularly where the research state is in the domain of flood risks. The term scour is included herein since this erosional process is increased during flood events and has been regarded as one of the leading causes of bridge failures worldwide. As a result, a vast amount of research has been conducted on modeling this phenomenon and its influence on bridge safety. Then, each system characteristic from Group 2 is linked with Group 3 through the Boolean operator "AND" (n_5 – n_8).

The fourth group corresponds to the state of knowledge with regard to the treatment of uncertainties and dependencies. The Boolean operator "AND" is used to link all system characteristics from Group 2 (n_{OR}) with each term from Group 4 (n_9 and n_{10}). Finally, the fifth group corresponds to the governance and management of the system, where the aim is to identify the preferences, attributes (or criteria), and objectives of decision makers. Similarly to Group 4, the Boolean operator "AND" is used to link all system characteristics from Group 2 (n_{OR}) with the search query from Group 5 (n_{11}). It should be mentioned that the term "objective" is not included in the search query of Group 5 since this term is too general and retrieves many results along the lines of "the objective of this study", "the objective of the paper", and others. The complete search queries are provided in the appendix table A.2.

2.2.2.2 Data collection and cleaning

The search queries defined are used to collect the records from the Scopus bibliographic database. The major advantage of choosing the Scopus database is its greater publication coverage for the research domain under study. Essentially, in addition to articles, the Scopus database contains other documents, such as conference proceedings and books. The queries were employed to search in the titles and abstracts field (TITLE-ABS) or author keywords field (AUTHKEY) of the Scopus database. As a general rule in the search queries, results from health sciences fields were excluded, as well as some specific life sciences such as Immunology and Microbiology, Pharmacology, among others (refer to appendix table A.3

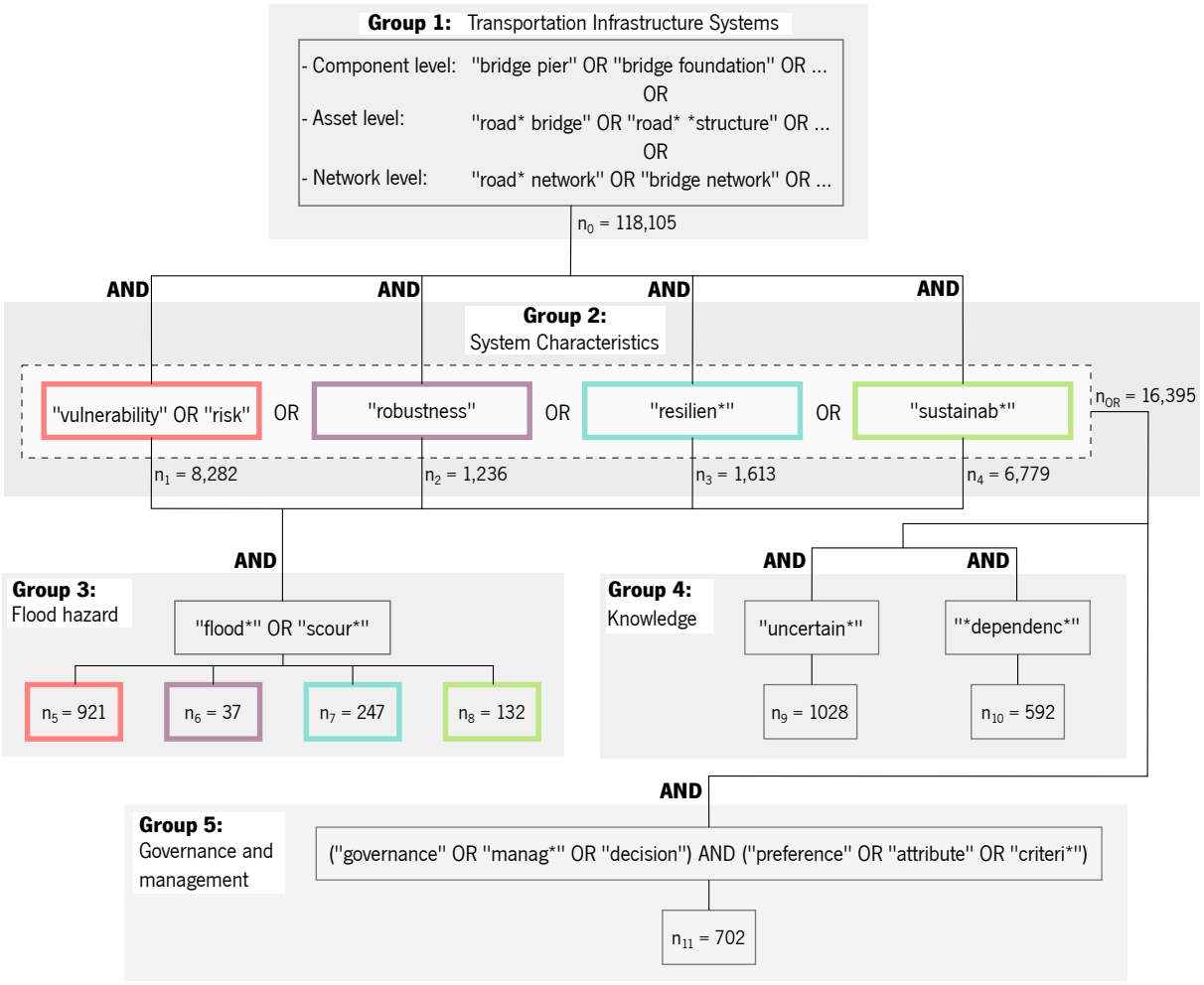


Figure 2.4: Workflow of search queries for the bibliometric analysis

for the full list), as these subject areas were not deemed of relevance to the scope of this study. All papers in the historical series since 1990 have been considered until December 2022.

The Group 1 search (n_0) returned a total of 118,105 records. Then, when linked with the combined search of all system characteristics with the "OR" operator (n_{O_R}), the search returned a total of 16,870 records. These latter records were extracted and screened to remove duplicates and exclude documents from different context areas, e.g., space transportation systems, traffic signal control systems, and others (refer to appendix table A.4 for the full list). A total of 16,395 unique records were finally used in this study. The number of records for each search query after data cleaning can be observed in Figure 2.4. It can be seen that when the flood exposure is added (n_5 – n_8), the number of records for all system characteristics drops significantly. In fact, the resulting dataset from search query n_6 is so small (37 records) that its use

for a bibliometric analysis is not recommended since forcing the analysis in such a small sample would be an overkill [74]. Then, the bibliometric analysis for search query n_6 is not performed.

2.2.3 Step III: Bibliometric networks construction

Bibliometric networks are the way bibliometric research is visualized. A bibliometric network consists of nodes and edges, where nodes can be publications, journals, researchers, or keywords, and the edges represent the relations between pairs of nodes. Among the different types of available bibliometric networks, this study uses co-occurrence of terms extracted from titles, abstracts, and keywords, which allows exploring the relationships among topics in a research field and therefore supports the identification of potential research gaps, which is one of the main goals of the study. In addition, bibliographic coupling networks of authors and countries are also selected to analyze the relationships among expert communities and the distribution of research globally. VOSviewer [87] was used to construct both types of bibliometric networks. VOSviewer is a software tool for constructing and visualizing bibliometric networks, which provides distance-based visualizations, i.e., the distance between two nodes approximately indicates the relatedness of the nodes. Moreover, it provides three visualizations for a map: network visualization, overlay visualization, and density visualization. Further details regarding the construction of the bibliometric networks are provided in the following.

2.2.3.1 Term co-occurrence network visualizations

VOSviewer offers a text-mining functionality to construct and visualize co-occurrence networks of relevant terms extracted from textual data. The software tool performs part-of-speech tagging and utilizes a linguistic filter to identify noun phrases (terms) for which a relevance score is computed. A low relevance score shows that a word co-occurs with other terms randomly, while a high relevance score is assigned to noun phrases that co-occur with a limited group of other noun phrases [88]. Terms were derived from the titles and abstracts from publications collected in Step II. Terms with low relevance scores were excluded, as well as too general and non-context-specific terms (e.g., article, author, challenge, literature). Applying

these filters shifts the focus to more specific and informative terms. The full list of excluded terms can be found in appendix table A.5.

Network visualizations are chosen to display the co-occurrence of terms. The network visualizations are comprised of items (terms) and links. Terms are represented by their label and a circle, which size depends on the number of publications that contain the term in the title or abstract. There are two counting methods available, binary or full counting. In the binary option, only the presence or the absence of a term in a publication matters. Conversely, in the full counting option, all occurrences of a term in a publication are counted [88]. The binary option is chosen, so a term that occurs only once is treated the same way as one that occurs multiple times. The minimum number of occurrences of a term for its inclusion in the network is adjusted for each search aiming to obtain medium size network visualizations of 120 terms (refer to Appendix table A.6). This helps to deal with the problem of very large networks being perceptually difficult to visualize and very small networks less informative due to few terms. On the other hand, links represent the connection or relationships that exist between two terms. Each link has a strength determined by the number of publications in which the two terms appear. The thicker the line in the visualization, the stronger the link. Terms that co-occur frequently are located closely, while terms with no or practically no co-occurrence are farther away. Additionally, terms are grouped together into clusters. A cluster represents a set of terms closely related, and each cluster has a distinctive color. Each term in a network belongs to one cluster only. The clustering technique employed by VOSviewer requires an algorithm for solving an optimization problem and is discussed in detail in [89] and [90]. Analyzing the clusters in the network visualizations makes it possible to identify the research area domains (fields and subfields) contributing to the knowledge.

2.2.3.2 Bibliographic coupling network visualizations

Bibliographic coupling networks were also constructed using the VOSviewer software for two items: authors and countries. In this type of network, the relatedness of items is based on the number of references they share. In other words, the larger the number of references two publications have in common, the stronger the bibliographic coupling relation between them [88]. There are two counting methods available, full counting and fractional counting. In the full counting method, each bibliographic coupling has

the same weight. Conversely, in the fractional counting method, the weight of a link is fractionalized to diminish the importance of highly cited publications or publications with a long reference list (e.g., review articles) [88]. As recommended by the authors, the fractional counting method is selected to include perspectives beyond citation numbers.

Density visualizations are chosen to display the bibliographic coupling of authors since they help to identify knowledge hubs and subject experts intuitively visually. In this type of format, authors are represented by their labels, and each point in the density visualization has a color that indicates the density of authors at that point. A rainbow color palette is used, which ranges from blue to green to red, to reflect the density of authors at each point. The 'hot' red zones of the map indicate a large number of authors in the neighborhood and high weights of the neighboring authors. Conversely, the 'cold' blue zones represent neighborhoods with a small number of authors and low weights of neighboring authors [87]. On the other hand, network visualizations have been used to display the bibliographic coupling for countries. Then, countries are represented by a label whose size indicates their relative importance, and the link between them indicates the relatedness of cited references. The bibliographic coupling networks were constructed from the publications collected in Step II. A minimum number of publications per author and per country for its inclusion in the networks were defined, aiming to obtain around 20-30 authors and 50-70 countries in each network (refer to appendix table A.7).

2.2.4 Step IV: Analysis of results

The data interpretation, analysis, and recommendations are the focus of the following sections.

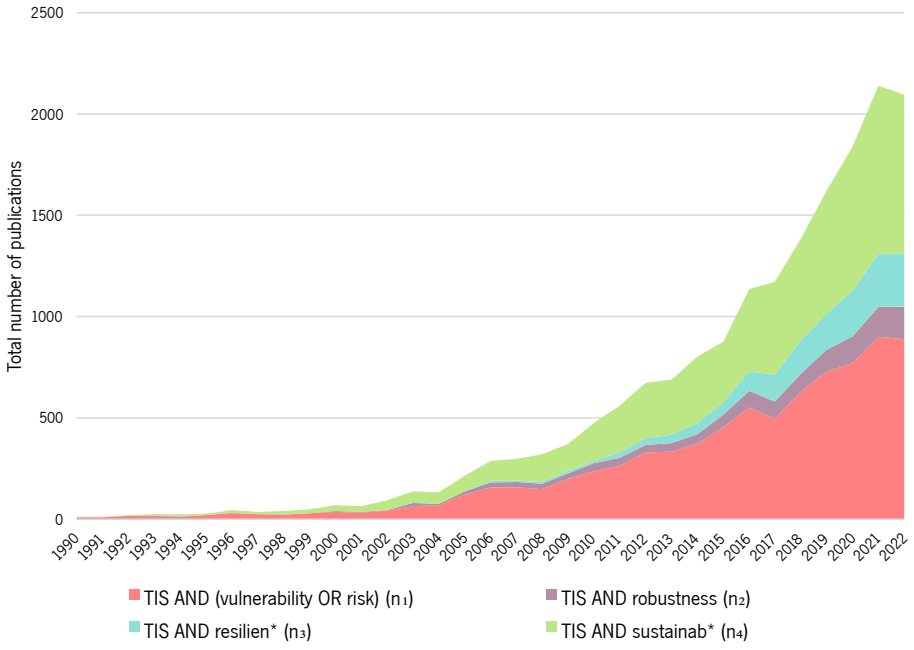
2.3 Results

2.3.1 Historical evolution and growth of research in system characteristics of TIS

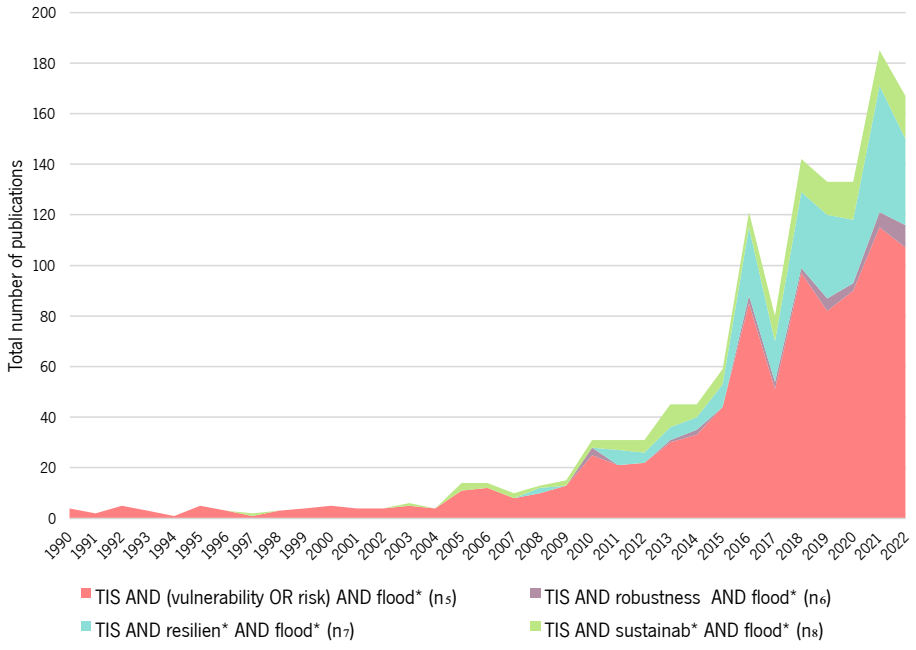
Figure 2.5 illustrates the historical evolution and volume of research in system characteristics of TIS. From Figure 2.5a, it can be observed that research in vulnerability and risk of TIS have the longest history and largest volume of publications, closely followed by sustainability research, while robustness has received less attention. All system characteristics show an upward trend, but risk and sustainability have increased at a higher rate in the last decade. When analyzing the system characteristics research in the specific context of flood exposure (Figure 2.5b), vulnerability and risk are by far the dominant research field, robustness research is marginal, and resilience gains more importance over sustainability. Interestingly, there are two peaks of publications in the years 2016 and 2018, which may be motivated by the occurrence of flooding events with large consequences worldwide during that period.

2.3.2 Multi-disciplinary composition of research in system characteristics of TIS

The distribution of subject areas in the domain of system characteristics research of TIS is shown in Figure 2.6. The top ten categories were selected for the non-hazard-specific queries (n_1 - n_4) and the flood-specific queries (n_5 - n_8). It can be observed that each bar chart contains around 11 to 12 subject areas, which means that the contribution of a discipline varies if the emphasis of the study is on flood exposure or not. Engineering is the predominant subject area for all system characteristics. However, when analyzing sustainability specifically under flood exposure, environmental science emerges as the leading subject area contributing to research. In general, the contribution from environmental science - and Earth planetary science - is significant in all search queries that include flood exposure. Another big contributing subject area is social sciences, which comes second in most system characteristics except for robustness research, where computer science becomes the second contributor. This is not a surprise since engineering disciplines heavily dominate research on robustness. Finally, decision sciences and



(a)



(b)

Figure 2.5: Evolution of research in (a) system characteristics of TIS (n_1 - n_4) (b) under flood exposure (n_5 - n_8)

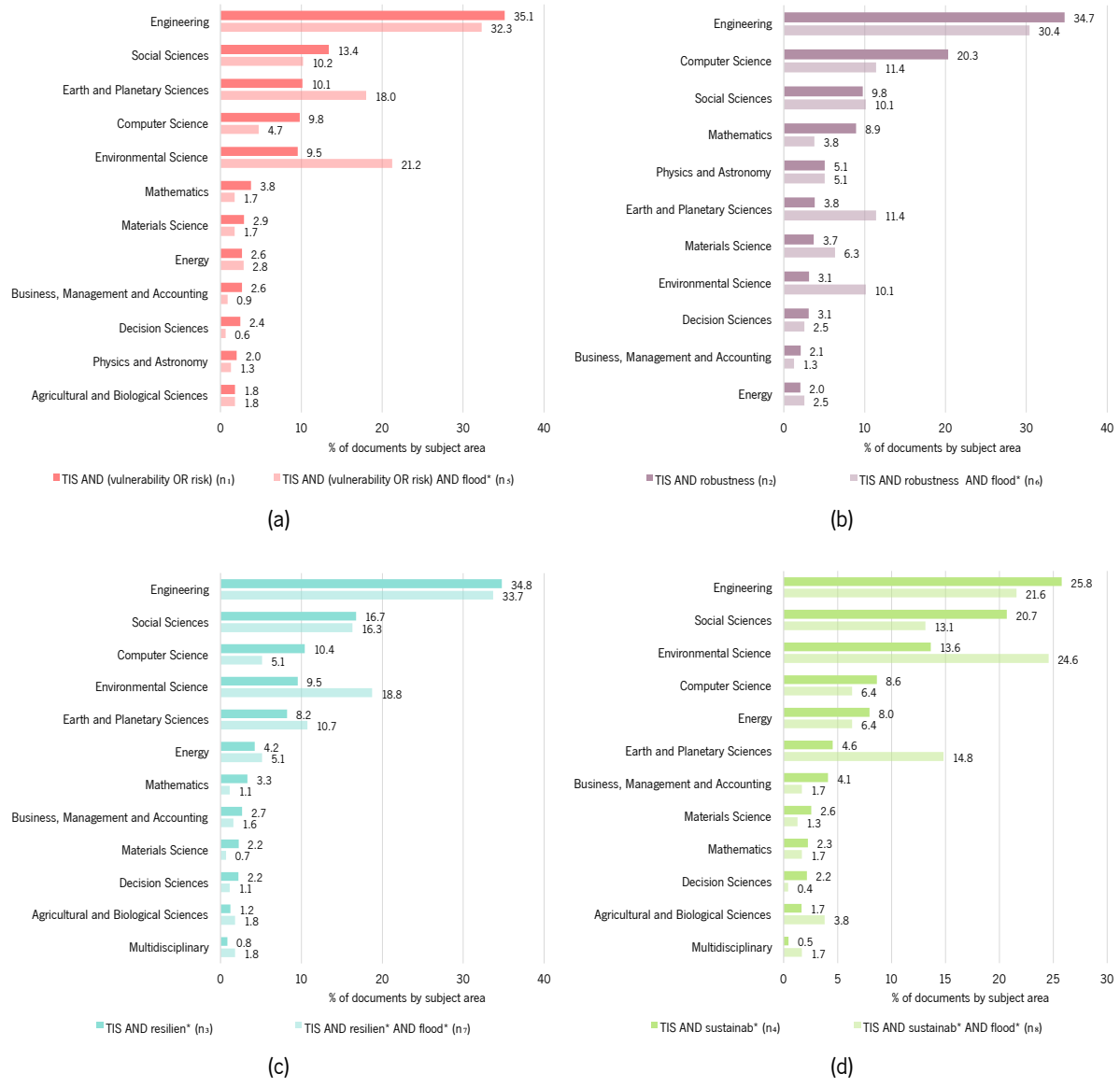


Figure 2.6: Main subject areas in TIS research on (a) risk and vulnerability (b) robustness (c) resilience (d) sustainability.

business, management, and accounting contribute to research at a minor level. Therefore, it could be said that the top contributing subject areas for all search queries approximately represent the ecological, engineered, and social systems perspectives.

2.3.3 Term co-occurrence analysis results

This section presents the term co-occurrence maps created with VOSviewer. As explained in section 2.2.3.1, the software uses a clustering technique to group related terms and assigns a specific color to each cluster. Then, the terms in each cluster are analyzed, and the research area that best represents the cluster is identified to name the cluster. It is acknowledged there is subjectivity involved in interpreting these maps. However, they are an efficient visualization tool to discover trends and patterns in large data sets and to identify potential research gaps based on the relationships between clusters. In addition, the networks will be explored in search of methods, techniques, tools, indicators, and metrics for modeling and managing TIS.

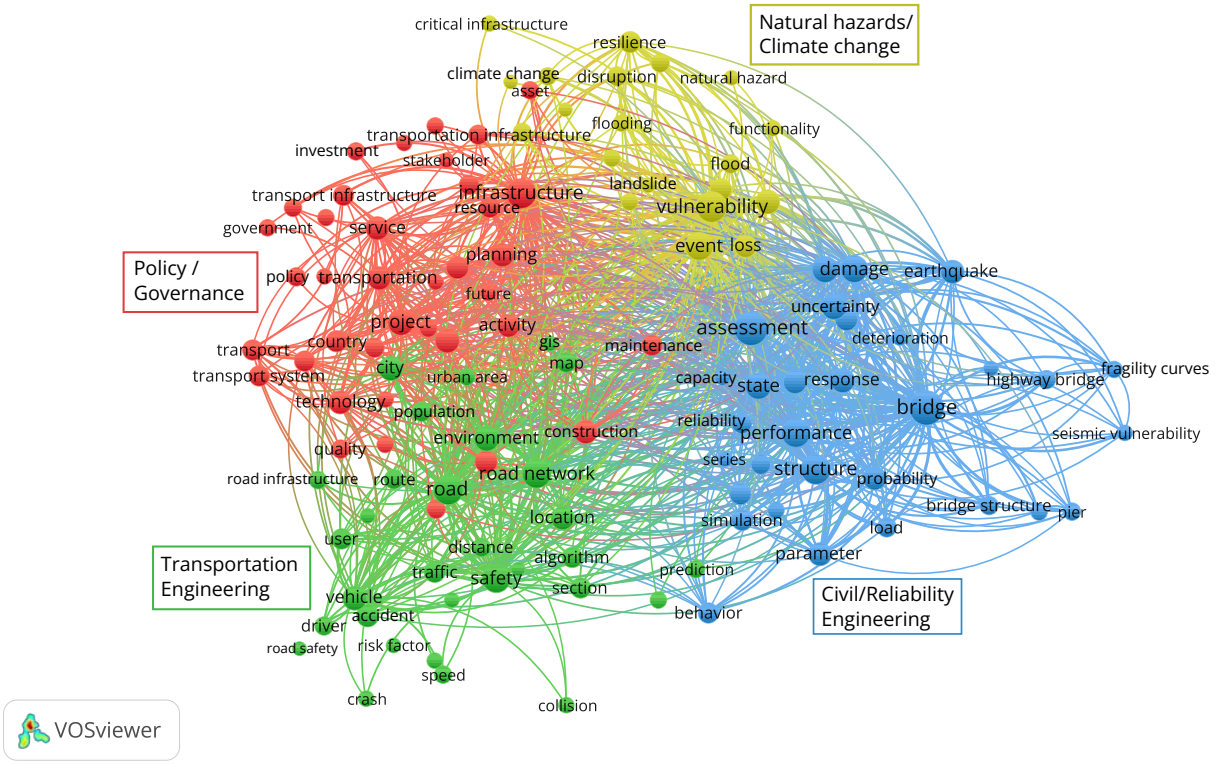
Figure 2.7a shows the network map combining the domains of vulnerability and risk of TIS. In this non-hazard-specific search, there are four different clusters. The blue cluster corresponds to the civil/reliability engineering domain (probability, uncertainty, structure), which focuses on structural safety assessment. It can be observed that a large emphasis is given to seismic vulnerability, and the use of fragility curves comes up to characterize the performance of structures under different intensities of the hazard. In addition, considerations regarding the long-term performance of bridges are also found in this cluster (e.g., deterioration, (condition) state). The red cluster is the policy/governance (e.g., government, resource, stakeholder, planning), which is more concerned with management than assessment, and focuses on economic considerations (investment, economy). The green cluster is closely related to the red cluster and represents the transportation engineering community (e.g., traffic, route, vehicle, city), with considerations regarding road safety and the environment. Lastly, the yellow cluster is the natural hazards domain (flooding, landslide, climate), which focuses on weather-related hazards affected by climate change.

Figure 2.7b presents the network map combining the domains of vulnerability and risk of TIS exposed to flood events. The network shows two closely related clusters (green and red) located far from a third cluster (blue). The green cluster represents the transportation engineering domain (e.g., service, access, person, urban area), where the main considerations are service provision and accessibility for the population during disasters. Also, GIS tools appear to be commonly used in this cluster for mapping the extent of the inundation area. The red cluster is closely related and corresponds to the natural hazards and climate change domain (sea level rise, extreme weather event, storm). Even though the policy and governance

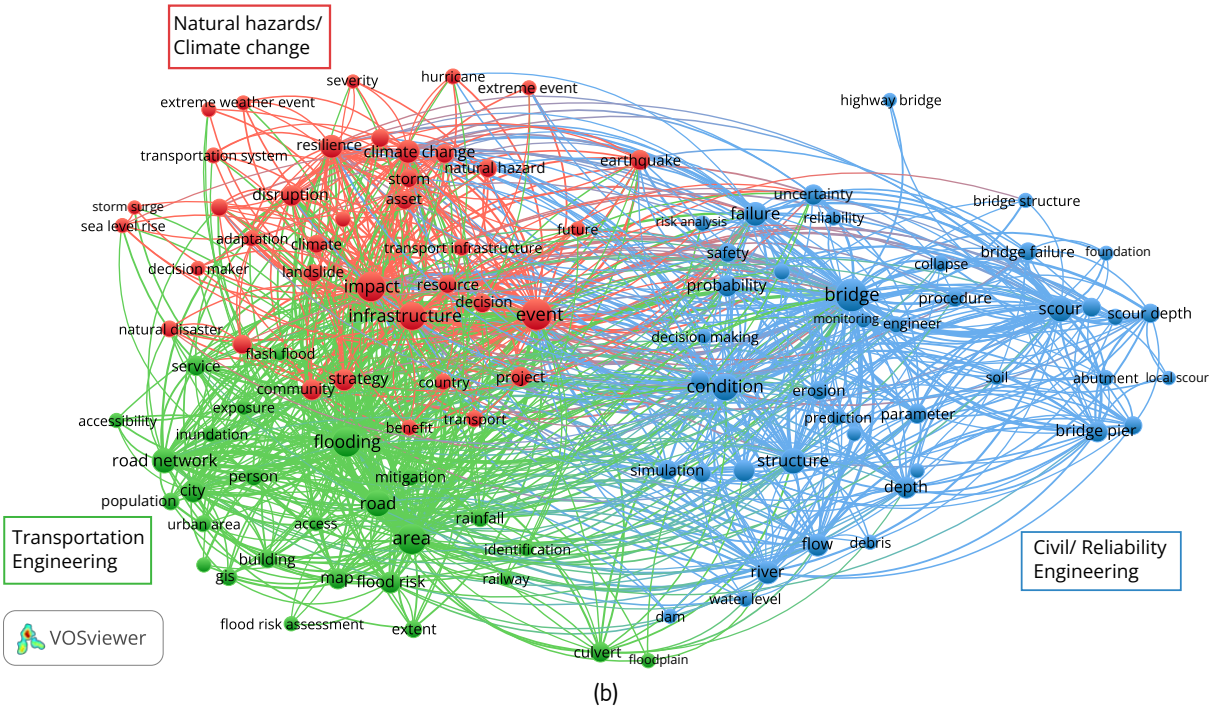
cluster from Figure 2.7a disappears when the flood exposure is included, some governance goes to the red cluster (e.g., decision maker, strategy, adaptation). The blue cluster, which represents the civil/reliability engineering (e.g., uncertainty, probability, safety), sits rather far from the other two clusters. In this cluster, there is a large contribution from the research community focused on bridge scour. Some considerations regarding long-term performance also take place, probably focusing on formulations for scour depth prediction (e.g., erosion, state, prediction). However, it can be seen that the term "fragility curves" disappears, meaning their use is not as frequent as in the case of seismic hazards. The distance of the blue cluster with the other clusters means that there might be a lack of integration of this community, more focused on the asset/bridge level analysis, with respect to transportation and natural hazards domains which focus on regional and country level scales.

Figure 2.8 shows the network map in the domain of robustness of TIS. The blue cluster corresponds to classical structural engineering (e.g., load, response, sensitivity analysis, numerical simulation), where structural assessment, damage identification, and structural health monitoring considerations are found. The green cluster is related to transportation engineering (e.g., vehicle, algorithm, technology, and intelligent transportation systems). This research domain has focused on developing new technologies for transportation/traffic systems, e.g., sensors and image detection. Considerations in this domain are accuracy, stability, and effectiveness of new solutions. However, these are classical terms and do not refer to systemic robustness as defined in Section 2.2.1.2, which also holds for the blue cluster. Conversely, the red cluster represents the systemic risk and resilience engineering perspective (e.g., redundancy, recovery, consequences, resilience, risk, vulnerability). This cluster includes important considerations such as network robustness, connectivity, travel time, and traffic congestion, which are relevant to quantify indirect losses due to network disruptions. It is worth noting that the flood-specific search for robustness research (n_6) returned insufficient records to perform a bibliometric analysis. Yet, this allows concluding that more research in this domain is still missing.

Figure 2.9a presents the network map in the domain of resilience of TIS. The red cluster is the densest and represents the policy/governance research (policy, planning, stakeholder, government). Besides economic aspects, this cluster has considerations with regard to the population, such as mobility, access(ibility), and quality of transportation service. Also, it is concerned with sustainability, adaptation to climate change, and some interdependency among different infrastructure systems, namely energy,



(a)



(b)

Figure 2.7: (a) Network map of research in the domain of risk and vulnerability of TIS (n_1) (b) under flood events (n_5)

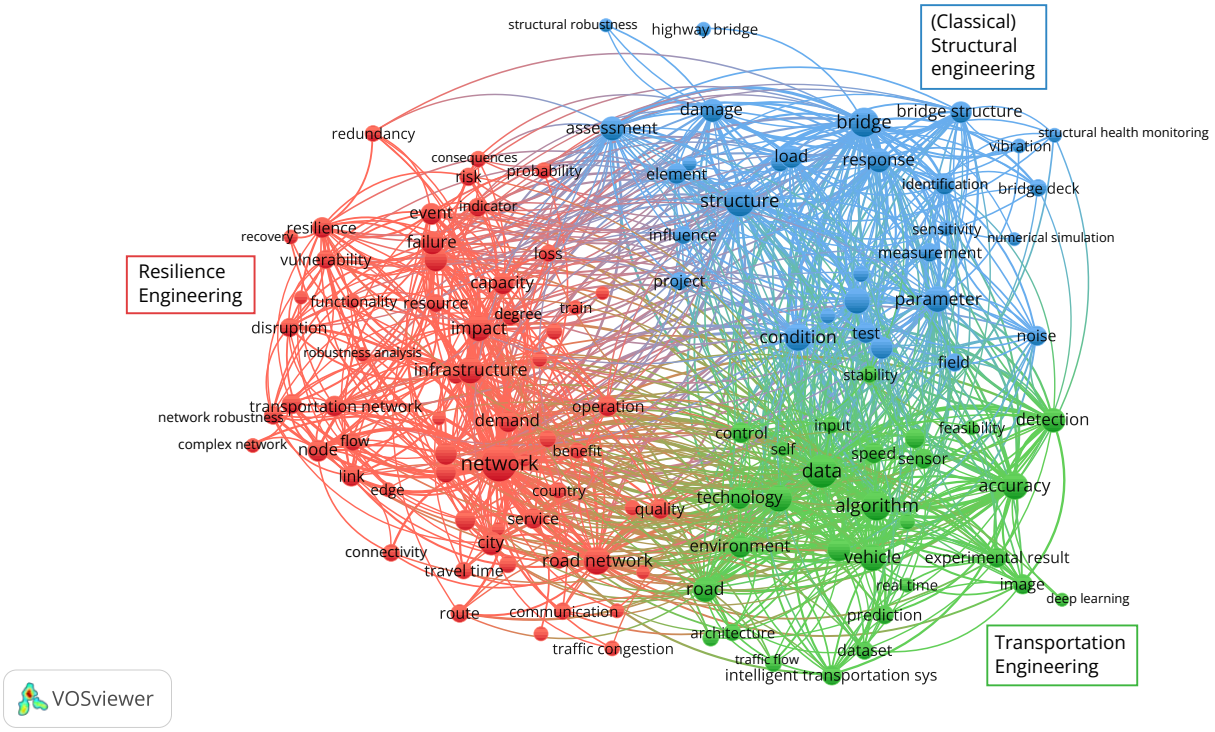


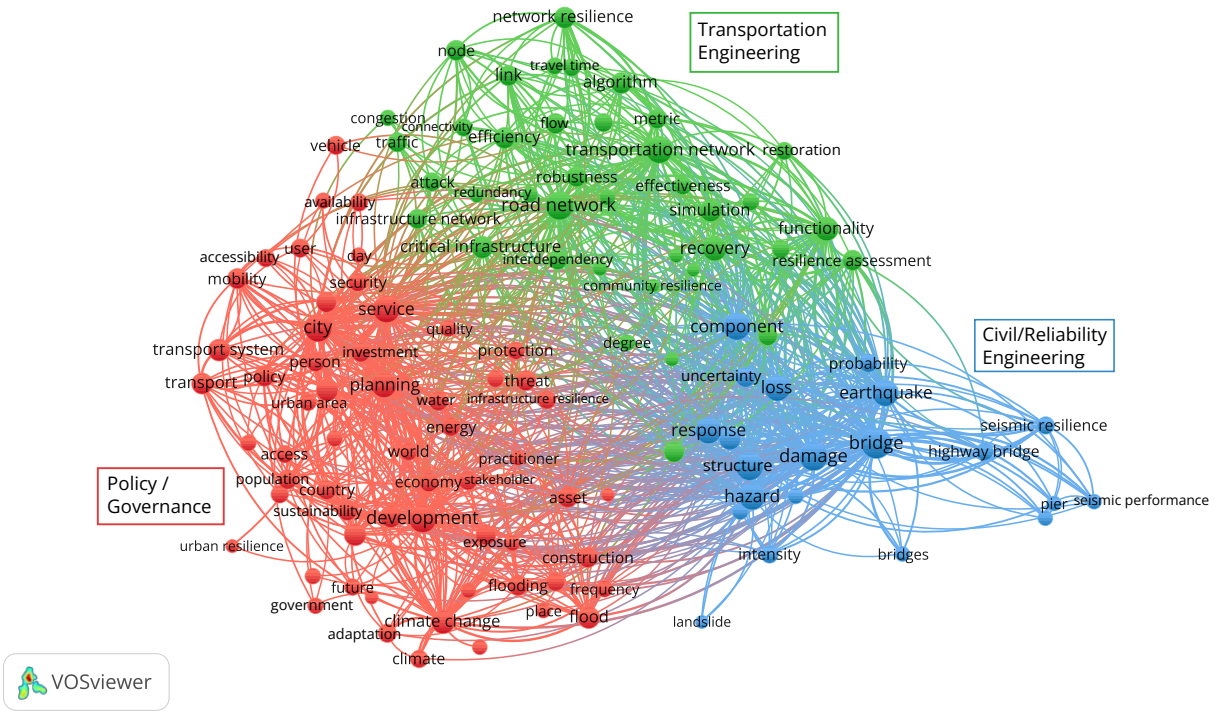
Figure 2.8: Network map of research in the domain of robustness of TIS (n_2)

water, transport, and other critical infrastructures. The blue cluster is the civil/reliability engineering (probability, uncertainty, response), which is focused on research at the component/bridge scale (e.g., damage, loss, structure, component), so the resilience metrics found are related to the level of structural damage after the occurrence of hazards, particularly from seismic hazards. Lastly, the green cluster represents transportation engineering research (traffic, congestion, flow, travel time). In this cluster, metrics to characterize the network resilience are identified, such as travel time, connectivity, and traffic flow, as well as resilience indicators like robustness and redundancy. This map shows that transportation engineering can play an important role in bridging the gap between policy and civil engineering research. On the right side, the nodes recovery and functionality from the transportation cluster are closely associated with the nodes component, response, and damage from the civil engineering cluster. This is expected since the time for recovering the complete functionality of the transportation network depends on the number of damaged components, their damage level, and the repair sequence. On the left side, nodes like traffic and connectivity from the transportation cluster are strongly linked with the service node in the governance cluster, which is a dominating node in this cluster.

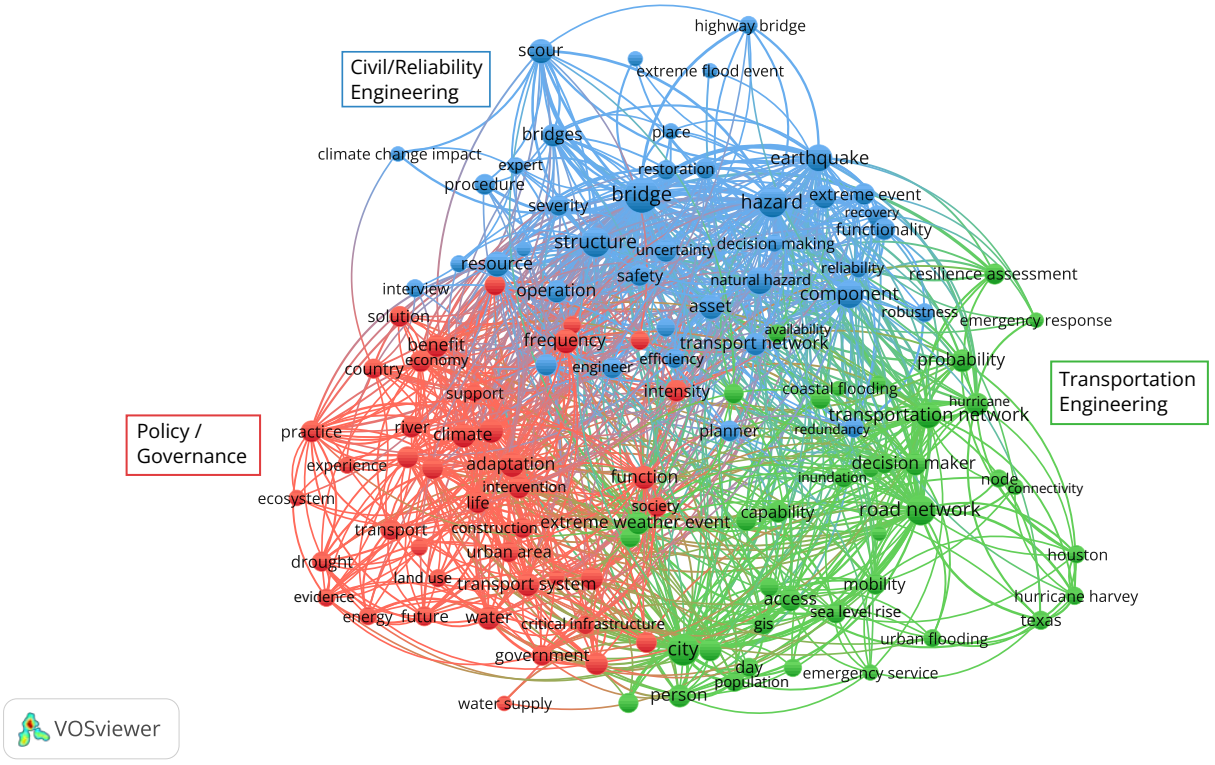
Figure 2.9b presents the network map in the domain of resilience of TIS under flood events. The same three clusters from the non-hazard-specific search are maintained. However, their composition is slightly different. For instance, the explicit modeling of the hazard/disturbance event does not appear to be relevant in the transportation engineering cluster from Figure 2.9a. Conversely, the transportation cluster from Figure 2.9b integrates natural hazards research of hydrological nature, such as coastal flooding, sea level rise, hurricanes, and their impacts on the road network service (inundation, access, mobility), particularly for emergency response. As a result, the prevailing metric to characterize resilience is connectivity. On the other hand, the civil/reliability engineering cluster (blue) gains more importance in this map. Besides research about the restoration of assets/bridges as a function of their damage severity and the recovery of functionality, this cluster includes resilience indicators like robustness and redundancy in close relationship with the green cluster. In fact, these two indicators were in the transportation cluster in Figure 2.9a, which indicates the relevance of these indicators to link both research communities. Finally, the policy/governance cluster (red) is similar to the non-hazard-specific map. Yet, it is less dense, and some relevant considerations with regard to the quality of the transportation service to the population and sustainability are missing.

Figure 2.10a presents a network map in the sustainability domain of TIS. This is a dense network with three clusters. The blue cluster is the civil engineering domain (e.g., construction, project, maintenance, infrastructure), where sustainability and environmental impacts are considered for managing the built environment, as well as risk and safety. The long-term performance of bridges appears to be considered (e.g., state, performance, year) to define maintenance strategies that ensure sustainability. The green cluster is the transportation engineering community, focused on sustainable mobility, e.g., reduction of traffic congestion, and energy consumption, as a means to reducing air pollution and emissions. Lastly, the red cluster is the policy/governance research (country, government, investment), which underlines the need for sustainable development, growth, and land use planning.

Figure 2.10b displays the network map in the sustainability domain of TIS under flood events. There are three interacting clusters, yet with some loosely connected nodes, which may be explained by the small dataset for this search (132 publications). In fact, this network map contains only 100 terms (rather than 120), since the minimum number of occurrences of a term was set in 5 instances to avoid the influence from one particular research group (see details in Appendix table A.6). The green cluster is the densest and



(a)



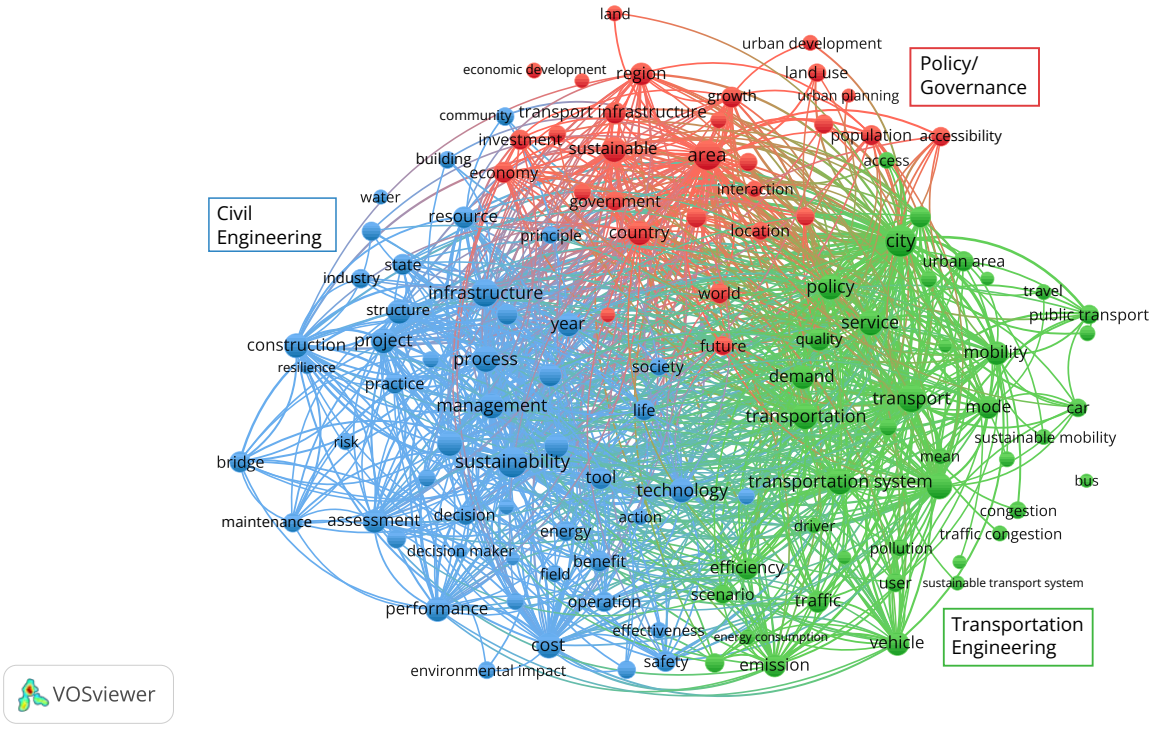
(b)

Figure 2.9: (a) Network map of research in the domain of resilience of TIS (n_3) (b) under flood events (n_7)

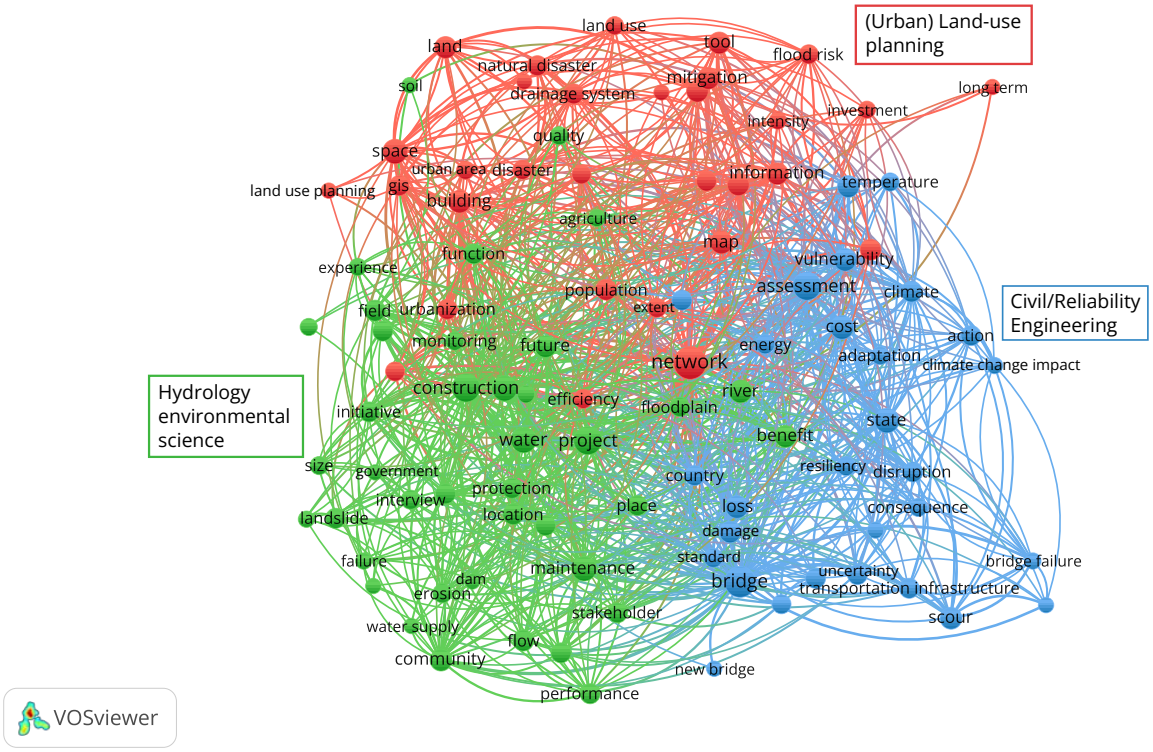
can be associated with hydrology environmental science research (river, floodplain, erosion, water supply). This knowledge hub integrates research on river/catchments modeling and how the built environment interacts with it. Its slight dominance in the network map is congruent with the finding in Figure 2.6d, where environmental science is the leading contributor to research for the sustainability search under flood events, followed by engineering. The red cluster is the urban land-use planning (urban area, land use, space, urbanization), which contains some governance aspects (investment, mitigation, long term). Lastly, the blue cluster is the civil/reliability engineering cluster (e.g., bridge failure, uncertainty, structure), where the main considerations are related to bridge damage, loss, consequences, and adaptation to climate change impacts.

Finally, the last three network maps correspond to the search queries related to knowledge, and governance and management. Figure 2.11a shows the network map in the domain of uncertainties in the system characteristics of TIS. The predominant cluster is the civil/reliability engineering in blue, with a major focus on bridges. The use of probabilistic approaches dominates the treatment of uncertainty in this cluster, and seismic fragility curves appear as a strong application that accounts for uncertainties in the assessment of structural vulnerability. On the other hand, the green cluster representing the transportation engineering community is comprised of loosely connected nodes. The approach for treating uncertainties in this cluster is not evident from the network map. Yet, this research community seems to acknowledge uncertainties in vehicle route choice, travel time, and traffic assignment solution algorithms. The red cluster corresponds to the policy/governance research. This is a more dense cluster with stronger links between nodes, yet it does not provide many insights either regarding the treatment of uncertainties. Lastly, the yellow cluster, which is the resilience engineering community (resilience, robustness, functionality), is a loosely connected cluster that appears to be making efforts to link the civil engineering community at the bridge level (blue cluster) with the infrastructure system level, through the assessment of the system functionality and characteristics like robustness and resilience. However, there is still a significant gap between the treatment of uncertainties at the asset level to the network level.

Figure 2.11b presents the network map of research in the domain of dependencies in the assessment of system characteristics of TIS. The network shows two closely related clusters (green and red) located far from a third cluster (blue). The blue cluster represents the systemic risk and resilience engineering



(a)



(b)

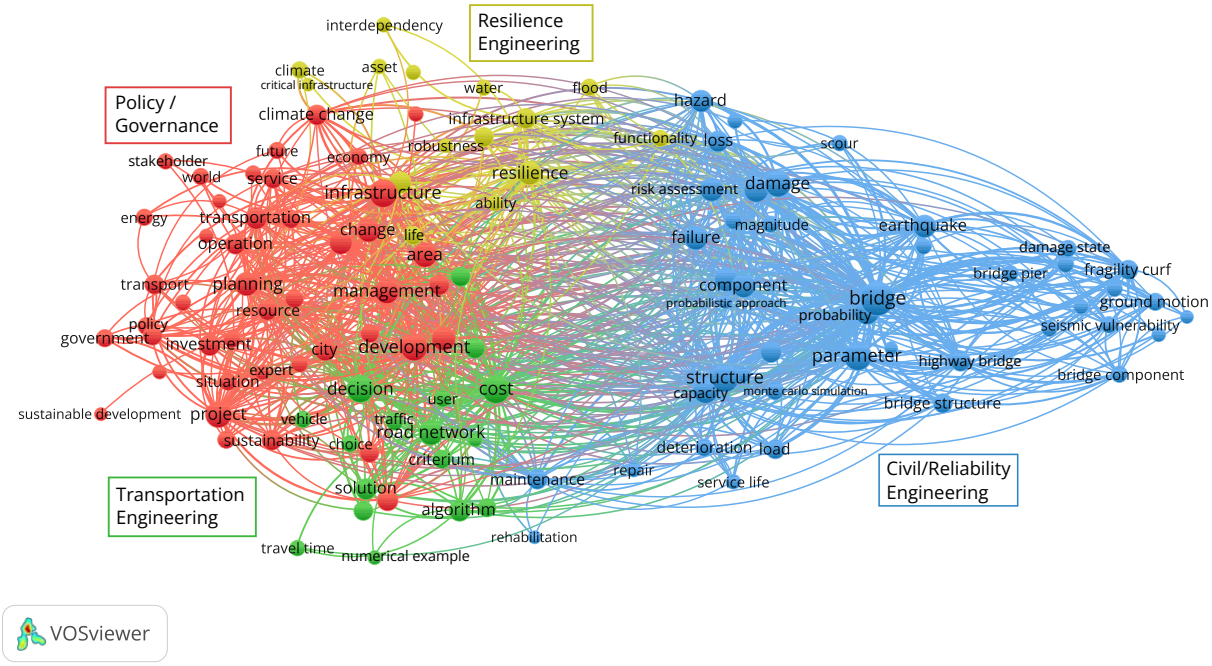
Figure 2.10: (a) Network map of research in the domain of sustainability of TIS (n_4) (b) under flood events (n_8)

perspective (vulnerability, risk assessment, robustness, functionality, resilience). The treatment of uncertainties is governed by the use of probabilities, and cascading effects are among the dependencies of random events underlined in this cluster. Also, there is great consideration of interdependency and cascading failures with other infrastructure systems: electricity/power, water, and telecommunication systems, as well as interdependencies with supply chains. The two other clusters located apart from the blue, are the green cluster which corresponds to transportation engineering (mobility, vehicle, traffic), and the red cluster, which represents the policy/governance (government, policy, country) from a societal infrastructure planning perspective. However, dependencies considered in these two clusters do not refer to the type of dependence related to knowledge as described in Section 2.2.1.2.

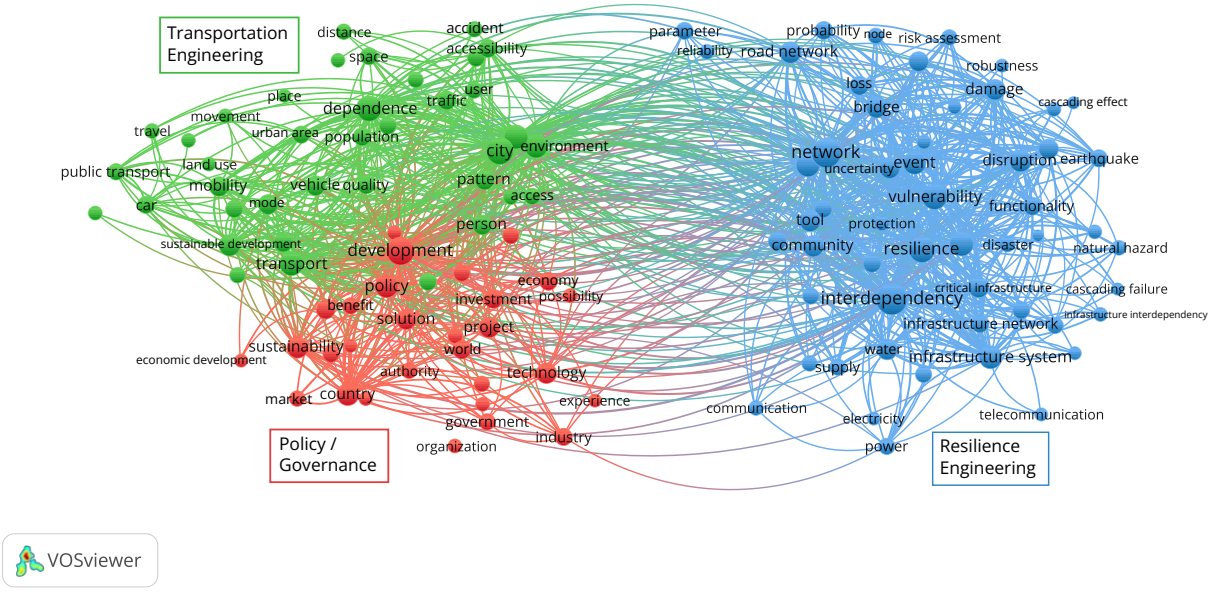
Lastly, in Figure 2.12, a network map in the domain of decision making of TIS under a normative context is given. There are three distinct clusters. The dominant cluster is the red one and represents the governance perspective (stakeholders, policy, country, investment). There is a lot of decision analysis in this cluster. Some preferences that arise are economy, sustainability with criteria like emissions, and some societal criteria related to mobility, such as availability, accessibility, and travel time. The green cluster belongs to the urban transportation planning (urban area, land use, route, road safety). In this cluster, decision-making methods appear like analytical hierarchical process (AHP) and multi-criteria decision analysis, with preferences like road safety and criteria like accidents. Lastly, the blue cluster represents the civil/reliability engineering perspective (risk, uncertainty, vulnerability), using risk-informed decision making. The concept of utility comes up in this cluster, very closely related to reliability and society which might be attributes accounted for and transformed into utility to assess the optimality of decision alternatives. Most certainly, decision making in this cluster is performed from an individual project perspective (bridge, structure, building), including long-term considerations for decision making (e.g., age, condition state, maintenance). The network analysis is thus more addressed by the green and red clusters.

2.3.4 Bibliographic coupling analysis results

In this section, the last results from the bibliometric analysis are presented, corresponding to the bibliographic coupling analysis. The bibliographic coupling networks are used to show the distribution of



(a)



(b)

Figure 2.11: Network map of research in the domain of (a) uncertainties in the system characteristics of TIS (n_9) and (b) dependencies (n_{10})

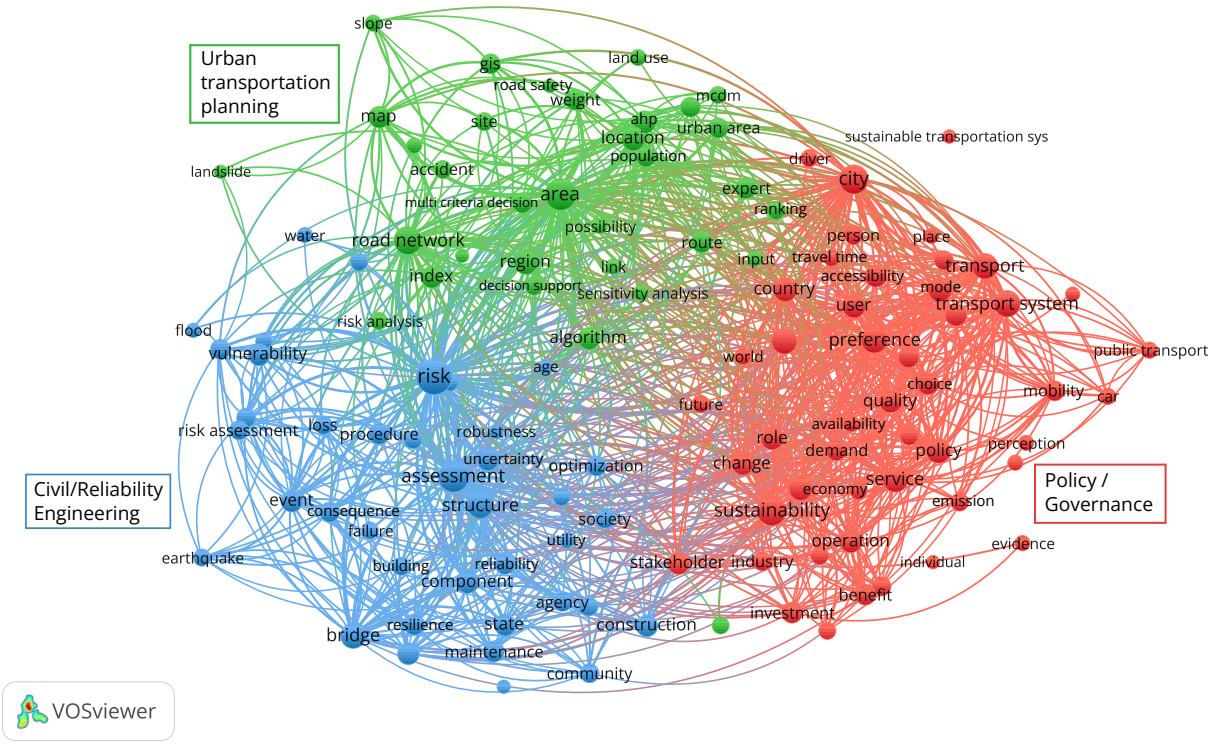


Figure 2.12: Network map of research in the domain of decision-making preferences for TIS management (n_{11})

knowledge by authors and countries in the system characteristics of TIS (search queries n_1-n_8). The use of bibliographic coupling of authors facilitates the identification of the relatedness of expert communities, or the fragmentation of research. Similarly, the bibliographic coupling of countries allows the observation of the major producers of research globally and collaborations among countries.

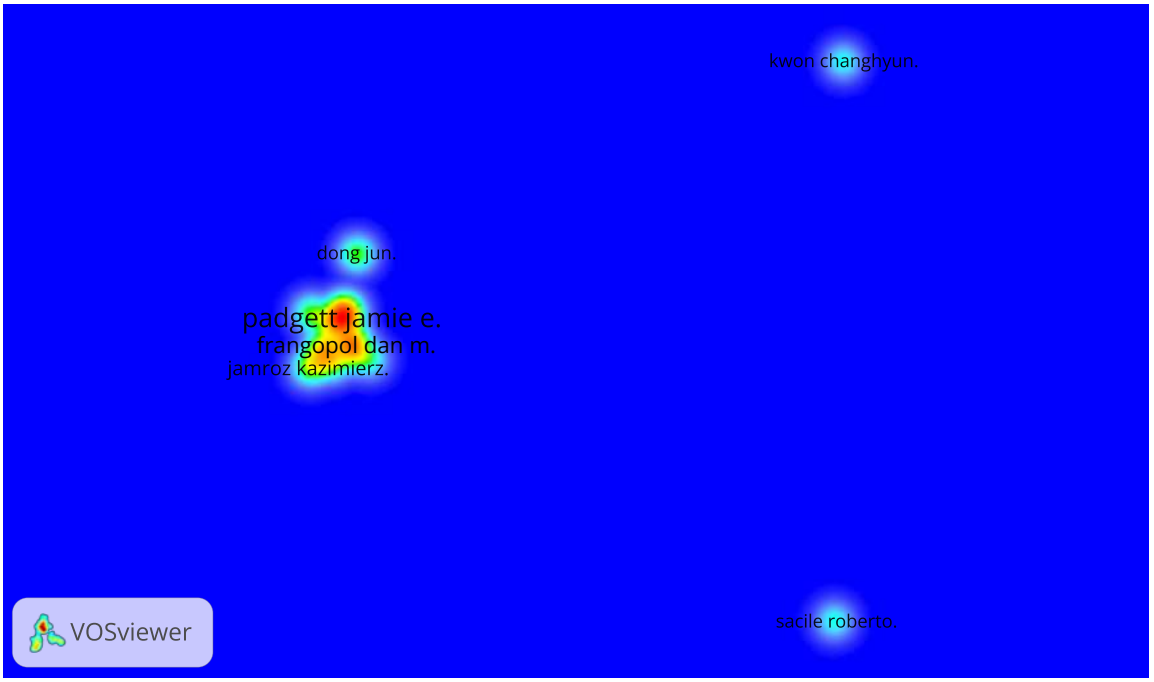
In Figure 2.13a, the bibliographic coupling by authors in research on vulnerability and risk of TIS is shown. There is a very interlinked group at the left and two distant authors at the right. These two authors are experts in risk management of hazardous materials transport on road networks. This division is interpreted as a result of the common practice of classifying hazards based on their source of origin, where hazardous material transport is not accounted for together with natural hazards, which is the main focus of the group from the left. Figure 2.13b presents the bibliographic coupling by countries for this search. The two dominant producers of research are the United States (USA) and China, although the exchange between them is not very strong. Conversely, there is a strong relationship between the former and the United Kingdom (UK). They both belong to the green cluster, together with some Scandinavian European countries. Australia also has proximity to the USA, although it belongs to the yellow cluster

together with some southeast Asian countries. Canada (hidden beneath China) has a strong relationship with China and belongs to the same cluster as South Korea and some Middle East countries. In the red cluster, several European countries are located, with Italy and Germany (hidden beneath Italy) having the lead and being strongly related. Russia is also a significant contributor to this cluster. The rest of the clusters have a smaller number of countries.

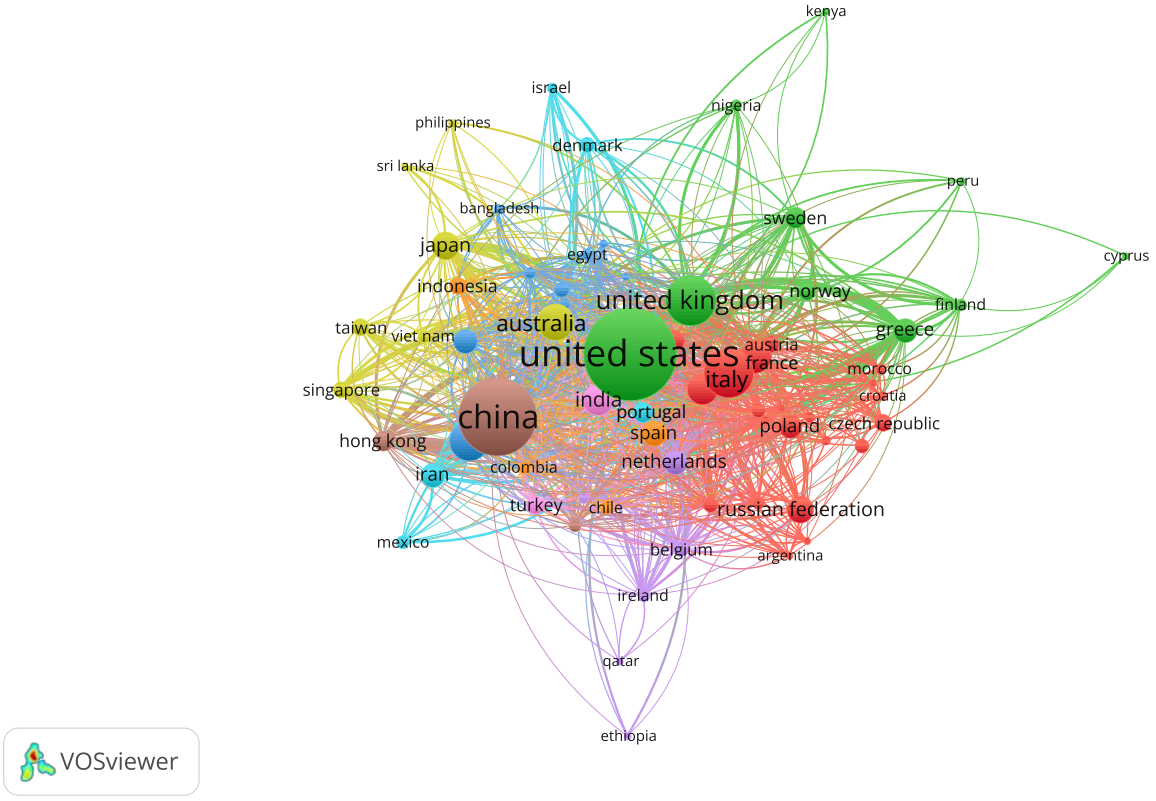
Figure 2.14a displays the bibliographic coupling by authors in research on vulnerability and risk of TIS under flood exposure. Similarly to Figure 2.13a, there is a very interconnected group at the left and two distant authors at the right. One of the author's expertise is in bridge hydraulics and scour research, while the other author's expertise is in urban planning and disaster management. This separation is partially explained by the different spatial scales used by the authors for the assessment of risks - from bridge level to network/regional level. Figure 2.14b presents the bibliographic coupling by countries for this search. Compared to the one from Figure 2.13b, which was not specific to flood hazard, the USA in the blue cluster is also a predominant producer of research, but the UK in the green cluster becomes the second more relevant, having a greater contribution than China. This finding can be explained by the fact that the UK has been severely affected by floods in the past years, which has motivated growing research in this area. Likewise, other countries greatly affected by floods are also relevant in this network including Italy, France, Australia, and Germany.

In Figure 2.15a, the bibliographic coupling by authors in research on the robustness of TIS is displayed. There are five different author groups, which are somehow related to those identified in Figure 2.8. Essentially, the largest group of authors on the left belongs to the classical structural engineering community, as well as the two small groups closer to this group. On the other hand, the medium size group of authors on the right, along with the last single author, belong to the transportation engineering community. The separation of these two research communities in the co-occurrence of terms network is therefore reflected in the bibliographic coupling of authors. Figure 2.15b shows the bibliographic coupling by countries for this search. In this map, China takes the lead in the production of research, closely followed by the USA, although weakly related among them.

In Figure 2.16a, the bibliographic coupling by authors in research on the resilience of TIS is shown. There are three groups of authors on the map. The author at the top of the figure is focused on transport

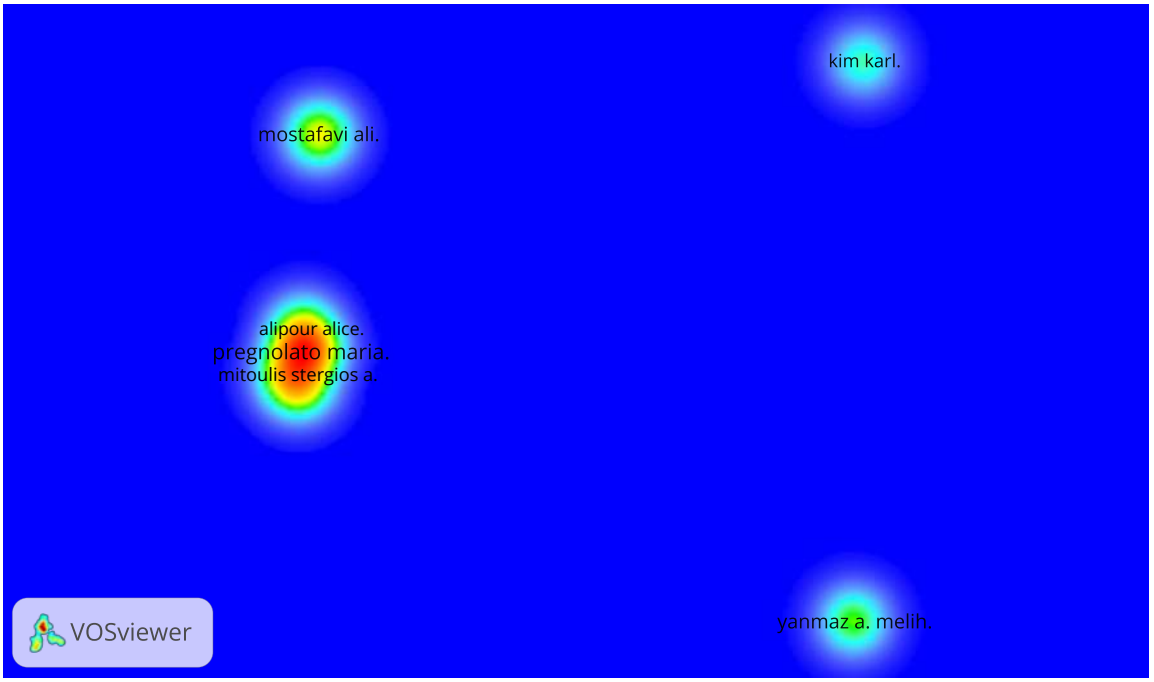


(a) Bibliographic coupling by author

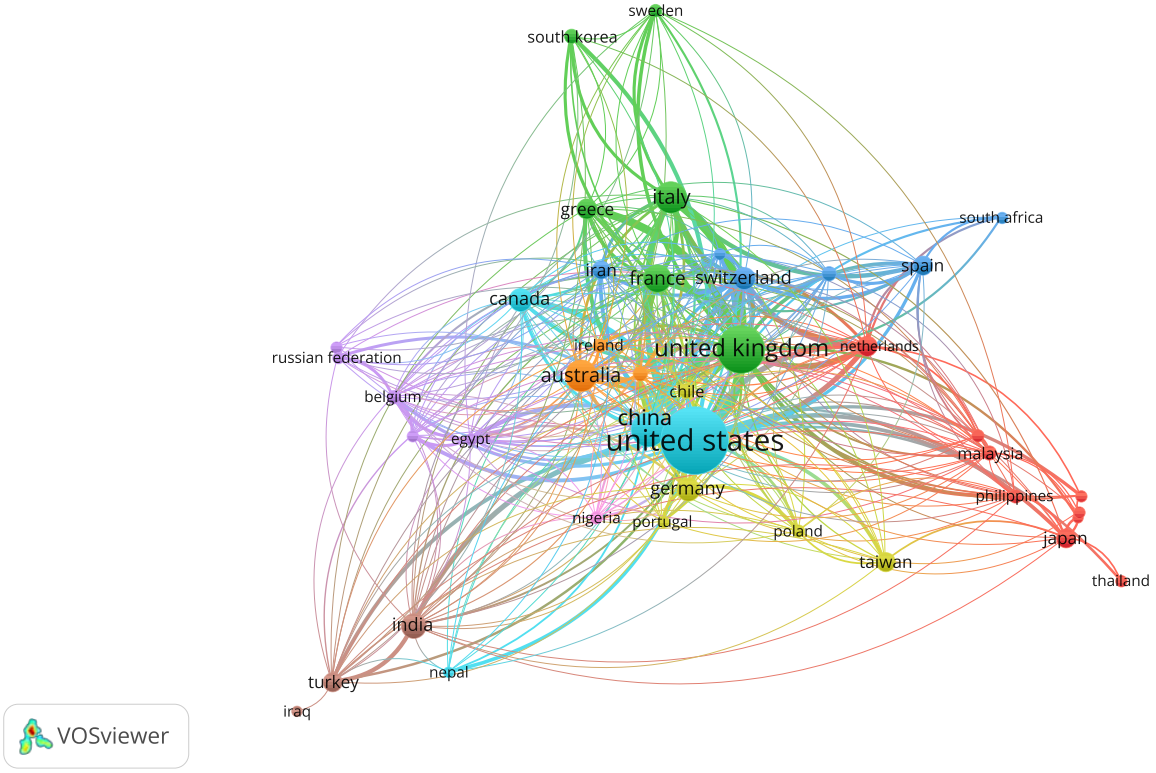


(b) Bibliographic coupling by country

Figure 2.13: Bibliographic coupling of vulnerability and risk of TIS

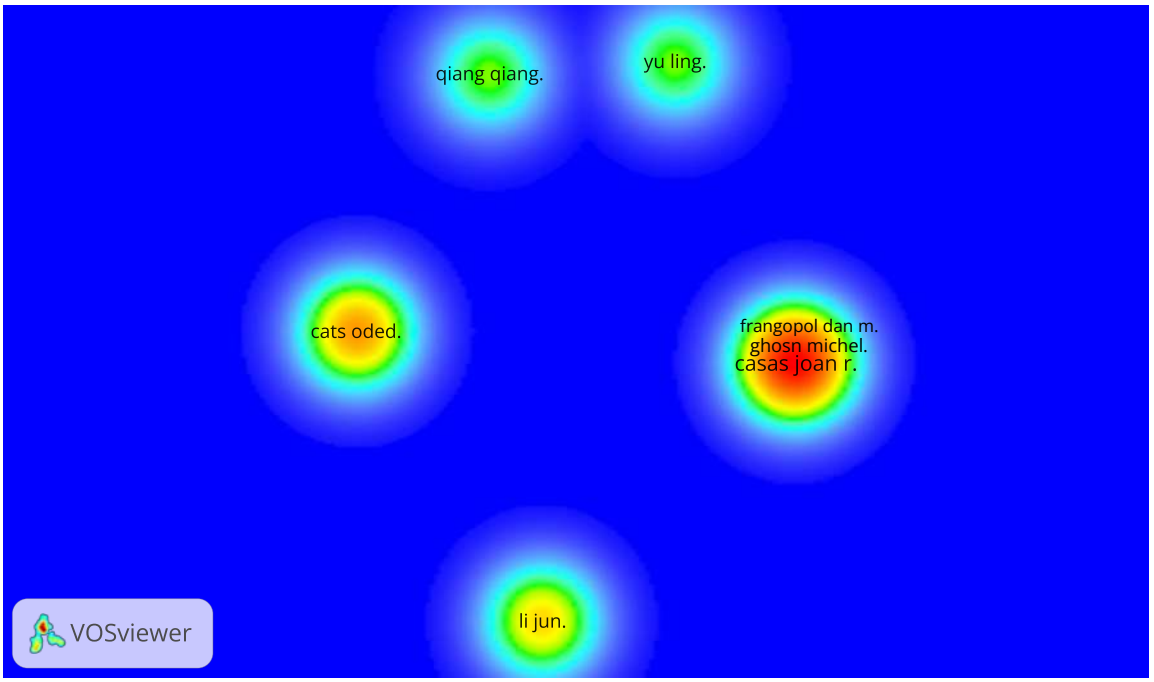


(a) Bibliographic coupling by author

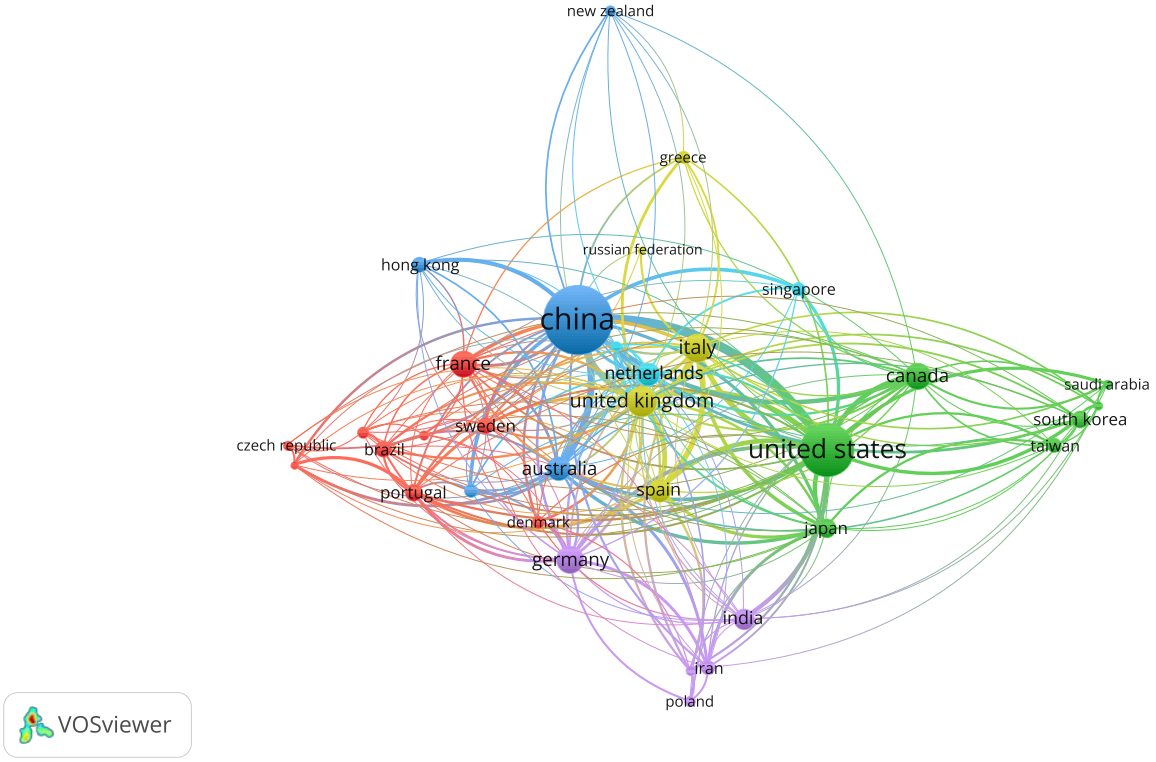


(b) Bibliographic coupling by country

Figure 2.14: Bibliographic coupling of vulnerability and risk of TIS under flood events



(a) Bibliographic coupling by author



(b) Bibliographic coupling by country

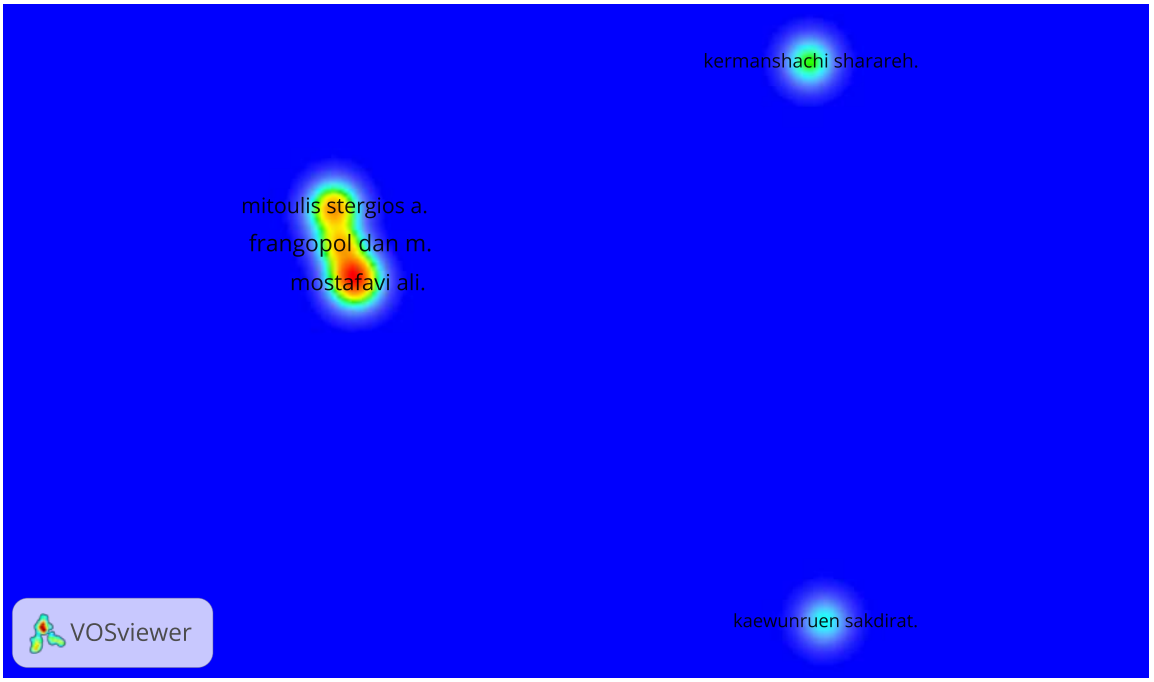
Figure 2.15: Bibliographic coupling of robustness of TIS

infrastructure resilience from a policy/governance perspective. This might explain the distance with the largest group of authors from the left, more related to transportation and civil/reliability engineering. The last group of authors located at the right is focused on railway infrastructure resilience. Despite belonging to civil/reliability engineering research, the distance from the large group of authors may be explained by the distinct structural behavior and characteristics of railway components and assets, which makes their bibliographic references dissimilar. The bibliographic coupling by country for this search is displayed in Figure 2.16b. The two dominant producers of research are the USA and China, followed by Italy and the UK.

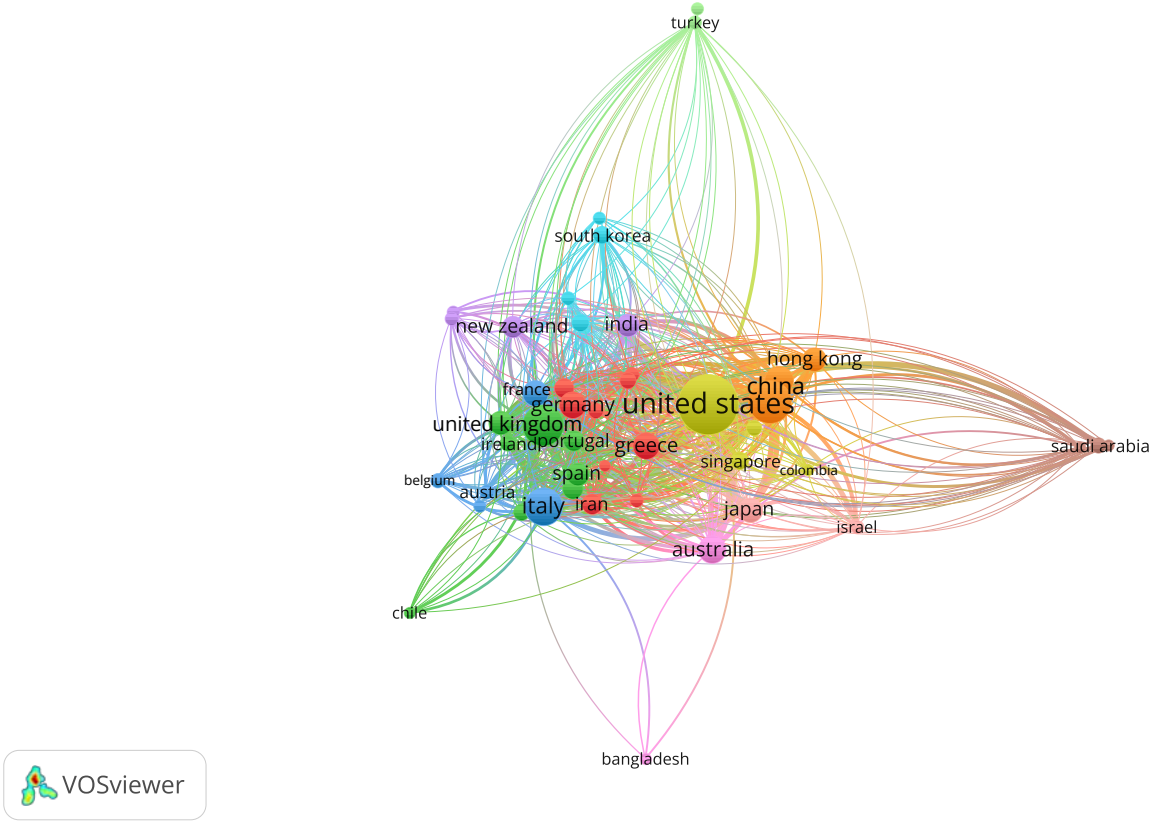
In Figure 2.17a presenting the bibliographic coupling by authors in research on the resilience of TIS under flood exposure, a similar trend to that from Figure 2.16a is exhibited. Essentially, there is one large group of connected authors on the left, along with a small group relatively close and connected to it, and three disconnected groups of authors on the right. Some of these authors are focused on adaptation planning from a policy/governance perspective, which explains their disconnection from the large group belonging to the engineering clusters. In addition, the other group is focused on pavements and underground infrastructures, which particular characteristics appear to have created some distance from research on bridges. The bibliographic coupling by country for this search is shown in Figure 2.17b. This map is dominated by what could be called the Anglo-Saxon group: USA, UK, Australia, and Canada, and to a lesser extent China.

Figure 2.18a shows the bibliographic coupling by authors in research on the sustainability of TIS. In this map, there are many groups with no connection among them. This evidences different perspectives, approaches, and diversity in research around the sustainability of TIS. This effect is also appreciated in the bibliographic coupling by country for this search in Figure 2.18b. Despite a larger contribution of research from the USA, China, and the UK, the distribution of research is quite spread around the world.

Finally, in Figure 2.19a the bibliographic coupling by authors in research on the sustainability of TIS under flood exposure is presented. However, only six authors have more than two publications in this search. Thus, the map does not represent all the expert communities but indicates that research on this topic is quite fragmented and comes from diverse research hubs. This is also evidenced in the bibliographic coupling by country (Figure 2.19b), where many countries are disconnected.

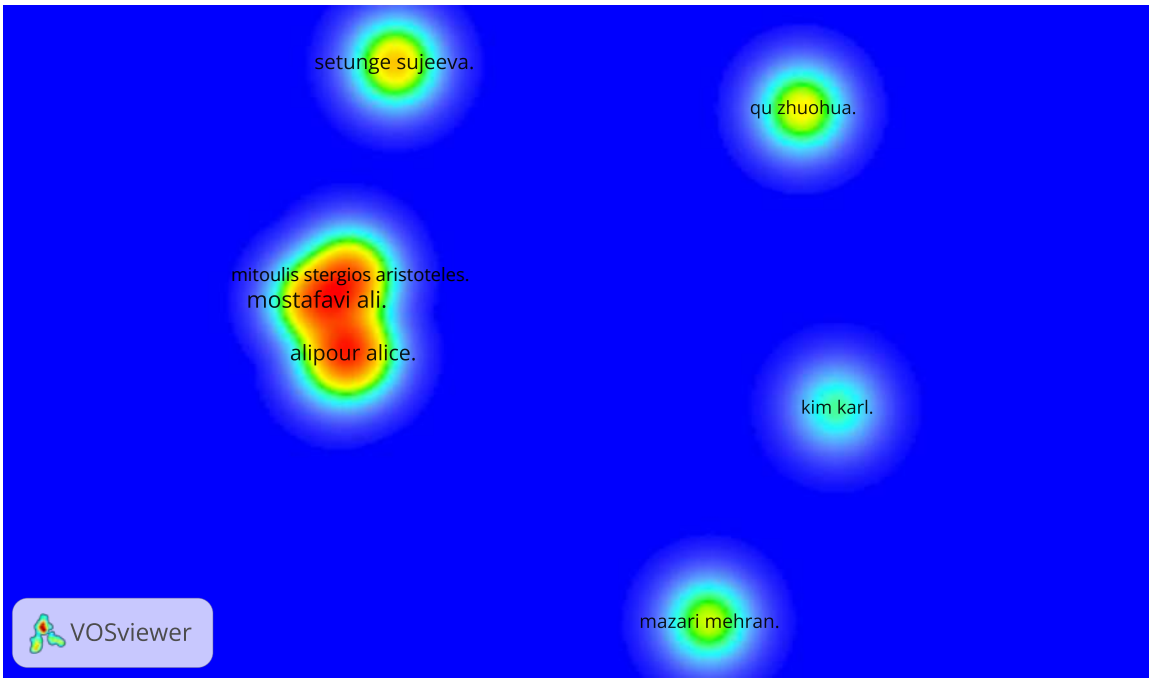


(a) Bibliographic coupling by author

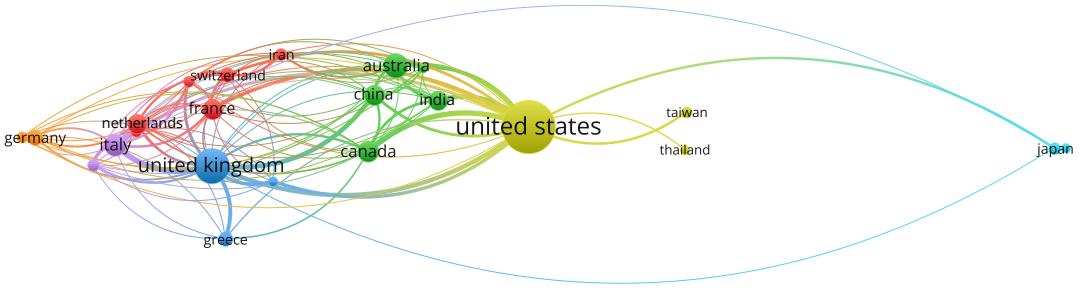


(b) Bibliographic coupling by country

Figure 2.16: Bibliographic coupling of resilience of TIS

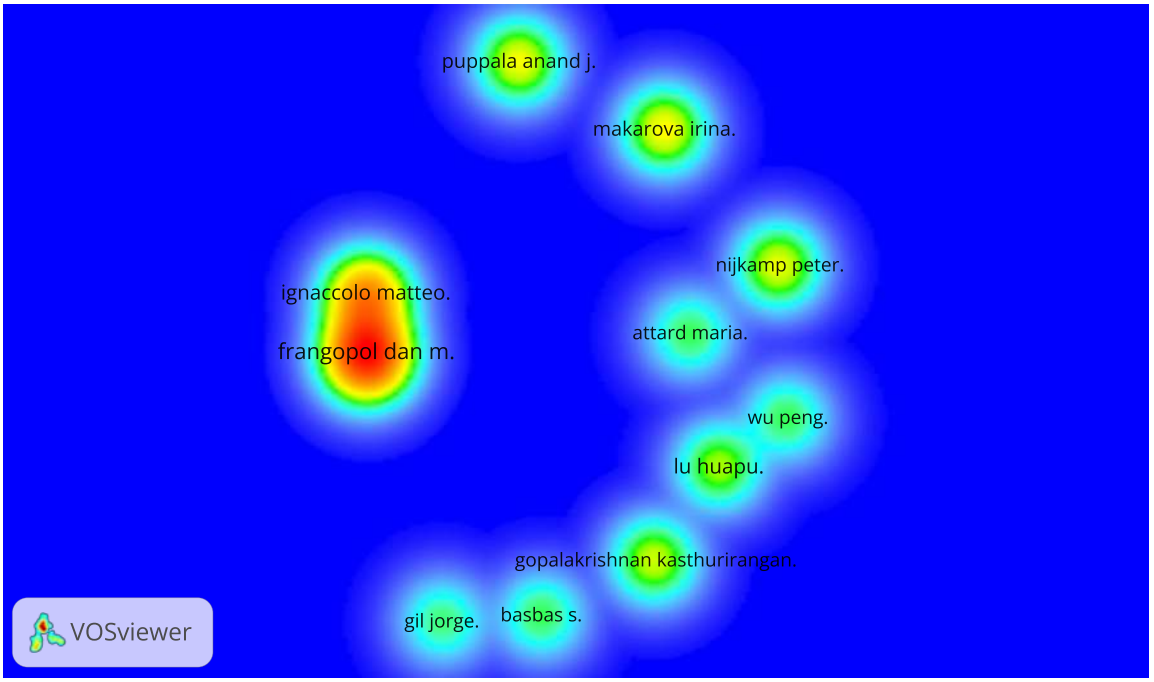


(a) Bibliographic coupling by author

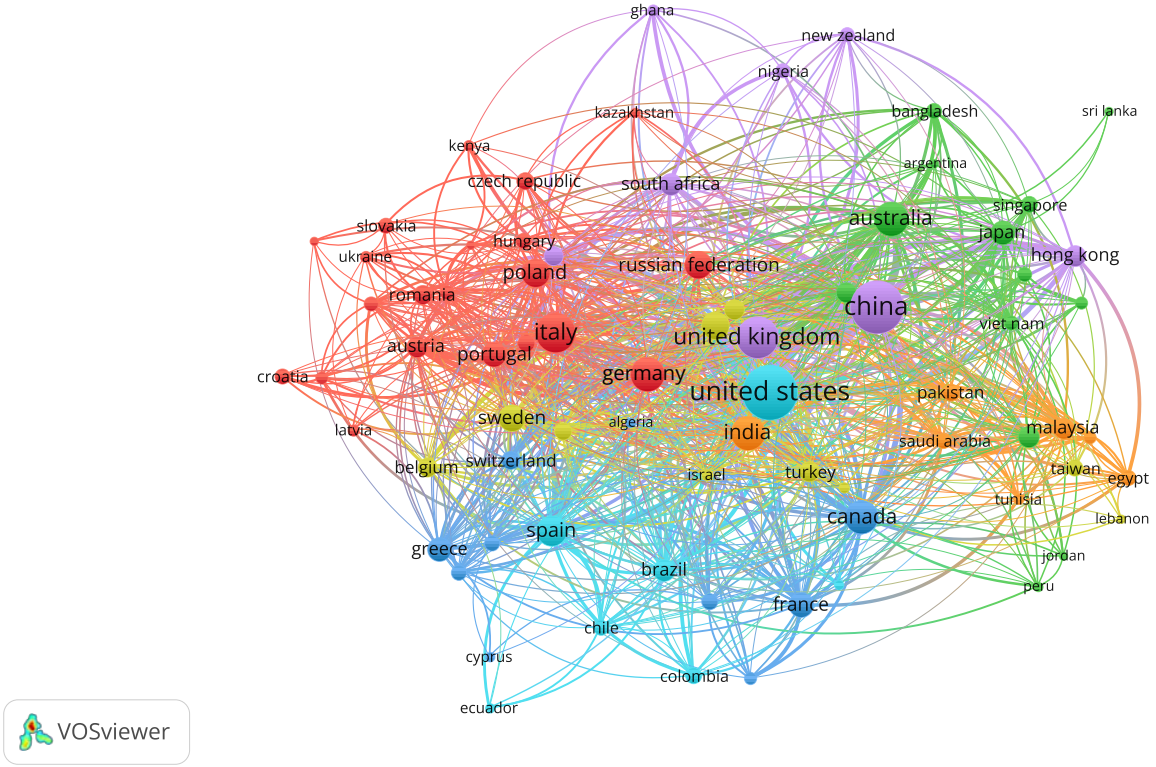


(b) Bibliographic coupling by country

Figure 2.17: Bibliographic coupling of resilience of TIS under flood events

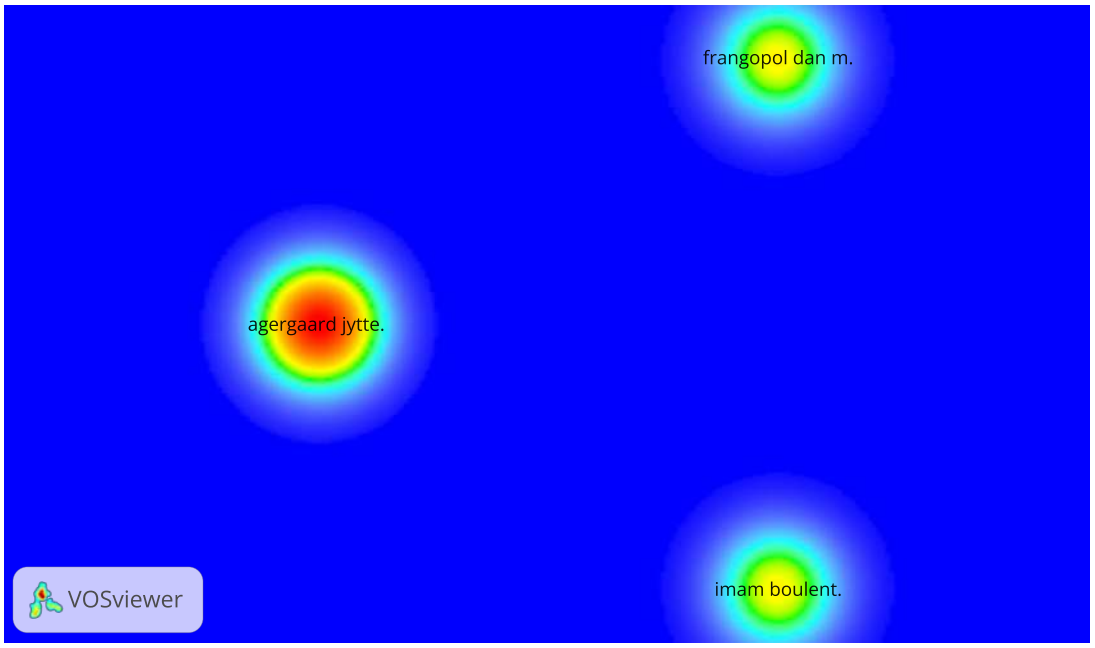


(a) Bibliographic coupling by author

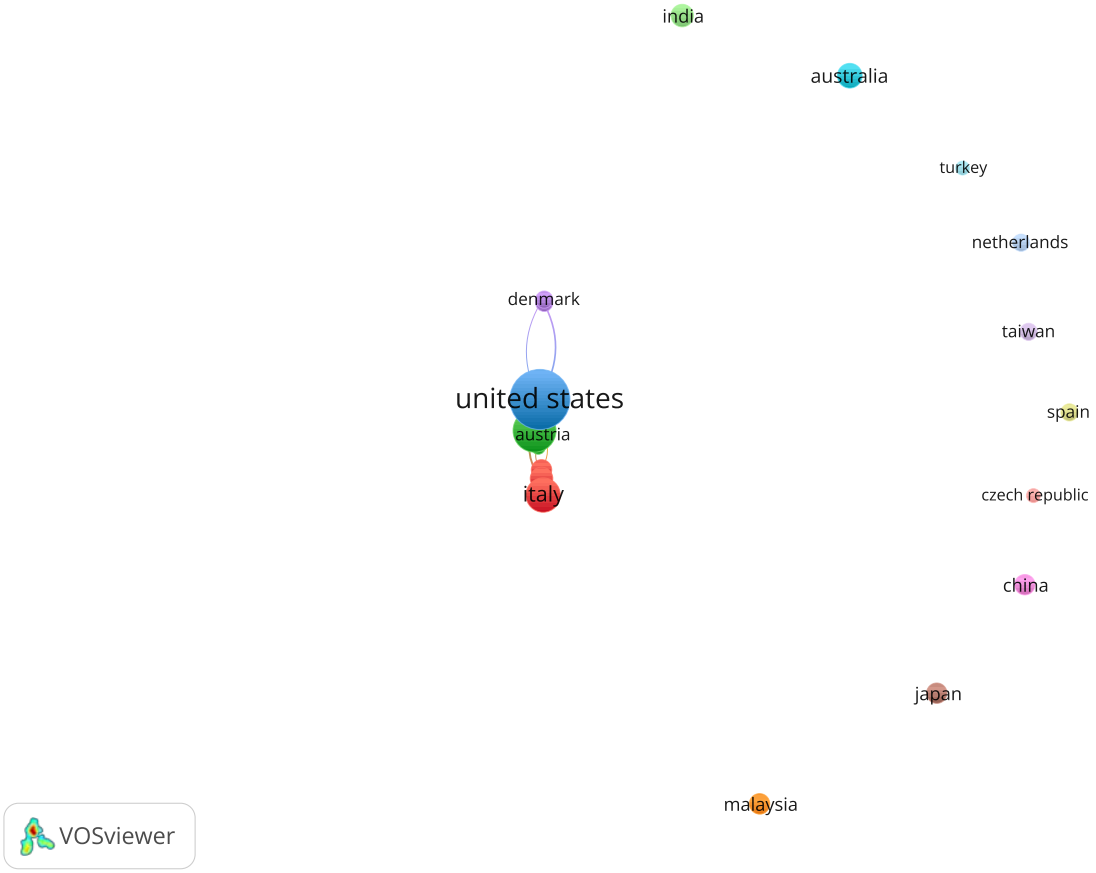


(b) Bibliographic coupling by country

Figure 2.18: Bibliographic coupling of sustainability of TIS



(a) Bibliographic coupling by author



(b) Bibliographic coupling by country

Figure 2.19: Bibliographic coupling of sustainability of TIS under flood events

2.4 Discussion

Through 24 bibliometric network maps, Section 2.3 illustrates the different disciplines, important authors, and geographic distribution in the production of research in risk, resilience, and sustainability management of TIS. Overall, the top three research domains contributing to knowledge in risk, resilience, and sustainability management of TIS are civil/reliability engineering, transportation engineering, and policy/-governance. In addition, the analysis of geographic distribution shows that the USA and China are the two major contributors to research in most of the search queries. This observation is predictable considering the larger number of researchers in these countries due to their large populations and large extents. However, countries that are more affected by floods contribute significantly to research in flood-specific search queries. This can be attributed to increased interest and government funding for research and development (R&D) aimed at understanding the risks and better preparing for these events.

One of the key problems identified in the bibliometric networks relates to the effect of the scale of the system representation. Basically, there is a substantial distance between clusters focused on research at the asset/bridge level to those focused on research at the network level, as shown in Figure 2.7-Figure 2.9. This distance suggests that there is a weak relatedness among asset- and network-level research. This effect is even more pronounced in Figure 2.7b, which evidences a potential gap in integrating flood risk and vulnerability research at the component and bridge level stemming from the civil/reliability engineering community, with research at the network/regional level coming from the transportation engineering community and the natural hazards domain. Future research developments should focus on bridging this gap related to the spatial scale of the systems modeling and how it affects optimal decision making across scales. Likewise, it would be relevant to examine how the temporal scale defined for the decision context influences the choices. For example, in the vulnerability and risk network maps (Figure 2.7), it can be seen that the civil/reliability engineering cluster includes considerations of the long-term performance of bridges (e.g., deterioration, erosion). In contrast, the resilience network maps (Figure 2.9) show a short-term view of the time scale, as the focus is on tactical management, i.e., ensuring optimal recovery and restoration in the aftermath of disaster events, without considering a long-term perspective. Conversely, the sustainability network map again shows some consideration of the long-term performance of bridges (Figure 2.10a), which is to be expected since sustainability in civil engineering has been assessed through

a life cycle perspective. These differences between the spatial and temporal boundaries of the system for addressing each concept may contribute to the apparent lack of integration of risk, resilience, and sustainability considerations for managing TIS. One observation that reflects this fragmentation is the substantial drop in the number of records in sustainability research when flood exposure is added (Figure 2.5b). This is interpreted as a lack of consideration of infrastructure safety - with respect to disturbance events such as natural hazards and the associated risks - in decisions concerning the sustainable development of TIS. This separation is also evidenced in Figure 2.7, where sustainability is an absent term in the network maps of research on risk and vulnerability of TIS. This lack of integration of risk, resilience, and sustainability from the engineering knowledge domain is also reflected in other disciplines taking the lead in the production of research. For instance, environmental science has been the greatest contributor to sustainability research of TIS under flood exposure (see Figure 2.6d). Moreover, it can be observed that the policy/governance research domain is the one attempting to integrate sustainability objectives in resilience research (Figure 2.9a), by including considerations of resource consumption of energy and water. However, the development and maintenance of TIS also have relevant impositions on the Earth system with regard to *material* consumption for construction and *emissions* of toxic substances to the environment (e.g., CO_2). None of these terms are found in the network map, which suggests that decisions about how to improve resilience are not comprehensively addressing their (positive or negative) impact on sustainability. Furthermore, the impositions to the environment generate a back-coupling between the exposures and the decisions to manage the infrastructure systems. In other words, since the management of TIS is associated with GHG emissions triggering climate change, the exposure to extreme weather events will change depending on the scenario of GHG emissions in accordance with our decisions to develop and maintain our infrastructures. Therefore, future research developments should explore further these interrelations, which enable making decisions that are safe, resilient, and sustainable.

Another issue that is observed in the bibliometric networks is the existence of multiple competing concept definitions. This is the case with the concept of robustness as observed in Figure 2.8. Essentially, the red cluster represents the systemic perspective where robustness is defined as the link between direct and indirect consequences (see Section 2.2.1.2), and the system is perfectly robust if consequences stop at direct consequences. On the other hand, in the blue cluster corresponding to classical structural engineering, robustness is the ability of a structure to withstand extreme events without being damaged to

an extent disproportionate to the original cause [91]. This definition does not provide a specific measure of robustness and does not relate to other system characteristics, such as vulnerability and risk. Likewise, in the green cluster representing transportation engineering, robustness is defined from a design optimization perspective, where a robust solution is the one that has the best performance/accuracy. It is evident that this inhomogeneity in concept definitions hinders communication among scientific experts from different research clusters. It also may explain why robustness research is so marginal compared to the other system characteristics individually, as shown in Figure 2.5. To address this issue, future research could focus on harmonizing concept definitions, thereby potentially promoting collaboration between experts from various disciplines. Similarly, this inhomogeneity issue is exhibited in the network maps of research in the domain of resilience of TIS, where multiple competing indicators and functionality metrics to measure resilience are found in each cluster. Essentially, the transportation engineering cluster in Figure 2.9a employs various metrics related to the functionality or service provided by the transportation network for the quantification of resilience. Some of the metrics found, such as connectivity, are usually measured through graph theory and represent topological features of a transportation network, while other functionality metrics found, such as travel time, traffic flow, and congestion index, are traffic-related and measure properties related to traffic flow and system capacity in addition to topological aspects. On the other hand, the policy/governance cluster employs resilience metrics more targeted to capture socioeconomic impacts from transportation service disruptions affecting the population, e.g., loss of mobility, accessibility, availability, security, and economy. Given that both perspectives are essential for quantifying resilience, future research is needed to harmonize resilience metrics across disciplines. Likewise, they should be harmonized for all types of hazards, as it can be observed in Figure 2.9b that resilience metrics under flood exposure are less exhaustive and vary from those in Figure 2.9a.

Finally, some relevant aspects were lacking in the network maps concerning the treatment of uncertainties (Figure 2.11a), which only has a role in the civil/reliability engineering cluster. Likewise, dependence related to Knowledge, as described in Section 2.2.1.2, only has a role in the resilience engineering cluster. This can be interpreted as a knowledge transfer need since the engineering community has the available knowledge which can be extended to other research communities. Similarly, available knowledge that has been identified within the earthquake engineering community regarding the concept of fragility curves for

vulnerability and risk assessment of TIS (observed in Figure 2.7a) can be transferred to characterize the performance of transport infrastructures under flooding events.

2.5 Conclusions

Research on risk, resilience, and sustainability of transportation infrastructure systems has gained attention in recent decades as the demand for efficient and reliable TIS to promote economic growth, social welfare, and environmental sustainability has increased. However, this goal is associated with many challenges that are addressed by different disciplines as the scope of TIS has broadened from a purely technical system perspective to a socio-technical system perspective. In this sense, understanding what the research field encompasses and what potential gaps exist is critical to identifying research and knowledge transfer needs.

To this end, an exploratory study using bibliometric networks has been used to understand the current state of the art in the management of TIS, with a focus on flood hazards. For the purpose of providing the basis for searching for relevant information, a generic and comprehensive system identification of TIS was outlined. This set the baseline for conducting the bibliometric analysis of 16,395 scientific works covering more than 30 years of research. The analysis showed that research in all system characteristics of TIS had seen a consistent upward trend, with research in vulnerability and risk having the longest history and largest volume of publications, followed by sustainability, resilience, and lastly, robustness, which has received little attention. In the context of flood exposure, the trend is similar, except that resilience gains importance over sustainability. Based on the assessment of the term co-occurrence network maps, it has been identified that the top three main disciplines contributing to the research domain are civil/reliability engineering, transportation engineering, and policy/governance. In addition, the examination of the bibliographic coupling networks of countries revealed that the USA and China are the two major contributors to the research domain. Nonetheless, the UK, Italy, France, Australia, and Germany, become significant contributors within the context of flood exposure, which can be attributed to the fact that they have been greatly affected by floods in the past years, which has motivated growing research in this area.

Furthermore, the study identified potential research gaps through the interpretation of the bibliometric networks. One of them relates to the spatial scale of the system modeling, which has created a separation between asset- and network-level research. This effect is evidenced both in the term co-occurrence networks as well as in the bibliographic coupling of authors, where the distances among clusters represent a weak relatedness and lack of collaboration among them. Therefore, future research developments should aim at bridging this gap to ensure optimal decision making of TIS across scales. Nonetheless, a prerequisite to promoting collaboration among these research clusters is to have a common understanding of the different concept definitions. However, it was found in several bibliometric networks that there exists inhomogeneity in concepts, as well as a large variety of indicators and metrics used by each discipline. Therefore, harmonization of concept definitions across various disciplines is also needed to enhance collaboration among them, together with an agreement on a set of indicators and metrics that could be adequate regardless of the scale of the system and the hazard under analysis. Another research gap that should receive more attention concerns the fragmentation of risk, resilience, and sustainability research for the management of TIS. Based on the analysis of the network maps, this lack of integration could be attributed to differences in how the spatial and temporal boundaries of the system are typically defined to address each concept individually. However, the three concepts are strongly linked, and there are relevant trade-offs that should be considered when managing TIS. For instance, considering the impacts of different decision alternatives with regard to sustainability facilitates that decisions with less environmental impacts, e.g., improving the preparedness of the governance system and the capacity to recover, are preferred over alternatives imposing material consumption and emissions to the environment. Therefore, it is necessary that future research developments focus attention on the trade-offs between acceptable risks, target levels of resilience, and sustainable developments, as well as the back-coupling effects between our decisions to manage the infrastructure systems and their effect on the exposures. Finally, a need for knowledge transfer has been identified from the reliability engineering knowledge domain to other disciplines with respect to the treatment of uncertainties. Essentially, resilience and sustainability of infrastructure systems can only be meaningfully approached and modeled probabilistically, like risk and robustness, given the lack of knowledge and inherent natural variability. However, there appears to be insufficient consideration of uncertainty treatment in some research domains - especially in those analyzing the system at a large spatial scale. Thus, reliability engineering knowledge could be introduced to these navigation domains for

appropriately representing and treating all uncertainties consistently across spatial and temporal scales. Likewise, insights from earthquake engineering concerning the development of fragility curves for vulnerability and risk assessment of TIS can be applied to assess transport infrastructure performance during floods.

It should be noted that the methodology implemented in this chapter to map the current state of the art in the management of TIS was based on a bibliometric analysis that enables identifying where the main research streams are. This does not exclude that there may be scientific literature looking at some of the specific gaps identified in this analysis. Yet, the main goal was to provide a big picture of where the majority of research activities are concentrated. This chapter presents some limitations due to the selection of search terms, which were the result of the system identification followed by several trials to ensure that the obtained datasets contained relevant studies for the intended analysis. In the process, some context areas were excluded to avoid unrelated articles, but this may have led to the exclusion of actually related ones. Moreover, the inclusion of additional databases may improve the coverage of scientific literature. Still, it was herein deemed unnecessary since the database with the greater publication coverage for the research domain under study was chosen. Future work could include other types of infrastructure systems in the bibliometric analysis, such as water distribution systems and/or electricity/power systems, as a way to further investigate the potential for introducing approaches from different research navigation domains and the interdependencies among infrastructure systems.

Chapter 3

Bayesian probabilistic representation of flood events on Transport Infrastructure Systems

Abstract: Flooding can significantly disrupt transportation infrastructure, causing immediate traffic disruptions and long-term delays due to infrastructure damage, among other socio-economic impacts. However, there are large uncertainties in the estimation of flood hazard exposure, and these are frequently not properly accounted for. This chapter proposes the implementation of Bayesian probabilistic modeling techniques to establish the representation of flood events on transport infrastructure systems. The proposed approach uses Bayesian networks (BNs) as a means to integrate expert knowledge, rainfall and streamflow observations, and flow data from hydrologic and hydraulic simulation outputs. Based on recent developments in BN learning, the graph structure and the model parameters are estimated from a data-driven approach. To illustrate the proposed modeling framework, a case study in the Tagus River basin in central Portugal is considered. The case study addresses the general aspects of developing the Bayesian probabilistic model. In addition, it discusses the applicability of the BN model for real-time decision support and for evaluating the performance of exposed transport infrastructures over their service life in a changing climate. By adopting this methodology, it is possible to capture the uncertainties associated

with flood hazard modeling, as well as the spatio-temporal representation of the flood actions at transport infrastructures, which is significantly relevant for risk quantification. Moreover, as more information on hazard intensities becomes available, the implemented Bayesian approach provides the advantage of updating the probabilistic models, which is of significant importance in the context of climate change.

3.1 Introduction

Transport Infrastructure Systems are vital for the functioning of modern societies, facilitating mobility and underpinning economic stability and welfare. However, these systems are increasingly vulnerable to natural hazards, particularly flooding [36], which can cause extensive damage to infrastructure and disrupt essential services. Accurately assessing the risks of transportation networks is a complex task, augmented by the uncertainties associated with flood hazard characterization and its impact on infrastructures. Fundamentally, extreme events with large footprints introduce spatial and temporal correlations in the hazard demand on transport infrastructures [92]. Then, accurate hazard modeling requires accounting for that stochastic variability. Several works have been done in the context of the seismic risk of transportation networks accounting for this variability (e.g., [67, 93–95]). In contrast, the probabilistic spatio-temporal characterization of flood hazards for risk assessment of transportation networks has received considerably less attention. Common modeling approaches approximate flood risk using flood maps with boundaries of inundation, water depth, and flow velocities with different probabilities of exceedance, and from these, consequences to the transportation network are derived (e.g., [46, 82, 96, 97]). These flood maps represent the best estimate of inundation areas for chosen probabilities of exceedance of flood magnitudes based on hydraulic model predictions. However, they are mapped deterministically since they do not explicitly account for the multiple sources of uncertainty when deriving these maps [98]. Some of these uncertainties are aleatory, i.e., related to the natural variability in the occurrence of floods, and others are epistemic, i.e., due to lack or incomplete knowledge, which may be differentiated into model uncertainties associated with the model chosen to represent the process (e.g., choice of a hydrologic and hydraulic models, model assumptions), and statistical uncertainties associated with the parameters of the model (e.g., floodplain topography and channel cross-sections, hydraulic roughness coefficients). On the other hand, fully probabilistic approaches adopt more simplified assumptions regarding the spatial modeling of

flow intensities at several sites during the same flood. For instance, Liu et al. [99] performed flood frequency analysis (FFA) to determine the probability density function of the peak flow discharge using gauge data from stream stations at two rivers. The correlation of the flood demand acting at different bridges was introduced through peak flow discharge ratios, assuming that for bridges located over the same river channel, the flow discharge was the same. In contrast, for bridges above different branches of the same river, the flow discharge was assumed to be proportional to the area of the riverbank cross-section at the bridge location, given the total discharge in the main channel. Besides being a simplified assumption, this flood hazard assessment approach is conditioned by the flow data availability at the sites of interest. An approach that addresses this issue involves physically modeling the complete hydrological process of dendritic watershed systems. This method, frequently called rainfall-runoff modeling, has been applied to investigate the climate change impact on scour risk for bridges in a transportation network [100]. However, Liu et al. [100] considered the spatial variation among flows in different reaches by sampling in the Monte Carlo (MC) simulation the watershed outlet flow, and flows in other reaches were determined based on the ratios of the historic baseflow in each reach to the historic baseflow at the watershed outlet. The use of baseflow ratios was attributed to the fact that they are more stable than extreme flows. However, water may be overtopping embankments during extreme flows, so the ratios will not hold under these events. Finally, more complex simulation engines have been developed for probabilistic rainfall-runoff-flood modeling coupled with damages, functional losses, traffic, and restoration modeling for quantifying the risks of roadway networks [44]. However, this advanced modeling approach is computationally intensive and time-consuming, limiting the number of simulated scenarios.

This chapter introduces a methodology employing Bayesian Networks (BNs) for the probabilistic spatial representation of flood events aimed at enhancing the assessment of flood hazard exposure for transport infrastructure systems. BNs are recognized for their ability to explicitly model uncertainty in a comprehensive probabilistic framework and are especially useful for capturing the joint distribution of multiple interrelated variables [4]. Given that they provide a transparent and concise representation of causal relationships among variables, they have been broadly applied in natural hazard risk assessment (e.g., [79, 101]). Furthermore, Bayesian probabilistic approaches have the potential to incorporate new data as it becomes available for the purpose of updating the probabilistic models efficiently and consistently,

which is crucial for risk management of natural hazards [102]. Recent advancements in data-driven approaches for BN learning have further promoted their use in various natural hazard applications, such as seismic hazard modeling [4] and offshore environmental load modeling [103, 104]. Particularly for spatial flood hazard modeling, previous BN approaches have predominantly relied on extensive observational data. For instance, [105] developed a dynamic object-oriented Bayesian network (OOBN) model to assess flood risk in a Mediterranean catchment, which required data from numerous stations to predict river level changes and the time it takes for the river to recover normality. Nonetheless, applying such an approach to characterize the flood hazard is challenging in river basins with limited data availability. Addressing this gap, the methodology proposed in this chapter seeks to integrate prior domain knowledge with available observations and simulation outputs from hydrological models, thereby facilitating consistent learning of BN model structures and parameters. This approach is designed to effectively characterize flood events at various locations of interest, such as infrastructure asset locations. Additionally, the potential impacts of climate change can be examined in the suggested approach by simulating shifts in the precipitation patterns and propagating this evidence through the BN model. Although this work does not delve into detailed climate projections, a sensitivity analysis is included to demonstrate the model's capability to inform the adaptation of transport infrastructure systems to climatic changes.

This chapter is organized as follows. Section 3.2 introduces the proposed methodology, which uses Bayesian networks as a means to integrate domain knowledge, rainfall and streamflow observations, and flow data from hydrologic and hydraulic simulation outputs. For a detailed introduction to BNs the reader is referred to [106]. In this chapter, only key aspects of the BN formalism are given together with a summary of BN learning techniques. Section 3.3 presents a case study in the Tagus River basin, central Portugal, to demonstrate the methodology. Section 3.4 discusses the results and provides a comprehensive discussion of the BN applications. The chapter concludes by summarizing the main contributions of this research for risk-informed decision support and the limitations that can be addressed in future research.

3.2 Methodology for probabilistic flood representation using Bayesian networks (BN)

A Bayesian network (BN) is a probabilistic graphical model that enables reasoning and learning within complex and uncertain domains. "Reasoning" denotes the process of performing probabilistic inference on one or multiple variables within the domain of interest, such as determining the (conditional) distribution of a variable, given the observed data on other variables within the model. "Learning" in this context involves developing the BN model, i.e., defining the model structure and parameters, based on a given training dataset [104]. Taking advantage of these two properties, a methodology for probabilistic flood representation using BNs is developed as depicted in Figure 3.1. The first step in the methodology consists of building a flood hazard database, which will be used to learn the BN model. The suggested steps for building the database are justified by the frequent lack of availability of flood discharge measurements at several locations of interest within a catchment. Then, observed precipitation can be used for extracting extreme values using a peak-over-threshold method. All the precipitation events exceeding the specified threshold are used as input to run a rainfall-runoff model to estimate the flood discharge at ungauged catchments (event-based hydrological simulations) and construct the database. The rest of the hydraulic parameters, namely flow velocity and water depth, are computed using hydrologic routing methods and rating curves. More detailed explanations about the database construction are given in the following sub-chapters. The second step in the methodology involves integrating expert knowledge with structure and parameter learning algorithms to develop the BN system representation of flood events. Finally, the third step involves performing probabilistic inference over the variables of interest, given the observed data. Since the primary goal of the BN model is to characterize the flood event at each infrastructure location consistently, it is particularly relevant to determine the conditional distribution of hydrologic and hydraulic variables at each location, given the observed evidence on rainfall depth. In addition, the effects of climate change can be incorporated into this last step. Fundamentally, evidence suggests that flooding is likely to become more frequent and intense due to changes in precipitation patterns, sea level rise, early snow melt, and extreme cyclonic events [21]. Therefore, the impacts of these changes can be simulated by increasing the frequency of extreme events (e.g., [107]) and/or by increasing the intensity (e.g., [108]). Both alternatives can be introduced when applying the proposed methodology in the context

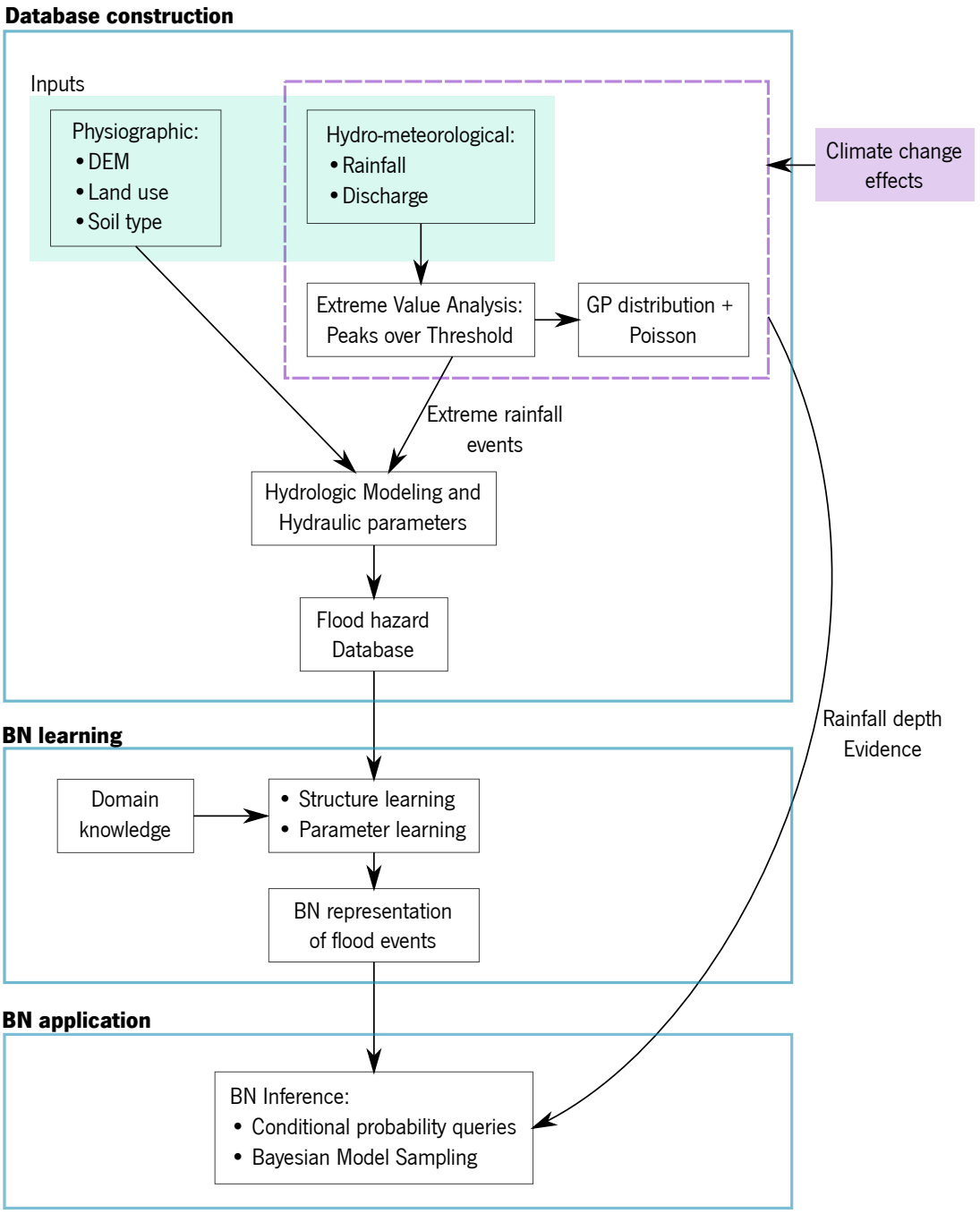


Figure 3.1: Proposed methodology for probabilistic representation of flood events

of the management of infrastructure systems. If the frequency of rainfall events exceeding the specified threshold is increased, more events will be realized during the life cycle of the infrastructure system. If the mean and/or variance of the extreme value distribution of the rainfall is increased, this new evidence can be introduced to perform probabilistic inference.

3.2.1 Extreme Value Analysis: Peak-over-thresholds

The most common approach for characterizing extreme hazardous events consists of fitting a probability distribution to observed records (e.g., rainfall depth, discharges, wind speed measurements). Extreme events from the time series of observed records can be analyzed through annual maximum series (AMS) or partial-duration series (PDS). AMS analysis is comparatively straightforward, as it uses only the largest event of each year, regardless of whether subsequent events within that year surpass the largest events in other years. In the context of floods, this method has limitations in regions characterized by semi-arid or arid conditions since the largest flood in a dry year may be zero or negligible, and it should not be considered an actual flood [109]. On the other hand, PDS analysis mitigates these issues by incorporating all events that surpass a designated threshold. Since the proposed methodology aims to construct a flood hazard database to learn the BN model, PDS is selected in this study to have simulation results from a larger number of rainfall events. Careful attention is paid to determining a suitable threshold level and identifying independent events that exceed this level (Section 3.3.2.1). In addition, PDS models typically employ a Poisson arrival model for the independent threshold exceedances, and the most common distributions used for describing the exceedances are the one-parameter exponential distribution and the two-parameter Generalized Pareto (GP) distribution [110].

3.2.2 Hydrologic and Hydraulic modeling

As previously mentioned, extreme value analysis of observed peak discharges for assessing the flood hazard is conditioned by the flow data availability at the site of interest. Then, another broadly applied approach consists of the physical modeling of the complete hydrological process of dendritic watershed systems, frequently referred to as rainfall-runoff modeling [111]. In the proposed approach, rainfall-runoff modeling is conducted using the Hydrologic Engineering Center-Hydrologic Modeling System (HEC-HMS) developed by the U.S. Army Corps of Engineers (USACE) [112]. HEC-HMS is a generalized modeling system designed to represent a variety of watersheds by decomposing the hydrologic cycle into manageable segments and delineating boundaries for the watershed under study. Several mathematical models are available to represent each hydrologic process, such as the computation of runoff volume, direct runoff,

baseflow, and channel flow routing. Selecting the appropriate models requires a comprehensive understanding of the specific watershed characteristics and depends on the study's objectives, e.g., how much detail and degree of accuracy is required [112]. Particularly for flow routing, the most appropriate method depends on several considerations, such as study constraints, data availability, output requirements, and physical considerations. For instance, the Muskingum-Cunge method combines the conservation of mass and the diffusion representation of the conservation of momentum. In this method, the routing parameters are recalculated every time step based on channel properties (length, slope, Manning's roughness coefficient, cross-sectional shape) and the flow depth. This method can account for floodplain effects since it computes the hydraulic properties of the overbank separately from the main channel. However, if there are significant backwater effects, i.e., an increase in the upstream water surface elevation resulting from, e.g., confluences, bridges, hydraulic structures, and other obstructions, a hydraulic model using, e.g., the Hydrologic Engineering Center-River Analysis System (HEC-RAS) [113], or the 2D diffusion wave method in HEC-HMS should be used to simulate this effect [112]. Both methods offer great accuracy in modeling complex flow patterns since they account for behavior variations on a grid-cell basis throughout the system. Yet, they require high-quality data inputs and significant computational resources to solve the Saint Venant equations. In this study, the Muskingum-Cunge routing method is selected since high-resolution data to develop an appropriate subgrid model is unavailable (e.g., high-resolution topographic data). This simplified method makes it possible to simulate many flood events, which is one of the study's objectives, and propagate hazard uncertainty. Nevertheless, it is assumed that backwater effects are negligible.

3.2.3 Bayesian networks (BNs)

The probabilistic framework of BNs has its source in the theorem postulated by Reverend Thomas Bayes (1702–1761), which outlines the method for updating probabilities when new evidence emerges. BNs combine probability theory with graph theory, representing probabilistic dependencies through an acyclic graphical model. In a BN model, the graph's nodes symbolize the random variables, and the presence or absence of edges between these nodes indicates the conditional dependencies or independencies among these variables [4]. In short, a BN model consists of the following [79, 106]:

1. $\boldsymbol{X}$: a set of random variables $X_i, i = 1, 2, 3, ...$

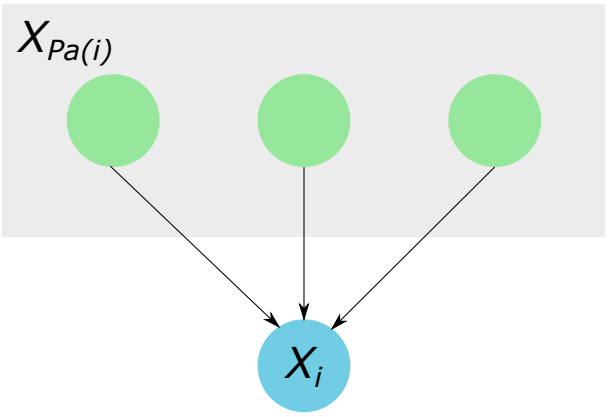


Figure 3.2: Illustration of a parent set $X_{Pa(i)}$ of a child node X_i in a BN (adapted from [4])

2. $\boldsymbol{E}$: a set of directed edges (or connections) showing dependence relations between variables. The variables $\boldsymbol{X}$, together with the directed edges $\boldsymbol{E}$, form a directed acyclic graph (DAG) $\mathcal{G}$.

3. $\boldsymbol{\Theta}_{\mathcal{G}}$: set of model parameters that define the conditional distribution of each variable X_i, given its parents $\boldsymbol{X}_{Pa(i)}$.

As depicted in Figure 3.2, the set of nodes from which edges are directed to a specific node, X_i, is the so-called parent set, $\boldsymbol{X}_{Pa(i)}$, of X_i. Thus, the conditional probability distribution of variable X_i is given conditioned on its parent set: $P(X_i \mid \boldsymbol{X}_{Pa(i)})$. It should be noted that the directions of the edges define the flow of information but do not necessarily indicate causality [4]. For discrete variables, the set of model parameters represent the probability masses of each combination of states: $\boldsymbol{\Theta}_{\mathcal{G}} = \bigcup\{P(x_i \mid \boldsymbol{x}_{Pa(i)}) = \Theta_{x_i|x_{Pa(i)}}\}$. For continuous variables, the set of model parameters corresponds to the required parameters to specify the probability density functions of the random variables [103].

Given the BN structure $\mathcal{G}$ and the set of model parameters $\boldsymbol{\Theta}_{\mathcal{G}}$, it follows from the axioms of probability theory that the joint distribution of all variables can be factorized into a product of conditional distributions as [4]:

$$P(\boldsymbol{X} \mid \mathcal{G}, \boldsymbol{\Theta}_{\mathcal{G}}) = \prod_i P(X_i \mid \boldsymbol{X}_{Pa(i)}), \tag{3.1}$$

3.2.4 Learning Bayesian networks

It follows from Eq. 3.1 that a BN can be entirely defined by its DAG $\mathcal{G}$ and its parameters $\boldsymbol{\Theta}_{\mathcal{G}}$. The process of determining the pair $\{\mathcal{G}, \boldsymbol{\Theta}_{\mathcal{G}}\}$ is called learning, and it is usually conducted in two steps: structure learning, which refers to the construction of the graph structure $\mathcal{G}$, and parameter learning, which relates to the specification of the model parameters $\boldsymbol{\Theta}_{\mathcal{G}}$. Both learning tasks may be performed using a bottom-up or top-down approach or a combination thereof [103]. In a top-down approach, also called a data-driven approach, the DAG and parameters are defined using information contained in a database. In a bottom-up approach, physical/empirical models are used, and/or domain experts are interviewed to identify the DAG and parameters [114, 115]. As previously noted, BNs are defined using conditional dependence relations and probabilistic properties without implying that the direction of the edges indicates causality in the DAG. Nonetheless, as highlighted by Pearl Pearl [116], causal BNs offer a more reliable and intuitive approach to representing knowledge about the problem. Therefore, a hybrid learning approach is recommended, where feasible, to optimally use the available and relevant knowledge and information about the system [103]. For instance, it has been demonstrated that combining data-driven algorithms with expert decisions enhances the robustness and reliability of BN models significantly [115].

The process of learning BNs from data involves identifying the pair DAG $\mathcal{G}$ and $\Theta_{\mathcal{G}}$ that could plausibly have generated the observed data D, as per the decomposition in Eq. 3.1. This task entails seeking a BN that maximizes a fitness score indicative of the BN's efficacy. However, this process must be undertaken with a keen awareness of common model selection challenges, such as overfitting and generalization. Various approaches to determining BN fitness scores have been proposed, each rooted in distinct theoretical concepts [4]. Herein, a Bayesian approach to learning is chosen, which involves that prior beliefs are defined with respect to $\{\mathcal{G}, \boldsymbol{\Theta}_{\mathcal{G}}\}$. Given the observed data D, the (current) prior distribution $P(\mathcal{G}, \boldsymbol{\Theta}_{\mathcal{G}})$ may be updated using Bayes' theorem to obtain the posterior distribution as [4]:

$$\underbrace{P(\mathcal{G}, \boldsymbol{\Theta}_{\mathcal{G}} \mid D)}_{\text{posterior}} \propto \underbrace{P(D \mid \mathcal{G}, \boldsymbol{\Theta}_{\mathcal{G}})}_{\text{likelihood}} \cdot \underbrace{P(\mathcal{G}, \boldsymbol{\Theta}_{\mathcal{G}})}_{\text{prior}}. \tag{3.2}$$

Therefore, the pair DAG $\mathcal{G}$ and $\Theta_{\mathcal{G}}$ that has the highest probability for the observed data D and thus maximizes the joint posterior is searched [4]. In this context, the data set $D = \{x_n\}_{n=1}^{N}$ is composed of N independent and identically distributed realizations.

3.2.4.1 Parameter Learning

Parameter learning focuses on estimating the parameters of a Bayesian network for a given dataset D when the corresponding DAG $\mathcal{G}$ is given. In this regard, parameter learning is generally performed by searching for a set of parameters in $\mathbf{\Theta}_{\mathcal{G}}$ that maximizes [104]:

$$P(\mathbf{\Theta}_{\mathcal{G}} \mid \mathcal{G}, D) = \frac{P(\mathcal{G}, \mathbf{\Theta}_{\mathcal{G}} \mid D)}{P(\mathcal{G})} \propto P(D \mid \mathcal{G}, \mathbf{\Theta}_{\mathcal{G}}) P(\mathbf{\Theta}_{\mathcal{G}} \mid \mathcal{G}), \tag{3.3}$$

where $P(\mathcal{G}, \mathbf{\Theta}_{\mathcal{G}}) = P(\mathbf{\Theta}_{\mathcal{G}} \mid \mathcal{G}) P(\mathcal{G})$. The likelihood $P(D \mid \mathcal{G}, \mathbf{\Theta}_{\mathcal{G}})$ factorizes according to $\mathcal{G}$, and the prior $P(\mathbf{\Theta}_{\mathcal{G}} \mid \mathcal{G})$ can be decomposed by assuming global and local parameter independence. In addition, a Dirichlet equivalent uniform prior can be used for the parent configurations in the factors, ensuring an unbiased initial estimation. Following these assumptions, Eq. 3.3 has a closed form when the available dataset D is complete [117].

3.2.4.2 Structure Learning

Taking basis in Eq. 3.2, structure learning is generally performed by searching for a DAG $\mathcal{G}$ that maximizes [104]:

$$P(\mathcal{G} \mid D) \propto P(\mathcal{G}) P(D \mid \mathcal{G}) = P(\mathcal{G}) \int P(D \mid \mathcal{G}, \mathbf{\Theta}_{\mathcal{G}}) P(\mathbf{\Theta}_{\mathcal{G}} \mid \mathcal{G}) d\mathbf{\Theta}_{\mathcal{G}}, \tag{3.4}$$

where $P(\mathcal{G}, \mathbf{\Theta}_{\mathcal{G}}) = P(\mathbf{\Theta}_{\mathcal{G}} \mid \mathcal{G}) P(\mathcal{G})$, and the prior over structures $P(\mathcal{G})$ are frequently assumed to be uniform. It is evident from Eq. 3.4, that structure learning is not possible without considering the parameters $\mathbf{\Theta}_{\mathcal{G}}$ of the BN model. Thus, $\mathbf{\Theta}_{\mathcal{G}}$ has to be integrated out of the equation to make $P(\mathcal{G} \mid D)$

independent of any specific choice of $\boldsymbol{\Theta}_{\mathcal{G}}$ [117]. As previously stated, $P(D \mid \mathcal{G})$ may be expressed in a closed form when the data set is complete. However, finding a DAG that maximizes Eq. 3.4 is NP-Complete [118]. Two strategies that may be adopted to approach this issue are score-based and constrained-based structure learning methods. The former method employs heuristic search strategies, such as hill-climbing, to identify a DAG that yields a high score. Conversely, the latter method avoids establishing a goodness-of-fit metric for $\mathcal{G}$. Instead, it uses conditional independence tests on the dataset D to construct a DAG progressively, adding one edge at a time [104, 117].

3.2.5 Bayesian Inference

As previously mentioned, a BN model enables probabilistic inference on one or multiple variables within the domain of interest. One of the most common inferences made in BNs is the so-called conditional probability query. A conditional probability query evaluates the posterior distribution $P(\boldsymbol{Y} \mid \boldsymbol{E}_v = \boldsymbol{e}_v)$ of a subset $\boldsymbol{Y}$ of the variables in the BN, given a set of evidence $\boldsymbol{E}_v = \boldsymbol{e}_v$ on some of the other variables in the network. By the definition of conditional probability, the probability query can be written as [104]:

$$P(\boldsymbol{Y} \mid \boldsymbol{E}_v = \boldsymbol{e}_v) = \frac{P(\boldsymbol{Y}, \boldsymbol{e}_v)}{P(\boldsymbol{e}_v)}. \tag{3.5}$$

In Eq. 3.5, the numerator is computed from the factorization of the joint distribution $P(\boldsymbol{X})$, defined by the BN, by marginalizing out the variables $\boldsymbol{W} = \boldsymbol{X} - \boldsymbol{Y} - \boldsymbol{E}_v$, which are neither query nor evidence variables:

$$P(\boldsymbol{Y}, \boldsymbol{e}_v) = \sum_{\boldsymbol{W}} P(\boldsymbol{Y}, \boldsymbol{W}, \boldsymbol{e}_v). \tag{3.6}$$

Since $\boldsymbol{Y}$, $\boldsymbol{W}$ and $\boldsymbol{E}_v$ are all the variables in the BN, each term in the summation $P(\boldsymbol{y}, \boldsymbol{w}, \boldsymbol{e}_v)$ represents one entry in the joint distribution. The denominator in Eq. 3.5 may then be computed as:

$$P(\boldsymbol{e}_v) = \sum_{\boldsymbol{Y}} P(\boldsymbol{Y}, \boldsymbol{e}_v), \tag{3.7}$$

This enables the reuse of the result of Eq. 3.6, instead of having to marginalize out both $\boldsymbol{Y}$ and $\boldsymbol{W}$ from the joint distribution $P(\boldsymbol{X})$ of all variables in the BN [117]. These considerations apply to the case where the variables are discrete. Still, integrals can replace the summations, where appropriate, for continuous variables or a combination of discrete and continuous variables [104].

Eq. 3.6 represents a sum-product method, an exhaustive computation approach for the determination of $P(\boldsymbol{Y} \mid \boldsymbol{E}_v)$. This technique needs the product of factors within the summation, followed by excluding variables $\boldsymbol{W}$ that are not of immediate interest through marginalization. Nonetheless, alternative algorithms, both exact (like the sum-product) and approximate, offer greater computational efficiency for inference. Some of these methods include variable elimination, belief propagation, particle-based techniques, and variational inference. For an in-depth explanation, see, e.g., [117].

3.3 Case Study Application

3.3.1 Study Area

The proposed framework was applied to a section of the Tagus River basin in Portugal (Figure 3.3). The Tagus is the longest river on the Iberian Peninsula (around 1100 km), and its drainage area (80,100 km^2) places it amongst the 20 largest in Europe. The lower valley of the Tagus River is where the most extreme flood events in Portugal have occurred in recent decades, resulting in an extensive floodplain (over 800 km^2) being completely submerged [119]. The study area is located in this region, corresponding to the Lower Tagus basin, the Almonda River basin, and the Alviela River basin, which drain a total area of 970 km^2 (see also Figure B.10).

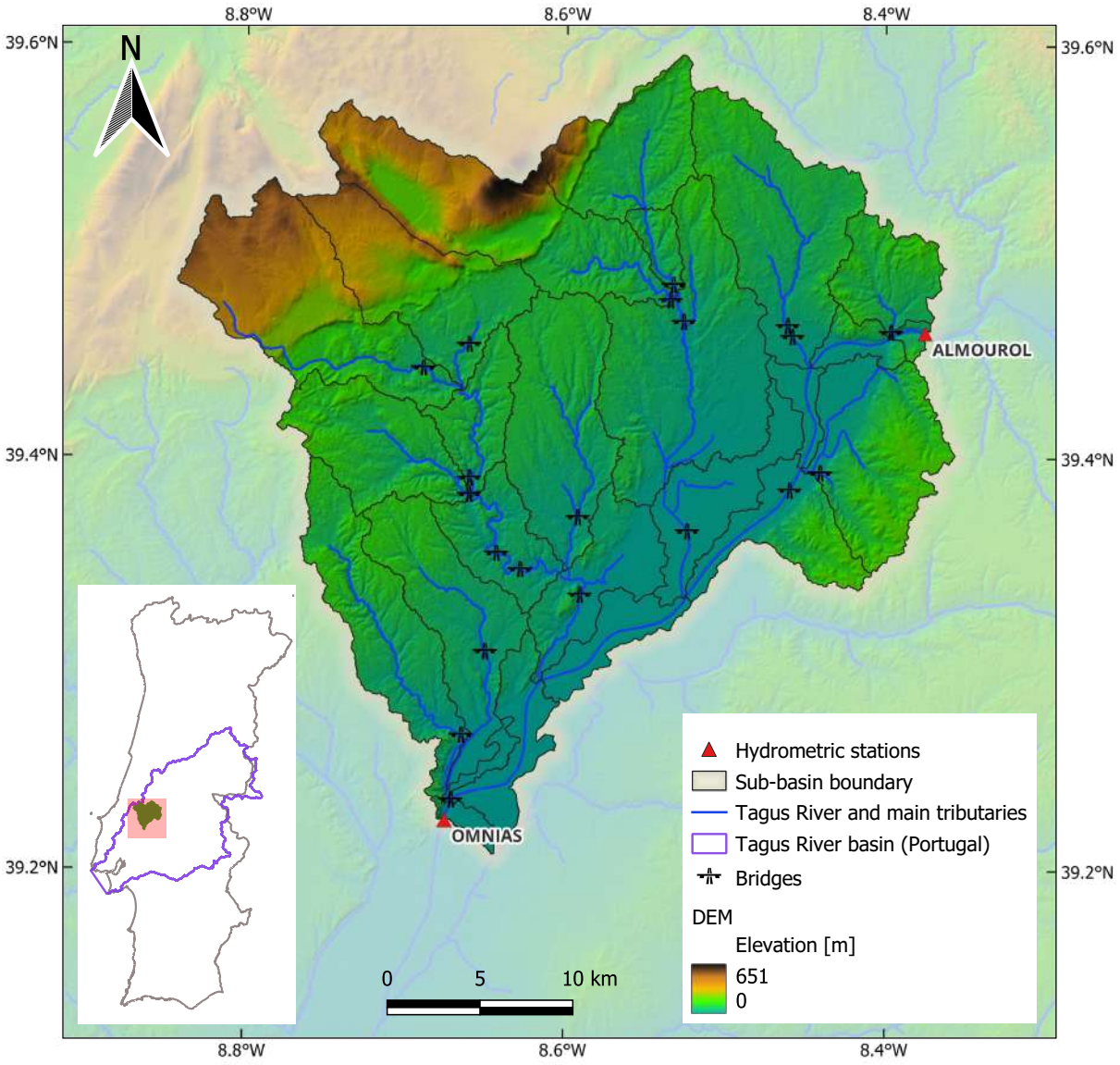


Figure 3.3: Location of the Central Tagus River basin and data observation locations (hydrometric stations). Source data: [5–7]

3.3.2 Data and Methods

The input data for the flood model building can be categorized into hydro-meteorological (rainfall and discharge) and physiographic (digital elevation model, land use, soil type) databases. Regarding the hydro-meteorological inputs, the National Information System for Water Resources (SNIRH) in Portugal provides access to the data recorded at hydrometric and weather stations on its website [5]. Two hydrometric stations are located within the study area, namely Almourol (station ID: 17G/02H) and Santarém/Ómnias

(station ID: 18E/04H) (see Figure 3.3). Almourol station is located upstream of the study area and defines the boundary conditions of the hydrologic model. Ómnias station is located downstream and coincides with the outlet of the hydrologic model. Discharge and stage time series data recorded at these stations have been available since 1973. However, Ómnias station has been discontinued in 2012. Therefore, the available period of records is used to calibrate the model (see Appendix B). Rainfall data is collected from the Chouto weather station (18G/01G), which corresponds to the most representative station for the central Tagus basin applying the Thiessen Spatial Interpolation Method [23] (see Figure B.2). Regarding physiographic data, the Digital Elevation Model (DEM) is derived from the Shuttle Radar Topographic Mission (SRTM) by SAR Interferometry, in an approximate resolution of 30 m, pre-processed for Portugal from NASA Earth Data [120]. The characterization of the sub-basins in terms of land use and soil type was done through the Curve Number (CN), a dimensionless parameter from the Soil Conservation Service (SCS) [28]. The CN value reflects the combined effects of soil type, vegetation cover type, land use, and the soil's antecedent moisture conditions (AMC) on runoff generation. APA provides the CN digital map for Portugal [121], corresponding to average antecedent moisture conditions (AMC_{II}).

3.3.2.1 Extreme Value Analysis: POT

As mentioned in Section- 3.2.1, the peaks-over-threshold (POT) method is selected for the extreme value analysis to include a larger number of rainfall events in the flood hazard database construction. Essentially, to extract the extreme values of POT, a threshold is chosen, and values higher than the threshold are selected. Then, these selected values are "declustered" to ensure the statistical independence of rainfall events. This is achieved by specifying a minimum distance between adjacent clusters, retaining only the maximum value within each cluster for analysis. For example, setting a minimum distance of 12 hours implies that clusters of exceedances separated by at least this duration are independent and identically distributed (IID). Such an assumption is necessary for describing the exceedances using either an exponential or GP distribution [8, 110]. Given that the selection of the threshold and declustering distance significantly influence the results, several tests can be performed to determine a suitable threshold value, e.g., mean residual life, parameter stability, and return value stability plots. To this end, pyextremes, a

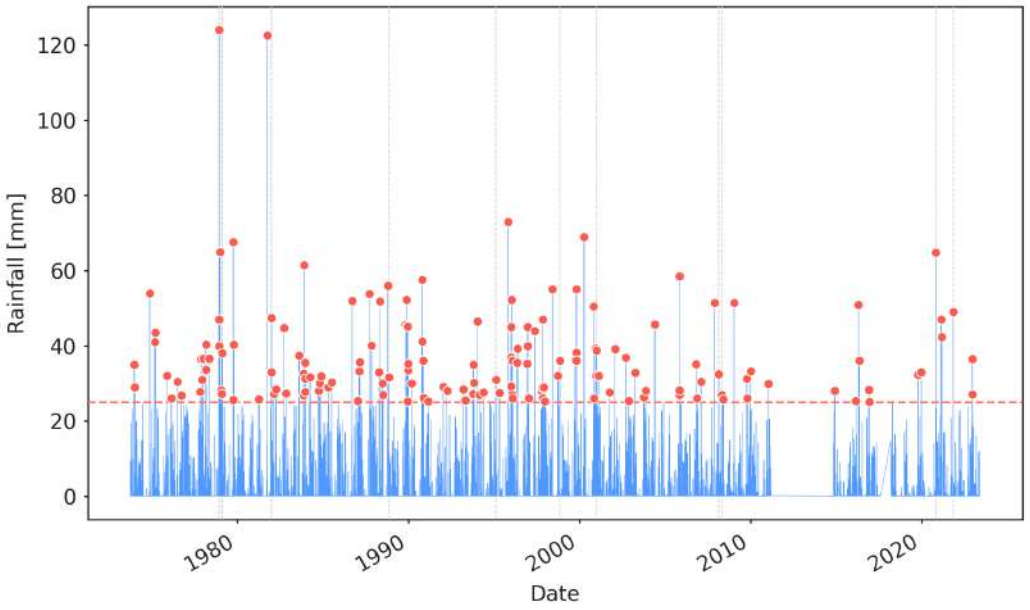


Figure 3.4: Daily rainfall at Chouto weather station exceeding a threshold of 25mm (generated with [8])

Python library that performs univariate extreme value analysis (EVA), is used to help with threshold selection [8]. The details regarding the analysis of different methods and the considerations for selecting the threshold are presented in Appendix B. Figure 3.4 displays the daily rainfall at Chouto weather station, where it can be observed that a total of 158 rainfall events (depicted as red dots) exceed the selected threshold of 25 mm with a 24-hour declustering distance. From this figure, it should be noted that even though rainfall data is available from 1973 until 2023, there is a period from 2011-2014 without records.

The next step is to fit an exponential and a GP distribution to the extracted extreme values. The maximum likelihood estimation (MLE) method is used to find the distribution parameters and calculate the confidence intervals using Bootstrap Monte Carlo. The distribution that best fits the data is selected using the Akaike Information Criterion (AIC). The results indicate that the GP distribution better describes the extreme values. Figure 3.5 shows the return period, probability density, Q-Q, and P-P plots resulting from fitting the GP distribution to the observed extreme values. The rainfall depth value calculated for a 50- and 100-year return period corresponds to approximately 100mm and 115mm, respectively. These values are comparable to those estimated by APA [25], of 101 mm and 111mm on average for the 50- and

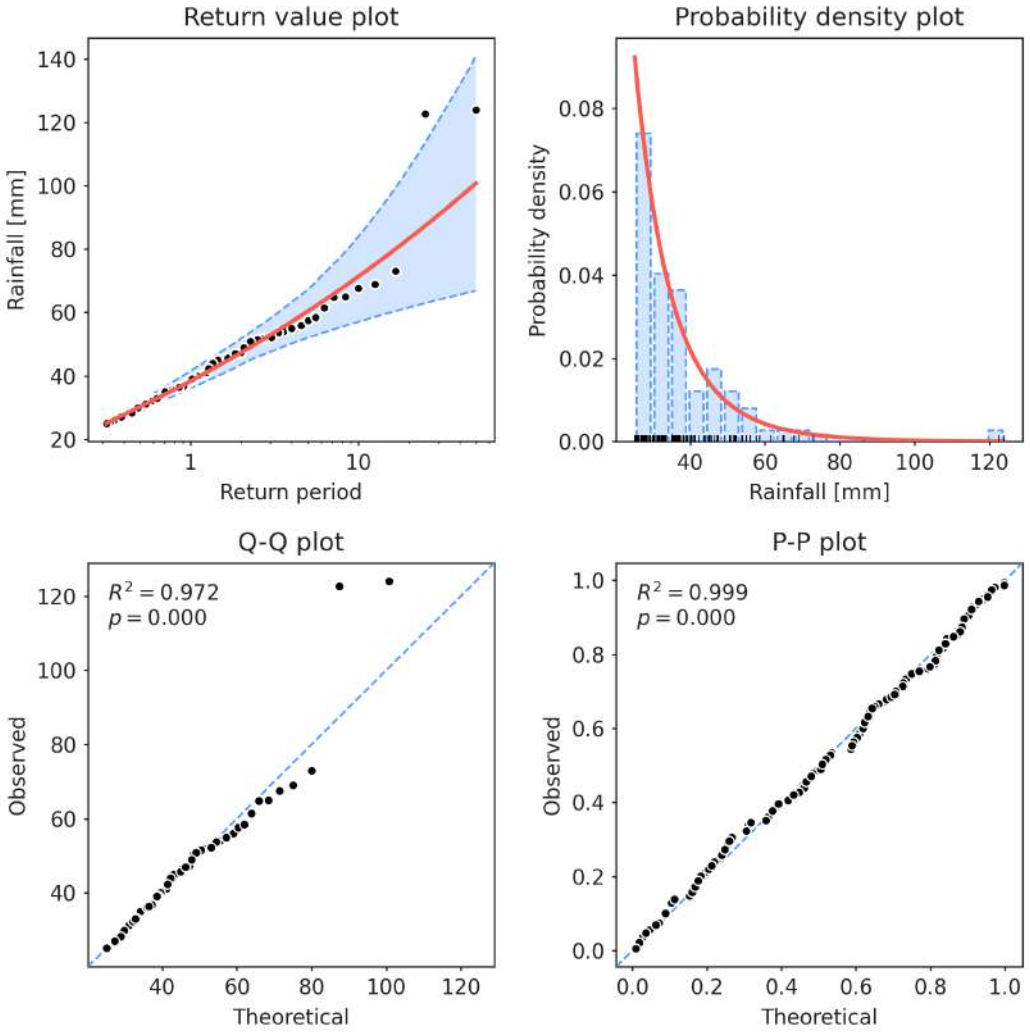


Figure 3.5: Diagnostic plot of the GP distribution fitting to observed extreme values (black dots), including return values, PDF, Q-Q, and P-P plots (generated with [8])

100-year return period, respectively, for the sub-basins located in the study area. These estimations were analyzed through AMS and fitted to a Gumbel distribution, which indicates consistency and confidence in the validity of the extreme value estimates despite the applied method.

3.3.2.2 Hydrologic Model

As stated in Section 3.2.2, this study uses the HEC-HMS hydrological model, which has been widely applied for flood hazard modeling, including the management plan of the Tagus basin [25]. The conceptual basin model was built using the Digital Elevation Model (DEM) and the physiographic characteristics of the basin with the support of QGIS software. The resulting basin model was divided into 25 sub-basin elements and 14 reach elements (refer to Appendix B for the full list of hydrologic elements and Figure B.11 for their identification). Based on the basin characteristics, the objectives of this study, and the data availability, the most appropriate methods for simulating the hydrological processes critical for quantifying and predicting flood flows were selected [122]. Table 3.1 summarizes the methods chosen and the corresponding simulation parameters. It can be observed that event simulation methods were selected over continuous simulation methods since the main objective of the hydrological model is to simulate the response of the watershed to specific extreme precipitation events. These methods include the Specified Hyetograph method to define the exact rainfall time series to use at the sub-basins, the Soil Conservation Service (SCS) Curve Number loss method for calculating runoff volume through precipitation losses, the SCS Unit Hydrograph transform method for direct runoff modeling, the Recession Baseflow method to represent the gradual subsurface drainage of water from groundwater storage into channels, and the Muskingum-Cunge routing method for channel flow modeling. In addition, a source element is added to represent the boundary conditions of the basin model, i.e., the inflow from the upstream region of the river basin that was not explicitly included in the model, using the observed flow at Almourol station. As specified in Table 3.1, some simulation parameters can be derived from direct observation or physically measured from watershed and stream characteristics. For the rest of the parameters, a sensitivity analysis was performed by running several simulations and testing different parameter values to examine their impact on the predicted streamflow. It was found that the Curve Number (CN) had the most significant influence on the simulation results, which coincides with the findings of previous studies (e.g.,[122]). Therefore, the CN values are calibrated based on a range of possible values according to the land surface characteristics, particularly the antecedent soil moisture condition (AMC), which depends on the accumulated rainfall in the five preceding days [28] (see Table B.4). For the remaining parameters, values from the literature were adopted (as indicated in Table 3.1). The model was calibrated

and validated against observed discharge time series at Ómnias station to ensure that it satisfactorily reflects the hydrologic response of the study area. The performance of the hydrologic model was evaluated through the Nash-Sutcliffe efficiency (NSE) indicator and the percentage of bias (PBIAS). In the verification phase, an average PBIAS of 18% is obtained, which indicates good model performance, while the average NS value is 0.46, which represents a satisfactory model performance, according to the model evaluation guidelines provided in [123]. Further explanation regarding the hydrologic modeling processes and model calibration and evaluation can be found in Appendix B.

Table 3.1: HEC-HMS components, methods and parameters

Model Component	**Method**	**Simulation parameters**	**Value**
Meteorological	Specified Hyetograph	Rainfall time-series	Rainfall observations [5]
Loss (runoff volume)	SCS Curve Number	Initial abstraction	Considered null [122]
		Curve number	Calibration process [121]
		Impervious	Considered null [122]
Transform (direct runoff)	SCS Unit Hydrograph	Lag time	Watershed characteristics [124]
Baseflow	Recession	Initial discharge	Streamflow observations [5]
		Recession constant	From literature [112]
		Ratio to peak	From literature [112]
Routing (channel flow)	Muskingum-Cunge	Length	Streams characteristics
		Slope	Streams characteristics
		Manning's coefficient	From literature [125]
		Cross-sectional shape	Streams characteristics

Finally, the simulation outputs of the hydrologic model for the 158 rainfall events are used to construct the flood hazard database. The variables selected to characterize the flood event are summarized in Table 3.2. In addition to rainfall depth (R_D), rainfall duration (R_W) is included in the database since it affects the peak discharge and the time to reach this peak. Similarly, the hydrograph duration (Q_W) is recorded along with the peak flow discharge (Q_P), given that a flood event with a long duration may increase the vulnerability of infrastructures, e.g., due to scour effects on foundations or levee breach due to a large flood volume, even under a moderate peak flow. Peak flow discharge and hydrograph duration variables are included at each hydrologic element of interest i, which matches the location of bridges

for this study. Likewise, water depth (H) and flow velocity (V) results are recorded at each hydrologic element i. Lastly, the database includes the AMC (A_M) condition in each simulation run to reflect how the degree of soil saturation and infiltration capacity influenced the runoff generated. This variable is chosen over the curve number of each sub-basin to reduce the number of variables in the database.

Table 3.2: Variables in the flood hazard database

Variable	Description	Unit
R_D	Rainfall depth	mm
R_W	Rainfall duration	min
A_M	Antecedent Moisture Condition (AMC)	AMC_I, AMC_{II}, AMC_{III}
Q_P^i	Peak flow discharge at element i	m^3/s
Q_W^i	Hydrograph duration at element i	min
H^i	Water depth at element i	m
V^i	Flow velocity at element i	m/s

3.3.2.3 BN representation

The variables contained in the flood hazard database are used to learn the BN. The first aspect to consider in the pre-processing phase is handling the continuous variables, which is crucial when using BNs in practical applications. A common approach is to assume the functional form of their distribution (e.g., [105]). To avoid making assumptions about the variable's distribution, this study implements a hierarchical clustering approach to discretization implemented in GeNIe [126], a graphical user interface (GUI) for BN model building and learning. The method starts by treating each record as an individual interval, resulting in as many initial intervals as there are data points. Later, an iterative process merges intervals based on the proximity of their mean values. Specifically, in each iteration, the two intervals with the slightest difference in their mean values are combined, thus reducing the total number of intervals by one. This process is repeated until the pre-defined target number of intervals is achieved. Figure 3.6 depicts the discretization for variables Q_P at "Almon-1" hydrologic element, and Q_P at "Alvie-1" hydrologic element. It can be observed that the hierarchical discretization with ten intervals offers a reasonable approximation of the continuous distribution probabilities (estimated using a kernel density on the variable dataset). Considering that the size of discrete BNs and the associated computational costs increase approximately exponentially with the number of discrete states of their nodes [127], ten intervals (bins) were specified

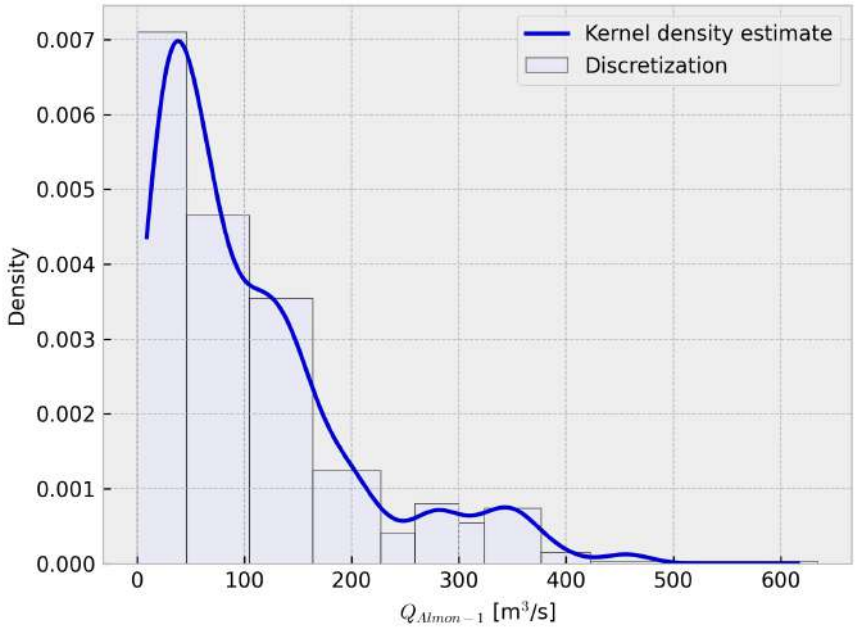
for all continuous variables. This number of intervals is deemed to satisfactorily reflect the important properties of the dataset while avoiding an escalation in computational demands. For the case of the AMC variable (A_M), only three intervals are defined, corresponding to the possible discrete values that the variable can take. Subsequently, structure learning is performed using a combined approach, i.e., the available domain knowledge and the information in the database. To this end, hill-climbing search strategies using a Bayesian Dirichlet equivalent score metric are applied to perform structure learning using functionalities from the publicly available Python Library pgmpy [128]. Heuristic hill-climbing implements a greedy local search that starts from a disconnected DAG $\mathcal{G}^{(t)}$ and defines all possible DAGs in the neighborhood that can be produced by performing single-edge manipulations (adding an edge, removing an edge, or reversing an edge). The DAG that has the highest score in the neighborhood is selected $\mathcal{G}^{(t+1)}$. The search proceeds iteratively and terminates once a local maximum is found. Given that this strategy only guarantees finding a local optimum, a tabu list of previously visited structures can be used to enforce a broader exploration of the search space. Lastly, the structure learning process is constrained by the prior causal understanding of the domain. This is achieved by providing a list of edges to the hill-climbing search as a "black list", i.e., edges that should be excluded from the search, and the resulting model will not contain any of those edges. This was applied mainly to force the direction of two related nodes. For instance, the initial graph structure learned, with no constraints, found an edge going from Q_W^i to R_W. Then, this edge was added to the "black list", and the hill-climbing search was run again. In the next run, the direction of this edge changed from R_W to Q_W^i, which aligns with the causal understanding that the rainfall event's duration affects the flood hydrograph's duration. After defining the graph structure, the set of model parameters $\mathbf{\Theta}_\mathcal{G}$ of the BN are estimated using Bayesian parameter estimation. This approach is preferred over MLE methods to avoid overfitting due to the sample size of the database, as there may not be enough observations, so the observed frequencies may not be representative. Conversely, the Bayesian parameter estimation approach starts with existing priors that reflect the beliefs before data is observed. A Bayesian Dirichlet equivalent uniform (BDeu) distribution is assumed for the prior in order to avoid encoding specific beliefs about the distributions of the variables. The hyperparameters of this distribution, often called pseudo-counts, represent the initial guess about the number of times the different outcomes occur. The sum of the pseudo-counts is the equivalent sample size, which reflects the

confidence in the priors. After data is observed, actual counts of the number of times each outcome occurred become available and can be used to update the prior beliefs [117]. Finally, the learned BN model $\{\mathcal{G}, \boldsymbol{\Theta}_{\mathcal{G}}\}$ may be used for different purposes, including inferring different (conditional) probability queries and sampling flood events over the service life of the infrastructure system for life cycle risk assessment (as presented in Chapter 6).

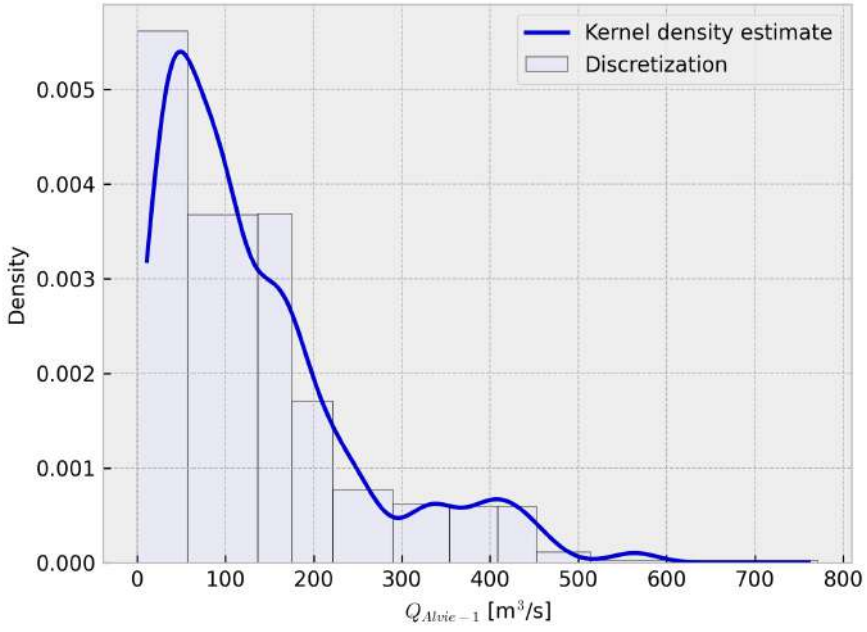
3.4 Results and discussion

The graph structure learned by applying the methodology previously described is shown in Figure 3.7. It can observed that the BN encodes a dependency between rainfall depth and rainfall duration. Moreover, as could be expected, there is a statistical dependence between the rainfall depth and the peak flow discharge, and the antecedent moisture condition and peak flow discharge. Likewise, there is a dependency between rainfall duration and the flood hydrograph duration. Dependencies among flow discharges were found between some hydrologic elements. This is the case of the flow discharge at the upstream element at Almourol ((see Figure 3.3), which strongly influences the flow discharge at the downstream elements (depicted as the edge from Q_P^0 to Q_P^1). However, not all the causal relations between flow discharges based on the spatial distribution of the hydrologic elements were included since those dependencies are expected to be learned from the database given their common parents R_D and A_M, which govern the flow discharge in small sub-basins. Finally, the BN learned the statistical dependence between the flow discharge and the water depth, and the water depth and flow velocity, per hydrological element.

Figure 3.8a displays the joint distribution of Q_P and H at "Almon-1" hydrologic element without evidence on the remaining variables. When some evidence is observed, e.g., the rainfall depth measured at a weather station, the conditional joint distribution of Q_P and H can be computed, as demonstrated in Figure 3.8b. In this case, by introducing evidence within the $[93 - 102]$ mm interval for R_D, it is observed that conditioning on this high rainfall depth, the likelihood of greater flow discharge and water depth increases. This type of conditional probability query is useful for real-time decision making. For instance, decisions regarding road closures for safety can be based on system observations during heavy rainfall, allowing for the inference of variables that directly affect the system's performance and lead to



(a)



(b)

Figure 3.6: Discretization of variables a) Q_P at "Almon-1" hydrologic element, and b) Q_P at "Alvie-1" hydrologic element

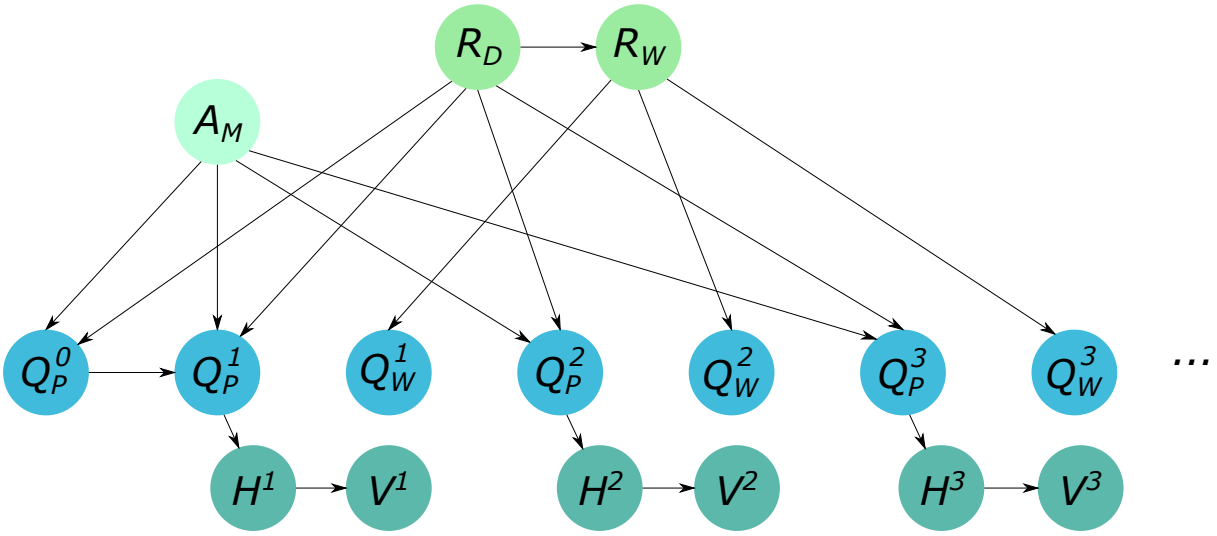


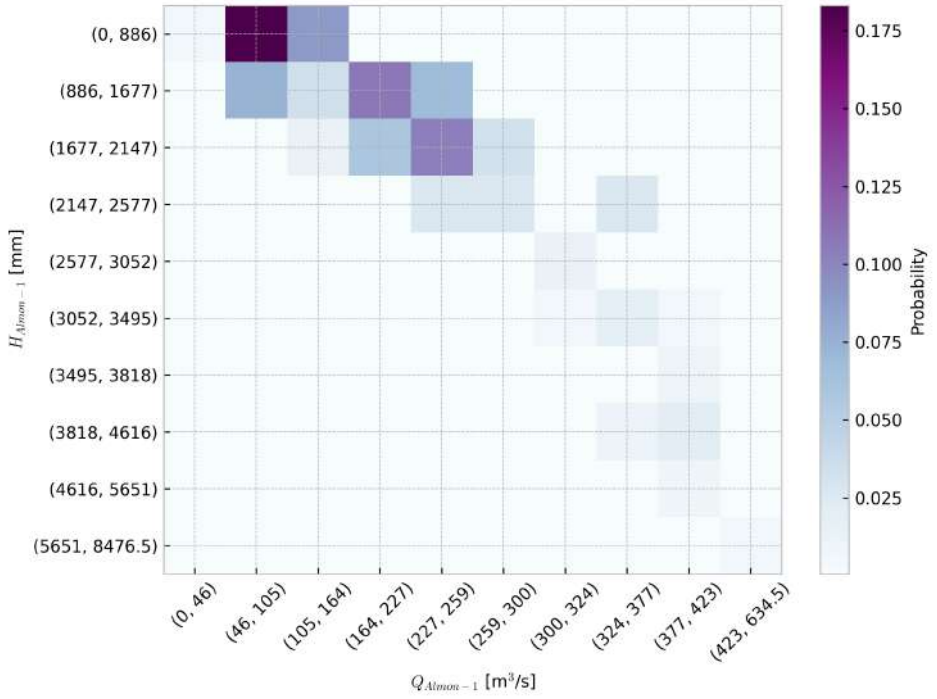
Figure 3.7: Illustration of the BN model structure learned

consequences. In addition, the BN model can be used in conjunction with the GP distribution model with Poisson arrivals for sampling flood events acting on the transport infrastructure systems over their service life. This approach is useful for implementing a scenario-based approach for risk assessment as the one suggested by the JCSS [38] (as introduced in Chapter 6). Finally, it is possible to investigate the impact of changes in precipitation patterns due to the climate system warming on flood events. This effect can be introduced in the proposed methodology by increasing the frequency of extreme events through the Poisson arrival rate, and/or by increasing the intensity and variability of the extreme value distribution, i.e., the GP distribution. While a comprehensive prediction of rainfall pattern changes would require the analysis of various climate models, such as general circulation models (GCMs) and regional climate models (RCMs), and the application of downscaling and bias correction methods (see, e.g., [108]), these procedures are beyond the scope of this thesis. Instead, a sensitivity analysis is undertaken to demonstrate how the BN model can incorporate potential future changes in rainfall depth. Figure 3.9 displays 1000 realizations of peak flow discharges at four hydrological elements sampled from the joint distribution of the BN model. Two scenarios are compared: the baseline scenario with the GP distribution parameters fitted to historical rainfall data, shown in blue, and a hypothetical scenario, shown in orange, where the GP distribution parameters are increased by 50% to simulate the potential impact of climate change. As expected, the climate-adjusted scenario results in increased variability in the flow discharges and a noticeable shift towards higher values. This type of sensitivity analysis can be used in the context

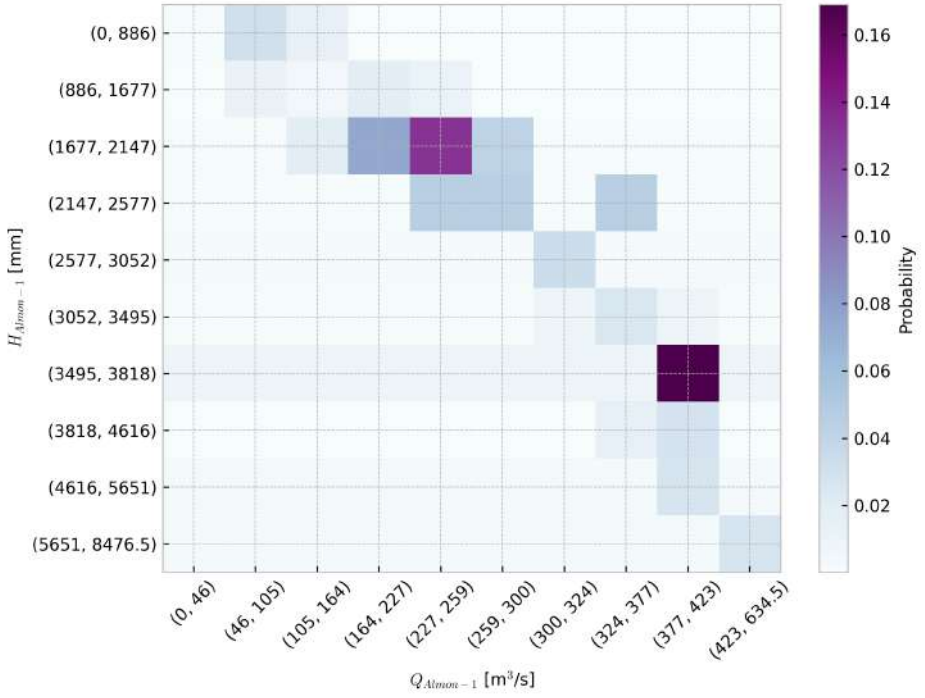
of adaptation of transport infrastructure systems to climate change.

3.5 Conclusions

A consistent probabilistic characterization of flood hazard exposure of transport infrastructure systems is crucial for estimating the associated risks. In this chapter, a methodology for probabilistic spatio-temporal representation of flood events using Bayesian Networks is outlined. The proposed approach integrates prior domain knowledge, observations collected from the system, namely rainfall and discharge records, and simulation outputs from a hydrologic model constructed for the main purpose of capturing the spatial and temporal dependencies of the development of floods within a watershed. Therefore, the advantage of this methodology is underlined for cases where there is a limited availability of spatially distributed records. The suggested methodology has been demonstrated in a real case study, where the type of approach proposed herein is essential to characterize the flood demand at different asset locations appropriately. Physiographic characteristics of the basin, together with hydro-meteorological observations, were used to build and calibrate a hydrological model and populate a flood hazard database with the responses of the watershed under past extreme rainfall events. The database was then exposed to recent developments in parameter and structure learning of BNs. The application of structure learning techniques enabled the discovery of interdependencies between rainfall characteristics and hydrological responses of the watershed system while also allowing the introduction of prior knowledge by forcing causal relationships between certain variables in accordance with the phenomenological understanding of the flooding process. In addition, parameter estimation through Bayesian methods was employed as the most adequate alternative for the database sample size, employing a Dirichlet equivalent uniform prior to ensuring an unbiased initial estimation. The developed BN model appropriately represented the complex relationships and dependencies of the flood hazard in the watershed, consistently accounting for uncertainties, thereby enabling their propagation for risk assessment of transportation networks. On the other hand, it was underlined how conditional probability queries enabled by the BN model are instrumental for real-time operational decisions, such as road closures during severe weather conditions. Moreover, the ability of the BN model to integrate changes in precipitation patterns attributable to climate warming further demonstrates its adaptability for evaluating the potential impacts of climate change on flood hazards.



(a) without evidence



(b) with evidence on the rainfall depth: $R_D = [93 - 102]$

Figure 3.8: Joint distribution of Q_P and H at "Almon-1" hydrologic element

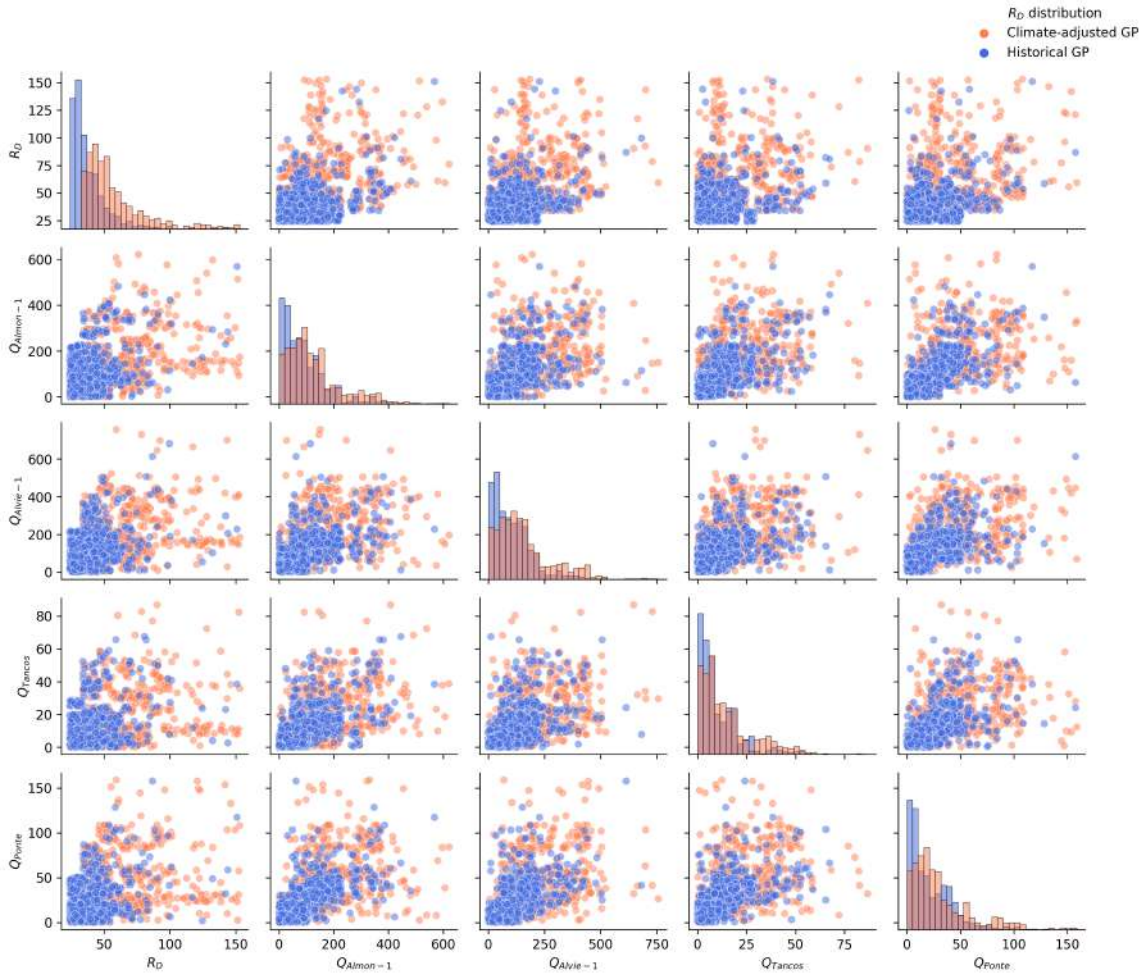


Figure 3.9: Samples from the joint distribution of the BN model given historical (blue) and climate-adjusted (orange) GP distributions

Although detailed climate projections were not within the scope of this work, the provided sensitivity analysis illustrates the model's capacity to incorporate changes in the distribution of extreme rainfall events. The analysis revealed that modifying the GP distribution parameters to reflect increased rainfall patterns resulted in a significant increase in the variability and magnitude of flow discharges. Such insights are valuable for strategically adapting transportation infrastructures to evolving climate conditions. However, future research is needed in this context since different scenarios of continued greenhouse gas (GHG) emissions can be realized in the future depending on societal developments, i.e., there is not one correct climate model but an ensemble of possible climate models. Therefore, there is a need for methodologies that allow accounting for these competing models and identifying robust decisions for designing and managing infrastructure regardless of the climate model that may realized in the future. Such a methodology is

on the agenda for future research (see Section 8.3). Finally, one limitation of this study was the use of hydrologic routing methods and rating curves rather than detailed hydraulic modeling to compute hydraulic parameters. While the Muskingum-Cunge method provided a practical solution given the constraints on data resolution and the need to simulate numerous flood events for hazard uncertainty propagation, it inherently assumes that backwater effects are minimal. Despite these constraints, the adopted methodology was appropriate for the study's objectives and available datasets and resources. Future work could enhance the model's accuracy by incorporating detailed hydraulic modeling, such as using HEC-RAS, which goes beyond the simplified routing methods by solving the full Saint-Venant equations to capture complex hydraulic phenomena such as backwater effects, hydraulic jumps, and flow transitions, pending the availability of high-resolution topographic data and increased computational capacity.

Chapter 4

Comparison of deterioration models for transport infrastructures

Based on "Comparison of forecasting models to predict concrete bridge decks performance"

Monica Santamaria Ariza, Ivan Zambon, Hélder S. Sousa, Jose Antonio Campos e Matos, Alfred Strauss

Structural Concrete

Volume 21, Issue 4, August 2020

https://doi.org/10.1002/suco.201900434

Abstract: The accuracy of forecasting models for the prediction of an infrastructure's deterioration process plays a significant role in the estimation of optimal maintenance, rehabilitation, and replacement strategies. Numerous approaches have been developed to overcome the limitations of existing forecasting models. In this chapter, a direct comparison is made between different models using the same input data to derive conclusions about their distinct performance. The models selected for the comparison were Markov, Semi Markov, Hidden Markov models, and Neural Networks (NN), which have been reported in the literature as reliable deterioration prediction models. A quality of fit was performed to measure how well the observed data corresponded to the predicted values and, therefore, objectively compare the performance of each model. The results demonstrated that the NN model accomplished the most accurate prediction. Nevertheless, all models presented differences with respect to typical values of concrete decks'

life expectancy, which is attributed to the inherent difficulties of the database. Additionally, the problem of visual inspection subjectivity was also regarded as one of the potential causes of the deviations found. Therefore, this chapter also discusses the shortcomings of current condition assessment practices and encourages future Bridge Management Systems to replace the classical methods with more sophisticated and objective tools.

4.1 Introduction

Bridge owners encounter great challenges in efficiently allocating funds to preserve and maintain their aging bridges. The ultimate goal of asset management programs consists of defining strategic and systematic processes to identify the sequence of maintenance, preservation, repair, rehabilitation, and replacement actions/interventions to ensure the safety, serviceability, and functionality of bridges within available budgets over their service life [129]. Many Bridge Management Systems (BMS) have been developed in recent decades. Typically, the architecture of a BMS consists of a database and modules dealing with condition and structural assessment, deterioration prediction, life cycle cost, and maintenance optimization [130]. Even though all modules are equally important, a reliable bridge condition assessment is needed as input for the deterioration prediction modules, which accuracy is a key element for the subsequent maintenance optimization strategies. Different condition assessment tools have been developed over the years, such as visual surveys, probing, non-destructive techniques (NDT), and structural health monitoring (SHM) [131]. Based on these assessment tools, the damage is estimated and expressed through performance indicators (PIs), which are metrics that define qualitatively and/or quantitatively the condition state of the bridge elements. Zanini et al. [131] classified the PIs into two main categories: operational and research indicators. Operational indicators are based on qualitative condition ratings, i.e., an adopted discrete scale where one value is defined as the as-built condition, and the remaining values represent the deviation from the as-built condition [132]. On the other hand, research indicators are based on a quantitative evaluation of the structural safety of the assets, i.e., computing the probability of failure for a given limit state [131]. Due to the distinction between the PIs, different forecasting models have been developed to predict the deterioration over time and the remaining service life of bridge elements.

For instance, a lot of research has been conducted on analytical deterioration models to describe common phenomena affecting reinforced concrete structures, such as chloride-induced corrosion [133–136], carbonation-induced corrosion [136, 137], alkali-aggregate reaction and freeze/thaw attack [138, 139], among others. Another approach has proposed using the reliability index as an indicator of the bridge performance and constructing a reliability profile, defined as the variation of the reliability index with time at a deterioration rate after the deterioration initiation time [140, 141]. Even though research PIs and their related forecasting models represent a more quantitative measure of the deterioration phenomena, their practical application on BMS is still limited due to the large number of assets that transportation agencies must manage. Therefore, operational PIs, i.e., condition ratings, have been predominantly the input parameters for deterioration models in existing BMS [130]. Literature on deterioration modeling approaches based on condition ratings is extensive and includes, but is not limited to, deterministic models (multiple linear regression [142], polynomial regressions [142–144], ordinal logistic regression [145]), stochastic models (Markov models [146–149], Semi Markov models [148–150], Hidden Markov models [148, 151]), Artificial Intelligence (AI) techniques (Neural Networks (NNs) [152–154], fuzzy logic [154, 155], Case-based Reasoning (CBR) [156]), Bayesian networks [157] and Petri-Nets [158]. Deterministic and stochastic Markov-chain models are the prevalent deterioration models currently used by most BMS [159, 160]. The main advantage of Markov chains over the deterministic models is their capability to reflect the uncertainty of the deterioration process while being computationally efficient and simple to manipulate networks with large a number of assets [147]. Nevertheless, it has been broadly discussed that some of the Markov-chains assumptions significantly affect the prediction accuracy [146, 149, 156]. Therefore, this study aims to objectively analyze the impact of those assumptions through a direct comparison of the prediction accuracy obtained by the Markov-chains model with other deterioration modeling approaches, namely Semi Markov models, Hidden Markov models, and Neural Networks. These models were selected as they have arisen as an enhancement/alternative to the Markov-chains model, while fulfilling desired characteristics for BMS. Furthermore, the implementation complexity of each model and the associated computational cost are also compared to provide recommendations for practice. To this end, a database containing inspection records from 766 different bridges with approximately 14 inspections (a time window of approximately 26 years) is employed to predict the evolution of concrete bridge deck conditions over time through each adopted model. The present work is organized as follows: Section 4.2

provides a description of the employed database and the conducted filtering procedure. The following sections present a brief conceptual description of the selected deterioration models and their application to the database. For a more detailed explanation of the theory of the models, the reader is referred to [148, 161–163]. Consequently, Section 4.7 compares the different deterioration patterns predicted by each model and uses some metrics to measure how well the observed data corresponds to the predicted values. Section 4.8 presents a discussion on the prediction capabilities of the models compared to that reported in the literature and the drawbacks encountered for the individual and general development of the models. Finally, concluding remarks, together with recommendations for future directions, are provided.

4.2 Database Pre-processing

The models were implemented using inspection records of bridges retrieved from the National Bridge Inventory (NBI) database managed by the U.S. Department of Transportation, Federal Highway Administration (FHWA) [27]. According to the 2017 ASCE's Report Card for America's Infrastructure [164], there were 614.387 bridges in the USA by 2016, 9.1% of which had been declared as structurally deficient. Even though, from a national perspective, the condition of the nation's bridges has improved over the past years, the highest percentage of structurally deficient bridges reached 24.9% for the state of Rhode Island. The inspection records corresponding to Rhode Island were selected for the implementation of the deterioration models in the present work, granting that the records from any other state would similarly accomplish the aim of the work. The visual inspection (VI) method is the predominant non-destructive evaluation (NDE) technique used for bridge inspections which are carried out biennially by certified inspectors [165]. The VI method examines the bridge members to identify deficiencies; for instance, detect concrete deck defects such as cracking, scaling, spalling, leaching, delamination, and full or partial depth failures. The bridge inspector is responsible for assigning a condition rating that properly characterizes the general condition of the entire component being rated based on the severity and extent of the deterioration [166]. The NBI specifies a condition rating ordinal scale from 0 to 9 (Table 4.1), where 0 represents a failed condition, and 9 represents an excellent condition. A condition rating of 4 is generally considered the threshold rating where rehabilitation or replacement measures must be performed (structurally deficient)

[129]. Separate condition ratings are assigned for each of the three major bridge components, namely substructure, superstructure, and deck. Herein, the deck ratings were selected to develop the models.

Table 4.1: Condition rating system for decks used in the National Bridge Inventory (NBI) [27]

Code	Condition	Description
9	Excellent	As new
8	Very good	No problems noted
7	Good	Some minor problems
6	Satisfactory	Structural elements show some minor deterioration
5	Fair	All primary structural elements are sound but may have minor section loss, cracking, spalling, or scour
4	Poor	Advanced section loss, deterioration, spalling or scour
3	Serious	Loss of section, deterioration, spalling, or scour have seriously affected primary structural components. Local failures are possible. Fatigue cracks in steel or shear cracks in concrete may be present
2	Critical	Advanced deterioration of primary structural elements. Fatigue cracks in steel or shear cracks in concrete may be present, or scour may have removed substructure support. Unless closely monitored, it may be necessary to close the bridge until corrective action is taken
1	"Imminent" failure	Major deterioration or section loss present in critical structural components or obvious vertical or horizontal movement affecting structure stability. The bridge is closed to traffic, but corrective action may put back in light service
0	Failed	Out of service, beyond corrective action

The database comprises inspection records from 766 different bridges by the year 2017. The earliest inspections date from 1990, covering a span of approximately 26 years. However, some bridges were built after that period (see Figure 4.1) or were not inspected biennially, resulting in a lower number of available inspections. Consequently, only bridges with the maximum possible number of records, i.e., 14 inspections, were used to build the models. It can be observed from Figure 4.1 that the predominant deck structure type corresponds to concrete cast-in-place and concrete precast panels. Hence, the database was refined to contain only concrete bridge decks.

Further filtering was applied to the NBI database to remove inconsistencies before its implementation in the models. For instance, records without condition deck ratings were removed, along with inspection records on bridges with reconstruction history, which do not characterize a natural deterioration trend. Additionally, there were cases where an improvement in the condition rating was observed. This effect can be attributed to non-recorded maintenance actions or visual inspection inaccuracy due to its inherent

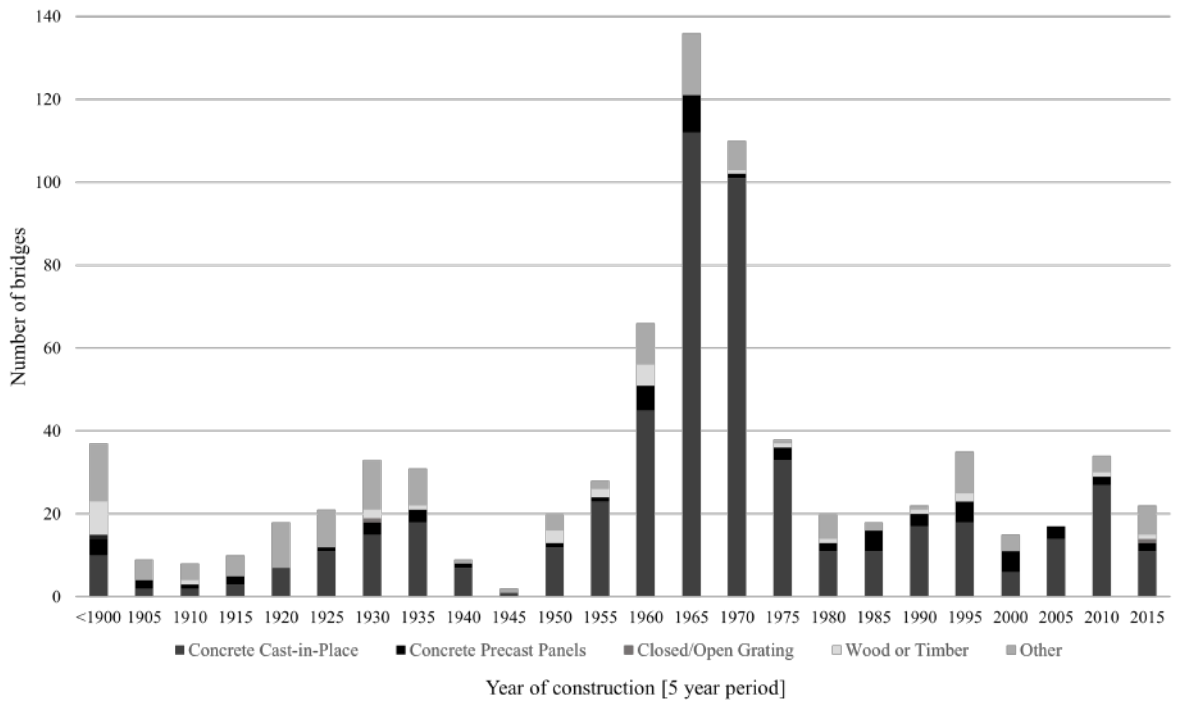


Figure 4.1: Distribution of bridges by year of construction and deck structure type

subjectivity. Both cases were herein studied, so "Dataset 1" discarded the complete sequence of observations where improved transitions were present. In contrast, a "Dataset 2" included the transitions towards better conditions up to two ratings assuming to represent the variability between inspectors [165]. All models implemented in the present work except the Hidden Markov model used Dataset 1. Finally, bridge decks with a condition rating of "2" or lower are posted for reduced load or closed to traffic, so they were removed because they are not in normal operation condition. It was also observed that there were no records on bridge decks with a condition rating of "9" following the filtering. Thus, the developed models were built to predict the deterioration from condition rating "8" to condition rating "3". Table 4.2 presents information on the distribution of bridges according to their main structure type, functional class, and recorded condition ratings for both considered datasets. It can be seen that there is a low number of very high and very low condition ratings in comparison with the number of available mid-condition ratings.

Table 4.2: Distribution of bridges according to selected parameters for each dataset

Main Structure Type						**Functional Class**[1]			**Condition Ratings**		
Kind of material and/or design			**Type of design and/or construction**								
	D1[2]	**D2**[3]		**D1**	**D2**		**D1**	**D2**		**D1**	**D2**
Concrete	18	34	Slab	12	25	RPI Arterial	4	8	CR 8	104	127
Concrete continuous	10	14	Stringer/Multi-beam/Girder	167	208	RP Arterial	7	7	CR 7	984	1260
Steel	119	149	Girder/Floorbeam	5	5	RMi Arterial	5	7	CR 6	1385	1769
Steel continuous	24	27	Tee beam	7	9	RMa Collector	9	14	CR 5	418	648
Prestressed concrete	42	56	Box Beam/Girders/Multiple	16	21	RMi Collector	2	5	CR 4	137	204
Wood or Timber	0	1	Frame	6	9	R Local	15	17	CR 3	24	24
Other	5	7	Truss - Thru	1	4	UPI Arterial	43	53			
			Arch - Deck	2	3	UP Arterial	18	25			
			Suspension	1	1	UPF Arterial	36	47			
			Other	1	3	UM Arterial	43	55			
						U Collector	19	28			
						U Local	17	22			

[1] Rural Principal (RP); Rural Principal Interstate (RPI); Rural Minor (RMi); Rural Major (RMa); Urban Principal Interstate (UPI); Urban Principal (UP); Urban Principal Freeways (UPF); Urban Minor (UM).
[2] Dataset 1 (D1) comprises a total of 218 bridges
[3] Dataset 2 (D2) comprises a total of 288 bridges.

4.3 Discrete Markov Models

Discrete Markov models are stochastic processes that describe physical systems where the probability that a system will be in a given state j at time t_2, may be obtained from a known state i at an earlier time t_1, but is independent of its history before time t_1 (i.e., Markov property) [167]. The probability of a transition between state i and j per unit of time is expressed as [148]:

$$P_{ij} = Pr\{X_{t+1} = j | X_t = i_0\} = Pr\{X_1 = j | X_0 = i\} \tag{4.1}$$

The probability of transitioning from all possible pairs (i, j) during a single period of time may be assembled in the transition probability matrix (TPM) of order (nxn), where n is the total number of condition states [148]:

$$P = \begin{bmatrix} P_{11} & P_{12} & \cdots & P_{1n} \\ P_{21} & P_{22} & \cdots & P_{2n} \\ \vdots & \vdots & \ddots & \vdots \\ P_{n1} & P_{n2} & \cdots & P_{nn} \end{bmatrix} \tag{4.2}$$

The elements of a TPM satisfy the following conditions [148]:

i $0 \leq P_{ij} \leq 1$ for all i, j

ii $\sum_{j=1}^{n} P_{ij} = 1$ for all i

iii $P_{ij} = 0$ for $i > j$

The third condition is assumed for the purpose of modeling deterioration. Therefore, the system will remain in the same state for a discrete period of time or will move to a more deteriorated state. There are different methods to estimate the transition probabilities. In this study, the percentage prediction method was used to derive the elements of the matrix [162]:

$$p_{ij} = \frac{n_{ij}}{n_i} \tag{4.3}$$

where: n_{ij} is the number of bridges that moved from state i to state j during a single period of time; n_i is the total number of bridges in state i before the transition Through the application of Eq. 4.3, the obtained TPM computed using the Dataset 1 described in Section 4.2 is equal to:

$$P = \begin{bmatrix} 0.59 & 0.41 & 0 & 0 & 0 & 0 \\ 0 & 0.87 & 0.13 & 0 & 0 & 0 \\ 0 & 0 & 0.94 & 0.06 & 0 & 0 \\ 0 & 0 & 0 & 0.93 & 0.07 & 0 \\ 0 & 0 & 0 & 0 & 0.97 & 0.03 \\ 0 & 0 & 0 & 0 & 0 & 1 \end{bmatrix} \tag{4.4}$$

By means of a discrete Markov process, the state vector Q_t, which corresponds to a vector containing the element rating for any time t, can be obtained as the initial condition state vector Q_0 multiplied by TPM to the power of t [146] :

$$Q_t = Q_0 \times P^t \tag{4.5}$$

For a newly constructed bridge element at the time of the first inspection, the initial state vector will be equal to $Q_0 = [1\,0\,0\,0\,0\,0]$ [146]. Finally, the estimation of the condition rating as a function of time $R_{(P,t)}$ is obtained as [146]:

$$R_{P,t} = Q_t \times R' \tag{4.6}$$

where R is a vector of condition ratings which for the processed database is equivalent to $R = [8\,7\,6\,5\,4\,3]$. Consequently, a deterioration curve can be constructed by computing the expected value of condition rating for each discrete time step over the lifetime of the network of bridges.

4.4 Semi Markov models

Aging is mathematically defined as an increasing probability of transition to a worse condition state as time progresses [148]. Semi Markov models are an extension of discrete Markov models where the aging effect can be captured through the random time inserted between state transitions [148]. This random time is referred to as sojourn (or waiting) time, denoted as T_{ij}, with probability density function (PDF) designated by f_{ij}, and survival function (SF) designated by S_{ij} [161]. In order to estimate the transition probabilities in a Semi Markov process, it is necessary to calculate the sum of the sojourn times in the states $(T_{i\to k})$, i.e., the time the process will take to move from state i to k, which can be expressed as [161]:

$$T_{i\to k} = \sum_{j=1}^{k-1} T_{j,j+1} \tag{4.7}$$

With $i = 1, 2, , n-1; k = 2, 3, , n$. Accordingly, the single-step transition probabilities can be determined as:

$$P_{i,i+1}^{t,t+1} = Pr\left[X\left(t+1\right) = i+1 \middle| X\left(t\right) = i\right] = \frac{f_{1\to i}(t)}{S_{1\to i}\left(t\right) - S_{1\to i-1}(t)} \tag{4.8}$$

where $f_{1\to i}(t)$ and $S_{1\to i}(t)$ are the PDF and SF of the sum of the sojourn times from state 1 to state i respectively. The TPM of the Semi Markov process is hence populated after generating all the transition

probabilities using Eq. 4.8:

$$P^{t,t+1} = \begin{bmatrix} {P_{11}}^{t,t+1} & {P_{12}}^{t,t+1} & 0 & \cdots & 0 \\ 0 & {P_{22}}^{t,t+1} & {P_{23}}^{t,t+1} & \cdots & 0 \\ \vdots & \vdots & \vdots & \ddots & \vdots \\ 0 & \cdots & \cdots & P_{n-1,n-1}^{t,t+1} & P_{n-1,n}^{t,t+1} \\ 0 & 0 & \cdots & 0 & 1 \end{bmatrix} \tag{4.9}$$

For the present work, the distribution of the sojourn times is assumed to follow a two-parameter Weibull distribution. Therefore, the PDF and SF of the sojourn times are given by [161]:

$$S_i\left(t\right) = e^{-(\lambda_i t)^{\beta_i}} \tag{4.10}$$

$$f_i\left(t\right) = \lambda_i \beta_i \ \left(\lambda_i t\right)^{\beta_i - 1} e^{-(\lambda_i t)^{\beta_i}} \tag{4.11}$$

The parameters λ_i and β_i are estimated from historical observations in Dataset 1. To this end, two intervals of time are defined, namely u and $v (u \neq v)$, and the probabilities of the bridge deck to remain in a certain condition rating i for more than u and v years are assessed, i.e., $x_{i,u}$ and $x_{i,v}$ respectively [161]. These probabilities are computed from the relative frequency of events similar to the Markov process [149], and the results for the selected intervals are shown in Table 4.3. Subsequently, the parameters λ_i and β_i are derived from the following expressions [161]:

$$\begin{cases} S_i(u) = e^{-(\lambda_i u)^{\beta_i}} \\ S_i(v) = e^{-(\lambda_i v)^{\beta_i}} \end{cases} \Rightarrow \begin{cases} \ln[S_i(u)] = -(\lambda_i u)^{\beta_i} \\ \ln[S_i(v)] = -(\lambda_i v)^{\beta_i} \end{cases} \Rightarrow \ln\left(\frac{\ln[S_i(u)]}{\ln[S_i(v)]}\right) = \beta_i \ln\left(\frac{u}{v}\right) \tag{4.12}$$

Once both parameters are evaluated for every i, the TPM for the Semi Markov process can be computed.

Table 4.3: Input parameters for the Semi Markov process

CR	$u(years)$	$x_{i,u}(\%)$	$v(years)$	$x_{i,v}(\%)$	β_i	$1/\lambda_i$	λ_i
8	30	0.000	50	0.000	0.950	3.178	0.315
7	30	0.110	50	0.028	0.950	13.029	0.077
6	30	0.396	50	0.222	0.950	32.548	0.031
5	30	0.309	50	0.149	0.950	25.361	0.039
4	30	0.592	50	0.426	0.950	59.125	0.017

4.5 Hidden Markov models

Monitoring data from historical inspections frequently contains measurement errors and selection biases [151], which affect the accuracy of the deterioration predictions. To address this issue, Hidden Markov models (HMM) have been used to incorporate the bias of the observations into the forecasting models [148, 151]. HMMs assume that there is some true condition state which is "hidden" to the observer [148]. In other words, the sequence of true states $S_1, S_2, \cdots, S_n$ at the inspection times $t_1, t_2, \cdots, t_n$ is hidden behind the sequence of the observed states $V_1, V_2, \cdots, V_n$ [148]. Therefore, considering the bias in the monitoring data allows the unobserved true condition states to be captured [151]. The sequence of the true states follows a simple Markov chain, so the probability a_{ij} representing the probability of moving to state S_j depends only on the state S_i, which can be expressed as $a_{ij} = P[q_{t+1} = S_j | q_t = S_i]$ [163]. On the contrary, the observed sequence does not hold the Markov property [148]. The conditional probability of the observations given the true states corresponds to [148]:

$$e_{ij} = Pr\left[V_k = j \middle| \, S_k = i\right] \tag{4.13}$$

These probabilities are collected in an error or misclassification matrix where $0 \leq e_{ij} \leq 1$, and $\sum_{j=0}^{n} e_{ij} = 1$ [148]:

$$E = \begin{bmatrix} e_{11} & e_{12} & \cdots & e_{1n} \\ e_{21} & e_{22} & \cdots & e_{2n} \\ \vdots & \vdots & \ddots & \vdots \\ e_{n1} & e_{n2} & \cdots & e_{nn} \end{bmatrix} \tag{4.14}$$

The probability of correctly identifying the condition state corresponds to e_{ii}, while for all $i \neq j$ there exists a misclassification reflecting the variability in the inspections [148]. This variation is attributed to the fact that the condition rating is a qualitative measure affected by the subjectivity of the inspectors. This phenomenon was investigated by the FHWA [165] who conducted a study to evaluate the reliability of the visual inspections. Forty-nine bridge inspectors completed routine and in-depth inspections of the same bridges. The results showed that 95% of the element condition ratings vary within ± 2 rating points around the mean, and 68% of these ratings vary within ± 1 rating point [165]. The error probabilities referred to as emission probabilities in the formal notation for Hidden Markov models may be assessed by expert judgment or by maximum likelihood [148]. One of the basic problems involved when using HMMs is to adjust the parameters of the model, i.e., the sequence of the states, the transition probabilities a_{ij} and the emission probabilities e_{ij}, to maximize the probability of the observation sequence given the model [163]. There is no analytical solution to maximize the probability of the observation sequence; hence, an iterative procedure such as the Baum-Welch algorithm can be used to locally maximize the observation sequence given a selected model λ, and re-estimate the model parameters $\bar{\lambda}$ until a stopping criterion is reached [163]. The mathematical description of this procedure is not herein presented, for a detailed explanation the reader is referred to [163, 168]. The MathWorks Inc. [169] function "hmmtrain" was used to estimate the transition and emission probabilities for the Hidden Markov model using the Baum-Welch algorithm. An initial estimation of the transition and emission probabilities matrices, together with the sequence of observations, are the inputs of the function. The initial guess for the transition probability matrix is computed with the same procedure described in Section 4.3 but using Dataset 2; in this manner, the model includes the inspectors' variability as explained in Section 4.2. The obtained matrix is equal to:

$$a_{ij} = \begin{bmatrix} 0.521 & 0.4455 & 0.0335 & 0 & 0 & 0 \\ 0.0014 & 0.8566 & 0.1335 & 0.0085 & 0 & 0 \\ 0.0044 & 0.0205 & 0.9044 & 0.0615 & 0.0092 & 0 \\ 0 & 0.024 & 0.0477 & 0.8747 & 0.0536 & 0 \\ 0 & 0 & 0.043 & 0.037 & 0.897 & 0.023 \\ 0 & 0 & 0 & 0 & 0 & 1 \end{bmatrix} \tag{4.15}$$

Note that the transitions to better states are allowed. Still, the increase is attributed to variability in

inspections rather than an improvement in the quality of the structure resulting from maintenance. The emission probability matrix assumes that the inspectors' misclassifications could be ± 2 condition ratings based on the FHWA findings [165]. The most likely values for the emission probabilities will be estimated through the Baum-Welch algorithm, so for the initial guess, all the non-zero elements of the matrix are assumed to be equal:

$$e_{ij} = \begin{bmatrix} \frac{1}{3} & \frac{1}{3} & \frac{1}{3} & 0 & 0 & 0 \\ \frac{1}{4} & \frac{1}{4} & \frac{1}{4} & \frac{1}{4} & 0 & 0 \\ \frac{1}{5} & \frac{1}{5} & \frac{1}{5} & \frac{1}{5} & \frac{1}{5} & 0 \\ 0 & \frac{1}{5} & \frac{1}{5} & \frac{1}{5} & \frac{1}{5} & \frac{1}{5} \\ 0 & 0 & \frac{1}{4} & \frac{1}{4} & \frac{1}{4} & \frac{1}{4} \\ 0 & 0 & 0 & \frac{1}{3} & \frac{1}{3} & \frac{1}{3} \end{bmatrix} \tag{4.16}$$

The sequence of observations corresponds to the succession of condition ratings along the years from each bridge deck. The transition and emission probabilities obtained through the Baum-Welch algorithm were:

$$\bar{a_{ij}} = \begin{bmatrix} 0.826 & 0.146 & 0.028 & 0 & 0 & 0 \\ 0.019 & 0.919 & 0.02 & 0.042 & 0 & 0 \\ 0.064 & 0.034 & 0.673 & 0.101 & 0.128 & 0 \\ 0 & 0.032 & 0.001 & 0.943 & 0.024 & 0 \\ 0 & 0 & 0.064 & 0 & 0.907 & 0.029 \\ 0 & 0 & 0 & 0 & 0 & 1 \end{bmatrix} \tag{4.17}$$

$$\bar{e_{ij}} = \begin{bmatrix} 0.091 & 0.904 & 0.005 & 0 & 0 & 0 \\ 0 & 0 & 0.999 & 0.001 & 0 & 0 \\ 0 & 0 & 0.138 & 0.808 & 0.054 & 0 \\ 0 & 0 & 0 & 1 & 0 & 0 \\ 0 & 0 & 0 & 0 & 1 & 0 \\ 0 & 0 & 0 & 0 & 0 & 1 \end{bmatrix} \tag{4.18}$$

Note that for the lower condition states, the obtained emission probabilities indicate that the true conditions are correctly observed by the inspector. In contrast, for the better condition ratings, the inspectors tend to assign lower than the true condition. This effect is in accordance with the FHWA research

[165], which concluded that inspectors are hesitant to assign high condition ratings for better condition elements. Based on the transition and emission probabilities previously obtained, the Matlab function "hmmgenerate" is used to generate random sequences of emission symbols (the observed states) and random sequences of states (true or hidden states) during a 100-year period. Then, the average of 10000 sequences of states is computed.

4.6 Neural Networks

Neural Networks (NN) are information-processing techniques conceptually motivated by the way the densely interconnected and parallel structure of the human brain processes information [152]. Several types of NN have been applied to solve the bridge deterioration modeling problem. One of the most widely used models that has demonstrated great capabilities to solve the prediction deterioration problem is multilayer perceptron networks (MLP). This model is based on fully connected, layered, feed-forward networks [152] that utilize the backpropagation technique for training. Additionally, other approaches have been developed, such as $i)$ case base reasoning, which looks for previous cases that are similar to the current problem and reuses them to solve the problem [156] $ii)$ ensemble of neural networks which is composed of a series of individual NNs working in parallel so predictions are made by collecting and combining the outputs of individual networks through a weighting process [154] $iii)$ Elman neural networks integrated with a backward prediction model which generates missing condition ratings when the input data is insufficient [153]. A MLP network has been used in the present work to model the deterioration of bridge decks based on Dataset 1. The input parameters for the network correspond to the variables that more significantly influence the condition of the bridge deck. The selection of the input variables is a crucial issue considering that the nature of the problem cannot be captured with only a few variables but can be over-fitted with redundant variables [154]. The NBI database comprises 116 bridge attributes (full list refer to [132]). Hence, a first selection of the potential influential parameters based on literature review and engineering judgment comprised 12 attributes, namely age, structure length, deck width, skew angle, type of design and/or construction, functional classification, design load, maintenance responsibility, kind of material and/or design, wearing surface, ADT (Average Daily Traffic) and ADTT (Average Daily Truck Traffic). Subsequently, statistical analysis was performed to validate the significance of the association

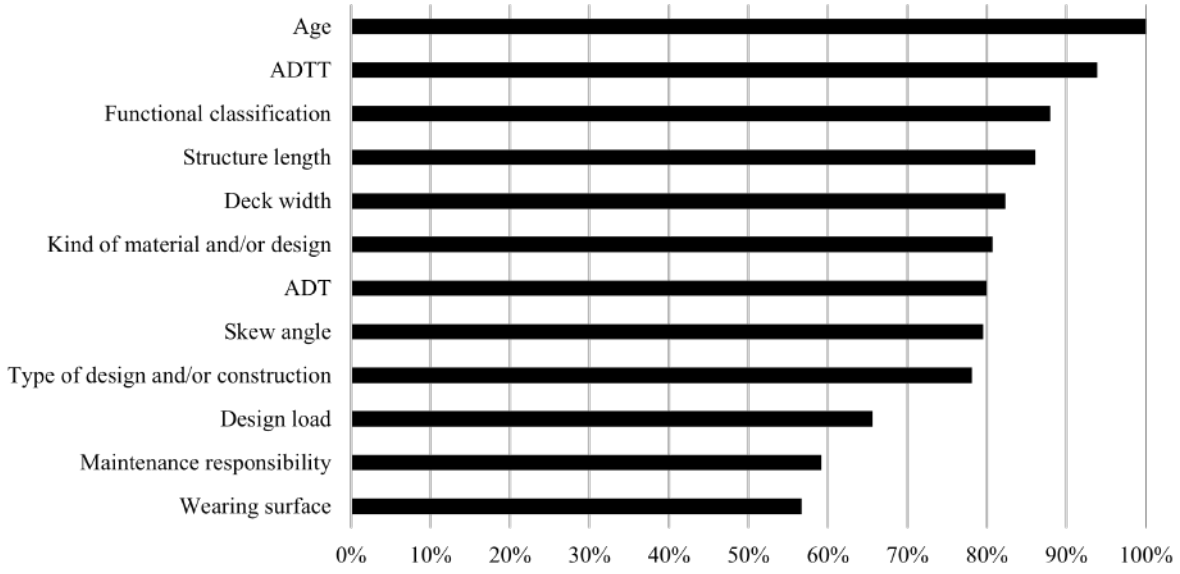


Figure 4.2: Normalized importance of the independent variables

and the correlation of the independent variables with the dependent variable. However, the database possesses complex multidimensional data, so the evidence obtained from the traditional statistical tests was not sufficiently strong to draw consistent conclusions. Therefore, the predictor selection was done through a variance-based sensitivity analysis that computes the importance of each predictor in determining the neural network, i.e., how much the network predicted value changes for different values of the independent variables [170]. The strength of this method is that it can deal with nonlinear responses and produces good estimations when the size of the dataset is large. After conducting the sensitivity analysis, the obtained normalized importance of the independent variables is shown in Figure 4.2.

The variables with the lowest importance were sequentially removed until the performance of the network reached its optimal value. The final parameters selected as input variables were age, structure length, deck width, functional classification, kind of material and/or design, and ADTT. The quantitative variables were standardized, and the categorical variables were transformed into a binary system before employing them in the model. Finally, Matlab Neural Network Toolbox [169] was used for the development of the MLP model. The network was trained with a Bayesian regularization backpropagation training function for its ability to reveal potentially complex relationships. 70%, 15%, and 15% of the input data were randomly allocated for training, validating, and testing the network, respectively. The number of hidden layers and the number of neurons in each layer were selected to be 3 and 20, respectively, after several iterations

to obtain the best network performance. The maximum number of epochs during the training was set at 10000. The activation function for the hidden layers was the hyperbolic tangent sigmoid transfer function, while the output layer uses a linear transfer function. The weights and biases obtained from the NN model are available as supplementary data in the published article [171].

4.7 Results

This section provides lifetime deterioration curves developed from the four previously presented models. To enable the comparison, a single plot with the deterioration curves representing the average condition of the bridge decks belonging to the network is shown in Figure 4.3. It can be noted that due to the variability in the inspections, the initial condition state for the NN model starts in a different state than state "8". It can also be observed that the three Markov processes predict a higher deterioration rate for the early years of the bridge decks compared to the NN. In general, the NN model maintains a good condition rating for longer than the rest of the models. However, at the end of the studied period, the hidden Markov model predicts the highest condition ratings. This effect can be explained by the fact that when considering the variability in the inspections, the model assigns a true condition rating higher than the observed for the better states. Hence, the accumulated deterioration at the end of the period is lower.

It can be seen that the deterioration curves developed by the different models produce distinct paths over the lifetime of the bridge decks. It is difficult to determine which of the models provides a better representation of the overall deterioration process of the bridge decks within the network. Hence, as an attempt to quantitatively measure the fitness of each model, the predictions are compared against the average condition rating recorded in the respective database per age (D1 average condition represented as dots in Figure 4.3). The metrics used to quantify how well the models matched the measured data were the mean square error (MSE), the mean absolute error (MAE), and the accuracy factor. MSE is more sensitive to outliers than MAE, which has led some authors to recommend using the latter for model fitness evaluation [172]. On the other hand, the accuracy factor indicates how much the predictions differ from observed data, where a value of "1" indicates a perfect model and can be expressed as [172]:

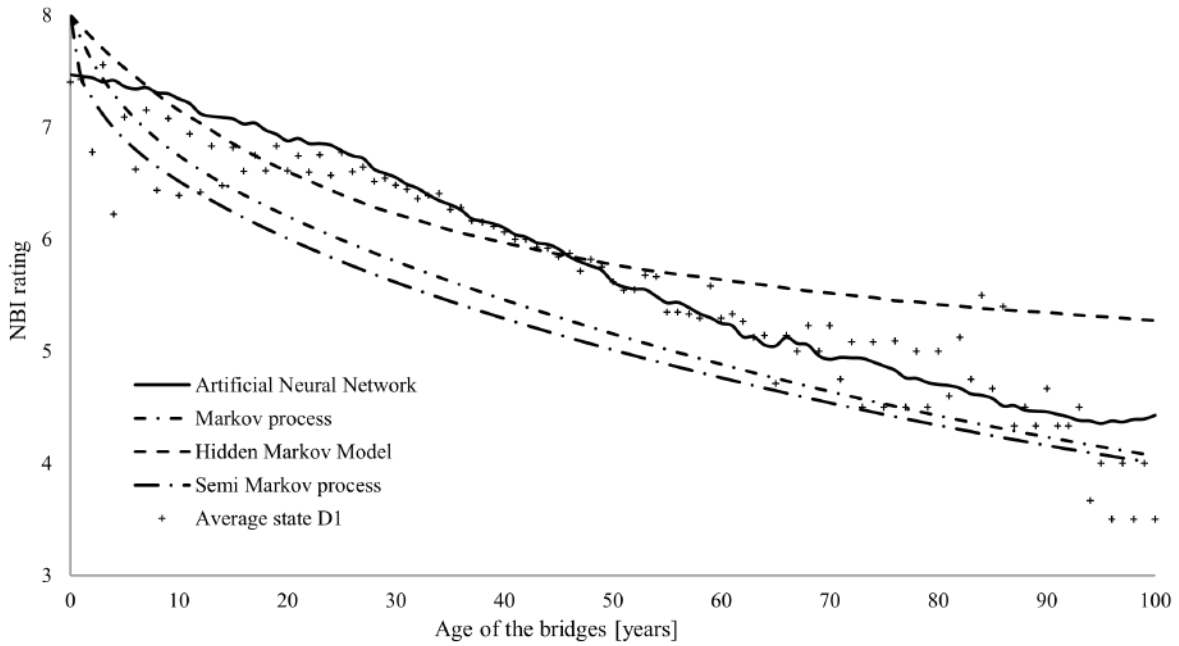


Figure 4.3: Deterioration curves for bridge decks

$$Accuracy\ factor = 10^{1/n} \sum_{i=1}^{n} \left| \log_{10} \left(\frac{predicted\ value}{observed\ value} \right) \right| \tag{4.19}$$

Table 4.4: MSE and MAE accuracy measures

Model	MSE	MAE	Accuracy factor
Neural Network	0.2068	0.3154	1.3552
Markov process	0.3336	0.5371	2.3312
Hidden Markov model	0.3302	0.4219	1.7521
Semi Markov process	0.4276	0.6086	2.6763

It is observed from Table 4.4 that the lowest errors and best accuracy factor are reached by the NN model. In contrast, the highest errors and worst accuracy factor correspond to the Semi Markov model. Based on the MSE measure, the Markov and the Hidden Markov models have approximately the same accuracy; nevertheless, the MAE measure indicates that the Hidden Markov model provides a better representation of the data than the Markov model. Likewise, the accuracy factor suggests that the HMM predictions diverge less from the measured data than the Markov model predictions.

4.8 Discussion

Overall, all the models evidenced a distinct deterioration pattern that concluded, at the end of the studied period, with a varying condition rating among the models. The worst condition was predicted by the Semi Markov model, followed closely by the Markov model, reaching a rating of 4, which is generally considered the threshold level to perform rehabilitation or replacement measures. NN model was also approaching the rating 4 while the Hidden Markov model was entering condition rating 5. As mentioned in Section 4.7, the better condition predicted by the HMM resulted from considering the variability in the inspections. However, the selection of this model might lead to inadequate maintenance activities considering that typical values of concrete deck life expectancy in the US are between 24-48 years [173]. In general, all the models are not in line with this experience. Even though Semi Markov models have been proposed extensively and their advantages over Markov chain models have been highlighted [148, 150], there were no significant differences among the obtained results. In fact, it was found that the Semi Markov model differed the most from the observed condition ratings. This might be attributed to the lack of historical data to appropriately estimate the parameters of the distribution of the waiting times. Some studies have employed expert judgment to define these parameters [161]. However, this approach adds subjectivity to the deterioration modeling. Maximum likelihood estimation (MLE) method has also been employed for parameter estimation [148]. Nonetheless, MLE can be heavily biased for small samples, which is the case for the estimation of the waiting times for the worst condition states, where the available data is limited due to the reconstructive efforts performed to prevent bridges from reaching structural deficient conditions (as seen in Table 4.2). Therefore, the estimation of the parameters for the Semi Markov model poses a higher complexity on its implementation from a mathematical point of view than the Markov chain model. Hence, unless sufficient data for reliable parameter estimation of the waiting times is available, Semi Markov models will not improve the prediction capabilities of Markov chains. On the other hand, the Hidden Markov model enabled the inclusion of inspection variability, which has been demonstrated to occur due to the subjective inspection procedure. Even though the HMM revealed a satisfactory accuracy compared to the rest of the models, the actual hidden process can never be observed [148], hence the model was fully determined by the data-based estimation of the emission probabilities, which conducted to an unrealistic result when compared to typical values of concrete decks life expectancy

as previously mentioned. The emission probabilities could have also been determined by expert judgment [148]. However, this involves a subjective estimation approach. Consequently, the estimation of the additional matrix increases the complexity of the implementation of HMM compared to Markov chain models. Finally, the NN model demonstrated a superiority in prediction accuracy. The most influencing parameters affecting the bridge deck condition were identified to construct a MLP network, which was able to correctly identify the condition ratings on average in 95% of the cases when exposed to the training data. The lowest percentage of correctly predicted values was obtained for the worst condition rating due to the database's low number of inspection records to train the network for transitions to this rating appropriately. Nonetheless, the number of data points was sufficient to obtain satisfactory predictions. These results are in accordance with the literature review where the NNs have always demonstrated great predictive capabilities [152, 154]. However, the training of the network involves high computational cost in comparison with Markov chain models, which can be seen as a limitation considering that the database is periodically updated, providing further knowledge about bridges that should be employed in predicting their future condition, but that will imply variations on the inputs to train the NN and consequently the weights and biases should be once again found. In general, the reliability of the predictions might have been affected by the inherent limitations of the models and aggravated by the accuracy of the database, which was found to contain data imbalance and deterioration trends that might not be realistic despite the filtering performed to remove effects from maintenance actions before developing the models (Section 4.2). For instance, some of the deck ratings over the complete span of 26 years did not vary significantly or did not vary at all. This behavior differs from what is expected and might be related to regular and minor maintenance activities not recorded in the database. This latter effect is particularly evidenced in several bridge decks with 70 years of age having ratings of 6 or 7. On the contrary, newly built bridges (0-5 years old) documented a deck rating of 6, i.e., satisfactory condition but with deterioration including cracks and around 2% of spalling or delamination in the deck area; which meant an unforeseen high deterioration rate at an early stage (decrease of 3 condition ratings in less than 5 years). As a consequence of the inconsistent deterioration trends observed in the NBI database, some studies have applied additional filtering to the data [143, 144]. For instance, in Hatami et al. [143], a maximum and minimum age for each condition rating was imposed, and data points outside the limits were removed. Similarly, in Bolukbasi et al. [144], it was assumed that any bridge deck should be reconstructed after the average

age at which reconstruction works occur, e.g., 30 years. Therefore, any deck rating assigned after that age should be eliminated. Nevertheless, these approaches are based on expected deterioration trends, so they might introduce subjectivity to the predictions depending on the selected ranks or restrict the available data for the development of the models.

4.9 Conclusions and future directions

Four different deterioration models, namely Markov models, Semi Markov models, Hidden Markov models, and Neural Networks, were implemented in this chapter to predict and compare the deterioration of bridge decks based on condition ratings retrieved from the NBI database. The Markov model herein applied consisted of a homogeneous Markov chain, the most frequently used model in the BMS. The simplicity of its implementation, together with its capabilities to capture the randomness of the deterioration process, are some of the main reasons for its selection. However, in a homogeneous Markov chain, the transition probabilities are not time-dependent, which is one of the features that has been widely criticized. For this reason, alternative deterioration modeling approaches were implemented to compare and analyze the impact of the Markov chain assumptions on the prediction results. It was shown that all models exhibited a distinct deterioration curve. However, there were no significant differences between the results obtained by the Markov and Semi Markov models. Nevertheless, the Semi Markov presented higher errors and a worse accuracy factor than the Markov model. Furthermore, it was found that the predictions obtained by the Hidden Markov model provided a better representation of the observed condition ratings than the Markov model. Amongst all, the NN model achieved the lowest errors and best accuracy factor. In addition to the higher prediction accuracy, the feature of employing the parameters affecting bridge deck deterioration for assessing the condition makes the NN model a more convenient alternative to be implemented on existing BMS to predict the condition of individual bridge decks. While the study focused on Rhode Island, the models and methodologies herein presented can be replicated in other regions using NBI data or similar databases to analyze whether different deterioration trends are obtained. Accordingly, the impact of each state's inspection and condition assessment practices on the development of deterioration models can be investigated. Moreover, additional deterioration modeling approaches, such as more advanced AI techniques and Petri-nets, could be included in the comparison. Finally, the deviation of the predictions

from the typical values of concrete decks' life expectancy as well as some challenges encountered during the development of the models, are attributed to i) an unbalanced and scattered database, ii) minor non-recorded maintenance actions preserving the condition without increasing the rating iii) shortcomings of VI as primary condition assessment tool, i.e. assessing a bridge condition only by VI is significantly subjected to variability of the condition ratings as demonstrated by Moore et al. [165], In order to overcome the latter limitation, NDE technologies have been used to detect and characterize the deteriorated condition of bridge elements more objectively. For instance, in Pailes [174], several NDE methods, namely electrical resistivity, half-cell potential, ground penetrating radar, impact echo, and chain drag, were combined to enable the identification of different deterioration phenomena for a complete assessment of concrete decks. Moreover, when a particular defect has been detected, e.g., active corrosion, condition assessment can be accompanied by additional measurements such as chloride content or carbonation depth, which quantify the severity of the deterioration phenomena. At present, NDE technologies are being used, but surveying large amounts of bridges for BMS is still cost- and time-consuming, usually involving traffic disruption and uncertainties in their measurements, which need to be carefully addressed. Similarly, structural health monitoring (SHM) systems are also a powerful and reliable technique for short- and long-term bridge condition assessment. Nevertheless, SHM systems are often costly, and their complexity resulting from data acquisition, structural modeling, big data analysis, and routine maintenance required for long-term operation limit their prompt adoption on BMS. Despite the current challenges of integrating NDE/SHM assessment tools into the BMS, research efforts should be undertaken in this direction so that bridge condition assessment could move from operational indicators (e.g., condition ratings) to research indicators, which address a bridge's structural safety and serviceability from a quantitative perspective. Consequently, deterioration modeling could be more realistic, considering that the input parameters will be based on quantitative resistance measures.

Chapter 5

Fragility assessment of transport infrastructures subjected to flood events

Abstract: In the face of increasing climate variability leading to more frequent and severe weather events, understanding the vulnerability of transport infrastructures to flooding is imperative. Current research in flood fragility assessment predominantly focuses on case-specific methodologies, limiting their scalability for implementing them for a portfolio of assets to assess network-level risks. This chapter develops a generic methodology for constructing flood fragility functions for transport infrastructures, particularly bridges, suitable for application at the infrastructure network scale. The proposed methodology systematically identifies failure modes for each bridge component, formulates limit state functions, defines bridge classes, and evaluates system fragility with time-dependent considerations. The approach is exemplified through its application to a Portuguese case study, showing how unique bridge classes may be defined to estimate flood fragility functions for a bridge portfolio. The case study indicates the essential attributes required to estimate flood fragility and underscores the absence of data in current bridge management system databases. The suggested methodology aims to support the identification of critical infrastructure assets and predominant failure modes that significantly contribute to network-level risks, thereby justifying the need for more detailed investigations.

5.1 Introduction

The assessment of the physical damage that transport infrastructures will experience when exposed to a given intensity of flood hazard is significantly relevant to estimating the direct and indirect impacts on the transportation system functionality. There are two common approaches for modeling vulnerabilities: the damage function approach and the fragility approach [175]. In the damage function approach, the consequences are modeled as a function of a hazard intensity, as illustrated in Figure 5.1a. Damage functions can be relative, meaning that the consequences are expressed as a percentage of the asset's value, or absolute, meaning that the consequences are expressed in monetary terms. These functions are often derived from statistical analysis of empirical damage data from past hazardous events (e.g.,[176, 177]). Alternatively, damage functions can be defined by expert knowledge, often referred to as judgemental, engineering models, or hybrid approaches. On the other hand, the fragility approach involves two modeling steps to determine the consequences of a hazard. Firstly, a fragility model determines the probability of the system being in a physical damage state DS_i for a given hazard intensity. Damage states are defined based on the level of damage caused by the hazard and typically include "Minor", "Moderate", "Extensive", and "Complete damage/collapse", corresponding to DS_1, DS_2, DS_3, and DS_4, respectively, in Figure 5.1b. In the second step, the direct consequences D are quantified as a function of the physical damage state of the system, $D = f(DS_i)$. Like damage functions, fragility models can be statistically inferred from empirical damage data. For instance, Lamb et al. [178] used historical observations of railway bridge failures in the United Kingdom to construct fragility curves that quantify the probability of failure as a function of the severity of a flood event. Even though this approach is useful for network risk analysis, it does not support the identification of individual bridge vulnerabilities. Moreover, due to the scarcity of data and the fact that data available is specific to exposed elements in a particular area, it has become more common to characterize the fragility of transport infrastructures with analytical models, as evidenced in a thorough review found in [179]).

As evidenced in the bibliometric analysis presented in Chapter 2, there is relatively less published literature on fragility functions for bridges that are susceptible to flood hazards compared to other natural disasters such as earthquakes (see Figure 2.7). The HAZUS-MH methodology for damage and loss assessment

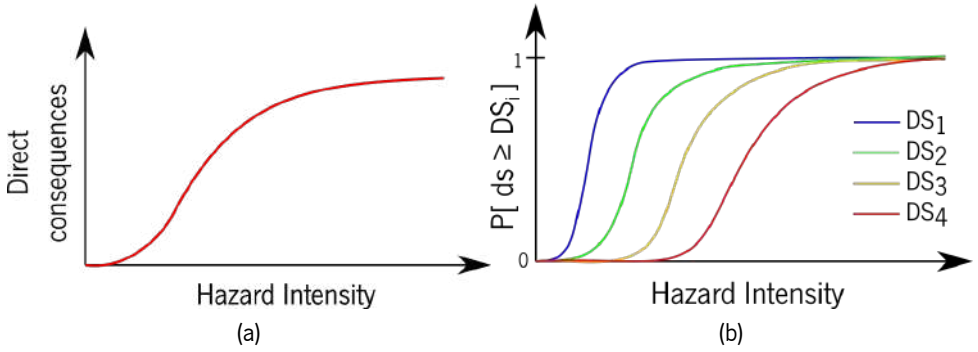


Figure 5.1: Schematic illustration of a) damage function model; b) fragility model

[180] was one of the first attempts to provide estimates of the fragility of bridges exposed to flood hazards. Therein, bridge failure probabilities for different flood return periods were given as a function of the scour potential, waterway adequacy, and span type, which are available attributes within the FHWA bridge inventory database [132]. However, the failure probabilities were defined by expert judgment as no comprehensive database of bridge damage due to flood hazards was identified, and no detailed structural analysis was conducted. Subsequent attempts have focused on analytical approaches to investigate bridge fragility under various flood actions. For instance, significant research has examined the effect of flood-induced scour on the seismic fragility of bridges (e.g., [181–184]. However, these studies accounted for scour as an aggravated seismic fragility condition rather than a collapse failure mechanism by itself. In this regard, Gehl [185] and Hackl et al. [44] obtained fragility curves for bridges that could fail due to local scour, assuming different thresholds of scour depth to describe minor to complete damage. Nonetheless, the definition of the thresholds was either not justified or based on the impact of scour depth on the bridge seismic response rather than the result of analyzing the behavior of scoured bridges under flood conditions. On the other hand, several studies have examined the nonlinear soil–pile–structure interactions of scoured bridges and have highlighted the importance of accounting for these effects when analyzing the response of all bridge components during flood events, including abutments, piles, and superstructure (e.g., [186–188]). Subsequently, recent studies have adopted numerical soil-pile-structure models for developing flood fragility functions for pile-supported bridges (e.g., [189–191]). Concerning other bridge types, Tanasić et al. [192] developed fragility functions for multiple-span reinforced concrete (RC) bridges supported on shallow foundations, where two failure modes were analyzed, namely the exceedance of the soil bearing capacity as a result of soil degradation due to scour, or the exceedance of the deformation

capacity of the superstructure as a result of pier sinking. Furthermore, the vulnerability of masonry arch bridges subjected to flood-induced scour has also received great attention due to their rigid behavior, significant sensitivity to settlements, and the typical use of shallow footing foundations in their construction [193–195]. Given the complexity of three-dimensional models to investigate the collapse mechanisms of masonry arch bridges, fragility functions have been developed using two-dimensional limit analysis models [196, 197]. Even though scour is one of the predominant causes of bridge failures worldwide [198], superstructure or pier failure due to extreme hydraulic pressures can also be present. In this respect, Turner [199] analyzed the deck failure induced by hydrodynamic forces to develop fragility curves for eight bridges. Also, Argyroudis and Mitoulis [200] developed fragility curves for prestressed concrete bridges accounting for various failure modes depending on the deck-pier connection (monolithically connected or supported on bearings) and resulting from the different flood actions, i.e., scour, debris accumulation, and hydrodynamic forces. Therein, the vulnerability of prestressed decks was underscored due to their non-ductile nature, which limits their ability to endure vertical displacements. Even slight movements induced by scour can significantly alter stress levels, affecting service limit states (SLS) and potentially leading to cracks in prestressed sections, which may impact the serviceability and durability of the deck [200]. Nevertheless, the impact of durability on the flood fragility of bridges throughout their service life has received little attention. To the authors' knowledge, the construction of flood fragility curves that consider the long-term performance of bridges has been limited to the work of Kim et al. [189] and Khandel and Soliman [191], who accounted for corrosion effects in RC piles and steel H-piles, respectively. The effects of other time-dependent deterioration mechanisms, such as deterioration of material properties or the impact of cumulative processes such as scour action, have yet to be investigated.

Based on the preceding review, it is noted that certain bridge types and failure modes have received more research attention than others. Moreover, it is apparent that the direct application of existing fragility curves for a portfolio of bridges is not yet feasible. This is partly due to the inhomogeneity in the methodologies to derive these functions, which vary in the level of complexity of the models, the treatment of uncertainties, and the inconsistency in the failure modes considered for the same bridge type. Additionally, the application of fragility functions at a network level requires defining classes to categorize each bridge within the network into a specific group and to select a fragility model that represents the entire class. This approach is necessary since developing fragility functions for every bridge in the network would be time-consuming

and computationally expensive. The definition of bridge classes has been broadly studied in the context of the fragility of bridges at seismic risk [201]. Conversely, bridge classes for the purpose of flood risk assessment have received considerably less attention. In this regard, Degan et al. [202] proposed a bridge taxonomy for riverine roadway bridges comprised of 20 attributes for identifying bridge classes for flood risk assessment. However, the taxonomy was not directly associated with bridge failure modes, and relevant attributes such as foundation type were not included. Therefore, this chapter introduces a generic methodology for developing flood fragility functions that facilitates the categorization of bridges into distinct classes, enabling its application at the bridge portfolio level. The suggested approach can be applied to any bridge type and allows for the inclusion of all plausible failure modes and time-dependent considerations. Lastly, the application of the methodology advocates for using simplified yet sufficiently accurate models, striking a balance with the required level of detail for assessing network-level risks.

The remainder of this chapter is organized as follows. Section 5.2 outlines the proposed methodology that includes identifying failure modes per bridge component type, formulating limit state functions, defining bridge classes, evaluating the system fragility, and including time-dependent considerations. To this end, Section 5.2.1 summarizes all the failure modes found in the literature review for different bridge component types. This thorough review aims to guide the development of fragility functions for a given bridge portfolio. Section 5.4 shows an application of the methodology to a bridge portfolio of a Portuguese case study. Finally, the chapter concludes by summarizing the key contributions of this research to bridge fragility assessment for quantification of network-level risks and the limitations that can be areas for future research.

5.2 Methodology for portfolio-level flood fragility functions

The generic methodology for developing flood fragility functions for a portfolio of n bridges is outlined in Figure 5.2. The first step in the methodology requires gathering a dataset containing all necessary bridge attributes to assess their performance. Considering that the focus of this study is on the fragility of bridges due to floods, the first verification involves selecting the bridges from the portfolio that are crossing rivers. This step is included as asset inventories typically encompass various structures, including

viaducts, overpasses, and underpasses, as illustrated in the application example (Section 5.4). The next step consists of analyzing the plausible bridge failure modes, denoted as n_f. To facilitate this task, an exhaustive literature review examining past failure events and insights from studies using analytical models was conducted in Section 5.2.1. The findings from the review are summarized in Table 5.1, which can be used in the methodology to support the identification of potential failure modes for different bridge components. For each bridge failure mode j, a limit state function denoted as G should be defined. Thus, each bridge i will have a vector of limit state functions $\boldsymbol{G_i}$ to evaluate its performance under flood events (further details are given in Section 5.2.2). Consequently, if two bridges have a common $\boldsymbol{G}$ vector, this indicates they share the same failure modes, and therefore their performance under flood events can be evaluated using the same limit state functions. In such instances, these bridges are classified under the same bridge class k. For each unique $\boldsymbol{G}$ vector, a new bridge class is established. Then, upon assessing all n bridges in the portfolio, the total number of bridge classes n_c is determined. Subsequently, given the relevance of incorporating deterioration effects into the long-term resistance of bridges, the methodology proposes the formulation of limit state functions that include time-dependent considerations. Thus, the limit state vector should be evaluated for each time t of analysis until the end of the bridge service life t_s. Moreover, this temporal aspect applies to the flood demand, which may change over time as explored in Chapter 3, with more details provided in Section 5.2.4. The flood demand in the limit state functions can be represented with physically observable or derivable quantities that characterize the load impacting the bridge during a flood event. The most common loading measures used in flood fragility analysis, often termed intensity measures (IM), include peak flow discharge, flow velocity, water level, and scour depth. To construct the fragility curve, the selected intensity measure is progressively increased, and the limit state vector is evaluated at each IM increment until reaching its maximum target value IM_{max}. Lastly, the probability of failure of the bridge system P_{Fi} is calculated for each intensity measure and time of analysis. The bridge is modeled as a series system, where failure occurs if any of the considered limit state functions is less than zero. The exact P_{Fi} depends on the correlation among failure modes, and the lower and upper bounds can be computed as detailed in Section 5.2.3. The complete procedure is repeated until the time-dependent fragility functions are obtained for all the river-crossing bridges in the portfolio. It is worth noting that even though the methodology outlines the steps for developing a fragility model that estimates the probability of the bridge system reaching a "Complete" damage state, it can be

adapted for assessing the probability of reaching intermediate damage states, e.g., "Minor", "Moderate", and "Extensive", by incorporating an additional iteration that evaluates the $\boldsymbol{G}$ vector for each DS_i.

5.2.1 Bridge component failure modes

Failure can be defined as complete or partial damage of bridge components leading to a reduction of the bridge's functional performance. A relatively large number of failure modes can be identified since each bridge component, depending on the bridge type, may fail differently when exposed to an extreme flood event due to the complex interaction between the resistance of the soil-bridge system and the diverse flood actions. This challenge has made defining failure modes a non-straightforward task, leading to inhomogeneity among authors. Birdsall and Hajdin [203] identified five different failure scenarios in which a flood can cause partial or complete failure of a bridge. Basically, if the characteristics of the flood conduct to bridge overtopping, (1) a roadway might be buried, (2) a superstructure might fail horizontally, or (3) the superstructure-substructure connection might fail horizontally or vertically. In addition, the bridge might fail due to (4) the undermining of its foundations if the characteristics of the streambed material subjected to the flow conditions result in scour on bridge foundations. Finally, (5) bridge piers might fail horizontally if the hydraulic loading exerted is beyond the design loads, e.g., when exacerbated by debris accumulation. Even though these scenarios broadly gathered most of the failure modes, they do not explicitly account for the possible interactions among bridge components, which can lead to additional failure mechanisms. In this regard, Van Leeuwen and Lamb [204] accounted for the interactions among the resistance of multiple bridge components by dividing the failure mechanisms as secondary mechanisms resulting from primary mechanisms. Essentially, scour can undermine shallow foundations or cause destabilization of deep foundations through erosion of the riverbed; this can lead to settlement or tilting of piers/abutments or tilting of the group of piles (primary mechanism), which in turn might result in structural damage to the superstructure, or deck sliding or falling off abutments/piers (secondary mechanism). Similarly, Argyroudis and Mitoulis [200] proposed a list of failure modes per bridge component, subdivided by primary (direct) and secondary (indirect) effects of flood stressors on bridges. This subdivision is equivalent to modeling the failure of a system as a two-phase phenomenon: the initiation phase and the propagation phase (see Figure 5.3). In the initiation phase, the hazard event causes damage or failures of some

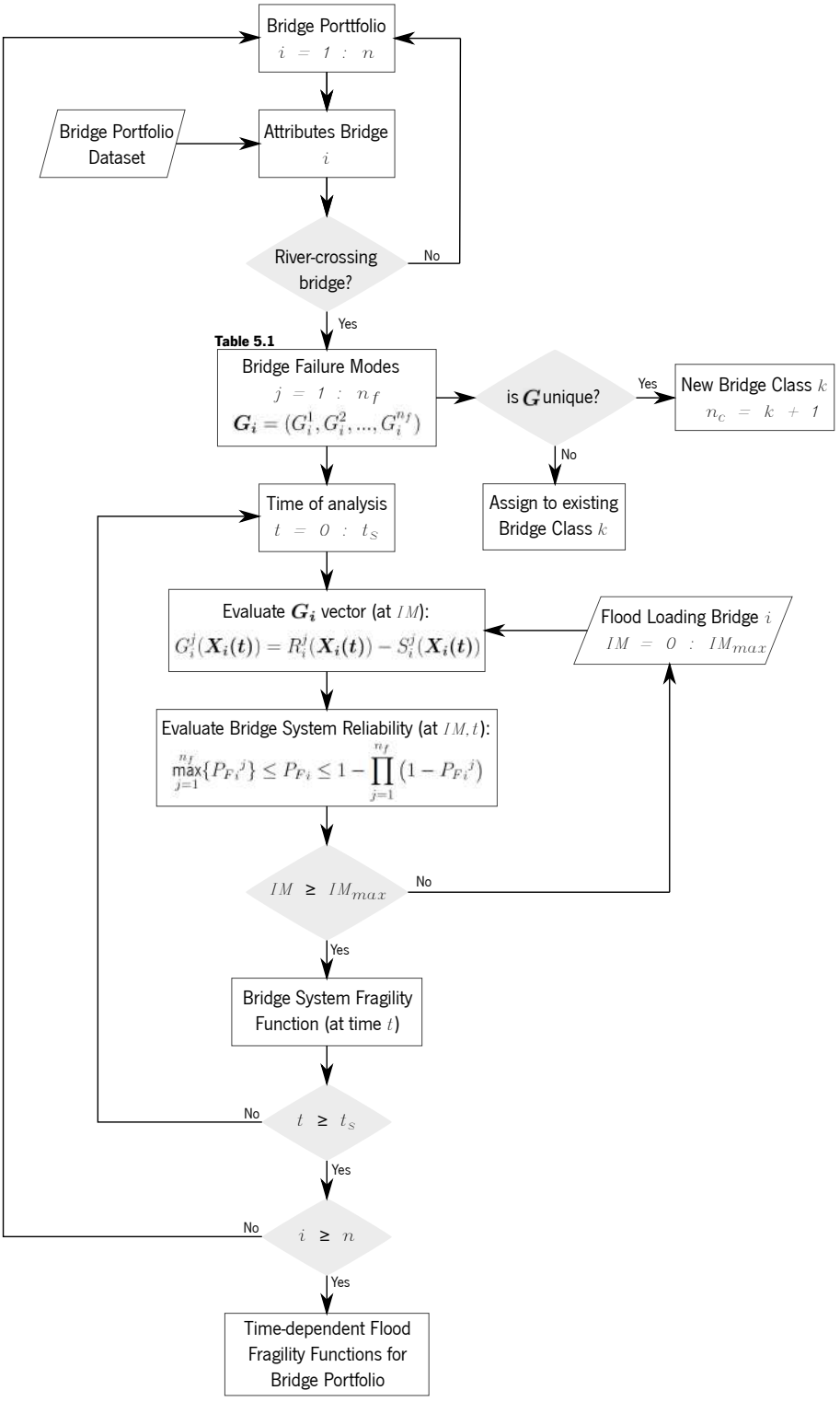


Figure 5.2: Methodology for time-dependent flood fragility functions for bridge portfolio

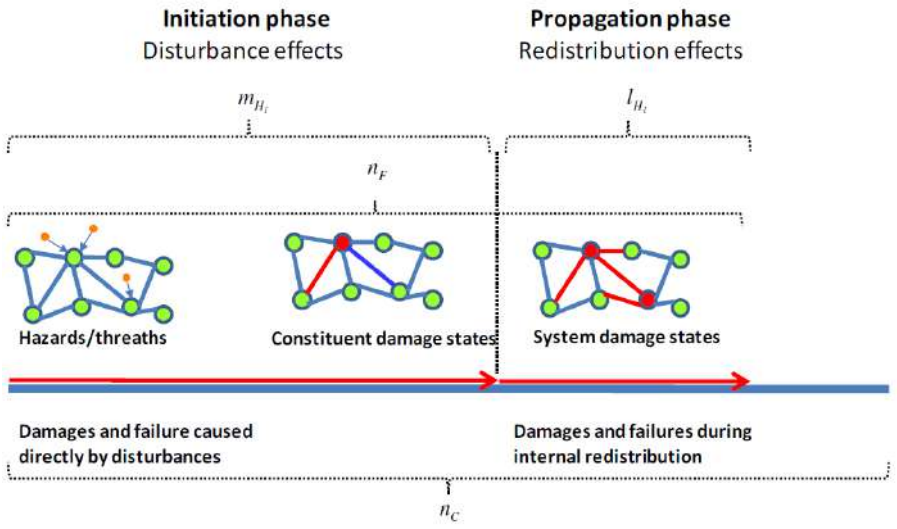


Figure 5.3: Illustration of the two-phase scenario-based failure propagation model. Source: [9]

constituents. In the propagation phase, the demands of the constituents of the system are redistributed until both internal and external demands are in equilibrium with the capacity of the system or until the system totally fails [9]. Analogously, an example of failure propagation in a bridge system during a flooding event can be explained as an initiation phase, where the disturbance effect consists of the hydraulic loads acting on the pier foundation and causing the first constituent damages, i.e., pier settlements due to scour at the foundation; and the propagation phase, where the internal redistribution of loads generates a high demand at the bridge deck due to the large settlements, which leads to deck failure.

Table 5.1 summarizes the failure modes found in the literature review for different bridge component types. It can be observed that some of the failure modes described in the table result directly from the flood demand acting on the components. For instance, hydrodynamic forces acting on (partially) submerged simply supported decks may cause transverse or uplift failure [11, 199], or yielding/cracking of girders [97]. However, other component failure modes result from the redistribution effects of previous component damage states, as explained in Figure 5.3. For instance, damage to the substructure components (piers and/or abutments), such as tilting or rotation due to local scour, will generate additional stresses at simply supported decks, which may cause damages such as concrete cracking, reinforcement yielding, deck unseating or even deck loss [205]. Similarly to simply supported decks, damage to the substructure components, such as differential settlement due to local scour, will cause a redistribution of forces at elastomeric bearings. Thus, bearings may fail under axial tension (cavitation) or

over-compression (buckling) and/or shear [200]. It can be seen from the table that significant research has been conducted on the behavior of pile-supported foundations subject to scour, even though bridges with this type of foundation are less vulnerable than those with shallow foundations. Nevertheless, it is undesirable for the piles to be exposed as this may compromise the lateral stability of the bridge, affect pile-bearing capacity, and trigger excessive settlements/rotations, which, among others, might damage the superstructure. Different failure modes have been formulated for this condition, in some cases accounting for the hydrodynamic forces acting on the scoured piles. For instance, Khandel and Soliman [191] defined four limit state functions for a bridge supported on steel H-piles foundations subjected to scour effects and hydrodynamic loads: 1) combined axial and flexural failure limit state, 2) shear failure limit state, 3) two serviceability limit states corresponding to lateral deformation, and 4) angular distortion. However, other research works assume different limit state functions, indicating that there is no full agreement between the failure modes defined for the same type of bridge. On the other hand, Table 5.1 shows that the behavior of masonry arch bridges (MAB) during floods has also received considerable attention, as they are deemed highly vulnerable to local scour [195]. The configuration of the local scour cavity at the foundation determines various failure modes in MAB, including fragmentation of piers/abutments, out-of-plane failures, and both symmetrical and asymmetrical in-plane failures [205]. In-plane failure modes have been analyzed with simplified analytical models (e.g., [193, 196, 197]), while out-of-plane failure modes require more advanced finite element models to examine the complex three-dimensional problem (e.g., [194, 195]). Less studied failure modes are those related to the bridge abutments, including the backfill and approaching roadway, even though significant damages to these components are frequently observed after extreme flooding events, e.g., extensive damage of abutments with partial or complete wash-away of the backfill was one of the predominant bridge failure modes observed after the 2020 Medicane Ianos floods in Greece [206]. Finally, debris built up due to water overtopping the deck is sometimes considered a failure mode since it involves certain functionality loss. However, as it does not threaten the stability of the bridge structure and the direct costs associated with cleaning are negligible compared to reconstruction costs, this failure mode is not included in the table. It is expected that Table 5.1 supports the identification of the predominant failure modes depending on the bridge and component types, thereby facilitating the definition of component limit state functions, as indicated in the next section.

Table 5.1: Common failure modes per bridge component type

Bridge component type	**Disturbance effect**	**Component Failure Mode**	**Ref.**
Simply supported deck	Hydrodynamic forces on (partially) submerged decks	Transverse failure	[11, 97]
		Uplift failure	[11, 199]
		Yielding/cracking of girders	[97]
	Differential settlement of pier and/or abutment	Deck damages/loss	[189, 200, 205]
	Tilting/rotation of substructure	Deck damages/loss	[200, 205]
	Loss of substructure	Deck failure in shear/flexure	[205]
	Debris loading or collision	Deck damages	[204]
Elastomeric bearings	Lateral hydrodynamic forces	Loss of frictional resistance, excessive shear deformation and strain	[97]
	Differential settlement of pier and/or abutment	Shear and/or tension/compression of bearings	[200]
Continuous deck	Unifom/differential abutment/pier settlement, tilting/rotation of abutment/pier	Plastic hinges in girders/deck	[192, 200, 205]
Intermediate RC piers	Hydrodynamic forces on pier (with potential debris)	Flexural and axial failure of bridge pier	[11, 200, 207]

Continued on next page

Table 5.1 – *Continued from previous page*

Bridge component type	**Disturbance effect**	**Component Failure Mode**	**Ref.**
		Shear failure of bridge pier	[11, 200]
Shallow foundation	Local scour at pier/abutment foundation	Soil bearing capacity exhausted	[192, 205]
Pile-supported foundation	Exposure of piles due to scour	Loss of soil bearing capacity (insufficient penetration for friction piles, undermine of pile tip for end bearing piles)	[207, 208]
		Pile buckling capacity	[191, 207]
	Hydrodynamic forces on scoured piles	Flexural and axial failure of pile group	[11, 191, 208]
		Shear failure under lateral loads	[191, 208]
		Lateral deformations	[190, 191]
		Angular distortion	[191]
		Lack of displacement ductility of piles	[189, 207]
		Steel reinforcement rupture of piles	[189]
		Pull-out failure of piles	[207, 208]
		Torsional failure due to skew flow	[207]

Continued on next page

Table 5.1 – *Continued from previous page*

Bridge component type	**Disturbance effect**	**Component Failure Mode**	**Ref.**
Masonry arch (arch + spandrel + backfill)	Local scour at pier foundation	Out-of-plane arch rotation and spandrel wall failure	[194, 195, 205]
		Symmetrical, in-plane arch failure	[193, 196, 197, 205]
		asymmetrical, in-plane arch failure	[193, 197, 205]
	Buoyancy effects due to water reaching the arch	Reduction of load-carrying capacity	[209]
Intermediate masonry piers	Local scour at pier foundation	Fragmentation of pier	[194, 195, 205]
Abutments	Local scour at abutments	Fragmentation of abutments	[205]
		Washout of embankment behind abutment (approach roadway)	[204]

5.2.2 Component Limit State Functions

Limit state functions (LSFs) can be formulated to represent each bridge component's failure modes. The general limit state function for each bridge failure mode j can be expressed as:

$$G_i^j(\boldsymbol{X_i}) = R_i^j(\boldsymbol{X_i}) - S_i^j(\boldsymbol{X_i}) \tag{5.1}$$

where G_i^j is the limit state function associated with bridge i and the j-th failure mode, $\boldsymbol{X_i}$ is the corresponding set of random variables of bridge i; and R_i^j and S_i^j are the capacity and the flood load intensity of bridge i associated with the j-th failure mode, respectively. The list of LSFs of bridge i can be denoted by a vector:

$$\boldsymbol{G_i} = (G_i^1, G_i^2, ..., G_i^{n_f}) \tag{5.2}$$

where n_f is the number of LSFs defined for bridge i. If any $G_i^{n_f}$ is less than zero, there are component failure events.

5.2.3 Bridge System Fragility

In the case where only one failure mode is considered for a bridge, e.g., $G_i^{j=1}$, the probability of failure of the bridge system i can be defined as:

$$P_{Fi} = P[G_i^1 \leq 0] \tag{5.3}$$

When several failure modes are considered, the bridge system fails if any of the LSF is less than zero. In other words, the bridge is modeled as a series system. For a series system where all failure modes exhibit full correlation, the probability of system failure is equal to that of the mode with the highest failure probability. This scenario represents a system wherein the weakest element can be distinctly identified. Given that the correlation among failure modes ranges between zero and one, the limits of failure probability for a series system can be established as [210]:

$$\max_{j=1}^{n_f}\{{P_{Fi}}^j\} \leq P_{Fi} \leq 1 - \prod_{j=1}^{n_f}\left(1 - {P_{Fi}}^j\right) \tag{5.4}$$

where the lower bound corresponds to the case of full correlation among failure modes and the upper bound to the case of zero correlation. The correlation among different failure modes depends on the

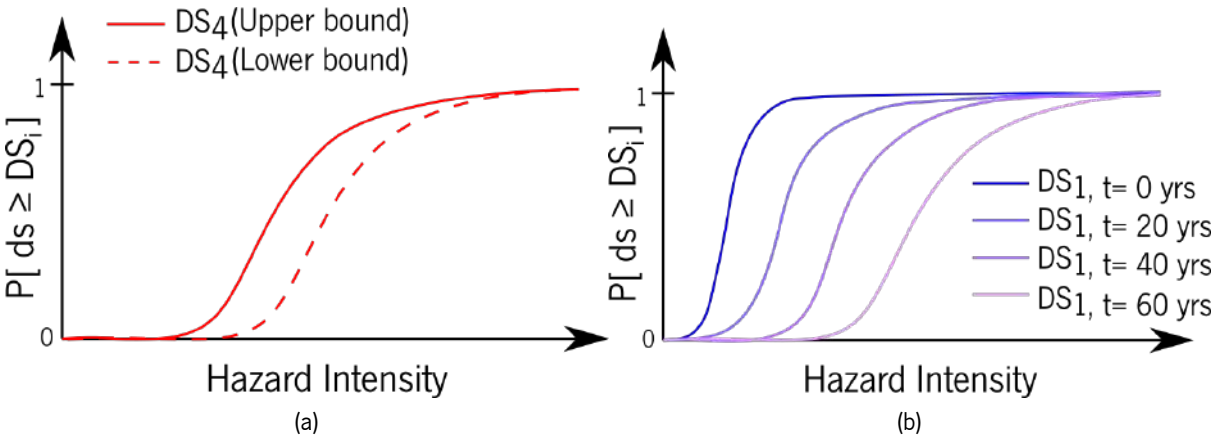


Figure 5.4: Schematic illustration of a) Bridge system fragility with upper and lower bounds; b) Bridge system fragility at different time periods

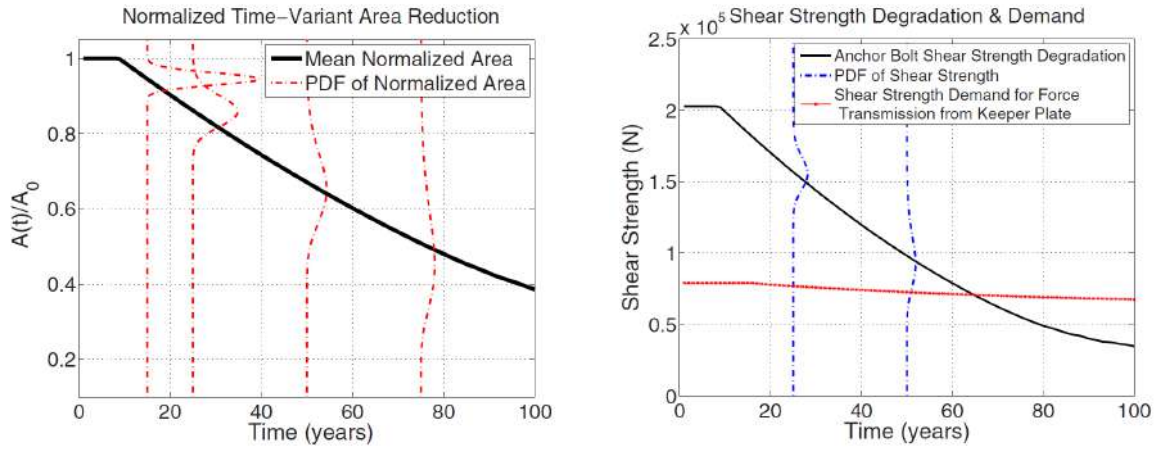
common random variables used in the LSFs. The dependencies between these variables in the different LSFs should be addressed to compute the bridge system reliability. Nonetheless, it is apparent that the flood event is what dominates these dependencies and ultimately determines the performance of the series system. Similar assumptions have been made to estimate the system reliability of bridges under seismic loading, where the dependencies that are taken into account are related to the common loading that is applied to the bridge components [185].

5.2.4 Time-dependent Fragility

As highlighted in Chapter 3, transportation infrastructure assets deteriorate due to exposure to adverse environmental and climatic conditions, aging, and changing load patterns, among other factors. These time-dependent deterioration effects can significantly increase the fragility of bridge components over time. Therefore, Eq. 5.1 can be generalized to account for deterioration effects at time t as:

$$G_i^j(\boldsymbol{X_i(t)}) = R_i^j(\boldsymbol{X_i(t)}) - S_i^j(\boldsymbol{X_i(t)}) \tag{5.5}$$

where $\boldsymbol{X_i(t)}$ denotes the set of random variables corresponding to bridge i at time t. The time-dependent random variables can be associated with both the bridge capacity and the flood load intensity acting at bridge i. In the case of the bridge capacity, it is expected that deterioration mechanisms will reduce the



(a) (b)

Figure 5.5: Modeling of corrosion effects on bridge components (a) Area reduction of the column reinforcement (b) Shear strength deterioration of anchor bolts. Source: [10]

resistance over time at a rate that depends on the specific deterioration process. Therefore, a higher bridge fragility is anticipated at the end of the bridge service life as depicted in Figure 5.4b. On the other hand, the flood load intensity acting at bridge components may increase over time due to climate change effects (as discussed in Chapter 3) or due to cumulative stressors (e.g. accumulated scour [211]), which ultimately may further increase the bridge fragility. The most studied deterioration process that has been considered for time-dependent fragility analysis of infrastructures under different hazards is the corrosion of reinforcing steel for concrete structural elements (e.g., [67, 189]). Corrosion is usually modeled by reducing the cross-section area of reinforcement as a function of time (Figure 5.5a), and secondary effects such as cracking and spalling of concrete, loss of bond strength, among others, have been also considered to investigate the total loss of structural strength due to corrosion [10]. Likewise, corrosion also affects steel bearings, anchor bolts, and keeper plates, reducing stiffness and ultimate strength in the bearing assemblies (Figure 5.5b).

Bridge substructures can also be affected by different deterioration mechanisms. For instance, during an underwater inspection, it was found that the I-10 bridge over the Jourdan River in Mississippi, USA, supported on friction steel piles, had an average of approximately 50% of steel pile cross-section loss due to severe corrosion. The corrosion was caused by significant scour that exposed the steel piles. As a result of the reduced cross-section, the web and flanges of the piles buckled locally [212]. On the

other hand, scour has also been regarded as a history-dependent and time-dependent phenomenon. Essentially, bridges are exposed during their service life to multiple floods, some of which exceed the discharge corresponding to the design return period, while others correspond to a very low return period but are still capable of causing scour. These latter events of minor intensity may not result in the critical scour depth being exceeded but may cause partial erosions, which accumulate due to multiple floods and may lead to bridge failures [211]. For instance, the cause of the collapse of the Malahide viaduct on the railway line from Dublin to Belfast on 21 August 2009 was reported as the result of a combination of factors, including the accumulative scour action over a long time period and the inappropriate inspection and maintenance activities [213]. Therefore, these time-dependent phenomena should be considered in the fragility assessment.

5.3 Flood actions on bridges

In the following section, a summary of different loads acting on bridges during flooding events is presented to facilitate the formulation of limit state functions for the different bridge component failure modes.

5.3.1 Hydrodynamic forces on bridge decks

Bridges are designed for a discharge with a given return period based on the conditions when the bridge was built. However, uncertain future conditions regarding climate, land use, and stream patterns can increase overtopping risk over the service life of bridges [214]. When the bridge superstructure is submerged, or partially submerged, the flowing water exerts hydrodynamic loads on the bridge deck, including *i)* a dragging force, $F_{D,d}$, acting parallel to flow; *ii)* a lifting force, $F_{L,d}$, acting vertically and perpendicular to flow; and *iii)* overturning moments, M_{CG}, due to unevenly distributed forces about the center of gravity (see Figure 5.6).

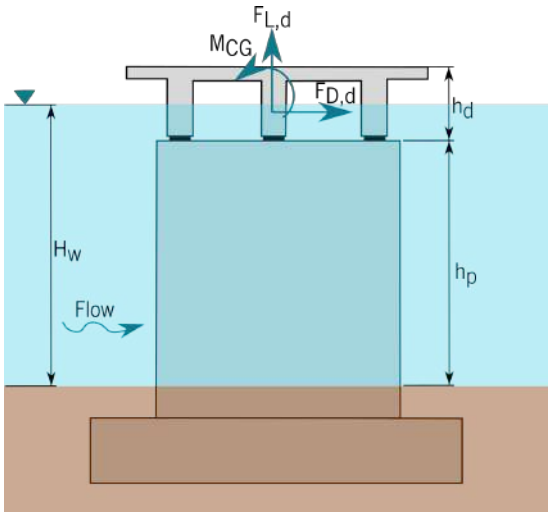


Figure 5.6: Hydrodynamic forces on inundated bridge decks (adapted from [11])

The dragging force acting on the bridge deck can be expressed as Kerenyi et al. [215]:

$$F_{D,d} = \frac{1}{2}\, C_{D,d}\, \rho\, V^2\, l_s\, h_d \qquad \text{if } h^* \geq 1.0 \tag{5.6}$$

$$F_{D,d} = \frac{1}{2}\, C_{D,d}\, \rho V^2\, l_s\, (H_w - h_p) \qquad \text{if } h^* < 1.0 \tag{5.7}$$

where h^* is the inundation ratio, i.e., higher values indicate the bridge is more submerged:

$$h^* = \frac{H_w - h_p}{h_d} \tag{5.8}$$

$C_{D,d}$ is the coefficient of drag on the deck, ρ is the density of water, V is the stream velocity, l_s is the span length, h_d is the deck thickness, H_w is the height of the water surface, and h_p is the height of the pier up to the low chord of the bridge deck, as depicted in Figure 5.6. The lifting force is the summation of the hydrodynamic lift force,HF_L, and the buoyancy force,BF_L [11]:

$$F_{L,d} = HF_L + BF_L \tag{5.9}$$

$$HF_L = \frac{1}{2}\, C_{L,d}\, \rho\, V^2\, l_s\, b_d \tag{5.10}$$

$$BF_L = vol\, \rho\, g \tag{5.11}$$

where $C_{L,d}$ is the coefficient for lift on the deck, b_d is the width of the bridge deck, vol is the displaced volume of water and g is the gravitational acceleration. Lastly, the overturning moment with respect to the bridge deck center of gravity is defined as:

$$M_{CG} = \frac{1}{2} C_{M,d} \rho V^2 (l_s {b_d}^2) \tag{5.12}$$

where $C_{M,d}$ is the coefficient for the flow-induced overturning moment on the deck. Drag, lift, and moment coefficients are usually provided by different guidelines and standards based on laboratory experiments. Alternatively, Kerenyi et al. [215] developed experimental tests and Computational Fluid Dynamics (CFD) models to develop force coefficients that can be used for design. The coefficients are a function of the bridge deck type (girder or streamlined) and the inundation ratio. The formulas can also be modified to compute dragging forces when debris accumulation has formed against the deck, i.e., the projected area of debris replaces the bridge deck area term. Even though experimental tests and CFD models have been used to derive the coefficients, the resulting mathematical model is subject to model uncertainties due to simplification and random effects that are neglected in the model. Ideally, model uncertainties should be obtained from a set of representative laboratory experiments and measurements on real structures. Nonetheless, this aspect is often overlooked, and model uncertainties should be based on engineering judgment.

5.3.2 Hydrodynamic forces on bridge piers

The direction of flow can be oriented at an angle relative to the pier's longitudinal axis (θ_f), leading to both lift and drag pressures on the pier (see Figure 5.7). The form of the water flow pressure distributed over the height of bridge piers can be assumed as uniform for both rectangular and circular piers, with very slight changes at both the top and bottom of the piers [216]. Thus, the drag ($F_{D,p}$) and lift ($F_{L,p}$)

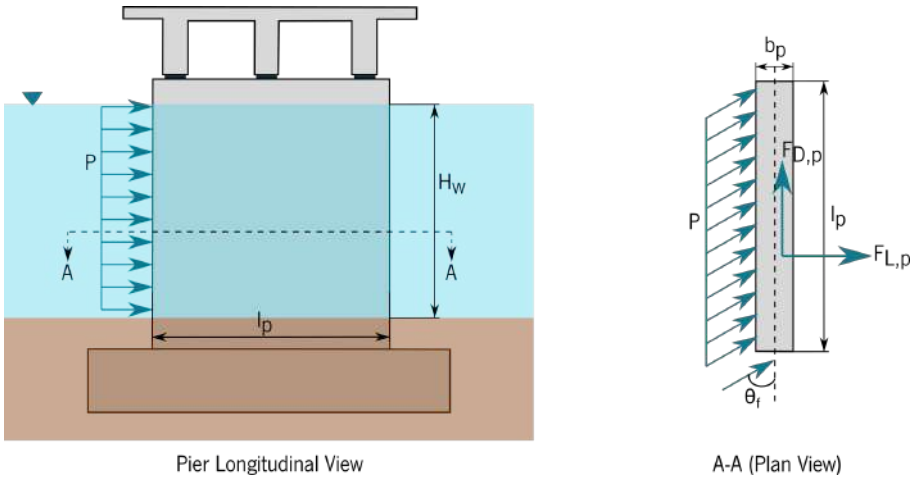


Figure 5.7: Hydrodynamic forces on submerged bridge piers

forces at piers can be expressed as:

$$F_{D,p} = \left(\frac{1}{2}\, C_{D,p}\, \frac{\gamma_w}{2g}\, V^2\right)\, b_p\, H_w \tag{5.13}$$

$$F_{L,p} = \left(\frac{1}{2}\, C_{L,p}\, \frac{\gamma_w}{2g}\, V^2\right)\, l_p\, H_w \tag{5.14}$$

where $C_{D,p}$ and $C_{L,p}$ are the coefficients of drag and lift on the pier, provided by different guidelines and standards (e.g. [217]), γ_w is the specific weight of water, b_p is the width of the pier, and l_p is the length of the pier. It should be noted that the dragging coefficient is usually established as a function of the shape of the pier, e.g., semicircular-nosed pier, square-ended pier, wedged-nosed pier, while the lifting coefficient is established as a function of the angle between the direction of flow and the longitudinal axis of the pier, with maximum values for larger angles (e.g. $C_{L,p} = 1$ for angles larger than $30°$ [217]).

5.3.3 Scour at substructures

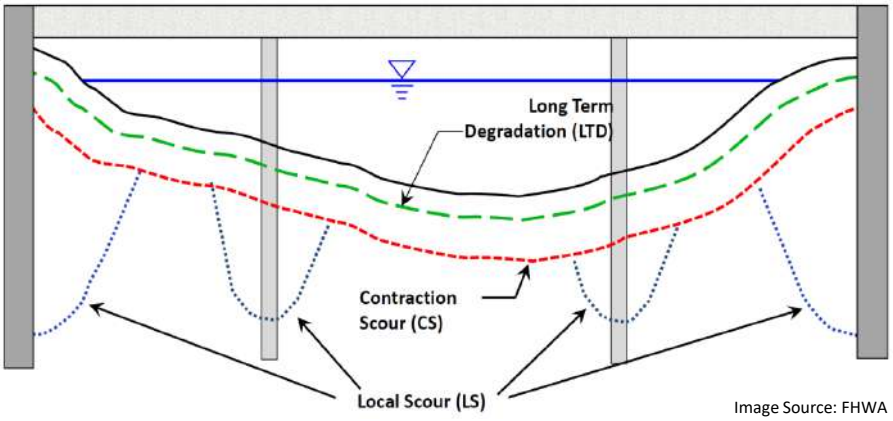
During flood events, the action of flowing water induces an erosion process of the bed material around bridge foundations referred to as scour [12]. Scour occurs naturally, and even though granular alluvial river beds and banks are more prone to this process, materials such as clay and even some kinds of rock are susceptible as well [204]. There are three main scour mechanisms known as long-term degradation,

contraction scour, and local scour. Degradation scour is a long-term process that occurs due to natural or human-made alterations to the catchment and river, which induces sediment removal due to a deficit in sediment supply from upstream; contraction scour is the removal of sediment due to the constriction of a river channel, e.g., due to the presence of bridge piers or abutments, which increases the velocity and shear stress at the streambed; and local scour is the removal of sediment around bridge piers and abutments, which is caused by the acceleration of flow and resulting vortices due to flow obstruction [12]. It can be conservatively assumed that the three components occur independently, and thus, their contribution can be added to obtain the total scour y_s at piers or abutments as:

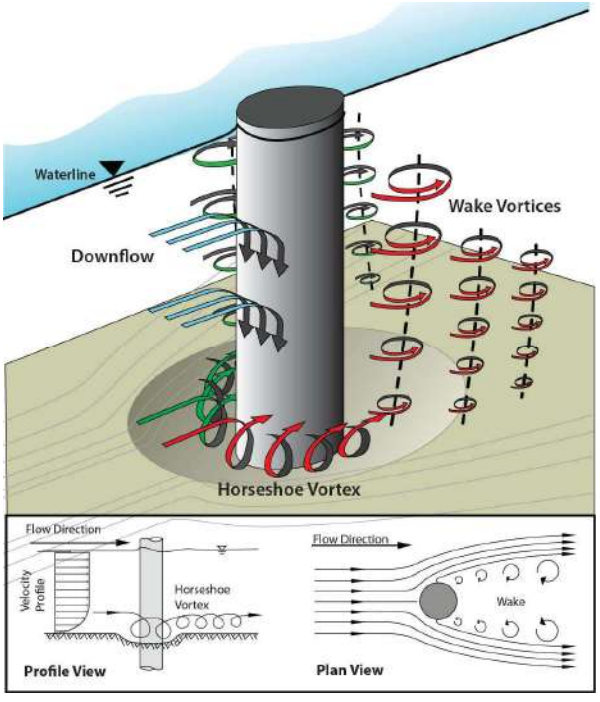
$$y_s = y_{s,loc} + y_{s,deg} + y_{s,con} \tag{5.15}$$

where $y_{s,loc}$ is the local scour, $y_{s,deg}$ is the long-term degradation, and $y_{s,con}$ is the contraction scour. Among the three scour components, local scour is often the ultimate cause of bridge failures during extreme flooding events [13].

Estimating local scour depth at piers has long posed challenges, largely owing to the complexities in both the flow field and pier configurations, as discussed by Ettema et al. [218]. Given the constraints of current computational capability, the use of numerical models for accurate scour simulation has been limited. Consequently, engineers continue to rely on empirical or semi-empirical formulas for determining equilibrium scour depths, which have been derived based on extensive hydraulics laboratory testing (flume tests) and available field data. To date, several prediction methods have been well-developed and widely adopted, including the HEC-18 method [12], the FDOT (Florida Department of Transportation) method [13], the Sheppard-Melville (S-M) method [219], and the TAMU method [220], previously referred to as the SRICOS-EFA (Scour Rate in Cohesive Soils - Erosion Function Apparatus) method. Ettema et al. [218] recommended adopting the S-M method for engineering practice. The concept of the S-M method was first proposed by Sheppard et al. [219] as a meld of two sets of equations: 1) the equation of Sheppard and Renna [13] for calculating equilibrium pier scour depth and 2) the equation adapted from Melville and Chiew [221] concerning the temporal evolution of time-dependent scour depth. Following this method, the time-dependent scour depth is evaluated depending on the flow intensity (V/V_c), which distinguishes



(a)



(b)

Figure 5.8: a) Total scour and scour components (source: [12]) ; b) Local scour processes at a cylindrical pier (source: [13])

whether clear water or live bed scour conditions prevail in the approach flow to the pier. The critical velocity V_c can be calculated using the logarithmic law of velocity distribution as [16]:

$$V_c = u_c \, 5.75 \, \log_{10}\left(\frac{5.53 \, H_w}{D_{50}}\right), \tag{5.16}$$

where D_{50} is the median diameter of bed sediment particles, and the critical shear velocity u_c may be computed as [221]:

$$u_c = \begin{cases} 0.0115 + 0.0125 \, D_{50}^{1.4} & \text{if } D_{50} \leq 1 \\ 0.0305 \, D_{50}^{0.5} - 0.0065 \, D_{50}^{-1} & \text{if } D_{50} > 1 \end{cases}. \tag{5.17}$$

In addition, the live bed velocity V_{lp} may be evaluated as:

$$V_{lp} = \max(5 \, V_c, 0.6 \, \sqrt{H_w \, 9.81}). \tag{5.18}$$

Then, the equilibrium local scour depth $y_{s,loc}$ may be calculated for each flow intensity condition as Sheppard and Renna [13]:

$$y_{s,loc} = \begin{cases} 2.5 \, f_1 \, f_2 \, f_3 \, D_{\text{eff}} & \text{if } 0.4 < \frac{V}{V_c} \leq 1 \\ D_{\text{eff}} \, f_1 \, \left(2.2 \, \frac{(V/V_c - 1)}{(V_{lp}/V_c - 1)} + 2.5 \, f_3 \, \frac{(V_{lp}/V_c - V/V_c)}{(V_{lp}/V_c - 1)}\right) & \text{if } 1 < \frac{V}{V_c} \leq \frac{V_{lp}}{V_c} \\ 2.2 \, f_1 \, D_{\text{eff}} & \text{otherwise} \end{cases} \tag{5.19}$$

where D_{eff} is the effective pier diameter (i.e. an equivalent diameter of a circular pile that would experience the same scour depth), and f_1, f_2 and f_3 represent, respectively:

$$
\begin{aligned}
f_1 &= \tanh\left(\left(H_w/D_{\text{eff}}\right)^{0.4}\right), \\
f_2 &= 1 - 1.2\left(\ln(V/V_c)\right)^2, \\
f_3 &= \frac{D_{\text{eff}}/(D_{50})}{0.4\left(D_{\text{eff}}/(D_{50})\right)^{1.2} + 10.6\left(D_{\text{eff}}/(D_{50})\right)^{-0.13}}.
\end{aligned}
\tag{5.20}
$$

Finally, the scour evolution over time $y_{st,loc}$ may be obtained by applying a factor K_t [221]:

$$
y_{st,loc} = y_{s,loc}\, K_t \tag{5.21}
$$

where,

$$
K_t = \exp\left(-0.04 \left|\frac{V_c}{V} \ln\left(\frac{t_c}{t_{\text{eq}}}\right)\right|^{1.6}\right) \tag{5.22}
$$

$$
t_{\text{eq}} = \begin{cases} 200\, \frac{D_{\text{eff}}}{V}\, \left(V/V_c - 0.4\right), & \text{if } H_w/D_{\text{eff}} > 6, \\ 127.8\, \frac{D_{\text{eff}}}{V}\, \left(V/V_c - 0.4\right)\, \left(H_w/D_{\text{eff}}\right)^{0.25}, & \text{otherwise.} \end{cases} \tag{5.23}
$$

where t_c is the peak flood duration in days. Figure 5.9 shows the results of predicted local scour depths for different flood durations using the S-M formulation, for the example presented in Eidsvig et al. [196], where the fragility of a masonry arch bridge to local scour was examined (this figure was not included in the published paper due to space limitations). It can be seen that the flood duration has a great influence on the local scour. Therefore, the assumption of the attainment of the equilibrium scour for assessing the bridge fragility may be over-conservative, as it was highlighted in [196], mainly when the discharge is inducing clear-water scour conditions.

Furthermore, it can be observed from Eqs. 5.19-5.23 that the method requires approximations to be made for D_{eff} when estimating scour at standard (noncylindrical) pier designs, given that it was originally developed for single cylindrical piers. In addition, more complex pier forms typically comprise several structural components, including a rectangular-section pier column supported by cylindrical piles beneath a pile cap, often located near the bed surface. The computation of local scour at these complex pier configurations requires, similarly, replacing the pier width of the original expression with an effective

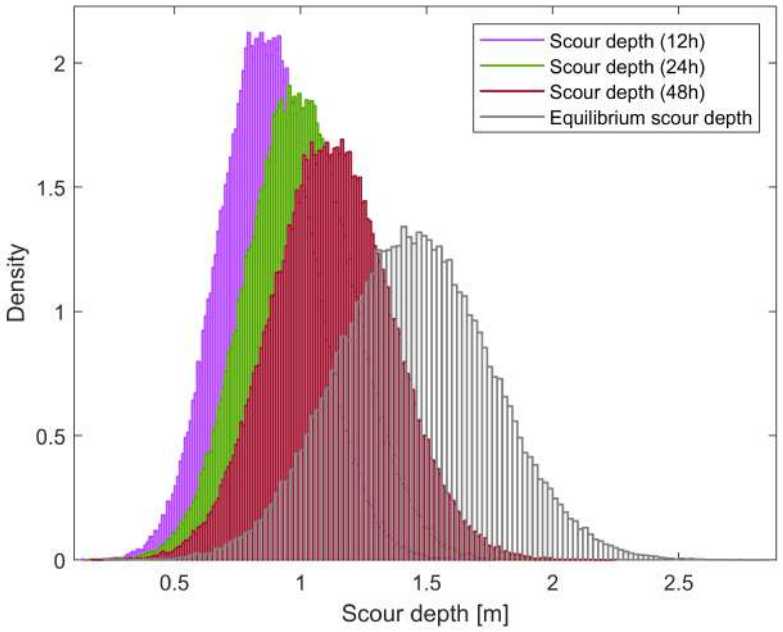


Figure 5.9: Example of predicted local scour depths for different flood durations

diameter. This adjustment ensures that the scour depth at a circular pile with this diameter matches the scour depth at the complex pier under identical sediment and flow conditions [219]. Nonetheless, these adaptations for complex piers are approximate and increase the uncertainty in the scour depth estimation [218]. On the other hand, local scour at abutments occurs due to the acceleration of the flow and the formation of vortices resulting from the abutment and the roadway embankment obstructing the flow [12]. Several equations have been formulated to estimate scour depth at abutments. Among them, Ettema et al. [222] developed abutment scour equations considering a range of abutment types, abutment locations, flow conditions, and sediment transport conditions. The equations consider abutment scour as a short contraction scour and apply a factor to amplify the scour depths estimated for flow through a long contraction and account for the large-scale turbulence that develops in the vicinity of the abutment [12]. Therefore, scour depth around an abutment $y_{s,ab}$ can be determined as Ettema et al. [222]:

$$y_{s,ab} = y_{\max} - y_0 \tag{5.24}$$

$$y_{\text{max}} = \alpha_A \, y_c \tag{5.25}$$

$$y_c = y_1 \left(\frac{q_{2c}}{q_1} \right)^{\frac{6}{7}} \tag{5.26}$$

where y_{max} is the maximum flow depth resulting from abutment scour, y_0 is the flow depth prior to scour, α_A is the amplification factor for condition A of abutment scour, y_c is the flow depth including live-bed or clear-water contraction scour, y_1 is the upstream flow depth, q_1 is the upstream unit discharge, and q_{2c} is the unit discharge in the constricted opening. For further details about the different abutment scour conditions and the amplification factors, readers may refer to, e.g., [12, 222]. Finally, it should be noted that describing a complex physical process as scour through the use of simplified mathematical expressions results in significant uncertainties. This aspect was examined in detail by Lagasse et al. [223], where the model uncertainty resulting from selecting a particular scour equation to estimate scour was estimated from laboratory and field data.

5.4 Case study of Santarém area bridges

The methodology from Section 5.2 is applied for fragility analysis of a portfolio of bridges in the Santarém district area (Figure 5.10). One of the first steps to implement the proposed methodology is to acquire a dataset of the bridge inventory from the case study containing the necessary structural parameters to estimate the capacity and demand given the hazard intensity. In Portugal, Infraestruturas de Portugal, S.A. (IP) is a public company managing the largest stock of assets. IP manages more than 15.000 km of roads, 2.600 km of railways, more than 7.500 bridges, and many sub-systems such as signaling, catenary, and power supply [224]. IP's Bridge Management System, SGOA, is a decision support tool implemented since 2006 with the main goal of prioritizing interventions. The SGOA comprises an inventory module that collects data regarding the assets; an inspection module that collects data from principal, routine, and sub-aquatic inspections and assesses the damages; and a maintenance, repair, rehabilitation, and replacement module for planning short-term intervention plans. IP provided the inventory data for 219

road transportation assets located in the Santarém study area (shown in Figure 5.10), within the scope of the SAFEWAY research project, which focused on enhancing the resilience of transport infrastructures across Europe [225]. Given that the inventory dataset did not contain all the required information for conducting the fragility analysis of bridges, additional data was obtained from bridge plans and inspection reports provided, as well as geo-information systems for deriving approximate channel geometries. The unavailability of high-quality data for the proper understanding of bridge performance is a current issue shared by many countries and highlighted by many researchers [226, 227]. This issue was tackled herein by using the available information from actual bridges and making assumptions in the absence of reliable data for the illustration and demonstration of the methodology.

As a next step in the methodology, only bridges crossing waterways are selected. Figure 5.11a provides an overview of the distribution of transport infrastructure types in the study area. It can be observed that 15.1% of the 219 assets correspond to river-crossing bridges, and 26.5% correspond to culverts. IP makes the differentiation between both types of assets as a function of their span. Essentially, bridges with a span length smaller than 10m are considered culverts, and their structural system is commonly pipe/box type. Even though culverts may exceed their capacity and become critical during flooding events [196], the focus here is on the structural behavior of bridges. Figure 5.11b provides an overview of the bridge structural types. It can be seen that multiple spans (48.5%), masonry arch bridges (24.2%), and simply supported decks (9.1%) comprise the three most frequent bridge types found in the study area. However, these categories are overly broad. Therefore, a detailed review of the bridge plans and inspection reports was essential prior to analyzing Table 5.1 in order to define the failure modes of the bridge components. After conducting this examination, five bridge classes were defined, namely single-span reinforced concrete (RC) bridges, multiple-span (continuous and simply supported) RC bridges with shallow foundations, multiple-span RC bridges with deep foundations, and masonry arch bridges with shallow foundations. It should be noted that two different classes were defined for multiple-span RC bridges given that bridges supported on shallow and deep foundations have a different resistance to scour, and thus, the LSF vector is defined differently for each case. Finally, a sixth bridge class was defined for some bridges found along the Tagus River (see Chapter 3), which are of great geographical importance since they link municipalities located on the riverbanks. In the next sub-sections, further details regarding the considerations for defining the failure modes for the bridge classes and the application of the methodology are provided. It is worth

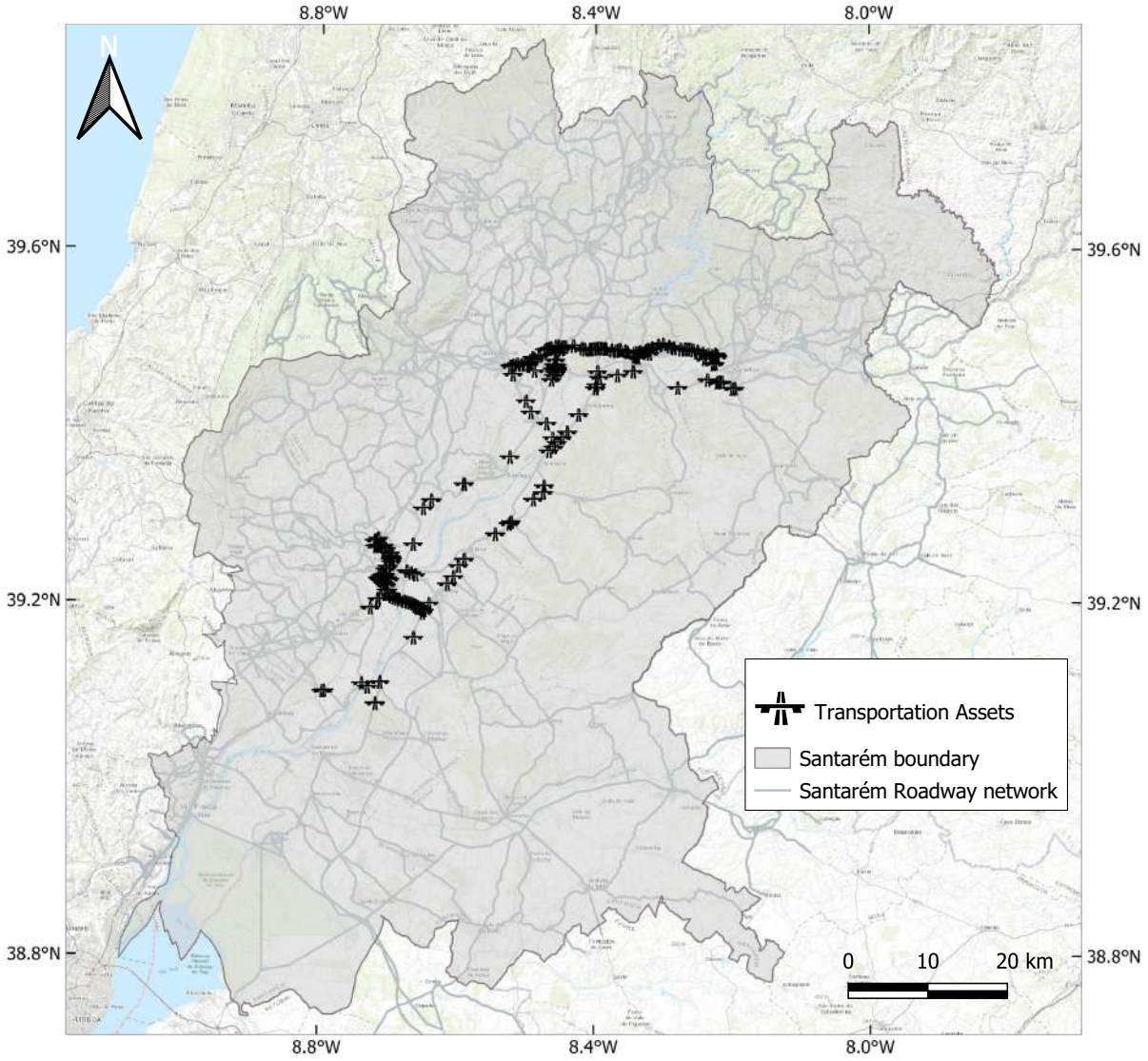


Figure 5.10: Location of transportation assets from the Santarém study area (source of data: Infraestruturas de Portugal)

noting that in the following assessments of bridge failures due to flooding, the assumption is made that there is no traffic on the bridge, thereby omitting live-load contributions from the analyses. Moreover, water depth was selected as the intensity measure for constructing the fragility functions, as it is deemed the most appropriate to characterize the load impacting the bridge across different failure modes. Based on this intensity measure, the remaining hydraulic properties at the bridge location are derived from the Bayesian Network elaborated in Chapter 3. Lastly, all the fragility functions presented in this section were constructed using one million Monte Carlo (MC) simulations to compute the probability of failure for each

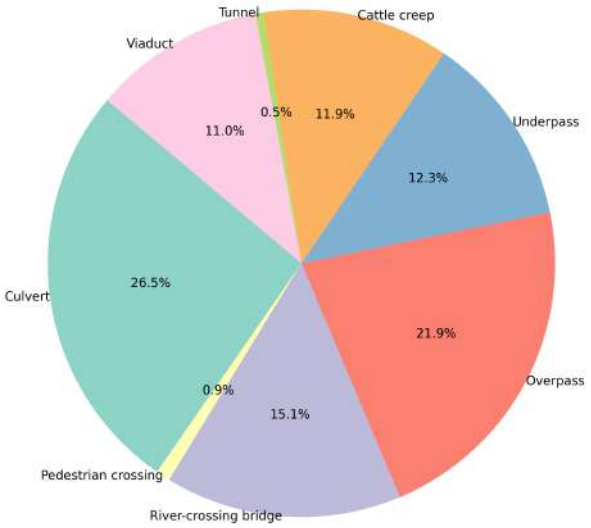
intensity measure.

5.4.1 Single span RC bridge

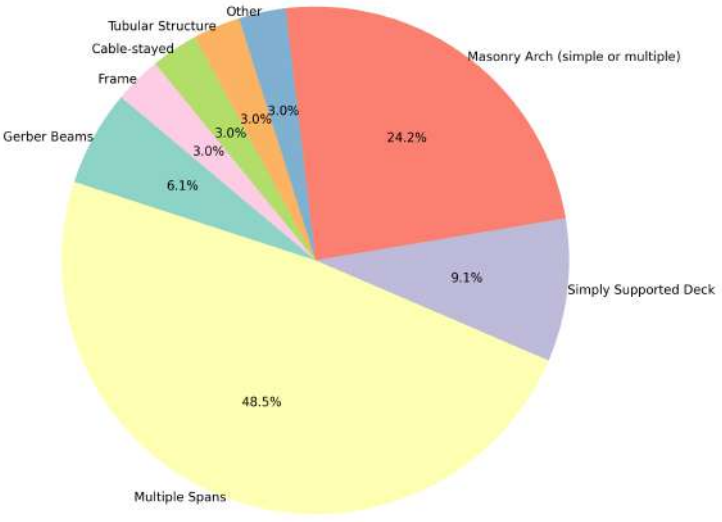
Figure 5.12 presents a schema of the first bridge class defined, which corresponds to single-span reinforced concrete (RC) bridges with simply supported decks (or limited deck-abutment connectivity). Following Table 5.1, hydrodynamic forces acting on simply supported decks may lead to a transverse, uplift, and/or overturning failure if the water depth exceeds the low chord of the bridge deck. The magnitude of these hydrodynamic forces can be computed as explained in Section 5.3.1. On the other hand, the vertical resistance of the deck to the uplift forces is comprised of the self-weight of the deck along with the strength of any connections present between the superstructure and the substructure. In the simplest case, the deck-pier connection is done through elastomeric bearings, which do not contribute to the vertical capacity. However, in cases where vertical connectivity is present, e.g., through anchor bolts, dowel bars, among others, its contribution to the capacity model should be considered. For instance, the contribution to the capacity of connections with dowel bars can be estimated as the pullout resistance or yield strength of the dowel bars [228]. Similarly, the transverse resistance depends on the deck-substructure connection. For decks with no transverse connections or restraints, the transverse capacity of the bridge deck corresponds to the friction force, which depends on the coefficient of friction between elastomeric bearings and concrete and the self-weight of the deck. Conversely, in the presence of any transverse restraint, e.g., shear keys, steel restrainers, anchor bolts, among others, their contribution to the transverse resistance should be added. In the following, the LSFs are formulated considering the simply supported decks with limited deck-abutment connectivity, i.e., dowel bars, as depicted in Figure 5.12, to provide a more general condition. Yet, if there are no connections, their contribution to the resistance can be disregarded.

Three limit state functions can be formulated for the deck failure modes of class 1 bridges $(G_{c1}^{d,t}, G_{c1}^{d,o}, G_{c1}^{d,u})$. First, the LSF for the transverse failure mode can be defined as:

$$G_{c1}^{d,t} = (\mu_b \ (D_L - F_{L,d}) + F_{ct,i}) \ (1 - D(t)) - F_{D,d} \tag{5.27}$$



(a)



(b)

Figure 5.11: Distribution of a) transport infrastructure types; b) river-crossing bridge structural types, in the Santarém case study (source of data: Infraestruturas de Portugal)

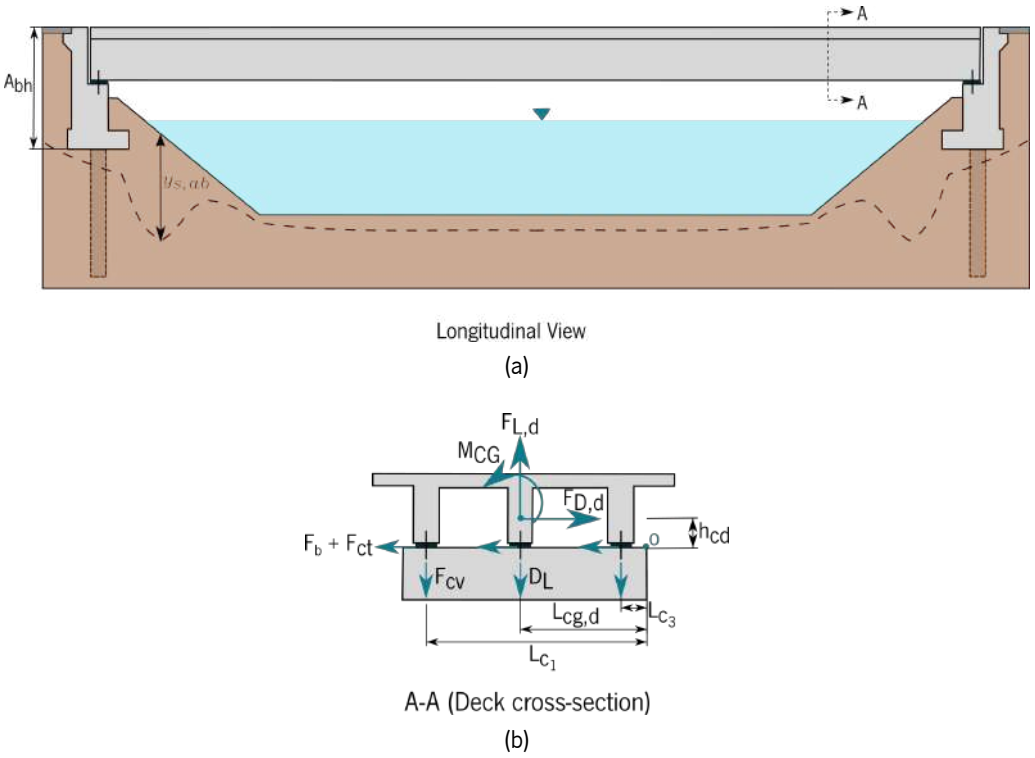


Figure 5.12: Illustration of bridges belonging to class 1: Single span RC bridges

where μ_b is the coefficient of friction between elastomeric bearings and concrete, D_L are the deck permanent loads, i.e. the deck self-weight plus additional dead loads, $F_{ct,i}$ is the contribution to the transverse capacity given by the connection i (if any exist), and $D(t)$ is a resistance deterioration function to account for potential deterioration effects affecting the deck fragility over time. Similarly, the LSFs for the overturning and uplift failure modes can be generalized as, respectively:

$$G_{c1}^{d,o} = ((D_L - F_{L,d})\ L_{cg,d} + F_{cv,i}\ L_{c,i})\ (1 - D(t)) - F_{D,d}\ h_{cd} + M_{CG} \tag{5.28}$$

$$G_{c1}^{d,u} = (D_L + F_{cv,i})\ (1 - D(t)) - F_{L,d} \tag{5.29}$$

where h_{cd} is the distance from the rotation point O (as depicted in Figure 5.12b) to the resultant dragging force which depends on the inundation ratio, $L_{cg,d}$ is the distance from the rotation point to the deck center of gravity, $F_{cv,i}$ is the contribution to the vertical capacity given by the connection i, and $L_{c,i}$

is the distance from the rotation point to the center of each connector. The coefficients for computing the hydrodynamic forces are determined following the fitting equations provided by [215] for the three girder bridges. These equations are a function of the inundation ratio so they vary for each intensity measure of the flood (see Appendix C for further details). It should be noted that the overturning moment M_{CG} takes a stabilizing behavior for low inundation ratios. However, as h_a values increase, the $C_{M,d}$ coefficient takes negative values, implying a destabilizing effect where the deck's upstream portion lifts when significantly submerged [229]. As highlighted in Section 5.3.1, the use of these coefficients to approximate the hydrodynamic forces on decks involves model uncertainties. Thus, all hydrodynamic loads ($F_{D,d}, F_{L,d}, M_{CG}$) are multiplied by a random variable θ_{hf}, which represents the model uncertainty associated with the estimation of hydrodynamic forces (it has been omitted from Eqs.5.27-5.29 to prevent redundancy). The contribution to the resistance provided by the dowel bars connecting the deck to the abutment is estimated following Ataei and Padgett [228]. Model uncertainty is not considered for the dowel bar strength equations, but uncertainty in the model parameters is considered, i.e., in the reinforcement yield strength F_y. Regarding the potential deterioration processes influencing the deck fragility, a resistance deterioration function is adopted in the following form:

$$D(t) = D(t-1) + \Delta_{D,t}, \quad \text{for } t \geq T_0, \tag{5.30}$$

where $\Delta_{D,t}$ represents the annual deterioration increment at year t, which accumulates over the service life, and $D(t-1)$ represents the accumulated deterioration up to year $t-1$. The deterioration process begins at time $t \geq T_0$. The mean values and standard deviation of the annual deterioration increment and the deterioration initiating time should be modeled in accordance with the deterioration phenomena. It is expected that deterioration mechanisms affecting the deck resistance to hydrodynamic loads are related to loss of frictional forces due to deterioration of the elastomeric bearings and corrosion of the dowel bars connectors (if any exist). The values assumed for these processes are presented in Table 5.2, estimated based on the findings presented in [10] regarding the strength deterioration of anchor bolts due to corrosion.

Lastly, a fourth failure mode is considered for bridges within class 1, consisting of local scour at abutments. As briefly mentioned in Section 5.3.3, scour at abutments depends on the flow conditions and the type

and location of the abutment. Considering the type of abutments in the study area for single-span RC bridges, scour condition A is more likely to take place since the abutments are in close proximity to the main channel (see [222] for reference). To formulate the limit state function for failure due to scour at abutments, the resistance of the soil-bridge system to scour has to be defined. It is worth mentioning that failure is defined as any abutment damage resulting in the bridge being closed to traffic. The maximum allowable scour depth the abutment can withstand depends on several factors, including the abutment type. In the case that abutments are supported on deep foundations, they frequently withstand deeper scour holes, and the failure can be associated with the loss of lateral stability and bearing capacity of piles (as will be introduced for bridges within class 4, i.e., multiple-span RC bridges with deep foundation). Nonetheless, even when the abutment is supported on deep foundations, a slope stability failure may occur, which would control the maximum scour depth to trigger failure since it is more critical than that to cause deep foundation failure [14] (see Figure 5.13). Thus, assuming slope stability failure as the controlling failure mode for bridge abutments in class 1, the LSF can be defined as:

$$G_{c1}^{a,s} = y_{s,max}\,\theta_{rs} \; - \left(y_{s,ab} + y_{s,deg}\left(t\right)\right)\,\theta_{sca} \tag{5.31}$$

where $y_{s,max}$ is the maximum allowable scour depth, θ_{rs} is the model uncertainty associated with the definition of this limit, and θ_{sca} is the model uncertainty of the abutment scour prediction model as explained in Section 5.3.3. Briaud et al. [14] investigated the failure scour depth $y_{s,max}$ controlled by slope stability failure of the abutment, based on a series of slope stability analyses of different scour scenarios using a 2D limit equilibrium slope stability program. Based on the effective stress analysis results, the calculation of the scour limit at abutments is recommended as [14]:

$$y_{s,max} = \frac{1.55\,\frac{c'_{\text{avg}}}{\gamma_s} - 0.1A_{bh}}{1 - 1.55\,\left(\tan\phi'\right)_{\text{avg}}} \tag{5.32}$$

where c'_{avg} and $\left(\tan\phi'\right)_{\text{avg}}$ are the average effective cohesion and the average effective friction angle tangent of the embankment and channel soil bed, respectively, γ_s is the soil unit weight, and A_{bh} is the total height of the abutment. No reference is made in [14] regarding the model uncertainty of this model, so θ_{rs} is assumed based on recommendations of the JCSS [230]. The model uncertainty associated with

the abutment scour prediction model (θ_{sca}) is considered normally distributed with the statistical properties obtained from the ratio of observed scour to predicted scour for the given equation, as suggested by Lagasse et al. [223]. Lastly, time-dependent deterioration effects are introduced in this LSF by accounting for the long-term degradation scour ($y_{s,deg}$), which may exacerbate the total scour depth at abutments. The degradation scour at time t can be computed as:

$$y_{s,deg}\left(t\right) = y_{s,deg}\left(t-1\right) + \Delta_{Ds,t} \tag{5.33}$$

where $\Delta_{Ds,t}$ represents the annual scour degradation increment at year t, which accumulates over the service life, and $y_{s,deg}\left(t-1\right)$ represents the accumulated degradation up to year $t-1$. The definition of an annual scour degradation increment would require the use of historical records showing trends in channel bed changes or other empirical methods to determine the potential for long-term degradation [12]. Given the lack of this type of data, the mean values and standard deviation of the annual rate of degradation scour are assumed in this study as detailed in Table 5.2.

Finally, the fragility of the bridge system is calculated using four LSFs:

$$\boldsymbol{G_{c1}} = (G_{c1}^{d,t}, G_{c1}^{d,o}, G_{c1}^{d,u}, G_{c1}^{a,s}) \tag{5.34}$$

Table 5.2 provides a summary of the distribution of the random variables considered for the evaluation of the limit state functions for bridges within class 1. Given that several bridges belong to this class, the specific values of bridge dimensions, connection details, and soil-related characteristics are not provided here but are summarized in Appendix C.

Results are herein presented for one bridge belonging to class 1, identified as bridge 19 (refer to Appendix C for identification). Four time periods of analysis are defined, namely at 0, 25, 50, and 75 years. Figure 5.14 presents the results of the upper and lower bounds of the system fragility functions for the selected time periods. It can be observed that after exceeding 4m of water depth, there is an abrupt



Figure 5.13: Slope stability failure of the abutment embankment. Source: [14]

Table 5.2: Distribution parameters for random variables to evaluate $G^{d,t}$, $G^{d,o}$, $G^{d,u}$, and $G^{a,s}$

Variable	Description	Dist.	Mean	Std	Ref.
D_L	Deck permanent loads	N[1]	μ_{D_L}	$0.1\mu_{D_L}$	[230]
F_y	Reinforcement yield strength	N	413 MPa	29 MPa	[230]
γ_s	Soil unit weight	LN[2]	μ_{γ_s}	$0.1\mu_{\gamma_s}$	[230]
c'	Effective cohesion	LN	$\mu_{c'}$	$0.2\mu_{c'}$	[230]
$\tan\phi'$	Effective friction angle	LN	$\mu_{\tan\phi'}$	$0.15\mu_{\tan\phi'}$	[230]
θ_{hf}	Model uncertainty hydrodynamic forces	LN	1	0.1	[230]
θ_{rs}	Model uncertainty slope stability	LN	1.1	0.1	[230]
θ_{sca}	Model uncertainty abutment scour formula	N	0.74	0.23	[223]
$\Delta_{Dd,t}$	Deck deterioration rate	LN	0.0025	0.0025	[10]
$\Delta_{Ds,t}$	Long-term degradation scour rate	LN	0.005	0.0025	-

[1] Normal distribution
[2] Lognormal distribution

increase in the probability of failure. This is explained by the deck being fully submerged, which significantly increases the hydrodynamic forces. Furthermore, the impact of deterioration processes over time is evident, with a substantial increase in the failure probability for the 75-year time period.

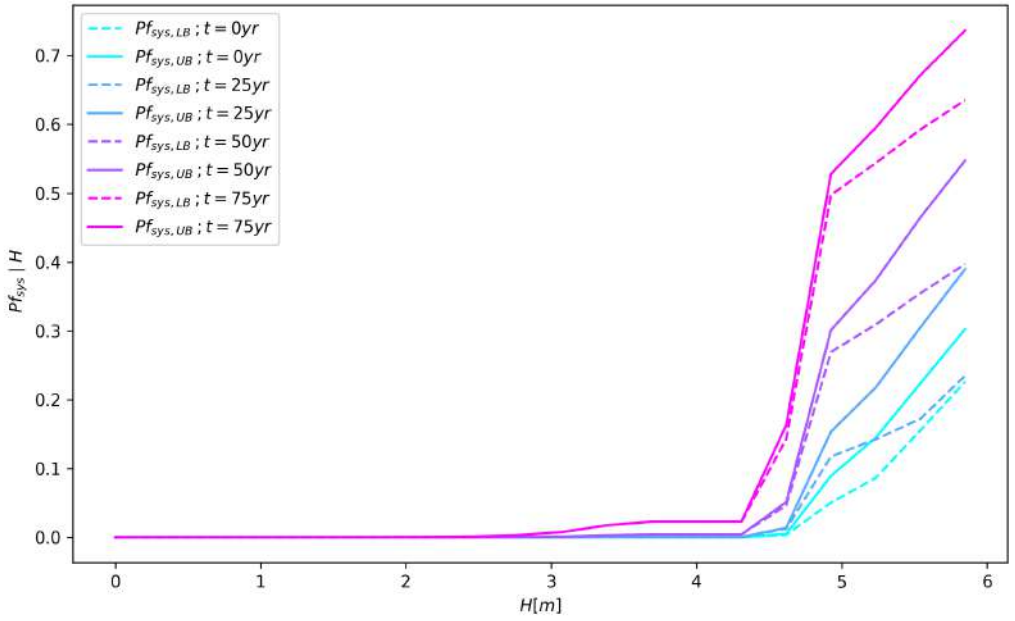


Figure 5.14: Time-dependent system fragility function for a single-span RC bridge (class 1)

5.4.2 Multiple-span RC bridge (continuous) with shallow foundation

Figure 5.15 presents a schema of the second bridge class defined, corresponding to multiple continuous span reinforced concrete (RC) bridges with shallow foundations. Given the deck's supporting conditions, the LSFs formulated for deck failure within class 1 bridges do not apply to this type of deck, even during inundated conditions. This is because the monolithic connection with the pier offers resistance against uplift, drag, and overturning of the deck induced by hydrodynamic forces. Following Table 5.1, there may exist also failure modes associated with the intermediate pier. Basically, the action of hydrodynamic forces on the bridge piers, simultaneously with axial, shear, and bending loads transferred from the deck, may cause pier failure [11]. However, it has been found that the probability of pier failure due to the effect of hydrodynamic forces alone leads to negligible values (< 1.0E-07 [11]). Even when potential debris accumulation exacerbating hydraulic forces is considered, the total dragging force acting on the pier is low and unlikely to affect the global behavior of the bridge [200]. Therefore, LSFs associated with pier failure due to hydrodynamic forces alone are not considered in the analysis. Nonetheless, the pier is supported on shallow foundations which makes it highly vulnerable to local scour. Thus, this failure

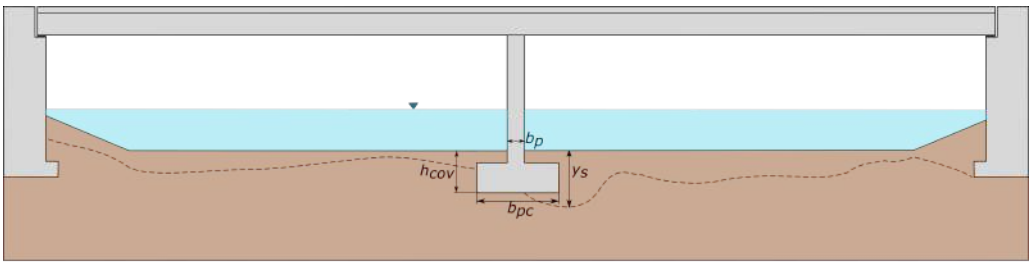


Figure 5.15: Illustration of bridges belonging to class 2: Multiple continuous-span RC bridges with shallow foundations

mode is thoroughly investigated for this bridge class. The scour depth at bridge piers can be computed as explained in Section 5.3.3 using the S-M method, given the hydraulic conditions, the soil properties, and the characteristics of the pier. Failure of bridges on shallow foundations is often anticipated when the estimated local scour depth reaches the foundation base, which is an assumption that has been proved to be conservative [16]. Fundamentally, bridge failure due to scour at pier foundations is governed by the combined resistance of the soil-bridge system, as depicted in Figure 5.16. The soil resistance to local scour is governed by the soil erodibility and its geotechnical properties: internal angle of friction, cohesion, and self-weight, while the bridge resistance is governed by its ability to redistribute the internal forces due to the removal of supporting soil at bridges substructures [15]. Therefore, the bridge's resistance to local scour action is significantly influenced by the quantities and detailing of reinforcement, type and detailing of bearings and joints between superstructure and substructure. Different methodologies can be implemented for the analysis of the soil-bridge system capacity, including detailed numerical modeling with 2D/3D finite element (FE) models (e.g., [200]). However, these approaches require extensive computation time, which hinders the possibility of applying them at a network-level scale, i.e., for a large portfolio of assets. On the other hand, Tanasić [16] elaborated on the concept of kinematic mechanisms to model the combined response of the supporting soil and the bridge structure (see Figure 5.16a). To this end, the bridge and supporting soil at substructures were represented with a rigid perfectly plastic soil-bridge model to apply the upper bound theorem of the theory of plasticity. Even though this approach is simple, it is comprehensive and sufficiently accurate for application on a portfolio level [15].

Based on the preceding discussion, the following limit state function can be formulated for the combined failure mode of class 2 bridges subjected to local scour at piers, (G^1_{c2}):

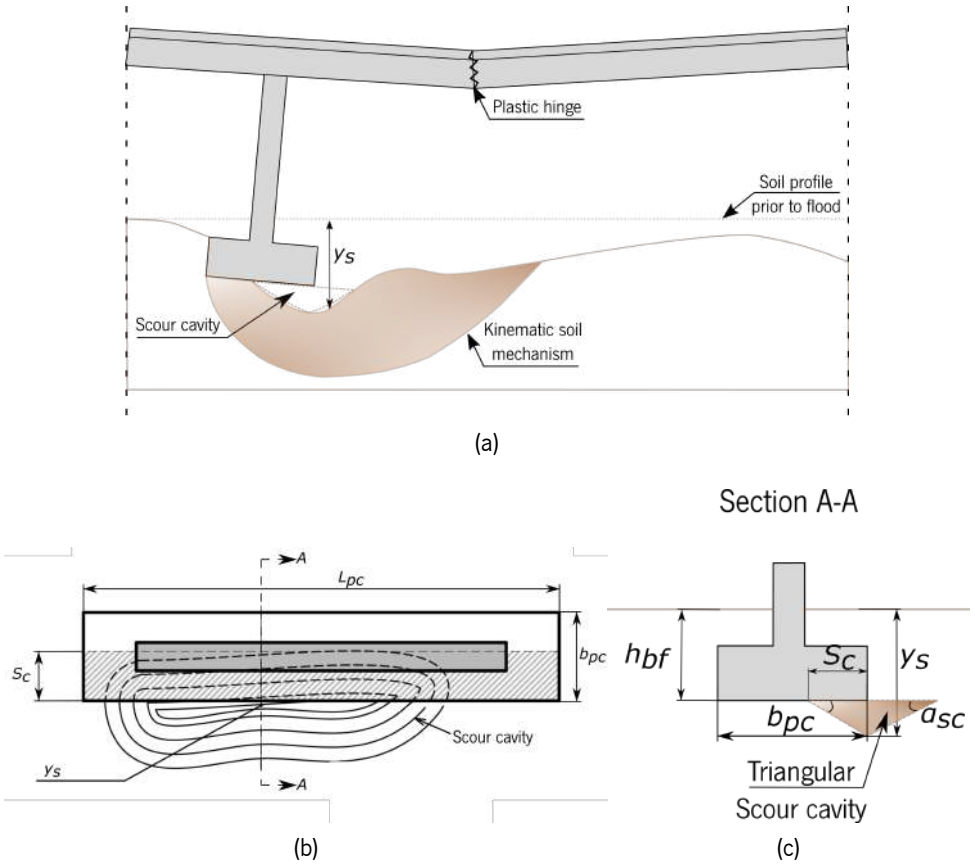


Figure 5.16: a) Combined bridge failure mode in the longitudinal direction; (b) local scour cavity at the affected pier foundation; (c) triangular scour cavity approximation. Source: [15]

$$G_{c2}^{p,u} = q_{\text{sbm}}(t)\ \theta_{ru}\ - q_{D_L}$$

where

$$q_{\text{sbm}}(t) = \begin{cases} q_{max} & \text{if } S_c(t) = 0, \\ q_{max}\left(1 - \frac{S_c(t)}{S_{c,max}}\right) & \text{otherwise} \end{cases} \tag{5.35}$$

where q_{sbm} is the limit load of the soil-bridge model at time t that depends on the scour cavity, i.e. the scour depth (y_s) and its horizontal extent (S_c), θ_{ru} is the model uncertainty associated with the response from the combined soil-bridge capacity model, and q_{D_L} is the contact pressure beneath the pier resulting from the superstructure self-weight and additional dead loads, and the self-weight of the pier foundation system. As illustrated in Figure 5.16c, the maximum scour cavities may be approximated as symmetrical, and the slope angles (α_{sc}) can be assumed equal to the soil internal friction angle for frictional soils, while

it can be considered as 45° for purely cohesive soils [16]. When the scour depth y_s has not reached the bottom of the foundation, q_{sbm} takes the value of the maximum soil bearing capacity (q_{max}). As the scour depth increases beneath the pier foundation level, the limit load decreases until the maximum scour extent $S_{c,max}$ that the soil-bridge model may withstand is reached. An example of the decrease of the limit load with the change in the horizontal scour extent is shown in Figure 5.17a. These functions were computed by Tanasić [16] using the rigid perfectly plastic soil-bridge model for different types of deck-substructure connection as illustrated in Figure 5.17b. These curves may be interpreted as the decrease of the safety factor at the pier foundation due to local scour growth. It can be observed that the type of deck-substructure connection has a significant impact on the resistance of the soil-bridge model to local scour. For bridges with no restraint on the top of the affected substructure (BT D in Figure 5.17b), there is no combined failure mode and a kinematic rotational soil mechanism is sufficient to trigger failure as the bridge superstructure does not constrain the foundation. Conversely, in the presence of horizontal restraint on the top of the affected substructure (BT A, BT B, and BT C in Figure 5.17b), the deck capacity and the adjacent deck-substructure connection type are relevant for the combined soil-bridge resistance. Bridges within class 2 in this study have wall-type piers, a fixed connection with the superstructure on the top of the pier, and a free connection on the adjacent supports, i.e., at the abutments. Therefore, a combined failure mode similar to the one encountered by the BT A from Figure 5.17 is expected. In order to estimate the ultimate horizontal scour extent beneath the foundation ($S_{c,max}$) for class 2 bridges, the rigid perfectly plastic soil-bridge model should be implemented. Nevertheless, project documentation with the reinforcement layout and detailing of the bridge elements is not available. In the absence of this information, one approach is to infer the quantity of reinforcement based on the design codes and regulations effective during the construction period. An alternative methodology, which has been adopted in this study, involves the assumption that the shape of the limit load functions depicted in Figure 5.17a reflect the mean behavior of the bridge type they represent and can be used to predict the maximum horizontal scour extent beneath the foundation for other bridges and evaluate the LSF of Eq. 5.35. Furthermore, the time-dependent deterioration effects are incorporated analogously to Class 1 bridges (Eq. 5.31), namely, through the addition of long-term degradation scour (Eq. 5.33) to the local scour depth at the piers. Nonetheless, deterioration associated with the corrosion of reinforcing steel, which impacts the deck and pier plastic moment, can also be considered, given their influence on the overall resistance of the soil-bridge system.

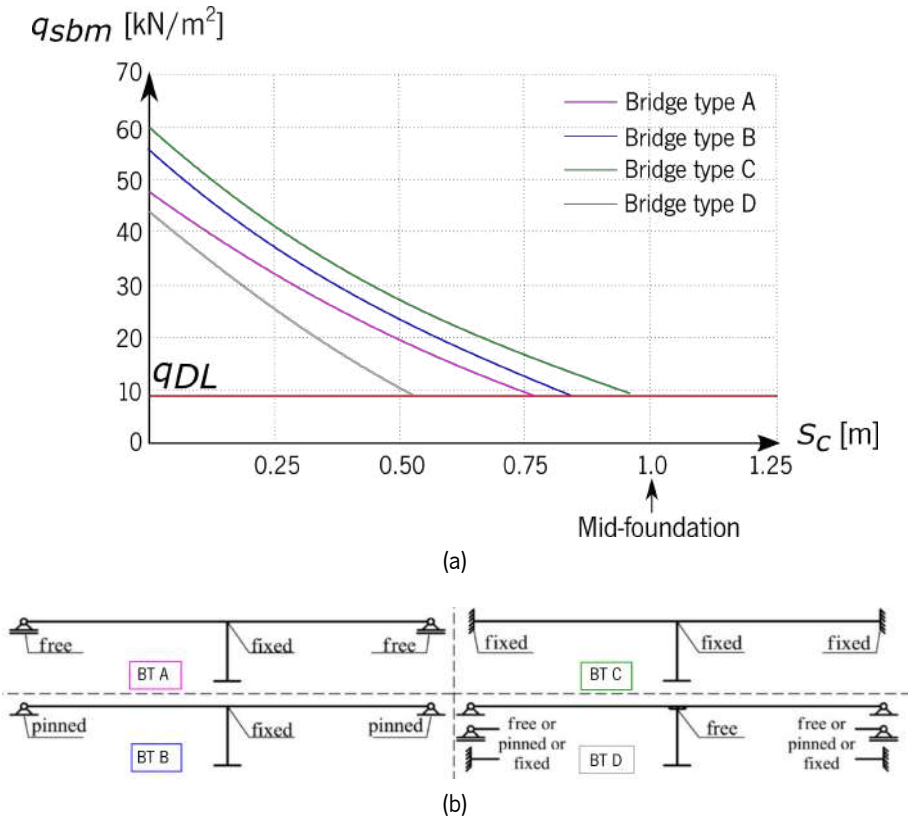


Figure 5.17: a) Decrease in limit load as a function of the horizontal scour extent; (b) Bridge types (BT) depending on adjacent deck support conditions and deck-pier connection. Source: [16]

Lastly, the type of abutments considered in this class correspond to vertical wall abutments with wing walls. As highlighted by Briaud et al. [14], in this type of abutment, the central vertical panel and the wing walls confine the embankment. This confinement provides a degree of protection against slope instability and embankment erosion. Consequently, the issue of determining the maximum allowable scour depth at vertical wall abutments is similar to that at bridge piers. In this scenario, the scour that leads to failure would be the depth that exposes the foundation components to a point where the load-bearing capacity is surpassed [14]. Therefore, the failure due to scour at abutments is formulated similarly to failure due to scour at pier foundations, but assuming the limit load function corresponding to bridges with no horizontal restriction at the top (BT D from Figure 5.17a) to determine the maximum horizontal scour extent beneath the abutment foundation. The LSF is then expressed as:

$$G_{c2}^{a,u} = q_{\text{sbm}}(t)\ \theta_{ru}\ - q_{D_L} \tag{5.36}$$

where the only distinction from the LSF of Eq. 5.35 relies on the limit load function to represent q_{sbm}. The fragility of the bridge system is finally calculated using the two LSFs:

$$\boldsymbol{G_{c2}} = (G_{c2}^{p,u}, G_{c2}^{a,u}) \tag{5.37}$$

Table 5.3 provides a summary of the distribution of the random variables considered for the evaluation of the limit state functions for bridges within class 2. The specific values of bridge dimensions and soil-related characteristics are not provided here but are summarized in Appendix C. It should be noted that similarly to the model uncertainty in the abutment scour formula considered for bridges in class 1, the model uncertainty in the pier scour formula is also assumed normally distributed with the statistical properties obtained from the ratio of observed scour to predicted scour for the FDOT equation, as suggested by Lagasse et al. [223].

Table 5.3: Distribution parameters for random variables to evaluate $G^{p,u}$ and $G^{a,u}$

Variable	Description	Dist.	Mean	Std	Ref.
D_{50}	Median diameter of bed sediment	LN[2]	$\mu_{D_{50}}$	$0.1\mu_{D_{50}}$	[223]
$\tan\phi'$	Effective friction angle	LN	$\mu_{\tan\phi'}$	$0.15\mu_{\tan\phi'}$	[230]
q_{D_L}	Contact pressure of permanent loads	N[1]	$\mu_{q_{D_L}}$	$0.1\mu_{q_{D_L}}$	[230]
q_{max}	Maximum soil bearing capacity	LN	$\mu_{q_{max}}$	$0.15\mu_{q_{max}}$	[230]
θ_{ru}	Uncertainty in soil-bridge resistance model	LN	1	0.25	-
θ_{sc}	Model uncertainty pier scour formula	N	0.78	0.20	[223]
θ_{sca}	Model uncertainty abutment scour formula	N	0.74	0.23	[223]
$\Delta_{Ds,t}$	Long-term degradation scour rate	LN	0.005	0.0025	-

[1] Normal distribution
[2] Lognormal distribution

Results are herein presented for one bridge belonging to class 2, identified as bridge 7 (refer to Appendix C for identification). Four time periods of analysis are defined, namely at 0, 25, 50, and 75 years. Figure 5.18 presents the results of the system fragility functions for the selected time periods. Although two LSFs were considered, the failure probability due to scour at abutments remained below 1E-6. Consequently, the combined failure mode governs the bridge system fragility due to local scour at piers (Eq. 5.35). Furthermore, the influence of long-term degradation scour is evidenced in the increasing failure probability over the years of analysis.

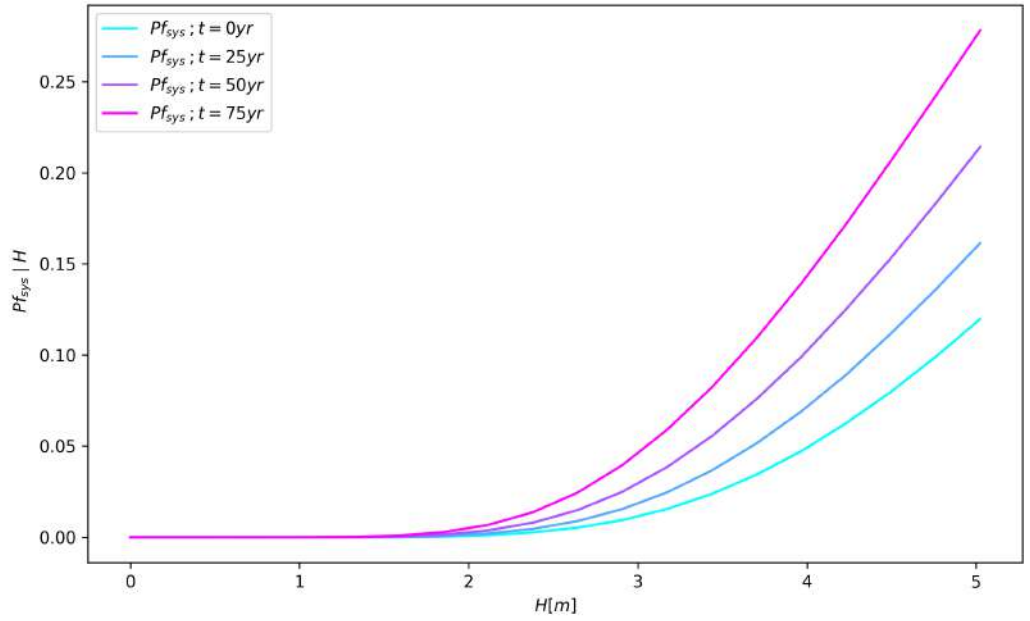


Figure 5.18: Time-dependent system fragility function for multiple continuous-span RC bridges with shallow foundations (class 2)

5.4.3 Multiple-span RC bridge (simply supported) with shallow foundation

As emphasized in the preceding section, the type of deck-substructure connection has a significant impact on the fragility of multiple-span bridges when exposed to scour. Therefore, the third class defined consists of multiple-span simply supported RC bridges with shallow foundations, as illustrated in Figure 5.19. Following the same approach employed for bridges in class 2, it can be seen that bridges in class 3 do not exhibit a combined failure mode due to the lack of restraint at the top of the affected pier. Instead, a kinematic rotational soil mechanism alone is sufficient to induce failure, as the bridge superstructure does not constrain the lifting of the foundation. Therefore, the failure due to scour at bridge piers within class 3 is formulated as per Eq. 5.35, assuming the limit load function corresponding to bridges with no horizontal restriction at the top (BT D from Figure 5.17a) to determine the maximum horizontal scour extent beneath the pier foundation. In addition, the condition of bridge abutments is equivalent to that of abutments within class 2. Thus, the LSF of Eq. 5.36 holds for bridge abutments within class 3. Finally, it is evident that given the supporting conditions of the decks, the same LSFs related to deck failure induced

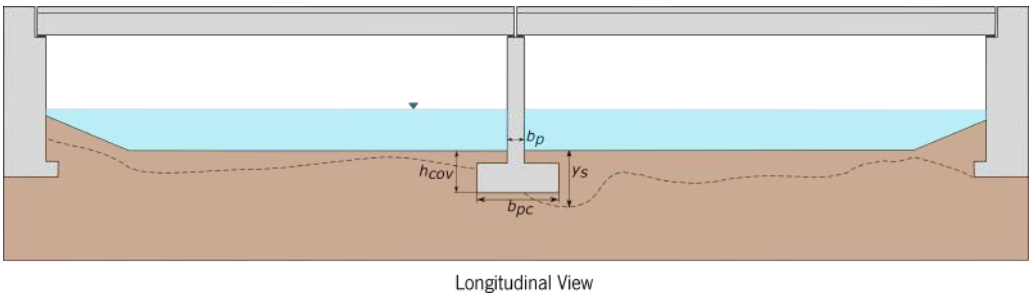


Figure 5.19: Illustration of bridges belonging to class 3: Multiple-span simply supported RC bridges with shallow foundations

by hydrodynamic forces from bridges within class 1 apply to decks in class 3. Then, the fragility of the bridge system is ultimately calculated using five LSFs:

$$\boldsymbol{G_{c3}} = (G_{c3}^{d,d}, G_{c3}^{d,o}, G_{c3}^{d,u}, G_{c3}^{p,u}, G_{c3}^{a,u}) \tag{5.38}$$

The summary of the distribution of the random variables considered for evaluating the LSFs in Eq. 5.38 is already provided in Tables 5.2-5.3. The specific values of bridge dimensions and soil-related characteristics are provided in Appendix C.

Results are herein presented for one bridge belonging to class 3, identified as bridge 15 (refer to Appendix C for identification). Figure 5.20 presents the results of the system fragility functions for the selected time periods of analysis, namely at 0, 25, 50, and 75 years. Like bridges in class 2, the system fragility is governed by the failure mode due to local scour at piers, while the probabilities for the other failure modes do not exceed 1E-6. It is recognized that an increase in water depth to a point where deck failure due to hydrodynamic forces becomes significant is plausible. Such a scenario would correspond to water levels surpassing 5m, i.e., the height of the bridge deck. Nevertheless, considering that the exceedance probability of a 4-meter water depth is only 0.1% at this bridge location (as derived from the Bayesian Network developed in Chapter 3), extending the intensity measure beyond this threshold is deemed unnecessary.

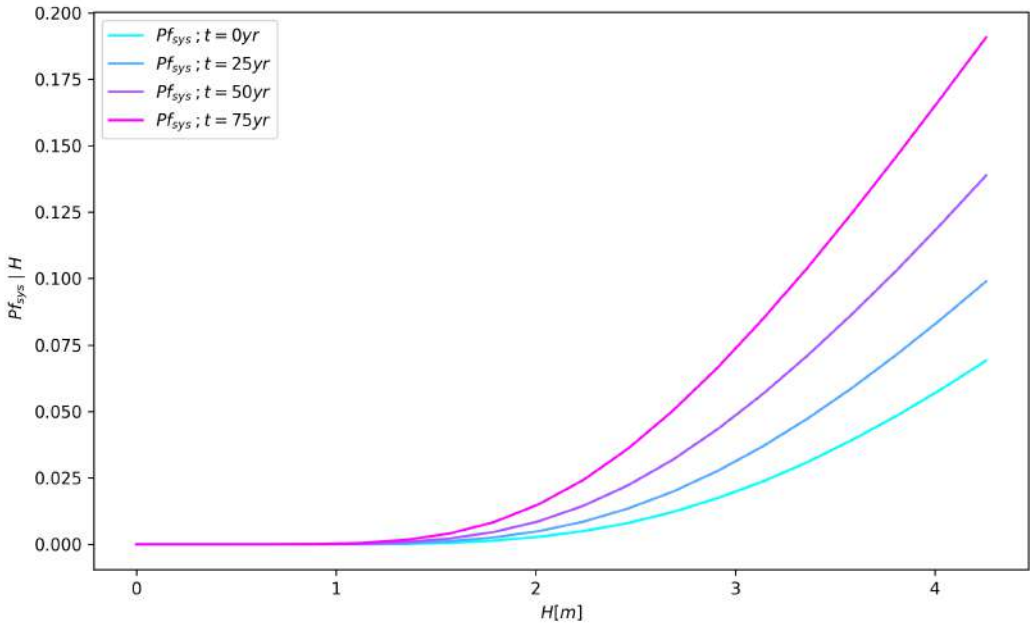


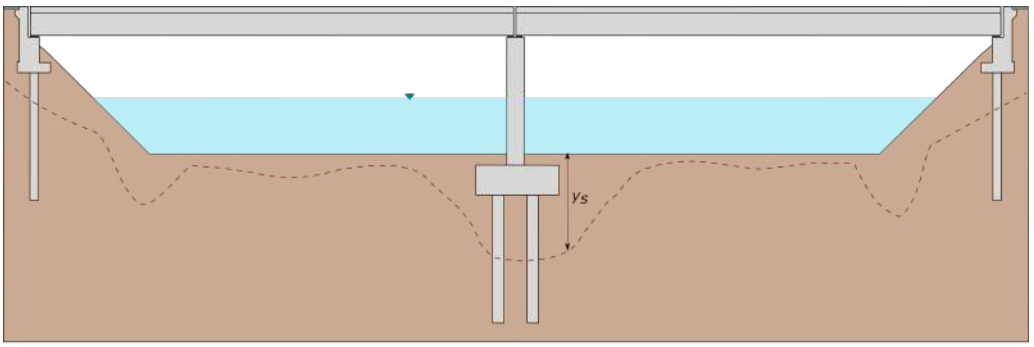
Figure 5.20: Time-dependent system fragility function for multiple-span simply supported RC bridges with shallow foundations (class 3)

5.4.4 Multiple-span RC bridge with deep foundation

Figure 5.21 illustrates the fourth bridge class defined, which corresponds to multiple-span simply supported RC bridges with deep foundations. Once again, given the supporting conditions of the decks, the same LSFs related to deck failure induced by hydrodynamic forces apply to decks in class 4. Other relevant failure modes for this bridge class concern those associated with scour at the pile-supported foundations. As mentioned in Section 5.2.1, bridges with pile foundations are less susceptible to scour damage or total collapse than those with shallow foundations. Nevertheless, exposed piles are undesirable as they compromise the bridge's stability. There are several challenges in estimating the reliability of bridges with deep foundations to flood-induced scour. On the one hand, predicting the scour depth at this type of bridge piers is particularly difficult due to the complex interactions between the flow field and bed materials for pier geometries comprised of multiple components, namely column, pile cap, and pile group [218]. Thus, as explained in Section 5.3.3, prediction formulas like the one suggested by the FDOT [219], require replacing the complex geometry (similar to that depicted in Figure 5.21b) with an

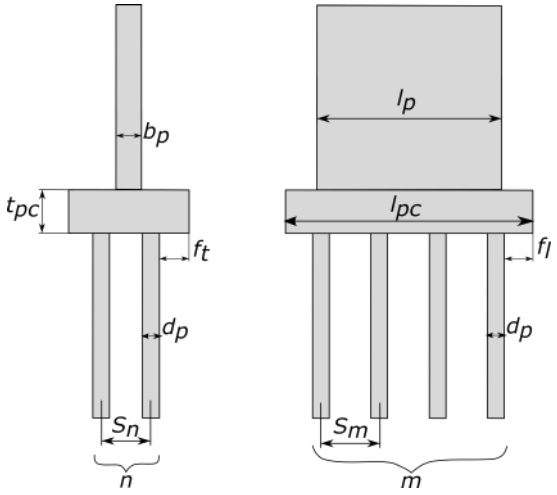
effective diameter. This adjustment aims to approximate the scour depth for a circular pile with the effective diameter to that of the actual pier geometry under the same sediment and flow conditions. The FDOT methodology [219] is adopted in this study to calculate the scour depth at complex piers. Nonetheless, the model uncertainty inherent in this methodology, when applied to complex piers, has not been previously addressed. Therefore, the θ_{sc} value estimated by Lagasse et al. [223] for the FDOT formula for cylindrical piers is used. Yet, it is recognized that the adaptations for complex piers increase the uncertainty in the scour depth estimation [218]. On the other hand, to accurately evaluate the response of bridges under extreme scour conditions and hydrodynamic forces, comprehensive nonlinear FE models accounting for the soil–pile–structure interactions have been proposed (e.g., [188–190]). Due to the high computational costs of conducting a probabilistic assessment involving FE modeling, surrogate modeling techniques, such as Neural Networks (NN), have been implemented to predict the response of pile-supported foundations under flood and flood-induced scour and thereby facilitate the development of fragility curves (e.g., [191]). In this study, a simplified methodology using analytical formulations has been implemented to evaluate two of the most frequent failure modes of pile-supported foundations, namely inadequate soil support and pile instability [207]. Essentially, multiple LSFs have been suggested by various authors as evidenced in Table 5.1. Assessing some of these LSFs necessitates access to project documentation detailing the reinforcement layout of the piles and the creation of nonlinear FE models, as previously stated. However, due to the unavailability of such documentation in this study and the considerable computational time required for applying nonlinear FE models on a network scale, evaluating the limit states linked to the bearing capacity and stability of the bridge foundation to flood-induced scour serves as an initial approximation. If the bridge failure probabilities calculated using these LSFs are found to be large, or if a network-level risk assessment deems the asset critical (as illustrated in Chapter 6), conducting a more detailed analysis is justified.

The first limit state function addresses bridge foundation failure under scour conditions owing to insufficient vertical bearing capacity. In the case of friction piles, this capacity is reduced as scour leads to a decrease in skin resistance by eroding the surrounding soil. Regarding end-bearing piles, their vertical bearing capacity is compromised when scour erodes the supporting layer (such as a hard stratum or bedrock) upon which the pile tips are resting on [207]. Then, this LSF can be generalized as:



Longitudinal View

(a)



(b)

Figure 5.21: Illustration of bridges belonging to class 4: Multiple-span RC bridges with deep foundation; a) longitudinal view; b) cross-section of the pier-foundation system

$$G_{c4}^{f,q} = Q_d\,(t)\;\theta_{rp}\; - Q_{D_L} \tag{5.39}$$

where Q_d is the bearing capacity of the group of piles, θ_{rp} is the model uncertainty associated with the piles bearing resistance calculation, and Q_{D_L} are the permanent loads at the bridge pier foundation. The time-dependent deterioration effects are incorporated via the bearing capacity estimation, as the scour process which erodes the surrounding soil, is potentially intensified by the long-term degradation of the channel bed ($y_{s,deg}$). Consequently, the computation of the bearing capacity accounts for the cumulative scour depth including the long-term degradation scour (Eq. 5.33).

The bearing capacity of piles ($Q_{d,p}$) can be determined as [231]:

$$\begin{aligned} Q_{d,p} &= Q_f + Q_p \\ &\text{where} \\ Q_f &= f_s \; A_{sp} \\ Q_p &= q_t \; A_{tp} \end{aligned} \tag{5.40}$$

where Q_f is the skin friction resistance, f_s is the unit skin friction capacity, A_{sp} is the side surface area of the pile, Q_p is the total end bearing capacity, q_t is the unit end bearing capacity, and A_{tp} is the gross end area of the pile. The skin friction capacity at any point along the pile may be calculated as suggested in API [231] for cohesionless and cohesive soils as:

$$\begin{aligned} f_s &= K_p \; p_o\prime \; \tan \delta_f \qquad \text{(cohesionless soil)} \\ f_s &= \alpha_f \; S_u \qquad\qquad\quad \text{(cohesive soil)} \end{aligned} \tag{5.41}$$

In the cohesionless soils formulation, K_p is a coefficient of lateral earth pressure, $p_o\prime$ is the effective overburden pressure at the analysis point, and δ_f is the friction angle between the soil and the pile wall. In the cohesive soils formulation, S_u is the undrained shear strength of the soil at the point in question, and α_f is a dimensionless factor that depends on the relation among S_u and $p_o\prime$. On the other hand, the unit end bearing capacity may be computed for cohesionless and cohesive soils as [231]:

$$\begin{aligned} q_t &= p_o\prime \; N_q \qquad \text{(cohesionless soil)} \\ q_t &= 9 \; S_u \qquad\quad \text{(cohesive soil)} \end{aligned} \tag{5.42}$$

In the cohesionless soils formulation, $p_o\prime$ refers to the effective overburden pressure at the pile tip, and N_q is a dimensionless bearing capacity factor.

Pile-supported foundations may also fail due to instability as scour progressively removes the surrounding soil, thereby extending the length of the pile without support. Under the influence of the axial load imposed by the bridge superstructure or a combination of axial and lateral loads, these slender piles are prone to

buckling [207, 212]. Therefore, a limit state function for evaluating the effect of scour on the buckling capacity of piles can be defined as:

$$G_{c4}^{f,b} = P_{cr,g}\,(t)\;\theta_{rb} - Q_{D_L} \tag{5.43}$$

where $P_{cr,g}$ is the critical axial force of the pile group and θ_{rb} is the uncertainty related to the buckling resistance model. Similar to Eq. 5.39, the incorporation of time-dependent deterioration effects is performed via the critical axial force estimation. In this case, the critical axial force can be impacted by the deterioration of the concrete buckling resistance as well as the increased unsupported length of the pile due to long-term degradation of the channel bed. In this study, only the latter effect is considered, but it can be extended to account for both.

The critical load that will cause the pile to buckle can be computed using Euler's formula for column buckling:

$$P_{cr} = \frac{\pi^2 E_c I_w}{(K_f(L_u + d_f))^2} \tag{5.44}$$

where E_c is the modulus of elasticity of the concrete piles, I_w is the weak axis moment of inertia of the pile, K_f is the effective length factor for the pile, L_u is the unsupported length of the pile due to the scour depth, and d_f is an embedded depth to assume fixity. The effective length factor K_f can be adopted as 1.0 since the rotation of the top of the piles subjected to scour is usually prevented by the mass and stiffness of the pier cap, while the lateral movement may occur due to the reduced soil confining pressure (fixed rotation and free translation condition) [232]. Furthermore, it can be seen that the unbraced length to resist buckling is taken as the sum of the unsupported length due to the scour effect plus an embedded depth to fixity (d_f), which can be approximated for cohesionless and cohesive soils as [232]:

$$d_f = 1.8 \left(\frac{E_c I_w}{n_h} \right)^{0.2} \quad \text{(cohesionless soil)}$$
$$d_f = 1.4 \left(\frac{E_c I_w}{E_s} \right)^{0.25} \quad \text{(cohesive Soil)} \tag{5.45}$$

where

$$E_s = 0.465\ S_u$$

where n_h is the rate of increase of soil modulus with depth, and E_s is the elastic modulus of cohesive soils [232]. It is recognized that this method has shortcomings due to the assumption that the soil modulus is constant or increases linearly with depth. A more realistic scenario would involve a soil modulus that changes with deflection at varying depths [233]. In addition, this formulation has a limitation for dealing with nonhomogeneous soils, i.e., layered soils. These shortcomings may be overcome by applying soil spring stiffness curves along the length of the piles to enable a comprehensive assessment of the buckling potential of exposed piles and verify the stability under vertical and lateral loads (as implemented in [188]). Nonetheless, such an analysis has not been pursued in this study due to the need for additional soil profile information to construct these curves and the increased computational demand to include this approach in the probabilistic analysis. Instead, the objective has been to retain simplified analytical expressions as previously stated.

Finally, it is evident that given the type of bridge abutments considered (as depicted in Figure 5.21a), the same LSF concerning slope stability failure due to scour at abutments defined for bridges in class 1, is applicable to abutments in class 4. Then, the fragility of the bridge system is ultimately calculated using the following six LSFs:

$$\boldsymbol{G_{c4}} = (G_{c4}^{d,d}, G_{c4}^{d,o}, G_{c4}^{d,u}, G_{c4}^{f,q}, G_{c4}^{f,b}, G_{c4}^{a,s}) \tag{5.46}$$

The summary of the distribution of the random variables considered for evaluating the LSFs in Eqs. 5.39-Eqs. 5.43 are provided in Table 5.4. The specific values of bridge dimensions and soil-related characteristics are provided in Appendix C.

Table 5.4: Distribution parameters for random variables to evaluate $G^{f,q}$ and $G^{f,b}$

Variable	Description	Dist.	Mean	Std	Ref.
D_{50}	Median diameter of bed sediment	LN[2]	$\mu_{D_{50}}$	$0.1\mu_{D_{50}}$	[223]
$\tan\phi'$	Effective friction angle	LN	$\mu_{\tan\phi'}$	$0.15\mu_{\tan\phi'}$	[230]
S_u	Effective friction angle	LN	μ_{S_u}	$0.15\mu_{S_u}$	[230]
Q_{D_L}	Permanent load at the bridge pier foundation	N[1]	$\mu_{q_{D_L}}$	$0.1\mu_{q_{D_L}}$	[230]
q_{max}	Maximum soil bearing capacity	LN	$\mu_{q_{max}}$	$0.15\mu_{q_{max}}$	[230]
E_c	Concrete Young's modulus	LN	2.8E4	4.2E3	[230]
θ_{sc}	Model uncertainty pier scour formula	N	0.78	0.20	[223]
θ_{rp}	Model uncertainty in piles bearing capacity	LN	1.0	0.25	[230]
θ_{rb}	Model uncertainty in buckling resistance model	LN	1.2	0.15	[230]
$\Delta_{Ds,t}$	Long-term degradation scour rate	LN	0.005	0.0025	-

[1] Normal distribution
[2] Lognormal distribution

Results are herein presented for one bridge belonging to class 4, identified as bridge 10 (refer to Appendix C for identification). Four time periods of analysis are defined, namely at 0, 25, 50, and 75 years. Figure 5.22 delineates the upper and lower bounds of the system fragility functions for the specified time intervals. Prior to the water depth attaining the deck height, the predominant failure modes correspond to insufficient pile-bearing capacity due to scour and abutment scour. These failure modes exhibit a gradual increase until reaching a water depth where, similar to the fragility function for Class 1 bridges, there is an abrupt increase in the failure probability, coinciding with the deck becoming fully submerged. Furthermore, the influence of deterioration processes is distinctly observable throughout the various time periods analyzed.

5.4.5 Masonry arch bridges with shallow foundation

As evidenced in Figure 5.10, masonry arch bridges (MAB) constitute a significant portion of the bridge inventory at the Santarém case study, accounting for 24.2%. As previously mentioned, MABs have been recognized as particularly vulnerable to local scour since they are often built on shallow foundations as depicted in Figure 5.23. Thus, failure modes related to local scour at MABs are examined for this bridge class.

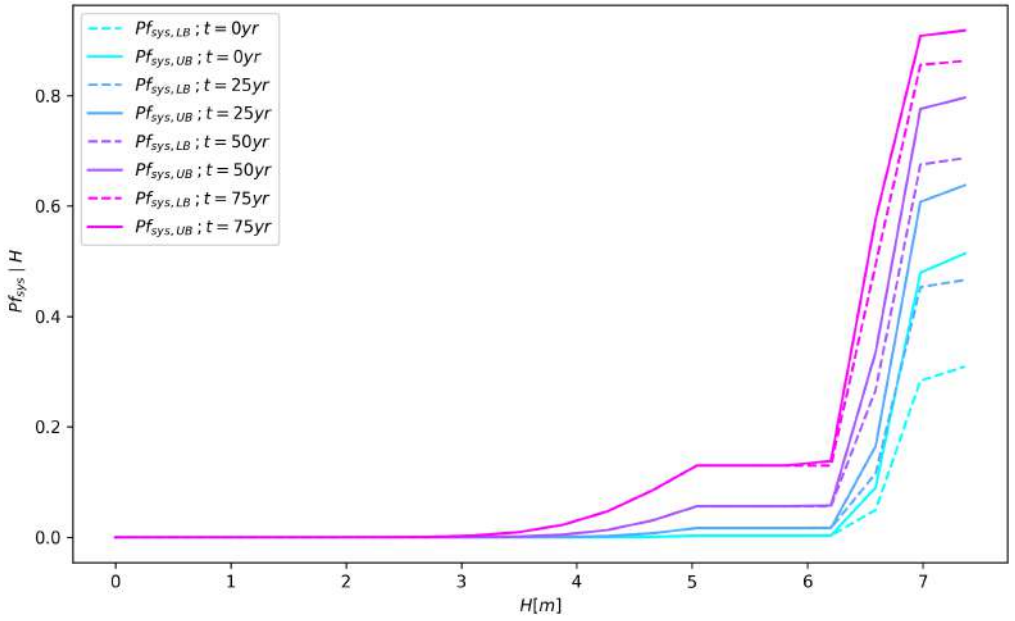
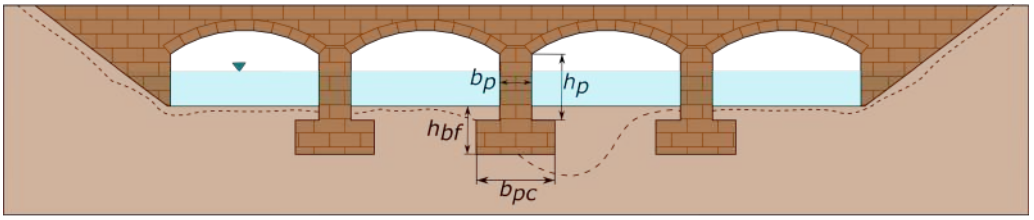


Figure 5.22: Time-dependent system fragility function for multiple-span simply supported RC bridges with deep foundations (class 4)

As outlined in Section 5.2.1, the shape of the local scour cavity at the masonry pier foundation can lead to various failure modes, including the fragmentation of piers/abutments, out-of-plane failures, and symmetrical or asymmetrical in-plane failures [205]. In most cases observed in the Santarém case study, masonry piers are squat in the transversal direction to the flow as shown in Figure 5.23. Therefore, an out-of-plane failure mechanism is unlikely, as small rotations are expected in the transversal section [193]. Conversely, depending on the pier alignment with regard to the direction of the water flow, a symmetrical or asymmetrical in-plane failure mechanism can develop. These failure modes have been analyzed using finite element modeling (e.g., [193]) and numerical limit analysis techniques (e.g.,[196, 197]). The advantage of the latter relies on the less costly but powerful computational alternative, which has been proven to be efficient for probabilistic analyses. Hence, this study employs discontinuity layout optimization (DLO) [234], an upper-bound limit analysis method integrated into the LimitState:GEO software, available for academic use [17]. LimitState:GEO has been used to assess the safety of MABs under operational loads [235]. It is applied here to estimate the collapse load of a MAB under various local scour configurations. Figure 5.24 illustrates an example of a multiple-span masonry arch bridge from the Santarém case study



Longitudinal View

(a)



(b)

Figure 5.23: a) Illustration of bridges belonging to class 5: Masonry arch bridges (MAB) with shallow foundation; b) MAB example in the study area (source: Infraestruturas de Portugal)

modeled in LimitState:GEO. Masonry units are represented using a rigid material model, while masonry joints are depicted through a Mohr–Coulomb model with zero cohesion and a friction angle based on the coefficient of friction. The same Mohr–Coulomb model is applied to the backfill and the foundation soil, along with interface elements that simulate the interaction between bridge elements and the soil. Moreover, a water table can be defined for using saturated unit weights below this level. The contribution of the spandrel walls to the overall capacity is not considered, as the contributions from the arch barrel and the backfill are substantially more significant [235]. Moreover, longitudinal cracks are generally formed in the arch barrel at the intersection with the piers [193], so it is assumed that there is no failure or excessive deformation in the spandrel walls.

The scour effect was simulated by removing soil around and beneath the foundation, assuming a triangular scour cavity as the one approximated for bridges within class 2, based on the soil's friction angle and the scour depth (Figure 5.16c). It is assumed that the scour acts primarily on the central pier, while the other piers did not experience this phenomenon significantly. This scenario is more critical since it

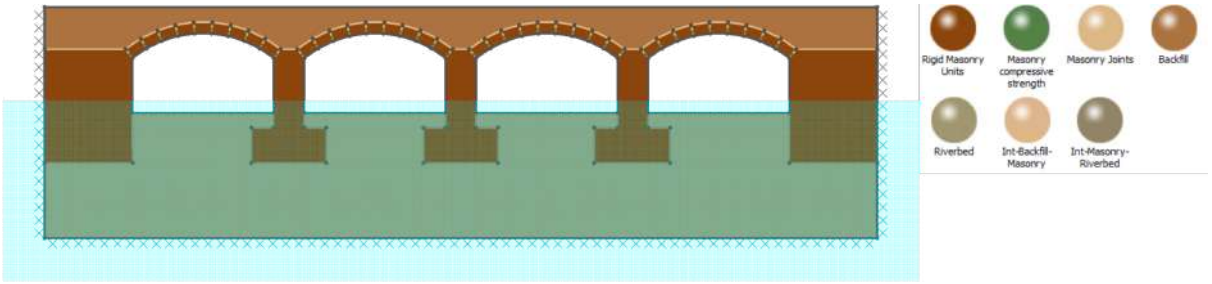


Figure 5.24: DLO model for the multiple span masonry arch bridge in LimitState:GEO [17]

induces higher stresses in the spans adjacent to the affected pier. Moreover, considering that the pier alignment with regard to the water flow direction varies at each bridge location, both symmetric and asymmetric scour configurations are considered. Essentially, if the water flow is aligned with respect to the pier plan orientation, a symmetrical in-plane failure mode is expected. Conversely, if the water flow is skewed with respect to the pier plan orientation, the expected failure mode would be asymmetrical. Figure 5.25 illustrates two symmetric scour depth configurations, i.e., 1m of scour depth (Fig. 5.25a) and 2m of scour depth leading to the soil underneath the pier foundation being eroded (Fig. 5.25c). For each scour configuration, LimitState:GEO employs advanced mathematical optimization techniques (DLO) to ascertain the critical layout of discontinuity lines that form at failure. These discontinuity lines are shown in Fig. 5.25b and Fig. 5.25d for the 1m and 2m scour depth cavities, respectively. Essentially, these lines delineate the boundaries between the moving rigid material blocks constituting the collapse mechanism. This mechanism is associated with a collapse load factor, representing an upper bound on the 'exact' load factor following established principles of plasticity theory [236]. For the case of asymmetric scour configurations, the cavities assumed are depicted in Figure 5.26a for a scour depth of 1m, and in Figure 5.26c for a 2m scour depth. It can be seen that even though the point of maximum scour depth is reached at one side of the pier, a lesser depth is assumed on the opposite side since the scour process envelops the entire pier [218]. Similarly to the symmetric case, the discontinuity lines delineating the boundaries of the collapse mechanisms for the asymmetric scour configurations are shown in Fig. 5.26b and Fig. 5.26d, for 1m and 2m of scour depth, respectively.

The collapse load is expressed in LimitState:GEO as an "adequacy factor" (AF), defined as the factor by which the specified loads need to be increased to bring the system to a state of collapse. Figure 5.27 shows the mean results of the adequacy factor variation at increasing dimensionless scour depths (y_s/h_{bf})

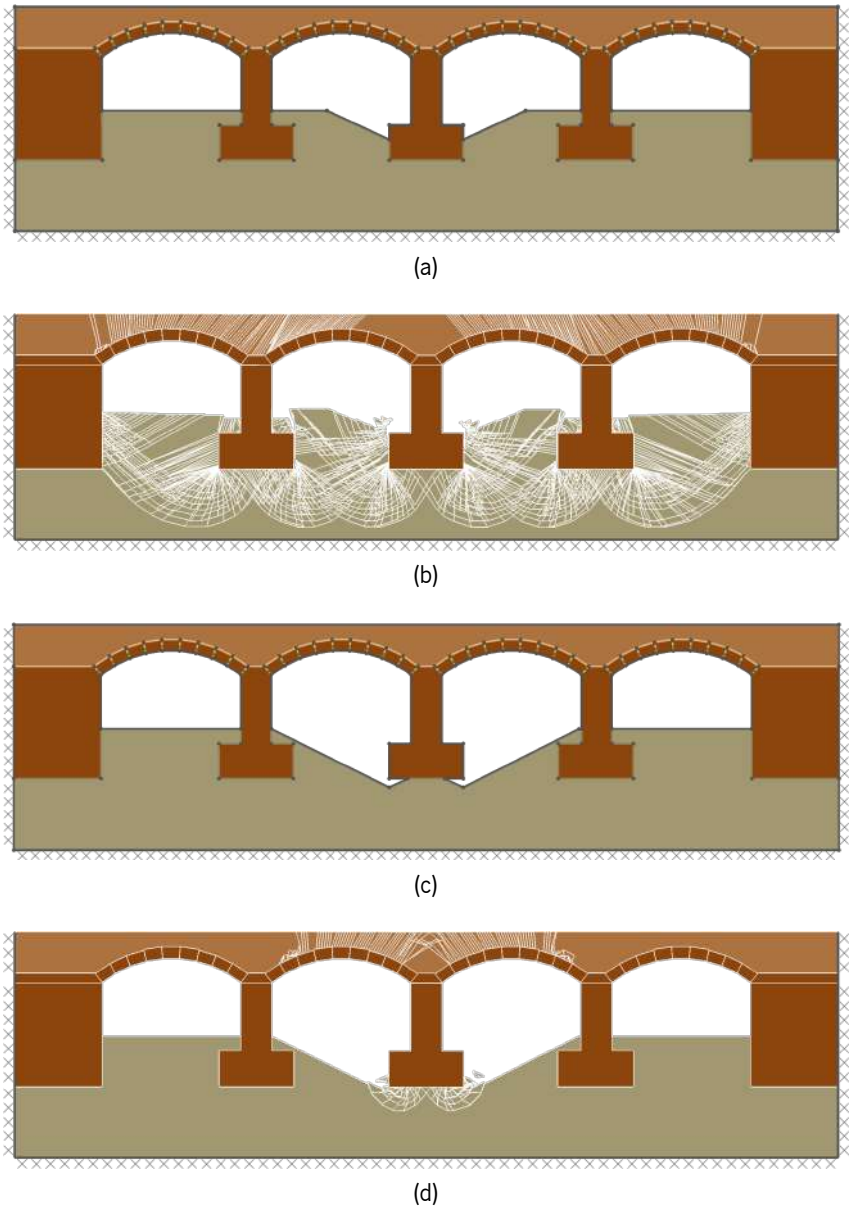


Figure 5.25: Symmetric scour configurations a) 1m scour depth cavity and its b) failure mechanism; c) 2m scour depth cavity and its d) failure mechanism, obtained through DLO in LimitState:GEO [17]

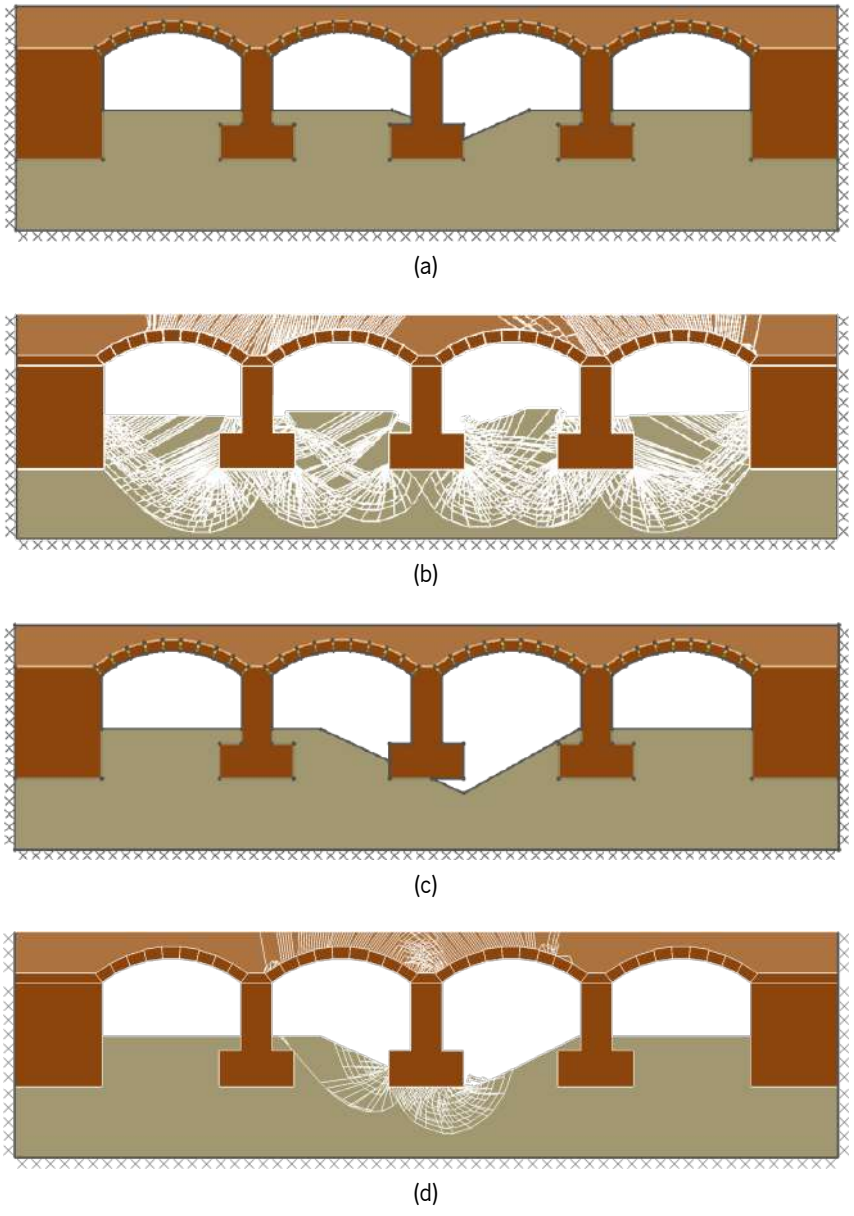


Figure 5.26: Asymmetric scour configurations a) 1m scour depth cavity and its b) failure mechanism; c) 2m scour depth cavity and its d) failure mechanism, obtained through DLO in LimitState:GEO [17]

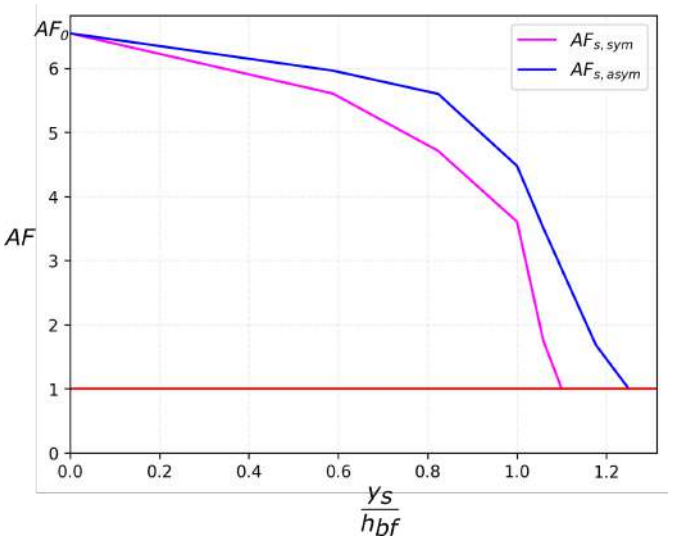


Figure 5.27: Mean Adequacy Factor (AF) variation at increasing dimensionless scour depths for both symmetric ($AF_{s,sym}$) and asymmetric configurations ($AF_{s,asym}$)

for both symmetric ($AF_{s,sym}$) and asymmetric configurations ($AF_{s,asym}$). Under no scour conditions, the initial adequacy factor (AF_0) corresponds to approximately 6.5. Then, in the presence of scour, AF_s reduces almost linearly until the scour depth approximates the foundation bottom ($y_s/h_{bf} \approx 1$). After this, the adequacy factor substantially reduces and rapidly reaches values lower than 1, which implies that the bridge does not withstand the acting loads. Moreover, it can be observed that piers in an asymmetric scour configuration generally endure greater scour depths compared to those in a symmetric arrangement. This effect is likely influenced by the presence of supporting soil on the side opposite to where the maximum scour depth occurs. Nevertheless, it should be noted that this does not imply that piers misaligned with the water flow have a higher resistance to scour. In fact, despite withstanding larger scour depths due to asymmetrical scour cavities, these piers exhibit a greater maximum scour depth than their aligned counterparts, rendering them more vulnerable (as demonstrated in Figure 5.28).

Based on the preceding discussion, the limit state function for MAB bridges can be formulated similarly to the combined failure mode of class 2 bridges subjected to local scour at piers:

$$G_{c5}^{ma,u} = q_{\text{sbm}}\left(t\right)\ \theta_{ru} - q_{A_L}$$

where

$$q_{\text{sbm}}\left(t\right) = \begin{cases} AF_0\ q_{A_L} & \text{if } y_s\left(t\right) = 0, \\ AF_s\ q_{A_L} & \text{otherwise} \end{cases} \tag{5.47}$$

where q_{sbm} is the resistance of the soil-bridge model at time t that depends on the adequacy factor AF_0 for the initial condition without scour, and AF_s for a given configuration and scour depth, θ_{ru} is the uncertainty related to the soil-bridge model generated using the upper bound theory of plasticity, and q_{A_L} are the acting loads in the model which correspond to the permanent dead loads. It is worth noting that hydrodynamic forces impacting the piers could have been included in the applied loads in the LimitState:GEO model. Nevertheless, only lifting forces are pertinent since dragging forces act perpendicularly to the analyzed plane (in an out-of-plane failure mode). Still, lifting forces arise only when the pier alignment diverges from the water flow direction, as depicted in Figure 5.7. Therefore, in symmetric scour configurations, lifting forces are absent. Conversely, in asymmetric scour cavities, the magnitude of the lifting force depends on the angle between the water flow and the pier but may serve as a stabilizing load, counteracting the sliding failure mechanism under the foundation, shown in Figure 5.26d. For this reason, lifting forces are disregarded from the asymmetric scour models.

To evaluate the LSF in Eq. 5.47, the adequacy factor AF_s is a function of the specific (symmetric or asymmetric) scour configuration which depends on the angle between the pier and the water flow (θ_f):

$$AF_s = \begin{cases} AF_{s,\text{sym}} & \text{if } \theta_f = 0, \\ AF_{s,\text{asym}} & \text{otherwise} \end{cases} \tag{5.48}$$

The adequacy factor for a given configuration and scour depth is determined by approximating the mean AF_s curves, as depicted in Figure 5.27, using two piecewise linear functions. In this manner, the two most significant patterns observed in the curves are captured. Lastly, the time-dependent deterioration effects introduced in Eq. 5.47 can be related to the deterioration and loss of masonry units and/or mortar joints, as well as the long-term degradation of the channel bed due to scour (Eq. 5.33). In this study, the

latter is considered the predominant deterioration process since it is deemed to diminish the soil-bridge capacity more critically. This assumption is based on the observation that MABs have proved to be long-lasting structures with low maintenance needs under gradual deterioration from traffic and environmental effects, compared to concrete and steel alternatives [237].

The summary of the distribution parameters for the random variables considered to evaluate the LSF in Eq. 5.47 is provided in Table 5.5. The specific values of bridge dimensions and soil-related characteristics are provided in Appendix C. Similarly to the previous bridge classes, the scour depth at the bridge pier is computed using the S-M method explained in Section 5.3.3, based on the hydraulic conditions, the soil properties, and the characteristics of the pier, and the model uncertainty associated with this prediction formula is also considered (θ_{sc}). It is important to note that the mean adequacy factor curves, presented in Figure 5.27, were obtained from the results of 100 models generated using LimitState:GEO for six scour depth values across both symmetric and asymmetric configurations and were executed through the command-line interface [236].

Table 5.5: Distribution parameters for random variables to evaluate $G^{ma,u}$

Variable	Description	Dist.	Mean	Std	Ref.
D_{50}	Median diameter of bed sediment	LN[2]	$\mu_{D_{50}}$	$0.1\mu_{D_{50}}$	[223]
γ_s	Soil unit weight	LN	μ_{γ_s}	$0.1\mu_{\gamma_s}$	[230]
c'	Effective cohesion	LN	$\mu_{c'}$	$0.2\mu_{c'}$	[230]
tan ϕ'	Effective soil friction angle	LN	$\mu_{\tan\phi'}$	$0.15\mu_{\tan\phi'}$	[230]
γ_m	Masonry unit weight	N[1]	μ_{γ_m}	$0.05\mu_{\gamma_m}$	[230]
f'_m	Masonry compressive strength	N	$\mu_{f'_m}$	$0.15\mu_{f'_m}$	[238]
ϕ_j	Masonry joints friction coefficient	N	μ_{ϕ_j}	$0.15\mu_{\phi_j}$	[238]
ϕ_b	Backfill angle of friction	N	μ_{ϕ_b}	$0.10\mu_{\phi_b}$	[238]
c_b	Backfill cohesion	N	μ_{c_b}	$0.15\mu_{c_b}$	[238]
γ_b	Backfill unit weight	N	μ_{γ_b}	$0.05\mu_{\gamma_b}$	[238]
q_{A_L}	Applied permanent dead loads	N	$\mu_{q_{A_L}}$	$0.1\mu_{q_{A_L}}$	[230]
θ_{ru}	Uncertainty in soil-bridge resistance model	LN	1	0.25	-
θ_{sc}	Model uncertainty pier scour formula	N	0.78	0.20	[223]
$\Delta_{Ds,t}$	Long-term degradation scour rate	LN	0.005	0.0025	-

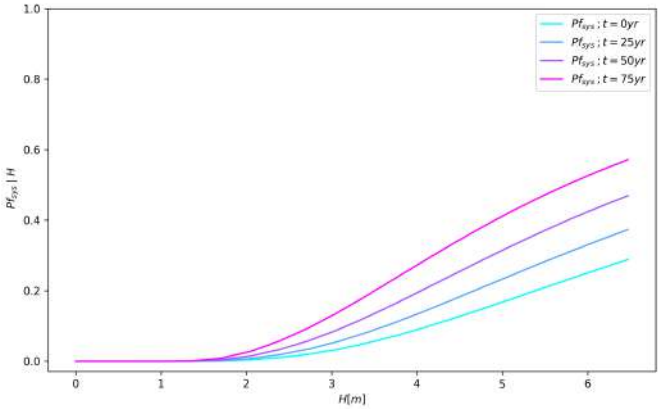
[1] Normal distribution
[2] Lognormal distribution

Results are herein presented for one bridge belonging to class 5, identified as bridge 12 (refer to Appendix C for identification). Figure 5.28a presents the results of the system fragility functions for the

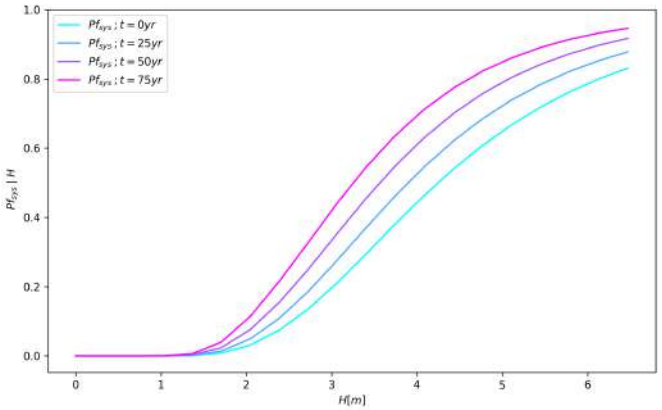
selected time periods, namely at 0, 25, 50, and 75 years. As anticipated, the impact of the deterioration processes is exhibited in the fragility curves. Additionally, to investigate the effect of the flow angle on the bridge fragility, two hypothetical angle flows, namely 15° and 30° are used to construct the fragility curves in Figure 5.28b and Figure 5.28c, respectively. These figures reveal the critical influence of the angle flow in the MAB fragility. As previously discussed, this behavior is expected as piers misaligned with the water flow exhibit a greater maximum scour depth than their aligned counterparts, rendering them more vulnerable.

5.4.6 Multiple-span steel truss bridges on masonry piers

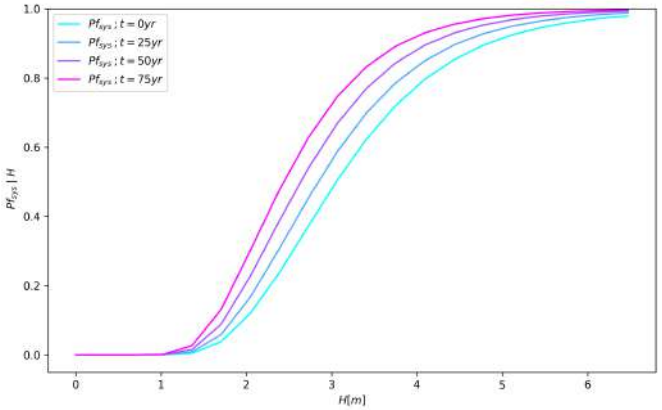
The last bridge class defined in the Santarém case study represents the type of bridges found along the Tagus River, which are of great geographical importance since they link municipalities located on the riverbanks. Moreover, these bridges were built between 110-150 years ago, so they have historical value. Figure 5.29 presents the general layout of these bridges, which are characterized by having multiple spans (with total span length between 400-600m), masonry wall piers, and simply supported steel truss structures for the deck. The foundation of these types of bridges consists of a deep prolongation of the piers until reaching a soil stratum with sufficient capacity, i.e., loads are transferred by direct bearing to dense soil. By analyzing the potential failure modes outlined in Table 5.1, it is evident that deck failure due to hydrodynamic forces acting on submerged decks is very unlikely. This is due to the wide geometry of the river channel and its floodplains, as well as the substantial bridge clearance above the water level. Specifically, with the deck situated >20m above the riverbed, the occurrence of deck overtopping is not anticipated. On the other hand, hydrodynamic forces alone acting on the piers are not expected to affect the global behavior of the bridge, as argued for bridges within class 2. Nonetheless, a condition that may affect the stability of these bridges can be associated with local scour at the piers. For instance, during sub-aquatic inspections of Dom Luís bridge, significant scour was found in several piers, reaching depths up to 1.5m as shown in Figure 5.30a. As a countermeasure, the riverbed was protected with rock-fill layers around piers. However, subsequent inspections revealed that these protective measures had been displaced or "washed away," as displayed in Figure 5.30b. Additionally, geotechnical surveys have indicated that some bridge piers rest on soils with low bearing capacity (refer to Figure C.3). Therefore, the



(a)



(b)



(c)

Figure 5.28: Time-dependent system fragility functions for masonry arch bridges with shallow foundations (class 5) for different flow angles: a) $0°$; b) $15°$; c) $30°$

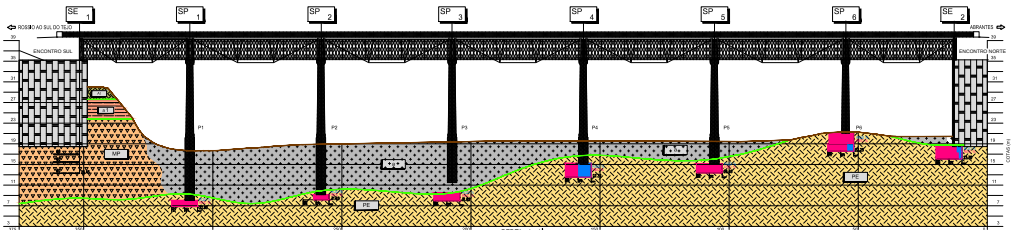


Figure 5.29: General layout of bridges belonging to class 6: Multiple-span steel truss bridges on masonry piers



(a) (b)

Figure 5.30: Presence of local scour in Dom Luís bridge (a) sub-aquatic inspection (b) "washed away" of protective fills. Source: Infraestruturas de Portugal

combined effect of lateral soil loss due to scour, the pier founded on weak soils, and significant hydrodynamic pressures acting against the piers during flood events may compromise pier stability, potentially leading to complete bridge failure. This failure mode was exhibited by the Hintze Ribeiro (North Portugal) bridge collapse, which featured a similar bridge design [239]. Thus, this failure mode is investigated for bridges belonging to class 6.

A similar approach to the one implemented for masonry arch bridges was applied to examine the fragility of this bridge class. Therefore, LimitState:GEO software [17] has been used to verify the stability of bridge piers under flood-induced scour conditions. Figure 5.31 illustrates an example of a typical masonry pier from bridges in class 6 modeled in LimitState:GEO. The acting loads included in the model consist of the dead load, i.e., self-weight from both the pier and bridge superstructure, along with the hydrodynamic dragging forces. It can be observed that in this analysis, unlike the approach taken for MABs, the bridge

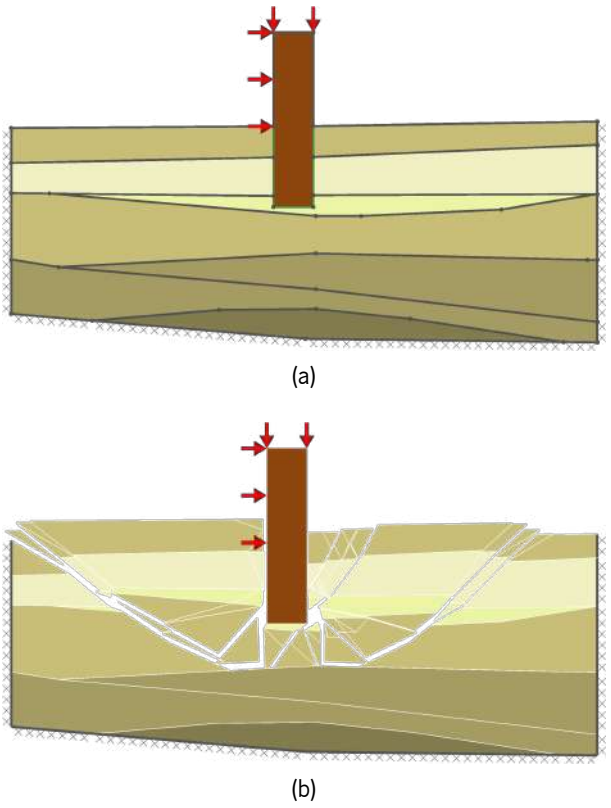


Figure 5.31: a) Example of a typical masonry pier of class 6 bridges and supporting soil modeled in LimitState:GEO, and its b) failure mechanism obtained through DLO [17]

pier is examined in the transversal direction. This distinction arises because the MABs being studied had squat piers, rendering an out-of-plane failure mechanism unlikely due to the minor rotations expected in the transversal section. In contrast, the piers in class 6 bridges are notably slender. Consequently, the loss of supporting soil will cause significant rotations in the transversal direction, which coupled with the dragging forces exerted on the pier during floods, is deemed a more critical condition for evaluating the safety of bridges in this class. The masonry pier is modeled as a rigid body since the failure mechanism implies the instability of the pier and its subsequent complete loss. Mohr-Coulomb models are employed to define the various soil layers based on data from geotechnical surveys that characterize each stratum. For the analysis, the soil stratigraphy for one of the piers resting on a low-bearing capacity soil is selected (further information can be found in Appendix C). Additionally, Mohr-Coulomb models are applied to the interface elements, which are used to simulate the interaction between the masonry pier and the respective soil layers. Figure 5.31b depicts the layout of the discontinuity lines that define the boundaries of the collapse mechanisms for the no-scour condition.

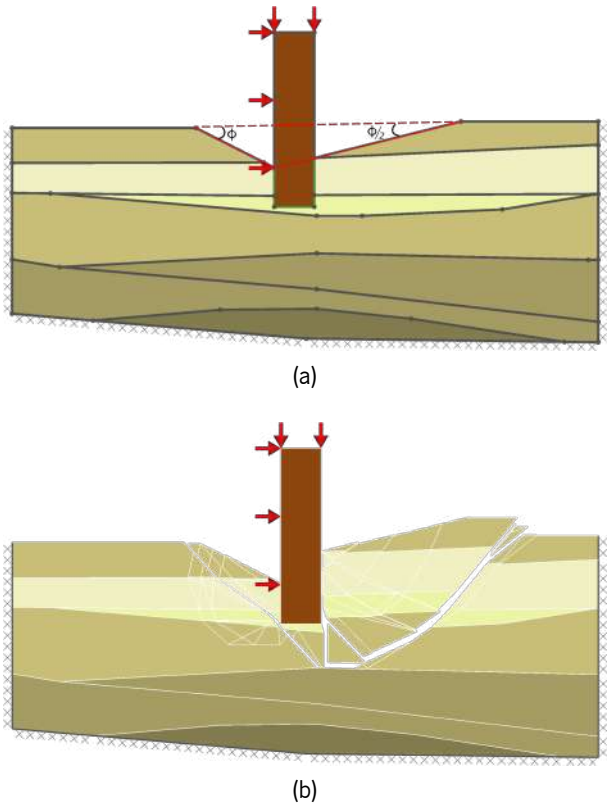


Figure 5.32: a) Modeling of scour cavity around the masonry pier for 8m of scour depth, and its b) failure mechanism obtained through DLO [17]

The modeling of scour was conducted by removing the lateral soil following the geometry for the scour cavity as detailed in [194, 195] for the longitudinal direction. Essentially, this approach approximates the scour cavity as an inverted pyramid, as depicted in Figure 5.32a. The vertex of the pyramid is positioned on the pier's upstream face. The upstream slope of the cavity is assumed equal to the soil's friction angle, while the downstream slope is estimated to be around half of this value. Figure 5.32b illustrates the collapse mechanism for 8m scour depth. It can be observed that the layout of the discontinuity lines changes from that of the no-scour condition and a sliding failure of the soil downstream governs the collapse mechanisms.

An increase in the scour depth to 16m results in the partial undermining of the pier, as illustrated in Figure 5.33a. The failure mechanism, in this case, depicts a significant rotation of the pier upstream, as shown in Figure 5.33b. The adequacy factor computed approaches zero, and LimitState:GEO issues an ′ ′unstable" warning, which indicates that under the applied forces, the problem has no viable means of resisting the loads [236]. This failure mechanism is consistent with observations from the Hintze Ribeiro

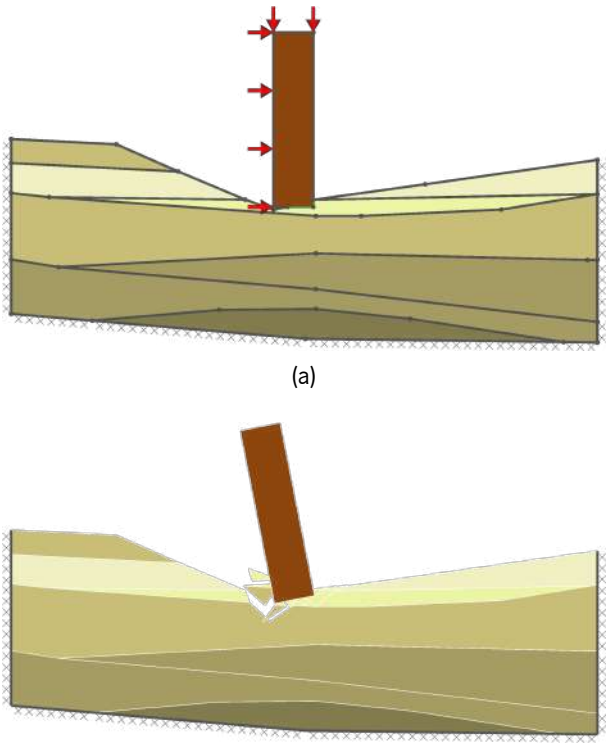


Figure 5.33: a) Extreme scour conditions undermining the pier foundation base and its b) failure mechanism obtained through DLO [17]

bridge collapse. Forensic studies indicate that the failed pier ′ ′P4" rotated and fell upstream during the collapse, which could only be justified by the undermining of the foundation base due to localized erosion [239].

The results of the mean adequacy factor for increasing scour depths around the masonry pier are displayed in Figure 5.34. In the absence of scour, the initial adequacy factor (AF_0) corresponds to approximately 8. Then, in the presence of scour, AF_s decreases approximately linearly until the scour depth reaches 14m. Beyond this depth, the reduction in the adequacy factor is more pronounced and reaches values lower than 1 when the scour depth exceeds the bottom of the pier foundation.

Analogously to masonry arch bridges, the LSF for the failure due to local scour at piers for bridges within class 6 can be formulated as:

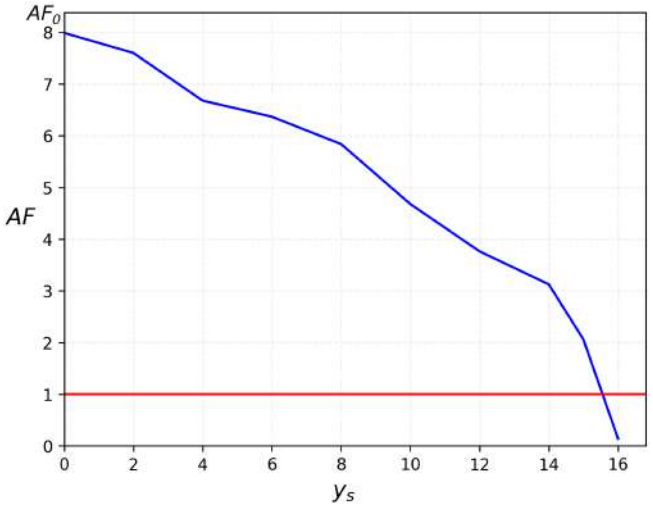


Figure 5.34: Mean Adequacy Factor (AF) variation at increasing scour depths around the masonry pier

$$G_{c6}^{mp,u} = q_{\text{sbm}}(t)\ \theta_{ru} - q_{A_L}$$

where

$$q_{\text{sbm}}(t) = \begin{cases} AF_0\ q_{A_L} & \text{if } y_s(t) = 0, \\ AF_s\ q_{A_L} & \text{otherwise} \end{cases} \tag{5.49}$$

where q_{sbm} denotes the resistance of the soil-bridge model at time t that depends on the adequacy factor AF_0 for the initial condition without scour and AF_s for a given scour depth, and q_{A_L} represents the acting loads in the model, comprising both the permanent dead loads and the hydrodynamic dragging force as previously discussed. Similarly to masonry arch bridges, the adequacy factor for a specified scour depth is ascertained by approximating the mean AF_s curve displayed in Figure 5.34, using two piecewise linear functions in order to capture the two most significant patterns observed in the curve. Lastly, the time-dependent deterioration effects incorporated in Eq. 5.49 are assumed to be related to long-term degradation of the channel bed (Eq. 5.33), given the evidence from bathymetric surveys of modifications of the channel profile. This phenomenon has had a significant impact on the performance of this type of bridge in the past. For example, the Hintze Ribeiro bridge experienced a considerable lowering of the channel bed over several years, primarily due to uncontrolled sand extraction, which increased the fragility of the bridge to withstand local scour at the piers during a sequence of intense floods and ended in the pier collapse as detailed in [239]. For this reason, and considering the high reliability of these bridges,

a particularly large degradation scour rate is assumed for this bridge class to investigate its effect on the bridge's fragility.

Table 5.6 summarizes the distribution parameters for the random variables used in evaluating Eq. 5.49. Details on specific bridge dimensions and soil characteristics are available in Appendix C. Similarly to other bridge classes, the scour depth at the bridge pier is calculated using the S-M method, as described in Section 5.3.3, and the model uncertainty associated with this prediction formula (θ_{sc}) is considered. It should be noted that the mean adequacy factor curves shown in Figure 5.34 were derived from 100 models generated in LimitState:GEO for ten different scour depths, and these models were executed using the command-line interface [236].

Table 5.6: Distribution parameters for random variables to evaluate $G^{mp,u}$

Variable	Description	Dist.	Mean	Std	Ref.
D_{50}	Median diameter of bed sediment	LN[2]	$\mu_{D_{50}}$	$0.1\mu_{D_{50}}$	[223]
$\gamma_{s,i}$	Soil unit weight of layer i	LN	$\mu_{\gamma_{s,i}}$	$0.1\mu_{\gamma_{s,i}}$	[230]
c'_i	Effective cohesion of layer i	LN	$\mu_{c'_i}$	$0.2\mu_{c'_i}$	[230]
$\tan\phi'_i$	Effective soil friction angle of layer i	LN	$\mu_{\tan\phi'_i}$	$0.15\mu_{\tan\phi'_i}$	[230]
q_{A_L}	Acting loads (Dead + Dragging forces)	N[1]	$\mu_{q_{A_L}}$	$0.1\mu_{q_{A_L}}$	[230]
θ_{ru}	Uncertainty in soil-bridge resistance model	LN	1	0.25	-
θ_{sc}	Model uncertainty pier scour formula	N	0.78	0.20	[223]
$\Delta_{Ds,t}$	Long-term degradation scour rate	LN	0.1	0.05	-

[1] Normal distribution
[2] Lognormal distribution

Results are herein presented for Dom Luís bridge, identified as bridge 20 (Appendix C). Figure 5.35 presents the results of the system fragility functions for the selected time periods, namely at 0, 25, 50, and 75 years. It can be observed that the bridge fragility is very low in the absence of deterioration effects, i.e., the failure probabilities for the initial 0 and 25-year periods are less than 1E-6. It is only after 50 years of enduring degradation scour that there is a perceptible increase in probability. The tangible impact of degradation scour becomes evident after 75 years, at which point there is a considerable increase in bridge fragility.

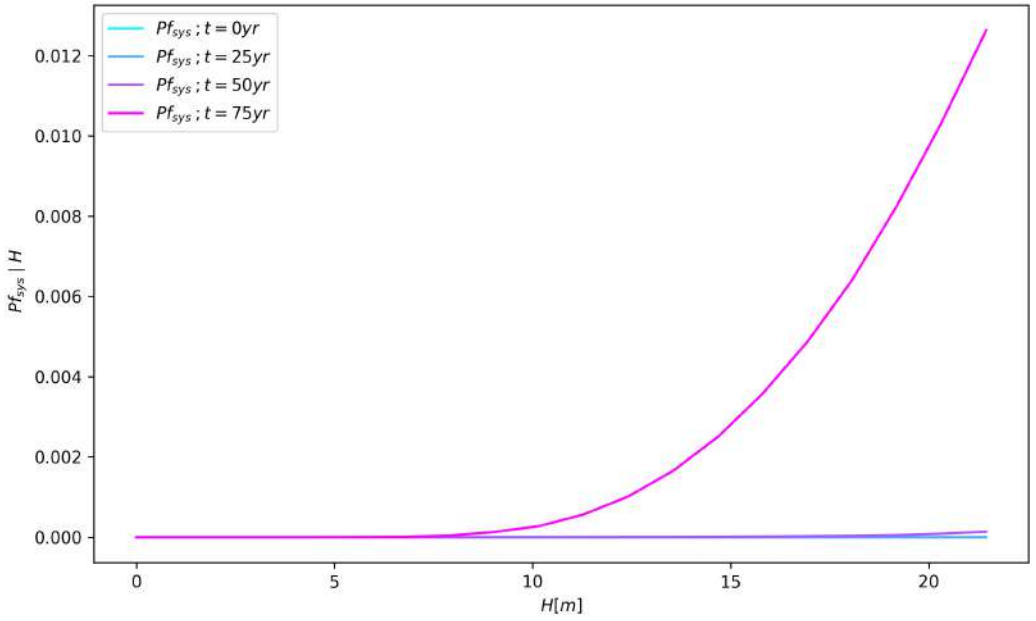


Figure 5.35: Time-dependent system fragility function for multiple-span steel truss bridges on masonry piers (class 6)

5.5 Conclusions

When considering the entire population of bridges managed by transportation agencies, a substantial effort is needed to assess their fragility under natural hazards, which poses a challenge to the risk assessment of transportation networks. Particularly for floods, various failure mechanisms may develop, depending on the bridge type and the complexities of the soil-structure interaction. After reviewing existing flood fragility functions, a significant gap in the direct application of these curves to bridge portfolios was underscored. Therefore, this chapter introduced a methodology for developing flood fragility functions that can be implemented at the bridge portfolio level and thereby supports the assessment of network-level risks. The suggested approach enables the definition of bridge classes, considering all plausible failure modes and including time-dependent considerations.

The proposed methodology has been applied to a portfolio of bridges in the Santarém district area. Through this case study, it has been demonstrated that the estimation of bridge fragility is a complex multidisciplinary problem that involves hydrologic, hydraulic, geotechnics, and structural assessment.

For this reason, most research efforts are very case-specific and time-consuming (involving finite element modeling), which hinders the possibility of implementing them at a network-level scale, i.e., for a large portfolio of assets. An alternative is to build simplified models while considering the important interaction between the soil-bridge system in the response to floods. It is argued that using these models goes in balance with the required accuracy to perform a risk assessment of transportation networks as conducted in Chapter 6. Consequently, if the failure scenarios involving a specific bridge are deemed to be relevant, i.e., the failure scenarios are dominating the risks, the simplified model can be adjusted for a more detailed analysis for a deep understanding of the particular failure mode or phenomena that are driving the system performance.

On the other hand, it was also evidenced how certain assets' characteristics may significantly change their vulnerability. For instance, it was highlighted how the superstructure-substructure connection in multiple-span RC bridges is extremely relevant for their fragility as the superstructure can contribute by limiting the rotation of the foundation. Moreover, it was exhibited how the angle between the pier and the water flow significantly impacts the fragility of masonry arch bridges. Therefore, having data regarding the river channel is also relevant to estimate the bridge fragility accurately. In this sense, the application of the methodology enabled the identification of all the random variables necessary to assess the performance of the different bridge classes. The extensive list of parameters is summarized in Appendix C and calls for the need to improve existing bridge inventories, which do not include such detailed variables. Moreover, the identification of all these necessary inputs, together with the methodology for the definition of bridge classes for fragility modeling, supports the development of a common taxonomy like the one that has been applied to other hazards like earthquakes.

A prominent result from the application of the methodology is that the assumption of fragility functions being lognormally distributed, which is very commonly adopted in seismic fragility analysis, has to be applied with caution. Essentially, it has been shown how certain effects can originate abrupt changes in the failure probabilities, which are not properly represented by a lognormal distribution. Moreover, the importance of considering model uncertainties in the fragility assessment was also underscored through the application of the methodology. Perhaps one of the most relevant concerns is the scour formulations, which carry large uncertainties, especially when the model is applied for a different type of structure than the one used for the model calibration.

One limitation of the application of the methodology was the need to make assumptions about the bridge due to the lack of detailed project documentation, which is a current issue shared by many countries and highlighted by many researchers, as previously discussed. This issue was tackled herein by using the available information from actual bridges and making assumptions in the absence of reliable data for the illustration and demonstration of the methodology. Further work can be done to evaluate the sensitivity of the results to the assumptions made in the face of a lack of project documentation. For instance, the reinforcement layout and detailing are usually lacking in bridge inventory databases. Therefore, the minimum reinforcement for each bridge element can be deduced from design codes and regulations applied during the construction period. However, this value can be varied within certain thresholds to evaluate the sensitivity of the bridge fragility results under different reinforcement amounts. Moreover, further work can be performed to study other common bridge types that were not analyzed in the case study of Santarém, such as prestressed concrete decks, which might be more vulnerable to scour. Therefore, evaluating the fragility under both conditions and how it impacts the risks can be of relevance.

Finally, the work can be extended to account for intermediate damage states in formulating the limit state functions. Nonetheless, this brings additional uncertainties in the definition of the thresholds for each of the damage states. Likewise, the methodology can be extended to account for bridge fragility for multiple hazards and harmonize the bridge classes with existing classifications, e.g., seismic classification with the obtained classes from the implementation of the proposed flood fragility classes defined in this work.

Chapter 6

Long-term flood risk and recovery prioritization for Resilient Transport Infrastructure Systems

Abstract: The exposure of transportation systems to natural and anthropogenic hazards, in combination with the inherent vulnerability of infrastructures, has led in the past to structural failures, traffic disruptions, injuries and fatalities, and damages to the environment. These past events have underscored the need to devise cost-efficient risk mitigation measures and increase the resilience of our transportation systems. This chapter proposes a methodology to support risk-informed decision making and recovery prioritization to increase the resilience of transport infrastructure systems. The proposed approach uses a scenario-based modeling framework suggested by the JCSS [38], where the probabilistic models of the exposure event and the fragility models of the infrastructure components are used to compute the scenarios of failure events and the corresponding direct and indirect consequences. Direct consequences are related to the structural failure of infrastructures, and indirect consequences are associated with functionality losses estimated with a traffic model and associated consequences to the economy, health, and the environment. To advance in the modeling of consequences, a neural network (NN) model is trained to predict the outputs from the traffic model. This model facilitates defining the optimal sequence of repair interventions to maximize resilience, i.e., by minimizing the indirect costs during the recovery period.

Moreover, different characteristics of the rapidity of the recovery are analyzed to support decisions on the target level of preparedness of the transportation system. The suggested approach is applied to a roadway network subject to flood events, where bridges are considered the most vulnerable assets. The application of the framework allows a thorough understanding of the infrastructure failures that significantly impact the expected total consequences at the road network level, facilitating the identification of critical infrastructure assets and predominant failure modes. Moreover, decisions on preparedness levels help infrastructure managers explore if they have sufficient capacity for recovery after an extreme event. Therefore, the methodology enhances the overall resilience of the transport infrastructure system.

6.1 Introduction

The evolving climate exposes Transport Infrastructure Systems (TIS) to a wide range of weather-related hazards, among which flooding stands out as a prominent threat around the world [36]. This situation underscores the need to devise cost-efficient risk mitigation measures and increase the resilience of our transportation systems. Conducting a risk assessment of TIS can help identify probable hazardous events, evaluate their impact on networks and users, and support planning for risk mitigation measures. Nonetheless, conducting such assessments can be a challenging task due to due to the numerous scenarios that must be considered, the modeling of these events, their interrelationships, and the availability of support tools for executing the models in an integrated manner [44]. Particularly, the spatial correlation that exists in TIS is one of the crucial aspects that need to be considered when assessing the risks. Fundamentally, TIS are composed of links connecting geographically dispersed communities, towns, and cities. As such, links in a transportation network form a spatially distributed system in which spatial correlation exists with respect to the link condition and its functionality in the network [240]. Due to this characteristic of spatially distributed systems, it has been demonstrated that risk assessment and management should be conducted at the network level, as the total indirect costs and optimal intervention sequences differ if the asset (e.g., bridge) failure is due to a common cause or not [241]. Modeling this spatial correlation is conventionally conducted using two approaches: event-based simulation (e.g., [67, 93–95]) and random field-based approximation [240]. In the first approach, hazards (either deterministic or stochastic) are hypothetically exposed upon a transportation network. The spatial correlation of link failure is then obtained

by simulating the asset performance under the hazards considering its location, age, type, and relative distances to other assets, among many other factors. This allows the consideration that geographically distributed network components (i.e., bridges and tunnels, among others) are exposed to different levels of hazards. For instance, the spatial distribution of seismic intensity (i.e., peak ground acceleration, spectral acceleration, among others) after an earthquake event attenuates from the source to the sites of interest, resulting in damage distribution within the network, which varies in space. This simulation-based technique has been used for various types of hazards such as earthquakes (e.g., [45]) and floods (e.g.,[108]). In the second approach, random field theory is used directly to approximate the spatial correlation of asset failures [92]. Instead of performing Monte Carlo simulation (MCS), this random field-based approximation can directly generate failure scenarios of assets (e.g., bridges) in a network. However, this approximation may compromise the actual correlation condition compared to event-based simulation.

On the other hand, the occurrence of natural and human-induced hazards may trigger numerous consequences for TIS. The assessment of probable consequences is essential so infrastructure managers can make informed decisions about the execution and prioritization of different risk-reducing interventions [242]. Furthermore, risk assessment of TIS also informs the recovery processes required to maintain functionality immediately following a severe event. For this reason, risk management has been extended to a resilience-based management concept that determines how a system can adapt to and recover rapidly from disturbance events and not just avoid or mitigate them [243]. Nonetheless, assessing consequences in TIS is a computationally expensive task since it requires the evaluation of traffic-related impacts to quantify the loss of functionality in the network. Thus, performing these operations for many scenarios can become prohibitive [240]. Addressing this gap, the methodology proposed in this chapter seeks to overcome the computational burden by introducing a neural network (NN) model trained to predict the outputs from the traffic model. Similar work in this regard has been conducted in [244]. However, the NN model therein was only used to estimate the additional travel time for damage scenarios. In this study, the NN model is extended to predict additional traffic-related metrics and is employed to determine the most effective sequence of restoration efforts to increase resilience, which is achieved by reducing the indirect costs throughout the restoration phase. In addition, various aspects of the rapidity of the recovery process are examined to aid in making informed choices regarding the target level of preparedness of the transportation system.

This chapter is organized as follows. Section 6.2 introduces the general risk modeling framework for decision-analysis of transport infrastructure systems. Section 6.3 presents the proposed methodology for risk-informed recovery to maximize resilience. Section 6.4 presents the application of the methodology to a case study in the Santarém district, Portugal, which has been affected by severe flood events. Section 6.5 discusses the results and their implications for supporting decisions to reduce risks and increase the resilience of transportation systems. The chapter concludes by summarizing the main contributions of this research to enhance the computation of risks and facilitate decision making, as well as the limitations that can be addressed in future research.

6.2 Risk modeling framework for decision-analysis of Transport Infrastructure Systems

When providing decision support for the management of systems, it is crucial to identify and establish a representation of the system that enables the ranking of different decision alternatives, consistent with the available knowledge and coherent with the objectives and preferences of decision-makers and stakeholders [38]. A modeling framework that facilitates decision analysis of systems is proposed in [9, 18] and is illustrated in Figure 6.1. This decision support framework can be applied to rank different decision alternatives for the design and management of systems according to their expected value of utility in accordance with the Bayesian decision analysis [41]. In addition, when modeling system characteristics such as resilience, the benefits from the service provided by the system should also be taken into account. For this reason, the modeling framework addresses both the benefit generation, which builds the system capacity (illustrated in green), and the losses, which represent the demand acting on the system (illustrated in red). Resilience failure may take place if one or more of the capacities of the system, namely economic, social, and/or environmental capacity, are exhausted. The concept of resilience failure event and its modeling are the focus of Chapter 7.

The system modeling approach from Figure 6.1 utilizes the scenario-based system representation proposed by the JCSS [38]. This generic system representation subdivides scenarios of events into three parts: *i)* the exposure events acting on the constituents of the system (e.g., natural hazards, operational

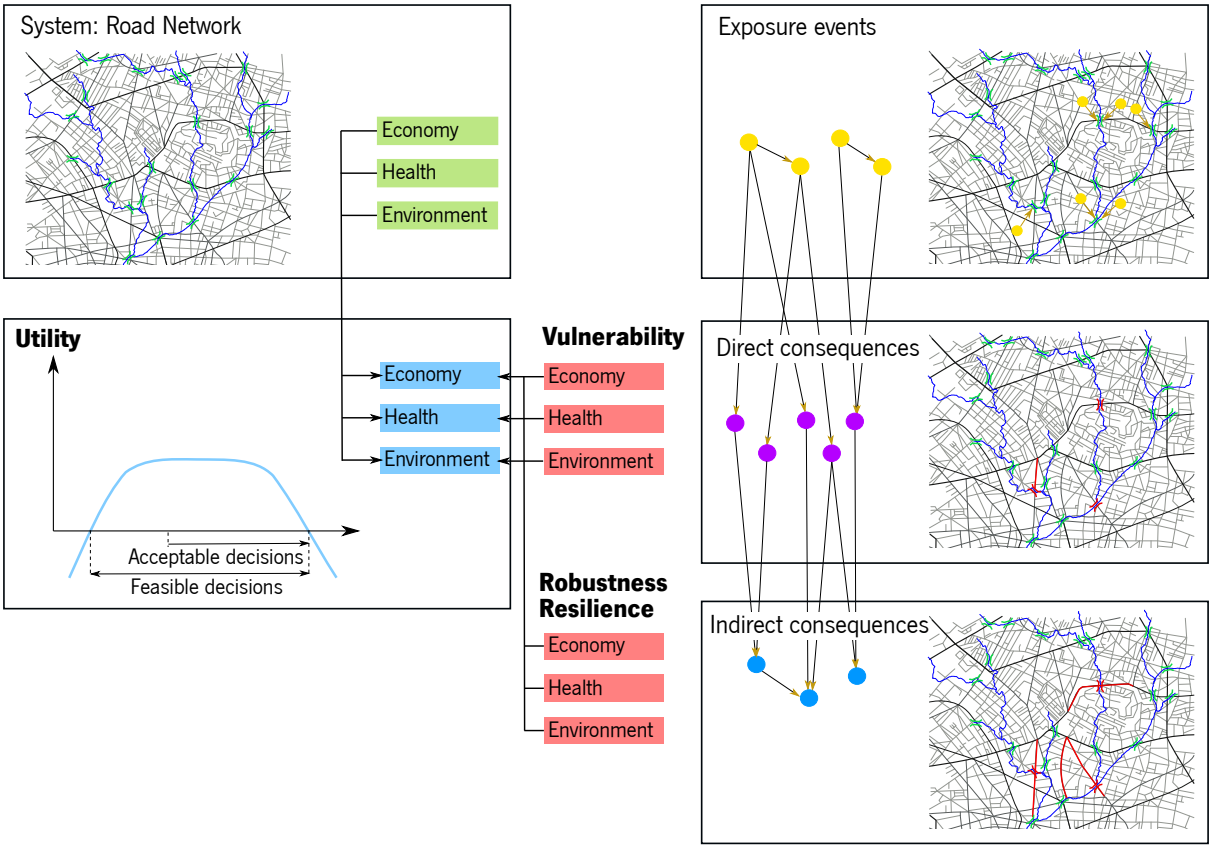


Figure 6.1: Illustration of systems modeling framework for decision analysis. Source: [18]

loads), *ii)* direct consequences that are associated with damages or failures of the constituents, and *iii)* indirect consequences that are related to the loss of functionality of the system as a result of one or more constituent failures. The consequences are manifold and generally depend strongly on the specific characteristics of the hazard as well as the location where it occurs and the assets that are exposed [38]. As a general rule, consequences should be assessed regarding loss of human lives and injuries, damages to the quality of the environment, and economic losses. As outlined in Section 2.2.1.2 and illustrated in Figure 6.1, distinguishing between direct and indirect consequences aids in modeling two relevant system characteristics: vulnerability and robustness. Vulnerability refers to the relationship between exposure and the resultant direct consequences. Robustness is associated with the link between direct and indirect consequences. Thus, a system's vulnerability is an indicator of the extent to which exposures lead to direct consequences. Meanwhile, robustness represents the system's capacity to contain or limit indirect consequences arising from a hazard event [39]. In general, a system is comprised of an ensemble of n

constituents interacting jointly to provide the desired functionality. In the case of transportation networks, the system can be modeled at different spatial scales (see Section 2.2.1.2). The definition of the system scale is particularly relevant for risk-informed decision making. Depending on the decision alternatives at hand, the appropriate scale of the system, which facilitates differentiating the expected value of benefit associated with the decision options, should be chosen [1]. In this chapter, the focus is given to identifying critical infrastructure assets within the network to guide decisions on the prioritization of mitigation and recovery actions. Accordingly, the scale of the system corresponds to the transportation network level, where different infrastructure assets, namely bridges, embankments, tunnels, retaining walls, and pavements, among others, interact with each other to provide their intended service, i.e., transportation for people and goods. In the following subsections, the formulation of probabilistic models for the performances of the transportation system and the modeling of consequences required for the application of this decision analytical framework are further addressed.

6.2.1 Exposure modeling

Extreme events with extensive geographical impacts introduce spatial and temporal correlations in the hazard demand at each transport infrastructure location. Then, accurate hazard modeling requires accounting for that stochastic variability. Chapter 3 presented an approach for modeling this spatial variability by means of a Bayesian network model, which is a representation of the joint probability distribution over its variables. As detailed in the proposed methodology from Figure 3.1, the BN model can be used to determine the conditional distribution of hydrologic and hydraulic variables at each infrastructure asset location, given the observed evidence of rainfall depth. Using this type of modeling, it is possible to generate a database of flood event realizations to be incorporated into the scenario-based framework from Figure 6.1.

6.2.2 Modeling of direct consequences: Vulnerability

As illustrated in Figure 6.1, the relationship between exposure or hazards and the direct consequences is termed vulnerability. Essentially, the vulnerability of a system indicates the degree to which exposures

generate direct consequences. The vulnerability of roadway networks can be defined as the risk due to all direct consequences from all infrastructure assets in the system (R_{D}), and it can be assessed by calculating the expected value of the conditional risk due to direct consequences, over all possible hazards and all asset damage states as [79]:

$$R_{\mathrm{D}} = \sum_{i} \sum_{j} P(D_j|H_i)\ P(H_i)\ C_{\mathrm{D},ij} \tag{6.1}$$

where $P(H_i)$ is the probability of hazard H_i, with $i = 1, 2, ..., n_s$ possible different scenarios of hazards; $P(D_j|H_i)$ is the probability of damage D_j given the hazard H_i, with $j = 1, 2, ..., n_{csta}$ possible set of infrastructure damage states; and $C_{\mathrm{D},ij}$ are the expected consequences of damage D_j due to hazard H_i.

The direct consequences depend on both the extent of damage sustained by the infrastructure asset and the specific failure mode. For instance, referring to Chapter 5, failure modes associated with deck unseating due to hydrodynamic forces primarily entail the costs of deck reconstruction. In contrast, failure modes pertaining to foundation failure due to scour would typically lead to a complete reconstruction of the bridge, including both the pier and the deck, as both components are likely to fail in such scenarios. Therefore, the direct costs of reconstruction can be quantified as a function of a damage ratio d_r as:

$$C_{\mathrm{D,reb}}(j) = b_d \cdot L_s(C_{reb} \cdot d_r(j)) \tag{6.2}$$

Frequently, the cost of debris removal is also included in the computation of direct costs of bridge rebuilding. In addition, repair and reconstruction activities are associated with environmental consequences associated with energy consumption and carbon dioxide emissions. These environmental impacts can also be quantified as a fraction of the damage ratio (d_r), as they are a function of the volume of the structural component requiring repair or reconstruction and the material used. Thus, the direct environmental consequences can be estimated as [182]:

$$C_{\mathrm{D,env}}(j) = \left(\sum_{m=1}^{n_m} V_{reb,m} \cdot \gamma_{E,m} \right) \cdot d_r(j) \tag{6.3}$$

where $V_{reb,m}$ is the volume of material m of the structural component to intervene, $\gamma_{E,m}$ is the environmental metric per unit volume of material m, e.g., embodied CO_2 emissions per kg/m^3, and n_m is the total number of materials used. Lastly, sudden bridge failures can result in the loss of human lives. To estimate the expected average number of fatalities and injuries, a statistical analysis based on past bridge failure events should be conducted (see, e.g., [245]). The average number of fatalities and injuries also depends on the bridge failure type, i.e., in the event of a complete bridge collapse, the likelihood of multiple fatalities is considerably higher compared to a scenario involving partial bridge failure [245]. In instances where a monetary valuation of life loss consequences is necessary to assess different decision alternatives, the concept of the Life Quality Index (LQI) can be introduced. The LQI concept, as formulated by Nathwani et al. [246], serves as a general principle to assist in decision-making processes related to activities that affect health and life safety in the public domain. Following Rackwitz [247], the LQI can be expressed in the following principal form:

$$\begin{aligned} LQI(g,l) &= g^q\, l \\ q &= \frac{1}{\beta}\,\frac{w}{1-w} \end{aligned} \tag{6.4}$$

where g represents the part of the gross domestic product per capita (GPD) available for investment into life safety, l the life expectancy at birth, and q is a measure of the trade-off between the resources available for consumption and the value of the time of a healthy life, which depends on the fraction of life spent to earn a living w, and a factor β that takes into account that only a part of the GDP is based on human labor [248]. Moreover, based on the LQI, compensation costs for a lost life can be assessed through the concept of the societal value of a statistical life (SVSL) [247]. Thus, the direct costs due to fatalities given bridge damage j can be estimated as:

$$\begin{aligned} C_{\text{D,fa}}(j) &= N_{pe,b}(j) \cdot SVSL \\ SVSL &= g/q \cdot E \end{aligned} \tag{6.5}$$

where $N_{pe,b}$ is the average number of fatalities associated with bridge damage j, and E is the so-called age-averaged discounted life expectancy at birth [247].

6.2.3 Modeling of indirect consequences: Robustness

The risk due to indirect consequences (R_{ID}) can be assessed through the expected value of the indirect consequences regarding all possible hazards and all asset damage states as:

$$R_{\mathsf{ID}} = \sum_{k} \sum_{i} \sum_{j} P(S_k|D_j \cap H_i) P(D_j|H_i) P(H_i) C_{\mathsf{ID},ijk} \tag{6.6}$$

where $P(S_k|D_j \cap H_i)$ is the probability of different network system states S_k given the damage of infrastructure assets D_j due to hazard event H_i; and $C_{\mathsf{ID},ijk}$ is the expected consequences of indirect damages due to system state S_k.

In contrast to direct costs, which can be determined from the condition of infrastructures after the hazardous event, indirect costs accumulate continually until the transportation network is fully restored. This emphasizes the importance of rapid and effective recovery strategies, as detailed in Section 6.3.2. The indirect consequences addressed in this study are those directly associated with the loss of traffic functionality, i.e., rerouting and loss of connectivity, in terms of economic consequences to users, environmental consequences, and consequences to health, i.e., injuries and fatalities. These consequences are further detailed in the following subsections.

The robustness of the transportation system may be assessed by means of a robustness index I_R expressed through the ratio between direct consequences and total consequences [38]:

$$I_{\mathsf{R}}(k) = \frac{C_{\mathsf{D}}(k)}{C_{\mathsf{ID}}(k)} \tag{6.7}$$

As the scenarios k are inherently random, the robustness index $I_R(k)$ is also a random variable. Consequently, robustness indexes can be probabilistically assessed, conditioned on factors such as the type and/or intensity of the hazard event, as well as the magnitude of direct, indirect, or total consequences [18].

6.2.3.1 Economic consequences to users

Travel-related consequences can be converted into monetary units by using the concept of generalized travel costs [249]. Essentially, in the case of failure of infrastructure assets, there will be a prolongation of travel time and distance since traffic flow is no longer possible through failed links. This will result in increased costs due to longer travel times for users, as well as additional vehicle operating costs when traveling longer distances owing to fuel consumption and vehicle maintenance. These indirect costs due to the prolongation of travel ($C_{\text{ID,pt}}$) can be estimated using Eq. 6.8, where U_{tt} is the value of travel time, U_{ov} are the vehicle operating costs, $t_{\text{l,0}}$ and $x_{\text{l,0}}$ are the travel time and the traffic flow at link l with length l_e, respectively, when the network is fully functional, and $t_{\text{l,t}}$ and $x_{\text{l,t}}$ are the travel time and the traffic flow at link l, respectively, at time t after a disturbance event, for a given damage network scenario k [44]:

$$C_{\text{ID,pt}}(k) = (t_{\text{l,t}}(k) \cdot x_{\text{l,t}}(k) - t_{\text{l,0}} \cdot x_{\text{l,0}}) \cdot U_{\text{tt}} + (x_{\text{l,t}}(k) - x_{\text{l,0}}(k)) \cdot l_e \cdot U_{\text{ov}} \tag{6.8}$$

In addition, the failure of certain infrastructure assets in the network may lead to a loss of connectivity between origin and destination (OD) pairs. This unsatisfied demand causes indirect costs due to decreased labor productivity during a time period, which can be estimated as [44]:

$$C_{\text{ID,lc}}(k) = \sum_{P_{\text{od}} \in P^{\text{lc}}_{\text{od,t}}(k)} OD_{\text{m,n}}(k) \cdot U_{\text{lt}} \tag{6.9}$$

where $P^{\text{lc}}_{\text{od,t}}(k)$ represents the OD-paths where no flow is possible (i.e., loss of connectivity between OD-pairs) for a given network system scenario k; $OD_{\text{m,n}}$ is the travel demand from origin m to destination n; U_{lt} is the monetary loss due to the missed trips. Then, the total indirect user costs are the sum of the prolongation of travel costs and the connectivity loss costs:

$$C_{\text{ID,uc}}(k) = C_{\text{ID,pt}} + C_{\text{ID,lc}} \tag{6.10}$$

6.2.3.2 Environmental consequences

Transportation network disruptions causing detours significantly increase the environmental consequences. This effect is attributed to the prolonged operating periods and extended distances covered, which elevate emissions such as CO_2, N_2O and CH_4 (methane), which are greenhouse gases (GHG) contributing to climate change [250]. The magnitude of these emissions is influenced by several factors, including the type of used fuel, the class of vehicle, driving speed, and other specific conditions [251]. Therefore, the GHG emissions can be determined by multiplying the vehicle kilometers for each vehicle type by their respective emission factors (in g/km) for the different GHGs (CO_2, N_2O, CH_4). Subsequently, by employing Global Warming Potentials (GWP), the emissions from these three GHGs can be aggregated to calculate the total CO_2 equivalent GHG emissions [21, 250]. Therefore, the indirect consequences due to environmental emissions for a given damage network scenario k can be estimated as:

$$C_{\text{ID,env}}(k) = (x_{\text{l,t}}(k) - x_{\text{l,0}}(k)) \cdot l_e \cdot E_{\text{CO}_2\text{eq}} \tag{6.11}$$

where $E_{\text{CO}_2\text{eq}}$ are the emissions of GHGs in grams of CO_2 equivalent per vehicle kilometer. Similarly to Eq. 6.8, $x_{\text{l,0}}$ is the traffic flow at link l with length l_e, when the network is fully functional, and $x_{\text{l,t}}$ is the traffic flow at link l, at time t after a disturbance event that resulted in a damage network scenario k. When a monetary valuation of environmental emissions is necessary to assess different decision alternatives, the costs per tonne CO_2 equivalent linked to various global warming impacts, such as sea level rise, loss of biodiversity, water management issues, increased frequency of extreme weather events, and crop failures - often termed as climate change cost - are approximately quantified [250]. One approach to quantify these climate change costs is to formulate them as avoidance costs, in line with the objectives set by the Paris Agreement. This agreement aims to limit global temperature increases to 1.5-2 degrees Celsius, which correlates to a maximum of 450 ppm (parts per million) CO_2 in the atmosphere. Therefore, the indirect consequences due to environmental emissions ($C_{\text{ID,env}}$) could be monetized using climate change avoidance costs in €per ton of CO_2 equivalent.

In instances where assessing decision alternatives requires valuing environmental emissions monetarily, the per tonne cost of CO_2 equivalent, linked to diverse global warming impacts like sea level elevation,

biodiversity diminution, water resource challenges, augmented incidence of severe weather occurrences, and agricultural yield reductions – often termed as climate change cost – are roughly quantified [250].

In addition to GHG emissions, traffic detours increase the emissions of local air pollutants due to combustion processes and dust emissions from road wear, tire particles, and debris from brakes, such as nitrogen oxides (NO_X), particles (PM_{10}, $PM_{2.5}$), and sulfur oxide (SO_2) [251]. The release of these pollutants is associated with various types of damage, among which health impacts are the most notable, as the inhalation of air pollutants increases the risk of respiratory and cardiovascular diseases [250]. These adverse health effects are addressed in the next section.

6.2.3.3 Consequences to health

When estimating the consequences of infrastructure failures in transportation systems, it is relevant to consider that detours may alter the risks for people. Essentially, the closure of a road segment in the network forces commuters to seek alternative routes. This rerouting increases travel distances and intensifies traffic density in other parts of the network, which can significantly escalate the likelihood of accidents. However, the relationship between traffic intensity and car accidents is complex, with various factors at play. Shefer and Rietveld [252] proposed a parabolic relationship between traffic density and fatal accidents, suggesting that congestion can reduce fatalities. Conversely, Wang et al. [253] found that traffic congestion negatively impacts road safety due to higher speed variance and erratic driving behavior. A recent study from Retallack and Ostendorf [254] summarizes these conflicting findings in the literature, with some studies showing a positive linear relationship between accidents and congestion, while others found a U-shaped relationship. Albalate and Fageda [19] investigated the relationship between traffic congestion and road accidents at the city level across 129 European cities from 2008 to 2017. Congestion represents the measured amount of extra travel time experienced by drivers due to traffic conditions. The dependent variable is the annual number of road accident fatalities at the city level, with data sourced from Eurostat. The main explanatory variable is the level of congestion. The study found evidence of a quadratic relationship between deaths in accidents and congestion, as depicted in Figure 6.2. This relationship indicates that up to a certain point, increased congestion could potentially reduce the number of

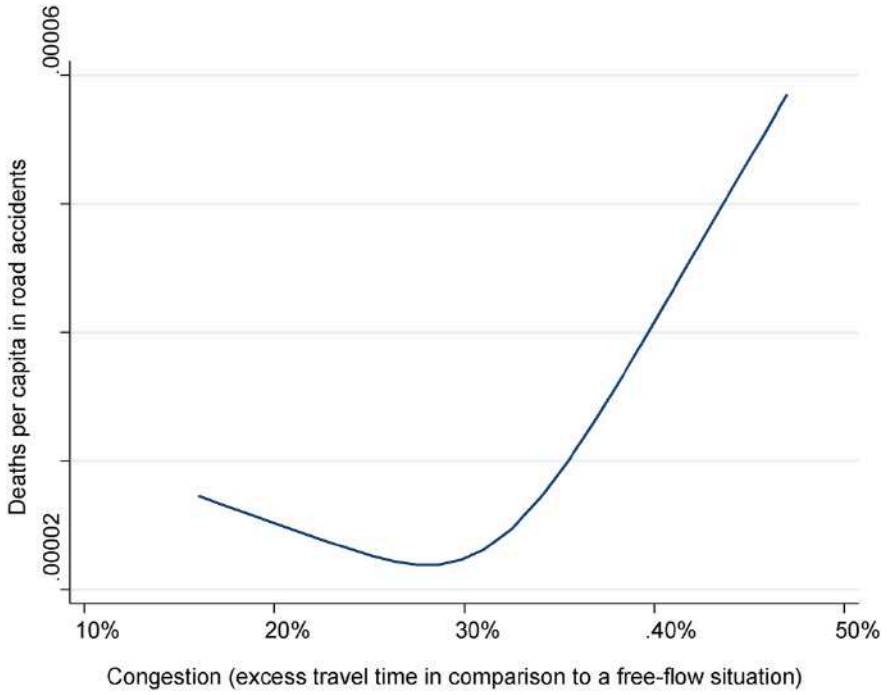


Figure 6.2: Relationship between traffic congestion and deaths due to road accidents. Source: [19]

deaths due to road accidents. However, beyond the 30% increase in travel time threshold, the relationship becomes positive, suggesting that further congestion increases could lead to more accidents.

As previously mentioned in section 6.2.2, a monetary valuation of life loss consequences can be made using the concept of LQI. Thus, the indirect costs due to road accident fatalities for a given damage network scenario k can be estimated as:

$$C_{\text{ID,fa}}(k) = N_{pe,a}(k) \cdot SVSL \tag{6.12}$$

where $N_{pe,a}$ is the average number of fatalities associated with road accidents given the traffic congestion in the damage network scenario k.

On the other hand, the increased traffic congestion leads to elevated noise levels, which causes more people to experience discomfort or adverse health impacts. Similarly, the release of air pollutants (as mentioned in the previous sub-section 6.2.3.2) is associated with adverse health effects, which result in costs for medical treatment, loss of productivity at work due to illness, and potentially fatalities. Therefore,

the costs related to these impacts can be quantified using established methodologies (e.g., [250]), and thus be incorporated into estimating indirect costs of human-related consequences.

6.3 Risk-informed Methodology for Resilient Transportation recovery

Figure 6.3 presents the methodology for risk-informed recovery of transportation systems to maximize resilience by minimizing the indirect costs during the recovery period. Initially, the scenario-based modeling approach will result in different damage network scenarios (k). To evaluate the recovery path for each of them, which minimizes the indirect costs, it is necessary to run the traffic modeling to obtain the different traffic-related metrics, including vehicle hours traveled (VHT), vehicle kilometers traveled (VKT), number of lost trips (LT) and the maximum congestion index (CI). Therefore, a number of damaged network scenarios are first run with the traffic model. Then, using these outputs, a neural network (NN) model is trained to predict the traffic-related metrics for different damage network scenarios. Subsequently, these outputs feed into a prioritization process that examines potential repair sequences, considering the indirect economic consequences associated with each link repair. This process yields the optimal bridge repair sequence that prioritizes actions to minimize the indirect costs, i.e., the sequence that most reduces risks and increases resilience. The following sub-chapters give more detailed explanations regarding the steps in the methodology.

6.3.1 NN model for Traffic Modeling

Transportation models may use different formulations to estimate how the traffic flows through the network in a way that satisfies both the demand and the capacity. The traffic flow volumes on network links can be predicted by traffic assignment. A transportation network is represented by a graph model containing nodes and links. Traffic demands are passenger car units (PCUs) that need to travel from an original node to a destination node. Such pairs of origin–destination (OD) nodes are referred to as OD pairs. There are several methods for performing traffic assignment. One of the most widespread methods is static

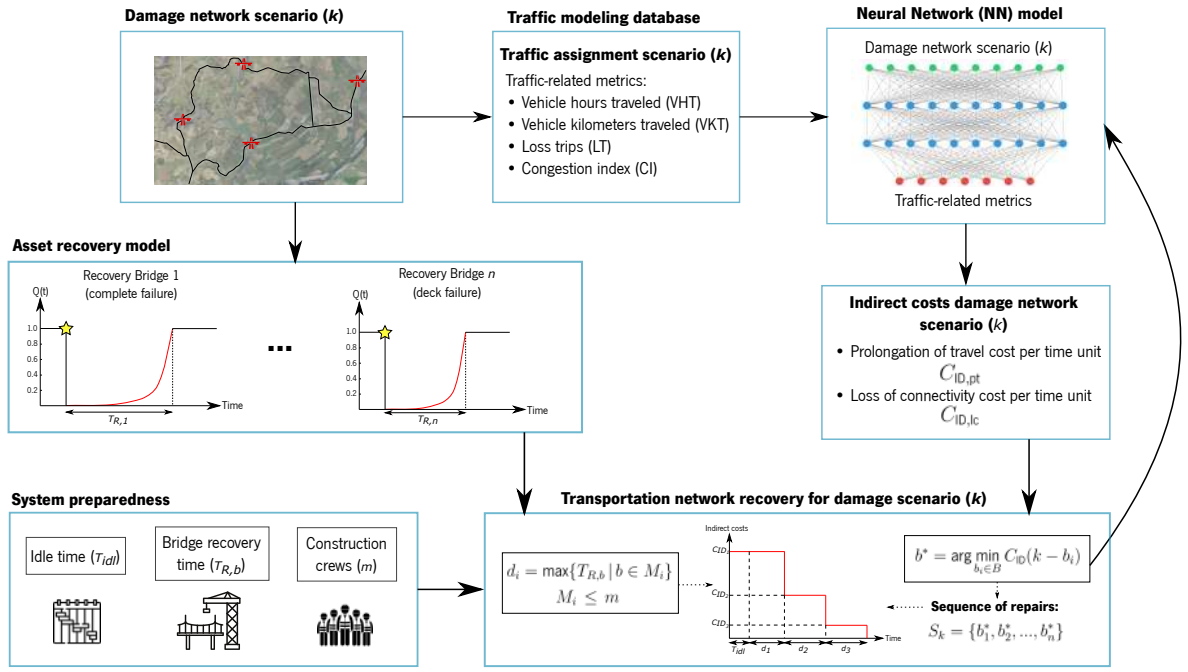


Figure 6.3: Methodology for risk-informed recovery of transportation networks after bridge failures

traffic assignment, based on fixed traffic demands to predict traffic flow volumes on network links based on the user equilibrium (UE) principle [255]. The UE principle may be used to estimate how traffic is flowing through the network. Based on this principle, all travelers are minimizing their travel costs and choosing their routes to minimize the total travel time in the transportation system [255]. Mathematically, traffic assignment based on the UE principle can be formulated as a convex optimization problem solved by the Frank–Wolfe algorithm with various shortest path subroutines to estimate the travel time on each link (e.g., Dijkstra's shortest path algorithm) [255]. This traffic assignment model assumes that traffic users have perfect information about their travel time and always behave accordingly to minimize it. In addition, traffic demands are rigid, meaning that the OD pairs and their associated demands do not vary. Despite these assumptions, the static traffic assignment model has been found to perform well in predicting steady-state traffic flow after a disturbance event such as bridge failure [256]. Nevertheless, other traffic assignment models, such as stochastic UE, can be used when perception uncertainties of traffic users are considered; gravitational models for traffic demand prediction can be integrated when demand variation (e.g., after a hazard) is taken into account, dynamic UE or agent-based modeling (ABM) can be applied when queueing behavior and short-term disturbance are investigated, e.g., when immediate

traffic delay after a hazard is of interest. However, as the complexity increases, the number of traffic assignment operations that can be performed will become limited as the computational cost can become prohibitive [240]. To overcome this limitation, a neural network (NN) model is introduced in the proposed methodology, as shown in Figure 6.3, to predict the outputs from the traffic model for different damage network scenarios. A NN is a model for processing data that consists of multiple interconnected layers of neurons inspired by the way the human brain processes information. In Section 4.6, a Multilayer Perceptron Network (MLP) was introduced and used to model the deterioration of bridge decks, where its higher accuracy was demonstrated. MLPs are also referred to as the (classical) feed-forward neural networks, as signals travel unidirectional only, i.e., from input to output, and there are no feedback loops. Thus, the output of any layer does not influence that same layer [257]. The construction of a NN model involves relevant choices on three primary aspects: (i) the choice of activation function for the hidden layers, (ii) the selection of an appropriate cost function for optimization, and (iii) the overall network architecture. Common practice suggests adopting the rectified linear unit (ReLU) as the activation function and cross-entropy as the cost function. However, various other combinations are documented and explored in existing literature. The structure of the suggested NN model for the multivariate regression task of predicting the traffic-related metrics for different damage network scenarios is shown in Figure 6.4. The input layer is comprised of the damage network scenario by specifying the state of each bridge in the network, i.e., survival or failure. The number of hidden layers and neurons for each layer can be either determined manually through several iterations to obtain the best network performance (as done in Chapter 4) or can be assisted through cross-validation methods such as grid search and random search to find the best combination of hyperparameters. The output of the NN model encompasses seven traffic-related metrics, including vehicle hours traveled (VHT), vehicle kilometers traveled (VKT), and the number of lost trips (LT), each categorized for cars and trucks independently, along with the maximum congestion index (CI). Subsequently, these outputs can be used to effectively compute the indirect consequences for different damage network scenarios.

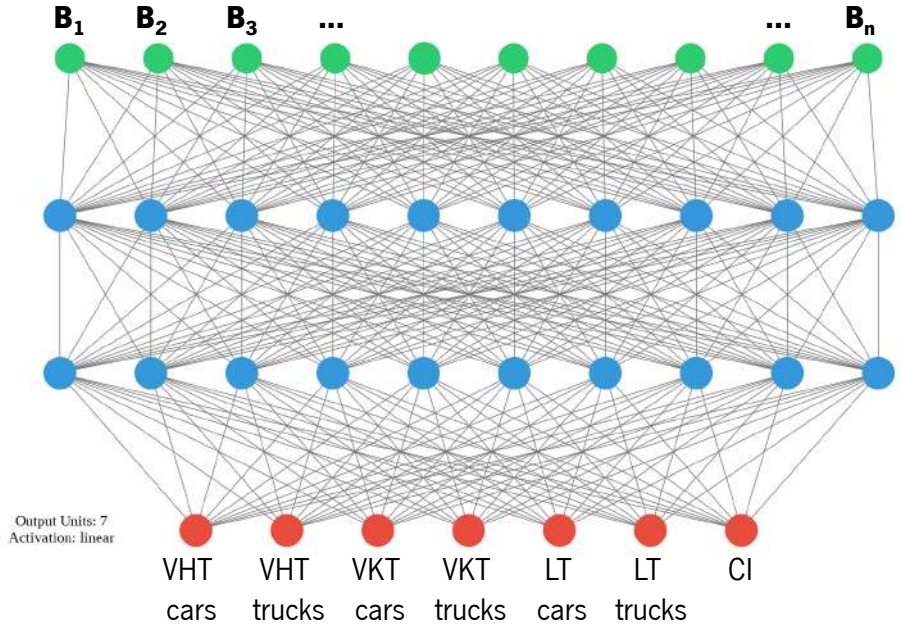


Figure 6.4: Schematic structure of the Neural Network (NN) model for traffic-related metrics

6.3.2 Recovery Modeling

After the occurrence of extreme hazardous events, infrastructure assets that experienced physical damages must be repaired to restore the functionality of the transportation system. Figure 6.5 illustrates three functionality recovery curves for a transportation system with different preparedness levels, namely low, moderate, and high preparedness. In this schema, the initial functionality provided by the system Q_0 drops to a residual functionality Q_R after the occurrence of the disturbance event. The recovery process is then comprised of an idle time and a restoration time. The idle time is conceptualized as the period between the occurrence of the event and the commencement of restoration activities. This duration encompasses a range of preparation and evaluation processes, which may include emergency response, clearing of debris, thorough inspections and condition assessments, site investigations, evaluations of structural and foundational integrity, design of remedial measures, and overcoming organizational barriers [258]. Subsequent to this period, the restoration time spans the duration of reconstruction and repair activities until the functionality of the system is restored. As depicted in Figure 6.5, this restoration can take place in several intermediate phases, which progressively increase the transportation system functionality. While Figure 6.5 depicts the complete recovery to the system's initial functionality, denoted as

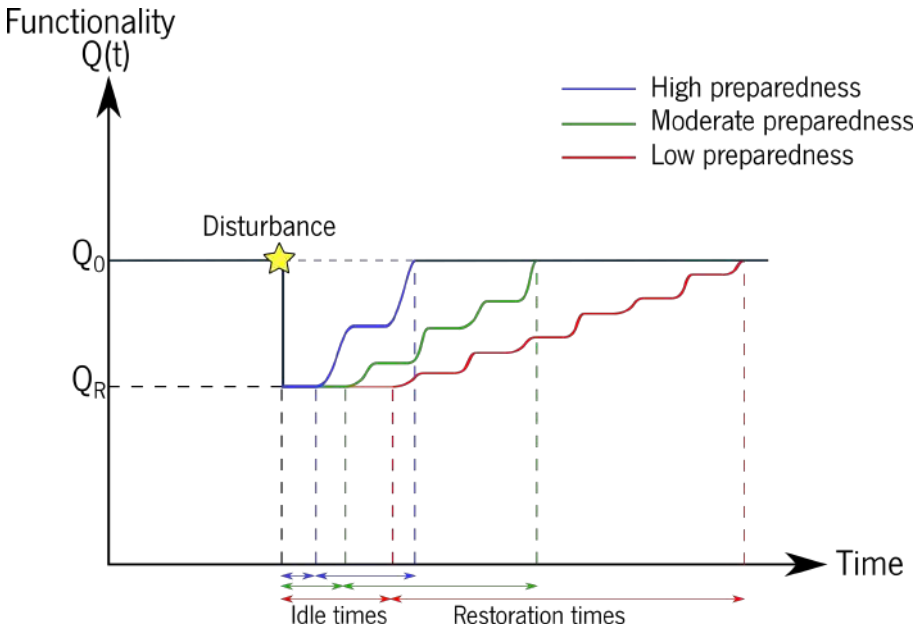


Figure 6.5: Functionality recovery curves for a transportation system

Q_0, it is important to recognize that recovery decisions may conduct to a higher/lower functionality level than before the disturbance event, as highlighted in [65].

The specific path of the functionality recovery curve depends on many factors, including the number and type of infrastructure assets affected in the network, the type and extent of their physical damage, construction techniques and scheduling, the available resources, and the governance capacity [258, 259]. Therefore, constructing reliable recovery functions is a complex task that involves analysis at both the infrastructure asset and transportation network levels. At the infrastructure asset level, recovery modeling has been typically supported by surveys and engineering judgment (e.g., [201]). For instance, Misra et al. [260] have recently conducted an online survey to experts in the field of roadway and bridge inspection and repair to characterize post-hazard restoration planning. Different levels of flood-related damages to bridge components were related to repair decisions, repair time, traffic closure decisions (partial/total closure), and closure times. Similarly, Mitoulis et al. [258] conducted a survey to elicit knowledge from experts and built recovery models for reinforced concrete bridges with spread and deep foundations for different damage levels after floods. The survey included questions regarding idle times, traffic capacity of the bridge after damage, restoration tasks duration, cost ratios, and prioritization. The data gathered from these studies can be used to fit various functions to the bridge functionality recovery for

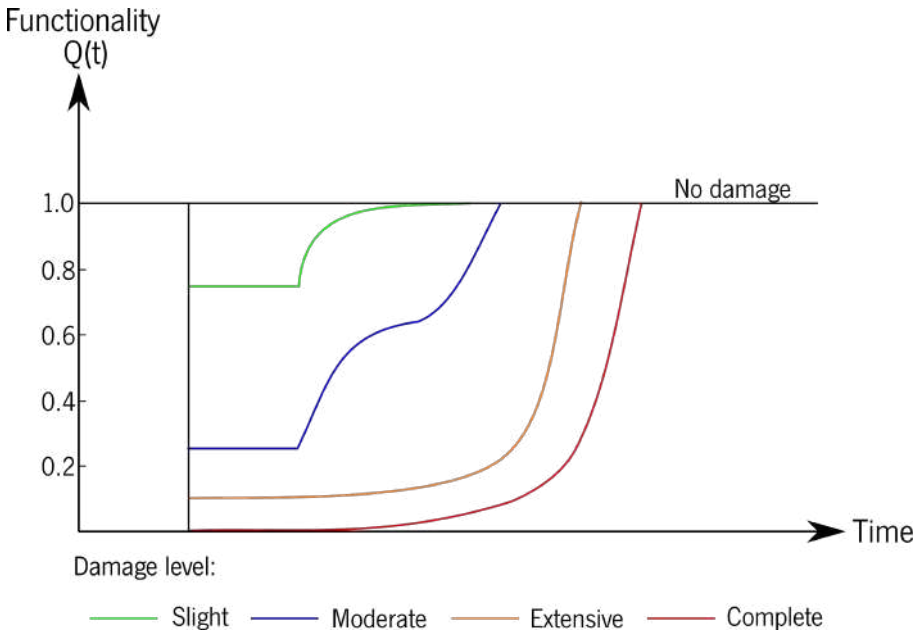


Figure 6.6: Bridge recovery patterns associated with different types of damage. Source: adapted from [20]

different damage levels and correlate this functionality with the traffic flow capacity. For instance, Bocchini and Frangopol [20] modeled the recovery pattern with a sinusoidal-based continuous function to capture different shapes approaching stepwise, linear, and positive and negative exponential functions, as depicted in Figure 6.6. In cases of slight damage (in green), there is a rapid recovery of functionality during the early stages of restoration, characterized by a negative exponential-type function. Conversely, for moderate damage (in blue), a stepwise-type curve is applied, reflecting partial traffic re-openings throughout the rehabilitation period. In situations of extensive and complete damage (in orange and red, respectively), a positive exponential-type pattern is adopted, indicating that the bridge becomes fully functional only upon completion of the rehabilitation process.

At the transportation network level, the functionality is recovered when every infrastructure asset that has suffered physical damage has been repaired, and the traffic flow capacity is fully restored. In addition to the number and severity of the infrastructure damages, the transportation system recovery is strongly influenced by the availability of resources to undertake the repair activities in terms of budget and labor resources (reconstruction crews) and organizational aspects. These factors are ultimately linked to the preparedness of the governance system for dealing with extreme events. Essentially, a transportation system with high preparedness would involve a governance system that reacts rapidly to the disturbance

event, efficiently plans the restoration activities (short idle time), and has sufficient resources to commission several construction crews to undertake the restoration activities. Conversely, a transportation system characterized by low preparedness reflects a governance system that requires an extended period to reorganize and initiate reconstruction activities (prolonged idle time) and has limited resources for restoration efforts, leading to a limited number of construction crews working concurrently and, consequently, extended restoration times. Irrespective of the system's preparedness level for dealing with extreme events, it is possible to identify an optimal restoration program utilizing the available means for recovery. Previous studies have searched for optimal restoration solutions to minimize the overall costs of recovery, including the identification of the type of repair and the schedule of the repairs, both with and without budget and reconstruction crew constraints, e.g., [69, 261, 262]. While most of these studies have employed optimization algorithms to determine the repair order, these solutions are computationally expensive, particularly for large and complex transportation networks. Alternative approaches that prioritize repairs using a network robustness index have shown comparable results to near-optimal heuristic algorithms based on simulated annealing (refer to [70]). Accordingly, this study employs a similar computationally efficient approach, where the order of repairs is determined by the bridge (network link) that minimizes indirect traffic-related costs. These costs encompass additional travel time, vehicle operating expenses, and loss of connectivity costs, as detailed in section 6.2.3.1. This method can be interpreted as prioritizing repairs based on a measure of the criticality of the bridge at the network level, thereby contributing to enhancing the resilience of the transportation system. The prioritization is conducted by sequentially evaluating the impact of every bridge repair on the indirect costs and selecting the option that results in the greatest reduction at each step. Essentially, in a given damage scenario k, involving n failed bridges, the indirect costs are determined by the state of the damaged network ($C_{\mathsf{ID}}(k)$). Thus, for a subset of bridges $B \subset \{b_1, b_2, ..., b_n\}$ requiring repair, the indirect costs of each potential repair are computed, i.e., the indirect costs of the network state in which bridge b_i has been repaired, denoted as $C_{\mathsf{ID}}(k - b_i)$. Then, the bridge whose repair minimizes the indirect costs is formulated as:

$$b^* = \arg\min_{b_i \in B} C_{\mathsf{ID}}(k - b_i) \tag{6.13}$$

where b^* is the bridge selected for repair. After this selection, the set B is updated by removing the

repaired bridge b^*, and the process continues sequentially until all bridges are repaired. This approach systematically reduces the indirect costs at each step. The prioritization is performed separately for each initial damage scenario k, and the output is a sequence vector S_k, representing the order in which the bridges should be repaired. This vector S_k is formulated as:

$$S_k = \{b_1^*, b_2^*, ..., b_n^*\} \tag{6.14}$$

where each b_i^* represents the i-th bridge to be repaired in the sequence for scenario k. It is worth noting that the proposed prioritization process entails estimating the indirect costs for numerous network states, many of which differ from the original damage scenarios. In light of this, the Neural Network (NN) model is an efficient tool for estimating the traffic-related metrics for these unseen scenarios and computing the indirect costs associated with the network state, as depicted in Figure 6.3.

Upon establishing the sequence of repairs, the functionality recovery path can be characterized by three main factors which are influenced by the level of preparedness, namely the idle time, the restoration time of the failed bridges, and the number of construction crews available, as illustrated in Figure 6.3. Following the idle time, the rapidity of the recovery is contingent on the number of construction crews working simultaneously and the duration of the restoration times for the bridges, which are dependent on the severity of the damage sustained. The focus of this study is on failure modes associated with the complete collapse of bridge components. Thus, intermediate stages of bridge restoration with partial bridge openings for traffic are not considered. A bridge is considered operational for traffic only after the full restoration period is completed (as illustrated in red in Figure 6.6). Consequently, the duration of each recovery phase (d_i) is determined by the longest restoration time among the bridges being repaired during that phase:

$$d_i = \max\{T_{R,b} \,|\, b \in M_i\} \quad \forall i \tag{6.15}$$

In this equation, $T_{R,b}$ is the restoration time for bridge b, and the set M_i comprises the bridges being repaired concurrently in the i-th phase, which is limited by the number of available construction crews

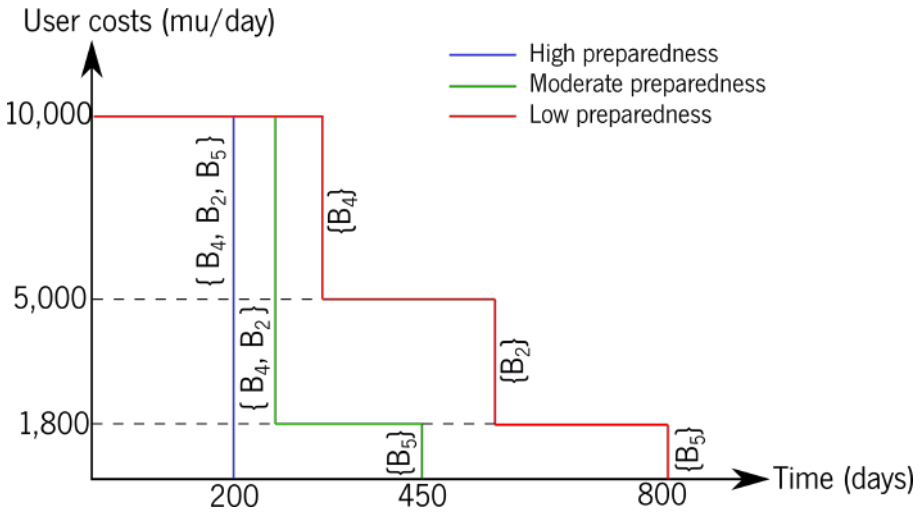


Figure 6.7: Illustrative traffic-related user costs during recovery period

m, ensuring that $M_i \leq m$. Budget constraints are not considered for characterizing the functionality recovery curve, as it is expected that the governance system will have the necessary resources to repair bridges that have sustained severe damage. This premise has been made in similar studies based on communications with transportation agencies (see [262]). Nonetheless, the case of not having this budget for reconstruction is formulated in Chapter 7 as a resilience failure event, where the economic capacity of the system is exhausted. This may be the case for a system with a very low preparedness level.

An example of the optimal sequence of repairs and the accumulated indirect costs to users during the recovery from a damage scenario consisting of three bridge failures is depicted in Figure 6.7, for three different preparedness levels, namely high (depicted in blue), moderate (green), or low (red) preparedness. It can be observed that each recovery path involves different indirect costs, given the different assumptions made for each preparedness level concerning the idle times, the bridge's restoration time, and the availability of construction crews. In this example, a single construction crew for bridge reconstruction is assumed for the low preparedness level, which has a strong influence on the total recovery time and, consequently, on the total indirect costs.

6.4 Case study: Santarém transportation network

As highlighted in Section 1.3.1, the region of Santarém has experienced severe flood incidents, which have led to the isolation of communities and road closures that have extended for weeks, inducing significant economic consequences and harmful social and health conditions [263]. Consequently, the system modeling approach from Figure 6.1 is utilized to model the scenarios of failure events and the corresponding consequences and evaluate flood risks within the transport infrastructure system. The estimation of consequences is enhanced by the application of the methodology proposed in Figure 6.3 for optimal system recovery after infrastructure failures. In applying this methodology, bridges are assumed to be the only assets within the network that result in significant disruptions following a flood event. Figure 6.8 depicts the transportation network comprised of 20 bridges. The information regarding each of the bridges considered is given in Appendix C.

6.4.1 Vulnerability modeling

For the exposure modeling, the Bayesian Network (BN) developed in Chapter 3 is employed to generate a database of flood event realizations to be incorporated into the scenario-based framework. The realizations appropriately characterize the flood demand at different asset locations, given the evidence in the rainfall depth.

Subsequently, the performance of each of the bridges is described by the limit state functions as detailed in Chapter 5, accounting for the deterioration effects over time. The results from the annual failure probabilities of the bridges in the network are shown in Figure 6.9. It can be observed that the probabilities increase during the life cycle due to the deterioration effects considered in the fragility analysis. Given that different deterioration mechanisms are modeled, it is noted that some bridges have a more pronounced increase in their annual failure probability at the end of the life cycle.

The application of the scenario-based modeling approach using 1 million Monte Carlo (MC) simulations resulted in 3444 unique damage network scenarios, i.e., distinct combinations of simultaneous bridge

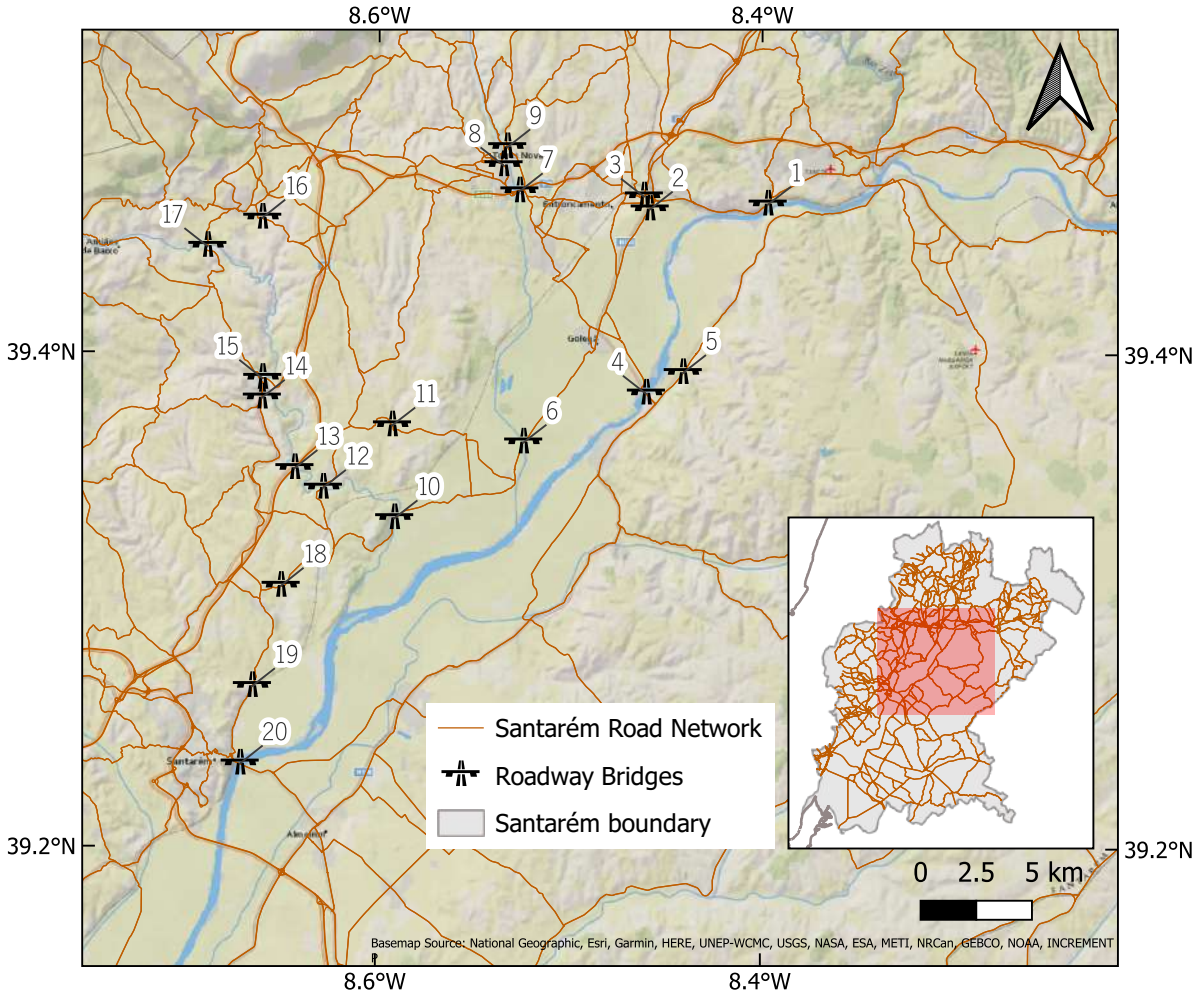
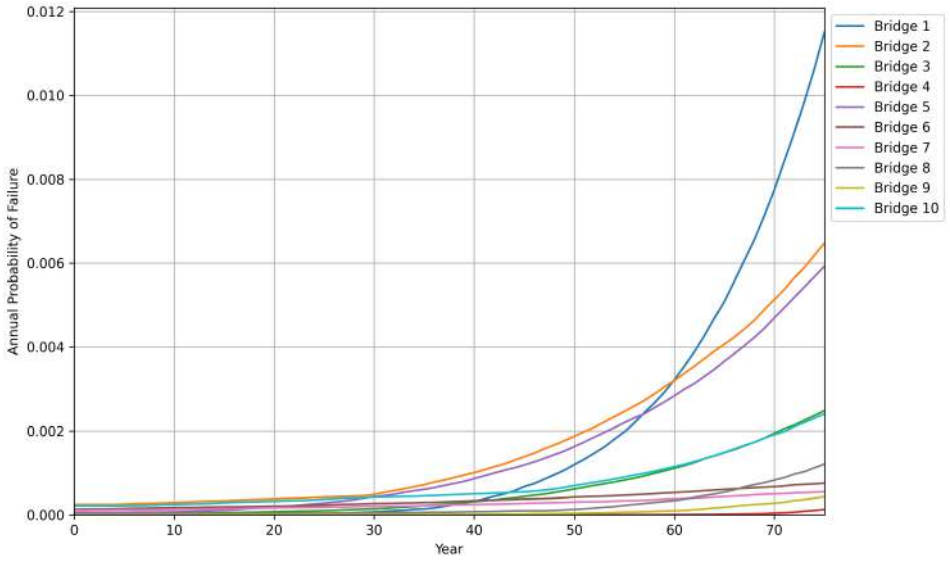


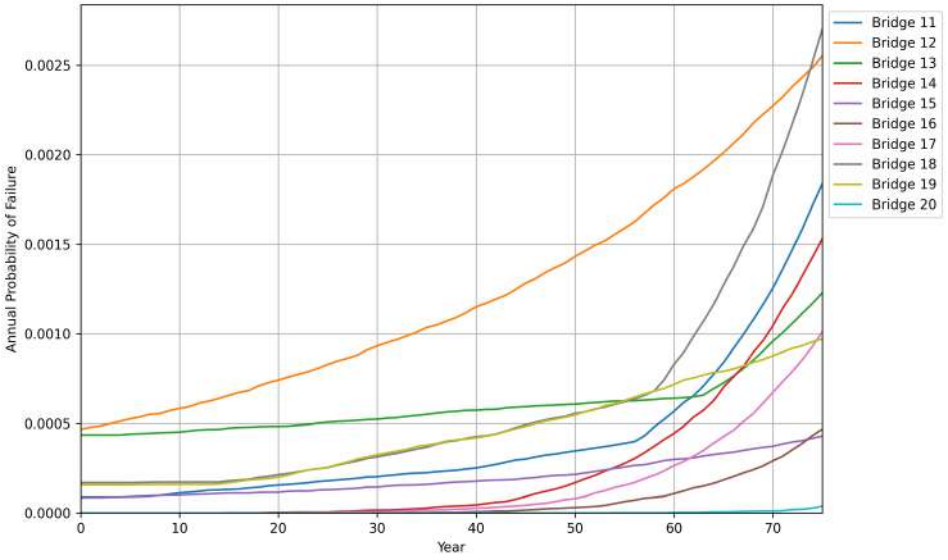
Figure 6.8: Bridge network in Santarém, Portugal

failures. Direct and indirect consequences should then be estimated for these damaged network scenarios. It is worth noting that despite the quite substantial number of scenarios, the application of the framework allows for reducing the space of likely combinations of damage network scenarios. Essentially, for the studied network with 20 bridges following binary failure states, i.e., survival or failure, the total number of failure scenarios encompass $2^{20} - 1 = 1.05E6$ distinct network damage states.

As mentioned in Section 6.2.2, the direct consequences associated with rebuilding depend on the damage level attained by the infrastructure. Since the performance of bridges is described by the limit state functions from Chapter 5, the damage levels correspond to the complete failure of bridge components, namely the deck, pier-foundation system, and/or abutment. Thus, there are three possible restoration



(a)



(b)

Figure 6.9: Annual failure probability of bridges over time

tasks depending on the particular failure mode and associated bridge component failure, as summarized in Table 6.1. The duration of these restoration tasks is adopted from the results from the survey conducted in [258]. Considering that the reference bridge to answer the questionnaire was a 3-span prestressed concrete bridge, an adjustment factor (F_{bt}) for other bridge types was introduced to increase or reduce the duration of the restoration activities accordingly (refer to Appendix C). Moreover, to quantify the associated direct costs (Eq. 6.2), the damage cost ratio (d_r) for each restoration task is given in Table 6.1 as a percentage of the total bridge replacement cost.

Table 6.1: Restoration tasks and duration per bridge failure mode for a reference 3-span prestressed concrete bridge

Failure mode	**Restoration task**	**Damage cost ratio (d_r)**	**Repair duration (days)[1]**		
			Min.	**Max.**	**Mean**
LSF 1,2,3	Deck replacement	0.3	22.2	51	36.6
LSF 4,5,6,7,10	Pier-foundation and adjacent deck spans reconstruction	0.6	88.8	334	211.4
LSF 8,9	Reconstruction of the abutment	0.4	31	72	51.5

[1] Duration source: [258]

The direct consequences associated with repair and/or rebuilding are evaluated in terms of monetary value. Therefore, to compare these costs over the years, the time-variant value of money has to be considered through the discount rate. Starting from the current year, the value of economic consequences for a certain year t can be computed as [182]:

$$C_{reb}(t) = C_{reb}(1 + r_d)^t \tag{6.16}$$

where $C_{reb}(t)$ is the future monetary value referred to year t, C_{reb} is the present monetary mean value of rebuilding, and r_d represents the annual monetary discount rate. A discount rate of 2% is assumed, which is intergenerationally acceptable for sustainable decision making [264]. The distribution parameters of the rebuilding costs are specified in Table 6.2, and the mean value for each bridge is provided in the Appendix C.

The environmental consequences associated with repair and reconstruction activities (Eq. 6.3) are also estimated using the damage ratios from Table 6.1. The environmental impacts considered are those from the embodied CO_2 emissions per kg/m^3 of volume of material to intervene. The corresponding γ_E mean values for each bridge construction material are summarized in Table 6.2. The volumes are quantified based on the bridge dimensions (Appendix C) and the damage ratios.

Lastly, a statistical analysis is required to estimate the number of fatalities and injuries due to complete or partial bridge collapse due to floods. However, as evidenced by statistics of 834 bridge failure incidents worldwide from 1966 to 2020 recorded in a database created within Task group 1.5 of the International Association of Bridge and Structural Engineering (IABSE) [265], fatalities and injuries in bridge collapses due to flooding are very rare. This can be explained as bridges are usually closed during such events, which was also the assumption made when formulating the limit state functions in Chapter 5. Then, fatalities due to bridge collapse during floods are not included in the direct consequence estimation.

Table 6.2: Parameters of random variables associated with direct consequences evaluation

Variable	Description	Dist.	Mean	CoV	Ref.
C_{reb}	Rebuilding costs per bridge type	LN[1]	$\mu_{C_{reb}}$[2]	0.2	[182]
$\gamma_{E,c}$	Concrete embodied CO_2 emissions	LN[1]	360 KgCO$_2$/m^3	0.2	[182, 266]
$\gamma_{E,s}$	Steel embodied CO_2 emissions	LN[1]	10,990 KgCO$_2$/m^3	0.2	[182, 266]
$\gamma_{E,b}$	Masonry embodied CO_2 emissions	LN[1]	180 KgCO$_2$/m^3	0.2	[182, 266]

[1] Lognormal distribution
[2] Refer to Appendix C for bridge type values

6.4.2 NN model for Static Traffic Assignment

The transportation network of the Santarém district is depicted in Figure 6.10, and comprises 7025 links and 879 nodes. The traffic demand data for the pilot zone were sourced from Infraestruturas de Portugal (IP), the public entity responsible for managing the most extensive portfolio of transportation assets in Portugal. The origin/destination (OD) matrix accounts for a daily vehicle volume of 462,720. The transportation network model in this study was developed utilizing AequilibraE, an open-source Python package for transportation network analysis [267]. The transportation model implemented in AequilibraE employs Static Traffic Assignment (STA), an extensively adopted macroscopic traffic modeling approach

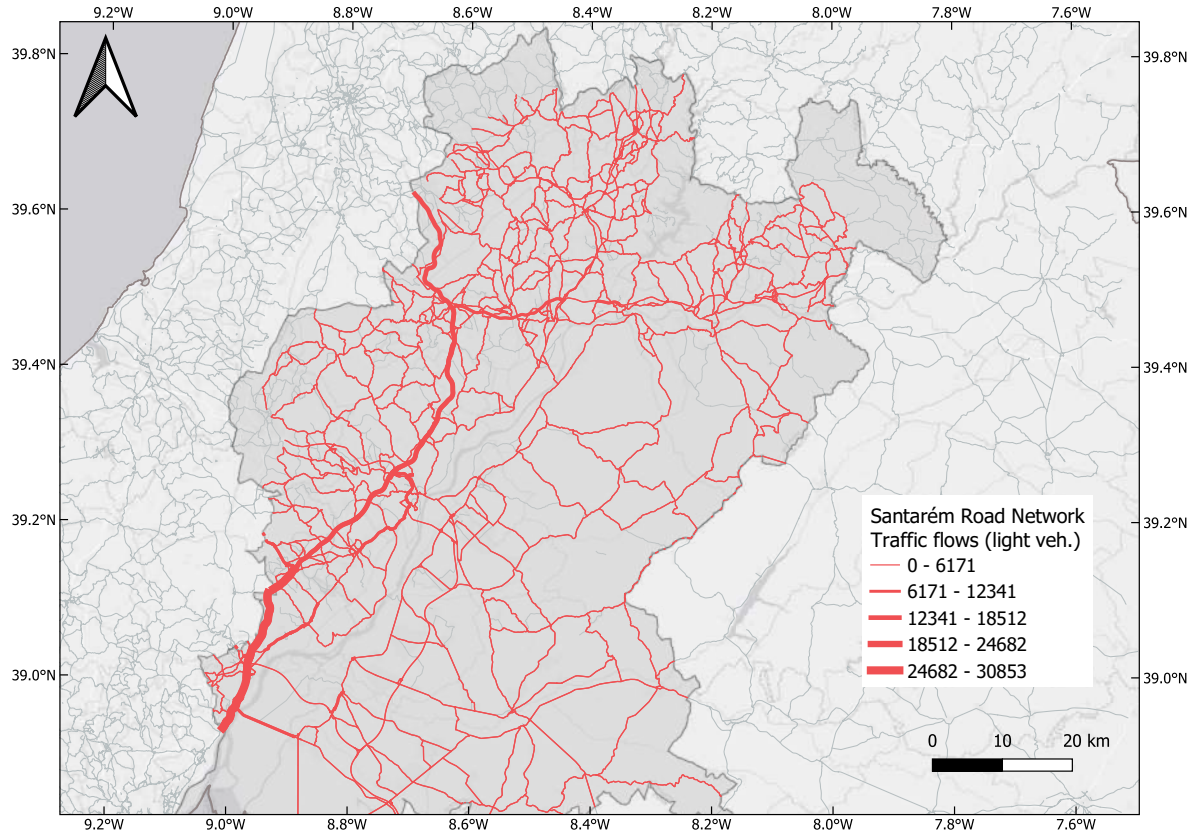


Figure 6.10: Traffic network of Santarém district, Portugal. Source of data: Infraestruturas de Portugal

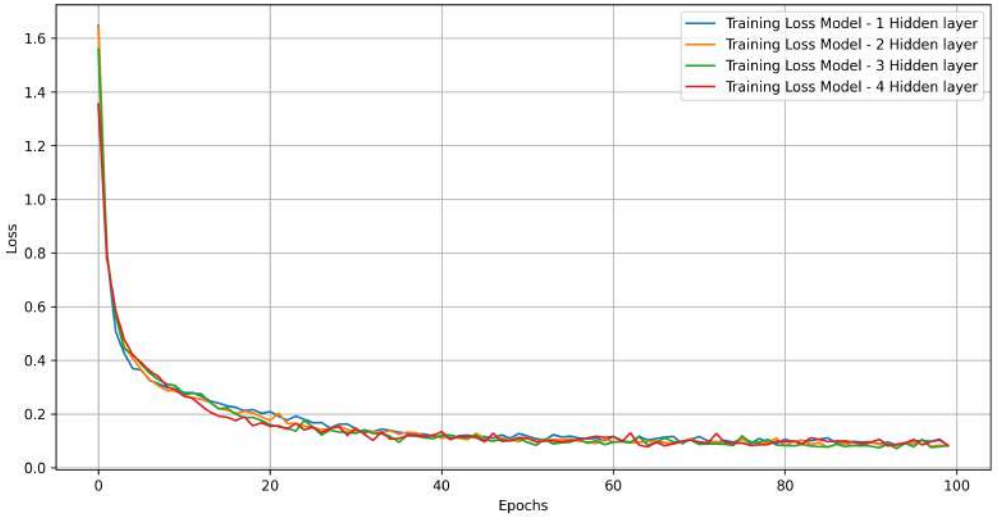
for determining traffic distribution across road networks. Even though macroscopic traffic modeling does not represent individual vehicles or people on the network, it is deemed sufficient for the intended type of analysis based on the assumption that the duration of reconstruction is sufficiently prolonged, allowing network users to adapt to the altered traffic conditions, seek alternative routes, and achieve a state of user equilibrium. For the same reason, traffic demand is assumed to be rigid, i.e., the flood event does not lead to any variation of scheduled trips. Similar considerations have been made in previous studies (e.g., [47]). Nonetheless, it is noted that the assumption that traffic is not altered after the disturbance event might lead to significantly lower estimates of the total induced traffic costs [68]. However, a detailed analysis regarding traffic variations after flood events is not available for the case study, which limits the incorporation of this aspect in the current study. The Biconjugate Frank-Wolfe algorithm is selected for solving the traffic assignment and estimating the travel time and traffic flow at each link, as well as the OD paths where no flow is possible for each damage scenario. Further details regarding the development and modeling considerations for the traffic model are provided in Appendix D.

As illustrated in the methodology shown in Figure 6.3, the traffic assignment (TA) problem is solved for various damage network scenarios, and the traffic-related outputs are stored in a database. Solving the TA for a single scenario takes approximately 2 minutes. Therefore, solving the 3444 unique damage network scenarios identified in the vulnerability modeling would require about 120 hours. To examine the impact of the number of scenarios used to train the neural network (NN) model, two subsets of the damage scenarios were chosen and solved using AequilibraE. The first subset encompassed 2500 scenarios, while the second included 1500 scenarios. The outcomes of these scenarios comprised the two datasets that were subsequently used to train the NN model for predicting the traffic-related metrics.

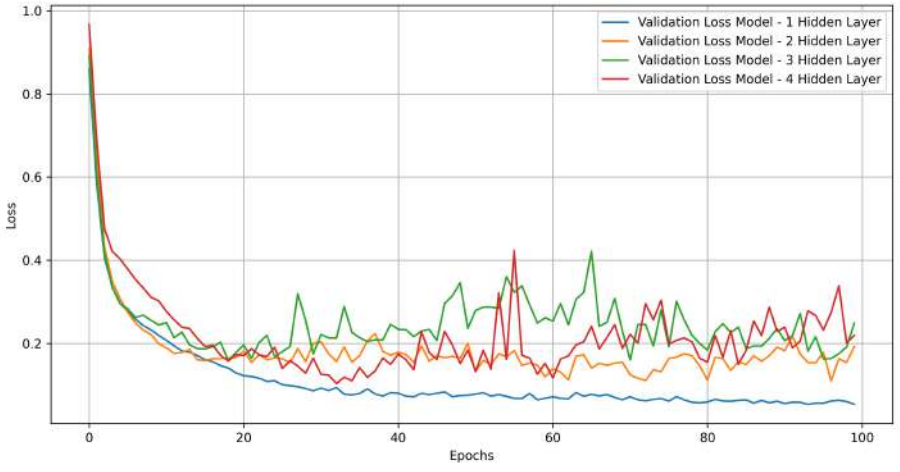
The NN model was developed using Keras and TensorFlow in Python. As explained in Section 6.3.1, the input layer is comprised of the damaged network scenario by specifying the state of each bridge in the network, i.e., survival or failure. The number of hidden layers and neurons per layer was determined through a manual search process by adjusting these settings to enhance the Multilayer Perceptron Network (MLP) performance. The rectified linear unit (ReLU) activation function is set for the hidden layers, as recommended for typical regression tasks of MLP networks [268] given its efficiency and effectiveness in non-linear transformations. The output layer encompasses the seven traffic-related metrics, so a linear activation function is employed for the output neurons to take any range of continuous values. The datasets are randomly split into training and testing datasets. Essentially, the model is trained on 80% of the provided input and output data, which ensures a substantial training dataset for the model to learn effectively, while the remaining 20% of the data is used for testing, allowing for an evaluation of the model's error in unseen scenarios. For this evaluation, the loss function used was the mean squared error (MSE). For the training of the NN model, the Adam optimizer is employed to optimize the weight settings for connections between neurons across the network layers. The choice of the Adam optimizer is based on its computational efficiency, minimal memory requirements, and suitability for problems that are large in terms of data/parameters, in comparison to other optimizers such as stochastic gradient descent [269]. Since the Adam optimizer is an adaptive learning rate algorithm, the learning rate hyperparameter requires less tuning. Then, the learning rate is set to its default value of 0.001. Lastly, the batch size is set as 20 as Batch Normalization is used to contribute to reducing overfitting, so the batch size should not be too small [268].

As suggested in [257] when defining the structure of MLPs, a uniform number of neurons is assumed as the default for all hidden layers to reduce the range of potential network structures. In this manner, only one width (number of neurons) and one depth (number of layers) parameters need to be selected. Thus, the manual search process involved first setting an arbitrary number of neurons and progressively increasing the number of hidden layers, ranging from one to four hidden layers. Figure 6.11 presents the comparison of the training and validation losses for the NN model with 30 neurons per hidden layer for the different depths considered, i.e., one to four hidden layers. In the training loss comparison (Figure 6.11a), all models seem to converge to a similar loss value as training progresses. However, in the validation loss comparison (Figure 6.11b), the models exhibit more variation in loss, especially after the initial sharp decrease. This large fluctuation in the validation loss is explained as the validation set is not used for training, so it represents the model's ability to generalize. A significant gap between training and validation loss can indicate overfitting. In this case, the model with one hidden layer (depicted in blue) maintains the lowest validation loss, suggesting it generalizes better than the others. In contrast, models with more hidden layers, especially the one with four hidden layers (depicted in red), show higher and more fluctuating validation losses, suggesting potential overfitting. Therefore, for the TA problem under study, a single hidden layer seems to provide the best performance, as adding more layers does not contribute to better generalization and may, in fact, lead to worse performance on unseen data.

After setting the NN model to one hidden layer, the number of neurons is varied to investigate their influence on the network performance. Figure 6.12 compares the training and validation losses for the NN model with one hidden layer for the different widths considered, i.e., 10, 30, 50, and 100 neurons. From the training loss plot of Figure 6.12a, it is seen that all models exhibit a steep decrease in training loss at the beginning, and as training progresses, the losses appear to converge to a similar value. In the validation loss plot shown in Figure 6.12b, the models with 30 and 50 neurons appear to have the most stable and lowest validation losses as training progresses. The model with 100 neurons, while exhibiting low losses, presents a slight divergence between training and validation loss, potentially indicating the onset of overfitting. Conversely, the model with 10 neurons has a slightly higher loss compared to the 30 and 50 neurons models, which may be indicative of slight underfitting or limited capacity to capture the complexity of the data. Therefore, the NN model with 30 neurons offers the best balance between complexity and performance on unseen data.

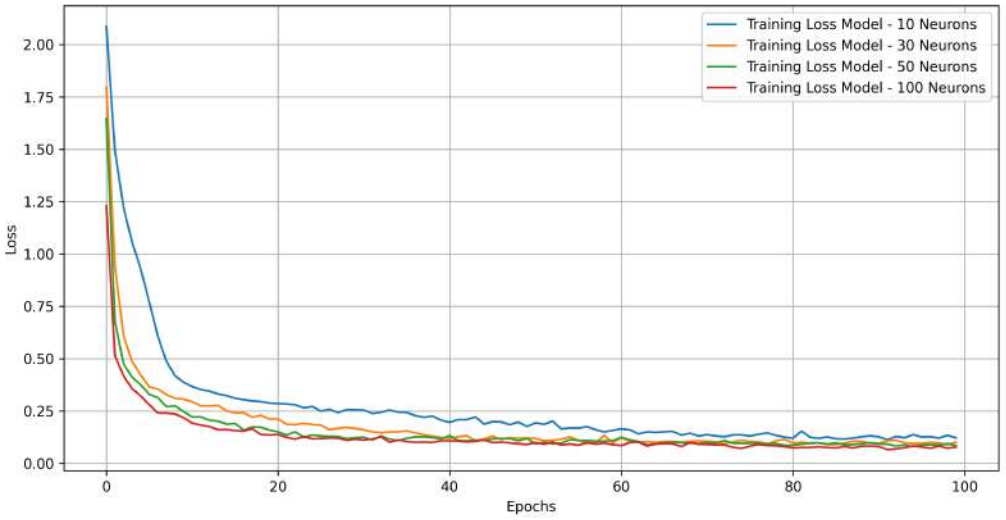


(a)

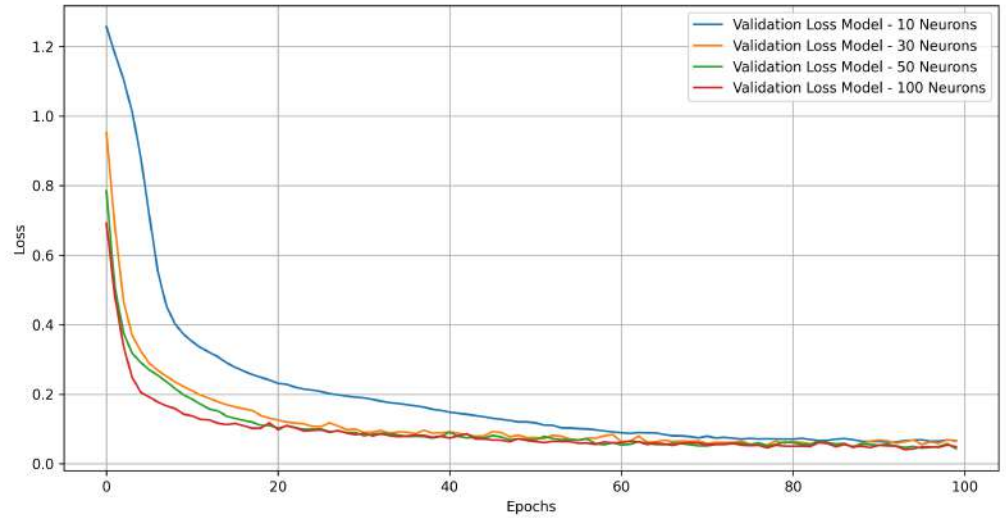


(b)

Figure 6.11: Comparison of training and validation losses of a NN model with various hidden layer sizes and 30 neurons



(a)



(b)

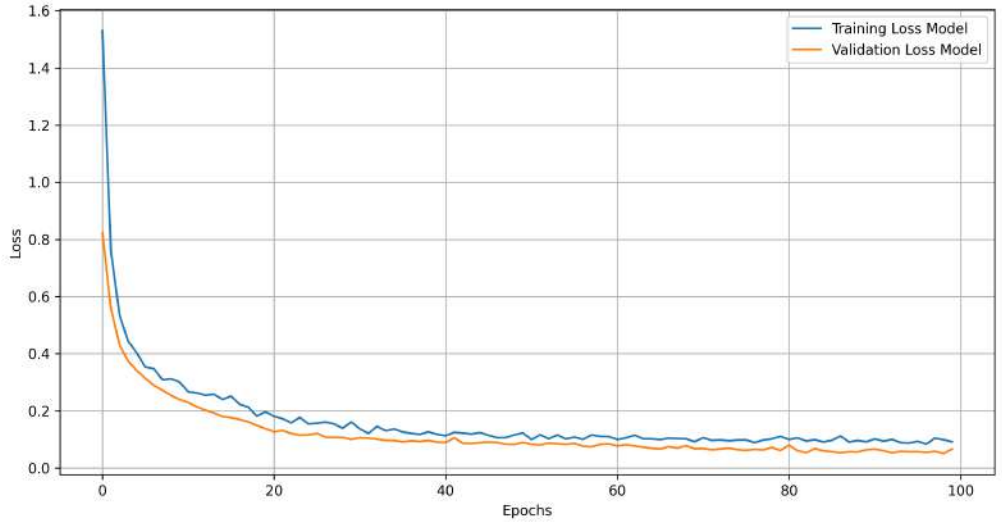
Figure 6.12: Comparison of training and validation losses of a NN model with various numbers of neurons and one hidden layer

The previous results were derived using the dataset containing the outcomes of the traffic assignment of 2500 damage scenarios. The same analysis for defining the number of hidden layers and neurons per layer was conducted on the smaller dataset with 1500 damage scenarios, yielding comparable results. Figure 6.13 shows the training and validation loss curves for both NN models with one hidden layer and 30 neurons, constructed using each dataset. It can be seen that that the NN model trained with the smaller dataset exhibits a similar performance to that using the larger dataset. In fact, the MSE of the NN model trained with the large dataset is 0.09, and the MSE for the NN model trained with the smaller dataset, even when assessed with the test set from the larger dataset, is 0.1. These results suggest that both datasets are adequate to train the NN model for predicting changes in traffic patterns for unseen bridge failure combinations. Employing the smaller dataset represents a considerable reduction in the computational cost compared to evaluating the traffic metrics of every damage scenario, which is a clear advantage of implementing the NN models.

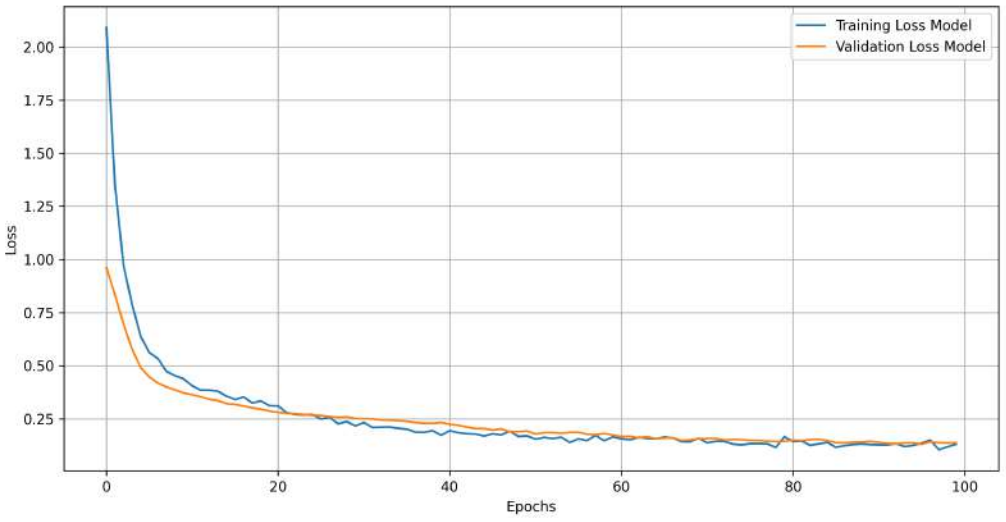
Lastly, Figure 6.14 depicts the scatter plots displaying the relationship between observed and predicted total kilometers driven by cars (Figure 6.14a) and total vehicle kilometers traveled by trucks (Figure 6.14b), as determined by the NN model. The plots reveal a high degree of predictive accuracy of the NN model, with the majority of data points closely aligning with the dashed line, which represents perfect prediction. However, the presence of outliers, more noticeable at higher values, suggests potential deviations in the model's predictions for scenarios possibly involving numerous bridge failures.

6.4.3 Indirect costs of failures

The traffic-related metrics are used to compute the indirect consequences to the economy, health, and environment, as detailed in Section 6.2.3. The parameters of the random variables associated with the evaluation of indirect consequences are summarized in Table 6.3. For the economic consequences to users, the mean values of travel time for light and heavy vehicles in Portugal are derived from [250]. For vehicle operating costs of light and heavy vehicles, the values are adopted from project technical reports conducted in Europe, as described in [47]. The opportunity costs arising from a loss of connectivity in the road network are related to the loss of labor productivity with respect to the canceled trip. Particular calculations of unit opportunity costs for Portugal are not available, so the values are assumed based on

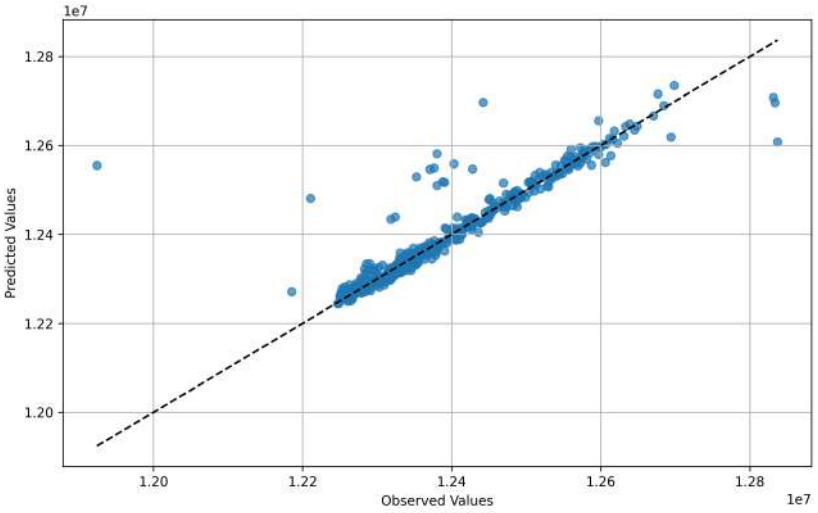


(a) Dataset with 2500 damage scenarios

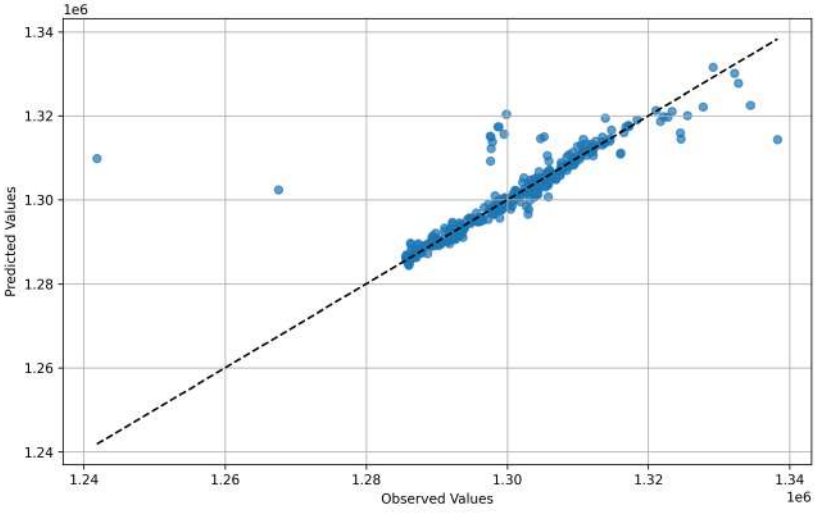


(b) Dataset with 1500 damage scenarios

Figure 6.13: Training and validation loss curves of the NN model for each dataset



(a) Total vehicle kilometers traveled by cars



(b) Total vehicle kilometers traveled by trucks

Figure 6.14: Observed versus predicted traffic-related metrics with the NN model

similar studies (e.g., [44, 46]). Regarding the environmental consequences, gasoline and diesel vehicles dominate the vehicle fleet in Portugal [225]. Therefore, the mean values of emissions of GHGs in grams of CO_2 equivalent per vehicle kilometer are derived from [225] by averaging the emission values for gasoline and diesel vehicles, for light and heavy vehicles in small towns. Lastly, for the health consequences, the relationship between traffic congestion and deaths due to road accidents proposed by [19] is implemented herein, assuming that the trends found in the study provide insights applicable to urban areas in Portugal, although it is not specific to the country. For the application of this relationship, a quadratic function is fitted to the values depicted in Figure 6.2, and the population of Santarém district is recorded at 425,000 inhabitants, as determined from the most recent census (2021) of the National Statistics Institute (INE) in Portugal. For the purpose of converting the expected deaths due to road accidents to monetary values, the LQI concept can be applied considering Portugal a developed country for which the necessary parameters for calculating the societal value of a statistical life (SVSL) are known [248]. Additional health consequences associated with air pollution and noise are not estimated, as the costs resulting from accidents in road transport have been demonstrated to be substantially greater than the combined effects of these two factors in Europe (refer to [250]).

Table 6.3: Parameters of random variables associated with indirect consequences evaluation

Variable	Description	Dist.	Mean	CoV	Ref.
$U_{\text{tt,l}}$	Value of travel time LV[2]	LN[1]	21.08 €/(veh hour)	0.2	[250]
$U_{\text{tt,h}}$	Value of travel time HV[3]	LN	37.68 €/(veh hour)	0.2	[250]
$U_{\text{ov,l}}$	Vehicle operating costs LV	LN	0.22 €/(veh km)	0.2	[47]
$U_{\text{ov,h}}$	Vehicle operating costs HV	LN	0.85 €/(veh km)	0.2	[47]
$U_{\text{lt,l}}$	Opportunity cost lost trip LV	LN	170 €/(veh)	0.2	-
$U_{\text{lt,h}}$	Opportunity cost lost trip HV	LN	650 €/(veh)	0.2	[44]
$E_{\text{CO}_2\text{eq,l}}$	Emissions of GHGs LV	LN	153 gCO_2eq / (veh km)	0.2	[44]
$E_{\text{CO}_2\text{eq,h}}$	Emissions of GHGs HV	LN	770 gCO_2eq / (veh km)	0.2	[44]
$SVSL$	Societal value of a statistical life	-	4.0 M €	-	[248]

[1] Lognormal distribution
[2] Light Vehicles (LV)
[3] Heavy Vehicles (HV)

6.4.4 Recovery model

As described in Section 6.3.2, the optimal sequence of repairs for each damage scenario is established by minimizing the indirect costs. This task is achieved by systematically evaluating the effect of each bridge repair on these costs. At each step, the repair option that yields the most substantial reduction in indirect costs is selected. The process is conducted sequentially until the restoration of all bridges is completed. Then, to characterize the functionality recovery path, three scenarios of preparedness for recovery in the case study are considered: low, moderate, and high preparedness. The main factors to characterize the recovery process for each preparedness level are given in Table 6.4. As previously outlined, the bridge restoration time depends on the failure mode and the associated restoration task, as given in Table 6.1, as well as an adjustment factor to account for the bridge type. Considering that the restoration times were adopted from the survey conducted in [258], it is assumed that the experts' responses align with a management system that is moderately prepared to cope with disasters, as they emphasize the importance of quick reinstatement and recognize the substantial indirect costs associated with delayed restoration. Therefore, for low and high preparedness levels, a mean restoration time factor is outlined in Table 6.4. This factor is applied to the restoration times listed in Table 6.1, which are assumed to follow a triangular distribution using the minimum, maximum, and mean values. The rationale behind this factor is to depict that a management system with low preparedness might implement sub-optimal reconstruction techniques due to inadequate practices, potentially leading to prolonged restoration times compared to a system with moderate preparedness. In contrast, a highly prepared management system, equipped with advanced reconstruction techniques such as accelerated construction or innovative technology, will likely achieve more expedient restoration times than a moderately prepared system. The remaining two factors to characterize the functionality recovery, namely idle times and number of construction crews available, were assumed for each preparedness level based on engineering judgment. The idle times have been assumed uniformly distributed, with the lower and upper bounds provided in Table 6.4.

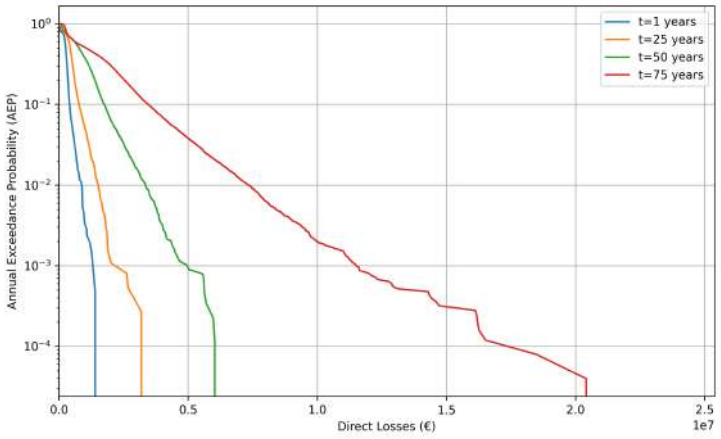
Table 6.4: Recovery factors and parameters for different preparedness levels

Preparedness parameter	High	Moderate	Low
Mean restoration time factor	0.8	1	1.2
Idle time (days)	U (30,60)	U (50,80)	U (70,100)
Construction crews	4	2	1

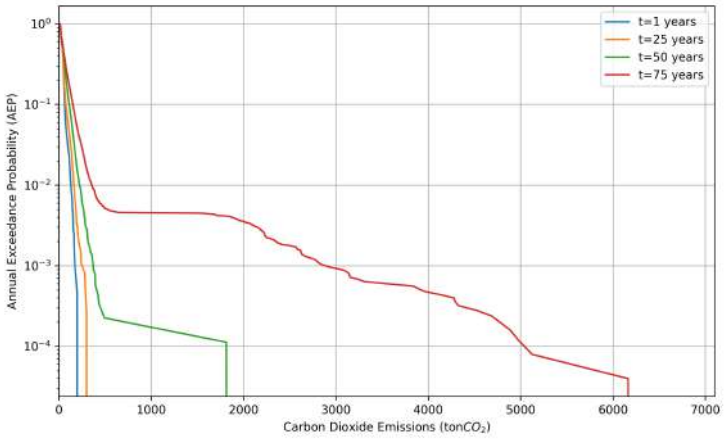
6.5 Results and discussion

Figure 6.15 presents annual exceedance probability curves of direct economic and environmental losses at various years of analysis, namely at 1, 25, 50, and 75 years. It can be observed that both direct economic and environmental losses increase for higher years of analysis, which demonstrates the influence of deterioration effects. This is more pronounced, especially for 75 years, which is anticipated as the probability of failure for most bridges increases substantially after 50 years. This effect is also evidenced in Figure 6.16, which depicts the time-variant expected value of direct economic losses (in €) and the expected value of direct emissions (in tons of CO_2).

Figure 6.17 presents the results of the accumulated user costs of 15 random samples of damage network scenarios when applying the methodology for resilient transportation system recovery for the three preparedness levels under analysis. It can be observed that user costs vary greatly depending on the combination of damaged bridges. Moreover, the influence of the preparedness levels on overall recovery time is evident, as the same damage combination under a high preparedness level (Figure 6.17c) is fully recovered in around 100 days, while it takes approximately 400 days in the low preparedness level (Figure 6.17a). These results are explained by the longer idle and restoration times for the low preparedness, exacerbated by the low number of construction crews available, which leads to several restoration phases depicted as sequential steps in the stepwise functions until all repairs are finalized. Conversely, most damage network scenarios are repaired simultaneously for the high preparedness level given the larger availability of construction crews, which explains the unique jump from indirect costs to zero, as shown in Figure 6.17c. The variation in total recovery time across these scenarios is influenced by the specific restoration duration of each bridge and their respective failure modes, as well as the uncertainties introduced in these values and in the idle time. At the moderate preparedness level (Figure 6.17b), the recovery progresses more slowly than at the high preparedness level, with certain network damage scenarios necessitating multiple phases to reach full recovery. Nonetheless, most scenarios achieve complete recovery in half the time required at the low preparedness level. These findings regarding the influence of preparedness levels on the recovery times extend to the results presented in Figure 6.18, which depicts the accumulated environmental consequences during transportation network recovery. Interestingly, the network damage scenarios associated with the greatest carbon dioxide emissions (in Kg CO_2 eq) due to



(a)



(b)

Figure 6.15: Annual Exceedance Probability curves of a) direct economic losses and b) direct environmental losses

detours do not necessarily coincide with those resulting in the highest user costs. This can be attributed to several factors, such as the congestion level that particularly increases travel time costs, whereas the environmental emissions only depend on the distance traveled. In addition, certain scenarios could lead to a loss of connectivity, incurring user costs due to productivity losses, while environmental emissions are actually reduced due to trips that are missed. These results are relevant when the objective is to compare multiple criteria, such as user costs and environmental impacts, for assessing different decision alternatives.

Figure 6.19 displays the annual exceedance probability (AEP) curves for indirect economic losses for the

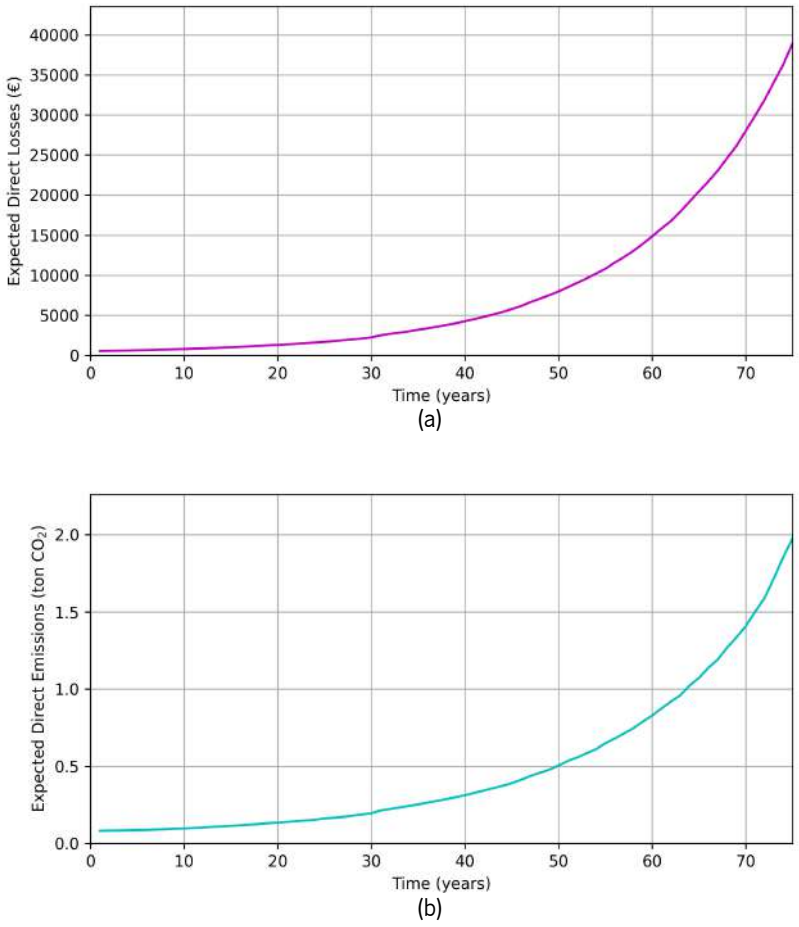
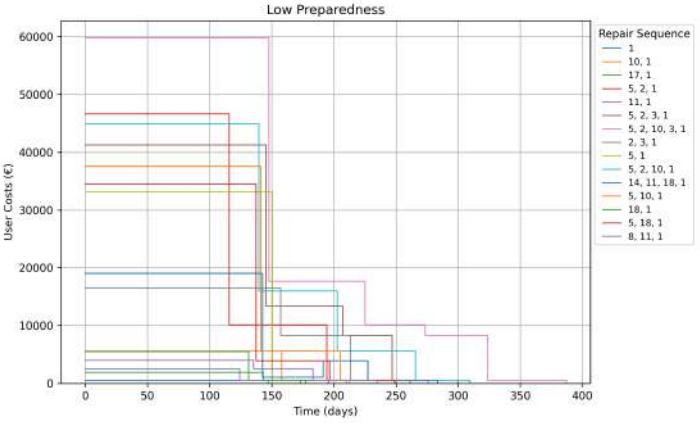
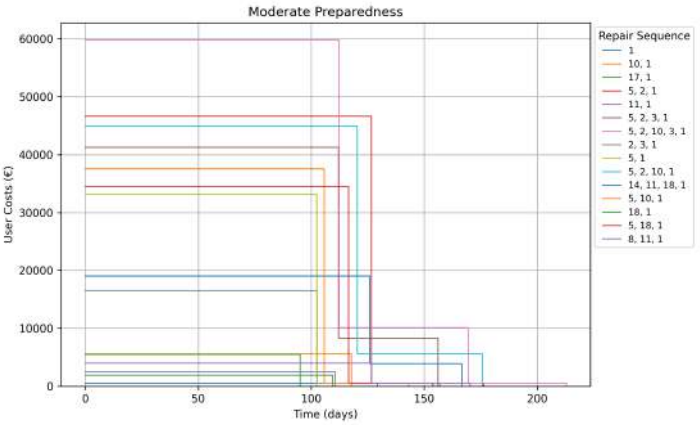


Figure 6.16: Time-variant expected value of a) direct economic losses and b) direct environmental losses

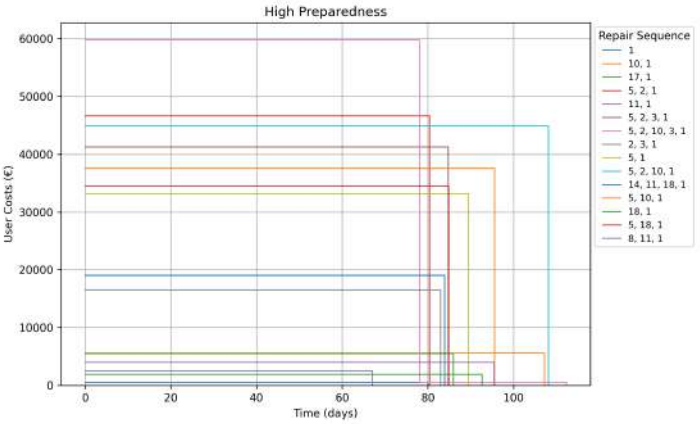
three levels of preparedness. As expected, the extended recovery duration associated with moderate and, more notably, low preparedness levels substantially impacts the total indirect losses. This effect is particularly pronounced for events with low annual exceedance probabilities, which involve multiple bridge failures and thus entail a recovery process characterized by numerous restoration phases. Moreover, the AEP curves are presented for the current year (Figure 6.19a) and for the projection of indirect losses after 75 years (Figure 6.19b). A comparison of both time frames reveals the marked impact of deterioration on indirect losses, as occurred with direct losses. Yet, when compared to the magnitude of direct economic losses, which are measured in millions, the indirect economic impacts are significantly greater, reaching into the billions. Similar trends are observed in Figure 6.20, which presents AEP curves of indirect environmental emissions for the three preparedness levels, both for the current year of analysis (Figure 6.20a)



(a)

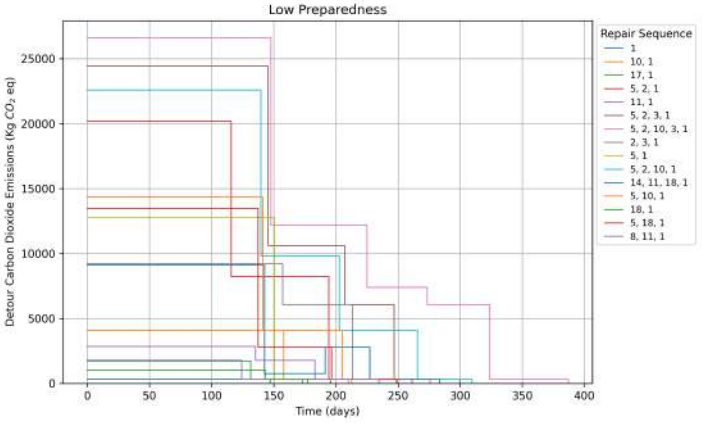


(b)

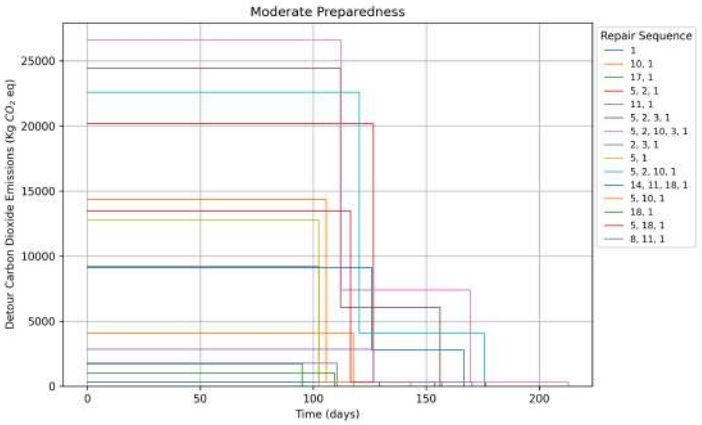


(c)

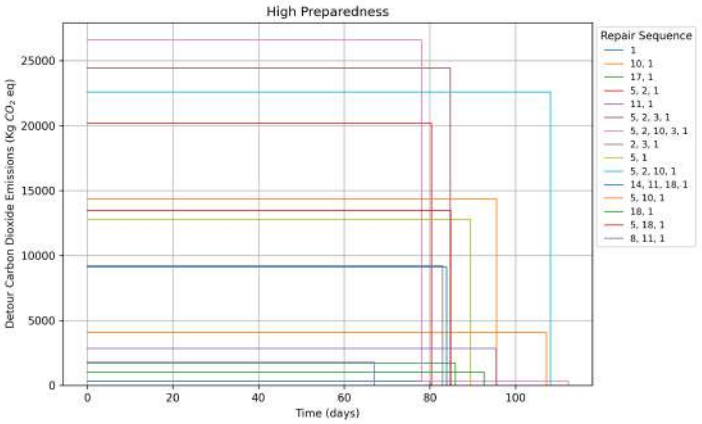
Figure 6.17: Accumulated indirect costs to users during transportation network recovery for different preparedness levels



(a)

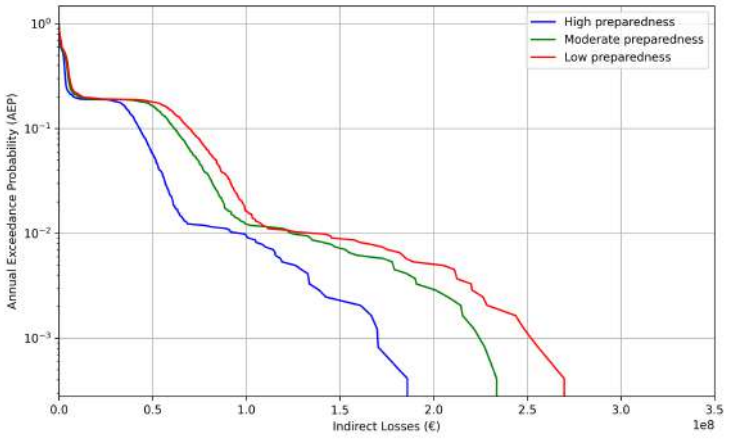


(b)

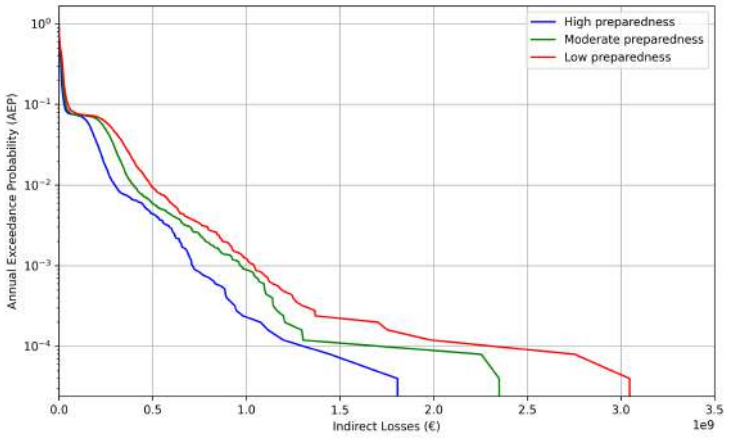


(c)

Figure 6.18: Accumulated indirect environmental consequences during transportation network recovery for different preparedness levels



(a)

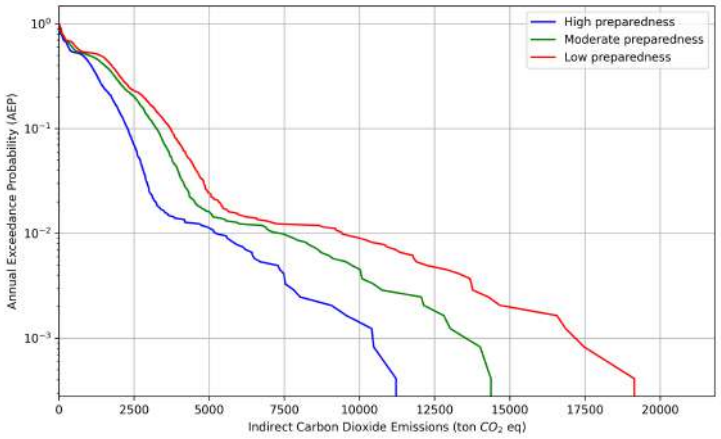


(b)

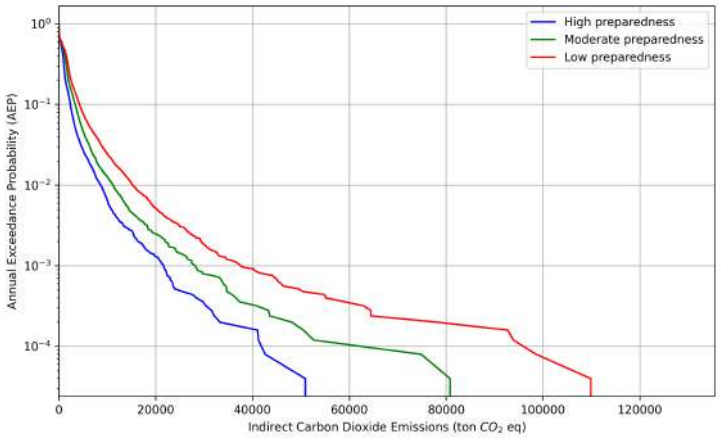
Figure 6.19: Annual Exceedance Probability curves of indirect economic losses at a) current year and b) projected for 75 years

and the projection after 75 years (Figure 6.20b). These figures indicate that the difference in environmental emissions between low and high preparedness levels is more pronounced than the differences noted in indirect economic losses among levels. Moreover, for the 75-year projections, the magnitude of direct carbon dioxide emissions measured in ton CO_2 equivalents is estimated in less than the tens of thousands, whereas indirect emissions from detours are projected to be in the hundreds of thousands for scenarios with low preparedness.

The evolution of the expected value of indirect economic losses and the expected indirect emissions over



(a)



(b)

Figure 6.20: Annual Exceedance Probability curves of indirect environmental losses at a) current year and b) projected for 75 years

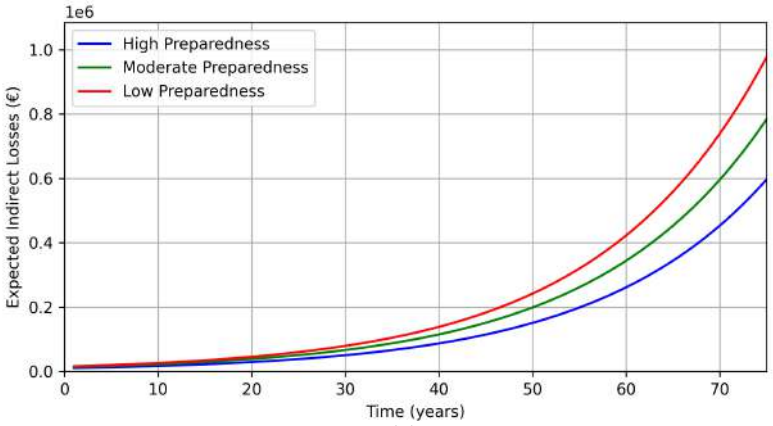
time is depicted in Figure 6.21. Additionally, Figure 6.21c illustrates the progression of expected fatality losses (in €) over time for different preparedness levels. The variation in expected fatalities across preparedness levels is attributed to the longer duration of recovery processes at moderate and low preparedness levels, i.e., leading to extended periods of higher congestion and, consequently, an increase in road accidents resulting in fatalities. For all three types of indirect impacts, there is a notable increase in the expected values after 50 years, which evidences the great relevance of accounting for long-term effects such as infrastructure deterioration when assessing the risks of transportation networks. Furthermore, it can be observed that the expected losses due to fatalities exceed those due to user costs, reflecting the

high societal value of a statistical life (SVSL). These two indirect losses considerably outweigh the direct economic losses incurred from bridge repairs. This highlights the critical importance of a rapid recovery, given the substantial indirect costs that arise from delays in restoration.

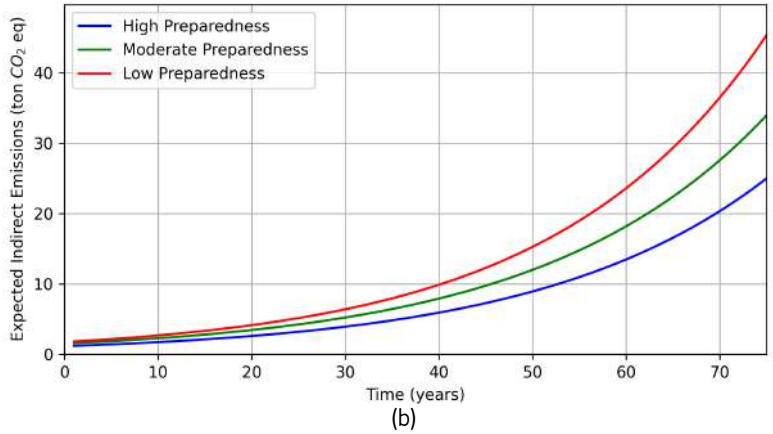
The cumulative distribution function (CDF) of the conditional robustness index for the three preparedness levels is depicted in Figure 6.22, computed for the economic losses (Figure 6.22a) and environmental losses (Figure 6.22a). It is observed that for both types of losses, the probability of a robustness index lower than x is larger for a low preparedness level than for a high preparedness level. This is expected as the low preparedness level involves the greatest indirect consequences. However, the robustness indexes are generally low for the three preparedness levels, given the large indirect losses associated with the traffic-related impacts.

The robustness indexes computed from the expected economic losses of individual bridge failure scenarios are used to define a bridge criticality within the transportation network. Four different criticality levels were defined, namely "Low", "Medium", "High" and "Very high". The thresholds for these classifications are as follows: bridge failures conducting to a robustness index I_R greater than 0.6 are deemed to have "Low" criticality, while those with an I_R between 0.3 and 0.6 are categorized as "Medium" criticality. Bridges with an I_R between 0.1 and 0.3 are classified as "High" criticality, and bridges with an I_R less than 0.1 are considered to have "Very high" criticality. Figure 6.23 displays the criticality level for each bridge in the transportation network based on the specified thresholds. From this figure, it is possible to identify the most critical bridges whose failure will result in large indirect consequences that outweigh the direct consequences, namely bridges 4, 5, 6, 13, and 14. In other words, the transportation system lacks robustness with respect to the failure of these bridges. Consequently, decision making strategies should be targeted to increase the robustness of the transportation network in relation to these identified critical failure scenarios.

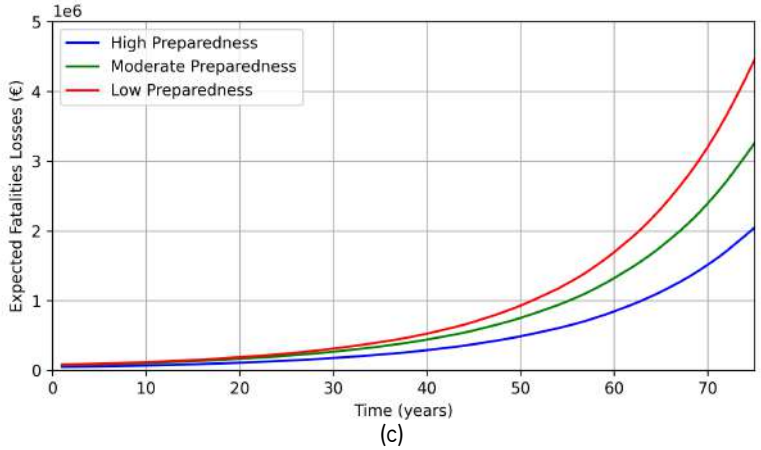
Additionally, the scenario-based approach facilitates the identification of specific failure scenarios, including the co-occurrence of bridge failures, that substantially contribute to the overall expected consequences (risks) and poor robustness performance. Figure 6.24a displays the critical failure scenarios associated with the expected economic losses exceeding the 99^{th} percentile, and Figure 6.24b shows the critical failure scenarios linked to expected environmental losses surpassing the 99^{th} percentile, both computed



(a)

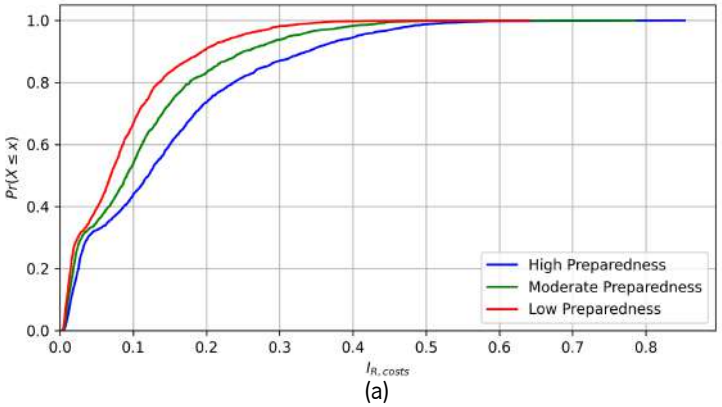


(b)

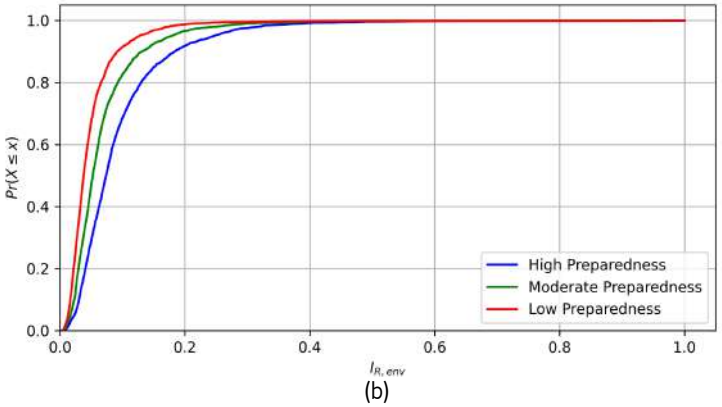


(c)

Figure 6.21: Time-variant expected value of indirect a) economic losses; b) environmental losses; and c) fatality losses



(a)



(b)

Figure 6.22: Cumulative distribution function (CDF) of the robustness index for the three preparedness levels a) economic losses and b) environmental losses.

at the time of 75 years. It can be seen that the individual failures of bridges 4, 5, 6, and 13, which were previously identified as lacking robustness, are also present in the scenarios resulting in the highest expected consequences. In addition to these individual failures, the co-occurrence of bridge failures such as [1,5], [6,12], as well as several combinations of bridge 13 with other bridges, e.g. [1,13], [2,13], [5,13], [12,13], are also critical in terms of large expected consequences and very poor robustness performance. These results indicate which bridge failures are the most critical and where mitigation strategies should be prioritized to reduce the expected value of losses. For instance, bridge 13, which appears in several failure scenarios, predominantly contributes to the transportation network's risk. This result is anticipated as the roadway link that will be disrupted in case of failure of bridge 13 corresponds to the highway that communicates the two largest cities in Portugal, Lisbon and Porto, with large traffic flows compared to the rest of the network as shown in Figure 6.10.

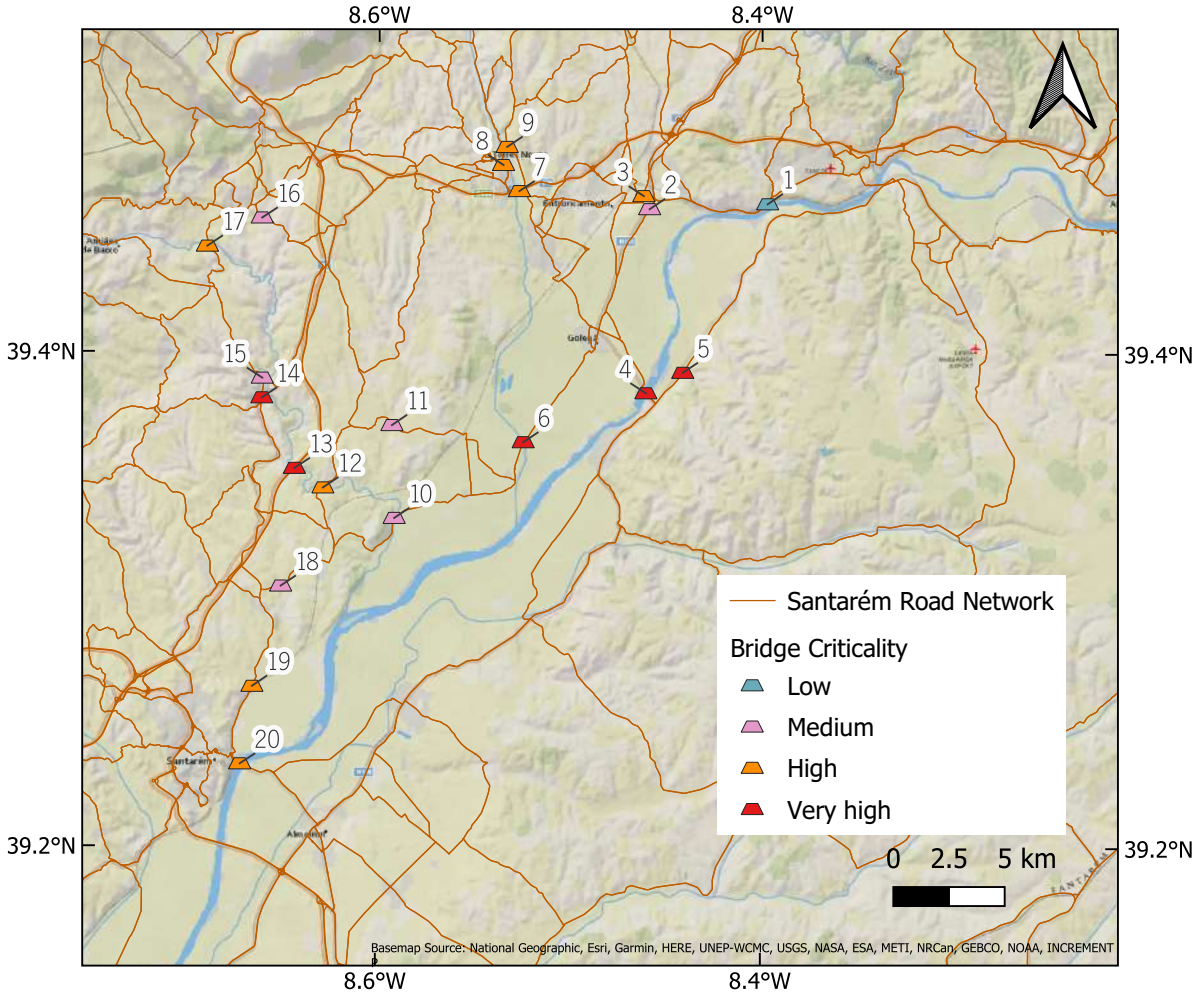
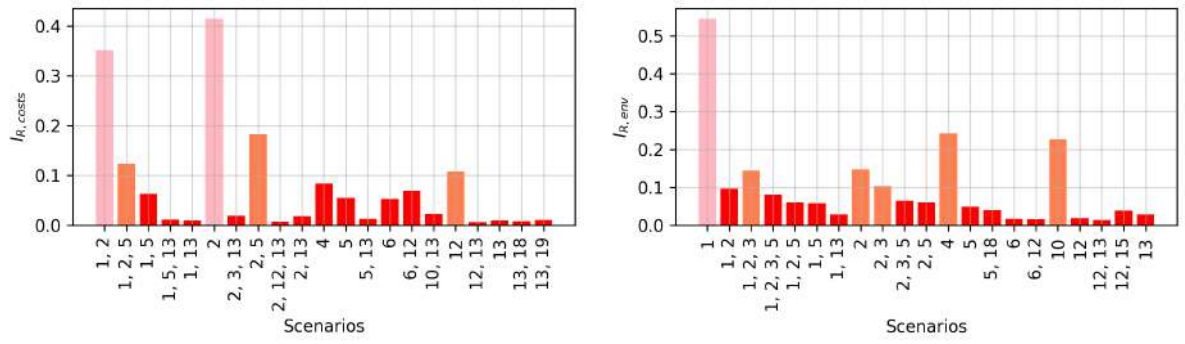


Figure 6.23: Bridge criticality in the roadway network based on the robustness index conditional on economic losses



(a) (b)

Figure 6.24: Critical damage failure scenarios exceeding the 99^{th} percentile of expected a) economic losses and b) environmental losses, computed at the time of 75 years.

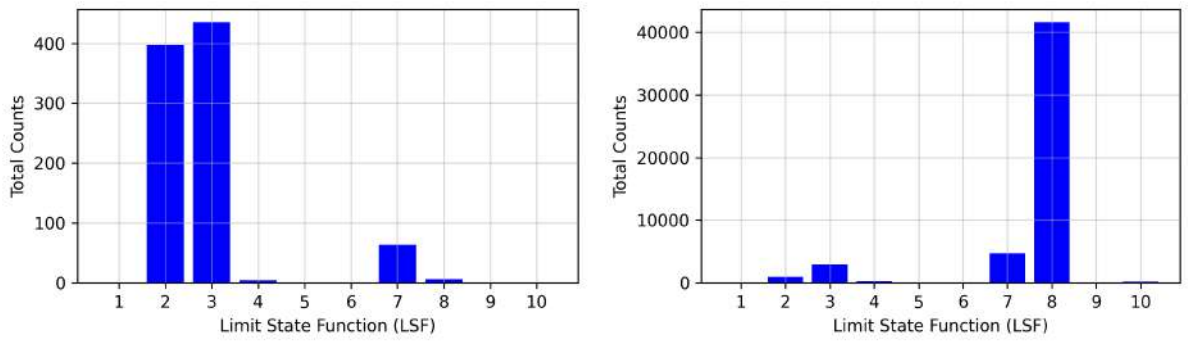


Figure 6.25: Predominant failure modes for critical failure scenarios computed at a) current year; and b) at the end of 75 years.

Finally, since the performance of bridges has been described by the limit state functions (LSF) as detailed in Chapter 5 (and summarized in Table C.1), it is possible to investigate which are the predominant failure modes for the identified critical damage failure scenarios. Figure 6.25 displays the frequency of occurrences where each LSF was less than zero, i.e., indicating failure. The results are presented for the critical failure scenarios exceeding the 99^{th} percentile of expected economic losses in the current year (Figure 6.25a), as well as the critical failure scenarios outlined in Figure 6.24a, corresponding to the time of 75 years (Figure 6.25b). It can be observed that for the current year, the predominant LSFs (LSF 2 and LSF 3) correspond to deck failure, while the predominant LSF at the end of 75 years (LSF 8) correspond to abutment failure. This notable distinction arises from the varying deterioration rates assigned to each failure mode. Specifically, the accumulated long-term scour degradation over 75 years, in the absence of any mitigation measures, has a more pronounced effect on bridge performance during flood-induced scour than deck resistance deterioration. This suggests long-term mitigation strategies should prioritize foundation protection, particularly if a significant annual scour degradation rate is confirmed. On the other hand, short-term mitigation plans might explore options to enhance resistance against deck overtopping or, alternatively, strategies for rapid deck replacement.

6.6 Conclusions

The assessment of probable consequences after natural hazards is crucial for making informed decisions about the prioritization of different risk-reduction interventions and for informing the recovery processes to restore functionality following a severe event rapidly. In this chapter, a methodology for identifying the optimal system recovery after infrastructure failures is proposed, aiming to minimize the indirect costs stemming from the transport functionality loss and their economic, health, and environmental consequences. The suggested methodology has been demonstrated in a real transportation network in Santarém, Portugal, which is exposed to flooding events. The proposed approach builds upon the scenario-based modeling framework recommended by the JCSS [38]. It employs the spatial probabilistic model developed in Chapter 3 to characterize the flood exposure at each bridge location, alongside the fragility models delineated in Chapter 5 to assess the performance of bridges during such hazards. To facilitate the estimation of indirect consequences arising from failure events, a neural network (NN) model is introduced to predict the outputs from the traffic model. It was found that the NN model efficiently predicted the traffic pattern changes under distinct bridge failure scenarios in the case study, using a reduced subset of damage network scenarios. This increased the computational efficiency to quantify the impacts of infrastructure failures and enhanced the application of the methodology for resilient transportation network recovery by facilitating the establishment of the optimal sequence of repairs that minimized the indirect costs. While these findings are specific and may not be directly applicable to other networks with different configurations and numbers of links considered for failure, they indicate the advantages of employing NN models for predicting traffic-related metrics under damage failure scenarios and thereby reducing the computational costs of evaluating every possible scenario, which has been a concern when quantifying the risks in complex transport infrastructures systems.

Moreover, the study delves into the effect of preparedness on the capacity of transport infrastructure systems to recover from disturbance events. Three levels of preparedness were considered in the case study application, represented by different idle times, restoration times, and number of available construction crews. The results demonstrated the considerable impact that system preparedness has on prolonging the duration of recovery and thereby increasing the accumulated user costs. Therefore, the proposed

methodology enables managers to evaluate their capacity for recovery post-disruption and support decisions to achieve the desired level of preparedness to enhance the transportation system resilience, e.g., decisions on emergency response plans, resources, crews available, and construction techniques, among others. Given that the primary objective of this study was to assess the impact of transportation system preparedness on the overall recovery process, the repair alternatives were predefined and dependent on the failure mode. Nonetheless, future work can extend the formulation of an optimal restoration program, including a detailed comparison of repair/reconstruction alternatives, aiming to minimize total costs by achieving a balance between faster recovery and lower direct costs.

Another outcome of this study is an improved understanding of which infrastructure failures, including the co-occurrence of bridge failures, substantially contribute to the overall expected consequences (risks) and poor robustness performance. To this end, the robustness index was used as a means for assessing the degree to which the transportation system can contain or limit the indirect consequences of hazards. Therefore, using this index for decision making ensures that the transportation system is designed and managed to possess an adequate level of robustness. Moreover, the scenario-based modeling framework enabled the identification of bridge failures that were driving the risks, together with the identification of the most relevant failure modes. These insights are crucial for strategic planning and investment in risk mitigation measures, as these can be prioritized per bridge and with regard to the governing failure modes, thereby effectively reducing the expected value of losses in the transportation system.

Finally, the quantification of time-variant risks accounting for long-term effects such as infrastructure deterioration highlighted the relevance of a life cycle perspective to support risk-informed decision making. Essentially, a significant increase in the risks was observed after 50 years, which evidences the need to perform timely maintenance activities to mitigate the effect of infrastructure deterioration, which significantly reduces structural performance. Consequently, the scheduling of the mitigation measures to be performed in future years should account for the evolving infrastructure performance. Future research can address additional time-dependent considerations in the quantification of life cycle risks, including long-term changes in consequence modeling, such as population changes, which would modify the traffic demands on the transportation network, and changes in the vehicle fleet due to the increase of electric vehicles, which would decrease the environmental consequences.

Chapter 7

Risk- and Resilience-informed decision making for Transport Infrastructure Systems

Abstract: Transport infrastructure systems play a pivotal role in economic development and welfare by facilitating access to markets, jobs, and social services. Consequently, when analyzing these systems, it is crucial to recognize that they do not exist in isolation but are interconnected with numerous other systems. In this chapter, transportation networks are modeled as interlinked systems comprised of a social system, infrastructure system, and geo-hazard system, all managed by governance and regulatory systems. The life cycle performance of each system and their dependencies are represented probabilistically. The scenario-based modeling approach from Chapter 6 to compute the expected value of losses is extended to account for the benefits of the interlinked system to the economy. This approach allows for comparing the economic benefits from different decision alternatives, including decisions on the level of safety for infrastructures, operational decisions of maintenance and repair activities, and the percentage of benefits saved for reconstruction and recovery after failures. Moreover, the framework allows the comparison of decision alternatives that may offer the same economic benefits but result in different environmental emissions and consequences to health. Finally, following the proposed formulation, it is also possible to quantify the probability of resilience failure, defined as the exhaustion of the transportation system's

capacity for re-establishing functionality within a life cycle framework. Therefore, the potential of each decision strategy for increasing the system's resilience can be analyzed.

7.1 Introduction

Transport infrastructure systems (TIS) are the backbone of modern societies, enabling the movement of people and goods, driving economic growth, and ensuring the well-being of communities. However, these systems are continually confronted by both natural and anthropogenic hazards, leading to significant interruptions that incur extensive socio-economic and environmental costs. This increasing awareness of vulnerabilities has highlighted the importance of enhancing TIS resilience. While the concept of resilience varies among disciplines, the definition provided by The National Academy of Science (NAS) [270] is widely accepted for infrastructure systems. This definition characterizes disaster resilience as the ability of a system "to prepare and plan for, absorb, recover from, or more successfully adapt to actual or potential adverse events". Several methodologies for resilience assessment of TIS have been proposed in the literature, ranging from qualitative and semi-qualitative to fully quantitative methods, using a wide variety of resilience indicators and metrics which are typically selected depending on the perspective, objective and scale of the analysis (see, e.g., [59–63] for an overview). In general, the resilience of TIS has been quantified using the system recovery curve, also known as the resilience curve, depicted in Figure 7.1. Based on this curve, resilience is characterized by the reduction in the system functionality after a disturbance event, which relates to the robustness of the system, and the particular shape of the recovery curve is related to system characteristics such as preparedness and adaptive capacity, which determine the time to fully recover the functionality and the rapidity of recovery. Resilience loss is then assessed by the difference between the functionality provided in the absence of a disturbance event and the functionality provided if a disturbance event occurs. Following this approach, the definition of a metric to adequately describe the system functionality (or level of service) is of crucial relevance when modeling and assessing the resilience of TIS. Several metrics have been proposed, such as connectivity, centrality, throughput, and travel time, among others. If the network functionality is defined in terms of accessibility, it may contribute to identifying the loss of access to critical facilities. If it is defined in terms of total travel time, it may facilitate the quantification of monetary losses of users due to trip delays and rerouting costs,

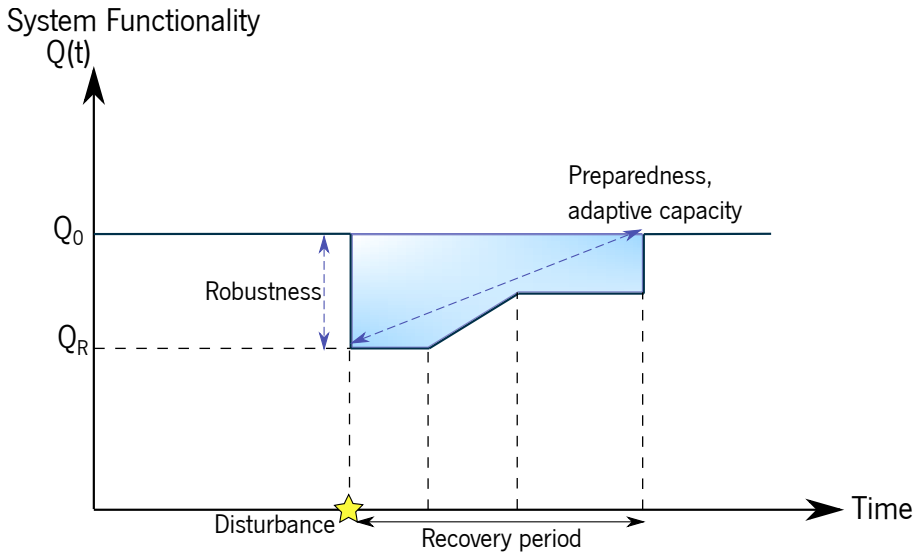


Figure 7.1: Illustration of principal model for resilience assessment

amongst others. Most studies select the most suitable functionality metric according to their main goal and quantify resilience based on the loss of that metric after a disturbance event until the system is fully recovered. However, the choice of the functionality metric significantly influences the measured resilience when following this approach (see [271]). Then, if multiple functionality metrics are defined, comparing and selecting the most optimal decision alternatives to increase resilience becomes challenging, as their impact is reflected differently on each chosen functionality metric.

Faber et al. [18] proposed a life cycle model of systems resilience, which provides a comprehensive approach to decision making. On the one hand, it incorporates a long-term perspective where all possible disturbance events during the service life of the infrastructure system are considered instead of focusing on particular disturbance scenarios, which has been a common approach when assessing the resilience of transportation systems. In addition, it highlights that resilience assessments should address the generation of system capacity for recovery beyond merely evaluating the loss of functionality [9]. This aspect is crucial for effective and prompt reorganization, adaptation, and recovery from disruptions. Fundamentally, socio-technical systems like transportation networks generate a benefit over time that contributes to socioeconomic growth, and some of these benefits should be allocated as reserves. The gradual accumulation of these reserves builds the capacity of the system to address disturbances. This explicit modeling of the system capacity facilitates the comparison of decision alternatives. This is because resilience can be formulated as a capacity-demand problem, where the demand can exceed the available capacity of

the system, similar to a structural reliability problem. Therefore, decisions can be guided to reduce the probability of resilience failure, defined as the event where a disturbance leads to a capacity loss of the system beyond its accumulated reserves [18]. The system capacity may encompass economic, social, and/or environmental capacity, as resilience modeling suggests a broad context in which infrastructure systems do not operate in isolation but are interlinked with other systems. This broader perspective further supports the connection of resilience with sustainability (refer to [3]).

This chapter introduces a probabilistic decision-making framework for enhancing the resilience of transport infrastructure systems. The framework builds upon the life cycle model of systems resilience from Faber et al. [18] and extends its application to the context of TIS. It specifically formulates the probability of resilience failure as the economic exhaustion of the transportation network's capacity to restore functionality. The proposed framework facilitates the comparison of different decision alternatives, including decisions on the level of safety for infrastructures, decisions on the investment into maintenance, and decisions on the percentage of benefit to be accumulated to address recovery after disturbance events. The framework ultimately supports comparing the potential of decision alternatives to increase the resilience of TIS, measured as the reduction in the probability of resilience failure. The application of the framework is illustrated in the Santarém case study. The findings demonstrate how the decision-making framework can be operationalized to support infrastructure managers and policymakers in making informed choices that align with resilience objectives.

7.2 System representation of TIS for assessing resilience

When analyzing infrastructure systems, it is crucial to understand that they do not exist in isolation but are deeply interconnected with various other systems. Therefore, when assessing resilience, the system representation from Figure 6.1 should be extended. Faber et al. [18] introduced a decision analysis framework for infrastructure systems modeled as interlinked systems, where the system representation included the infrastructure system itself, the geo-hazards or anthropological hazards system, the management system, which consists of the governance and regulatory systems, the Earth life-support system, and the social system, as depicted in Figure 7.2.

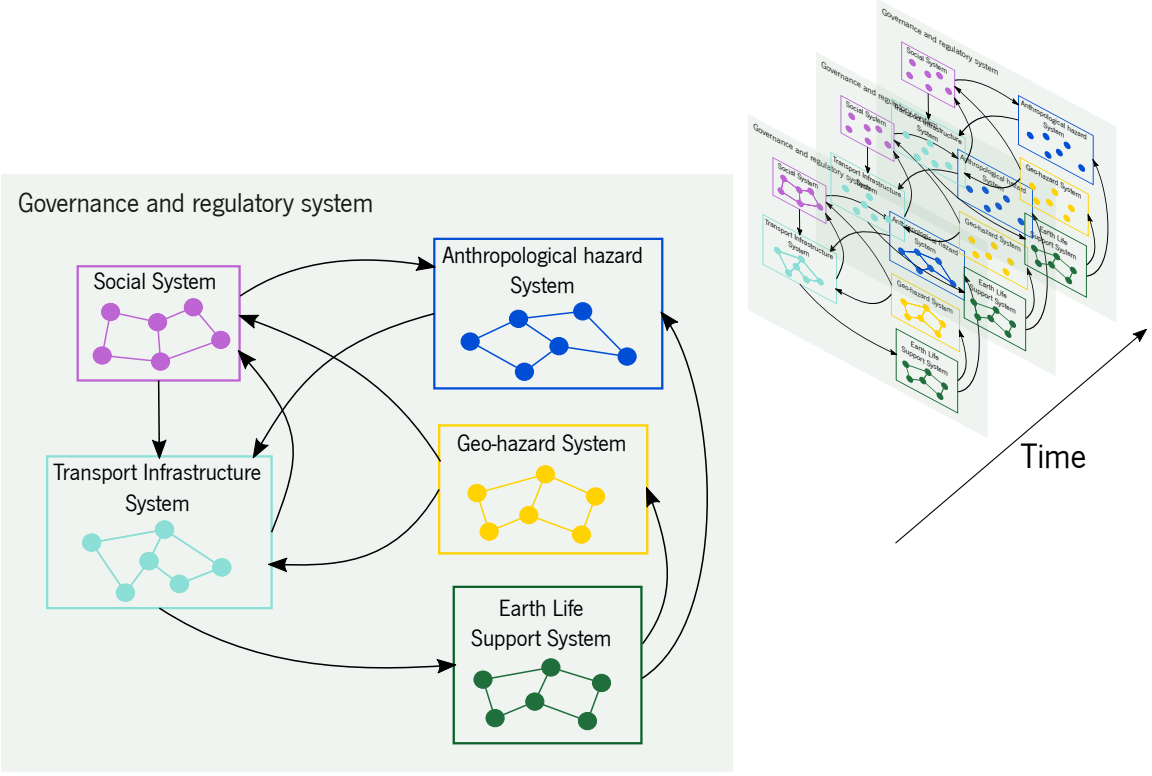


Figure 7.2: Illustration of interlinked systems for assessing resilience. Adapted from [9]

The regulatory system is assumed to manage the performance of the infrastructure system, representing the governance system concerning operational hazards and the geo-hazard system [18]. Typically, decision-makers and stakeholders are organized hierarchically at local, national, and global levels and are connected by governance structures. In the context of TIS, decision-makers at the local level (municipality or community level) are private or public asset infrastructure owners, managers, or operators in charge of operational decisions of maintenance and repair activities at the asset level in short- to mid-term as well as strategical decisions for the management of individual local projects at long-term. At the regional/state level, network managers are in charge of the entire transportation network or all infrastructure assets in a large geographical area. At the national to the global level, the governance system manages all previous levels based on its objectives, which include but are not limited to maximizing benefits, minimizing economic losses, satisfying population demands, maximizing the welfare of people, and minimizing environmental damage at local and global levels. The extent to which an objective is accomplished can be measured by attributes or criteria, e.g., safety, monetary cost, minimum level of service, life quality,

and environmental emissions, among others. The governance system ensures the achievement of its objectives by means of regulations. In other words, decision alternatives considered for the purpose of managing the system must comply with the boundary conditions and/or constraints imposed through codes, standards, and trans/national or global scale regulations [18]. For instance, in the National Annexes of the European civil engineering technical standards (Eurocodes), individual nations specify their National Determined Parameters (NDPs) and decide on the level of safety for the design of new structures and assessment of existing ones.

On the other hand, the development and management of infrastructure systems significantly impact Earth's life-support systems, affecting the boundary conditions essential for human existence. These interactions and impacts occur at multiple scales—ranging from local to global. For instance, at the local level, incidents such as toxic events can have dire consequences on community livelihoods. On a global scale, factors like CO_2 emissions from infrastructure systems have the potential to alter climate conditions.

Finally, the temporal dynamics of this interlinked system are captured through time-slicing. In other words, the state of the transportation system can be modeled, e.g., annually. Therefore, its condition at a specific time (e.g., one year) is influenced by its past performance.

7.2.1 Resilience modeling and quantification

Following the decision analytical framework proposed by [18], systems resilience models and assessments should concern not only the loss of functionality and recovery but also the generation of the system recovery capacity, which is critical for successfully and rapidly reorganizing, adapting, and recovering from disturbance events. Essentially, socio-technical systems such as transportation networks generate a benefit over time that favors economic growth. A percentage of that benefit should be collected as an economic reserve to respond to disturbances. Thus, the economic capacity with respect to resilience R_r of transport infrastructure systems may be described as the accumulation of the reserves over time [272]:

$$R_r(\boldsymbol{X}, \boldsymbol{a}, \chi, t) = R_r^0 + \int_0^t \frac{\chi\, b(\boldsymbol{X}, \boldsymbol{a}, \tau)}{(1 + r_\gamma)^\tau}\, d\tau \tag{7.1}$$

where R_{r}^{0} represents the starting capital reserve, which may be assumed to correspond to some percentage of the expected value of total benefits generated during the service life of the road infrastructure system, χ represents the percentage of benefit savings, $b(\boldsymbol{X}, \boldsymbol{a}, \tau)$ corresponds to the benefit generation over time, and r_{γ} is the discount rate. Benefits from TIS are generated from the service provision of mobility for people and goods in the form of taxes or toll roads. In some cases, infrastructure assets such as historic bridges provide cultural and economic services related to tourism (refer to [77]). Moreover, transport infrastructure assets can assume other functionalities that provide economic benefits, such as carrying power and telecommunication lines, oil and gas pipelines, or water pipelines. The quantification of benefits can be based on considerations of the relationship between choices of quantity and quality of transport infrastructures and their effect on societal economic growth. For instance, Nishijima and Faber [273] established this relationship through production functions from macroeconomics to identify the optimal investments into infrastructure subject to natural hazards, which ensure sustainable societal development.

Figure 7.3 illustrates a realization of benefit generation and the accumulated economic capacity. For simplicity, the evolution of benefit generation is assumed to be constant over time when the transportation network is fully functional. When the occurrence of a disturbance event at time τ results in damage or failure of infrastructure constituents in the network, both the benefit generation and the economic capacity of the transportation system will be reduced. The economic demand S_{r} caused by a disturbance event at time t may be expressed as ([272]):

$$S_{\mathrm{r}}(\boldsymbol{X}, \boldsymbol{a}, t) = \sum_{\tau \in \{\mathrm{t_F} \cap (0,t)\}} \frac{C(\boldsymbol{X}, \boldsymbol{a}, \tau)}{(1 + r_{\gamma})^{\tau}} \tag{7.2}$$

where $C(\boldsymbol{X}, \boldsymbol{a}, \tau)$ represents the costs for recovery after the failure event; $\mathrm{t_F}$ corresponds to the time domain when disturbance events happened within the service life of the infrastructure system $(0,t)$. If, at some point in time, the economic capacity is insufficient for re-establishing the functionality of the transportation system, i.e., reserves are exhausted, this can be defined as a resilience failure event (dashed line from Figure 7.3). Thus, the probability of resilience failure P_{RF} may be defined and assessed probabilistically as [9]:

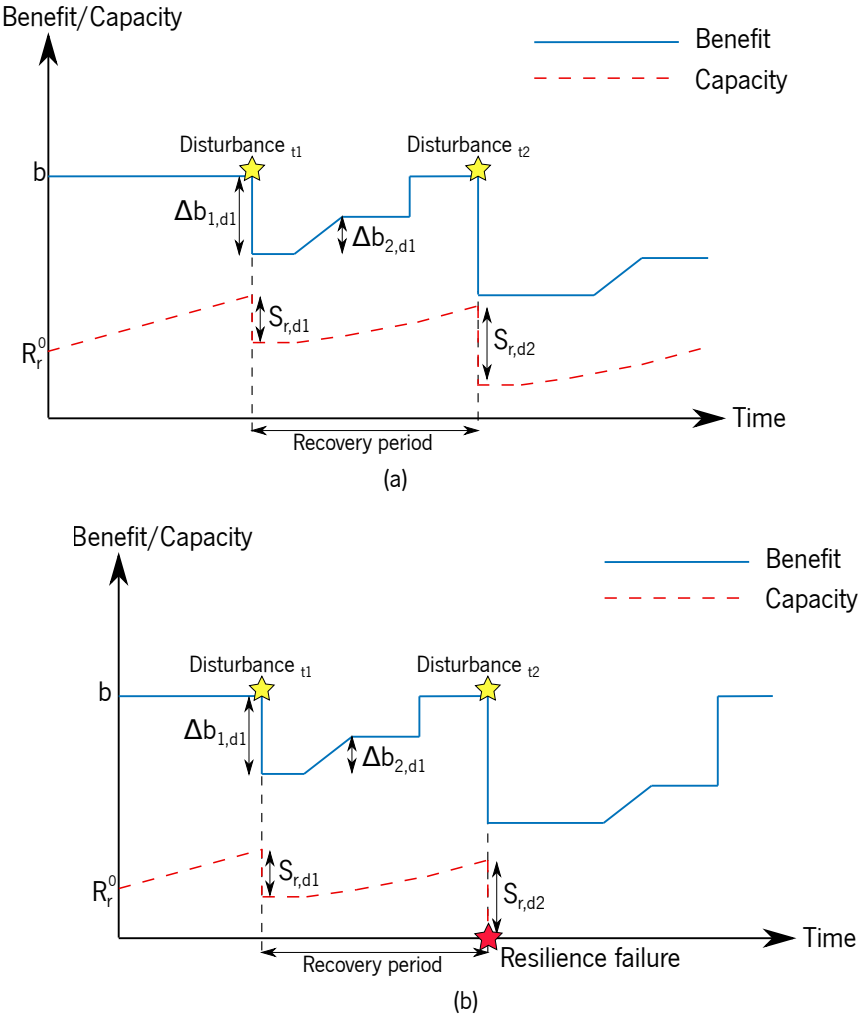


Figure 7.3: Resilience model in terms of benefit generation and economic capacity (a) Scenario with no resilience failure (b) Scenario with resilience failure

$$P_{\text{RF}}(\boldsymbol{a}, \chi, t) = 1 - P[\ \{R_{\text{r}}(\boldsymbol{X}(\tau), \boldsymbol{a}, \chi) - S_{\text{r}}(\boldsymbol{X}(\tau), \boldsymbol{a})\} > 0, \forall\ \tau \in [0, t]\ ] \tag{7.3}$$

The formulation of Eqs. 7.1-7.2 have focused on the exhaustion of the economic capacity. Nonetheless, as previously stated, the system capacity in the context of resilience modeling may encompass social and environmental capacity as well. The social capacity in the context of TIS encompasses the ability of the governance system (comprised of infrastructure owners/operators, local and national public authorities) to deal with hazardous events in terms of reorganization, restructuring, and adaptive learning in and

after an event. This social capacity can be represented through the concept of Life Quality Index (LQI) [18]. Moreover, the environmental capacity may relate to, e.g., emissions of CO_2 exhausting the Earth's capacity [274] or the availability of natural resources for the development and maintenance of TIS, such as raw materials, space, and water. The exhaustion of the environmental capacity may occur due to both large resource consumption and environmental impacts associated with construction, operation and maintenance, and failure of TIS. Therefore, the formulation of resilience with regard to the environmental capacity considering the global scale, i.e., the Earth system, is equivalent to sustainability [3, 18]. The formulation of resilience failure due to the exhaustion of the social and environmental capacity of TIS is beyond the scope of this thesis. However, social and environmental considerations are integrated into the decision support framework proposed in the next section.

7.3 Decision support framework for interlinked TIS

Building upon the interlinked system representation from Section 7.2, a decision-making methodology for transport infrastructure systems (TIS) is outlined in Figure 7.4. The proposed framework focuses on the interconnections between various systems and plausible decisions to enhance resilience in the face of geo-hazard events. Fundamentally, TIS are influenced by the geo-hazard or threats system, which may encompass operational and natural hazards. These hazards can lead to infrastructure failures, resulting in traffic-related consequences, such as increased travel times and accidents, and necessitating reconstruction and recovery efforts. The consequences of these failures extend to environmental impacts, such as increased emissions, as well as health-related impacts, including injuries and fatalities due to accidents. The management system establishes decisions regarding the reliability level of infrastructures, investments in maintenance, and the allocation of funds for benefit savings. These decisions affect the system's economic capacity, which is a function of the benefits generated from the operation of TIS, the savings allocated for reconstruction and recovery, and the operational costs of infrastructure maintenance. On the other hand, the social system's functionality heavily depends on the development of the economy, e.g., measured through the Gross Domestic Product (GDP), which influences the system's preparedness to recover from disturbances over time. At the same time, it influences the economic capacity as building preparedness requires saving some benefits as reserves to cope with disturbance

events. Finally, the decision criteria measure the extent to which objectives are achieved across different domains, such as environmental, health, and economic factors. These are quantified through expected net benefits, emissions from reconstruction and maintenance, emissions due to rerouting, fatalities due to accidents from rerouting, and the annual probability of resilience failure, allowing for a multi-criteria assessment of the system's performance under the different decision scenarios. The framework can be extended by incorporating utility theory, transforming these attributes into a single utility metric, enabling a consistent reflection of decision-maker preferences, and facilitating the assessment of the optimality of various decision alternatives (e.g., [275, 276]).

7.4 Santarém Case Study

The proposed decision support framework for transport infrastructure systems is applied to the Santarém case study. To this end, the bridge network described in Section 6.4 is examined in this chapter from an interlinked systems perspective. As such, the case study is modeled as the interaction between the geo-hazard system, the transport infrastructure system, the management system, and the social system. It should be noted that some modifications to the original case study were made, as the proposed approach is illustrative, and some specific parameters for its application to the real case study are unavailable.

7.4.1 System representation of roadway networks for decision support

7.4.1.1 Management system

The management system in the context of the Santarém roadway network is comprised of transport infrastructure managers, who are concerned about managing the system efficiently by ensuring reliable transportation service for people and goods on the basis of their available resources. The management system is constrained by the governance system through regulations imposed in national codes and standards. These regulations set the requirements to ensure infrastructure safety during their service life. In addition, the governance system can evaluate decisions concerning preparedness to cope with

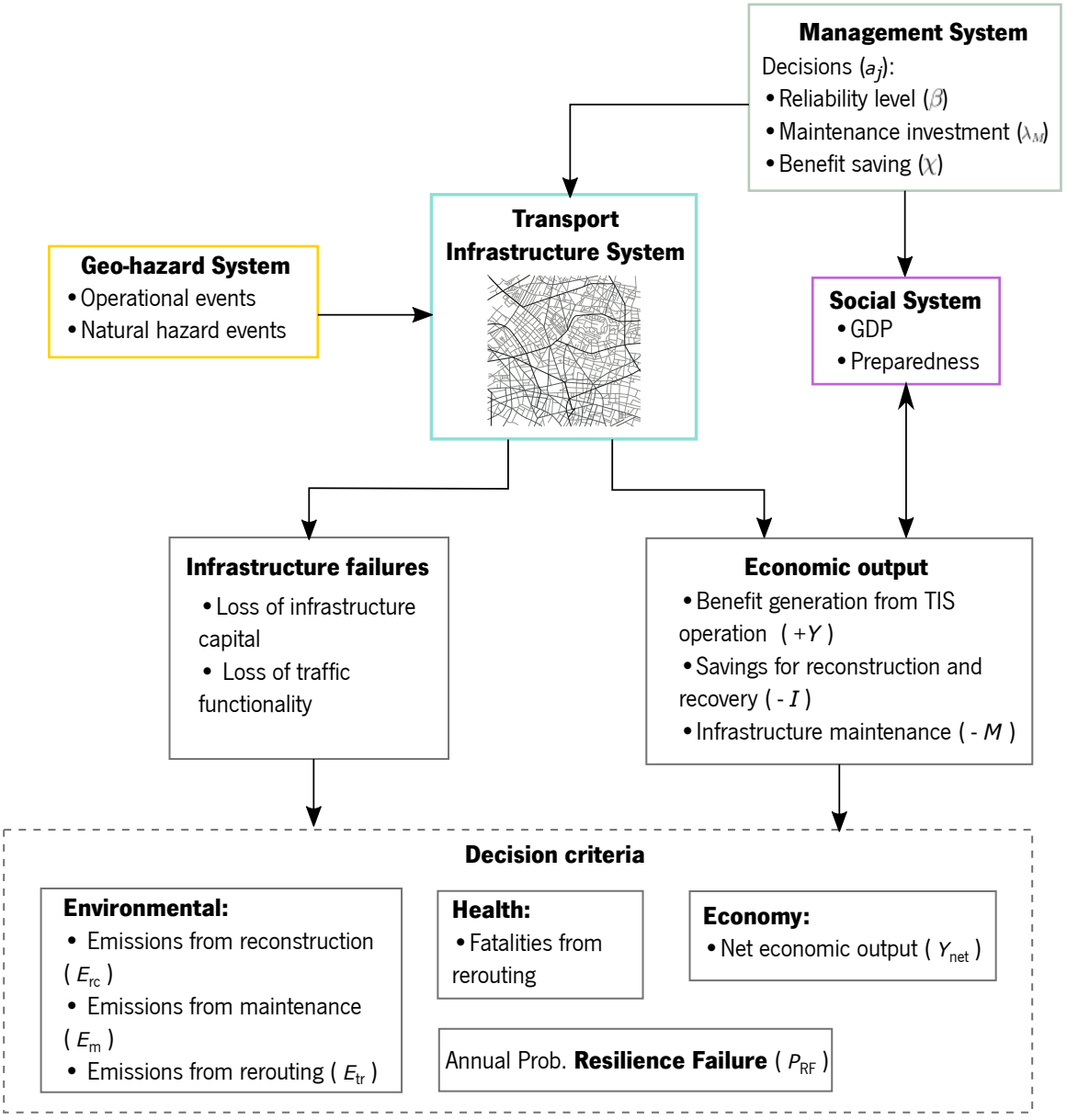


Figure 7.4: Decision support framework for interlinked Transport Infrastructure Systems

disaster events. Therefore, the following three types of decision alternatives are considered for the purpose of managing the system:

$$\boldsymbol{a_j} = \{\boldsymbol{a_1}, \boldsymbol{a_2}, \boldsymbol{a_3}\} \tag{7.4}$$

where,

- $\boldsymbol{a_1}$ = $\{\beta_{\mathsf{l}}, \beta_{\mathsf{m}}, \beta_{\mathsf{h}}\}$ represents the decisions on the target annual reliability level of bridges;
- $\boldsymbol{a_2}$ = $\{\chi_{\mathsf{l}}, \chi_{\mathsf{m}}, \chi_{\mathsf{h}}\}$ represents the decisions on the percentage of benefits saved for reconstruction and recovery after failure;
- $\boldsymbol{a_3}$ = $\{\lambda_{\mathsf{l}}, \lambda_{\mathsf{m}}, \lambda_{\mathsf{h}}\}$ represents the decisions on the maintenance investment ratio into infrastructures;

For each of these decisions, three levels are considered, namely low (l), medium (m), and high (h). The values assumed for each level of the decision alternatives vectors are defined as:

- $\boldsymbol{a_1}$ = $\{3.7(P_{\mathsf{f}} \approx 10e^{-4}), 4.2(P_{\mathsf{f}} \approx 10e^{-5}), 4.7(P_{\mathsf{f}} \approx 10e^{-6}\})$ to evaluate the effect of low, medium, and high levels of target annual reliability, β;
- $\boldsymbol{a_2}$ = $\{0.02, 0.04, 0.06\}$ to evaluate the effect of low, medium, and high levels of percentage of benefits saved for reconstruction and recovery after failure, χ;
- $\boldsymbol{a_3}$ = $\{0.02, 0.05, 0.1\}$ to evaluate the effect of low, medium, and high levels of maintenance investment ratio into infrastructures, λ_M;

These decision alternatives are combined into 27 unique decision scenarios, summarized in Table 7.1, to evaluate the influence of each management alternative on the decision criteria from Figure 7.4.

Table 7.1: Decision scenarios with predefined levels (low (l), medium (m), and high (h))

Decision Scenario (a_j)	**Target Design Reliability (β)**	**Benefits Savings Ratio (χ)**	**Maintenance Investment Ratio (λ_M)**
a_1	β_l	χ_l	λ_l
a_2	β_l	χ_l	λ_m
a_3	β_l	χ_l	λ_h
a_4	β_l	χ_m	λ_l
a_5	β_l	χ_m	λ_m
a_6	β_l	χ_m	λ_h
a_7	β_l	χ_h	λ_l
a_8	β_l	χ_h	λ_m
a_9	β_l	χ_h	λ_h
a_{10}	β_m	χ_l	λ_l
a_{11}	β_m	χ_l	λ_m
a_{12}	β_m	χ_l	λ_h
a_{13}	β_m	χ_m	λ_l
a_{14}	β_m	χ_m	λ_m
a_{15}	β_m	χ_m	λ_h
a_{16}	β_m	χ_h	λ_l
a_{17}	β_m	χ_h	λ_m
a_{18}	β_m	χ_h	λ_h
a_{19}	β_h	χ_l	λ_l
a_{20}	β_h	χ_l	λ_m
a_{21}	β_h	χ_l	λ_h
a_{22}	β_h	χ_m	λ_l
a_{23}	β_h	χ_m	λ_m
a_{24}	β_h	χ_m	λ_h
a_{25}	β_h	χ_h	λ_l
a_{26}	β_h	χ_h	λ_m
a_{27}	β_h	χ_h	λ_h

7.4.1.2 Infrastructure system

The infrastructure system consists of the transportation network of the Santarém region, which has been extensively detailed in Chapter 6. Nonetheless, the bridges in the network have distinct annual failure probabilities as well as different deterioration patterns, as evidenced in Figure 6.9. Thus, to facilitate the evaluation of the type of decision alternatives considered for managing the system, the following time-dependent limit state function is assumed to represent the failure of all bridges in the transportation network with respect to the geo-hazard disturbance, i.e., the flooding event:

$$g_i(t) = z\ R_{0,i}\ (1 - D(t))\ X_r - S_i\ X_s \tag{7.5}$$

where $R_{0,i}$ is the initial resistance of bridge $i = 1, .., 20$ with respect to the flood event intensity, z is the safety design parameter, S_i is the flood load intensity at bridge i, X_r and X_s are the model uncertainties in the resistance and demand, respectively, and $D(t)$ is a resistance deterioration function which increases with time. The incorporation of the safety design parameter z facilitates the calibration of the failure probabilities for the three decision alternatives' levels. Table 7.2 provides a summary of the distribution of the random variables considered for evaluating the limit state function of Eq. 7.5.

Regarding the deterioration process influencing the overall bridge resistance over time, a deterioration function is adopted in the following form:

$$D(t) = D(t-1) + \Delta_{D,t}, \quad \text{for } t \geq T_0, \tag{7.6}$$

where $\Delta_{D,t}$ represents the annual deterioration increment at year t, which accumulates over the service life, and $D(t-1)$ represents the accumulated deterioration up to year $t-1$. The deterioration process begins at time $t \geq T_0$. To illustrate the influence of decisions on maintenance investments, three levels of deterioration are assumed: low, medium, and high. Essentially, a high level of maintenance investment will lead to a low deterioration rate due to effective maintenance practices. Conversely, a low level of maintenance investment will lead to a high deterioration rate due to poor maintenance practices.

The mean values and standard deviation of $\Delta_{D,t}$ and deterioration initiation times T_0 for the three deterioration levels are adopted according to values for reinforced concrete bridges subjected to corrosion [277, 278]. The summary of the distribution parameters for the different $\Delta_{D,t}$ levels is given in Table 7.2. Following [277], the expected value of the deterioration initiation time when experiencing low deterioration is assumed to begin after 10 years, for cases of medium deterioration after 5 years, and for high deterioration conditions, starts as early as 2.5 years.

Lastly, the structural capacity of the portfolio of bridges exhibits some correlation influenced by various factors, including structural type, construction period, and design standards ([79, 240]). Thus, it is

assumed that the correlation coefficient between the structural capacities of bridges is ρ_R = 0.5 for the same bridge type (defined in Chapter 5) and ρ_R = 0.3 for the remaining cases.

Table 7.2: Distribution parameters for the Limit State Function

Variable	Distribution	Mean	Standard deviation
R_0	Lognormal	1	0.1
X_r	Lognormal	1	0.1
X_s	Lognormal	1	0.1
$\Delta_{Dl,t}$	Lognormal	0.001	0.001
$\Delta_{Dm,t}$	Lognormal	0.0025	0.001
$\Delta_{Dh,t}$	Lognormal	0.005	0.001

7.4.1.3 Geo-hazard system

Similarly to Chapter 6, the realization of geo-hazard disturbance events over time, i.e., flood events, is achieved using the Bayesian Network (BN) developed in Chapter 3. However, to conform with the limit state function of Eq. 7.5, the flood load intensity variables at each bridge location are normalized such that the mean value is one. Figure 7.5 presents the histograms of the flood load intensity S_i for bridges 1 to 6 (refer to Appendix C for identification).

7.4.1.4 Social system

The social system in the context of managing roadway networks is assumed to be represented by the system's capacity to respond to infrastructure failures caused by the geo-hazard system, including the ability to reorganize, adapt, and recover efficiently. This capacity is strongly linked to the development of the economy and its societal welfare (as depicted in Figure 7.4). Therefore, it is assumed that the decision on the percentage of benefits saved for reconstruction and recovery (χ) determines the level of social preparedness of the transportation system to deal with disturbances. For instance, a high percentage of benefit savings would involve a transportation system that is building a high preparedness to react rapidly to disturbance events, to plan efficiently the restoration activities (short idle time), and has sufficient resources to commission several construction crews to undertake the restoration activities, as described thoroughly in Chapter 6. Therefore, the three preparedness levels for recovery detailed in Section 6.4.4,

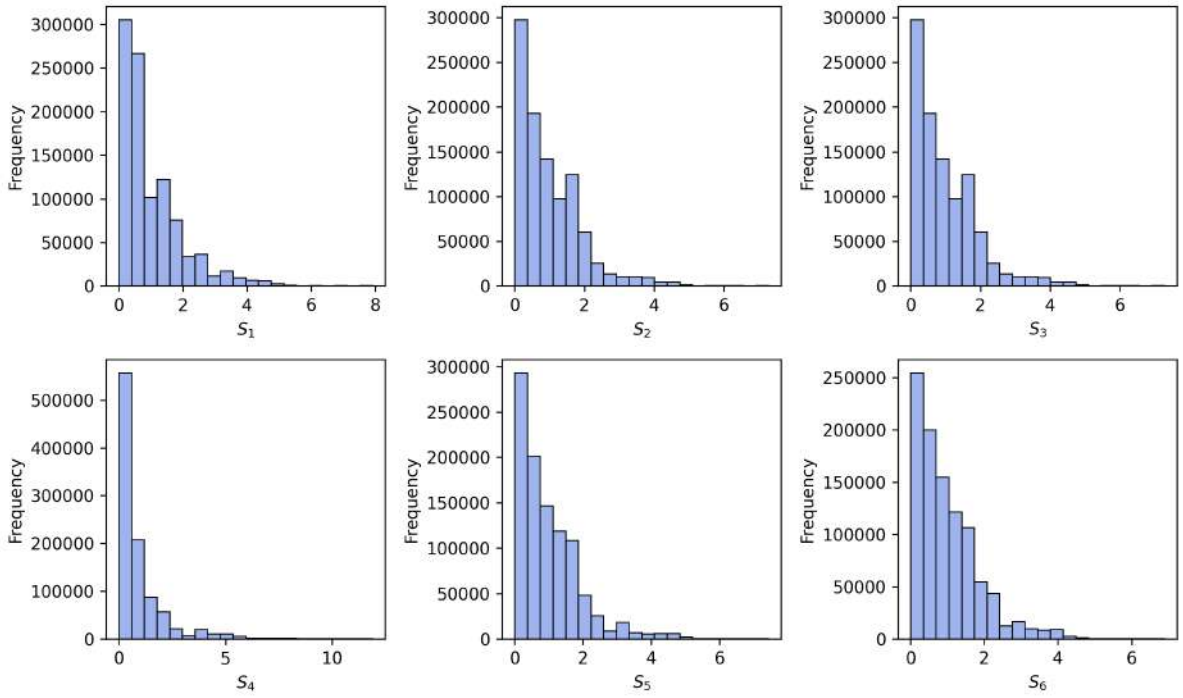


Figure 7.5: Flood load intensity S_i at the first six bridges

namely low, moderate, and high preparedness, are considered to characterize the transportation system recovery for decisions of low (χ_l), medium (χ_m), and high (χ_h) levels of percentage of benefits, respectively, using the factors and parameters specified in Table 6.4. Considering that the performance of the bridges in the transportation network is described by the limit state function from Eq. 7.5, the failure does not refer to a specific failure mode as specified in Chapter 6 but to complete bridge failure. Thus, the restoration tasks are assumed to correspond to the pier-foundation system and adjacent deck span reconstruction, with a duration adopted from Table 6.1.

7.4.2 Economic Model

Given that the system under analysis is a transportation network with certain societal functionality, it can be assumed that its impact on the national economic development can be represented from a macroeconomic perspective. Under this view, the impact of infrastructure is commonly depicted through production functions, i.e., functions to relate the level of economic output given the amounts of different types of capital, e.g., human capital, physical capital, among others [273]:

$$Y = f(K^{(1)}, K^{(2)}, \ldots) \tag{7.7}$$

where Y denotes the economic output for a specific period, $K^{(i)}$ (where $i = 1, 2, \ldots$) represents the quantities of various kinds of capitals. The degree of capital differentiation depends on the depth of analysis and data availability. For example, $K^{(n)}$ could embody the cumulative capital related to diverse forms of infrastructure or represent one specific type of infrastructure. Additionally, it is feasible that $K^{(m)}$ denotes the quantity of capital differentiated by its significance but still pertaining to the same class of infrastructure; for instance, road networks linking major cities as opposed to road networks in isolated regions [273]. A production function may be approximated through the utilization of historical data via time-series analysis and/or cross-sectional investigations. In these estimations, capitals are quantified either in physical units, e.g., kilowatts of electrical generation capacity, length of road, or in monetary terms by converting the physical measurements using corresponding prices [273].

Following [273], a single type of capital affecting economic production, i.e., infrastructures, can be considered to evaluate the effect of design and management decisions on societal economic growth. Therefore, the economic model used for the Santarém case study assumes that roadway infrastructure is the only capital that affects the economic production in society, and the production function from Eq. 7.7 can be formulated as [273]:

$$Y = A\, K^{\alpha_c} \tag{7.8}$$

where the infrastructure capital K is measured in physical terms, A is a coefficient that represents societal technology, and α_c indicates the marginal increase in economic output relative to the infrastructure capital [273]. In this study, the A coefficient is assumed as 10, and the α_c value is set at 0.2. It should be noted that this economic model is idealized, and other models can be formulated to relate the benefits of roadway infrastructure to society's functionality.

The initial infrastructure capital denoted as K_0 is a function of the reliability level of bridges and can be described as [279]:

$$K_0(z) = K_{\text{base}} \frac{f}{z} \tag{7.9}$$

where f is a factor used to capture the links between the quality of infrastructure, denoted by the safety design parameter z, and its construction cost and CO_2 emission impacts, and K_{base} denotes the initial amount of capital when $z = f$, which corresponds to the total number of bridges, i.e., 20. In this study, f is calibrated so that $f = z$ when $P_{\text{f}}(z) = 10^{-4}$.

The amount of infrastructure capital evolves over time due to new construction, occurrences of infrastructure failures, and reconstruction, which are influenced by the decision alternatives. Therefore, the capital $K(t)$ represents the quantity of infrastructure at a specific point in time. For a specific time interval $[t, t + \Delta t]$, the increase in infrastructure capital $\Delta K(t)$ can be formulated as [273]:

$$\Delta K(t, \boldsymbol{a}) = K_c(t, \boldsymbol{a}) - K_f(t, \boldsymbol{a}) \tag{7.10}$$

where $\boldsymbol{a}$ is a vector that encompasses all decisions related to the quality and quantity of infrastructures, $K_c(t, \boldsymbol{a})$ represents the amount of newly constructed infrastructure capital, and $K_f(t, \boldsymbol{a})$ is the amount of failed infrastructure capital due to the occurrence of geo-hazard events and deterioration effects. K_f is influenced by decisions concerning the quality of infrastructures, such as safety policies (type $\boldsymbol{a}_1$ decisions) and maintenance choices (type $\boldsymbol{a}_3$ decisions), among others. K_c also depends on these quality-related decisions, which determine the infrastructure construction cost, together with decisions on the investment into new construction. The type of decision alternatives considered for managing the system (outlined in Section 7.4.1.1) do not include investments in new construction. Therefore, the K_c component in Eq. 7.10 will be considered only if there is failed infrastructure capital that should be reconstructed at a specific time t.

On the other hand, the execution of management decisions necessitates budget allocation. Therefore, a part of the economic output should be directed towards investing in infrastructure. Therefore, the net economic output ($Y_{net}(t)$) can be calculated as [279]:

$$\begin{aligned} Y_{net}(t) &= Y(t) - G(t) \\ G(t) &= I(t) + M(t) \end{aligned} \tag{7.11}$$

where $G(t)$ is the budget allocated for investing in infrastructure at time t, which may be divided into investment for new construction $I(t)$ and investment for maintenance $M(t)$ [273]. As previously mentioned, the decision alternatives do not consider the construction of new bridges. Thus, the investment $I(t)$ herein refers to the savings for reconstructing failed infrastructures. These investments can be specified as a fraction of the economic output at time t, represented by the percentage of savings χ and the maintenance investment ratio λ_M, corresponding to $I(t)$ and $M(t)$, respectively:

$$\begin{aligned} I(t) &= \chi\, Y(t) \\ M(t) &= \lambda_M\, Y(t) \end{aligned} \tag{7.12}$$

The accumulation of savings for reconstruction over time builds the economic capacity of the transportation system with respect to resilience. Therefore, the economic capacity at time t can be estimated as:

$$R_r(t, \boldsymbol{a}) = R_r^0 + \int_0^t \frac{\chi\, Y(\boldsymbol{a}, \tau)}{(1 + r_\gamma)^\tau}\, d\tau \tag{7.13}$$

where R_r^0 that represents the starting reserve is assumed to be a percentage equal to χ of the expected value of total net economic output generated during the service life of the transportation system. On the other hand, the economic demand at time t consists of the reconstruction expenses attributed to the number of failed infrastructures $K_f(t)$, which can be calculated as follows:

$$S_r(t, \boldsymbol{a}) = \sum_{\tau \in \{t_F \cap (0,t)\}} \frac{K_f(\boldsymbol{a}, t)\; q_c(\boldsymbol{a})}{(1 + r_\gamma)^\tau} \tag{7.14}$$

where q_c is the construction cost per infrastructure, which is determined by the quality-related decisions, i.e., the safety design parameter z. Thus, the construction cost can be computed as [279]:

$$q_c(z) = q_{c,\text{base}} \frac{z}{f} \tag{7.15}$$

where $q_{c,\text{base}}$ represents the construction cost when $z = f$, and is assumed to be 1.

The accumulated reserves measured in terms of economic outputs and the economic demands for recovery occurring in the future are discounted assuming a discount rate of 2%, which is deemed intergenerationally acceptable for sustainable decision making [264].

Finally, the probability of resilience failure P_{RF} at time t, characterized by the economic demand exceeding the economic capacity (as explained in Section 7.2.1), can be computed by evaluating Eq. 7.3.

7.4.3 System failure consequences

Similarly to Chapter 6, the failure consequences assumed in this study focus on consequences to the economy, health, and the environment. The economic consequences encompass reconstruction costs, as well as user costs due to the prolongation of travel time and the loss of connectivity, given the disturbances in traffic functionality after infrastructure failures. These economic consequences are implicitly accounted for in the economic model from Section 7.4.2 by means of the reduction in the infrastructure capital due to failures, consequently leading to a decrease in the economic output (Eqs. 7.8-7.10), i.e., reduced economic benefits to the society.

Regarding consequences to health, accidents leading to fatalities may escalate as a result of road closures due to infrastructure failures that force commuters to seek alternative routes. These consequences to health are estimated as outlined in Section 6.2.3.3. Similarly, environmental consequences are also increased due to prolonged operating periods and extended distances covered in case of road closures, which elevate CO_2 emissions. These environmental emissions, denoted as E_{tr}, are computed as described in Section 6.2.3.2. Moreover, environmental impacts due to emissions from bridge reconstruction

and maintenance activities are also assessed. Emissions due to maintenance activities, denoted as E_m, are strongly influenced by decisions on the investment in maintenance, and emissions due to reconstruction, denoted as E_{rc}, are largely determined by decisions on the reliability level. Over a specific time frame $[t, t + \Delta t]$, E_m can be estimated from the increment in the volume consumed in maintenance ΔV_m, while E_{rc} can be computed from the increment in the volume consumed in reconstruction ΔV_{rc} [279]:

$$\Delta V_m(t, \boldsymbol{a}) = v_m(\boldsymbol{a}) \, \frac{M(t, \boldsymbol{a})}{q_c(\boldsymbol{a})} \tag{7.16}$$

$$\Delta V_{rc}(t, \boldsymbol{a}) = v_{rc}(\boldsymbol{a}) \, K_f(t, \boldsymbol{a}) \tag{7.17}$$

where the variables v_m and v_{rc} denote the material consumption per-unit structure, which is determined by the quality-related decisions, i.e., the safety design parameter z, and can be estimated as [279]:

$$v_m(z) = v_{m,\text{base}} \, \frac{z}{f} \tag{7.18}$$

$$v_{rc}(z) = v_{rc,\text{base}} \, \frac{z}{f} \tag{7.19}$$

where $v_{m,\text{base}}$ and $v_{rc,\text{base}}$ represent the maintenance and reconstruction material consumption per-unit structure when $z = f$, respectively, and are both assumed to be 0.1. Subsequently, the associated emissions from these two components can be computed as [279]:

$$\begin{aligned} \Delta E_m(t, \boldsymbol{a}) &= \Delta V_m(t, \boldsymbol{a}) \, \gamma_E \\ \Delta E_{rc}(t, \boldsymbol{a}) &= \Delta V_{rc}(t, \boldsymbol{a}) \, \gamma_E \end{aligned} \tag{7.20}$$

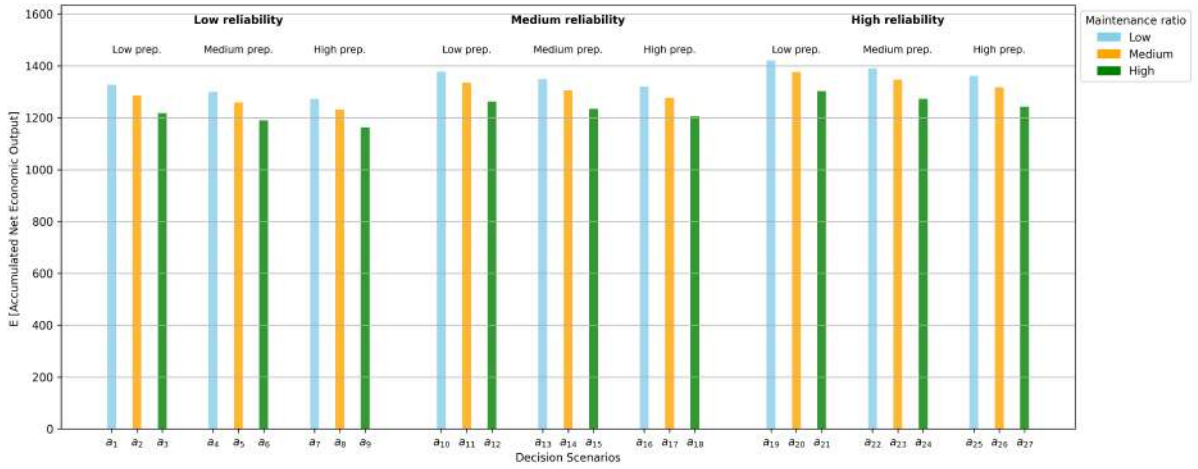


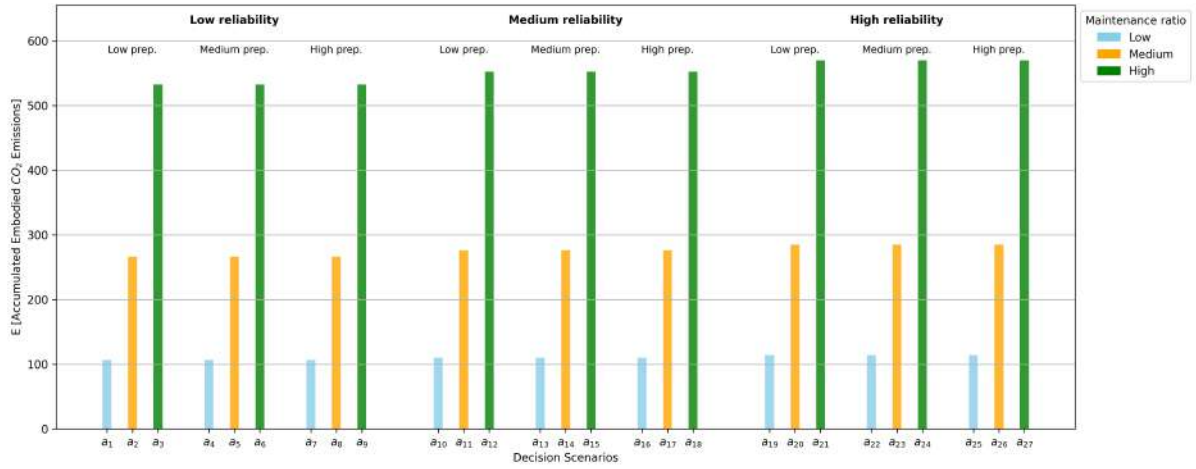
Figure 7.6: Expected net economic output (benefit) over the life cycle for the different decision alternatives

where γ_E represents the embodied CO_2 per unit of the material under consideration, which is assumed as 1.

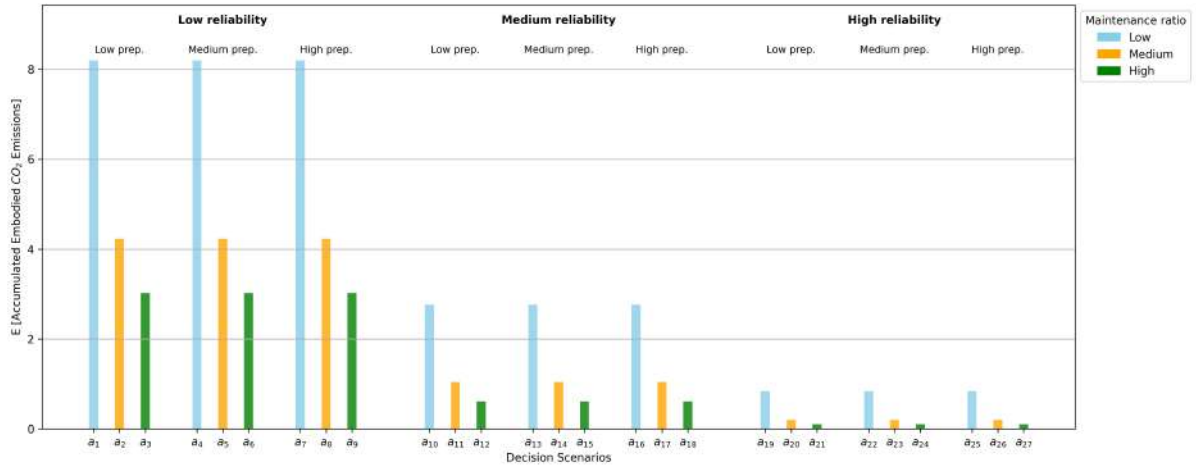
7.5 Results and discussion

The results of the interlinked system performance for the 27 decision scenarios a_j are presented below. The analysis has been run assuming a service life of 75 years. Figure 7.6 presents the expected net economic output over the service life. It can be seen that decisions of high reliability ($a_{19} - a_{27}$) lead to the highest net economic outputs. Regarding maintenance decisions, which are depicted by the different bar colors, it can be observed that the high investments in maintenance reduce the net economic output considerably. Similarly, decisions on a high preparedness level diminish the net economic output. However, the impact is less pronounced due to the lower percentages assumed for savings investments compared to maintenance investments.

Figure 7.7a presents the results of cumulative embodied emissions due to maintenance actions over the life cycle. As anticipated, high investments in maintenance result in higher embodied emissions, and these results are independent of the rest of the decision alternatives, i.e., reliability and preparedness levels. However, high maintenance ratios delay deterioration and consequently reduce the number of



(a)



(b)

Figure 7.7: Expected embodied emissions over the life cycle for the different decision alternatives due to a) maintenance and b) reconstruction

infrastructure failures, which contributes to reduced emissions due to reconstruction. This effect is captured in Figure 7.7b, where low maintenance ratios are significantly contributing to emissions due to reconstruction, particularly for the low reliability level.

Furthermore, Figure 7.8 presents the results of cumulative emissions from rerouting over the life cycle. It can be observed that preparedness levels, as well as reliability levels, have a significant impact in this case. Essentially, under low reliability levels, more infrastructure failures occur, forcing commuters to seek alternative routes with prolonged operating periods and extended distances covered, which elevates emissions. The impacts of expected emissions are exacerbated under low preparedness levels, which increase the recovery time and thereby accumulate emissions during a longer restoration period.

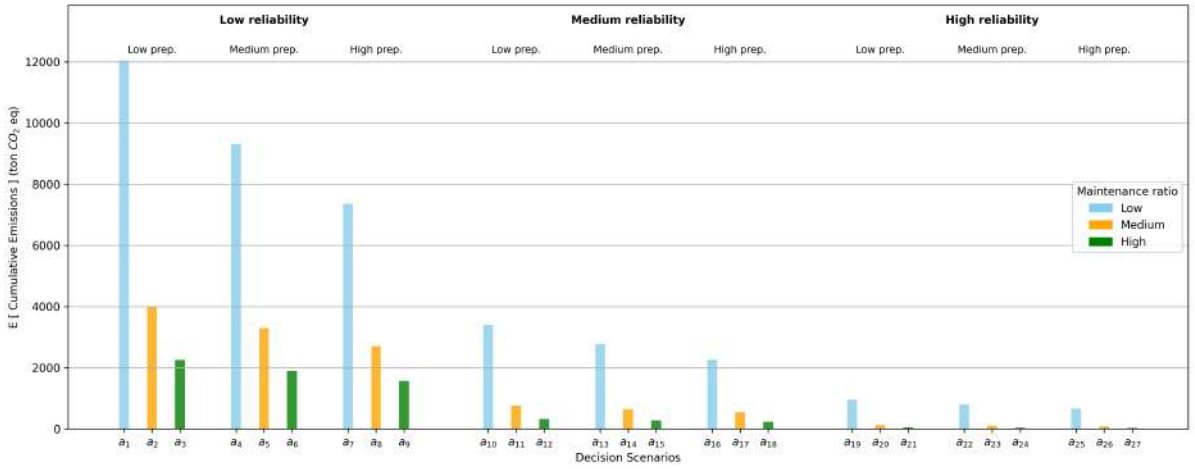


Figure 7.8: Expected emissions from rerouting over the life cycle for the different decision alternatives

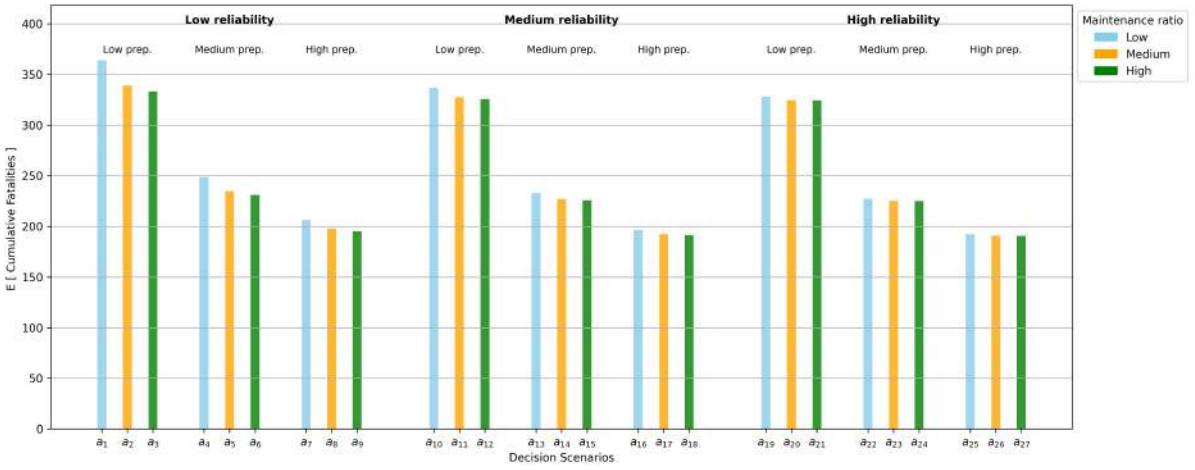


Figure 7.9: Expected fatalities over the life cycle for the different decision alternatives

Lastly, Figure 7.9 displays the expected fatalities over the life cycle. Similar to the emissions from rerouting, the reliability and the preparedness level have the most significant effect on the results. A higher reliability reduces the number of infrastructure failures and, consequently, the number of fatalities due to reduced exposure to abnormal traffic conditions. Moreover, a high preparedness level supports faster recovery after disturbance events, which diminishes the exposure time to traffic congestion.

Finally, Figures 7.10-7.12 presents the results of the annual probability of resilience failure for the different decision alternatives. It can be seen that the decisions on maintenance levels have a significant effect on the annual increase of the resilience failure probability. This can be explained by the fact that low maintenance investment ratios represent high deterioration rates due to poor maintenance practices.

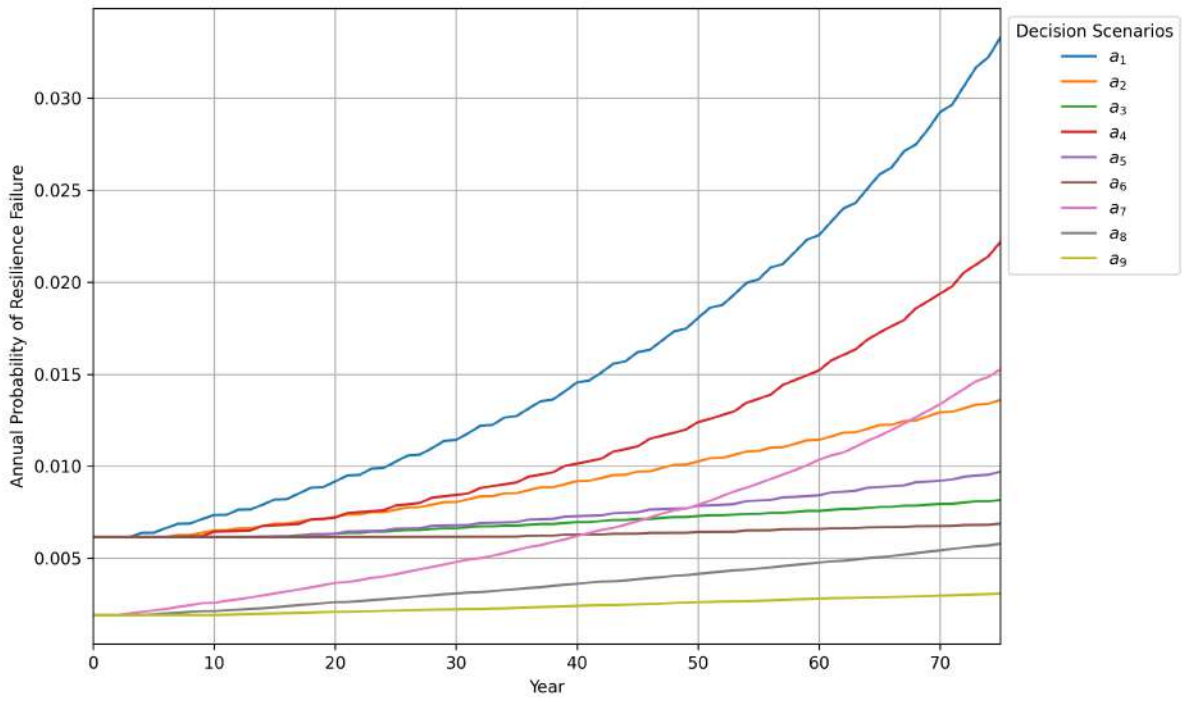


Figure 7.10: Annual Probability of Resilience Failure: Low-reliability decision alternatives

Therefore, the number of infrastructure failures under this condition increases substantially, imposing high economic demands, which result in the exhaustion of the accumulated economic capacity for recovery. The decisions on the benefit savings ratio also influence the probability of resilience failure, with high levels of savings leading to low failure probability. However, in some cases (e.g., a_7), the effect of high benefit savings is diminished by the effect of poor maintenance, which over time becomes very critical and increases the probability of resilience failure despite the high savings level.

The analysis of the results indicates the presence of multiple conflicting criteria that need to be balanced to reach optimal decisions. For instance, a low maintenance ratio leads to greater net economic output and low embodied emissions due to maintenance. However, it results in larger infrastructure failures, incrementing embodied emissions due to reconstruction, emissions and fatalities due to the rerouting, and leads to a high probability of resilience failure. Therefore, these criteria (or attributes) can be transformed (weighted) into a single metric - utility, which consistently reflects the preferences of decision makers. Then, utility theory allows ranking the optimality of different decision alternatives according to their expected value of utility, which is facilitated by Bayesian decision analysis [41]. It should be noted that the utility function used for transforming (weighing) the attributes into utility is a property of the decision

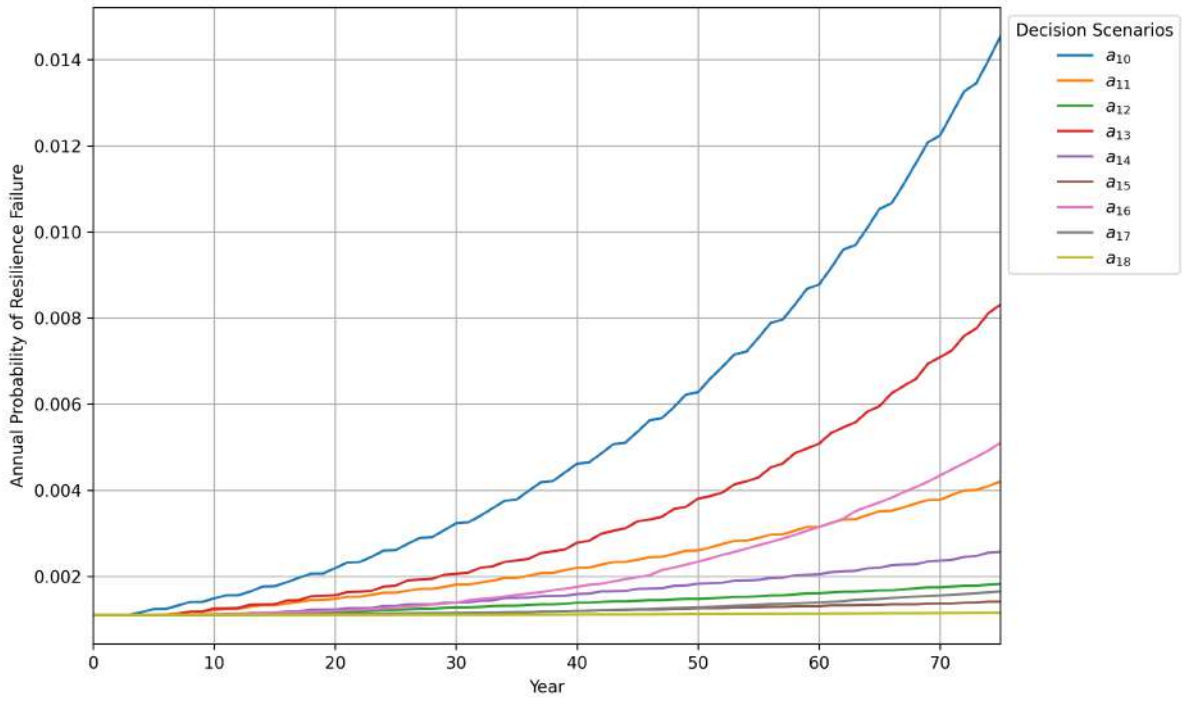


Figure 7.11: Annual Probability of Resilience Failure: Medium-reliability decision alternatives

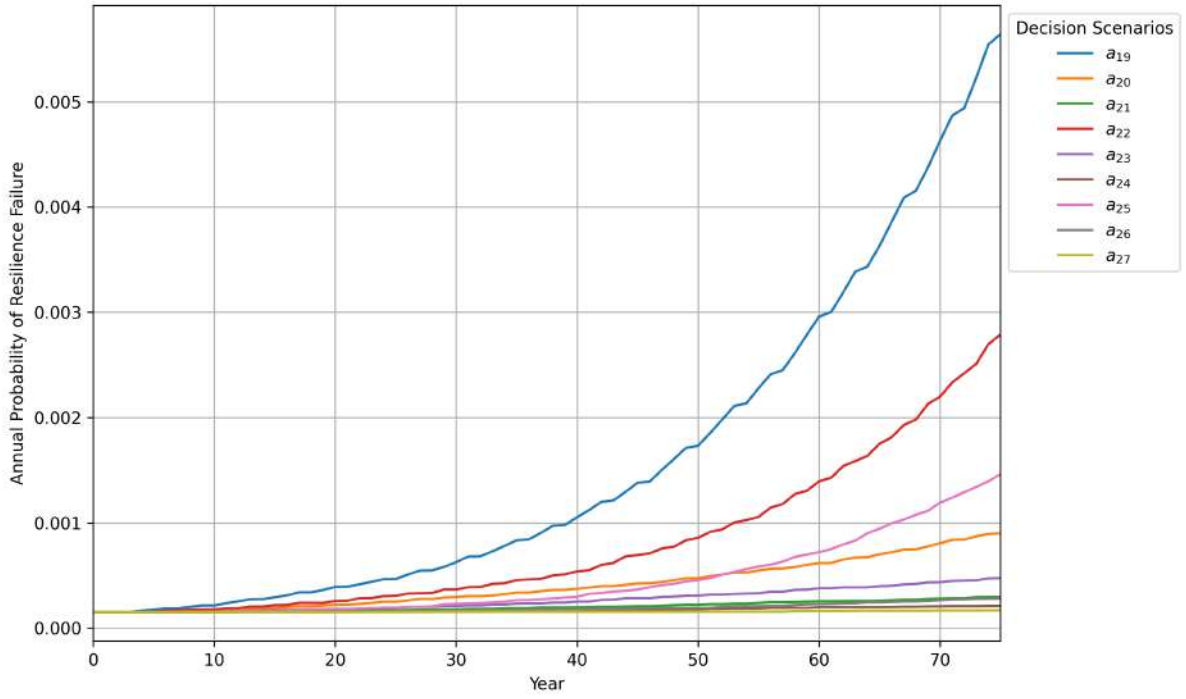


Figure 7.12: Annual Probability of Resilience Failure: High-reliability decision alternatives

maker since it describes her/his preferences. Thus, different decision makers will have different utility functions [280].

7.6 Conclusions

Optimal decisions for designing and managing transport infrastructure systems (TIS) are crucial for ensuring adequate functionality under operational loads and geo-hazard events. This chapter introduces a probabilistic decision-making framework aimed at enhancing the resilience of TIS during their service life. The framework conceptualizes TIS as interlinked systems, aiming to capture the dependencies among social, infrastructure, geo-hazard, and management systems. The proposed approach allows for the comparison of different decision alternatives, including decisions on the level of structural safety, decisions on the maintenance investment, and decisions on the percentage of the benefit that should be accumulated to cope with adaptation and recovery after disturbance events. In addition, the resilience life cycle modeling implemented in this chapter allows the consideration of all potential hazardous events throughout the infrastructures' service life rather than limiting the analysis to a single event, and it explicitly accounts for the generation of the system's capacity to recover from hazards.

The decision support framework has been exemplified in the transportation network in Santarém, Portugal. The proposed methodology enabled the comparison of several criteria for each of the decision alternatives considered for managing the system. Particularly, the results demonstrated that increasing the safety level of infrastructures increased the net economic output (benefit). Additionally, increasing preparedness greatly reduced the impacts on health and the environment in case of infrastructure failures, while it did not reduce the net economic output substantially. Therefore, these results facilitate the inclusion of sustainability considerations in the decision-making process, in the form of environmental emissions and social impacts, and enable the prioritization of decisions according to the preferences of decision-makers. To this end, future research can extend the decision support framework by incorporating utility theory, which transforms the different criteria into a single utility metric by means of weights and facilitates the ranking of various decision alternatives. Moreover, the probability of resilience failure can be incorporated into the decision-making process as a constraint, similar to target reliability levels that must be fulfilled and

are provided in standards. However, future research is needed regarding the definition of an acceptable annual probability of resilience failure.

Finally, one limitation of the application of the methodology was the absence of historical data or specific cross-sectional studies that examined the relationship between transport infrastructures and their economic benefits in the case study. Consequently, a macroeconomic model derived from production functions, commonly dedicated to policy-making, was implemented. The model related the amount and quality of transport infrastructure to economic outputs, and the function parameters were adopted from the literature to demonstrate the methodology. Future work can implement more refined economic models to estimate the benefits of the transportation system more accurately and integrate these models within the proposed decision-making methodology.

Chapter 8

Conclusions and future developments

The exploratory bibliometric analysis presented in Chapter 2 facilitated the identification of research gaps in risk, resilience, and sustainability management of Transport Infrastructure Systems (TIS). The research conducted in this thesis intended to address several of these gaps, making relevant contributions to the field. This section summarizes the key contributions towards each identified gap, highlights the primary findings, recognizes the study's limitations, and proposes potential directions for future research.

8.1 Contributions to research domain

Table 8.1: Research gaps from bibliometric analysis

Research gap	Ch. 3	Ch. 4	Ch. 5	Ch. 6	Ch. 7
1. Fragmentation of research among spatial scales of the systems modeling	✓		✓	✓	✓
2. Lack of long-term perspective for decision making	✓	✓	✓	✓	✓
3. Potential for transfer of knowledge from seismic domain regarding fragility curves			✓		
4. Lack of consistent treatment of uncertainties and dependencies	✓	✓	✓	✓	✓
5. Lack of integration of risk, resilience, and sustainability considerations for decision making					✓

Table 8.1 summarizes the research gaps and the thesis' Chapters where they have been addressed. The first gap concerned the fragmentation of research at the asset and network level. Essentially, there was a potential gap in integrating flood risk and vulnerability research at the component and bridge level stemming from the civil/reliability engineering community, with research at the network/regional level coming from the transportation engineering community and the natural hazards domain. This problem was addressed across several chapters by integrating different spatial scales in the modeling. In Chapter 3, the methodology introduced for the probabilistic spatial representation of the flood actions at transport infrastructures using Bayesian Networks was performed at the network level. Subsequently, Chapter 5 proposed a methodology for constructing flood fragility functions for transport infrastructures at the asset level. Then, the integration of both scales was conducted in Chapter 6 to quantify the transportation network risks, including traffic modeling at the regional level, to understand the indirect consequences of asset failures. This integration enabled the identification of the infrastructure assets that contributed the most to the transportation network risks. Therefore, optimal decision making across scales was enhanced. Moreover, this integration was also conducted in Chapter 7 for the estimation of the transportation system resilience.

Another research gap identified in the bibliometric analysis relates to a lack of a long-term perspective for decision making on resilient infrastructures. Most of the focus of resilience management has been given to ensuring optimal recovery and restoration in the aftermath of disaster events, i.e., tactical management. However, decisions should be made from a life cycle perspective, considering the long-term performance of transport infrastructures. This thesis aimed to address this issue across all chapters by analyzing likely climate change effects in flood hazard modeling (Chapter 3), deterioration effects in the performance of bridges under operational and flooding events (Chapter 4 and Chapter 5, respectively), and implementing a life cycle risk and resilience modeling (Chapter 6 and Chapter 7) to support decision making.

Furthermore, it was evidenced from the bibliometric analysis that the concept of fragility curves, which has been thoroughly developed in earthquake engineering, represented available knowledge that can be transferred to characterize the performance of transport infrastructures under flooding events. In this regard, Chapter 5 aimed to contribute with a generic methodology for constructing fragility curves for different flood failure modes considering uncertainties and time-dependent considerations.

One research gap addressed in every Chapter is the lack of consistent treatment of uncertainties. From the bibliometric analysis in Chapter 2 it was observed that they had a significant role in civil/reliability engineering at the asset level. However, the consistent treatment of uncertainties across scales and disciplines was limited. In this thesis, uncertainties were considered in all the components, including the flood hazard model, the fragility analysis, the consequence modeling, and the resilience quantification.

Finally, one relevant gap was the lack of integration of risk, resilience, and sustainability for managing TIS from the engineering knowledge domain. Chapter 7 aimed to contribute to this fragmentation by including sustainability considerations, in the form of embodied carbon and CO_2 emissions due to detours, when deciding on the most optimal alternatives to improve resilience and how these decisions positively or negatively impact sustainability.

8.2 Conclusions

Detailed conclusions have been presented in each of the preceding chapters. In this section, the key conclusions derived from this work are summarized in relation to the research objectives:

1. *Implementation of Bayesian probabilistic modeling techniques to establish the representation of flood events impacting transport infrastructure systems, consistently integrating available and potential future knowledge and information while systematically addressing uncertainties inherent in exposure modeling.*

   Chapter 3 introduced a methodology for the probabilistic spatio-temporal representation of flood occurrences utilizing Bayesian Networks. The strength of this proposed approach lies in its ability to combine prior domain knowledge, observed data from the system, specifically rainfall and discharge records, and results from a hydrological model. The construction of the model was specifically intended to capture the spatial dependencies involved in the progression of floods across a watershed.

   One potential application of this modeling approach was demonstrated in Chapter 6 and Chapter 7. In these chapters, a Bayesian Network (BN) was employed to simulate flood events throughout the

life cycle of transport infrastructure systems. This approach effectively characterized the flood hazard at each infrastructure location while also incorporating uncertainties, enabling their propagation in the risk assessment and resilience modeling of transport infrastructure systems conducted therein.

In addition, through a sensitivity analysis, the capability of the BN model to integrate shifts in precipitation patterns resulting from climate warming and evaluate the potential impacts on flood hazards was demonstrated. These insights are crucial for strategically adapting transportation infrastructures to changing climate conditions.

2. *Application of big data analysis techniques for improving the understanding of transport infrastructure systems performance and reducing the computational cost associated with complex consequence modeling tasks while maintaining a high level of model accuracy.*

   In Chapter 4, several models were implemented to predict the deterioration of transport infrastructures due to aging and environmental stressors. Among these, machine learning techniques, namely Neural Networks (NN), offered a superior accuracy factor and achieved the lowest prediction errors. Therefore, it was proved that the application of these techniques represents a convenient alternative to predict the performance of infrastructures over their life cycle, thereby aiding the quantification of long-term risks in transportation systems.

   Additionally, Chapter 6 presented a NN model as a means to improve computational efficiency in evaluating the consequences of infrastructure failures within transportation networks. The NN model was trained to predict the outputs from the traffic model under damaged failure scenarios resulting from the probabilistic vulnerability analysis. The NN model proved to be efficient in predicting the traffic-related metrics under the disrupted scenarios and thereby assisting in the quantification of economic, health, and environmental consequences. It also contributed to identifying the optimal sequence of restoration efforts to enhance resilience by reducing the indirect costs throughout the restoration phase.

3. *Quantification of life cycle risks at the network level scale, accounting for individual infrastructure's response to the common hazard event throughout their service life, with consistent treatment*

of uncertainties and dependencies, and aggregating consequences at the transportation network level.

Chapter 5 outlined a methodology for systematically identifying bridge failure modes and assessing their fragility in the context of flooding events while considering the effects of long-term deterioration. This method facilitated the recognition of key factors influencing the flood vulnerability of bridges. Additionally, it enabled the subsequent identification of the predominant failure modes that significantly contributed to network-level risks. This aspect is particularly relevant in guiding the selection of appropriate mitigation strategies.

Furthermore, building upon the hazard modeling methodology from Chapter 3 and the infrastructure fragility models from Chapter 5, a scenario-based modeling approach was introduced in Chapter 6. This framework effectively quantified life cycle risks at the transportation network level with consistent treatment of uncertainties. The NN model facilitated the aggregation of consequences, as previously stated. The application of the framework enabled a better understanding of the failure scenarios that significantly impacted the network-level risks, thereby aiding in the identification of critical infrastructures and predominant failure modes.

4. *Establishment of a decision-making methodology integrating resilience concepts to facilitate the identification of decision alternatives that reduce the risks, improve the resilience of the transport infrastructure system, and examine the impacts of these decisions on sustainability.*

   Chapter 6 outlined a methodology that contributed to informing decisions about recovery prioritization, aiming to reduce indirect costs and thereby enhancing transportation resilience through the efficient restoration of functionality following disruptions. Moreover, the scenario-based modeling framework described in this chapter aided decision making concerning the prioritization of mitigation strategies, given its capability to recognize critical infrastructures and failure modes significantly contributing to the risks, as previously mentioned.

   In addition, Chapter 7 introduced a decision framework that evaluated the economic benefits arising from various decision alternatives. These alternatives encompassed choices about infrastructure safety levels, operational decisions regarding maintenance and repair activities, and the percentage of benefits allocated for reconstruction and recovery after failures, which is critical to ensuring

a resilient transport infrastructure system. Furthermore, this framework allowed for comparing decision alternatives that, while yielding similar economic benefits, resulted in varying environmental emissions and health-related consequences. Thus, it enabled the incorporation of decision-makers preferences into the framework, allowing for selecting options that aligned with their specific priorities.

8.3 Limitations and recommendations for future research

This final section outlines the limitations of some approaches implemented in this thesis and suggests directions for future work. The recommendations are focused on extending the methods presented in this study and promoting the exploration of related perspectives.

- The bibliometric analysis conducted in Chapter 2 focused on mapping the current state of the art in the management of TIS, which facilitated the identification of research gaps and the potential for transfer of knowledge across sub-fields, particularly from seismic to flood hazard research. Future work could broaden the bibliometric analysis to encompass additional infrastructure systems beyond transportation, including water distribution and electricity/power systems, which share similar characteristics, such as being geographically distributed systems with societal functionality exposed to hazardous events. This could reveal approaches that can potentially be transferred to the management of transportation systems and contribute to understanding interdependencies among these systems.

- Changes in the precipitation patterns attributable to climate warming were analyzed using sensitivity analysis to demonstrate the BN capability to evaluate the impacts on the flood hazard. However, global and regional climate modeling can be down-scaled and bias-corrected to derive projections for a specific region. Nonetheless, there is a large variation in the projections between models and emission scenarios, which leads to substantial uncertainty about how the distribution of precipitation will change in the future [21]. From a systems modeling context, it can be said that the actual system under consideration is unknown. In other words, since different scenarios of continued

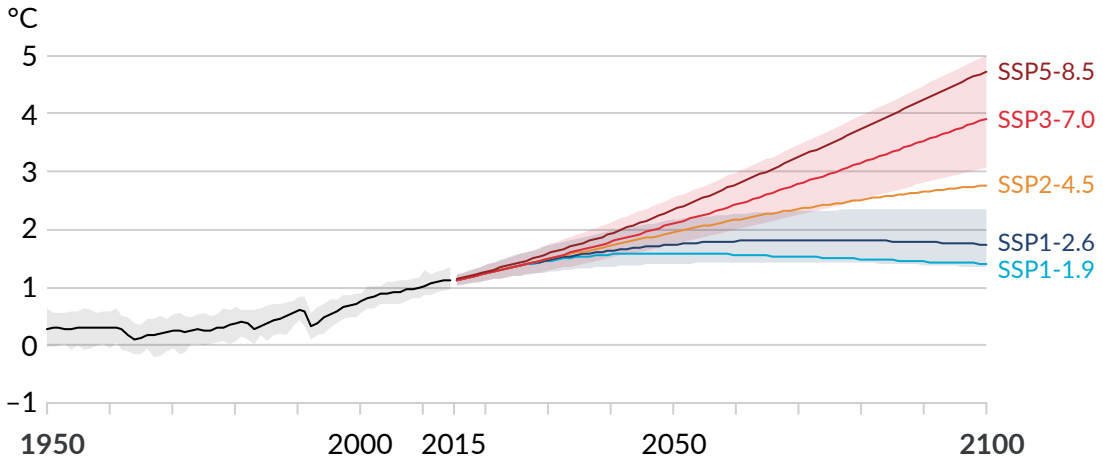


Figure 8.1: Global surface temperature change relative to 1850–1900. Source: [21]

greenhouse gas (GHG) emissions can be realized in the future depending on our societal developments, there is not one correct climate model but an ensemble of possible climate models, as depicted in Figure 8.1. Therefore, all these scenarios can be seen as competing system models, and it is necessary that the decision-making framework accounts for the possibility of these competing models to identify robust decisions for designing and managing infrastructure, regardless of the climate scenario that may be realized in the future [281]. The conceptual framework for such a decision analysis approach is available in [282]. Future research is needed to relate the climate scenarios to probabilities and consistently account for all competing systems in the decision framework. Previous work has successfully applied this framework in the context of the evacuation of offshore structures, given information on competing realizations of an emerging storm event (see [103]).

- The models implemented in Chapter 4 to predict the deterioration of transport infrastructures due to aging and environmental stressors were built from condition ratings obtained from visual inspections as the performance indicator. However, some shortcomings of using these indicators for deterioration modeling were discussed in that chapter, including the subjectivity of inspectors when assigning the condition ratings and the qualitative nature of these indicators, which challenges using the model results for structural safety assessment. Therefore, recent condition assessment practices have incorporated non-destructive techniques (NDT) and structural health monitoring (SHM) systems to improve the indicators used to quantify the impacts of damages on infrastructure

safety. Despite the emergence of these techniques, their implementation has been limited due to the costs associated with their acquisition, maintenance, use, and decommissioning. In this regard, the concept of Value of Information (VoI) from Bayesian decision analysis [41] has been proposed in recent years to quantify the benefit of collecting information with these techniques before their adoption. As briefly explained in Chapter 1, collecting information can be seen as a type of decision alternative to improve our knowledge about the performance of the infrastructures, thereby improving our models and the ranking of decisions. Future research in the application of VoI for large infrastructure systems such as transportation networks is crucial for identifying optimal locations in the network where to collect information.

- The implementation of the methodology outlined in Chapter 5 exhibited the large amount of data required to assess the performance of bridges under flooding events. Given the frequent lack of this data in existing bridge inventories, future research can be conducted to evaluate the sensitivity of the results to the assumptions made in the face of incomplete documentation. Moreover, the work presented in that chapter can be extended to account for intermediate damage states as it has been commonly addressed in the context of seismic fragility analysis. Ultimately, research efforts should aim at harmonizing the methodologies for fragility assessment under multiple hazards and the definition of bridge classes.

- The framework presented in Chapter 7 aimed at including sustainability considerations in the form of environmental emissions and social impacts in the decision-making process. Nonetheless, there is a back-coupling effect between the exposure and the decisions to manage the infrastructure systems that is not considered in the framework. Essentially, our decisions for managing transport infrastructure systems impose GHG emissions, triggering changes in the Earth's Life Support System, as illustrated in Figure 7.2. Consequently, the exposure to extreme weather events is subject to variation in accordance with the prevailing state of the ELSS under different GHG emission scenarios. Therefore, future research developments should further explore these interrelations and their influence on the definition of management strategies for transport infrastructure systems.

- The application of the decision analysis framework from Chapter 7 requires the modeling of the economic capacity of the transport infrastructure system. This capacity builds upon the benefits

that the transportation system provides to society. In that chapter, the benefit was derived from macroeconomic production functions, where the amount and quality of infrastructures were related to the economic outputs. Future work can be conducted to incorporate more advanced economic models into the decision analysis framework.

Appendix A

Bibliometric networks construction

Table A.1: Full search query of Group 1: Transport Infrastructure Systems (TIS)

Component level	"bridge pier" OR "bridge pile" OR "bridge foundation" OR "bridge abutment" OR "bridge deck" OR "bridge component" OR...
Asset level	"bridge *structur*" OR road* W/1 bridge OR "rail* bridge"OR"highway bridge"OR"coastal bridge"OR"river* bridge"OR"waterway bridge" OR "river crossing bridge" OR "culvert" OR "transport* asset" OR "transport* *structure" OR "road* *structure" OR "road* segment" OR...
Network level	"road* network" OR "bridge network" OR "highway network" OR... "transport* network" AND ("road*" OR "rail*" OR "bridge" OR "urban" OR "highway" OR "infrastructure")[1]OR... "transport* system" AND ("road*" OR "rail*" OR "bridge" OR "urban" OR "highway" OR "infrastructure")[1]OR... "traffic network" AND ("road*" OR "rail*" OR "bridge" OR "urban" OR "highway")[1]OR... "traffic system" AND ("road*" OR "rail*" OR "bridge" OR "urban" OR "highway")[2]OR... "infrastructure system" AND ("road*" OR "rail*" OR "bridge" OR "highway" OR "transport*" OR "traffic")[2]OR... "infrastructure network" AND ("road*" OR "rail*" OR "bridge" OR "highway" OR "transport*" OR "traffic")[2]

[1] Search query after AND gives context to transportation systems and infrastructure that enables the traveling of people and goods (transport/traffic systems and traffic networks are sometimes used in different context areas).

[2] Search query after AND gives context to transportation.

Table A.2: Search query combinations

Search query		**Results**
n_0	TIS	118,105
n_1	TIS AND (“vulnerability” OR “risk”)	8,282
n_2	TIS AND “robustness”	1,236
n_3	TIS AND “resilien*”	1,613
n_4	TIS AND “sustainab*”	6,779
n_{OR}	TIS AND (“vulnerability” OR “risk” OR “robustness” OR “resilien*” OR “sustainab*”)	16,395
n_5	TIS AND (“vulnerability” OR “risk”) AND (“flood*” OR “scour*”)	921
n_6	TIS AND “robustness” AND (“flood*” OR “scour*”)	37
n_7	TIS AND “resilien*” AND (“flood*” OR “scour*”)	247
n_8	TIS AND ‘sustainab*” AND (“flood*” OR “scour*”)	132
n_9	TIS AND (“vulnerability” OR “risk” OR “robustness” OR “resilien*” OR “sustainab*”) AND “uncertain*”	1028
n_{10}	TIS AND (“vulnerability” OR “risk” OR “robustness” OR “resilien*” OR “sustainab*”) AND “*dependenc*”	592
n_{11}	TIS AND n_{OR} AND (“governance” OR “manag*” OR “decision”) AND (“preference” OR “attribute” OR “criteri*”)	702

Table A.3: Scopus subject areas excluded from the search

Health Sciences	Life Sciences
Medicine(MEDI)	Biochemistry, Genetics and Molecular Biology (BIOC)
Nursing (NURS)	Immunology and Microbiology (IMMU)
Veterinary (VETE)	Neuroscience (NEUR)
Dentistry (DENT)	Pharmacology, Toxicology and Pharmaceutics (PHAR)
Health Professions (HEAL)	Chemistry (CHEM) (Physical Sciences)

Table A.4: Context areas excluded from the search

Research context	Keywords to exclude in search query
Computer networking and communication	vehic* ad hoc networks (vanets)
	broadcast
	transmission flood*
Traffic signal systems	signal control*
	traffic control*
	traffic signal
Connected, automated and electric vehicles	autonomous W/2 vehicle
	autonomous W/2 buses
	"platoon*"
	"recharg*" or "charg*" or "batter*"
Location Privacy and Security	"mobile users"
	"map matching"
Space transportation systems	"moon" or "mars" or "lunar"

Table A.5: Non-context-specific terms excluded from visualizations

knowledge	question	comparison	attention	cause
account	advantage	article	author	challenge
improvement	requirement	view	case study	concept
perspective	problem	difference	presence	concern
addition	basis	consideration	effort	goal
face	focus	form	gap	good
example	order	estimation	(important) role	insight
chapter	lack	application	type	issue
characteristic	point	end	limitation	new method
need	research(er)	review	feature	principal
investigation	overview	recent year	regard	set
literature	need	hand	set	use
kind	study area	context	variety	variation
methodology	characterization	understanding	factor	way
wide range	implementation			

Table A.6: VOSviewer specifications for term co-occurrence analysis networks

Search query	n_1	n_2	n_3	n_4	n_5	n_7	n_8	n_9	n_{10}	n_{11}
Total number of records	8282	1236	1613	6779	921	247	132	1028	592	702
Binary count	Yes	Yes	Yes	Yes	Yes	Yes	Yes	Yes	Yes	Yes
Min. no. of occurrences of a term[1]	170	23	37	150	25	8	5	23	15	18
No. of terms	170	174	171	169	175	170	148	170	177	168
% of relevant terms[2]	71%	69%	70%	71%	69%	71%	68%	71%	68%	71%
Final no. of terms selected	120	120	120	120	120	120	100	120	120	120
No. of clusters	4	3	3	3	3	3	4	4	3	3
No. of links	7064	6256	6506	7135	5232	4316	2788	6136	5973	6164
Total link strength	309949	49606	48598	413514	45836	8958	4862	42480	29648	29909

[1] The minimum number of occurrences of a term is adjusted aiming to obtain medium size network visualizations of 120 terms

[2] Percentage of terms to be selected based on their relevance score (set to exclude around 30% of terms with low relevance score)

Table A.7: VOSviewer specifications for bibliographic coupling analysis networks

Search query	n_1	n_2	n_3	n_4	n_5	n_7	n_8
Total no. of records	8282	1236	1613	6779	921	247	132
Fractional counting	Yes	Yes	Yes	Yes	Yes	Yes	Yes
Min. no. documents per author	10	5	6	8	5	3	2
No. of authors	32	11	31	24	18	29	8
Min. no. documents per country	10	5	5	10	5	3	3
No. of countries	69	34	47	76	44	23	22

Appendix B

Supplementary information for the flood hazard modeling

B.1 Study Area

The Tagus River basin extends from Spain to Portugal, as shown in Figure B.1. It should be noted that the Tagus River has suffered human intervention that has modified its hydrological behavior due to the construction of dams. However, the period of records used in this study corresponds to the post-dam regimen. In addition, the model domain was set to the Central Tagus River basin, corresponding to the area of interest in the Santarém district. Then, the HEC-HMS model was used to simulate a subset of the area from the Tagus River basin.

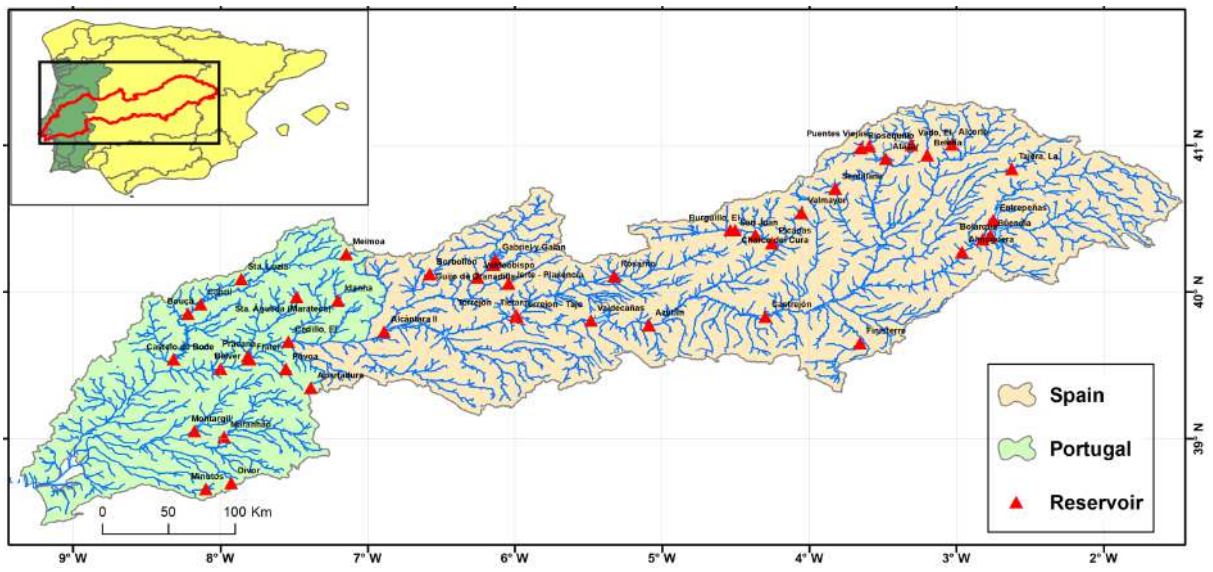


Figure B.1: Location of Tagus River basin and reservoirs. Source: [22]

B.2 Input Data Treatment

B.2.1 Rainfall data

Figure B.2 shows the spatial distribution of annual precipitation in the Tagus River basin. It can be seen that the basin presents significant differences throughout the river basin, with notably low rainfall in the upper Tagus, the region near the border with Spain. The central Tagus has higher precipitation levels, and it is in this region that flood events occur more frequently [23]. The most representative station for the Central Tagus applying the Thiessen Spatial Interpolation Method corresponds to the Chouto weather station (18G/01G) (see Figure B.2).

Daily and hourly precipitation records are accessible free of charge through the National Information System for Water Resources (SNIRH) website [5]. Hourly rainfall for the period 2001-2023 was available. For the period between 1973 to 2000, daily rainfall was available. NEOPRENE, a Python library for rainfall disaggregation was used [24]. Regarding the distribution of precipitation throughout the hydrological year (beginning in October), it is observed that the first quarter is the wettest, with the highest daily precipitation values recorded during this period (Figure B.3).

Figure B.5 shows the disaggregation plot for the rainfall corresponding to the month of February 1995.

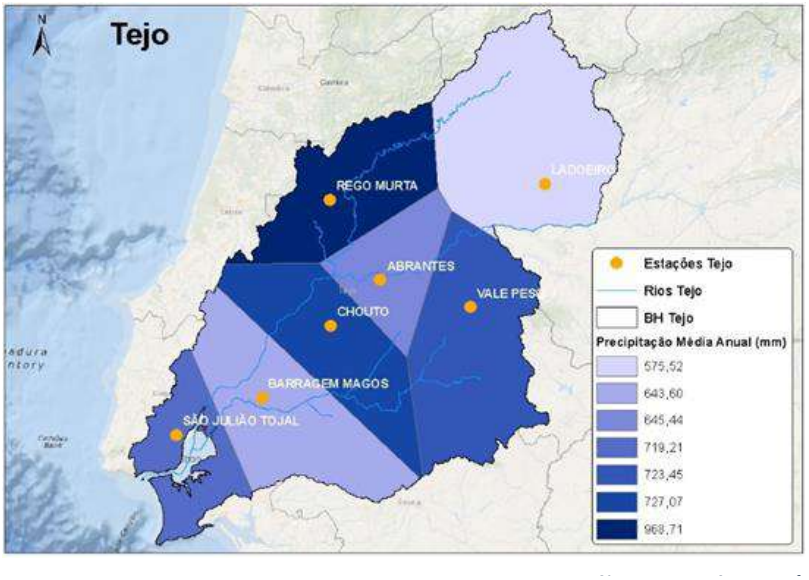


Figure B.2: Annual and Monthly Average Precipitation in the Tagus River Basin. Source: [23]

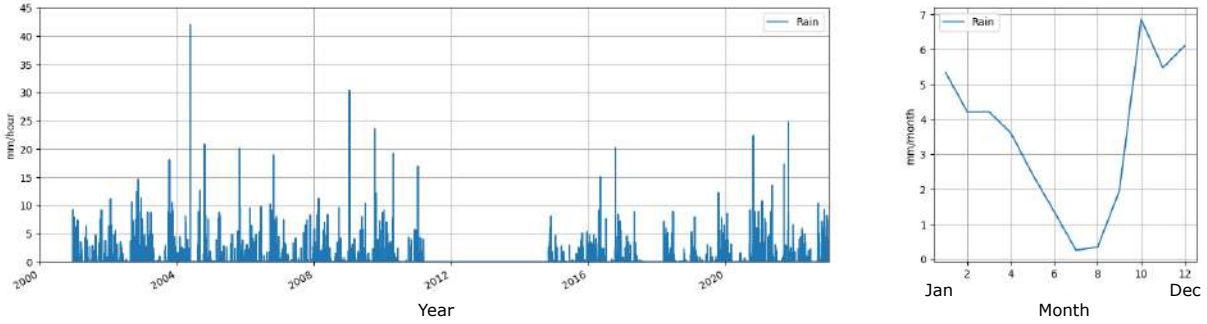


Figure B.3: Hourly precipitation recorded at Chouto station and monthly seasonality

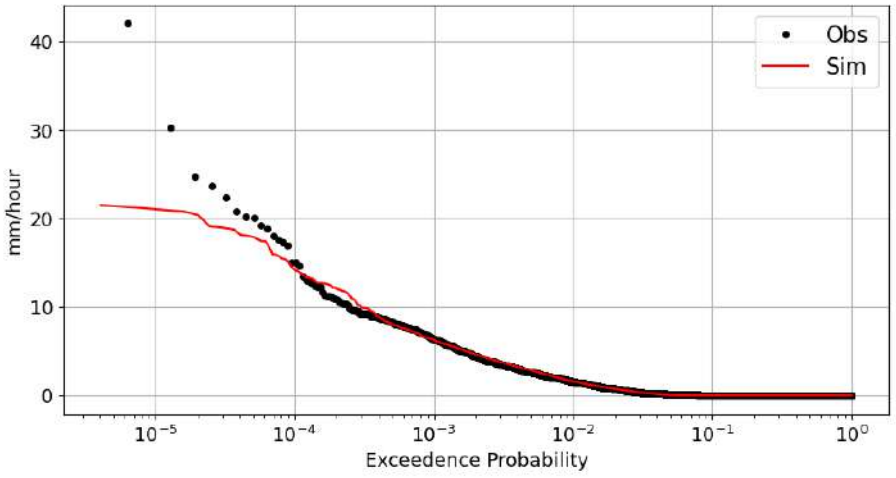


Figure B.4: Exceedance probability of observed (black dots) and simulated (red line) hourly rainfall values (generated with NEOPRENE [24])

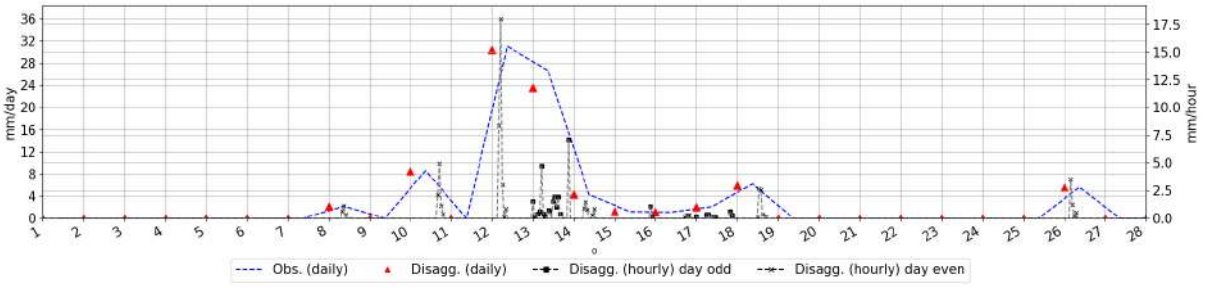


Figure B.5: Rainfall disaggregation plot. Blue (observation) and red (simulated) lines correspond to observed and simulated series at a daily scale, respectively. Back lines indicate the hourly disaggretation simulated with the model (generated with NEOPRENE [24])

B.3 Extreme Value Analysis - Peak Over Threshold

As mentioned in Section 3.3.2.1, the selection of the threshold and declustering distance significantly influence the results of the extreme value analysis. Higher threshold values yield fewer extreme events, resulting in considerable variability in the results (i.e., wider confidence intervals). In contrast, lower threshold values result in a sample that poorly approximates the GP distribution. Therefore, the optimal threshold selection involves identifying the smallest threshold value that ensures that the extracted extreme values conform to the GP distribution [8]. In the following, several tests are performed to determine a suitable threshold value using pyextremes [8]. A 24-hour declustering distance is assumed to be a reasonably good separation of independent heavy rainfall events.

B.3.1 Mean Residual Life

The mean residual life plot displays the average excess value beyond a specified threshold across a range of thresholds. The concept is that this plot will exhibit an approximately linear trend at and above a threshold where the GP distribution model is valid. Figure B.6 presents the mean residual plot where it can be observed that the exceedance values maintain an approximate linearity in the threshold interval between 5 and 30. This delineates a threshold value range for examination through additional tests.

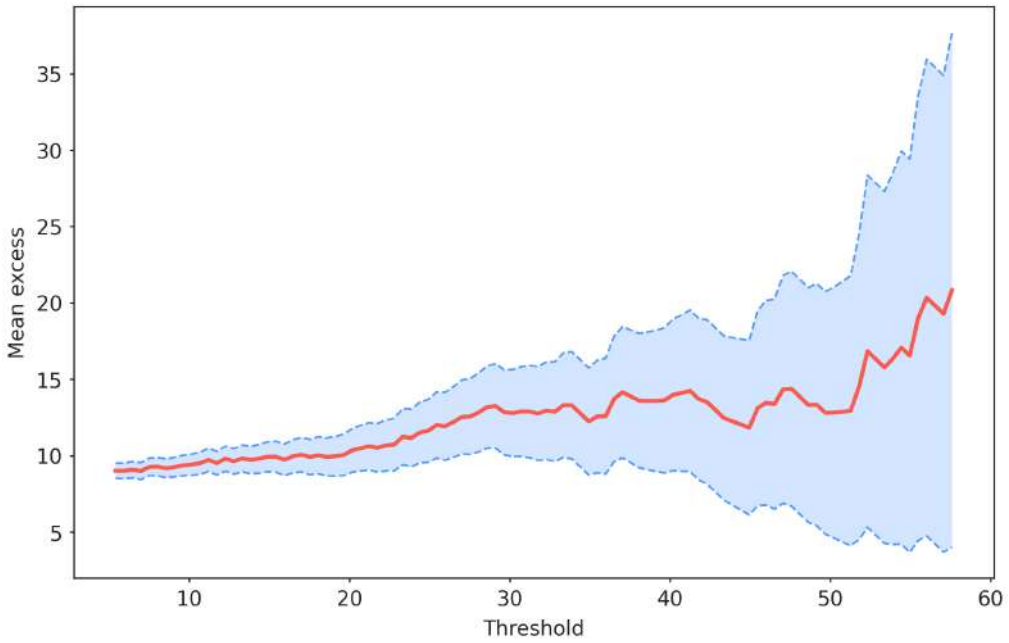


Figure B.6: Mean residual plot (generated with [8])

B.3.2 Parameter Stability

The parameter stability plot illustrates the variations in the shape ξ and modified scale $\sigma*$ parameters of the GP distribution across different threshold values. The expectation is that these parameters should exhibit stability within a valid threshold range, i.e., changing minimally. Figure B.7 depicts the parameter stability plot, where it can be seen that both parameters seem to be stable within a range of values between 5 and 33, with later values displaying increased variance due to the reduced number of exceedances.

B.3.3 Return Value Stability

Building upon the parameter stability, the return value stability examines the consistency of a specific return value across a range of thresholds for a given return period. This approach offers a more straightforward measure of model stability [8]. Figure B.8 shows the return value stability plot for a 100-year return period. For the exponential distribution, it can be seen that the model is very stable across the entire range of investigated thresholds. However, for the GP distribution, it can be observed that the model is more stable for threshold values above 25.

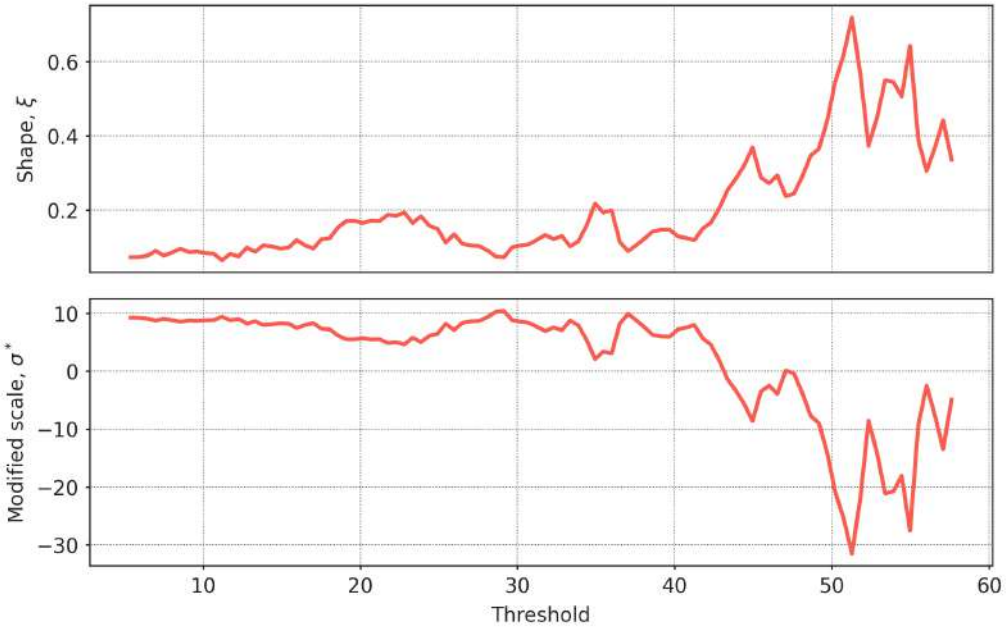


Figure B.7: Parameter stability plot (generated with [8])

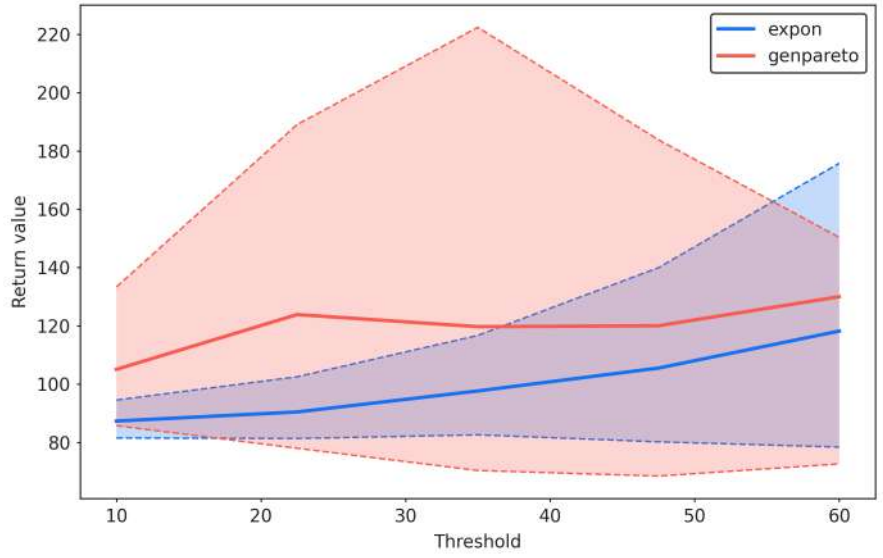


Figure B.8: Return value stability plot (generated with [8])

Based on the analysis of the three performed tests, it is concluded that the smallest threshold value that ensures that the extracted extreme values are stable and conform to the GP distributions is around 25mm. Therefore, the extreme values exceeding this threshold are extracted and used to fit the GP distribution. The results of the model fitting are presented in Section 3.3.2.1 (Figure 3.5).

B.4 Hydrological Model in HEC-HMS

The general flowchart for developing the hydrologic model in HEC-HMS is illustrated in Figure B.9. The complete rainfall time series is given as an input to the meteorological component in HEC-HMS. However, as the purpose of the hydrological model is to simulate the response of the watershed to extreme rainfall events, the start and end dates of the rainfall events exceeding the threshold are specified in the control specifications to establish the duration of the event simulation. Subsequently, the basin component, which comprises the conceptual simulations of various physical phenomena, calculates the streamflow value at the different hydrological elements. Further details regarding the basin model and the methods chosen for simulating the hydrological processes are given in the following sub-chapters.

B.4.1 Basin Model

The GIS capabilities of HEC-HMS were used to delineate the sub-basins using the Digital Elevation Model (DEM), derived from the Shuttle Radar Topographic Mission (SRTM) by SAR Interferometry, in an approximate resolution of 30 m, pre-processed for Portugal from NASA Earth Data [120]. Terrain reconditioning tools were also implemented, i.e., a building walls procedure for coincidence with the sub-basins delineated by the Portuguese Environmental Agency (APA) [6] (see Figure B.10). Similarly, a burning streams procedure was also implemented for coincidence with the stream network by APA [7]. The hydrologic elements derived from this process can be observed in the representation of the HEC-HMS model in Figure B.11. In addition, a source element was added to represent the boundary conditions of the basin model, i.e., the inflow from the upstream region of the river basin that was not explicitly included in the model, using the observed flow at Almourol station. Finally, the sink (or outlet) of the hydrologic model

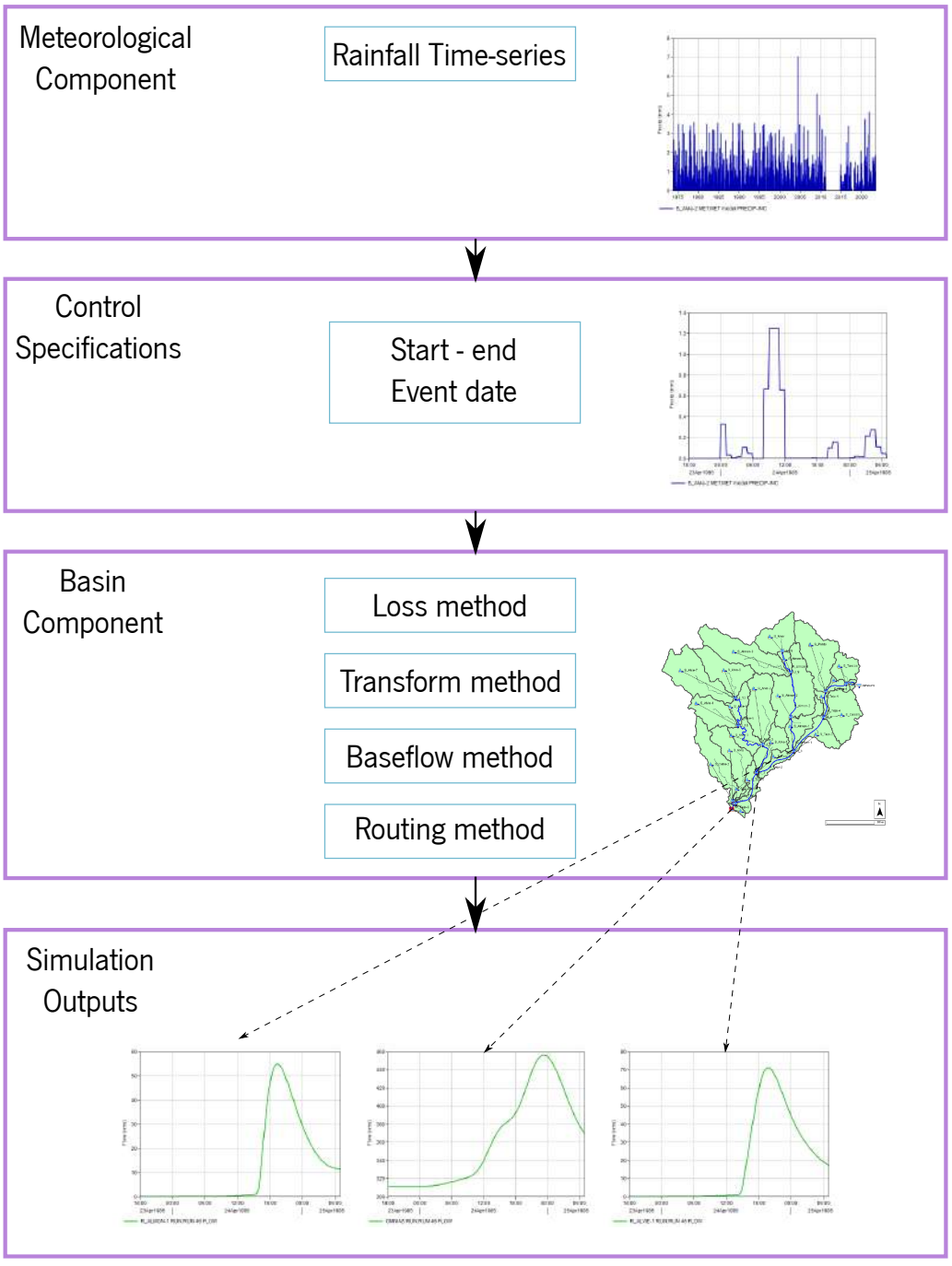


Figure B.9: Flowchart for the development of HEC-HMS model

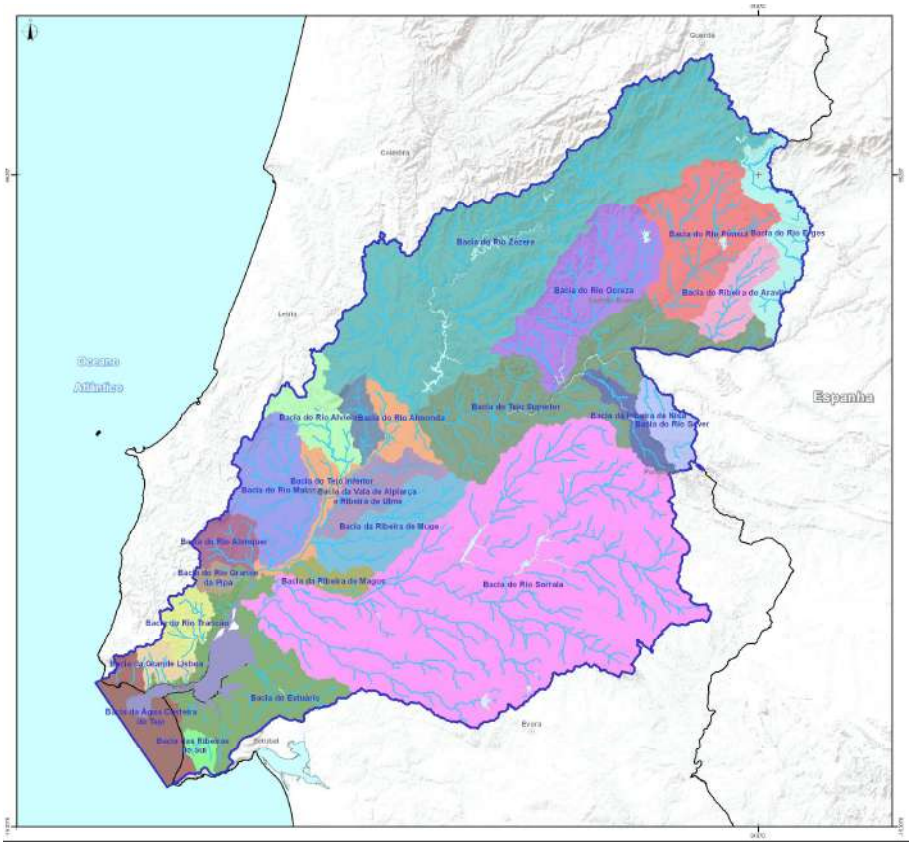


Figure B.10: Sub-basins of the Tagus River basin. Source: [25]

coincides with Ómnias station. Then, the streamflow observations at this station are used to calibrate and validate the model.

The main characteristics of the hydrologic elements identified in Figure B.11 can be found in Table B.1 and Table B.2, for sub-basins and reach elements, respectively.

B.4.2 Loss method

The loss method represents the amount of water lost to the ground due to infiltration. HEC-HMS has many methods to compute infiltration losses. Some are meant explicitly for continuous simulation, while others are for event simulation. In this study, the most commonly used SCS Curve number method is selected to compute losses and obtain the excess rainfall from the total rainfall.

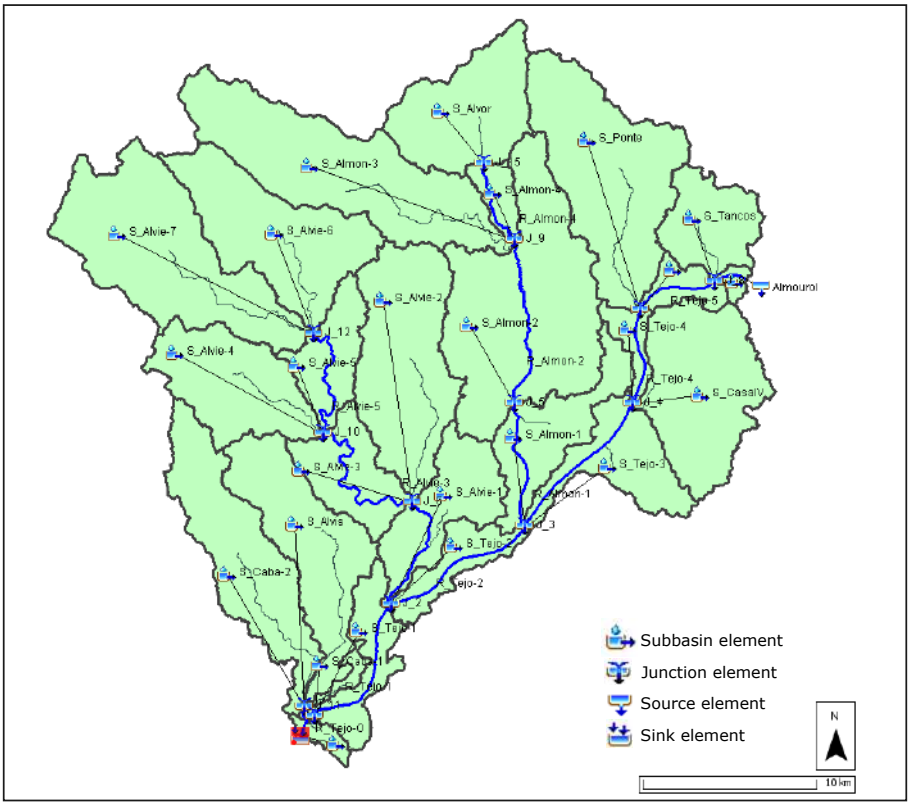


Figure B.11: HEC-HMS model of Central Tagus River Basin

The SCS method, developed by the Soil Conservation Service, can be used for larger areas than the rational method, which is generally limited to less than 60 acres (approximately 0.25 square kilometers). This method is used to estimate runoff for a given rainfall amount. It calculates surface runoff (or excess rainfall) using the Curve Number (CN), which correlates with land use and land cover, antecedent soil moisture, hydrologic condition, and soil moisture retention capacity. This method uses the following equations [28]:

$$P_e = \frac{(P - I_a)^2}{P - I_a + S'} \tag{B.1}$$

$$I_a = 0.2S \tag{B.2}$$

Table B.1: Sub-basins characteristics

Subbasin	Area (km^2)	Longest flowpath length (km)	Basin slope (m/m)
S_Almon-1	32.55	21	0.0249
S_Almon-2	98.01	19	0.0704
S_Almon-3	83.19	31	0.1502
S_Almon-4	8.21	6	0.1383
S_Alvie-1	33.39	16	0.0588
S_Alvie-2	65.11	19	0.0812
S_Alvie-3	27.32	15	0.0989
S_Alvie-4	44.19	14	0.1192
S_Alvie-5	22.28	13	0.1172
S_Alvie-6	59.22	20	0.1065
S_Alvie-7	81.94	23	0.1018
S_Alvis	53.49	22	0.0742
S_Alvor	45.37	10	0.1359
S_Caba-1	3.69	7	0.0284
S_Caba-2	56.36	25	0.1047
S_CasalV	58.42	16	0.1034
S_Ponte	76.15	20	0.0737
S_Tancos	26.29	8	0.1066
S_Tejo-O	4.16	4	0.0536
S_Tejo-1	22.29	13	0.0347
S_Tejo-2	17.27	10	0.0211
S_Tejo-3	30.62	15	0.0875
S_Tejo-4	8.17	9	0.0328
S_Tejo-5	9.50	7	0.0956
S_Tejo-6	2.73	4	0.1276

$$S = \frac{25400 - 254CN}{CN} \tag{B.3}$$

where P_e signifies the accumulated precipitation excess at time t, P denotes the accumulated rainfall depth at time t, I_a represents the initial abstraction, and S is the potential maximum retention. The CN parameter reflects hydrological conditions, land use, soil type, and prior moisture levels and can be determined using guidelines from authoritative sources. To account for variations due to the antecedent moisture conditions (AMC), the CN values should be adjusted to represent the appropriate moisture level: AMC I denotes drier conditions, AMC II indicates average moisture conditions, and AMC III corresponds to wetter states. The CN values pertinent to Portugal are available in a raster map from APA [121] for

Table B.2: Characteristics of reach elements

Reach	Length [km]	Slope [m/m]
R_Almon-1	8.27359	0.00040
R_Almon-2	11.94376	0.00159
R_Almon-4	5.66080	0.00283
R_Alvie-1	8.18823	0.00040
R_Alvie-3	12.69391	0.00110
R_Alvie-5	9.51200	0.00252
R_Caba-1	0.86222	0.00696
R_Tejo-0	1.10037	0.00040
R_Tejo-1	9.80338	0.00040
R_Tejo-2	9.92771	0.00040
R_Tejo-3	9.93387	0.00040
R_Tejo-4	6.10228	0.00040
R_Tejo-5	5.14369	0.00040
R_Tejo-6	2.10707	0.00040

the average moisture condition (AMC II). For AMC I and AMC III, CN values can be adjusted as follows to represent drier (CN I) and wetter (CN III) conditions, respectively [28]:

$$CN_I = \frac{CN_{II}}{2.281 - 0.01281 CN_{II}} \tag{B.4}$$

$$CN_{III} = \frac{CN_{II}}{0.427 + 0.00573 CN_{II}} \tag{B.5}$$

The CN II values were extracted for each sub-basin using zonal statistics operations in QGIS, calculating the mean of the cell values of the raster map within the zones defined by the sub-basins. Table B.3 summarizes the CN II values derived for each sub-basin and the estimated CN I and CN III values using Eq. B.4 and Eq.B.5, respectively.

The total precipitation in the five days prior to the simulation is used to define the AMC level. Mishra and Singh [28] provide thresholds of total precipitation to define the AMC level depending on the planting seasons. In the studied region of Portugal, agriculture is relatively active throughout the year, with different crops planted in different seasons. This continuous cycle of planting and harvesting suggests that there may not be a distinct dormant season as seen in other regions with more extreme seasonal temperature

Table B.3: Estimated CN values per sub-basin for each AMC level

Sub-basin	CN_I	CN_{II}	CN_{III}
S_Almon-1	70.91	84.76	92.87
S_Almon-2	56.67	74.89	87.48
S_Almon-3	68.17	83.01	91.96
S_Almon-4	59.59	77.09	88.74
S_Alvie-1	59.87	77.29	88.85
S_Alvie-2	69.00	83.55	92.24
S_Alvie-3	70.70	84.62	92.80
S_Alvie-4	64.42	80.51	90.63
S_Alvie-5	68.92	83.49	92.22
S_Alvie-6	69.40	83.80	92.38
S_Alvie-7	66.95	82.21	91.54
S_Alvis	70.19	84.30	92.63
S_Alvor	66.06	81.62	91.23
S_Caba-1	70.14	84.27	92.62
S_Caba-2	67.35	82.47	91.68
S_CasalV	57.90	75.83	88.02
S_Ponte	56.32	74.63	87.32
S_Tancos	49.95	69.48	84.20
S_Tejo-O	73.82	86.54	93.77
S_Tejo-1	76.50	88.13	94.56
S_Tejo-2	60.72	77.91	89.20
S_Tejo-3	74.11	86.72	93.86
S_Tejo-4	52.42	71.54	85.48
S_Tejo-5	61.18	78.24	89.38
S_Tejo-6	71.20	84.94	92.96

variations. Therefore, the thresholds of total precipitation for the growth period are adopted as shown in Table B.4.

Table B.4: Antecedent moisture conditions relative to the total precipitation in the five days prior [28]

Total Precipitation in the last five days (mm)	**AMC level**
< 36	AMC I
36 to 53	AMC II
> 53	AMC III

B.4.3 Transform method

The transform method represents the transformation of excess rainfall (total rainfall minus the losses) to direct runoff. In this study, the SCS Unit Hydrograph method is selected. The watershed response time (or lag time), denoted as t_{lag}, can be estimated through an iterative calibration process. In the absence of adequate data for calibration, SCS advises that the lag time is assumed to be 60% of the basin's concentration time, t_c [112]:

$$t_{lag} = 0.6t_c, \tag{B.6}$$

Additionally, the concentration time can be computed as follows, according to Hipólito and Vaz [124]:

$$t_c = 0.093 \left(\frac{L^{0.8}}{i^{0.5}} \left(\frac{1000}{CN} - 9 \right)^{0.7} \right) \tag{B.7}$$

where L is the distance to the reference section from the furthest point in the sub-basin, i is the mean slope of the sub-basin, and CN represents the curve number. Following Eqs.B.6-B.7, the response time and the concentration time for each sub-basin are estimated and presented in Table B.5.

B.4.4 Baseflow method

The baseflow method represents the sub-surface processes and computes the contribution of water flowing within the sub-surface into the streams [112]. In this study, the recession baseflow method, primarily used for event simulation, is selected to approximate the typical exponential decline of channel flow in watersheds after rainfall events [112]. In this method, a recession constant should be specified, which describes the rate at which baseflow recedes between rainfall events. Its value is subject to temporal variations influenced by groundwater recharge. It ranges from 0 to 1, where lower values represent a more rapid reduction of baseflow, and values approaching 1 suggest a slower decrease [122]. Moreover, a ratio to peak parameter should be specified, determining when the baseflow recession curve is added

Table B.5: Estimated response time and concentration time for each sub-basin

Sub-basin	T_{c,CN_I}	$T_{c,CN_{II}}$	$T_{c,CN_{III}}$	T_{lag,CN_I}	$T_{lag,CN_{II}}$	$T_{lag,CN_{III}}$
S_Almon-1	21.04	13.82	10.02	12.62	8.29	6.01
S_Almon-2	17.02	10.53	7.00	10.21	6.32	4.20
S_Almon-3	12.62	8.17	5.82	7.57	4.90	3.49
S_Almon-4	4.67	2.92	1.97	2.80	1.75	1.18
S_Alvie-1	14.51	9.07	6.14	8.70	5.44	3.68
S_Alvie-2	11.26	7.32	5.24	6.75	4.39	3.14
S_Alvie-3	8.31	5.45	3.95	4.98	3.27	2.37
S_Alvie-4	8.22	5.23	3.64	4.93	3.14	2.18
S_Alvie-5	6.82	4.43	3.17	4.09	2.66	1.90
S_Alvie-6	10.13	6.60	4.74	6.08	3.96	2.84
S_Alvie-7	12.59	8.10	5.72	7.55	4.86	3.43
S_Alvis	13.06	8.54	6.16	7.83	5.12	3.70
S_Alvor	5.80	3.72	2.61	3.48	2.23	1.57
S_Caba-1	8.84	5.78	4.17	5.30	3.47	2.50
S_Caba-2	13.07	8.43	5.97	7.84	5.06	3.58
S_CasalV	11.80	7.32	4.90	7.08	4.39	2.94
S_Ponte	17.08	10.55	7.01	10.25	6.33	4.20
S_Tancos	8.36	5.07	3.26	5.02	3.04	1.96
S_Tejo-0	3.72	2.49	1.84	2.23	1.49	1.10
S_Tejo-1	10.64	7.23	5.47	6.38	4.34	3.28
S_Tejo-2	17.00	10.66	7.25	10.20	6.40	4.35
S_Tejo-3	7.78	5.21	3.87	4.67	3.12	2.32
S_Tejo-4	14.80	9.03	5.89	8.88	5.42	3.53
S_Tejo-5	5.87	3.69	2.52	3.52	2.21	1.51
S_Tejo-6	2.33	1.53	1.11	1.40	0.92	0.67

to the total runoff hydrograph [112]. Based on the literature, the recession constant value is set as 0.8, and the ratio to peak is established as 0.2 [112, 122].

B.4.5 Routing method

A reach element represents a river (or stream) and has two methods: routing and loss/gain. The routing method accounts for the storage effects as the water travels downstream through the reach, while the loss/gain method accounts for water exchange/interaction between the stream and the subsurface [112]. In this study, the Muskingum-Cunge method is selected, as it aligns well with the characteristics of natural watercourses. This method computes parameters X and K using the relations below [112]:

$$K = \frac{\Delta x}{c} \tag{B.8}$$

$$X = \frac{1}{2}\left(1 - \frac{Q}{BS_0 c\Delta x}\right), \tag{B.9}$$

where Δx denotes the length of the river reach, c is the wave celerity, Q represents the flow rate during floods, B is the width of the floodplain, and S_0 is the channel slope. In the Muskingum-Cunge method, hydraulic parameters are computed at each time step based on the physical properties of the channel. Hence, the length, slope, cross-sectional shape, and Manning's roughness coefficient should be specified. A Manning number of 0.05 was adopted for all sections of the hydrographic network, corresponding to a value commonly used for natural watercourses [125]. The remaining physical properties were derived from the DEM.

B.4.6 Model Calibration and Evaluation

In this study, the main goal of the hydrologic model is to simulate the response of the watershed under various extreme rainfall events in order to capture the spatial and temporal dependencies in the streamflows, thus enabling the prediction of the development of floods across the watershed. Therefore, when used for prediction purposes, the calibration process should consider the variation of the model parameters over time, mainly in response to changing weather affecting the hydrological conditions [122]. To this aim, a similar procedure to that outlined in [122] is followed to calibrate and validate the hydrologic model. The methodology consists of finding the optimal values of the calibration parameters to model the observed streamflow for various hydro-meteorological states. After performing a sensitivity analysis by running several simulations and testing different parameter values to examine their impact on the predicted streamflow, it was found that the CN number had the most significant influence on the simulation results. Therefore, the CN number was established as the calibration parameter, whose value was correlated to the total precipitation in the 5 days preceding the event simulation, i.e., correlated to the antecedent moisture condition level, to account for the hydro-meteorological state of the watershed

at each simulation. The values from Table B.3 are used as the initial CN numbers for each sub-basin, considering the AMC condition associated with the simulation run. These values are then calibrated using a selection of rainfall events for each AMC condition, and the model with the calibrated parameters is validated in the remaining simulation runs.

Two accuracy statistics are used to evaluate the performance of the hydrological model, namely the Nash-Sutcliffe efficiency (NSE) and the percentage of bias (PBIAS). The NSE is a normalized statistic that reflects the correspondence of observed versus simulated data in a 1 to 1 line plot, which can be computed as [123]:

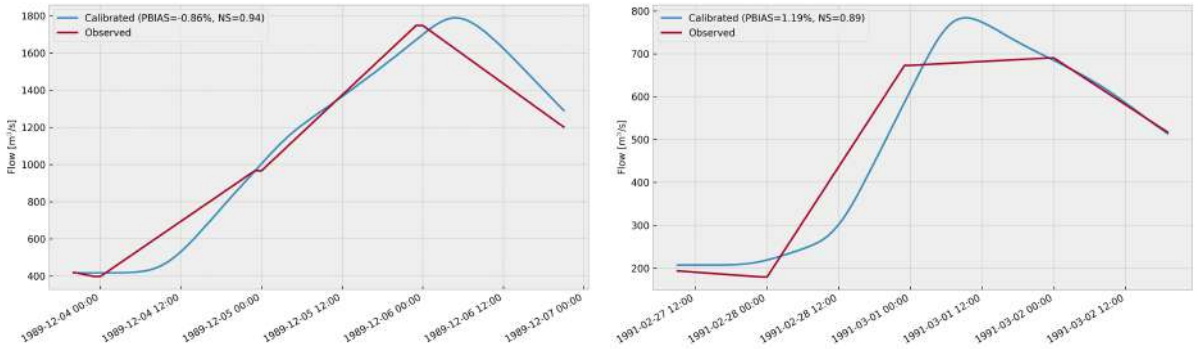
$$NSE = 1 - \frac{\sum_{i=1}^{n}(Y_i^{\text{obs}} - Y_i^{\text{sim}})^2}{\sum_{i=1}^{n}(Y_i^{\text{obs}} - \bar{Y}^{\text{mean}})^2} \tag{B.10}$$

where Y_i^{obs} is the ith observed flow, Y_i^{sim} is the ith simulated flow, $\bar{Y}^{\text{mean}}$ is the mean of observed flow, and n is the total number of observations or simulated data points. The second performance measure, PBIAS, evaluates the average tendency of the simulated data to either exceed or not reach the corresponding observed values. An ideal PBIAS score is zero, implying that low-magnitude values represent accurate model simulations. A positive PBIAS value suggests a bias toward underestimation by the model, whereas a negative value reveals a tendency for overestimation [123]. The PBIAS expressed in percentage can be computed as:

$$PBIAS = \frac{\sum_{i=1}^{n}(Y_i^{\text{obs}} - Y_i^{\text{sim}}) \times 100}{\sum_{i=1}^{n} Y_i^{\text{obs}}} \tag{B.11}$$

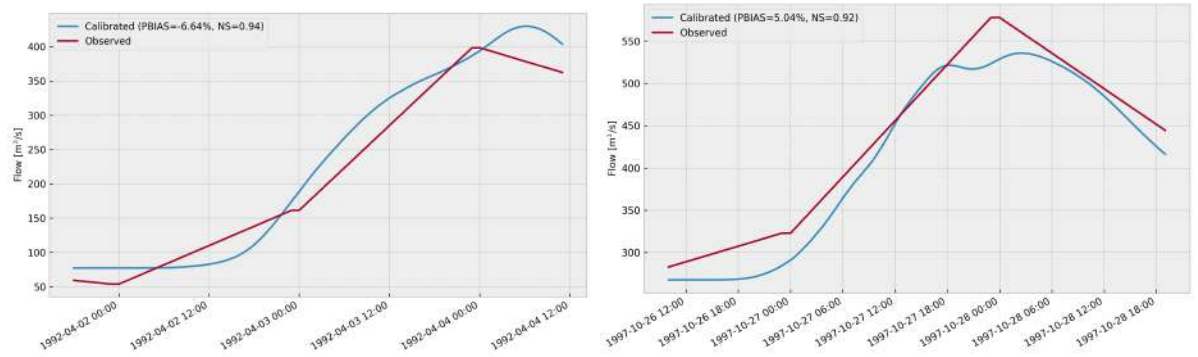
According to Moriasi et al. [123], the model simulation for streamflow can be deemed as satisfactory if $|PBIAS| < 25\%$ and $NS > 0.5$, good when $|PBIAS| < 15\%$ and $NS > 0.65$, and very good when $|PBIAS| < 10\%$ and $NS > 0.75$.

The results of some simulation runs after calibrating the CN numbers are presented in Figures B.12-B.13 for each AMC condition. The simulated flows are compared to the observed flows at Ómnias station, and the NSE and PBIAS statistics are computed to measure the accuracy of the hydrologic model and are plotted in each figure. Overall, the model simulations for the calibrated rainfall events present good



(a) (b)

Figure B.12: Comparison of the observed flow with simulation outputs performed with the calibrated CN values for AMC I

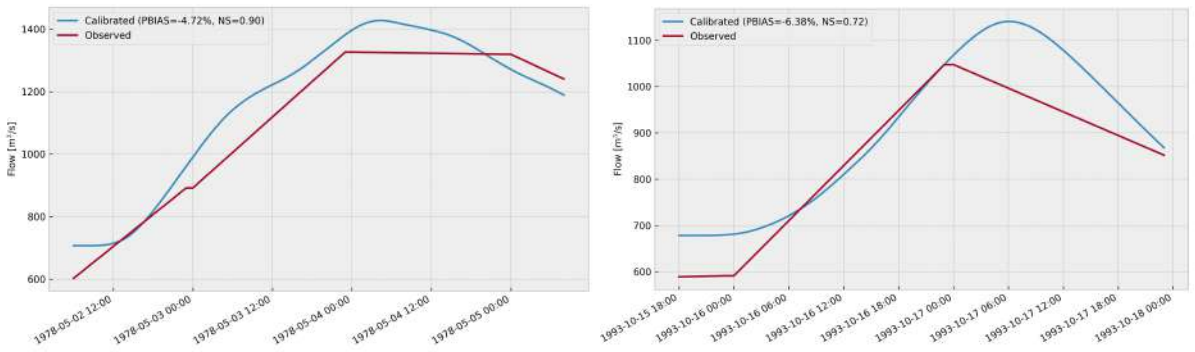


(a) (b)

Figure B.13: Comparison of the observed flow with simulation outputs performed with the calibrated CN values for AMC II

results, with PBIAS < 15% and NSE > 0.70. It is worth noting that one of the reasons for the observed graphical differences is attributed to the fact that observations at Ómnias station are provided as daily mean streamflows. Conversely, the simulation step of the hydrologic model is set at 10 minutes. Therefore, the actual maximum peak flow at Ómnias might not be recorded as inferred by Figure B.12b, where the peak flow from the model occurs at the middle of the observed time interval and is higher than the bounded recorded values.

Finally, when evaluating the accuracy of the remaining simulations, an average PBIAS of 18% is obtained, which indicates good model performance, while the average NS value is 0.46, which represents a satisfactory model performance.



(a) (b)

Figure B.14: Comparison of the observed flow with simulation outputs performed with the calibrated CN values for AMC III

Appendix C

Dataset of Roadway bridges

This appendix contains the inventory data required in Chapter 5 to assess the performance of bridges under flooding events. It focuses on 20 bridges from the Santarém case study as shown in Figure C.1, which are subsequently used in the risk assessment from Chapter 6. It is worth mentioning that the available information from the actual bridges was limited. Thus, several assumptions were made for the demonstration of the methodology. Consequently, the results presented in this study are not precise representations of the actual conditions.

C.1 Hydrodynamic forces on decks

As explained in Chapter 5, the coefficients for computing the hydrodynamic forces are determined following the fitting equations provided by [215] for the three girder bridges. These equations are a function of the inundation ratio h_a and are defined for this study as:

$$C_{D,d} = 1.8 \ \exp(-2\, h_a^2) - 2 \ \exp(-0.75\, h_a^2) + 1.95 \tag{C.1}$$

$$C_{L,d} = 2 \ (\exp(-3.5\, h_a^2) - \exp(-0.6\, h_a^{1.7})) \tag{C.2}$$

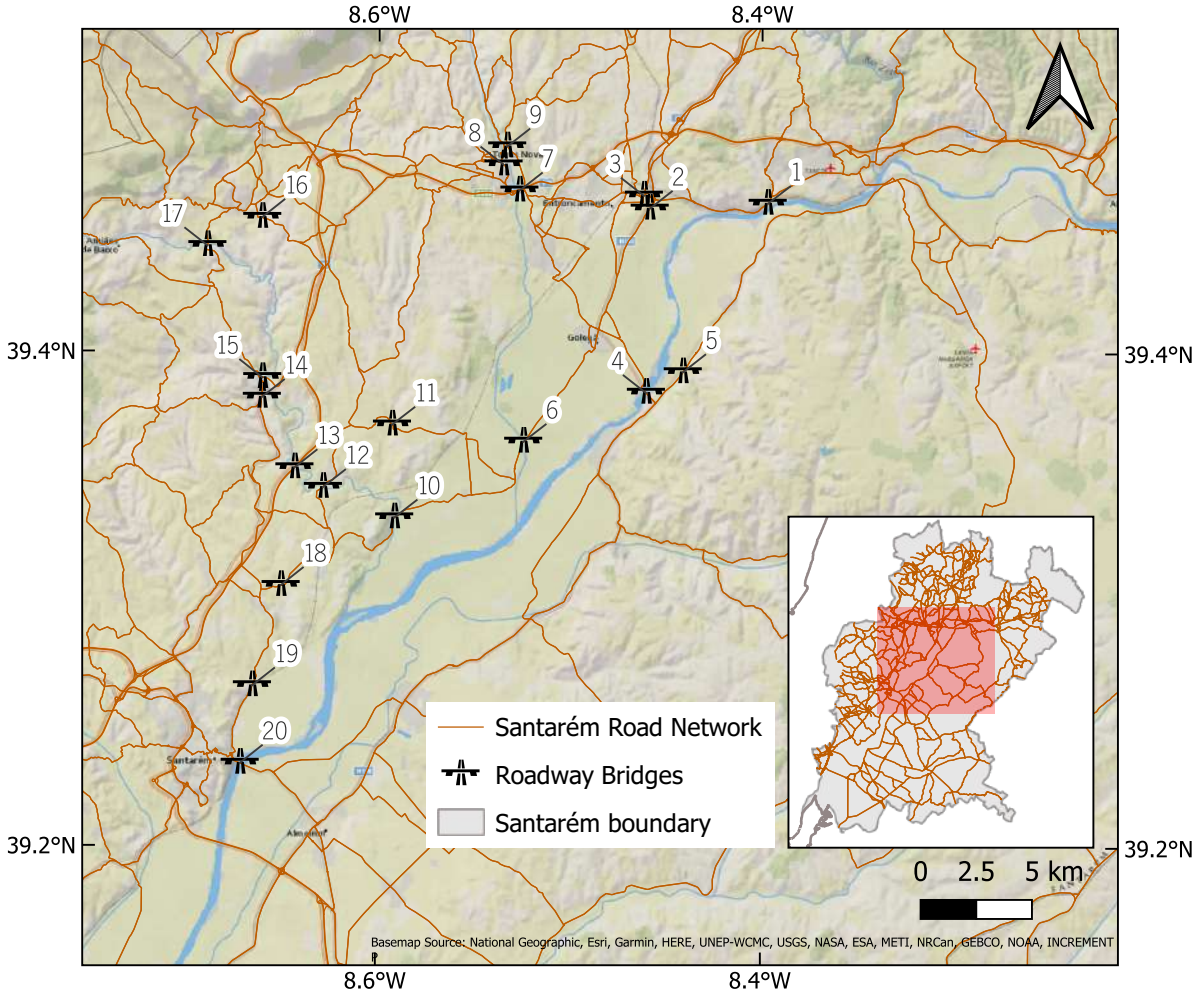


Figure C.1: Bridge network in Santarém, Portugal (reproduced from Chapter 6)

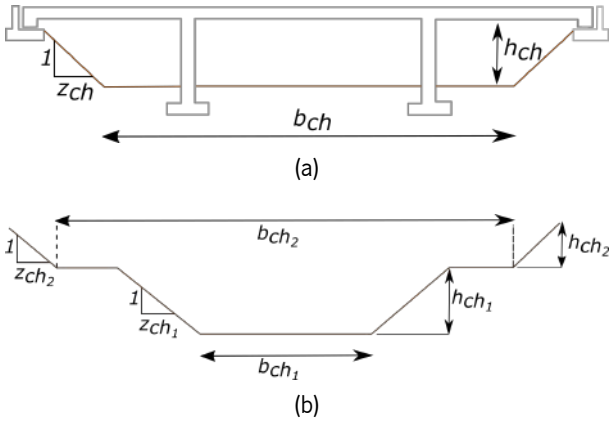


Figure C.2: River channel approximation as a) Trapezoidal channel; b) Compound channel

Table C.1: Applicable limit state functions (LSF) per bridge (1= Apply; 0=Not Apply)

ID	1: $G^{d,t}$	2: $G^{d,o}$	3: $G^{d,u}$	4: $G^{p,u}$	5: $G^{f,q}$	6: $G^{f,b}$	7: $G^{ma,u}$	8: $G^{a,s}$	9: $G^{a,u}$	10: $G^{mp,u}$
1	1	1	1	0	0	0	0	1	0	0
2	1	1	1	0	1	1	0	1	0	0
3	1	1	1	0	0	0	0	1	0	0
4	0	0	0	0	0	0	0	0	0	1
5	1	1	1	0	0	0	0	1	0	0
6	0	0	0	0	0	0	1	0	0	0
7	0	0	0	1	0	0	0	0	1	0
8	1	1	1	0	0	0	0	1	0	0
9	1	1	1	0	0	0	0	1	0	0
10	1	1	1	0	1	1	0	1	0	0
11	1	1	1	0	0	0	0	1	0	0
12	0	0	0	0	0	0	1	0	0	0
13	1	1	1	0	1	1	0	1	0	0
14	1	1	1	0	0	0	0	1	0	0
15	1	1	1	1	0	0	0	0	1	0
16	1	1	1	0	0	0	0	1	0	0
17	1	1	1	0	0	0	0	1	0	0
18	1	1	1	0	0	0	0	1	0	0
19	1	1	1	0	0	0	0	1	0	0
20	0	0	0	0	0	0	0	0	0	1

$$C_{M,d} = 0.8\, h_a^2\ \exp(-1.5\, h_a^2) - 0.11 \tag{C.3}$$

It can be inferred that the coefficient for the overturning moment on the deck $C_{M,d}$ can take positive and negative values. Essentially, for h_a values around 0.8, $C_{M,d}$ takes a maximum value of around 0.25 for three girder bridges, which suggests a stabilizing behavior. Conversely, as h_a increases, $C_{M,d}$ converges towards a constant value of -0.1, which implies a destabilizing effect where the deck's upstream portion lifts when significantly submerged [229]. This effect can be observed in Figure C.4, where the drag force, uplift force, and overturning moment are displayed for the bridge example of class 1 summarized in Chapter 5.

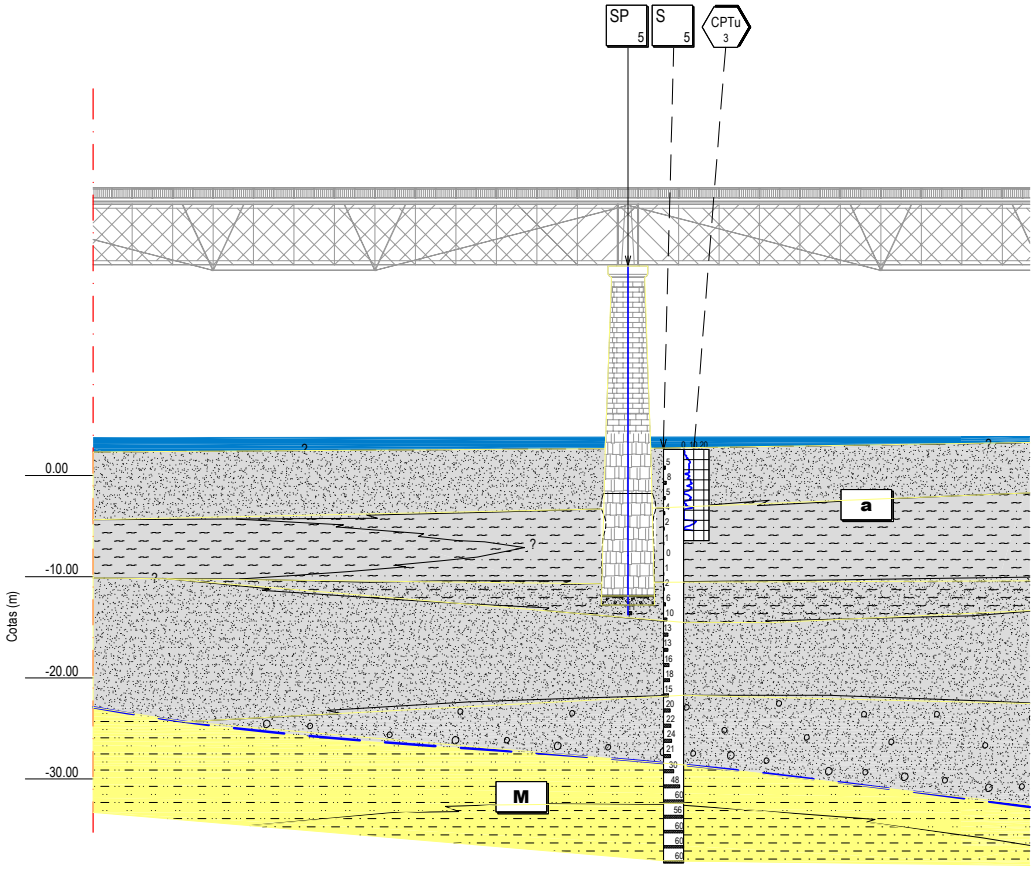


Figure C.3: Geotechnical profile at Pier 5 - Dom Luís bridge

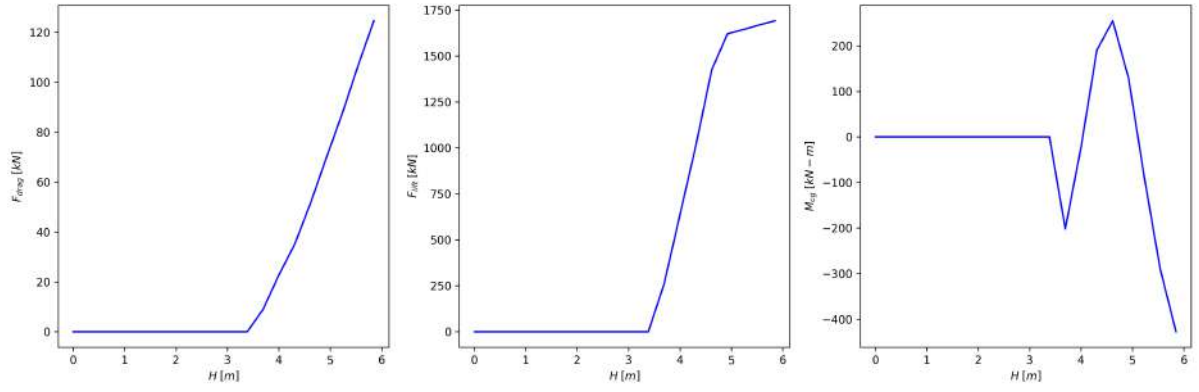


Figure C.4: Hydrodynamic forces on decks: Drag force (F_{drag}), Lift force (F_{lift} and Overturning moment (M_{cg})

Table C.2: Characteristics of the river channel at the asset location

Bridge ID	HMS element	h_{ch}	z_{ch}	b_{ch}	θ_f
1	S_Tancos	1.5	0.5	8.5	0
2	S_Ponte	4.05	0.5	10	20
3	S_Ponte	4.5	0.5	10	0
4	J_4[1]	-	-	-	15
5	S_CasalV	4	0.5	17.7	0
6	R_Almon-1	6	1	28	15
7	R_Almon-2	6	1	28	5
8	S_Almon-3	3	0.5	17	0
9	R_Almon-4	3	0.5	17	0
10	R_Alvie-1	5	1	50	20
11	S_Alvie-2	3	0.5	17	0
12	R_Alvie-3	5	1	30	0
13	R_Alvie-3	5	1	30	5
14	S_Alvie-4	3	0.5	12	0
15	R_Alvie-5	5	1	30	0
16	S_Alvie-6	3	0.5	12	0
17	S_Alvie-7	3	0.5	12	0
18	S_Alvis	3	0.5	13.5	0
19	S_Caba-2	3.5	0.5	13	0
20	J_1[1]	-	-	-	15

[1] Compound channel section

Table C.3: Bridge dimensions and rebuilding costs

Bridge ID	L_s	b_d	h_d	n_{beam}	n_{bars}	A_{bar} [mm^2]	C_{reb} [€/m^2]	F_{bt}
1	10	15.5	0.85	3	6	126.7	1000	0.85
2	26	15.5	1.5	3	12	506.7	1500	1
3	14	15.3	1.1	3	6	506.7	1000	0.85
4	75.3	8.5	8.5				2000	1.5
5	20	14.8	1.5	3	12	506.7	1000	0.85
6	20	7.4	1.5				1100	1.15
7	20	7.4	1.5	2			1200	1
8	20	7.4	1.5	2	4	506.7	1000	0.85
9	20	7.4	1.5	2	4	126.7	1000	0.85
10	30	10.5	1.8	3	12	506.7	1500	1
11	20	10.5	1.5	3	6	506.7	1000	0.85
12	20	10.5	1.5				1100	1.15
13	20	15.5	1.5	3	6	285.0	1500	1
14	15	10.5	1.15	3	6	506.7	1000	0.85
15	20	10.5	1.5	3			1200	1
16	15	10.5	1.15	3	6	126.7	1000	0.85
17	15	10.5	1.15	3	6	285.0	1000	0.85
18	16	9	1.25	2	4	506.7	1000	0.85
19	16	9	1.25	2	4	506.7	1000	0.85
20	58.6	8.5	8.5				2000	1.5

Table C.4: Mean values of soil-related parameters per bridge

Bridge ID	D_{50}	ϕ'_{s1}	γ_{s1}	c'_{s1}	de_{s1}	γ_{s1}	de_{s2}	Su_{s2}
1	0.25	28	19	5	3	17	7	337.5
2	0.25	34	19	5	3	17	7	337.5
3	0.25	28	19	5	3	17	7	337.5
4	0.5	30	17	0	3	17	7	337.5
5	1	34	19	5	3	17	7	337.5
6	4	34	19	5	3	17	7	337.5
7	4	34	19	5	3	17	7	337.5
8	4	34	19	5	3	17	7	337.5
9	4	34	19	5	3	17	7	337.5
10	16	34	19	5	3	17	7	337.5
11	16	34	19	5	3	17	7	337.5
12	16	34	19	5	3	17	7	337.5
13	16	34	19	5	3	17	7	337.5
14	16	34	19	5	3	17	7	337.5
15	16	34	19	5	3	17	7	337.5
16	16	34	19	5	3	17	7	337.5
17	16	34	19	5	3	17	7	337.5
18	1	34	19	5	3	17	7	337.5
19	1	34	19	5	3	17	7	337.5
20	0.5	30	17	0	3	17	7	337.5

Table C.5: Pier-foundation dimensions and characteristics (Shape: 0= Circular; 1=Rectangular)

Bridge ID	p_{shape}	b_p	h_p	l_p	pc_{shape}	b_{pc}	l_{pc}	t_{pc}	h_{bf}
2	1	1	4.05	14.5	1	3	15.5	1.5	0
4	1	3.85	18	7.7	-	-	-	-	-
6	1	2	6	6.4	1	4	8.4	1.2	2.5
7	1	0.5	6	6.4	1	2	8.4	1.5	2.5
10	1	0.5	5	9.5	1	2.5	10.5	1.5	0
12	1	1.7	5	9.5	1	3.4	11.5	1.2	2.5
13	1	1	5	14.5	1	3	15.5	1.5	0
15	1	1	5	9.5	1	2	11.5	1.5	2.5
20	1	3.85	18	7.7	-	-	-	-	-

Table C.6: Pile-supported foundation dimensions and characteristics (Shape: 0= Circular; 1=Rectangular)

Bridge ID	$pile_{shape}$	d_p	n_p	m_p	S_n	S_m	f_l	f_t
2	0	0.5	2	4	2	4	0.5	1
10	0	0.5	2	3	2	3	0.5	1
13	0	0.5	2	3	2	4	0.5	1

Appendix D

Traffic Model

As mentioned in Chapter 6, the traffic model was developed using AequilibraE, an open-source Python package for transportation network analysis [267]. The input data for the development of the model has been provided by Infraestruturas de Portugal (IP). Therefore, the modeling bases of IP's traffic model are summarized in Section D.1, based on the thorough description provided in [26]. Subsequently, the modeling bases adopted for the AequilibraE traffic model are outlined in Section D.3, with a validation of the obtained results compared with IP's traffic model results.

D.1 Traffic Model: Infraestruturas de Portugal

The Portuguese national traffic model has been designed, developed, and implemented using INRO's EMME software to estimate traffic volumes for both light and heavy vehicles (Figure D.1) [26]. The traffic demand was initially characterized based on a road mobility survey conducted in 2005 at 54 strategically placed locations throughout the national road network. Since 2010, the traffic model has been based on a parish-level zoning system. Currently, the national traffic model encompasses 4,084 zones, defining origin and destination (OD) matrices for both light and heavy vehicles [26]. The OD matrices are annually and periodically updated using data published by the National Institute of Statistics (INE) regarding the modal split of trips taken by the resident population per parish. This pertains to individuals who work

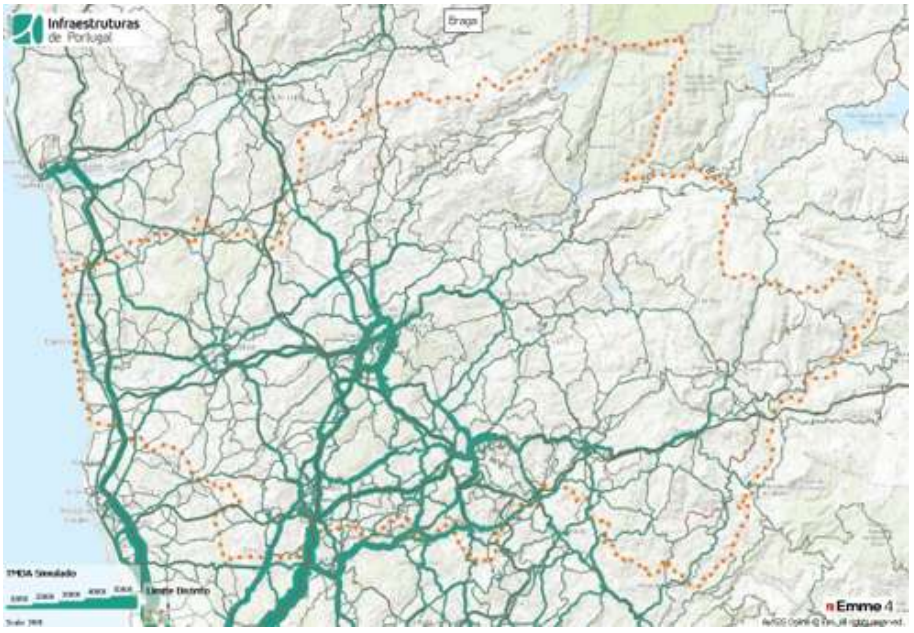


Figure D.1: Traffic Model Infraestruturas de Portugal (IP). Source: [26]

or study within the same parish, another parish within the same municipality, or a parish in a different municipality [26]. Additionally, models for trip generation and distribution have been developed. These models rely on factors such as the resident population, employed population, vehicle fleet, and factors related to distance, time, and toll cost transformed into time [26].

To characterize the traffic supply, i.e., the traffic capacity, an extensive and detailed characterization of the existing road network in Portugal was conducted. The geographic database includes the number of one-way lanes, type of road, free flow speed, toll information for each link, mode of transport supported on each link, and traffic volume recorded for monitored links (with counters). Currently, the supply is characterized by around 45,000 nodes and about 105,000 one-way links representing the road infrastructure, achieving coverage of about 50,000 km [26].

To perform the traffic assignment, the impact of road capacity on travel time is assessed using volume-delay functions ($t(v)$), which describe the travel time (or cost) on a road segment as a function of traffic volume (v). Typically, these functions are represented as the free flow time (t_0) multiplied by a normalized congestion function ($f(x)$) [283]:

$$t(v) = t_0 \; f(v/c) \tag{D.1}$$

where v/c represents the ratio of traffic volume to road capacity, with c indicating the road's capacity. Numerous volume-delay functions have been suggested and implemented in practice, with the BPR function being the most commonly applied (Bureau of Public Roads) [284]. IP's traffic model implements a conical congestion function, which can be defined as [283]:

$$t^c(v) = t_0 \left(2 - \beta - \alpha \left(1 - \frac{v}{c} \right) + \sqrt{\alpha^2 \left(1 - \frac{v}{c} \right)^2 + \beta^2} \right) \tag{D.2}$$

where t^c is the congested time, α is any number larger than 1, and β can be estimated as [283]:

$$\beta = \frac{2\alpha - 1}{2\alpha - 2} \tag{D.3}$$

The main attributes of each link type defined in IP's traffic model are summarized in Table D.1, with the parameters for the conical volume-delay functions adopted, which are depicted in Figure D.2.

Table D.1: Characteristics of links and VDF functions. Source: Infraestruturas de Portugal

ID	Link Type	Capacity	Free flow speed (km/h)	α	β^2
2	Toll-free highways	26000 PCE * lanes	120	12	1.093
3	Multi-lane roads	24000 PCE * lanes	55-75	12	1.093
4	Single-lane roads	16000 PCE * lanes	30-75	12	1.093
5	Highway (with tolls)	26000 PCE * lanes	120	12	1.093

Finally, the Portuguese national model has been calibrated through an iterative process to minimize the error between the actual traffic counts and the simulated volumes on monitored links in the roadway network [26]. Figure D.3 displays the correlation between the simulated volumes for light vehicles and the actual traffic counts for the year 2017. The regression analysis indicates a high degree of accuracy of the traffic model, evidenced by a coefficient of determination of 0.991.

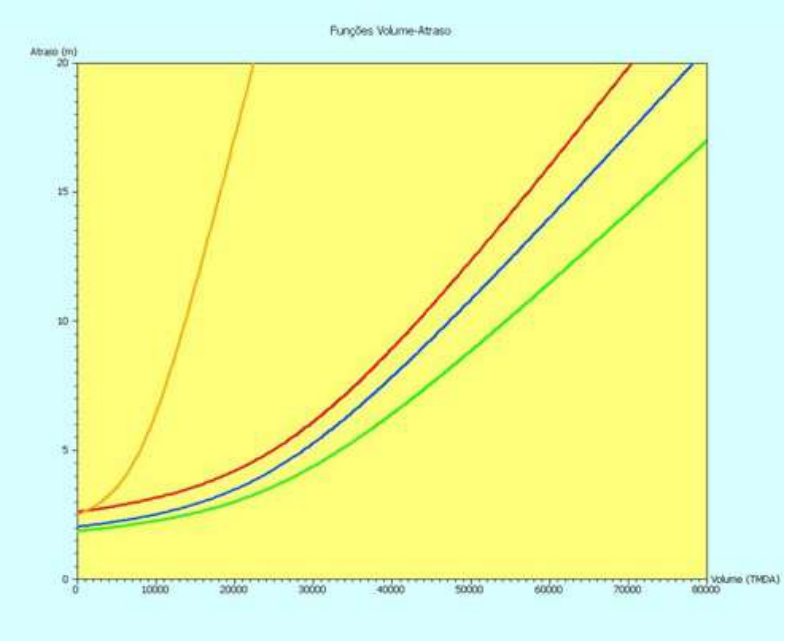


Figure D.2: Volume-delay functions for each link type in IP's traffic model. Source: [26]

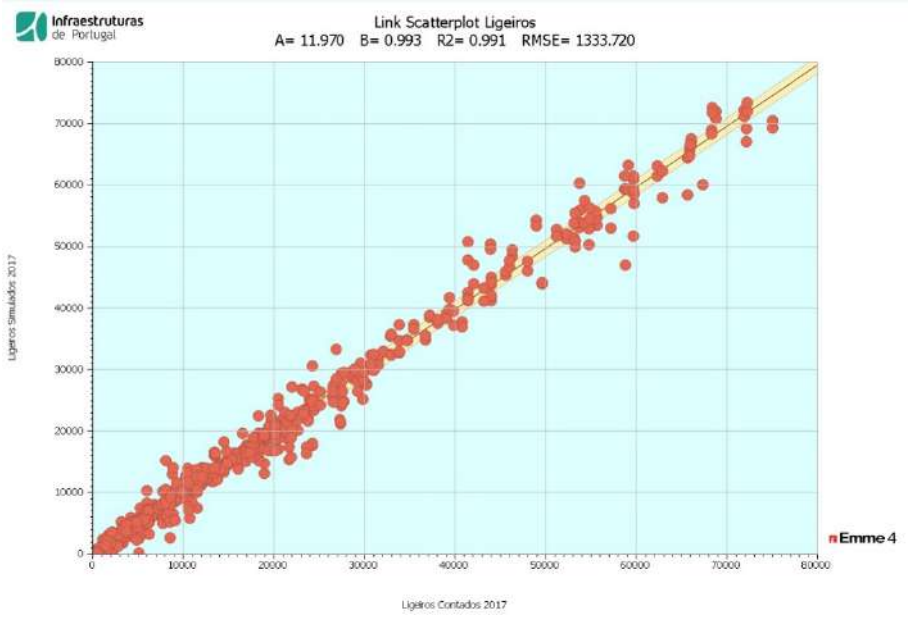


Figure D.3: Accurracy of IP's Traffic Model. Source: [26]

D.2 Santarém Roadway Network

The transportation network of the Santarém district has been extracted from the Portuguese national model and comprises 7,025 links and 879 nodes (Figure D.4). The origin/destination (OD) matrix accounts for a daily volume of 462,720 light vehicles and 32,190 heavy vehicles. As explained in Chapter 6, traffic demands are assumed to be rigid, meaning that flood events do not lead to any variation in the OD pairs and their associated demands. IP's traffic model assigns centroids representing the points of origin and destination for the matrix's trips. These are specific points in the network from where the traffic flows and define the trips in and out of the parish zones. Figure D.4 displays the centroids of the Santarém roadway network, identified as red dots, whose size varies according to the number of trips attracted to the node. The connectors, which are links that join the centroids to the roadway network, are represented by red links. It should be noted that the centroids and the connectors are virtual nodes and links, so they do not exist in reality. Figure 6.10 depicts the traffic flows of light vehicles, and Figure D.5 shows the traffic flows of heavy vehicles from the traffic assignment using IP's model. Moreover, Figure D.6 illustrates the capacity of each link in the roadway network in passenger car equivalents (PCE).

D.3 AequilibraE Traffic Model

The input data from the Santarém roadway network described in the previous section is used to develop the AequilibraE (AE) traffic model. To perform the multi-class equilibrium assignment, a factor of 1.75 PCE is assigned to the heavy vehicles. This factor is consistent with the one used in IP's traffic model, although the methodologies vary. In IP's approach, the process is sequential: the traffic assignment for heavy vehicles is conducted initially, and the results are saved. Subsequently, the traffic assignment for light vehicles is performed, with background traffic equivalent to 1.75 times the heavy vehicles. The conical volume delay function is used in the AE model with the parameters from Table D.1. In addition, fixed costs, i.e., tolls, associated with the traversal of certain links in the network are specified in the AE traffic model according to the values provided in [26] for light and heavy vehicles. Lastly, due to its fastest convergence time, the Biconjugate Frank-Wolfe algorithm is selected to solve the traffic assignment problem.

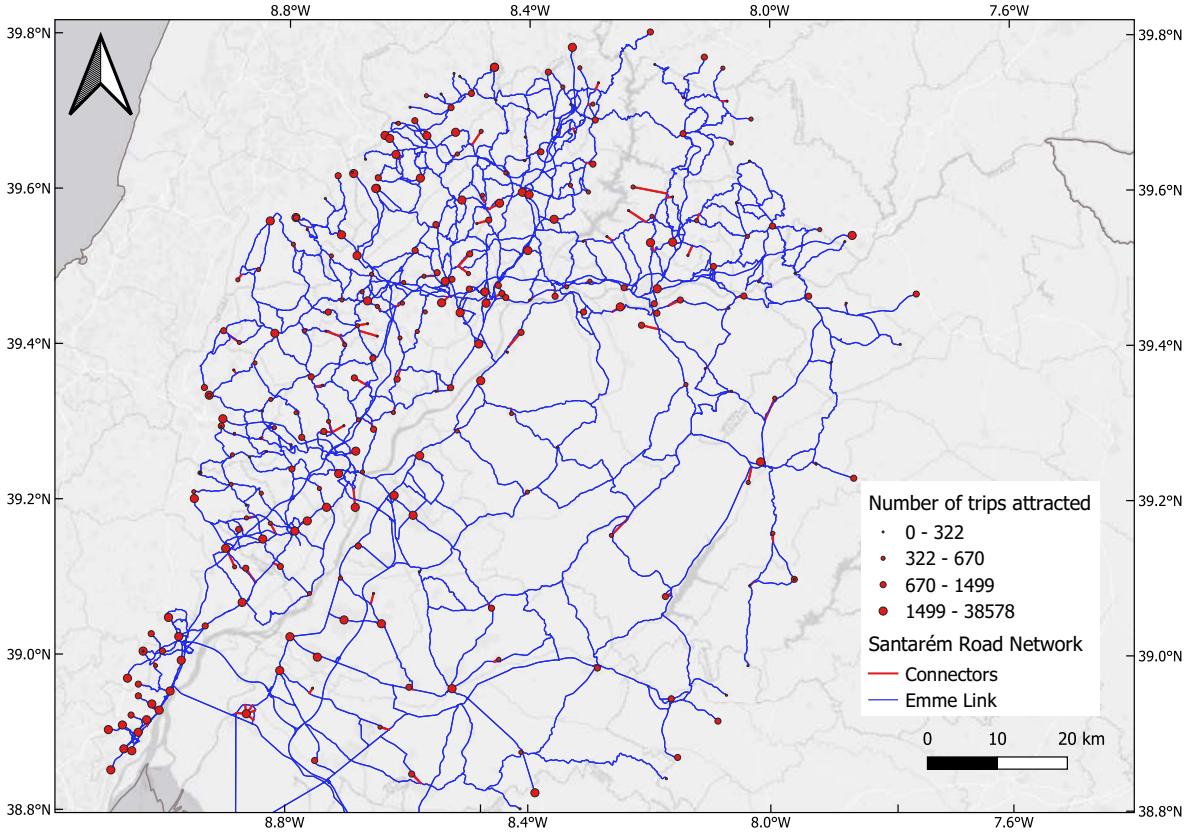


Figure D.4: Roadway network of Santarém district, Portugal. Source of data: Infraestruturas de Portugal

To validate the AE traffic model, the estimated travel time at each link is compared to the results of the calibrated IP model. Similarly to Chapter 4, the metrics used to quantify how well the AE traffic model matches IP's model are the mean square error (MSE), the mean absolute error (MAE), and the mean absolute percentage error (MAPE), as per [285]:

$$MAPE = \frac{1}{n}\sum_{t=1}^{n}\left|\frac{t_{l,IP} - t_{l,AE}}{t_{l,IP}}\right| \times 100 \tag{D.4}$$

where n is the number of links, $t_{l,IP}$ is the travel time per link obtained by IP's traffic model, and $t_{l,AE}$ is the predicted travel time per link obtained by AE's traffic model. The obtained metrics are MSE = 0.000104, MAE = 0.001706, and MAPE = 0.538426 %. Therefore, the AE model is considered to appropriately characterize the traffic in the Santarém roadway network under normal conditions. Finally, given the lack of traffic data during flooding events, validating the results from the disturbance scenarios analyzed in

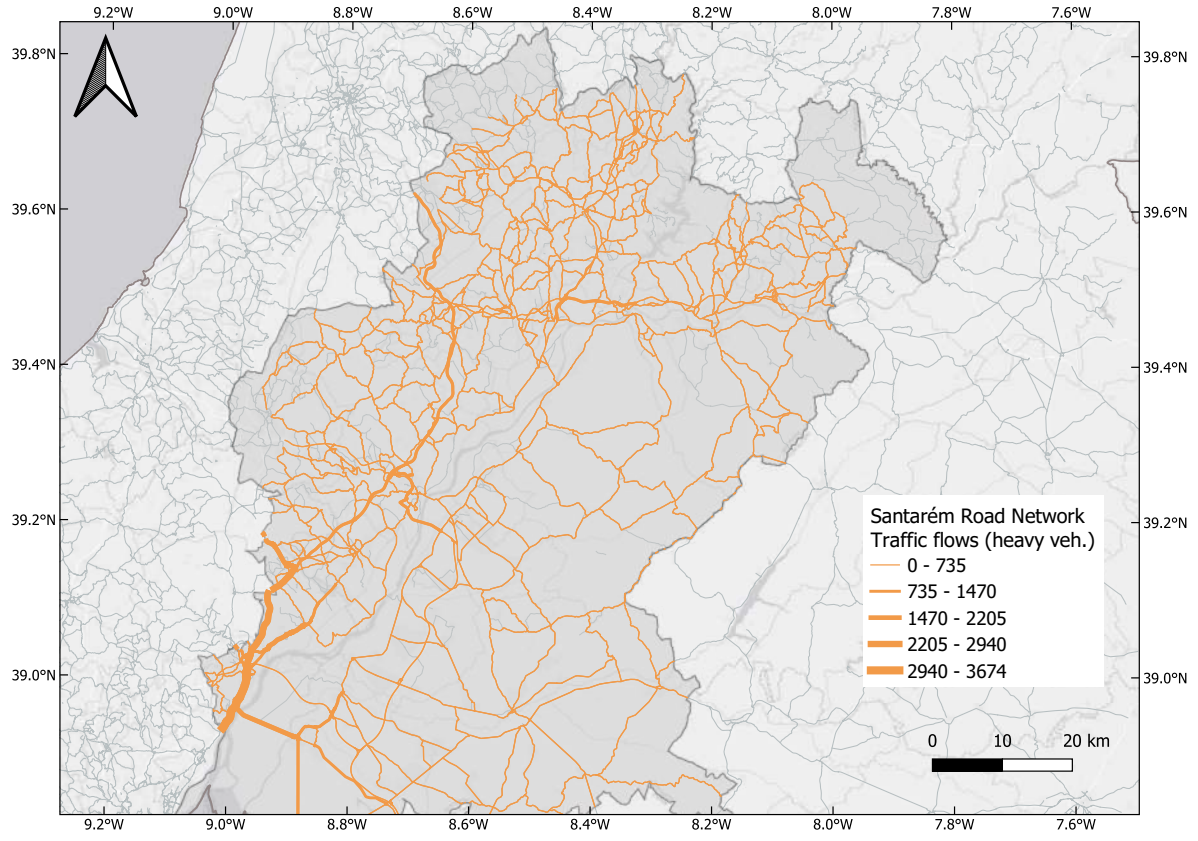


Figure D.5: Traffic flows (heavy vehicles) in Santarém roadway network. Source of data: Infraestruturas de Portugal

Chapter 6 is not feasible. Thus, it is assumed that the validation of the model with traffic counts during normal conditions is sufficient to predict traffic under disrupted conditions.

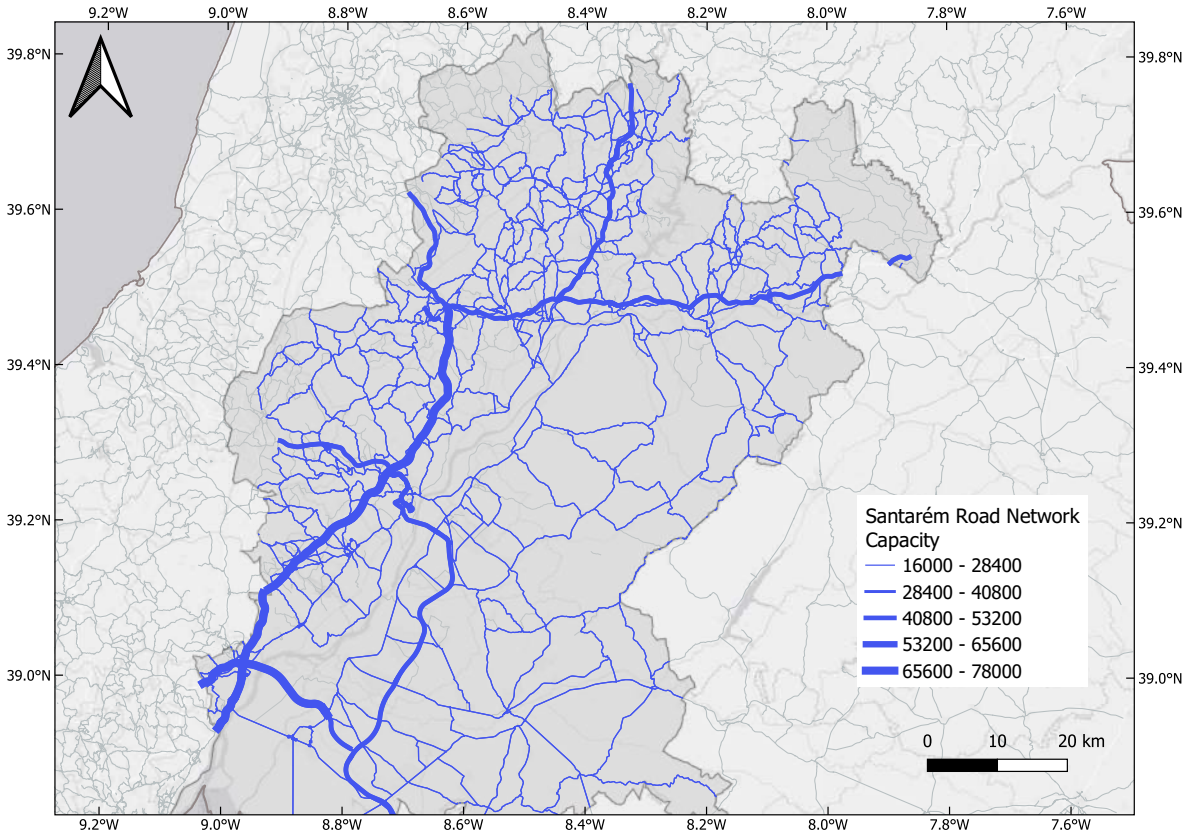


Figure D.6: Link capacity of Santarém roadway network. Source of data: Infraestruturas de Portugal

Bibliography

[1] Michael Havbro Faber. Risk informed structural systems integrity management: a decision analytical perspective. In *International Conference on Offshore Mechanics and Arctic Engineering*, volume 57779, page V009T12A040. American Society of Mechanical Engineers, 2017.

[2] Portugal Fotografia Aerea. Cheias do rio tejo. Available at: https://portugalfotografiaaerea.blogspot.com/2013/04/cheias-do-rio-tejo.html, 2013. Accessed: 20/06/20.

[3] Michael Havbro Faber. *On sustainability and resilience of engineered systems*. Routledge Abingdon, 2018.

[4] Kristin Vogel, Carsten Riggelsen, Oliver Korup, and Frank Scherbaum. Bayesian network learning for natural hazard analyses. *Natural Hazards and Earth System Sciences*, 14(9):2605–2626, 2014.

[5] Departamento de Monitorização de Recursos Hídricos da Agência Portuguesa do Ambiente (APA), I.P. Sistema nacional de informação de recursos hídricos. Available at: https://snirh.apambiente.pt/. Accessed on 03/11/2021.

[6] Agência Portuguesa do Ambiente (APA), I.P. Bacias hidrográficas das massas de Água de portugal continental: Conjunto de dados geográficos sniamb. Available at: https://sniambgeoviewer.apambiente.pt/Geodocs/shpzips/wise_vw_surfacewaterbody_basin_ptcont.zip, 2018. Accessed on 03/11/2021.

[7] Agência Portuguesa do Ambiente (APA), I.P. Massas de Água superficiais rios de portugal continental: Conjunto de dados geográficos sniamb. Available at: https://sniambgeoviewer.

apambiente.pt/Geodocs/shpzips/wise_vw_surfacewaterbody_river_line_ptcont.zip, 2018. Accessed on 03/11/2021.

[8] Georgii Bocharov. pyextremes. https://georgebv.github.io/pyextremes, 2023.

[9] Michael H Faber, Jianjun Qin, Simona Miraglia, and Sebastian Thöns. On the probabilistic characterization of robustness and resilience. *Procedia engineering*, 198:1070–1083, 2017.

[10] Jayadipta Ghosh and Jamie E Padgett. Aging considerations in the development of time-dependent seismic fragility curves. *Journal of Structural Engineering*, 136(12):1497–1511, 2010.

[11] Alysson Mondoro and Dan M Frangopol. Risk-based cost-benefit analysis for the retrofit of bridges exposed to extreme hydrologic events considering multiple failure modes. *Engineering Structures*, 159:310–319, 2018.

[12] LA Arneson. Evaluating scour at bridges. Technical report, United States. Federal Highway Administration, 2013.

[13] D.M. Sheppard and R. Renna. *Bridge Scour Manual*. State of Florida Department of Transportation, Tallahassee, FL, USA, 2010.

[14] Jean-Louis Briaud, Mabel Chedid, et al. Allowable limit contraction and abutment scour at bridges: Technical report. Technical report, Texas A&M Transportation Institute, 2019.

[15] Nikola Tanasić and Rade Hajdin. Management of bridges with shallow foundations exposed to local scour. *Structure and Infrastructure Engineering*, 14(4):468–476, 2018.

[16] Nikola S Tanasić. Vulnerability of reinforced concrete bridges to local scour in bridge management. *University of Belgrade*, 2015.

[17] LimitState. LimitStateGEO: Geotechnical analysis software. Available at: https://www.limitstate.com/geo, n.d.

[18] Michael H Faber, Simona Miraglia, Jianjun Qin, and Mark G Stewart. Bridging resilience and sustainability-decision analysis for design and management of infrastructure systems. *Sustainable and Resilient Infrastructure*, 5(1-2):102–124, 2020.

[19] Daniel Albalate and Xavier Fageda. On the relationship between congestion and road safety in cities. *Transport policy*, 105:145–152, 2021.

[20] Paolo Bocchini and Dan M Frangopol. Restoration of bridge networks after an earthquake: Multicriteria intervention optimization. *Earthquake Spectra*, 28(2):427–455, 2012.

[21] Sonia I. Seneviratne, Muhammad Adnan, Wafae Badi, Claudine Dereczynski, Alejandro Di Luca, Subimal Ghosh, Iskhaq Iskandar, James Kossin, Sophie Lewis, Friederike Otto, Izidine Pinto, Masaki Satoh, Sergio M. Vicente-Serrano, Michael Wehner, and Botao Zhou. *Weather and Climate Extreme Events in a Changing Climate*, pages 1513 – 1766. Cambridge University Press, Cambridge, 2022.

[22] Rodrigo Proença de Oliveira. Os caudais no rio tejo: enquadramento na convenção de albufeira e diretiva quadro da Água. Available at: https://aprh.pt/wp-content/uploads/2022/05/Tejo30Out2019_RodrigoOliveira.pdf, 2019.

[23] Agência Portuguesa do Ambiente (APA), I.P. Cartas de zonas inundáveis de riscos de inundações da rh5a – tejo e ribeiras do oeste. Available at: https://www.apambiente.pt/agua/2o-ciclo-de-planeamento-2016-2021, 2020.

[24] Javier Diez-Sierra, Salvador Navas, and Manuel del Jesus. Neoprene v1. 0.1: A python library for generating spatial rainfall based on the neyman-scott process. *EGUsphere*, 2023:1–19, 2023.

[25] I.P. Agência Portuguesa do Ambiente (APA). Plano de gestão da região hidrográfica do tejo. Available at: https://www.apambiente.pt/agua/1o-ciclo-de-planeamento-2010-2015, 2012.

[26] José Alexandre Narigueta Maçarico, Bruno Miguel Aldeia Correia, and Idalina Conceição Nunes. O modelo nacional de tráfego e a sua evolução natural para um modelo nacional multimodal de transportes. In *9º Congresso Rodoviário Português*, Lisboa, LNEC, Maio 2019.

[27] U.S. Department of Transportation Federal Highway Administration. NBI ASCII files - National Bridge Inventory - Bridge Inspection - Safety - Bridges & Structures - Federal Highway Administration, 2019.

[28] Surendra Kumar Mishra and Vijay Singh. *Soil conservation service curve number (SCS-CN) methodology*, volume 42. Springer Science & Business Media, 2003.

[29] Samuel A. Markolf, Christopher Hoehne, Andrew Fraser, Mikhail V. Chester, and B. Shane Underwood. Transportation resilience to climate change and extreme weather events – beyond risk and robustness. *Transport Policy*, 74:174–186, 2019. ISSN 0967-070X. doi: https://doi.org/10.1016/j.tranpol.2018.11.003. URL https://www.sciencedirect.com/science/article/pii/S0967070X17305000.

[30] Gkoumas K, Marques Dos Santos F, Van Balen M, Tsakalidis A, Ortega Hortelano A, Grosso M, Haq A, and Pekar F. Research and innovation in bridge maintenance, inspection and monitoring. Scientific analysis or review KJ-1A-29650-EN-N (online),KJ-1A-29650-EN-C (print), Luxembourg (Luxembourg), 2019.

[31] Maurizio Morgese, Farhad Ansari, Marco Domaneschi, and Gian Paolo Cimellaro. Post-collapse analysis of morandi's polcevera viaduct in genoa italy. *Journal of Civil Structural Health Monitoring*, 10:69–85, 2020.

[32] Elco Koks, Kees Van Ginkel, Margreet Van Marle, and Anne Lemnitzer. Critical infrastructure impacts of the 2021 mid-july western european flood event. In *EGU General Assembly Conference Abstracts*, pages EGU22–13096, 2022.

[33] Alessandro Pucci, Daniel Eickmeier, Hélder S Sousa, Linda Giresini, José C Matos, and Ralph Holst. Fragility analysis based on damaged bridges during the 2021 flood in germany. *Applied Sciences*, 13(18):10454, 2023.

[34] Mark Stewart and Robert E Melchers. *Probabilistic risk assessment of engineering systems*. Springer, 1997.

[35] Michael H Faber and Mark G Stewart. Risk assessment for civil engineering facilities: critical overview and discussion. *Reliability engineering & system safety*, 80(2):173–184, 2003.

[36] Elco E Koks, Julie Rozenberg, Conrad Zorn, Mersedeh Tariverdi, Michalis Vousdoukas, SA Fraser, JW Hall, and Stephane Hallegatte. A global multi-hazard risk analysis of road and railway infrastructure assets. *Nature communications*, 10(1):1–11, 2019.

[37] Linda Nielsen, Sebastian Tølbøll Glavind, Jianjun Qin, and Michael H. Faber. Faith and fakes – dealing with critical information in decision analysis. *Civil Engineering and Environmental Systems*, 36(1):32–54, 2019. doi: 10.1080/10286608.2019.1615476.

[38] JCSS. Risk assessment in engineering—principles, system representation & risk criteria. *Joint Committee on Structural Safety*, 2008.

[39] MH Faber. Codified risk informed decision making for structures. In *Symposium on Reliability of Engineering System, SRES2015, Hangzou, China*, pages 15–17, 2015.

[40] JCSS. Risk assessment in engineering—principles, system representation & risk criteria. *Joint Committee on Structural Safety*, 2008.

[41] Robert Schlaifer and Howard Raiffa. *Applied statistical decision theory*. MIT Press, 1961.

[42] Sebastian Thöns and Michael Havbro Faber. Assessing the value of structural health monitoring. In *ICOSSAR'13-11th International conference on structural safety and reliability-Safety, reliability, risk and life-cycle performance of structures and infrastructures (Proceedings)*, pages 1–8. CRC Press, 2013.

[43] Wei-Heng Zhang, Da-Gang Lu, Jianjun Qin, Sebastian Thöns, and Michael Havbro Faber. Value of information analysis in civil and infrastructure engineering: a review. *Journal of Infrastructure Preservation and Resilience*, 2(1):16, 2021.

[44] Jürgen Hackl, Juan Carlos Lam, Magnus Heitzler, Bryan T Adey, and Lorenz Hurni. Estimating network related risks: A methodology and an application in the transport sector. *Natural Hazards and Earth System Sciences*, 18(8):2273–2293, 2018.

[45] Ioannis Kilanitis and Anastasios Sextos. Integrated seismic risk and resilience assessment of roadway networks in earthquake prone areas. *Bulletin of earthquake engineering*, 17(1):181–210, 2019.

[46] Ning Zhang and Alice Alipour. Flood risk assessment and application of risk curves for design of mitigation strategies. *International Journal of Critical Infrastructure Protection*, 36:100490, 2022.

[47] Matteo Maria Messore, Luca Capacci, and Fabio Biondini. Life-cycle cost-based risk assessment of aging bridge networks. *Structure and Infrastructure Engineering*, 17(4):515–533, 2020.

[48] SAFEWAY. GIS-based Infrastructure Management System for Optimized Response to Extreme Events on Terrestrial Transport Networks. Grant Agreement No. 769255. Available at:https://www.safeway-project.eu/, 2019.

[49] Agência Lusa. Médio tejo: Municípios reivindicam apoios do governo para prejuízos da tempestade 'elsa'. Available at: https://www.mediotejo.net/medio-tejo-municipios-reivindicam-apoios-do-governo-para-prejuizos-da-tempestade-elsa-c-audio/, 2020. Accessed: 20/06/20.

[50] Agência Portuguesa do Ambiente (APA), I.P. Risk associated with flood-prone areas. Available at: https://rea.apambiente.pt/content/risk-associated-flood-prone-areas?language=en, 2016. Accessed: 20/06/20.

[51] Mark Roberts, Theophile Bougna, Martin Melecky, and Yan Xu. Transport corridors and their wider economic benefits: A critical review of the literature. *World Bank Policy Research Working Paper*, 1(8302), 2018.

[52] Julie Rozenberg and Marianne Fay. *Beyond the gap: How countries can afford the infrastructure they need while protecting the planet*. World Bank Publications, 2019.

[53] Stephane Hallegatte, Jun Rentschler, and Julie Rozenberg. *Lifelines: The resilient infrastructure opportunity*. World Bank Publications, 2019.

[54] World Meteorological Association et al. Wmo atlas of mortality and economic losses from weather, climate and water extremes (1970–2019). Technical report, Technical Report, 2021.

[55] ISO. Iso 31010:2009; risk management — risk assessment techniques, 2009.

[56] ISO. Iso 13824:2009; bases for design of structures — general principles on risk assessment of systems involving structures, 2009.

[57] Paolo Gardoni and Colleen Murphy. Society-based design: promoting societal well-being by designing sustainable and resilient infrastructure. *Sustainable and Resilient Infrastructure*, 5(1-2):4–19, 2020. doi: 10.1080/23789689.2018.1448667.

[58] Crawford S Holling. Resilience and stability of ecological systems. *Annual review of ecology and systematics*, 4(1):1–23, 1973.

[59] Wenjuan Sun, Paolo Bocchini, and Brian D. Davison. Resilience metrics and measurement methods for transportation infrastructure: the state of the art. *Sustainable and Resilient Infrastructure*, 5(3):168–199, 2020. doi: 10.1080/23789689.2018.1448663. URL https://doi.org/10.1080/23789689.2018.1448663.

[60] Luca Capacci, Fabio Biondini, and Dan M Frangopol. Resilience of aging structures and infrastructure systems with emphasis on seismic resilience of bridges and road networks. *Resilient Cities and Structures*, 1(2):23–41, 2022.

[61] Sotirios A Argyroudis. Resilience metrics for transport networks: a review and practical examples for bridges. In *Proceedings of the Institution of Civil Engineers-Bridge Engineering*, pages 1–14. Thomas Telford Ltd, 2022.

[62] Shouzheng Pan, Hai Yan, Jia He, and Zhengbing He. Vulnerability and resilience of transportation systems: A recent literature review. *Physica A: Statistical Mechanics and its Applications*, 581: 126235, 2021.

[63] Maria Nogal and Alan O'Connor. Resilience assessment of transportation networks. In *Routledge Handbook of Sustainable and Resilient Infrastructure*, pages 199–215. Routledge, 2018.

[64] Michel Bruneau, Stephanie E Chang, Ronald T Eguchi, George C Lee, Thomas D O'Rourke, Andrei M Reinhorn, Masanobu Shinozuka, Kathleen Tierney, William A Wallace, and Detlof Von Winterfeldt. A framework to quantitatively assess and enhance the seismic resilience of communities. *Earthquake spectra*, 19(4):733–752, 2003.

[65] Bilal M Ayyub. Systems resilience for multihazard environments: Definition, metrics, and valuation for decision making. *Risk analysis*, 34(2):340–355, 2014.

[66] Neetesh Sharma, Armin Tabandeh, and Paolo Gardoni. Resilience analysis: A mathematical formulation to model resilience of engineering systems. *Sustainable and Resilient Infrastructure*, 3 (2):49–67, 2018.

[67] Alice Alipour and Behrouz Shafei. Seismic resilience of transportation networks with deteriorating components. *Journal of Structural Engineering*, 142(8):C4015015, 2016.

[68] Ioannis Kilanitis and Anastasios Sextos. Impact of earthquake-induced bridge damage and time evolving traffic demand on the road network resilience. *Journal of traffic and transportation engineering (English edition)*, 6(1):35–48, 2019.

[69] Eric D Vugrin, Mark A Turnquist, and Nathanael JK Brown. Optimal recovery sequencing for enhanced resilience and service restoration in transportation networks. *International Journal of Critical Infrastructures*, 10(3-4):218–246, 2014.

[70] YuanChi Liu, Sue McNeil, Jürgen Hackl, and Bryan T Adey. Prioritizing transportation network recovery using a resilience measure. *Sustainable and Resilient Infrastructure*, 7(1):70–81, 2022.

[71] WSA Saunders and JS Becker. A discussion of resilience and sustainability: Land use planning recovery from the canterbury earthquake sequence, new zealand. *International journal of disaster risk reduction*, 14:73–81, 2015.

[72] Zoubir Lounis and Therese P McAllister. Risk-based decision making for sustainable and resilient infrastructure systems. *Journal of Structural Engineering*, 142(9):F4016005, 2016.

[73] Paolo Gardoni. *Routledge handbook of sustainable and resilient infrastructure*. Routledge, 2018.

[74] Naveen Donthu, Satish Kumar, Debmalya Mukherjee, Nitesh Pandey, and Weng Marc Lim. How to conduct a bibliometric analysis: An overview and guidelines. *Journal of Business Research*, 133: 285–296, 2021.

[75] Linda Nielsen and Michael H. Faber. Impacts of sustainability and resilience research on risk governance, management and education. *Sustainable and Resilient Infrastructure*, 6(6):339–384, 2021. doi: 10.1080/23789689.2019.1611056.

[76] Michael Havbro Faber, Marc A Maes, Jack W Baker, Ton Vrouwenvelder, and Tsuyoshi Takada. Principles of risk assessment of engineered systems. In *10th International Conference on Application of Statistic and Probability in Civil Engineering (ICASP10)*, 2007.

[77] Zehra Irem Turksezer, Maria Pina Limongelli, and Michael Havbro Faber. On a generic framework for systems resilience modelling of bridges - accounting for historic and cultural values. *Sustainable and Resilient Infrastructure*, 0(0):1–14, 2020. doi: 10.1080/23789689.2020.1859272. URL https://doi.org/10.1080/23789689.2020.1859272.

[78] Daniel Straub. Lecture notes in engineering risk analysis, 2018.

[79] Yahya Y Bayraktarli and Michael H Faber. Bayesian probabilistic network approach for managing earthquake risks of cities. *Georisk*, 5(1):2–24, 2011.

[80] Oskar Morgenstern and John Von Neumann. *Theory of games and economic behavior*. Princeton university press, 1953.

[81] Ning Zhang and Alice Alipour. Multi-scale robustness model for highway networks under flood events. *Transportation research part D: transport and environment*, 83:102281, 2020.

[82] Ning Zhang and Alice Alipour. A multi-step assessment framework for optimization of flood mitigation strategies in transportation networks. *International Journal of Disaster Risk Reduction*, 63: 102439, 2021.

[83] William HK Lam, Hu Shao, and Agachai Sumalee. Modeling impacts of adverse weather conditions on a road network with uncertainties in demand and supply. *Transportation research part B: methodological*, 42(10):890–910, 2008.

[84] Sotirios Argyroudis, Jacopo Selva, Pierre Gehl, and Kyriazis Pitilakis. Systemic seismic risk assessment of road networks considering interactions with the built environment. *Computer-Aided Civil and Infrastructure Engineering*, 30(7):524–540, 2015.

[85] Pierre Gehl and Dina D'ayala. System loss assessment of bridge networks accounting for multi-hazard interactions. *Structure and Infrastructure Engineering*, 14(10):1355–1371, 2018.

[86] Maria Nogal, Alan O'Connor, Brian Caulfield, and Beatriz Martinez-Pastor. Resilience of traffic networks: From perturbation to recovery via a dynamic restricted equilibrium model. *Reliability Engineering & System Safety*, 156:84–96, 2016.

[87] Nees Jan van Eck and Ludo Waltman. Vosviewer manual version 1.6.17, 2021.

[88] Nees Jan Van Eck and Ludo Waltman. Visualizing bibliometric networks. In *Measuring scholarly impact*, pages 285–320. Springer, 2014.

[89] Ludo Waltman, Nees Jan Van Eck, and Ed CM Noyons. A unified approach to mapping and clustering of bibliometric networks. *Journal of informetrics*, 4(4):629–635, 2010.

[90] Ludo Waltman and Nees Jan Van Eck. A smart local moving algorithm for large-scale modularity-based community detection. *The European physical journal B*, 86(11):1–14, 2013.

[91] CEN. Eurocode 1: Actions on structures; part 1-7: General action - accidental action. *European Committee for Standardization*, 2003.

[92] Weili Zhang and Naiyu Wang. Resilience-based risk mitigation for road networks. *Structural Safety*, 62:57–65, 2016.

[93] Anne Kiremidjian, James Moore, Yue Yue Fan, Ozgur Yazlali, Nesrin Basoz, and Meredith Williams. Seismic risk assessment of transportation network systems. *Journal of Earthquake Engineering*, 11(3):371–382, 2007.

[94] Nobuhiko Shiraki, Masanobu Shinozuka, James E Moore, Stephanie E Chang, Hiroyuki Kameda, and Satoshi Tanaka. System risk curves: Probabilistic performance scenarios for highway networks subject to earthquake damage. *Journal of Infrastructure Systems*, 13(1):43–54, 2007.

[95] Evangelos C Stergiou and Anne S Kiremidjian. Risk assessment of transportation systems with network functionality losses. *Structure and Infrastructure Engineering*, 6(1-2):111–125, 2010.

[96] Ning Zhang and Alice Alipour. Integrated framework for risk and resilience assessment of the road network under inland flooding. *Transportation research record*, 2673(12):182–190, 2019.

[97] Maria Pregnolato, Andrew O Winter, Dakota Mascarenas, Andrew D Sen, Paul Bates, and Michael R Motley. Assessing flooding impact to riverine bridges: an integrated analysis. *Natural Hazards and Earth System Sciences*, 22(5):1559–1576, 2022.

[98] Keith Beven, Dave Leedal, and Simon McCarthy. Framework for assessing uncertainty in fluvial flood risk mapping, 2014.

[99] Liang Liu, Dan M Frangopol, Alysson Mondoro, and David Y Yang. Sustainability-informed bridge ranking under scour based on transportation network performance and multiattribute utility. *Journal of Bridge Engineering*, 23(10):04018082, 2018.

[100] Liang Liu, David Y Yang, and Dan M Frangopol. Network-level risk-based framework for optimal bridge adaptation management considering scour and climate change. *Journal of Infrastructure Systems*, 26(1):04019037, 2020.

[101] Adrienne Grêt-Regamey and Daniel Straub. Spatially explicit avalanche risk assessment linking bayesian networks to a gis. *Natural Hazards and Earth System Sciences*, 6(6):911–926, 2006.

[102] Mathias Graf, Kazuyoshi Nishijima, and Michael H Faber. Bayesian updating in natural hazard risk assessment. *Australian Journal of Structural Engineering*, 9(1):35–44, 2009.

[103] Sebastian T Glavind and Michael H Faber. A framework for offshore load environment modeling. *Journal of Offshore Mechanics and Arctic Engineering*, 142(2):021702, 2020.

[104] Sebastian T Glavind, Henning Brüske, Erik D Christensen, and Michael H Faber. Bayesian probabilistic representation of complex systems: With application to wave load modeling. *Computer-Aided Civil and Infrastructure Engineering*, 37(8):935–955, 2022.

[105] M Julia Flores, Rosa F Ropero, and Rafael Rumí. Assessment of flood risk in mediterranean catchments: an approach based on bayesian networks. *Stochastic Environmental Research and Risk Assessment*, 33:1991–2005, 2019.

[106] Finn V Jensen and Thomas Dyhre Nielsen. *Bayesian networks and decision graphs*, volume 2. Springer, 2007.

[107] M. Santamaria-Ariza, M. Liu, H.S. Sousa, J.C. Matos, and M.H. Faber. Probabilistic resilience model for management of road infrastructure systems subject to flood events. In *International Conference on Applications of Statistics and Probability in Civil Engineering (ICASP 14)*, Dublin, Ireland, July 2023.

[108] David Y Yang and Dan M Frangopol. Physics-based assessment of climate change impact on long-term regional bridge scour risk using hydrologic modeling: application to lehigh river watershed. *Journal of Bridge Engineering*, 24(11):04019099, 2019.

[109] Eduardo S Martins and Jery R Stedinger. Generalized maximum likelihood pareto-poisson estimators for partial duration series. *Water Resources Research*, 37(10):2551–2557, 2001.

[110] Jery R Stedinger. Frequency analysis of extreme events. *Handbook of hydrology*, 1993.

[111] Keith J Beven. *Rainfall-runoff modelling: the primer*. John Wiley & Sons, 2011.

[112] A.D. Feldman and Hydrologic Engineering Center (U.S.). *Hydrologic Modeling System HEC-HMS: Technical Reference Manual*. US Army Corps of Engineers, Hydrologic Engineering Center, 2000.

[113] Gary W Brunner. Hec-ras river analysis system: Hydraulic reference manual, version 5.0. *US Army Corps of Engineers–Hydrologic Engineering Center*, 547, 2016.

[114] K Zwirglmaier and D Straub. Approaches to bayesian network structure elicitation. *Risk, Reliability and Safety: Innovating Theory and Practice: Proceedings of ESREL 2016 (Glasgow, Scotland, 25-29 September 2016)*, page 333, 2016.

[115] Hélder S Sousa, Francisco Prieto-Castrillo, José C Matos, Jorge M Branco, and Paulo B Lourenço. Combination of expert decision and learned based bayesian networks for multi-scale mechanical analysis of timber elements. *Expert Systems with Applications*, 93:156–168, 2018.

[116] Judea Pearl. *Probabilistic reasoning in intelligent systems: networks of plausible inference*. Morgan kaufmann, 1988.

[117] Daphne Koller and Nir Friedman. *Probabilistic graphical models: principles and techniques*. MIT press, 2009.

[118] David Maxwell Chickering. Learning bayesian networks is np-complete. *Learning from data: Artificial intelligence and statistics V*, pages 121–130, 1996.

[119] Catarina Ramos and Eusébio Reis. Floods in southern portugal: their physical and human causes, impacts and human response. *Mitigation and Adaptation Strategies for Global Change*, 7(3): 267–284, 2002.

[120] José Alberto Gonçalves and André Pinhal. DEM data for Portugal. Available at:https://www.fc.up.pt/pessoas/jagoncal/dems/, n.d. Accessed on 03/11/2021.

[121] Agência Portuguesa do Ambiente (APA), I.P. Atlas da Água - números de escoamento. Available at: https://sniambgeoviewer.apambiente.pt/GeoDocs/shpzips/AtAgua_cn2_2000_500.zip, note = Accessed on 03/11/2021, 2021.

[122] Juliana Mendes and Rodrigo Maia. Hydrologic modelling calibration for operational flood forecasting. *Water Resources Management*, 30:5671–5685, 2016.

[123] Daniel N Moriasi, Jeffrey G Arnold, Michael W Van Liew, Ronald L Bingner, R Daren Harmel, and Tamie L Veith. Model evaluation guidelines for systematic quantification of accuracy in watershed simulations. *Transactions of the ASABE*, 50(3):885–900, 2007.

[124] João Reis Hipólito and AC Vaz. Hidrologia e recursos hídricos. *Editora Universitaria do Instituto Superior Tecnico, Lisboa*, 2011.

[125] A Lencastre and FM Franco. Lições de hidrologia 3ª edição revista. *Lisboa: Fundação da Faculdade de Ciências e Tecnologia da Universidade Nova de Lisboa*, 2006.

[126] BayesFusion, LLC. *GeNIe Modeler User Manual*, 2022.

[127] Kilian Zwirglmaier and Daniel Straub. A discretization procedure for rare events in bayesian networks. *Reliability Engineering & System Safety*, 153:96–109, 2016.

[128] Ankur Ankan and Abinash Panda. pgmpy: Probabilistic graphical models using python. In *Proceedings of the 14th Python in Science Conference (SCIPY 2015)*. Citeseer, 2015.

[129] FHWA (Federal Highway Administration). Bridge preservation guide: Maintaining a resilient infrastructure to preserve mobility, 2018.

[130] Tarek Omar and Moncef L Nehdi. Condition assessment of reinforced concrete bridges: Current practice and research challenges. *Infrastructures*, 3(3):36, 2018.

[131] Mariano Angelo Zanini, Flora Faleschini, and Joan Ramon Casas. State-of-research on performance indicators for bridge quality control and management. *Frontiers in built environment*, 5:22, 2019.

[132] FHWA. Recording and coding guide for the structure inventory and appraisal of the nation's bridges. *Federal Highway Administration Report No. FHWA-PD-96-001*, 1995.

[133] Schalk R Bezuidenhout and Gideon PAG van Zijl. Corrosion propagation in cracked reinforced concrete, toward determining residual service life. *Structural Concrete*, 20(6):2183–2193, 2019.

[134] Ahsana Parammel Vatteri, K Balaji Rao, and Anoop M Bharathan. Time-variant reliability analysis of rc bridge girders subjected to corrosion-shear limit state. *Structural Concrete*, 17(2):162–174, 2016.

[135] C Gehlen, S v Greve-Dierfeld, J Gulikers, S Helland, A Rahimi, et al. *fib Bulletin 76: Benchmarking of Deemed-to-Satisfy Provisions in Standards–Durability of Reinforced Concrete Structures Exposed to Chlorides*. fib - The International Federation for Structural Concrete, 2015.

[136] C Gehlen, C Andrade, M Bartholomew, J Cairns, J Gulikers, F Javier Leon, S Matthews, P McKenna, K Osterminski, A Paeglitis, et al. *fib Bulletin 59. Condition control and assessment of reinforced concrete structures exposed to corrosive environments (carbonation/chlorides)*. fib - The International Federation for Structural Concrete, 2011.

[137] Ivan Zambon, Anja Vidović, Alfred Strauss, and Jose Matos. Condition prediction of existing concrete bridges as a combination of visual inspection and analytical models of deterioration. *Applied Sciences*, 9(1):148, 2019.

[138] JC Walraven and AQC Van Der Horst. *fib model code for concrete structures 2010*. fib - The International Federation for Structural Concrete, 2013.

[139] fib Task Group 5.6. fib bulletin 34. model code for service life design, 2006.

[140] Palle Thoft-Christensen. Assessment of the reliability profiles for concrete bridges. *Engineering structures*, 20(11):1004–1009, 1998.

[141] Dan M Frangopol, Jung S Kong, and Emhaidy S Gharaibeh. Reliability-based life-cycle management of highway bridges. *Journal of computing in civil engineering*, 15(1):27–34, 2001.

[142] Denver Tolliver and Pan Lu. Analysis of bridge deterioration rates: A case study of the northern plains region. In *Journal of the Transportation Research Forum*, volume 50, pages 87–100, 2011.

[143] Afshin Hatami, George Morcous, et al. Developing deterioration models for nebraska bridges. Technical report, Nebraska Transportation Center, 2011.

[144] Melik Bolukbasi, Jamshid Mohammadi, and David Arditi. Estimating the future condition of highway bridge components using national bridge inventory data. *Practice Periodical on Structural Design and Construction*, 9(1):16–25, 2004.

[145] Pan Lu, Hao Wang, Denver Tolliver, et al. Prediction of bridge component ratings using ordinal logistic regression model. *Mathematical problems in engineering*, 2019, 2019.

[146] Anil K Agrawal, Akira Kawaguchi, and Zheng Chen. Deterioration rates of typical bridge elements in new york. *Journal of Bridge Engineering*, 15(4):419–429, 2010.

[147] George Morcous. Performance prediction of bridge deck systems using markov chains. *Journal of performance of Constructed Facilities*, 20(2):146–155, 2006.

[148] Maatern-Jan Kallen. Markov processes for maintenance optimization of civil infrastructure in the netherlands, 2007.

[149] Ivan Zambon, Anja Vidovic, Alfred Strauss, Jose Matos, and Joao Amado. Comparison of stochastic prediction models based on visual inspections of bridge decks. *Journal of Civil Engineering and Management*, 23(5):553–561, 2017.

[150] See-King Ng and Fred Moses. Bridge deterioration modeling using semi-markov theory. *A. A. Balkema Uitgevers B. V, Structural Safety and Reliability.*, 1:113–120, 1998.

[151] Kiyoshi Kobayashi, Kiyoyuki Kaito, and Nam Lethanh. A statistical deterioration forecasting method using hidden markov model for infrastructure management. *Transportation Research Part B: Methodological*, 46(4):544–561, 2012.

[152] Ying-Hua Huang. Artificial neural network model of bridge deterioration. *Journal of Performance of Constructed Facilities*, 24(6):597–602, 2010.

[153] GP Bu, JH Lee, H Guan, YC Loo, and M Blumenstein. Prediction of long-term bridge performance: Integrated deterioration approach with case studies. *Journal of Performance of Constructed Facilities*, 29(3):04014089, 2015.

[154] Zhe Li and Rigoberto Burgueño. Using soft computing to analyze inspection results for bridge evaluation and management. *Journal of Bridge Engineering*, 15(4):430–438, 2010.

[155] Amir Tarighat and Ayaho Miyamoto. Fuzzy concrete bridge deck condition rating method for practical bridge management system. *Expert Systems with Applications*, 36(10):12077–12085, 2009.

[156] George Morcous, H Rivard, and AM Hanna. Modeling bridge deterioration using case-based reasoning. *Journal of Infrastructure Systems*, 8(3):86–95, 2002.

[157] Haoyuan Zhang and D William R Marsh. Multi-state deterioration prediction for infrastructure asset: Learning from uncertain data, knowledge and similar groups. *Information Sciences*, 529:197–213, 2020.

[158] Bryant Le and John Andrews. Petri net modelling of bridge asset management using maintenance-related state conditions. *Structure and Infrastructure Engineering*, 12(6):730–751, 2016.

[159] M. Santamaria Ariza, J. Fernandes, and J. Matos. Overview on performance predictive models: Application to bridge management systems. In *IABSE Symposium 2019 Guimarães. Towards a Resilient Built Environment - Risk and Asset Management*, pages 1222–1229, Guimarães, Portugal, March 2019. IABSE. ISBN 978-3-85748-163-5.

[160] Zanyar Mirzaei, Bryan T Adey, Leo Klatter, and P Thompson. The iabmas bridge management committee overview of existing bridge management systems. *International Association for Bridge Maintenance and Safety (IABMAS), Sapporo, Japan*, 2014.

[161] Yehuda Kleiner. Scheduling inspection and renewal of large infrastructure assets. *Journal of infrastructure systems*, 7(4):136–143, 2001.

[162] L. Collins. An introduction to markov chains analysis. In *Concepts and Techniques in Modern Geography (CATMOG)*. GEO ABSTRACTS, University of East Anglia, 1975.

[163] Lawrence R Rabiner. A tutorial on hidden markov models and selected applications in speech recognition. *Proceedings of the IEEE*, 77(2):257–286, 1989.

[164] ASCE. American society of civil engineers (asce) 2017 infrastructure report card: Roads, 2017.

[165] Mark Moore, Brent M Phares, Benjamin Graybeal, Dennis Rolander, Glenn Washer, Janney Wiss, et al. Reliability of visual inspection for highway bridges, volume i. Technical report, Turner-Fairbank Highway Research Center, 2001.

[166] T Ryan, A Hartle, J Mann, and J Danovich. Bridge inspector's reference manual (birm), volume 1 (6). *US Federal Highway Admin, Washington, DC*, 20590, 2012.

[167] Emanuel Parzen. *Stochastic processes*. Society for Industrial and Applied Mathematics (SIAM), 1999.

[168] Iain L MacDonald and Walter Zucchini. *Hidden Markov and other models for discrete-valued time series*, volume 110. CRC Press, 1997.

[169] The MathWorks Inc. *MATLAB Neural Network Toolbox Release 2016a*. Natick, MA, 2016.

[170] Andrea Saltelli, Stefano Tarantola, Francesca Campolongo, Marco Ratto, et al. *Sensitivity analysis in practice: a guide to assessing scientific models*, volume 1. Wiley Online Library, 2004.

[171] Monica Santamaria Ariza, Ivan Zambon, Hélder S. Sousa, Jose Antonio Campos e Matos, and Alfred Strauss. Comparison of forecasting models to predict concrete bridge decks performance. *Structural Concrete*, 21(4):1240–1253, 2020.

[172] Lihui Zhao, Yuhuan Chen, and Donald W Schaffner. Comparison of logistic regression and linear regression in modeling percentage data. *Applied and environmental microbiology*, 67(5): 2129–2135, 2001.

[173] Allen C Estes and Dan M Frangopol. Bridge lifetime system reliability under multiple limit states. *Journal of bridge engineering*, 6(6):523–528, 2001.

[174] Brian M Pailes. *Damage identification, progression, and condition rating of bridge decks using multi-modal non-destructive testing*. Rutgers The State University of New Jersey, School of Graduate Studies, 2014.

[175] Rocco Custer. *Hierarchical modelling of flood risk for engineering decision analysis*. Technical University of Denmark, Department of Civil Engineering., 2015.

[176] Uzielli, Marco, Vangelsten, Bjørn Vidar, and Eidsvig, Unni. Probabilistic modeling of vulnerability of road infrastructures to floods. *E3S Web Conf.*, 7:04009, 2016. doi: 10.1051/e3sconf/20160704009. URL https://doi.org/10.1051/e3sconf/20160704009.

[177] Nathan Miner and Alice Alipour. Bridge damage, repair costs, and fragilities for inland flood events. *Journal of Bridge Engineering*, 27(8):04022057, 2022.

[178] Rob Lamb, Paige Garside, Raghav Pant, and Jim W Hall. A probabilistic model of the economic risk to britain's railway network from bridge scour during floods. *Risk analysis*, 39(11):2457–2478, 2019.

[179] Sotirios A Argyroudis, Stergios A Mitoulis, Mike G Winter, and Amir M Kaynia. Fragility of transport assets exposed to multiple hazards: State-of-the-art review toward infrastructural resilience. *Reliability Engineering & System Safety*, 191:106567, 2019.

[180] Federal Emergency Management Agency (FEMA). Multi-hazard loss estimation methodology: Flood model. hazus-mh technical manual 2.1. Technical report, US Department of Transportation, Washington, DC, USA, 2009. URL https://www.fema.gov/sites/default/files/2020-09/fema_hazus_flood-model_technicalmanual_2.1.pdf.

[181] Azadeh Alipour, Behrouz Shafei, and Masanobu Shinozuka. Reliability-based calibration of load and resistance factors for design of rc bridges under multiple extreme events: Scour and earthquake. *Journal of Bridge Engineering*, 18(5):362–371, 2013.

[182] You Dong, Dan M Frangopol, and Duygu Saydam. Time-variant sustainability assessment of seismically vulnerable bridges subjected to multiple hazards. *Earthquake Engineering & Structural Dynamics*, 42(10):1451–1467, 2013.

[183] Gautham Ganesh Prasad and Swagata Banerjee. The impact of flood-induced scour on seismic fragility characteristics of bridges. *Journal of Earthquake Engineering*, 17(6):803–828, 2013.

[184] Taner Yilmaz, Swagata Banerjee, and Peggy A Johnson. Uncertainty in risk of highway bridges assessed for integrated seismic and flood hazards. *Structure and infrastructure engineering*, 14 (9):1182–1196, 2018.

[185] Pierre Gehl. *Bayesian networks for the multi-risk assessment of road infrastructure*. PhD thesis, UCL (University College London), 2017.

[186] Cheng Lin, Caroline Bennett, Jie Han, and Robert L Parsons. Integrated analysis of the performance of pile-supported bridges under scoured conditions. *Engineering structures*, 36:27–38, 2012.

[187] Chung-Chan Hung and Wen-Gi Yau. Behavior of scoured bridge piers subjected to flood-induced loads. *Engineering structures*, 80:241–250, 2014.

[188] John V Klinga and Alice Alipour. Assessment of structural integrity of bridges under extreme scour conditions. *Engineering Structures*, 82:55–71, 2015.

[189] Hyunjun Kim, Sung-Han Sim, Jaebeom Lee, Young-Joo Lee, and Jin-Man Kim. Flood fragility analysis for bridges with multiple failure modes. *Advances in Mechanical Engineering*, 9(3): 1687814017696415, 2017.

[190] Touhid Ahamed, Jennifer G Duan, and Hongki Jo. Flood-fragility analysis of instream bridges–consideration of flow hydraulics, geotechnical uncertainties, and variable scour depth. *Structure and Infrastructure Engineering*, 17(11):1494–1507, 2021.

[191] Omid Khandel and Mohamed Soliman. Integrated framework for assessment of time-variant flood fragility of bridges using deep learning neural networks. *Journal of Infrastructure Systems*, 27(1): 04020045, 2021.

[192] Nikola Tanasić, Vladan Ilić, and Rade Hajdin. Vulnerability assessment of bridges exposed to scour. *Transportation research record*, 2360(1):36–44, 2013.

[193] Paolo Zampieri, Mariano Angelo Zanini, Flora Faleschini, Lorenzo Hofer, and Carlo Pellegrino. Failure analysis of masonry arch bridges subject to local pier scour. *Engineering Failure Analysis*, 79:371–384, 2017.

[194] Enrico Tubaldi, Lorenzo Macorini, and Bassam A Izzuddin. Three-dimensional mesoscale modelling of multi-span masonry arch bridges subjected to scour. *Engineering Structures*, 165:486–500, 2018.

[195] Fabrizio Scozzese, Laura Ragni, Enrico Tubaldi, and Fabrizio Gara. Modal properties variation and collapse assessment of masonry arch bridges under scour action. *Engineering Structures*, 199: 109665, 2019.

[196] Unni Eidsvig, Monica Santamaría, Neryvaldo Galvão, Nikola Tanasic, Luca Piciullo, Rade Hajdin, Farrokh Nadim, Hélder S Sousa, and José Matos. Risk assessment of terrestrial transportation infrastructures exposed to extreme events. *Infrastructures*, 6(11):163, 2021.

[197] Carlos Mendoza Cabanzo, Mónica Santamaría, Hélder S Sousa, and José C Matos. In-plane fragility and parametric analyses of masonry arch bridges exposed to flood hazard using surrogate modeling techniques. *Applied Sciences*, 12(4):1886, 2022.

[198] Dirk Proske. *Bridge collapse frequencies versus failure probabilities*. Springer, 2018.

[199] David Turner. *Fragility assessment of bridge superstructures under hydrodynamic forces*. PhD thesis, Colorado State University, 2015.

[200] Sotirios A Argyroudis and Stergios Aristoteles Mitoulis. Vulnerability of bridges to individual and multiple hazards-floods and earthquakes. *Reliability engineering & system safety*, 210:107564, 2021.

[201] Federal Emergency Management Agency (FEMA). Hazus-mh: multi-hazard loss estimation methodology: Earthquake model-technical manual. Technical report, Department of Homeland Security ..., Washington, DC, USA, 2003.

[202] Giuseppe D Degan, Andre R Barbosa, and Maria Pregnolato. A taxonomy of bridges at risk of flooding: towards bridge classes and damage models. In *Proceedings of the Institution of Civil Engineers-Bridge Engineering*, volume 175-3, pages 172–178. Thomas Telford Ltd, 2022.

[203] J Birdsall and RADE Hajdin. Vulnerability assessment of individual infrastructure objects subjected to natural hazards. *International Bridge and Structure Management*, page 339, 2008.

[204] Z Van Leeuwen and R Lamb. Flood and scour related failure incidents at railway assets between 1846 and 2013. *Railway Safety & Standards Board*, 2014.

[205] R Hajdin, M Kušar, S Mašović, P Linneberg, J Amado, and N Tanasić. Wg3 technical report. establishment of a quality control plan. *COST TU*, 1406, 2018.

[206] Marianna Loli, Stergios Aristoteles Mitoulis, Angelos Tsatsis, John Manousakis, Rallis Kourkoulis, and Dimitrios Zekkos. Flood characterization based on forensic analysis of bridge collapse using uav reconnaissance and cfd simulations. *Science of the Total Environment*, 822:153661, 2022.

[207] Cheng Lin, Jie Han, Caroline Bennett, and Robert L. Parsons. *Case History Analysis of Bridge Failures due to Scour*, pages 204–216. American Society of Civil Engineers (ASCE), 2014. doi: 10.1061/9780784413326.021.

[208] Kuo-Wei Liao, Yasunori Muto, Wei-Lun Chen, and Bang-Ho Wu. A probabilistic bridge safety evaluation against floods. *SpringerPlus*, 5:1–19, 2016.

[209] Kent M Hulet, Colin C Smith, and Matthew Gilbert. Load-carrying capacity of flooded masonry arch bridges. In *Proceedings of the Institution of Civil Engineers-Bridge Engineering*, volume 159-3, pages 97–103. Thomas Telford Ltd, 2006.

[210] Michael Havbro Faber. Risk and safety in civil engineering. *Lecture Notes. Swiss Federal Institute of Technology, Zurich*, 2007.

[211] Enrico Tubaldi, Lorenzo Macorini, Bassam A Izzuddin, Costantino Manes, and Francesco Laio. A framework for probabilistic assessment of clear-water scour around bridge piers. *Structural safety*, 69:11–22, 2017.

[212] R Richard Avent and Mohamed Alawady. Bridge scour and substructure deterioration: Case study. *Journal of Bridge Engineering*, 10(3):247–254, 2005.

[213] Jeremy Benn. Railway bridge failure during flooding in the uk and ireland. *Proceedings of the Institution of Civil Engineers-Forensic Engineering*, 166(4):163–170, 2013.

[214] Yawen Shen, Jonathan L Goodall, and Steven B Chase. Method for rapidly assessing the overtopping risk of bridges due to flooding over a large geographic region. *JAWRA Journal of the American Water Resources Association*, 53(6):1437–1452, 2017.

[215] Kornel Kerenyi, Tanju Sofu, and Junke Guo. Hydrodynamic forces on inundated bridge decks. Technical Report FHWA-HRT-09-028, Federal Highway Administration, 2009.

[216] Maryam Nasim, Sujeeva Setunge, Shiwei Zhou, and Hessam Mohseni. An investigation of waterflow pressure distribution on bridge piers under flood loading. *Structure and Infrastructure Engineering*, 15(2):219–229, 2019.

[217] AASHTO. Lrfd bridge design specifications, 2012.

[218] Robert Ettema, George Constantinescu, and Bruce W Melville. Flow-field complexity and design estimation of pier-scour depth: Sixty years since laursen and toch. *Journal of Hydraulic Engineering*, 143(9):03117006, 2017.

[219] Donald Max Sheppard, Huseyin Demir, and Bruce W Melville. *Scour at wide piers and long skewed piers*, volume 682. Transportation Research Board, 2011.

[220] Jean-Louis Briaud. Scour depth at bridges: Method including soil properties. i: Maximum scour depth prediction. *Journal of Geotechnical and Geoenvironmental Engineering*, 141(2):04014104, 2015.

[221] Bruce W Melville and Yee-Meng Chiew. Time scale for local scour at bridge piers. *Journal of Hydraulic Engineering*, 125(1):59–65, 1999.

[222] Robert Ettema, Tatsuaki Nakato, and Marian Muste. Estimation of scour depth at bridge abutments. nchrp 24-20. *Transportation Research Board, Washington, DC*, 2010.

[223] PF Lagasse, M Ghosn, PA Johnson, LW Zevenbergen, and PE Clopper. Risk-based approach for bridge scour prediction. *National Cooperative Highway Research Program Transportation Research Board National Research Council: Washington, DC, USA*, 20, 2013.

[224] J Morgado, J Amado, N Carlos, and M Pinheiro. The development of multi-asset performance indicators for the management of the portuguese road and rail networks. *Towards a Resilient Built Environment-Risk and Asset Management*, pages 1643–1650, 2019.

[225] M. Santamaria-Ariza, E. Arango, F. Jafari, H.S. Sousa, U. Eidsvig, F. Nadim, L. Piciullo, I.H. Steinholt, R. Klaeboe, J. Ludvigsen, G. Hadjidemetriou, J.C. Matos, and M. Morais. Dynamic risk-based predictive models. Deliverable 5.1, SAFEWAY, 2021. Grant Agreement No. 769255.

[226] R Hajdin, JR Casas, and J Campos e Matos. Inspection of existing bridges–moving on from condition rating. iabse symp. towar. a resilient built environ. risk asset manag., guimarães, portugal: Iabse; 2019, 2019.

[227] Maria Pregnolato. Bridge safety is not for granted–a novel approach to bridge management. *Engineering Structures*, 196:109193, 2019.

[228] Navid Ataei and Jamie E Padgett. Probabilistic modeling of bridge deck unseating during hurricane events. *Journal of Bridge Engineering*, 18(4):275–286, 2013.

[229] Kevin Oudenbroek, Nader Naderi, Jeremy D Bricker, Yuguang Yang, Cor Van der Veen, Wim Uijttewaal, Shuji Moriguchi, and Sebastiaan N Jonkman. Hydrodynamic and debris-damming failure of bridge decks and piers in steady flow. *Geosciences*, 8(11):409, 2018.

[230] Joint Committee on Structural Safety. Probabilistic model code. Available at: https://www.jcss-lc.org/jcss-probabilistic-model-code/, 2001. Accessed: 03/09/2020.

[231] API. *API 2A-WSD: Recommended practice for planning, designing and constructing fixed offshore platforms-working stress design*. American Petroleum Institute, 2000.

[232] Patrick J Hannigan, F Rausche, GE Likins, Brent Robinson, Matthew Becker, Ryan R Berg, et al. Design and construction of driven pile foundations–volume i. Technical report, National Highway Institute (US), 2016.

[233] Cheng Lin, Caroline Bennett, Jie Han, and Robert L Parsons. Py based approach for buckling analysis of axially loaded piles under scoured conditions. In *Structures Congress 2010*, pages 110–120, 2010.

[234] Colin Smith and Matthew Gilbert. Application of discontinuity layout optimization to plane plasticity problems. *Proceedings of the Royal Society A: Mathematical, Physical and Engineering Sciences*, 463(2086):2461–2484, 2007.

[235] Matthew Gilbert, John Valentino, Colin Smith, and Tom Pritchard. Limit analysis of masonry arch bridges using discontinuity layout optimization. In *Proceedings of ARCH 2019: 9th International Conference on Arch Bridges*, pages 307–314. Springer, 2020.

[236] LimitState Ltd. Limitstate:geo manual. https://www.limitstate.com/geo-documentation, 2019.

[237] A Tomor. Life-cycle assessment and deterioration models for masonry arch bridges. *WIT Transactions on Ecology and the Environment*, 179:535–546, 2013.

[238] Borja Conde, José C Matos, Daniel V Oliveira, and Belén Riveiro. Probabilistic-based structural assessment of a historic stone arch bridge. *Structure and Infrastructure Engineering*, 17(3):379–391, 2021.

[239] João Soromenho Rocha, José Simão Antunes do Carmo, Luís Joaquim Leal Lemos, Vítor Dias da Silva, and Carlos Alberto da Silva Rebelo. Pontes construídas sobre fundos aluvionares: O colapso da ponte hintze ribeiro. *Recursos Hídricos*, 29(2), 2008.

[240] David Y Yang and Dan M Frangopol. Life-cycle management of deteriorating bridge networks with network-level risk bounds and system reliability analysis. *Structural Safety*, 83:101911, 2020.

[241] Bryan Adey, Rade Hajdin, and Eugen Brühwiler. Effect of common cause failures on indirect costs. *Journal of Bridge Engineering*, 9(2):200–208, 2004.

[242] Juan Carlos Lam and Bryan T Adey. Functional loss assessment and restoration analysis to quantify indirect consequences of hazards. *ASCE-ASME Journal of Risk and Uncertainty in Engineering Systems, Part A: Civil Engineering*, 2(4):04016008, 2016.

[243] Sotirios A. Argyroudis, Stergios A. Mitoulis, Lorenzo Hofer, Mariano Angelo Zanini, Enrico Tubaldi, and Dan M. Frangopol. Resilience assessment framework for critical infrastructure in a multi-hazard environment: Case study on transport assets. *Science of The Total Environment*, 714: 136854, 2020. ISSN 0048-9697. doi: https://doi.org/10.1016/j.scitotenv.2020.136854. URL https://www.sciencedirect.com/science/article/pii/S0048969720303648.

[244] Mohammad Reza Yazdi-Samadi and Mojtaba Mahsuli. Time-variant seismic risk analysis of transportation networks considering economic and socioeconomic impacts. *Journal of Earthquake Engineering*, 24(5):745–773, 2020.

[245] Graziano Fiorillo and Michel Ghosn. Risk-based importance factors for bridge networks under highway traffic loads. *Structure and Infrastructure Engineering*, 15(1):113–126, 2019.

[246] Jatin S Nathwani, Niels Christian Lind, and Mahesh D Pandey. Affordable safety by choice: the life quality method. *INSTITUTE FOR RISK RESEARCH, WATERLOO, ON(CANADA). 245*, page 1997, 1997.

[247] Rudiger Rackwitz. The philosophy behind the life quality index and empirical verification. *Updated memorandum to JCSS, Technical University Munich, Munich*, 2005.

[248] Michael Havbro Faber and Edgar Virguez-Rodriguez. Supporting decisions on global health and life safety investments. *Applications of Statistics and Probability in Civil Engineering*, 16(13):10, 2011.

[249] Alex Erath, James Birdsall, Kay W Axhausen, and Rade Hajdin. Vulnerability assessment methodology for swiss road network. *Transportation Research Record*, 2137(1):118–126, 2009.

[250] CE Delft et al. Handbook on the external costs of transport: version 2019–1.1. 2020.

[251] Benedikt Notter, M Keller, H Althaus, B Cox, W Knörr, C Heidt, K Biemann, D Räder, and M Jamet. The handbook of emission factors for road transport (hbefa) 4.1. Available at: https://www.hbefa.net/.

[252] Daniel Shefer and Piet Rietveld. Congestion and safety on highways: towards an analytical model. *Urban Studies*, 34(4):679–692, 1997.

[253] Chao Wang, Mohammed Quddus, and Stephen Ison. A spatiotemporal analysis of the impact of congestion on traffic safety on major roads in the uk. *Transportmetrica A: Transport Science*, 9(2): 124–148, 2013.

[254] Angus Eugene Retallack and Bertram Ostendorf. Current understanding of the effects of congestion on traffic accidents. *International journal of environmental research and public health*, 16(18): 3400, 2019.

[255] Michael Patriksson. *The traffic assignment problem: models and methods*. Courier Dover Publications, 2015.

[256] Il Moore, E James, Geunyoung Kim, Seongdil Cho, Hsi-hwa Hu, and Rong Xu. Evaluating system atmis technologies via rapid estimation of network flows. 1997.

[257] Ian Goodfellow, Yoshua Bengio, and Aaron Courville. *Deep learning*. MIT press, 2016.

[258] Stergios Aristoteles Mitoulis, Sotirios A Argyroudis, Marianna Loli, and Boulent Imam. Restoration models for quantifying flood resilience of bridges. *Engineering structures*, 238:112180, 2021.

[259] Ehsan Minaie and Franklin Moon. Practical and simplified approach for quantifying bridge resilience. *Journal of Infrastructure Systems*, 23(4):04017016, 2017.

[260] Sushreyo Misra, Jamie E Padgett, Andre R Barbosa, and Bret M Webb. An expert opinion survey on post-hazard restoration of roadways and bridges: Data and key insights. *Earthquake Spectra*, 36(2):983–1004, 2020.

[261] Jürgen Hackl, Bryan T Adey, and Nam Lethanh. Determination of near-optimal restoration programs for transportation networks following natural hazard events using simulated annealing. *Computer-Aided Civil and Infrastructure Engineering*, 33(8):618–637, 2018.

[262] Ning Zhang and Alice Alipour. A stochastic programming approach to enhance the resilience of infrastructure under weather-related risk. *Computer-Aided Civil and Infrastructure Engineering*, 38 (4):411–432, 2023.

[263] Pedro Pinto Santos, Susana Pereira, José Luís Zêzere, Alexandre Oliveira Tavares, Eusébio Reis, Ricardo AC Garcia, and Sérgio Cruz Oliveira. A comprehensive approach to understanding flood risk drivers at the municipal level. *Journal of environmental management*, 260:110127, 2020.

[264] R Rackwitz, A Lentz, and M Faber. Socio-economically sustainable civil engineering infrastructures by optimization. *Structural safety*, 27(3):187–229, 2005.

[265] N. Galvão, H. Sousa, S. Fernandes, A. Pucci, J. Matos, N. Tanasić, et al. Impact of human-made hazards. Deliverable 2.2, SAFEWAY, 2019. Grant Agreement No. 769255.

[266] Soheyl Sazedj, António José Morais, and Said Jalali. Comparison of environmental benchmarks of masonry and concrete structure based on a building model. *Construction and Building Materials*, 141:36–43, 2017.

[267] Pedro Camargo. Aequilibrae: Python package for transportation modeling, 2014. URL https://github.com/AequilibraE/aequilibrae.

[268] Aurélien Géron. *Hands-on machine learning with Scikit-Learn, Keras, and TensorFlow*. " O'Reilly Media, Inc.", 2022.

[269] Diederik P Kingma and Jimmy Ba. Adam: A method for stochastic optimization. *arXiv preprint arXiv:1412.6980*, 2014.

[270] National Research Council. *Disaster Resilience: A National Imperative*. The National Academies Press, 2012.

[271] Navya Vishnu, Sabarethinam Kameshwar, and Jamie E Padgett. A framework for resilience assessment of highway transportation networks. In *Routledge handbook of sustainable and resilient infrastructure*, pages 216–238. Routledge, 2018.

[272] Min Liu, Jianjun Qin, Da-Gang Lu, Wei-Heng Zhang, Jiang-Sheng Zhu, and Michael Havbro Faber. Towards resilience of offshore wind farms: A framework and application to asset integrity management. *Applied Energy*, 322:119429, 2022.

[273] Kazuyoshi Nishijima and Michael Havbro Faber. Societal performance of infrastructure subject to natural hazards. *Australian journal of structural engineering*, 9(1):9–16, 2009.

[274] Will Steffen, Katherine Richardson, Johan Rockström, Sarah E Cornell, Ingo Fetzer, Elena M Bennett, Reinette Biggs, Stephen R Carpenter, Wim De Vries, Cynthia A De Wit, Carl Folke, Dieter Gerten, Jens Heinke, Georgina M. Mace, Linn M. Persson, Veerabhadran Ramanathan, Belinda Reyers, and Sverker Sörlin. Planetary boundaries: Guiding human development on a changing planet. *Science*, 347(6223):1259855, 2015.

[275] Zaharah Allah Bukhsh, Irina Stipanovic, Giel Klanker, Alan O'Connor, and Andre G Doree. Network level bridges maintenance planning using multi-attribute utility theory. *Structure and infrastructure engineering*, 15(7):872–885, 2019.

[276] Zaharah Allah Bukhsh, Irina Stipanovic, and Andre G Doree. Multi-year maintenance planning framework using multi-attribute utility theory and genetic algorithms. *European Transport Research Review*, 12:1–13, 2020.

[277] Michael P Enright and Dan M Frangopol. Service-life prediction of deteriorating concrete bridges. *Journal of Structural engineering*, 124(3):309–317, 1998.

[278] Lijia Long, Michael Döhler, and Sebastian Thöns. Determination of structural and damage detection system influencing parameters on the value of information. *Structural Health Monitoring*, 21(1): 19–36, 2022.

[279] Min Liu, Jianjun Qin, Da-Gang Lu, Wei-Heng Zhang, and Michael Havbro Faber. On co2 efficiency and trade-off's between sustainability, resilience and safety in infrastructure development, 2023. Unpublished manuscript.

[280] Daniel Straub and Isabell Welpe. Decision-making under risk: A normative and behavioral perspective. In *Risk-A Multidisciplinary Introduction*, pages 63–93. Springer, 2014.

[281] Michael Havbro Faber. On the governance of global and catastrophic risks. *International Journal of Risk Assessment and Management*, 15(5-6):400–416, 2011.

[282] Marc A Maes and Michael H Faber. Epistemic uncertainties and system choice in decision making. In *Safety and reliability of engineering systems and structures: proceedings of the Ninth International Conference on Structural Safety and Reliability, ICOSSAR'05, Rome, Italy 19-23 June 2005*, pages 3519–3526. Millpress, 2005.

[283] Heinz Spiess. Conical volume-delay functions. *Transportation Science*, 24(2):153–158, 1990.

[284] Traffic Assignment Manual. Bureau of public roads, us dept. *Commerce, Urban Planning Division, Washington, DC, USA*, 1964.

[285] Fereshteh Jafari Shahdani, Mónica Santamaria-Ariza, Hélder S Sousa, Mário Coelho, and José C Matos. Assessing flood indirect impacts on road transport networks applying mesoscopic traffic modelling: the case study of santarém, portugal. *Applied Sciences*, 12(6):3076, 2022.